Investigating the Use of Energy Absorbing Connections (EAC) to Enhance the Performance of Mass Timber Structures Subjected to Blast Loading

by

Antoine Bérubé

Thesis submitted to the University of Ottawa

in partial fulfillment of the requirements for the degree of

Master of Applied Science

in Civil Engineering

Under the auspices of the Ottawa-Carleton Institute for Civil Engineering

uOttawa

Department of Civil Engineering

Faculty of Engineering

University of Ottawa

ABSTRACT

Wood structural elements are more vulnerable to blast loading due to the inherent brittle nature and low density of the material, as demonstrated by recent significant research efforts on the behaviour of timber elements subjected to the effect of blast loading. These studies showed that wood performs poorly under blast loading. A way of improving this performance is to provide additional ductility or energy absorption capabilities to wooden elements. Recently, there was interest in investigating and developing energy-absorbing connections (EAC) to improve timber assemblies' ductility and energy absorption capabilities. Although some research effort has been made to investigate the use of EACs to enhance the ductility of reinforced concrete or structural steel members, only limited work is available on this topic about timber elements. The current study aims to systematically investigate the use of various shapes of EACs to be used to enhance the post-peak performance of timber assemblies.

Preliminary finite element analysis led to selecting nine steel EACs with varying geometries for further experimental investigation. A total of eighteen specimens were tested statically. In comparison, a total of eighteen specimens were tested dynamically in the shock tube facility of the University of Ottawa to simulate the effects of far-field blast explosions. The experimental results showed that decreasing the leg length or increasing the thickness of EACs manufactured with steel angles and reducing the diameter of EACs manufactured with circular HSS caused an increase in yield load and elastic stiffness while reducing the densification displacement. Connections with angles and a centre weld, and connections with 90-degree arcs from circular HSS, were identified as unsuitable for the application of EACs. The experimental program also showed that EACs manufactured from angles offer a well-defined plateau able to absorb a large quantity of energy, making them particularly suitable for blast mitigation. EACs manufactured from multiple circular HSS were shown to achieve multiple load-displacement plateaus and present an interesting option for systems with multiple failure modes occurring at different levels. SDOF analysis and FEA were conducted to predict the experimental behaviour with some success. The importance of the weld type was also highlighted from both the analytical and experimental results. A methodology for developing idealized load-displacement curves from experimental results of EACs was also proposed and evaluated.

ACKNOWLEDGEMENTS

Although this project required a lot of motivation, work, and patience on my end, it would definitely not have been possible without the support and encouragement from many.

Firstly, I would like to thank my supervisor, Dr. Ghasan Doudak, for his support, guidance, patience, and financial support during this research project. I am extremely grateful for the many opportunities you have provided during this project. I look forward to pursuing a PhD under your supervision and to keep learning from your deep pool of knowledge and experience.

I would also like to thank my colleague and friend, Dr. Christian Viau, for teaching me the ropes and always being available for help, support, and guidance throughout the project, even when you were not involved directly. Notably, your help in the lab was extremely appreciated and made me avoid many headaches. I look forward to potential future collaborations with you.

To my other colleagues: Damian Oliveira, Laith Gharaibeh, Mohammad Masroor, Dalu Xing, and Andrew McGrath, thank you for the assistance and support prior to and throughout the project. Without all your help in and outside the lab, this project would not have been possible. Also, a special thank you to my colleagues at the NRC who contributed indirectly to this project by offering me many opportunities during my internship with them.

À mes amis: Patrick Lauzon, Bianca Martindale, Mathieu Lemaire-Paul, Jacob Mongenais, François Léveillé, et beaucoup d'autres, merci pour votre amitié, encouragement et support depuis bien des années. Ce projet n'aurait pas été possible sans vous! Merci beaucoup!

Enfin, et surtout, un très grand merci à mes parents, Denise et Marc, mon frère, Pascal, et au reste de ma famille, pour votre encouragement, support, aide et amour pendant ma maitrise et bien avant!

TABLE OF CONTENTS

ABSTRACT ii

ACKNOWLEDGEMENTS iii

LIST OF TABLES viii

LIST OF FIGURES ix

NOTATIONS xiv

CHAPTER 1 - Introduction 1

1.1 Introduction 1

1.2 Research Needs 2

1.3 Blast Loading 5

1.3.1 Blast Phenomena and Shock Waves 5

1.3.2 Scaling 7

1.4 Dynamic Analysis 8

1.4.1 General 8

1.4.2 Equivalent SDOF Analysis 10

1.4.3 Resistance Function 10

1.5 Research Objectives 11

1.6 Scope 12

1.7 Structure of Thesis 12

CHAPTER 2 - Literature Review 14

2.1 General 14

2.2 Wood 14

2.2.1 Wood as a Construction Material 14

2.2.2 Mechanical Properties of Wood 15

2.2.3 Engineered Wood Products 16

2.2.4 Ductility of Connections in Wood Systems 17
2.3 High Strain Rate Loading of Wood Elements 18
2.3.1 Wood Under Impact Loading 18
2.3.2 Light-Frame Wood Stud Walls Under Blast Loading 19
2.3.3 Glulam Beams and Columns Under Blast Loading 19
2.3.4 CLT Panels Under Blast Loading 20
2.3.5 High Strain Rate Loading of Wood Connections 20
2.3.6 Wood Connections Under Blast Loading 21
2.4 Energy Absorption 22
2.4.1 Cellular Materials 23
2.4.2 Tube Compressed by Two Flat Plates 25
2.4.3 Steel Under High Strain Rates 26
2.4.4 Energy Absorbing Connections (EACs) 27
2.5 Summary 37
CHAPTER 3 - Specimen Selection, Design and Manufacturing 39
3.1 General 39
3.2 Preliminary Finite Element Analysis 39
3.2.1 General 39
3.2.2 Methodology and Procedure 44
3.2.3 Scalability Verification 46
3.2.4 Summary of Preliminary Results 46
3.3 Specimen Selection 56
3.4 Specimen Design and Manufacturing 57
CHAPTER 4 - Experimental Program 61
4.1 General 61

4.2 Static Tests 61
4.3 Dynamic tests 62
4.3.1 General 62
4.3.2 Shock Tube Test Facility 62
4.3.3 Test Setup 65
4.4 Tensile Coupon Tests 68
CHAPTER 5 - Experimental Results 69
5.1 General 69
5.2 As-built Dimension and Mass Measurements 69
5.3 Static Test Results 70
5.3.1 Tensile Coupons Tests Results 70
5.3.2 Connection-level Test Results 71
5.4 Dynamic Test Results 83
5.4.1 Specimens D-Ia-1 and D-Ia-2 85
5.4.2 Specimens D-Ib-1 and D-Ib-2 86
5.4.3 Specimens D-Ic-1 and D-Ic-2 86
5.4.4 Specimens D-Id-1 and D-Id-2 87
5.4.5 Specimens D-IIa-1 and D-IIa-2 88
5.4.6 Specimens D-IIb-1 and D-IIb-2 90
5.4.7 Specimens D-IIc-1 and D-IIc-2 90
5.4.8 Specimens D-IId-1 and D-IId-2 91
5.4.9 Specimens D-IIe-1 and D-IIe-2 92
CHAPTER 6 - Analytical Modelling and Results 94
6.1 General 94
6.2 SDOF Analysis 94

6.2.1 SDOF Model Results and Comparison 96
6.3 Characterization of EAC Load-displacement Properties 99
6.3.1 Idealized and Experimental Load-displacement Parameters 99
6.3.2 Comparison of Idealized and Experimental Load-displacement Parameters and Behaviour 104
6.4 Revised FEA Model 107
6.4.1 Limitations of Preliminary FEA Model and Introduction of the Revised FEA Model 107
6.4.2 Mesh Sensitivity Analysis 109
6.4.3 Comparison of Revised FEA Model and Experimental Static Results 111
CHAPTER 7 - Discussion 115
7.1 General 115
7.2 Comparison between Static and Dynamic Tests Results 115
7.3 Effect of Geometry and Weld Type on EAC Load-displacement Behaviour 116
7.3.1 EACs Manufactured from Angles 116
7.3.2 Circular EACs 119
7.4 Application of EACs to Timber Assemblies and Design Considerations 123
7.4.1 Design Considerations 131
CHAPTER 8 - Conclusions 133
8.1 Recommendations for Future Work 134
References 135
APPENDIX A – Preliminary Finite Element Analysis Results 145
APPENDIX B – Drawings of Specimens 193
APPENDIX C – Static and Dynamic Connection Level Test Results 197
APPENDIX D – Analytical Results 252

LIST OF TABLES

Table 2.1: DIFs in CSA S850-12 (CSA 2012) 27
Table 3.1: Steel sections used in the analysis 41
Table 3.2: Mild steel material properties (Chapel Steel 2021; CSA 2021) 45
Table 3.3: Selected specimen type for experimental program 57
Table 3.4: Weld force capacity verification 58
Table 5.1: EAC specimen as-built dimensions 69
Table 5.2: Measured thicknesses of steel sections 69
Table 5.3: Measured mass of specimens 70
Table 5.4: Measured yield and ultimate strength 71
Table 5.5: Maximum reflected pressure and impulse 84
Table 6.1: Experimental and SDOF maximum displacement and time to maximum displacement 98
Table 6.2: Ratio of SDOF value to experimental value 99
Table 6.3: Idealized and experimental parameters for specimens tested statically 102
Table 6.4: Idealized and experimental parameters for specimens tested dynamically 103
Table 6.5: Ratio of idealized to experimental values 104
Table 6.6: Number of elements and nodes for varying global size 109
Table 7.1: Geometry percent change in relation to specimen type Ia and corresponding property percent change 117
Table 7.2: Property percent change due to addition of centre weld 119
Table 7.3: Geometry percent change in relation to specimen IIa and corresponding property percent change 121
Table 7.4: Manufacturer provided mechanical property for glulam 24f-ES (Nordic 2020) 125
Table 7.5: Summary of bending moment capacity calculation 125
Table 7.6: Summary of elastic stiffness calculation 126
Table 7.7: Unscaled and scaled properties for EAC specimens 128

LIST OF FIGURES

Figure 1.1: Damaged exposition building in Halifax, NS, after the 1917 explosion (George Grantham Bain Collection 2021) 1
Figure 1.2: Former Alfred P. Murrah federal building in Oklahoma City, after the 1995 bombing (Murphy 2020) 1
Figure 1.3: Example of an EAC 3
Figure 1.4: Glulam post and beam assembly with EACs 4
Figure 1.5: CLT wall and floor/diaphragm assembly with EACs (Viau and Doudak 2021b) 4
Figure 1.6: Blast source and propagation of shock wave (Dusenberry 2010) 5
Figure 1.7: Shock wave from a detonation (Dusenberry 2010) 5
Figure 1.8: Reflected pressure vs. side-on overpressure (Cormie et al. 2009) 6
Figure 1.9: Linear-elastic-plastic resistance function 11
Figure 2.1: Light frame construction (naturallywood.com 2021) 15
Figure 2.2: Mass timber structure – Wythe I Building (Nordic Structures 2021) 15
Figure 2.3: Load-displacement graphs of timber loaded parallel to grain (Dinwoodie 2017) 16
Figure 2.4: (a) OSB and (b) plywood (APA 2021) 16
Figure 2.5: (a) Glulam and (b) CLT (CWC 2021) 17
Figure 2.6: Load-displacement curve of (a) overdesigned 2×3 bolted connection and (b) more ductile 2×1 connection (Viau and Doudak 2021a) 22
Figure 2.7: Honeycomb with hexagonal cells, with in-plane properties relating to the x_2 and x_1 directions (Gibson and Ashby 1999) 23
Figure 2.8: In-plane compressive stress-strain curve of honeycombs with varying thickness over length ratios (Gibson and Ashby 1999) 24
Figure 2.9: Stress-strain graph (left) and energy absorption graph (right) of foams (Gibson and Ashby 1999) 25
Figure 2.10: (a) Undeformed tube, (b) DeRuntz and Hodge (1963) collapse mode, and (c) Burton and Craig collapse mode (1963) (Reid and Reddy 1978) 26
Figure 2.11: Typical load-deformation curves for tubes of zircaloy and mild steel (Reddy and Reid 1979) 26
Figure 2.12: Deformed and undeformed shapes of EAC (Whitney 1996) 28
Figure 2.13: Types of tested EAC in Oswald (2018) 29

Figure 2.14: EACs force vs deflection graphs (Oswald 2018) 30
Figure 2.15: States of loading and deformation for (a) members without EACs and (b) with EACs. 30
Figure 2.16: Force-deformation of a circular HSS 7”×0.25” and deformed shape (Lavarnway and Pollino 2015)..... 31
Figure 2.17: Front and section view of EAC specimen (Wang et al. 2019) 32
Figure 2.18: Load-displacement curve and energy absorption efficiency (Wang et al. 2019)..... 32
Figure 2.19: Deformation mechanisms of EACs without aluminium foam (Wang et al. 2017) .. 33
Figure 2.20: Deformation mechanisms of EACs with aluminium foam (Wang et al. 2017) 33
Figure 2.21: Force-displacement curves of (a) EACs without aluminium foam and (b) with aluminium foam where P represents angles and C represents circular HSS in the legend (Wang et al. 2017) 34
Figure 2.22: Nested oblong tube system (a) without dampers and (b) with dampers 35
Figure 2.23: Comparison of energy absorbed by a CLT angle connection (blue) and EAC connection (red) (Viau and Doudak 2021b) 36
Figure 2.24: Failure sequence of an EAC assembly based on probabilistic principles (Viau and Doudak 2021b)..... 36
Figure 2.25: Idealized load-displacement graph of an EAC..... 37
Figure 3.1: Typical EAC cross-sections representing half the shapes, and used for preliminary analysis..... 44
Figure 3.2: Boundary conditions of preliminary FEA model..... 45
Figure 3.3: Scalability verification 46
Figure 3.4: FEA results for angles 47
Figure 3.5: FEA results for welded angles..... 48
Figure 3.6: FEA results for angles with central plate 48
Figure 3.7: Comparison of angle geometry effects on results 49
Figure 3.8: FEA results for circular HSS..... 50
Figure 3.9: FEA results for circular HSS arcs 51
Figure 3.10: FEA results for 2 circular HSS..... 52
Figure 3.11: FEA results for 3 circular HSS..... 52
Figure 3.12: Comparison of results for multiple circular HSS 53

Figure 3.13: FEA results for angles plus circular HSS 54
Figure 3.14: Effect of thickness variation 54
Figure 3.15: Comparison with constituting parts 55
Figure 3.16: Fillet weld cross-section (CSA W59-13) 58
Figure 3.17: Welding jig 59
Figure 3.18: Welding jig for angle EAC 60
Figure 3.19: Welding jig for circular HSS EAC 60
Figure 4.1: Static test setup with specimen S-Ia-1 62
Figure 4.2: Shock tube (Lacroix 2013) 64
Figure 4.3: Shock tube internal view and end frame 64
Figure 4.4: Dynamic test setup 66
Figure 4.5: Specimen in test set up 67
Figure 4.6: Shock tube test setup sketch 67
Figure 4.7: Tensile coupon test setup 68
Figure 5.1: Static measured load-displacement curve for specimens S-Ia-1 and S-Ia-2 72
Figure 5.2: Initial and deformed shape of specimens S-Ia-1 and S-Ia-2 72
Figure 5.3: Static measured load-displacement curve for specimens S-Ib-1 and S-Ib-2 73
Figure 5.4: Initial and deformed shape of specimens S-Ib-1 and S-Ib-2 74
Figure 5.5: Static measured load-displacement curve for specimens S-Ic-1 and S-Ic-2 74
Figure 5.6: Initial and deformed shape of specimens S-Ic-1 and S-Ic-2 75
Figure 5.7: Static measured load-displacement curve for specimens S-Id-1 and S-Id-2 75
Figure 5.8: Initial and deformed shape of specimens S-Id-1 and S-Id-2 76
Figure 5.9: Static measured load-displacement curve for specimens S-IIa-1 and S-IIa-2 77
Figure 5.10: Initial and deformed shape of specimens S-IIa-1 and S-IIa-2 77
Figure 5.11: Static measured load-displacement curve for specimens S-IIb-1 and S-IIb-2 78
Figure 5.12: Initial and deformed shape of specimens S-IIb-1 and S-IIb-2 79
Figure 5.13: Static measured load-displacement curve for specimens S-IIc-1 and S-IIc-2 79
Figure 5.14: Initial and deformed shape of specimens S-IIc-1 and S-IIc-2 80
Figure 5.15: Static measured load-displacement curve for specimens S-IId-1 and S-IId-2 81
Figure 5.16: Initial and deformed shape of specimens S-IId-1 and S-IId-2 81
Figure 5.17: Static measured load-displacement curve for specimens S-IIe-1 and S-IIe-2 82

Figure 5.18: Initial and deformed shape of specimens S-IIe-1 and S-IIe-2 83
Figure 5.19: Typical pressure and impulse time-history 84
Figure 5.20: Typical time-history for reaction load and displacement 85
Figure 5.21: Dynamic measured load-displacement curve for specimens D-Ia-1 and D-Ia-2 85
Figure 5.22: Dynamic measured load-displacement curve for specimens D-Ib-1 and D-Ib-2 86
Figure 5.23: Dynamic measured load-displacement curve for specimens D-Ic-1 and D-Ic-2 87
Figure 5.24: Dynamic measured load-displacement curve for specimens D-Id-1 and D-Id-2 88
Figure 5.25: Dynamic measured load-displacement curve for specimens D-IIa-1 and D-IIa-2 ... 89
Figure 5.26: Initial and deformed shape of specimens D-IIa-1 and D-IIa-2 89
Figure 5.27: Dynamic measured load-displacement curve for specimens D-IIb-1 and D-IIb-2 .. 90
Figure 5.28: Dynamic measured load-displacement curve for specimens D-IIc-1 and D-IIc-2 ... 91
Figure 5.29: Dynamic measured load-displacement curve for specimens D-IId-1 and D-IId-2 .. 92
Figure 5.30: Dynamic measured load-displacement curve for specimens D-IIe-1 and D-IIe-2 ... 93
Figure 6.1: Pressure and impulse time histories for specimen D-Ia-1 95
Figure 6.2: Dynamic load-displacement curve of specimen D-Ia-1 96
Figure 6.3: Displacement time-histories for specimen D-Ia-1 97
Figure 6.4: Idealized load-displacement curve 100
Figure 6.5: Determination of displacement at the onset of densification 101
Figure 6.6: Experimental Static and Idealized Load-displacement Curve for Specimen S-Ia-1 105
Figure 6.7: Experimental Static and Idealized Load-displacement Curve for Specimen S-IIa-1 106
Figure 6.8: Experimental Static and Idealized Load-displacement Curve for Specimen S-Id-1 107
Figure 6.9: Revised FEA mesh for specimen Ia 108
Figure 6.10: Revised FEA mesh for specimen IIa with weld type 1 108
Figure 6.11: Revised FEA mesh for specimen IIa with weld type 2 108
Figure 6.12: Boundary conditions of revised FEA model 109
Figure 6.13: Global size and resulting number of elements and nodes 110
Figure 6.14: Revised FEA model mesh for a global size of 4 (left) and 2 (right), respectively. 110
Figure 6.15: Mesh sensitivity analysis of load-displacement FEA model results 111
Figure 6.16: Revised FEA model – Id 112
Figure 6.17: Revised FEA model – IIa 112
Figure 6.18: Revised FEA model – IIb 113

Figure 6.19: Revised FEA model – IId 113
Figure 6.20: Deflected shape for specimen type IIa with weld type 1 114
Figure 6.21: Deflected shape for specimen type IIa with weld type 2 114
Figure 7.1: Static and dynamic load-displacement curves for specimen type Ia 115
Figure 7.2: Comparison of the static load-displacement results for specimen types Ia, Ib, and Ic 116
Figure 7.3: Specimen type Ia (left) and Id (right) 118
Figure 7.4: Comparison of the static load-displacement results for specimen types Ia and Id... 118
Figure 7.5: Comparison of static (Weld Type 1) and dynamic (Weld Type 2) load-displacement results for specimen type IIa 120
Figure 7.6: Comparison of the static load-displacement results for specimen types IIa, IIb, and IIc 121
Figure 7.7: Comparison of the static load-displacement results for specimen type IIa and IId . 122
Figure 7.8: Comparison of the static load-displacement results for specimen types IIa and IIe 123
Figure 7.9: Conceptual Scenario 124
Figure 7.10: Glulam member and EAC resistance curves 127
Figure 7.11: System displacement time-histories 130
Figure 7.12: Individual DOF displacement time-histories for system with specimen IIc 130
Figure 7.13: Displacement time-histories for EAC-to-wood stiffness ratio of 0.5, 1.0, and 2.0 131

NOTATIONS

Acronym	Definition
EAC	Energy Absorbing Connection
CLT	Cross-Laminated Timber
HSS	Hollow Steel Section
FEA	Finite Element Analysis
DIF	Dynamic Increase Factor
SIF	Strength Increase Factor
CSA	Canadian Standards Association
ASTM	American Society for Testing and Materials
SDOF	Single Degree of Freedom
TDOF	Two Degree of Freedom
LTD	Load-Transfer Device
LVDT	Linear Variable Differential Transducers
UTM	Universal Testing Machine
CoV	Coefficient of Variation

Symbol	Definition
P_o	Ambient Pressure
P_{so}	Peak positive side-on overpressure
$P_s(t)$	Time varying positive overpressure
P_r	Peak reflected overpressure
i_s	Positive-phase-specific impulse
t_A	Time of arrival
t_o	Positive phase duration
P_{so}^-	Peak negative side-on overpressure
$P_s^-(t)$	Time varying negative overpressure
i_s^-	Negative-phase-specific impulse
t_o^-	Negative phase duration
t_d	Idealized positive phase duration
b	Waveform parameter
$P_r(t)$	Time varying reflected pressure
I^+	Positive impulse
I^-	Negative impulse
R	Standoff Distance
W_{TNT}	Charge weight equivalent to TNT
Z	Scaled distance
A	Tributary area
$F(t)$	Forcing function
F_1	Maximum force
m	Mass
c	Damping coefficient
k	Stiffness
ω_n	Natural frequency
t	Time
y	Displacement
$\dot{y}$	Velocity
$\ddot{y}$	Acceleration
DLF	Dynamic load factor
y_{st}	Static displacement
K_M	Mass transformation factor
K_L	Load (Force) transformation factor
K_R	Resistance transformation factor

K_{LM}	Load-mass transformation factor
$\bar{m}(x)$	Distributed mass per unit length
$\varphi(x)$	Shape function
L	Length
$f(x,t)$	Distributed forcing function per unit length
$R(y)$	Resistance function
R_e	Yield resistance
F_y	Yield force
P_y	Yield load
f_y	Yield Strength or Stress
Δ_y	Yield displacement
k_e	Elastic stiffness
L_a	Angle leg length
t_a	Angle thickness
w	EAC width
L_p	Plate length
$\varnothing$	Circular HSS outer diameter
t_c	Circular HSS thickness
θ	Arc angle
t_p	Plate thickness
H	EAC height
$\mathbb{Q}$	Centerline
f_d	Dynamic stress
f_s	Static stress
$\dot{\varepsilon}_p$	Plastic strain rate
η	Energy absorption efficiency
W	Work or energy absorbed
F	Force
P	Load
σ	Stress
Δ	Displacement or deformation
ε	Strain
α_y	Overstrength factor
Z_{95th}	Standard score for the 95th percentile
Z_{5th}	Standard score for the 5th percentile

$CoV_{F_{y,wood}}$	Coefficient of variation for the wood member ultimate failure load
$CoV_{F_{u,conn}}$	Coefficient of variation for the EAC yielding load
DIF	Dynamic Increase Factor
V_{base}	Base metal shear force capacity
S_1,S_2	Effective sizes of leg of fillet
ℓ	Length of weld
F_{y1}, F_{y2}	Base metal yield strength
V_{weld}	Weld shear force capacity
t_w	Effective throat of the weld
X_u	Ultimate tensile strength
Δ_D	Displacement at onset of densification
W_m	Maximum energy absorbed prior to densification
K_D	Densification stiffness

CHAPTER 1 - Introduction

1.1 Introduction

Past intentional or accidental explosions have highlighted the devastating effects that blast loads can cause on infrastructure. Some examples of accidental explosions include the 1917 Halifax explosion (Kernaghan and Foot 2017), the 1968 Ronan point apartment tower collapse (Pearson and Delatte 2005), the 2005 BP Texas City disaster (CSB 2007), the 2014 Lac-Mégantic rail disaster (TSB 2014) and the 2020 Beirut explosion (WHO 2020). Examples of explosions caused by intentional attacks include the 1995 Oklahoma City bombing (Corley et al. 1998) and the 2001 World Trade Center Towers collapse (NIST 2005). Figure 1.1 and Figure 1.2 show the potential damage following an explosion.

Figure 1.1: Damaged exposition building in Halifax, NS, after the 1917 explosion (George Grantham Bain Collection 2021)

Figure 1.2: Former Alfred P. Murrah federal building in Oklahoma City, after the 1995 bombing (Murphy 2020)

Other catastrophes, such as earthquakes, tsunamis, and high winds and their impact on buildings and other infrastructures seem to be well understood and documented in various codes and standards. Loading and design provisions from such events are readily available to designers based on years of research and practice. For example, research on earthquake and wind loads began in the early 20th century with substantial work worldwide since then. Research on the behaviour of structural elements to the effects of explosions has recently gained increased interest, notably due to recent events and heightened awareness of the need for security, not only of targeted infrastructure but also its surroundings. Presently, it is recognized that heightened risks to infrastructure and human life exists, and considerable research has been underway to address this issue and mitigate against such risk.

Design provisions in Canada do not directly require blast loads to be considered in the design of buildings (NRC 2018). It is therefore left to the discretion of the building owner or local authorities whether to consider blast load in the design of structural members and introduce other measures to mitigate risks. To assist with such design, various codes standards, guidelines and provisions have been developed (CSA 2012; DHS 2011; Office of the Deputy Prime Minister 2004; USACE 2008; USADD 2008, 2009). The need for research work to assist in further developing design provisions, especially for wood structures, is discussed next.

1.2 Research Needs

A substantial part of the overall literature available on blast effects focuses on reinforced concrete structural elements (Burrell 2012; Jacques et al. 2013; Jacques and Saatcioglu 2020; Li and Aoude 2020; Mays et al. 1999; Pantelides et al. 2014; Silva and Lu 2009; Williams and Williamson 2011; Yu et al. 2014, 2018) and structural steel elements (Cannon and Clubley 2021; Krishnappa et al. 2014; Nassr et al. 2014; Shabanlou et al. 2021; Soroushian and Choi 1987; Tetougueni et al. 2020; Warn and Bruneau 2009).

Wood structural elements are more vulnerable to blast loading due to the inherent brittle nature and low density of the material. Recent technologies have led to a larger inventory of available engineered wood products and recent environmental concerns have led to an increase in the number of wooden buildings being built. This development has been accompanied by significant research effort, especially at the University of Ottawa, which has led to significant improvement in understanding the behaviour of timber elements subjected to the effect of blast loading (Côté and Doudak 2019; Lacroix and Doudak 2020, 2018a; McGrath and Doudak 2021; Poulin et al. 2018; Viau and Doudak 2019, 2021b; c). Further work has focussed on improving the performance of timber buildings exposed to blast by investigating the possible use of fibre-reinforced polymers (FRP) (Lacroix and Doudak 2020) to enhance the post-peak performance of the structural elements itself, as well as enhancing the performance of timber assemblies with realistic boundary connections using commercially available fasteners (McGrath and Doudak 2021; Viau and Doudak 2019, 2021b; c) or joints specifically designed to dissipate energy (McGrath and Doudak 2021; Viau and Doudak 2019, 2021b; c). The latter is of particular interest to the current study and forms the basis of the research investigation.

A way of improving this performance is to provide additional ductility or energy absorption capabilities to wooden elements. There was recently interest in investigating and developing energy-absorbing connections (EAC) to improve timber assemblies' ductility and energy absorption capabilities (Viau and Doudak 2021b). An example of the principle of an EAC is illustrated in Figure 1.3. Although some research effort has been made to investigate the use of EACs to enhance the ductility of reinforced concrete or structural steel members (Lavarnway and Pollino 2015; Oswald 2018; Whitney 1996), only limited work is available on this topic pertaining to timber elements (Viau and Doudak 2021b). The current study aims to systematically investigate the use of various shapes of EACs to be used to enhance the post-peak performance of timber assemblies.

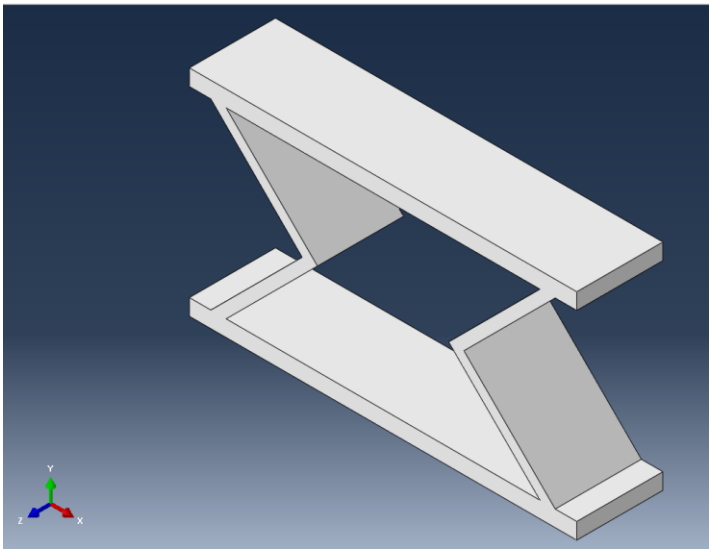

Figure 1.3: Example of an EAC

EACs are sacrificial elements designed to yield prior to the main member's ultimate failure while being able to undergo large inelastic deformations. If these conditions are met, EACs have the potential to significantly increase the ductility of the assembly and provide additional energy absorption. A typical timber assembly could have EACs implemented between the cladding or façade and the structural system or between two or more main structural components. Bolts, screws, dowels, or other fasteners would typically be used to connect the EACs to the main structural components. Figure 1.4 and Figure 1.5 show an illustration of how EACs could be used to connect a glulam column to a beam and a CLT wall to a floor, respectively.

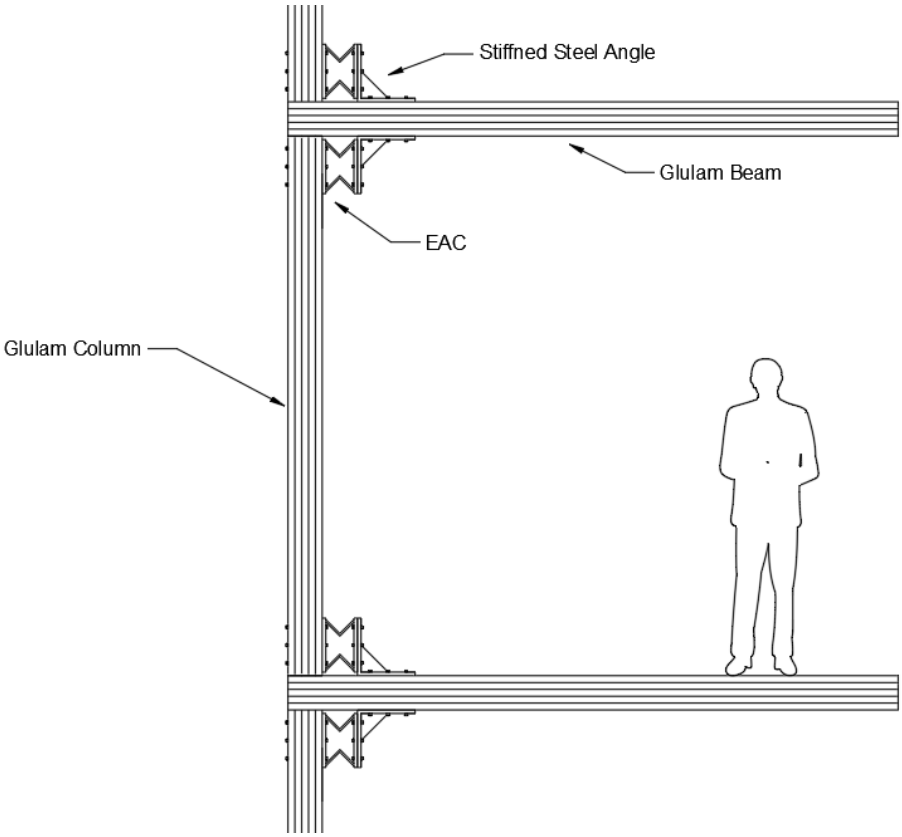

Figure 1.4: Glulam post and beam assembly with EACs

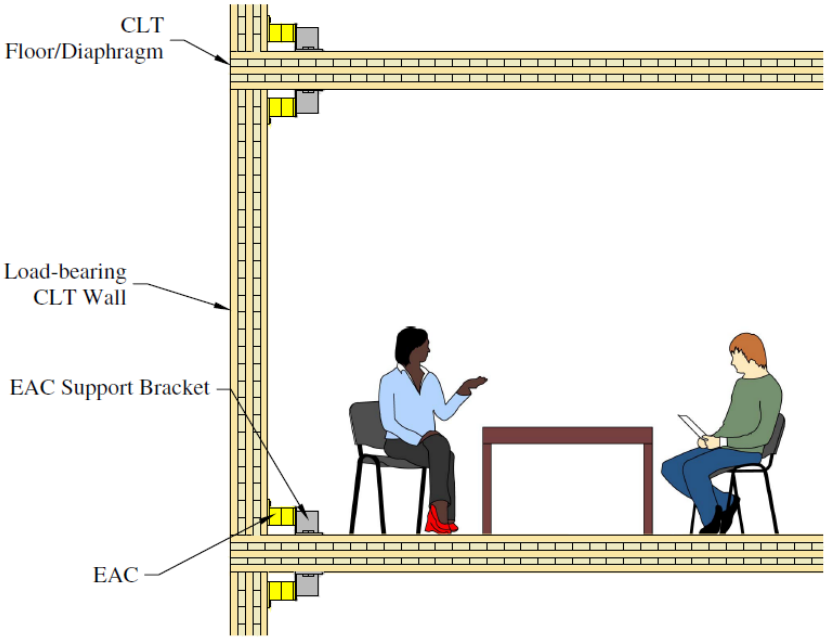

Figure 1.5: CLT wall and floor/diaphragm assembly with EACs (Viau and Doudak 2021b)

1.3 Blast Loading

1.3.1 Blast Phenomena and Shock Waves

Blast loads are generated by a rapid release of energy resulting in a shock wave propagating away from the source (Figure 1.6). Blast can be generated from high explosives, propellants, gases, etc. The shock waves generated cause an almost immediate increase in pressure, referred to as overpressure, above the atmospheric ambient pressure (i.e. ~101.3 kPa at sea level), which then diminishes with time (Figure 1.7). Blast loads can be approximated with empirical methods or more complex computational fluid dynamics software (Dusenberry 2010).

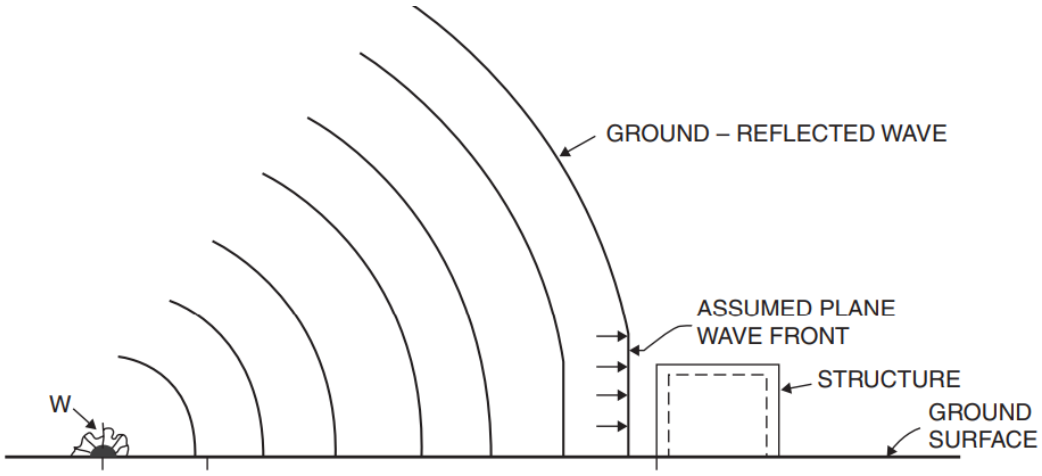

Figure 1.6: Blast source and propagation of shock wave (Dusenberry 2010)

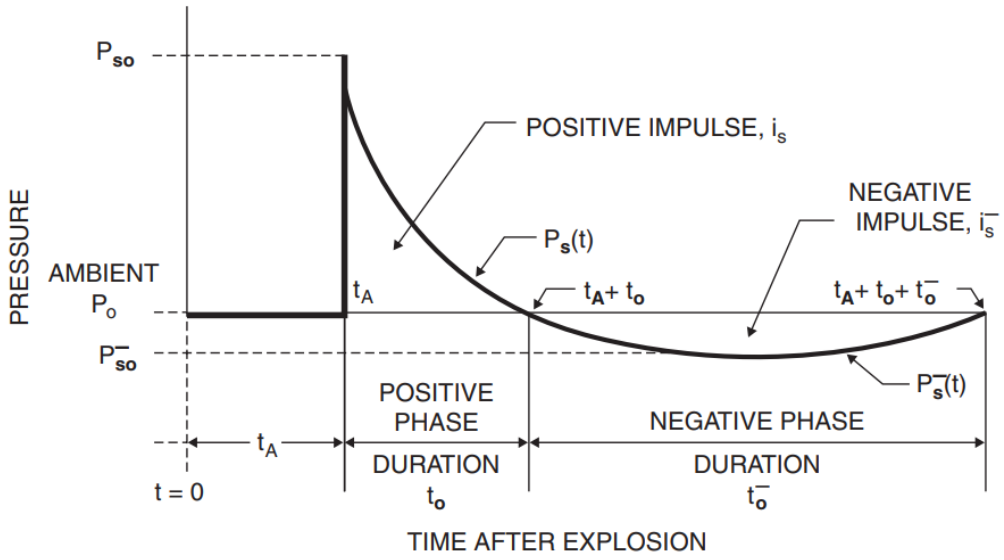

Figure 1.7: Shock wave from a detonation (Dusenberry 2010)

Shock waves, generated from detonations, travel at supersonic speeds through the air and generate high pressures. Lower pressure waves, generated by deflagrations, travel at subsonic speeds and have a lower potential of causing damage or harm. As the shock wave travels away from its origin, the overpressure diminishes but its duration increases. Once shockwaves hit a structure, a positive overpressure phase is first experienced. As time goes on, the pressure is further diminished to the point of reaching a negative pressure phase (Figure 1.7). Typically, only the positive phase is considered in design due to the greater loads experienced during this phase (Dusenberry 2010).

When the pressure wave interacts with a structure, it will reflect off the surface of the structure, generated what is termed reflected pressure. The reflected pressure is generally larger than the side-on overpressure (Figure 1.8). The angle of incidence at which the shock wave hits the building can reduce the pressure on the structure. Due to the complexity of the pressure profile on a building, several simplifications are usually assumed in the analysis (Cormie et al. 2009; Dusenberry 2010).

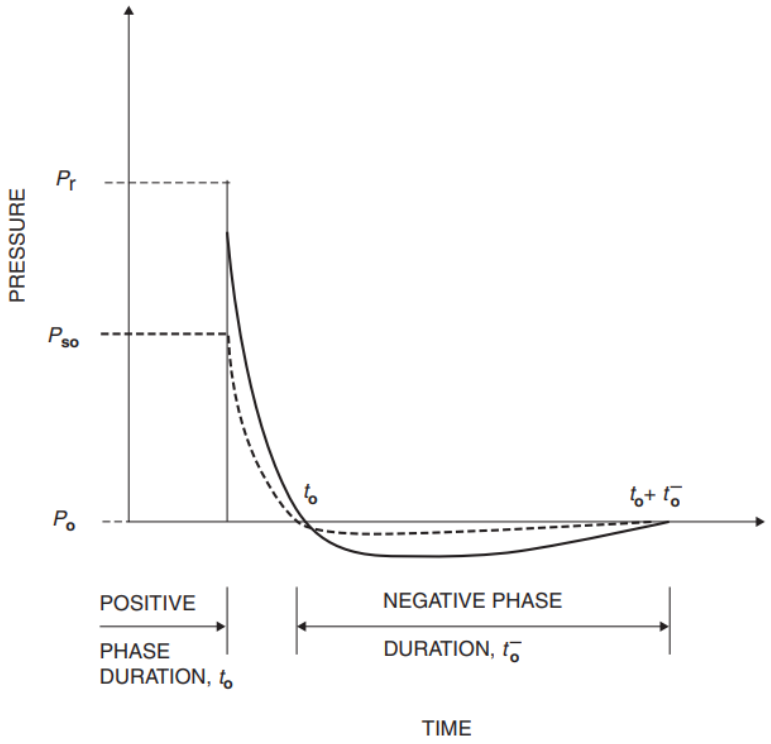

Figure 1.8: Reflected pressure vs. side-on overpressure (Cormie et al. 2009)

The time-varying reflected pressure, shown in Figure 1.8, can be approximated by expressions such as the Friedlander exponential expression, presented in Equation 1.1 with idealized parameters (Cormie et al. 2009). Additionally, the positive and negative impulses caused by the time-varying function can be determined by integration, as demonstrated in Equation 1.2 and Equation 1.3, respectively. Numerically, this can be done by summing the area under the pressure-time history.

$$P_r(t) = P_r\left(1 - \frac{t}{t_d}\right)e^{-b\left(\frac{t}{t_d}\right)} \qquad \text{Equation 1.1}$$

$$I^+ = \int_{t_A}^{t_A+t_o} P_r(t)dt \qquad \text{Equation 1.2}$$

$$I^- = \int_{t_A+t_o}^{t_A+t_o+t_o^-} P_r(t)dt \qquad \text{Equation 1.3}$$

Where P_r is the peak reflected pressure, t is time, t_d is the idealized positive phase duration, and b is the waveform parameter.

1.3.2 Scaling

To simplify the determination of pressure-time history parameters presented in the previous section, scaling laws are used for explosives. Scaling laws allows for data from one explosive (typically TNT due to a large inventory of experimental results) to be scaled and used for other explosives.

Charges set off closer to the structure or with larger TNT weight will cause a shock wave with larger pressures on the structure. Thus, the standoff distance (R) and the equivalent TNT charge weight (W_{TNT}) are used to define the scaled distance. Cubic root scaling is typically used for this purpose, where the inverse cubic root of the explosion energy (TNT weight) is used to scale the standoff distance, as shown in Equation 1.4 (Dusenberry 2010; Krauthammer 2008).

$$Z = \frac{R}{\sqrt[3]{W_{TNT}}} \qquad \text{Equation 1.4}$$

Where Z is the scaled distance, R is the standoff distance and, W_{TNT} is the equivalent TNT weight.

Once the pressure-time history parameters have been determined, an equivalent triangular loading, or forcing function, is typically used in analysis and design. The forcing function is shown in

Equation 1.5. Additionally, the peak initial force can be approximated from the peak reflected pressure and the area on which this peak reflected pressure is being transferred (Equation 1.6) (Dusenberry 2010).

$$F(t) = F_1\left(1 - \frac{t}{t_d}\right) \quad \text{Equation 1.5}$$

$$F_1 = AP_r \quad \text{Equation 1.6}$$

Where A is the tributary area and P_r is the peak reflected pressure.

1.4 Dynamic Analysis

1.4.1 General

Blast loads are typically of short duration, especially when compared to other loads such as earthquake and wind loads. This short duration causes inertial forces and kinetic energy to be a substantial portion of the behaviour. For this reason, dynamic analysis is used to establish the performance of structural elements subjected to blast loads. Often, single-degree-of-freedom (SDOF) analysis is adequate to simulate blast behaviour of structural elements considered in isolation, and where loading, boundary conditions, and failure mode are well defined. This observation has been supported by several studies confirming that SDOF method is adequate in predicting the response of structural elements subjected to blast (Burrell 2012; Jacques 2011; Lacroix 2017; Viau 2020). For assemblies, where multiple failure modes are possible, more sophisticated modelling techniques, such as multi-degree-of-freedom (MDOF) analysis, may be required to capture the overall system behaviour. More advanced modelling techniques, such as finite element analysis (FEA), are typically less often employed in blast analysis due to the increased uncertainty associated with both loading and material properties (Biggs 1964).

Dynamic analysis for single-degree-of-freedom systems involves solving the differential equation of motion of a forced vibration system composed of mass, stiffness, and damping components, as presented in Equation 1.7 (Biggs 1964; Chopra 2017).

$$m\ddot{y} + c\dot{y} + ky = F(t) \quad \text{Equation 1.7}$$

Where m is the system mass, c is the damping coefficient, k is the stiffness, and F(t) is the external forcing function. $\ddot{y}$, $\dot{y}$, and y are the acceleration, velocity, and displacement of the system for each time step, respectively.

Since blast is of short duration, damping is not generated in time to significantly impact the overall response. Also, only maximum response is required for most applications. For both of these reasons, damping is typically neglected (Biggs 1964; Jansson 1992). This assumption simplifies the equation of motion to that presented in Equation 1.8.

$$m\ddot{y} + ky = F(t) \qquad \text{Equation 1.8}$$

The solution of the equation of motion (Eq. Equation 1.8) can be solved for a forcing function idealized as triangular, as shown in Equation 1.9. Following the end of the forcing function, the solution becomes that shown in Equation 1.10. This solution is only valid for a SDOF system where the mass, stiffness and forcing function are all applied at a single point and where forces act in the same direction.

$$y(t) = \frac{F_1}{k}\left(\frac{\sin(\omega_n t)}{\omega_n t_d} - \cos(\omega_n t) - \frac{t}{t_d} + 1\right) \qquad \text{Equation 1.9}$$

$$y(t) = \frac{F_1}{k}\left(\frac{\sin(\omega_n t) - \sin(\omega_n (t - t_d))}{t_d} - \cos(\omega_n t)\right) \qquad \text{Equation 1.10}$$

Where F_1 is the maximum force at the arrival of the shock wave front, k is the stiffness, t_d is the idealized positive phase duration of the triangular forcing function and, ω_n is the natural frequency as shown in Equation 1.11.

$$\omega_n = \sqrt{\frac{k}{m}} \qquad \text{Equation 1.11}$$

For more complex forcing functions, numerical methods such as Duhamel integral may be required. Solutions for other simple forcing functions, including damping, can be found in the literature (Biggs 1964; Chopra 2017).

The dynamic displacement from Equation 1.9 and Equation 1.10 can also be used to determine the dynamic load factor (DLF), representing the ratio between dynamic and static displacements, as shown in Equation 1.12.

$$DLF(t) = \frac{y(t)}{y_{st}} \qquad \text{Equation 1.12}$$

1.4.2 Equivalent SDOF Analysis

Mass, stiffness and forces are in reality distributed (e.g. along the length of a beam) and not concentrated at a single point. However, in order to provide analysis containing mathematical simplicity, the distributed mass, stiffness, and forces are lumped into a single point. This is done by introducing transformation factors for mass (K_M), stiffness (K_R) and forces (K_L) to convert the distributed system into a lumped system. Additionally, the stiffness portion of the equation of motion is replaced by a resistance function that can accommodate different material behaviours and loss of stiffness following yielding, for instance, linear-elastic-plastic behaviour (Biggs 1964). The equivalent equation of motion can be seen in Equation 1.13.

$$K_M(m\ddot{y}) + K_R R(y) = K_L F(t) \qquad \text{Equation 1.13}$$

The mass and load transformation factors can be determined using Equation 1.14 and Equation 1.15, respectively. K_R and K_L have the same value since they both represent similar force distributions. Since K_M represents the inertia force, which is more dynamic in nature, it has a different value (Biggs 1964).

$$K_M = \frac{\int_0^L [\bar{m}(x)\varphi^2(x)]dx}{\int_0^L [\bar{m}(x)]dx} \qquad \text{Equation 1.14}$$

$$K_L = \frac{\int_0^L [f(x,t)\varphi(x)]dx}{\int_0^L [f(x,t)]dx} \qquad \text{Equation 1.15}$$

Where $\bar{m}(x)$ is the distributed mass, $f(x,t)$ is the distributed forcing function, $\varphi(x)$ is the assumed shape function and, L is the length of the element with distributed force, stiffness, and mass.

The equation of motion can be further simplified to that shown in Equation 1.16 by presenting a single transformation factor, K_{LM}, as defined in Equation 1.17 (Biggs 1964).

$$K_{LM}(m\ddot{y}) + R(y) = F(t) \qquad \text{Equation 1.16}$$

$$K_{LM} = \frac{K_M}{K_L} \qquad \text{Equation 1.17}$$

1.4.3 Resistance Function

The resistance function represents the resistance of the structural member as a function of the displacement it undergoes. This function can be either linear or nonlinear. The resistance function is closely related to the stress-strain relationship of the material that makes up the element. For

systems characterized by a linear-elastic-plastic behaviour, the resistance function is a simple bilinear relationship, such as shown in Figure 1.9 (Biggs 1964).

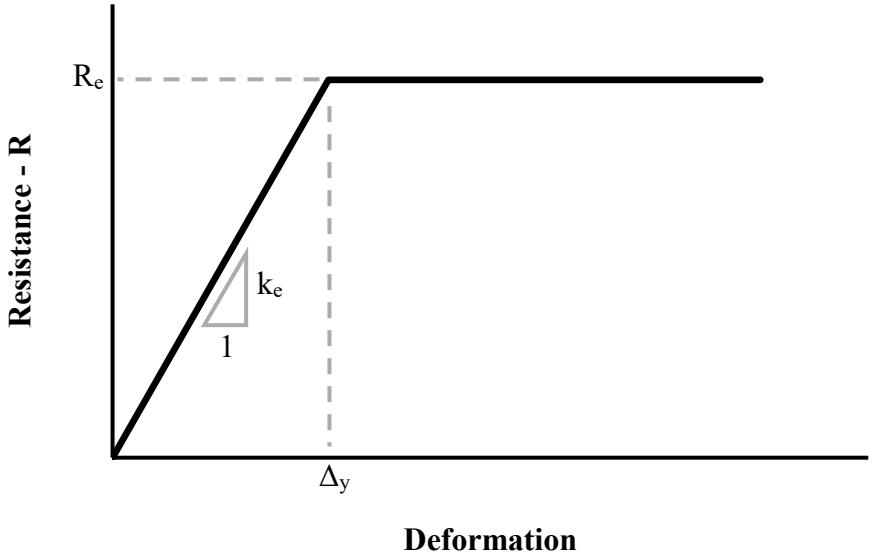

Figure 1.9: Linear-elastic-plastic resistance function

Where R_e is the yield resistance (i.e. F_y), Δ_y is the yield deformation, and k_e is the elastic stiffness.

1.5 Research Objectives

This research project aims to enhance the energy dissipation and overall performance of timber structural elements by investigating and developing energy-absorbing connections (EAC's). Specific objectives include:

I. Developing easy to manufacture steel joints that have the ability to deform inelastically and absorb energy;
II. Conducting static and dynamic testing of the developed joints in order to establish load-deformation relationships and dynamic properties that can be used as input in the analysis of timber assemblies containing such joints;
III. Developing analysis procedures to predict the behaviour of the joints in isolation and as part of structural systems.
IV. Investigation various types of joints capable of improving the blast performance of structural timber elements and recommending optimized section shapes

1.6 Scope

The research objectives are achieved through the following approach:

i. Carry a literature review on the behaviour of wood systems, steel connections and, EAC's under blast or impact loads;
ii. Model sample EAC's of different shapes in FEA software to select the most favourable ones for further investigation.
iii. Investigate the requirements related to welding for the EAC's manufacturing.
iv. Manufacture selected EAC's for testing.
v. Conduct static tests on manufactured EAC specimens to establish their static properties.
vi. Conduct dynamic tests on manufactured EAC specimens to establish their dynamic properties;
vii. Analyze experimental results of static and dynamic tests to determine the appropriate load-displacement relationships to be used in the analysis;
viii. Conduct tensile tests on steel coupons from the same material used to manufacture the EACs in order to characterize their material behaviour;
ix. Model the EAC's using FEA to obtain refined load-displacement relationships using the improved information from experimental testing on steel coupons;
x. Compare experimental load-displacement relationships with those from models, and;
xi. Discuss the results and potential code implementation.

1.7 Structure of Thesis

Chapter 1 introduces relevant background material on blast, presents research needs, objectives and scope of work.

Chapter 2 presents a literature review on relevant current knowledge, including subjects such as blast and dynamic behaviour of steel connections, wood systems and EAC's.

Chapter 3 presents specimen selection through initial finite element analysis, specimen design and manufacturing details.

Chapter 4 presents the experimental program, including test setup and methodology.

Chapter 5 presents the results obtained from the experimental program, including static, dynamic and tensile coupon testing.

Chapter 6 presents the analytical modelling methodology and results.

Chapter 7 compares and discusses the experimental and analytical results.

Chapter 9 summarizes the research findings and proposes potential future work and research topics.

Appendix A presents the preliminary finite element analysis results introduced in Chapter 3.

Appendix B presents drawings of the selected specimens for experimental testing.

Appendix C presents the experimental results introduced in Chapter 5.

Appendix D presents the analytical results introduced in Chapter 6.

CHAPTER 2 - Literature Review

2.1 General

This Chapter presents the background information and overview of the literature for three topics of importance to this project. Section 2.2 will present the background information on wood as a construction material, mechanical properties of wood, engineered wood products, and recent research in the ductility of connections in wood systems. Section 2.3 will present the recent research related to the performance of wood components under high strain rate loading such as impact and blast. Section 2.3 will present background information in energy absorption and cellular materials and will present the recent research in steel under high strain rate and energy-absorbing connections (EACs).

2.2 Wood

2.2.1 Wood as a Construction Material

Wood has been used as a construction material since prehistoric times. Since then, a significant evolution in the understanding of the material has been achieved. As a result, modern wooden (timber) construction is now based on engineering and scientific principles. Modern wooden construction generally falls into two categories: light-frame construction (Figure 2.1) and heavy timber or mass timber construction (Figure 2.2). Light frame construction is common in North America, especially for single-family dwellings and low-to-mid rise residential and commercial buildings. It consists of dimensional sawn lumber (i.e. 2×4, 2×6, etc.) framed with structural or non-structural sheathing panels (i.e. Oriented Strand Board (OSB), Plywood, Gypsum, etc.) connected with metal fasteners (commonly nails or screws). Heavy timber and mass timber construction have recently regained interest due to environmental and architectural reasons. This construction consists of larger size sawn timber members, glue-laminated (Glulam) members, cross-laminated timber (CLT) panels, and other Engineered Wood Products (EWPs) framed in different configurations (Green and Taggart 2017; Thelandersson and Larsen 2003).

Figure 2.1: Light frame construction (naturallywood.com 2021)

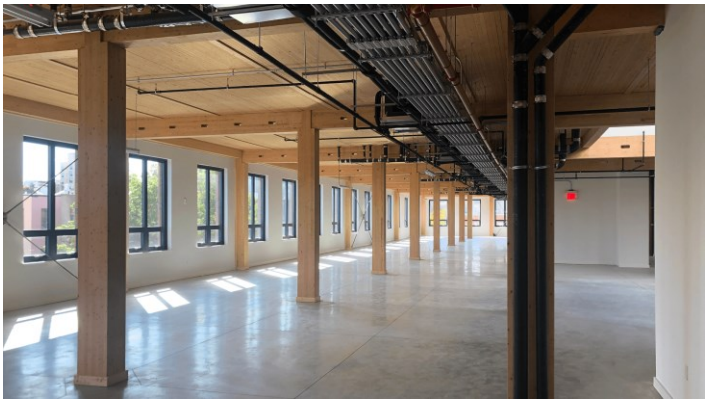

Figure 2.2: Mass timber structure – Wythe I Building (Nordic Structures 2021)

2.2.2 Mechanical Properties of Wood

Wood is an anisotropic (i.e. properties depend upon direction) and non-homogenous material produced by biological processes during the growth of trees. The wood structure comprises fibres optimized to have maximum strength in stressed directions, referred to as the grain orientations. However, since wood is a natural material, no two pieces of lumber are identical and have the same properties. To create some uniformity in the mechanical properties, wood is graded visually or mechanically according to standards.

Typically, wood is stronger and stiffer when loaded parallel to the grain than perpendicular to the grain and is stronger in tension than in compression (Figure 2.3). Other factors such as loading duration, species and climate exposure can also affect mechanical properties. Wood strength is also highly dependent on the rate of loading and duration of loading. In typical engineering design, a load duration factor is applied to account for these effects. For long-term durations, a strength reduction is applied, while for shorter load durations, an increase in the apparent strength has been observed (Dinwoodie 2017; Green and Taggart 2017; Thelandersson and Larsen 2003).

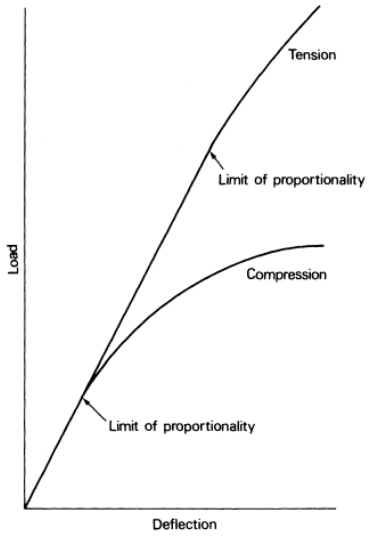

Figure 2.3: Load-displacement graphs of timber loaded parallel to grain (Dinwoodie 2017)

2.2.3 Engineered Wood Products

Engineered wood products (EWPs) include products that have been manufactured to improve the mechanical properties of the constituting wood material. These products often include glue to bound various laminations, veneers, strands, or sawdust, as required in the manufacturing process. EWPs are not limited by the size of the tree and can be manufactured to larger sizes to accommodate greater structural demand for height or span. Also, wood defects can be removed or placed in such a way that the mechanical properties of the EWP are better predictable than a sawn lumber member of the same size (Thelandersson and Larsen 2003). Examples of EWPs include Glulam (Figure 2.5a), CLT (Figure 2.5b), OSB (Figure 2.4a), laminated veneer lumber (LVL), Nailed-laminated timber (NLT), plywood (Figure 2.4b) and parallel-strand lumber (PSL).

(a) (b)

Figure 2.4: (a) OSB and (b) plywood (APA 2021)

(a) (b)

Figure 2.5: (a) Glulam and (b) CLT (CWC 2021)

2.2.4 Ductility of Connections in Wood Systems

Wood components in timber structures are typically joined together using connections that include metal dowel fasteners (i.e. bolts, nails, screws, dowels etc.), metal plates, or adhesives (i.e. glue). Timber connections often require large spacing between the individual fasteners in order to avoid brittle failures in the wood material, such as splitting (i.e. tension perpendicular to grain failure) (Thelandersson and Larsen 2003).

Connections are often used in timber structures to provide ductility to the system (Mpidi Bita et al. 2018; Pirinen 2014; Thelandersson and Larsen 2003). Fasteners in connections act as structural fuses that can dissipate energy and thus delay or avoid brittle failure in the wood material. The performance of wooden structures during extreme loading events such as earthquakes or blasts is thus greatly influenced by the performance of individual connections and their ability to undergo large inelastic deformation (Viau 2020).

Techniques have been employed to prevent brittle failure in connections through other means, including reinforcement of the timber joints by using densification (Blaß and Schädle 2011; Wang et al. 2015) or self-tapping screws (Lam et al. 2008; Wang et al. 2015).

Jorissen and Fragiacomo (2011) outlined a procedure based on capacity design to ensure that the design strength capacity of a ductile element (i.e. connection) is less than the capacity of the brittle timber element, using an overstrength factor, defined as the ratio between the capacities of the timber member and connections. This overstrength factor must account for the variation in resistance of both the timber member and connection. To achieve this, the variation in strength and stiffness must be known and based on statistically significant databases of experimental tests

results. This procedure has been successfully used by Nolet et al. (2019) for the design of CLT shear walls with ductile wall components (i.e. hold downs) under in-plane seismic loading and Viau et al. (2021b) for the design of Energy Absorbing Connections (EACs) to be used as sacrificial elements with Glulam or CLT elements under blast loading.

2.3 High Strain Rate Loading of Wood Elements

2.3.1 Wood Under Impact Loading

Impact loading differs from blast loading in that it consists of the direct physical application of a high magnitude load as opposed to the shock wave propagation of blast loading. Compression and flexure testing on small clear wood samples by Markwardt and Liska (1956) indicated that an increase of 10% to 40% in the apparent ultimate strength could be achieved for a tenfold increase in loading rate.

Nadeau et al. (1982) tested specimens with or without intentional notching on the tension side under strain rates in the range of 3×10^{-7} to 6×10^{-2} s^{-1} to investigate the effects of material variability. These tests showed a similar increase in the apparent ultimate strength to Markwardt and Liska (1956) for unnotched specimens only. This was later corroborated by Spencer (1978) and Jansson (1992). It was reported that higher strength lumber had a more substantial dynamic strength increase than lower strength lumber. The study by Jansson (1992) is of particular interest since it used specimens representative of those used in construction instead of small clear specimens. Specimens with defects were observed to be more likely to fail under flexure near defects and with a crack-dependent failure at lower strain rates, shifting to a brash failure for higher strain rates.

Sukontasukkul et al. (2000) observed a similar bending strength increase for PSL beams, while compressive strength increase in the range of 16 to 41% was observed by Syron (2008) for LSL. Syron (2008) also observed an increase of up to 28% for the compressive modulus of elasticity and did not observe any increase due to high strain rates for LSL in tension.

A different experimental procedure, the split-hopkinson bar test, was used to investigate high strain rate effects on softwood typical of construction by Gilbertson and Bulleit (2013). A significant increase in the compressive strength (between 1.9 and 2.4) of the softwood specimens was

observed when comparing static testing (70×10^{-3}-150×10^{-3} s^{-1}) to dynamic testing (70-340 s^{-1}). These observations were later corroborated by Wouts et al. (2016).

2.3.2 Light-Frame Wood Stud Walls Under Blast Loading

Jacques et al. (2014) investigated the dynamic flexural response of 8 ft long 2×6 spruce-pine-fir (SPF) visually graded studs. Specimens were tested statically and dynamically at the University of Ottawa's shock tube facility. Statistical analysis of the experimental results indicated that a DIF of 1.41 could be justified for the modulus of rupture for strain rates of 0.1 s^{-1} to 0.4 s^{-1}. However, no increase in the modulus of elasticity could be substantiated due to the sample size.

Lacroix and Doudak (2015) tested full-scale light-frame shear walls using simply supported boundary conditions. It was reported that a DIF of 1.40 could be achieved for the modulus of rupture and of 1.18 for the modulus of elasticity based on static and shock tube dynamic testing. Strain rates in the range of 0.12 to 0.55 s^{-1} were achieved. The study also found that the failure mode shifted from a splintering tension failure under static loading to a brash tension failure under dynamic loading.

Once brittle failures in the studs were identified, subsequent research work aimed at providing possible retrofit options to mitigate damage and projectile generation from sheathing tearing at high pressures. Options that showed favourable outcomes include using thicker sheathing panels or replacing sheathing panels with corrugated metal panels (Lacroix et al. 2014) or adding welded wire mesh between studs and sheathing (Viau and Doudak 2016b).

2.3.3 Glulam Beams and Columns Under Blast Loading

Lacroix and Doudak (2018a) investigated the performance of glulam beams and columns under simply supported boundary conditions exposed to blast loading and found that a DIF of 1.14 could be achieved for the modulus of rupture. However, when finger joints were present through the entire width of a member in the high moment region of the tension laminate, no DIF was observed. Also, no significant DIF on the modulus of elasticity was observed from these tests. The authors showed that SDOF modelling with a linear elastic resistance curve was adequate at simulating the dynamic response of the tested beams. Glulam columns, subjected to combined blast lateral loading and variable static axial loading, were also investigated (Lacroix and Doudak 2018b), and a material predictive model was developed to capture the additional effects induced by the axial loading.

Research aimed at using fibre-reinforced polymers to strengthen and improve the brittle failure mode of glulam beams during blast loading was undertaken by Lacroix and Doudak (2020, 2018c). The authors observed an increase in maximum deflection and resistance of approximately 30 to 65% due to FRP tension laminates.

2.3.4 CLT Panels Under Blast Loading

Blast testing of CLT was first conducted with a shock tube by Lowak (2015, 2016), with a reported strength increase factor of 1.6. However, these tests were only loaded slightly past their elastic limit, and no post-peak behaviour was investigated. These tests were later supplemented by live blast tests by Weaver et al. (2017).

Poulin et al. (2018) investigated the performance of simply supported CLT panels under blast loading and determined a DIF of 1.28 on the resistance while no increase was observed for stiffness. Differences in failure modes were also reported between static and dynamic testing. Two resistance material models, accounting for high strain rates effects and post-peak response, were developed to describe both failure modes.

2.3.5 High Strain Rate Loading of Wood Connections

Girhammar and Andersson (1988) investigated the performance of nailed connections under high strain rates effects at deformation rates of 0.033 mm/s to 1000 mm/s. The study found that the ultimate load capacity increased while deformation capacity decreased with increased strain rate. It was also observed that the failure mode was governed by combined bending and embedment failure (wood crushing). Although a small increase in the strength of nails was observed at higher strain rates, the authors also observed that this increase was significantly lower than the strength increase occurring in the wood. Varying DIF was observed for the different failure modes and tests, with values as high as 1.58. However, similar tests by Rosowsky and Reinhold (1999) did not find enough evidence to show a correlation between strength and strain rates effects. The authors attribute this to the premature failure of the joints, which prevented the development of wood crushing and nail bending.

Daneff (1997) investigated the performance of bolted connections at loading rates of 0.042 mm/s and 25 mm/s. For connections in the parallel-to-grain direction, embedment failure in the wood was observed, followed by splitting, which was more significant at higher strain rates. Significant splitting failure was observed at all strain rates in the perpendicular-to-grain direction, with some

embedment failure. Connections loaded at higher strain rates were observed to be stiffer and reached higher yield loads than those at lower strain rates.

2.3.6 Wood Connections Under Blast Loading

Viau and Doudak (2016a) investigated realistic boundary conditions and the use of prescriptive connections in light-frame shear walls exposed to blast loading. These connections were detailed for low and high seismic and wind regions. The results showed that these prescriptive connections did not perform well under blast loading. Although designed connections performed well, findings indicated that basing the connection solely on capacity might be inadequate. This study also showed that SDOF analysis of the assembly is only accurate when damage in the connection is limited.

CLT wall assemblies with realistic boundary connections were investigated by Côté and Doudak (2019). Configurations with seismic detailing were considered in order to evaluate their applicability to blast loading. Connections typically used in construction to resist gravity and lateral loads and specially designed connections for blast loading were investigated. The results indicated that connection detailing significantly affected the behaviour of the CLT shear walls. Self-tapping screws connecting floor to wall were observed to perform poorly and fail in a brittle manner, while angle bracket connections performed well with ductile yielding of the fasteners or brackets. Deformation of the connections provided a significant amount of energy dissipation and reduced the damage in the CLT panels.

Viau and Doudak (2019) also investigated the blast performance of CLT panels with idealized and realistic boundary conditions. Connections included angle brackets and screw fasteners. A two-degree-of-freedom (TDOF) analysis software was also developed and validated using the experimental results. A later study by the same authors validated the TDOF analysis software with different experimental results of timber assemblies from published literature (Viau and Doudak 2021c). The study noted that SDOF analysis was only accurate when boundary conditions are specifically designed to remain elastic with a stiffness that is at least ten times that of the wood member (Viau and Doudak 2021c).

Viau and Doudak (2021a) investigated the behaviour of Glulam beams with bolted connections under blast loads. Full-scale testing of glulam beam was performed, and the results showed that bolted connections designed to yield in bolt bending performed better than over-designed bolts.

Furthermore, proper detailing of the bolt group geometry was sufficient to achieve a specific failure sequence. The use of self-tapping screws to reinforce the glulam beam assembly was also investigated. The authors observed that using self-tapping screws shifted the failure mode from splitting to a combination of bolt yielding and wood crushing, thus providing additional ductility to the system. The authors emphasized the importance of limiting brittle failure modes in the connections. An approach was thus proposed to ensure that ultimate failure does not occur in the load-bearing timber elements prior to connection yielding, thus providing additional energy absorption potential. This can be observed in Figure 2.6a, where an overdesigned 2×3 connection absorbs less energy than the more ductile 2×1 connection (Figure 2.6b) (Viau and Doudak 2021a).

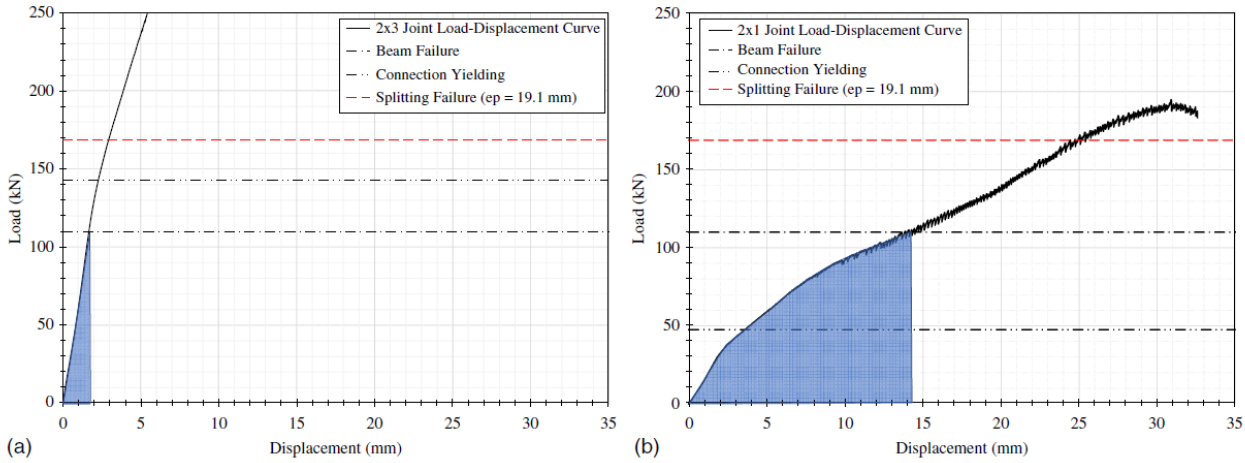

Figure 2.6: Load-displacement curve of (a) overdesigned 2×3 bolted connection and (b) more ductile 2×1 connection (Viau and Doudak 2021a)

McGrath and Doudak (2021) investigated the performance of steel-wood-steel connections under blast loading. Static testing, as well as dynamic testing in a shock tube, were performed. The authors observed an apparent increase in resistance of about 1.2, as well as an increase of 1.5 and 1.9 for stiffness parallel and perpendicular to the grain, respectively. However, this was only the case when failure was dominated by embedment (wood crushing) in both parallel and perpendicular to grain directions. The results also showed that failure modes involving fastener bending exhibited improved performance over those with wood crushing alone.

2.4 Energy Absorption

Substantial work has been undertaken to study the energy absorption capabilities of rings and ring systems as well as cellular materials such as honeycombs and foams.

2.4.1 Cellular Materials

Cellular materials, or cellular solids, are materials with an internal structure made up of clusters of cells (i.e., small compartments, enclosed space). Cellular materials can be natural, such as wood or cork, or made by non-natural processes, such as honeycombs and foams. Modern technologies have allowed cellular materials to be manufactured from polymers, metals and ceramics, broadening their applications.

2.4.1.1 Honeycombs

An example of a honeycomb is presented in Figure 2.7. The typical compressive stress-strain relationship of honeycombs is presented in Figure 2.8 for different relative densities. This stress-strain relationship typically experiences three regimes during deformation: elastic, plateau, and densification.

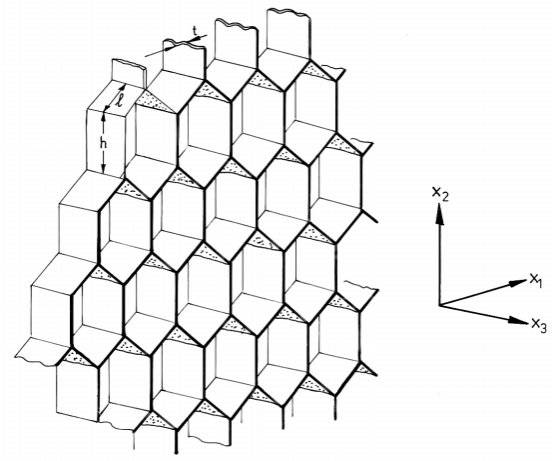

Figure 2.7: Honeycomb with hexagonal cells, with in-plane properties relating to the x_2 and x_1 directions (Gibson and Ashby 1999)

Elastic in-plane deformations (x_1 and x_2 directions in Figure 2.7) are typically governed by bending, while out-of-plane deformations are typically governed by buckling (x_3 direction in Figure 2.7). Densification represents the point where cell walls begin to touch each other, which causes a dramatic increase in stiffness.

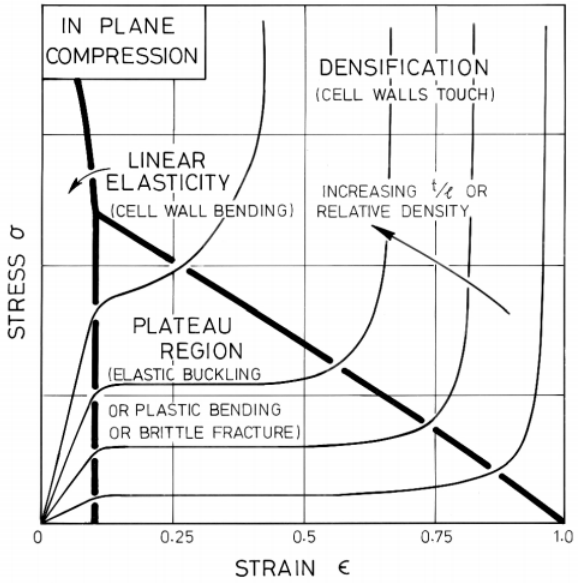

Figure 2.8: In-plane compressive stress-strain curve of honeycombs with varying thickness over length ratios (Gibson and Ashby 1999)

Increasing the relative density (or t/l) modifies the stress-strain curve in two ways. It increases the yield strength and elastic stiffness and shifts the densification strain to the left since smaller voids require less strain to reach contact between cell walls.

2.4.1.2 Foams

Foams are capable of absorbing energy since they deform with ductile mechanisms such as plastic bending at stress levels lower than the applied peak stress. To assess the energy absorption capacity of a given foam, an energy absorption graph can be drawn from the stress-strain or load-displacement graph, as shown in Figure 2.9 (Gibson and Ashby 1999).

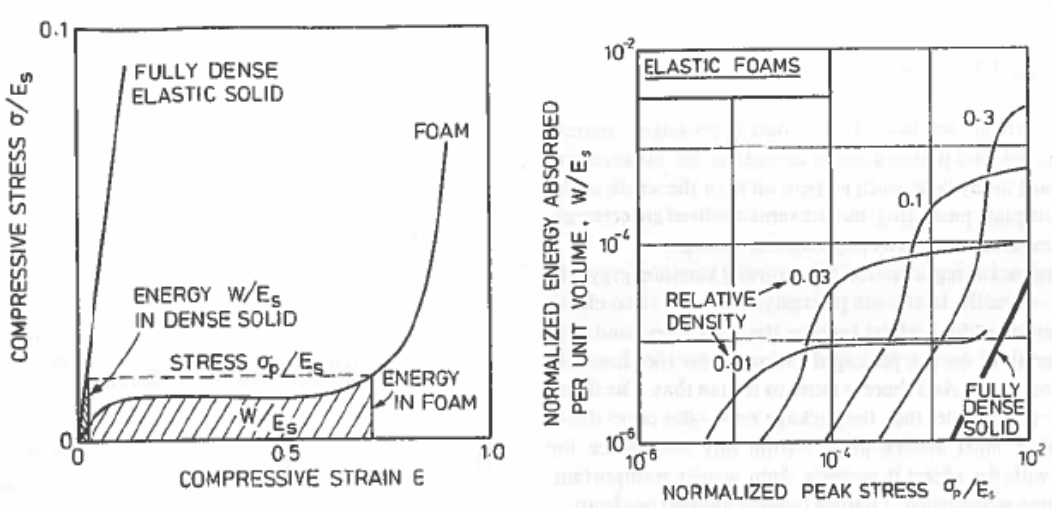

Figure 2.9: Stress-strain graph (left) and energy absorption graph (right) of foams (Gibson and Ashby 1999)

It can be observed that for a given peak stress (σ_p), the energy absorption is much higher in a foam than a fully dense solid of the same material. Gibson and Ashby (1999) present the energy absorption graph as the normalized energy absorbed per unit volume (W/E_s), as a function of the normalized peak stress (σ_p/E_s). The work done by the stress-strain curve, which represents the energy absorption at a given deformation level, can be calculated with Equation 2.1, or numerically with Equation 2.2.

$$W(\varepsilon) = \int_0^{\varepsilon} \sigma(\varepsilon)\, d\varepsilon \qquad \text{Equation 2.1}$$

$$W_i = W_{i-1} + \sigma_i \cdot |\varepsilon_i - \varepsilon_{i-1}| \qquad \text{Equation 2.2}$$

Where W is the work done by the deformation mechanism, σ is the peak stress, and ε is the strain.

2.4.2 Tube Compressed by Two Flat Plates

Tubes, rings, or circular hollow steel sections (HSS) compressed by two flat plates can be used as an energy-absorbing mechanism, due to the formation of plastic hinges, as shown in Figure 2.10. Approximate load-displacement curves for these deformation modes have also been developed (Burton and Craig 1963; DeRuntz and Hodge 1963; Lu and Yu 2003; Reddy and Reid 1980; Reid and Reddy 1978). An example is shown in Figure 2.11 (Reid and Reddy 1978) and similar results have been observed by Avalle and Goglio (1997) and Gupta et al. (2005).

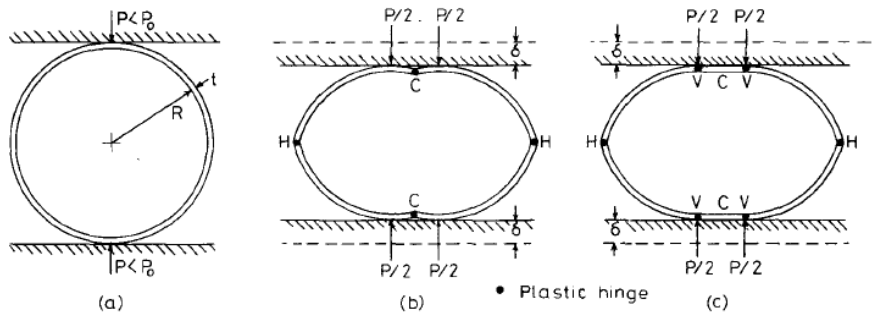

Figure 2.10: (a) Undeformed tube, (b) DeRuntz and Hodge (1963) collapse mode, and (c) Burton and Craig collapse mode (1963) (Reid and Reddy 1978)

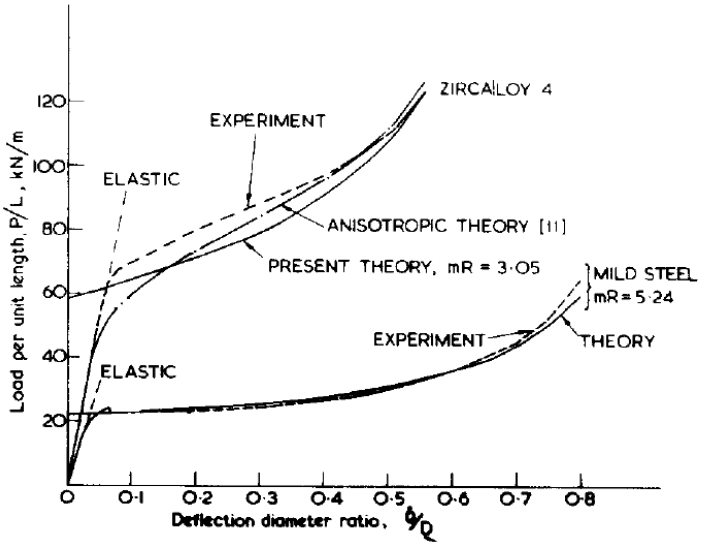

Figure 2.11: Typical load-deformation curves for tubes of zircaloy and mild steel (Reddy and Reid 1979)

2.4.3 Steel Under High Strain Rates

The effects of high strain rates on steel have been well documented in the literature (Chen 2010; CSA 2012). At quasi-static strain rates (i.e. 10^{-4} to 10^{-2} s^{-1}), the distribution of stresses in a steel member can be assumed to be time-independent. However, intermediate strain rates (i.e. 1 to 100 s^{-1}) and high strain rates (i.e. 1000 s^{-1} and up) require that additional consideration be taken. When the strain rate becomes intermediate, the distribution of stresses is mostly continuous but is dependent on inertia effects. High strain rates require that the stress wave propagation effect be considered in addition to the inertia effects. Typically, the true stress, including yield, will increase when the strain rate increases (Chen 2010).

Chen (2010) experimentally tested mild steel of grade 44W with tensile coupon testing. It was observed that the Cowper-Symonds power-law equation (Equation 2.3) (Cowper and Symonds 1957) was able to predict the dynamic yield stress for mild steels up to a strain rate of 1 s^{-1} and the flow stress at a strain rate up to 1000 s^{-1}. Values of 40.4 s^{-1} for D and 5 for q were recommended by Symonds (1967). It was also observed that the ductility, rupture strain and engineering strain at fracture of mild steel were not affected by strain rates up to 1.0 s^{-1} (Chen 2010).

$$\frac{f_d}{f_s} = 1 + \left(\frac{\dot{\varepsilon}_p}{D}\right)^{\frac{1}{q}} \qquad \text{Equation 2.3}$$

Where f_d/f_s is the ratio of the dynamic stress over the static stress, $\dot{\varepsilon}_p$ is the plastic strain rate, and D and q are material constants.

Dynamic increase factors (DIFs) are often employed to consider the effects of high strain rates or high loading rates. CSA S850 provides DIFs values of common Canadian materials for far-field and near-field blasts, as shown in Table 2.1 (CSA 2012).

Table 2.1: DIFs in CSA S850-12 (CSA 2012)

Material	**Material Property**	**Failure Mode**			
		Far field		**Near field**	
		Flexure	**Compression**	**Flexure**	**Compression**
Structural Steel 350W or 350WT	Yield Strength	1.2	1.1	1.3	1.2
	Ultimate Strength	1.1	1.1	1.1	1.1
Visually-graded lumber Machine-graded lumber (MSR)	Any	1.4	1.4	1.4	1.4
Glulam Engineered wood products	Any	1.4	1.4	Not provided	Not provided

2.4.4 Energy Absorbing Connections (EACs)

Energy-absorbing connections, referred to as EACs, are sacrificial elements meant to absorb large quantities of energy to reduce damage to more crucial elements during blast or impact loading. Many of these connections are made out of angular or hexagonal shapes. Research on such elements ranges from simple angular EACs (i.e. Whitney (1996), Oswald (2018), and Wang et al.

(2017, 2019)) that rely on deformation mechanisms such as plastic hinging to absorb energy, to more complex systems that may rely on other mechanisms (i.e. Cao et al. (2018)).

Whitney (1996) investigated the use of deformable EAC for supporting pre-cast reinforced concrete panels attached directly to an existing reinforced concrete frame subjected to blast waves through dynamic analysis and physical testing. These connectors were selected for their potential to reduce the damage in the the panel and the loads transferred to supporting frames. Figure 2.12 shows the deformed and undeformed shapes of one type of EAC at full-scale, half-scale, and quarter-scale, respectively. These specimens were manufactured from A-36 steel with strengths that can vary from 36 ksi to 50 ksi, since steel not meeting A-50 specification may be stamped as A-36 steel.

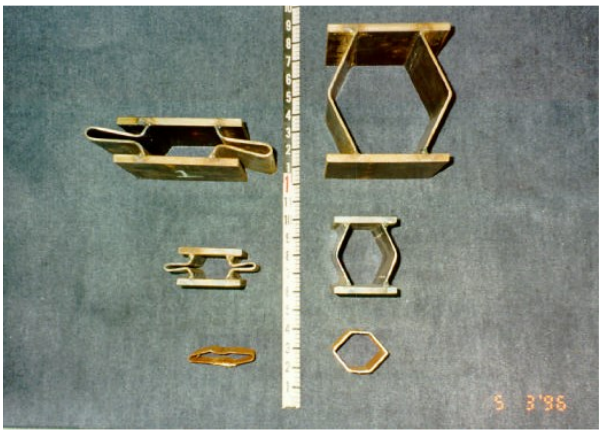

Figure 2.12: Deformed and undeformed shapes of EAC (Whitney 1996)

The welds used in manufacturing were continuous and welded on the entire depth of the EAC to avoid weld failure leading to a lack of plastic hinge development. The experimental program consisted of blast testing in a shock tube at pressures up to 25 psi and at durations up to 100 ms. The specimens were also tested statically to establish load-displacement curves. Panels up to 8 ft by 8 ft were tested in combination with the EACs (Whitney 1996). The system was analyzed using a SDOF model under the assumption that the connector resistance remains lower than the panel capacity. The model was idealized so that all deflection is assumed to occur in the connector while mass is entirely provided by the panel. This was deemed appropriate since the panel experienced negligible deflections during experimental testing. Also, the elastic portion of the connector response was neglected under the assumption that the elastic response is much smaller than the plastic response, mimicking true rigid response (Whitney 1996).

It was observed that the EAC with a hexagonal steel tube, such as shown in Figure 2.12, provided the best performance. An initial elastic response region is achieved for the hexagonal EAC until the connector yields. This is followed by a plastic response region where the load stays relatively constant, achieving much larger displacements than the elastic response region. The rigid-plastic model predicted conservative overestimates of the connector's permanent deformation (Whitney 1996).

Oswald (2018) conducted a series of shock tube tests of pre-cast panels supported by EACs and compared the results to those of rigid supports and under static loading. Shock loads similar to those from large high explosive threats were investigated, including the negative phase of loading. The EAC's investigated consisted of two 3"×3"×0.25" Grade 50 steel angles welded to 3/8" thick top and bottom plates with or without additional aluminium honeycomb material (Figure 2.13). The energy absorbed was approximated by multiplying the yield load of the EAC and the deflection.

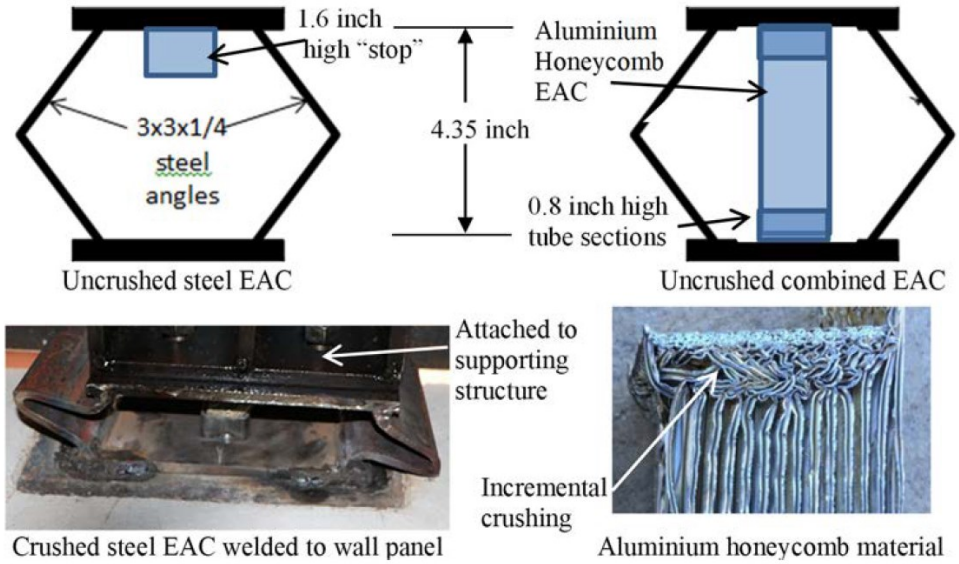

Figure 2.13: Types of tested EAC in Oswald (2018)

Oswald (2018) observed that both the steel EAC and aluminium honeycomb material yielded at small compressive axial strains (<5%). This was followed by a plateau of nearly constant force (i.e. yield load) up to large axial strains (~65%) where lockup or steel fracture occurred. The axial strain was approximated as the axial deflection divided by the original EAC height and was limited to 65% by steel tube "stops" to avoid fracture during peak inbound response.

The dynamic testing confirmed that using EACs reduced the peak midspan deflection of panels and the peak dynamic reaction loads to that experienced with rigid supports. The peak dynamic reaction force was observed to be reduced by 25-40% of that experienced with rigid supports, while the peak midspan deflection was reduced by 20-40%, with the yield or plateau load being an important factor to these reductions. Figure 2.14 shows the typical dynamic force vs. deflection relationships of the tested EACs.

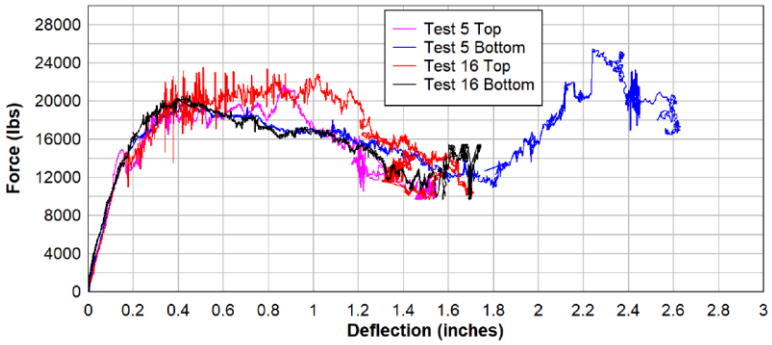

Figure 2.14: EACs force vs deflection graphs (Oswald 2018)

Lavarnway and Pollino (2015) investigated the use of circular EACs, referred to as blast-resistant ductile connectors (BRDCs). Simplified dynamic analysis based on conservation of energy was used. This was assumed to be adequate since the EACs do not add substantial mass and thus do not significantly modify the natural period of the system but do provide a substantial contribution in energy absorption capability. In addition, nonlinear dynamic and static FEA was performed as well as quasi-static experimental testing.

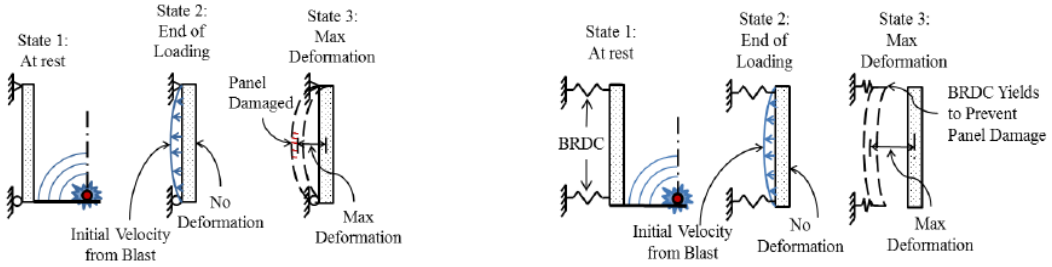

(a) (b)

Figure 2.15: States of loading and deformation for (a) members without EACs and (b) with EACs.

Results similar to Withney (1996) and Oswald (2018) with regards to the feasibility and performance of EACs were observed. In particular, the reduction in damage on the members connected to the EACs (Figure 2.15) was further confirmed. It was also found that circular HSS EACs could resist and transfer forces through the large deformations and strains imposed during loading. The shape of the force-deformation curve from both FEA and experimental results (Figure 2.16) was similar to the results obtained by Reid and Reddy (1978).

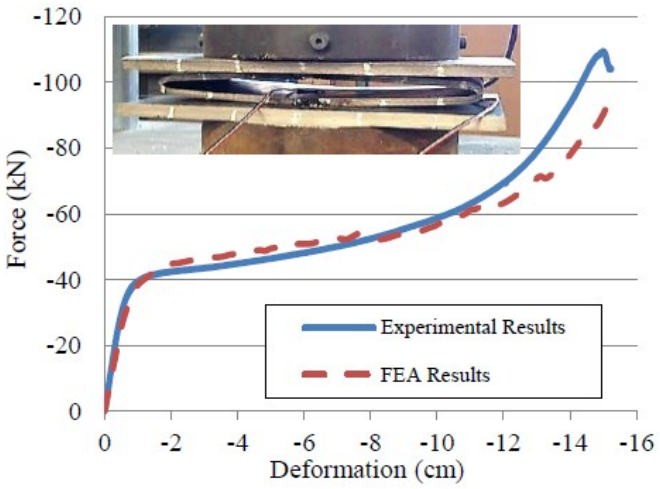

Figure 2.16: Force-deformation of a circular HSS 7”×0.25” and deformed shape (Lavarnway and Pollino 2015)

Wang et al. (2017, 2019) investigated similar mild steel angular connections to Whitney (1996) and Oswald (2018) but using unequal angle legs. Additional aluminium and polyurethane foam were used as a filler between the steel sections, and their effects on the performance were investigated under quasi-static loading (0.5 to 4 mm/min). One other key difference is that the steel sections were not welded but bolted to the top and bottom steel plates, as shown in Figure 2.17.

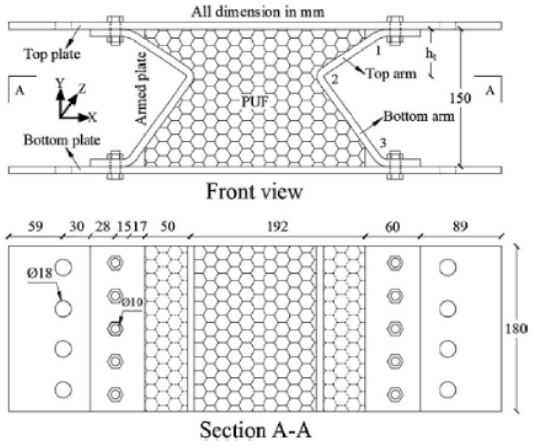

Figure 2.17: Front and section view of EAC specimen (Wang et al. 2019)

Numerical and analytical model consistent with experimental results were developed to predict the energy absorption performance. The energy absorption efficiency (η) was approximated with Equation 2.4 and was adopted to define the onset of densification. When η is at its maximum, it is an indication that densification is beginning, as shown in Figure 2.18.

$$\eta = \frac{W}{FH} \qquad \text{Equation 2.4}$$

Where W is the work (energy absorbed) by the load-displacement curve, Δ is the displacement, F is the load-displacement curve, and H is the maximum height of the EAC (i.e. before loading).

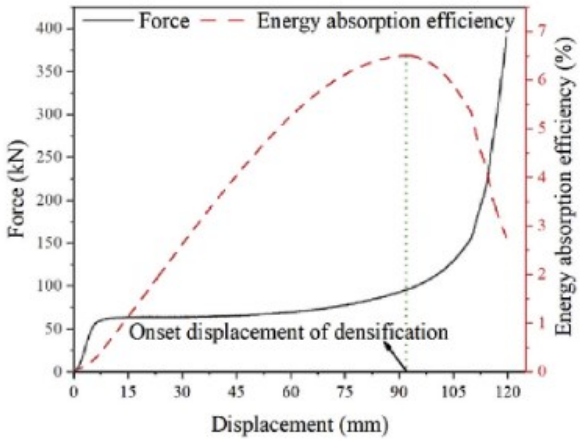

Figure 2.18: Load-displacement curve and energy absorption efficiency (Wang et al. 2019)

Figure 2.19 shows the observed plastic hinging deformation mechanism experienced by the compressed steel sections alone. The addition of aluminium foam introduced additional

deformation mechanisms to the connection, namely the cracking of cell walls (Figure 2.20), introducing additional force capacity and energy absorption potential (Figure 2.21).

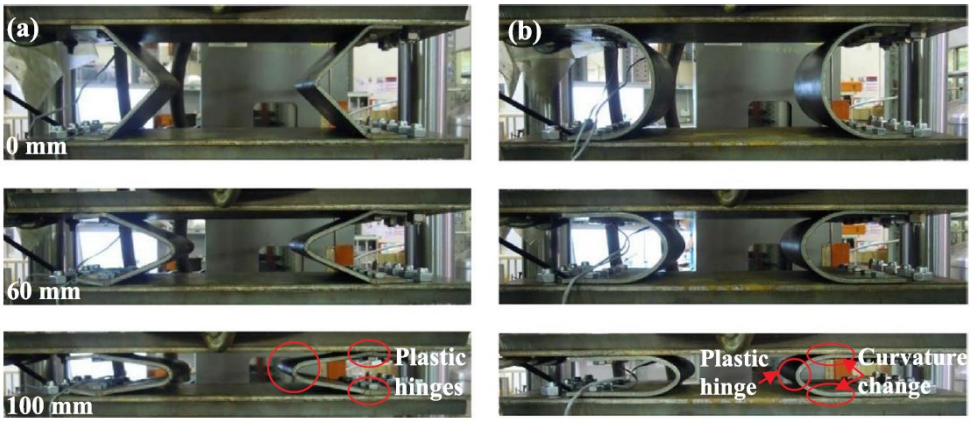

Figure 2.19: Deformation mechanisms of EACs without aluminium foam (Wang et al. 2017)

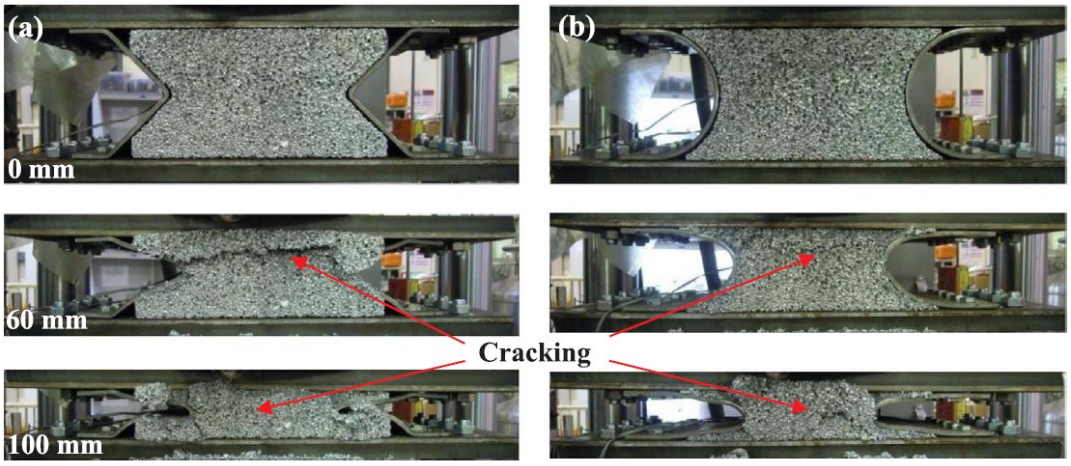

Figure 2.20: Deformation mechanisms of EACs with aluminium foam (Wang et al. 2017)

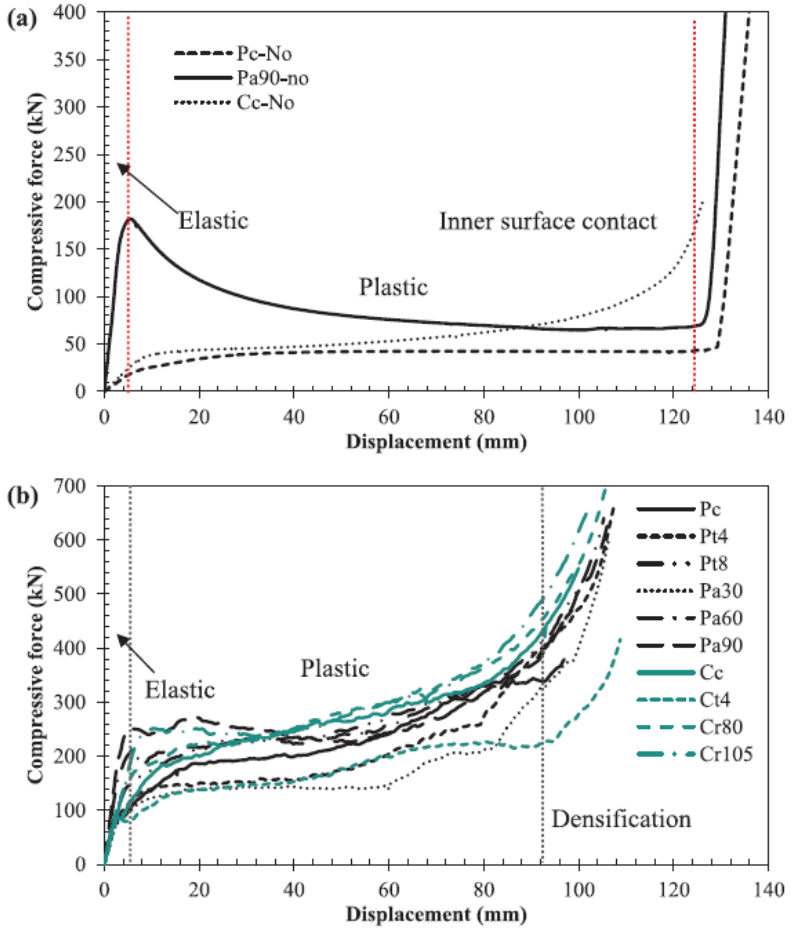

Figure 2.21: Force-displacement curves of (a) EACs without aluminium foam and (b) with aluminium foam where P represents angles and C represents circular HSS in the legend (Wang et al. 2017)

Wang et al. (2017, 2019) thus observed that the energy absorption performance of EACs could be improved by using foams. Additionally, it was observed that increasing the thickness and reducing the height of the angles or circular HSS could also provide improved performance. In particular, the use of foam filler increased the energy absorption per unit displacement and per unit mass, thus leading to a more efficient connection of the same size. Similar results were observed by Yonghui et al. (2019) with EACs of different geometry.

Oblong tubes have also been tested as a potential shape for energy-absorbing systems (Baroutaji et al. 2014; Olabi et al. 2008). These tubes are manufactured by stretching circular HSS sections along a line until it forms a shape like that shown in Figure 2.22. Olabi et al. (2008) investigated

the use of multiple nested oblong tubes under two configurations, as shown in Figure 2.22. Both impact testing and FEA were used to obtain the force-displacement relationships of the specimens.

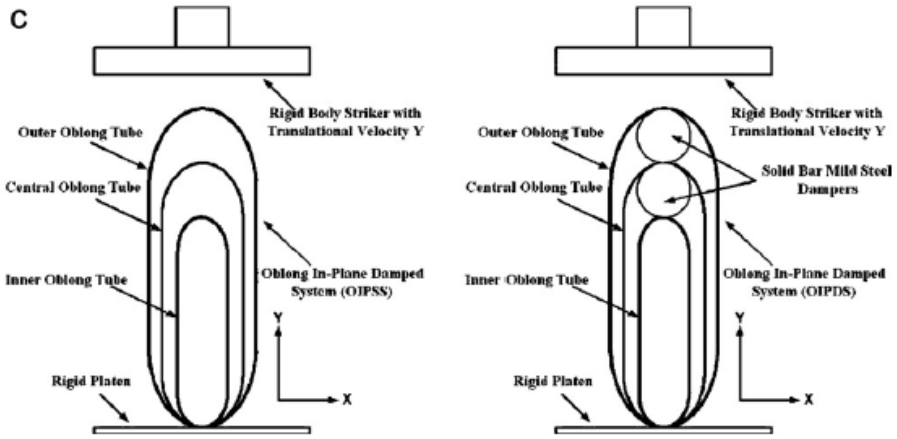

Figure 2.22: Nested oblong tube system (a) without dampers and (b) with dampers

Olabi et al. (2008) observed that providing dampers caused the force to remain mostly constant during testing due to the transfer of forces to each oblong tube during the entirety of testing. It was also observed that providing no dampers causes delayed jumps in the force capacity when the top tube comes into contact with lower tubes. Providing dampers thus increased the energy absorption capacity of the system.

Viau and Doudak (2021b) were the first to investigate the use of EACs in heavy timber assemblies subjected to blast loads. Static and shock tube testing of angular EACs showed that when properly designed, EACs could allow assemblies to withstand a greater amount of energy than typical connections and provide increased ductility to the system (Figure 2.23). A probabilistic approach was thus developed to be used in the design of EACs to ensure that brittle flexure failure of wood elements does not occur prior to sufficient energy dissipation from the EACs. This was achieved by ensuring that the ultimate strength of the wood element ($F_{u,wood}$) remains larger than the yield strength ($F_{y,conn}$) and lower than the ultimate strength ($F_{u,conn}$) of the EAC (see Figure 2.24). Factors α_y and α_u, seen in Figure 2.24, represent the overstrength allocated to ensure proper failure sequence. They are based on the distribution of wood and EAC strength, as shown in Equation 2.5. A TDOF analysis was also conducted by discretizing the timber and EAC components and was capable of predicting the behaviour of the full-scale assemblies.

$$\alpha_y \geq \frac{1 + Z_{95th} CoV_{F_{y,conn}}}{1 + Z_{5th} CoV_{F_{u,wood}}} \qquad \text{Equation 2.5}$$

Where Z_{95th} and Z_{5th} are the standard score for the 95th and 5th percentiles, respectively, and where $CoV_{F_{y,wood}}$ and $CoV_{F_{u,conn}}$ are the coefficient of variation for the wood member ultimate failure load and the EAC yielding load, respectively.

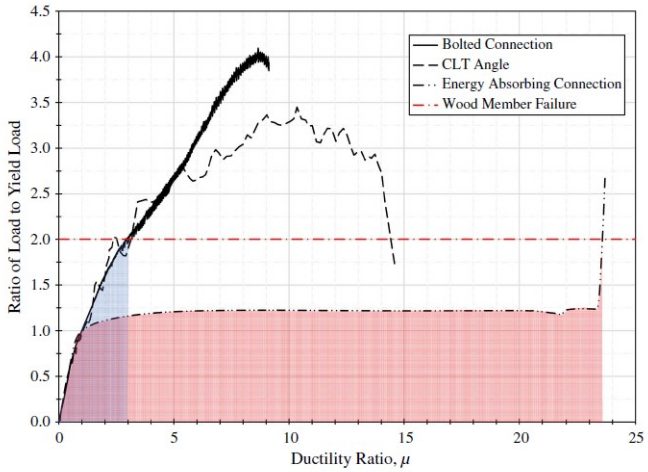

Figure 2.23: Comparison of energy absorbed by a CLT angle connection (blue) and EAC connection (red) (Viau and Doudak 2021b)

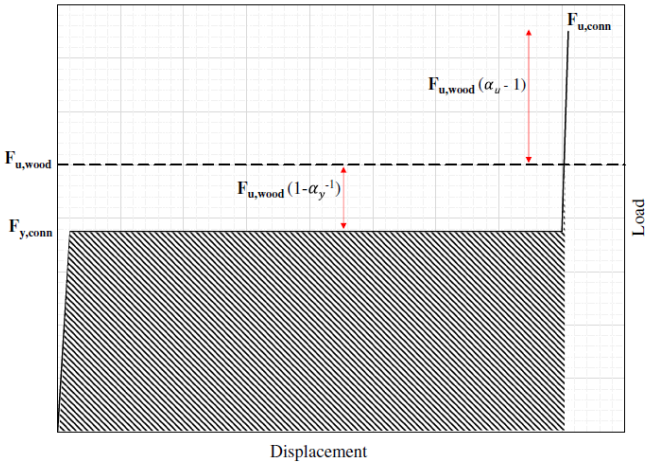

Figure 2.24: Failure sequence of an EAC assembly based on probabilistic principles (Viau and Doudak 2021b)

The concept presented in Section 2.4.1 provides the basic concepts to determine the energy absorption potential of EACs. The equations for work (Equation 2.1 and Equation 2.2) can be modified for force-displacement relationships (Figure 2.25) by replacing the stress component

with force and the strain component with displacement. The energy absorbed will thus be the area under the load-displacement graph up to densification (grey area in Figure 2.25). This modification is more adequate to the application of EACs due to their non-isotropic nature and the more common load-displacement experimental measurements. Equation 2.6 and Equation 2.7 show the modified work equations adapted for EACs.

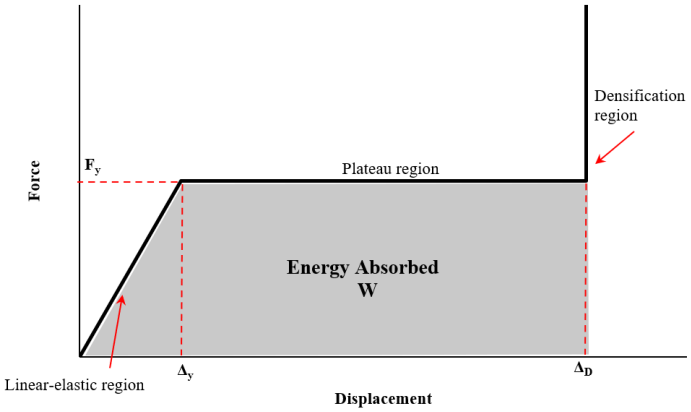

Figure 2.25: Idealized load-displacement graph of an EAC

$$W = \int_0^{\Delta_D} F(\Delta)\, d\Delta \qquad \text{Equation 2.6}$$

$$W_i = W_{i-1} + F_i \cdot |\Delta_i - \Delta_{i-1}| \qquad \text{Equation 2.7}$$

Where W is the work done by the force-displacement curve, Δ_D is the displacement at the beginning of the densification region (Figure 2.25), F is the force, and Δ is the displacement.

2.5 Summary

Although extensive work has been done in the study of timber assemblies under blast loading, including members and connections, work has only begun on the application of EACs in timber assemblies. Most studies on timber assemblies subjected to blast loading do not focus on improving energy absorption capability. Improving the energy absorption, for example by using EACs, can offer great potential in mitigating the effects of blast loading. However, only one study has investigated the use of EACs with timber assemblies and only considered one EAC geometry. The present study thus aims at filling the gap by investigating the effect of geometry on the load-displacement performance of EACs. This study also aims at investigating whether the selected EACs are appropriate to timber assemblies subjected to blast loading. EACs geometries were

either selected for their original shape (i.e. not investigated in the literature) or if the load-displacement performance presented in the literature showed compelling results while not considering timber assemblies as a potential application. Although some shapes have already been investigated in the literature, they were chosen to verify that the manufacturing process used in this project could replicate the EAC performance. Also, none of the published studies investigated the effects of depth scaling, which could be utilized to modify the yield and stiffness to that required in design. It should also be noted that published literature has been limited to EACs used in conjunction with much stiffer materials such as reinforced concrete. The following Chapter will present the process used to select EAC specimens of varying geometry for experimental testing and which EAC specimens were selected for the present study.

CHAPTER 3 - Specimen Selection, Design and Manufacturing

3.1 General

This chapter summarizes the specimen selection, design, and manufacturing process. Section 3.2 presents the preliminary finite element analysis (FEA) performed to generate load-displacement graphs of different EAC configurations, while Section 3.3 presents the reasoning behind the choice of the 9 EACs configurations selected for the experimental program. Section 3.4 presents additional design and manufacturing details and requirements.

3.2 Preliminary Finite Element Analysis

3.2.1 General

FEA models were generated and analyzed to obtain approximate load-displacement graphs of potential EAC specimens. A number of possible shapes and configurations were investigated based on a sample of commercially available structural steel sections (

Table 3.1). These included steel plates, equal leg angles, and circular hollow steel sections (HSS). Welded joints at the intersections of the different steel sections were assumed to be of the same material, thus having identical mechanical properties. More detailed FEA models were developed following the experimental program and are presented in Chapter 6.

Table 3.1: Steel sections used in the analysis

Section and ID	Description	Sketch
Plate	Width (w): Any Depth (d): Any Thickness (t_p): 0.313” Grade: 44W/300W Hot Rolled Steel	
Angle 2×2×0.125	Depth (d): Any Leg length (L_a): 2” Thickness (t_a): 0.125” Grade: 44W/300W Hot Rolled Steel	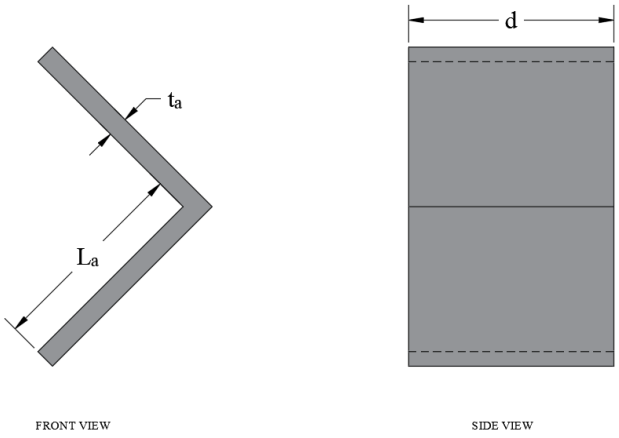
Angle 2×2×0.25	Depth (d): Any Leg length (L_a): 2” Thickness (t_a): 0.25” Grade: 44W/300W Hot Rolled Steel	
Angle 3×3×0.188	Depth (d): Any Leg length (L_a): 3” Thickness (t_a): 0.188” Grade: 44W/300W Hot Rolled Steel	
Angle 3×3×0.25	Depth (d): Any Leg length (L_a): 3” Thickness (t_a): 0.25” Grade: 44W/300W Hot Rolled Steel	
Angle 4×4×0.25	Depth (d): Any Leg length (L_a): 4” Thickness (t_a): 0.25” Grade: 44W/300W Hot Rolled Steel	
Circular HSS 2.375×0.125	Depth (d): Any Outside Diameter (⌀): 2.375” Thickness (t_c): 0.125” Grade: 1018 Hot Rolled Steel	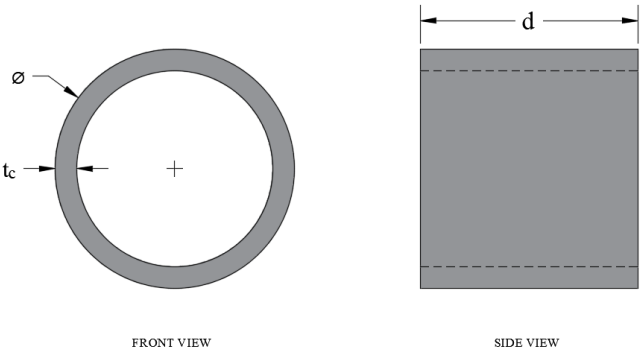
Circular HSS 3.5×0.125	Depth (d): Any Outside Diameter (⌀): 3.5” Thickness (t_c): 0.125” Grade: 1018 Hot Rolled Steel	
Circular HSS 3.5×0.25	Depth (d): Any Outside Diameter (⌀): 3.5” Thickness (t_c): 0.25” Grade: 1018 Hot Rolled Steel	
Circular HSS 5×0.125	Depth (d): Any Outside Diameter (⌀): 5” Thickness (t_c): 0.125” Grade: 1018 Hot Rolled Steel	
Circular HSS 5×0.25	Depth (d): Any Outside Diameter (⌀): 5” Thickness (t_c): 0.25” Grade: 1018 Hot Rolled Steel	

EACs assembled from the steel sections shown in

Table 3.1 were modelled to investigate the effects of varying different geometrical parameters on the load-displacement behaviour. The reasoning behind modelling such a large inventory of geometrical shapes was to identify the EACs with a well-defined yield plateau, which is required to enhance the performance of timber assemblies. Typical EAC geometries considered in this study are shown in Figure 3.1, where the varied parameters are listed below. It should be noted that the geometries presented in Figure 3.1 represent only half of the EAC shape, mirrored along the centerline (℄).

I. EACs with a cross-sectional shape made up of steel angles.
    a. Varying the leg length of the angles (L_a);
    b. Varying the thickness of the angles (t_a);
    c. Including welds and plates of different lengths (L_p) at the center of the connection;
    d. Adding four angles instead of two angles per connection.

II. EACs with a cross-sectional shape made up of circular HSS.
    a. Varying the circular HSS outer diameter (⌀);
    b. Varying the circular HSS thickness (t_c);
    c. Using an arc of the circular HSS with angle (θ);
    d. Using additional circular HSS of varying thicknesses and outer diameters.

III. EACs with a cross-sectional shape made up of a combination of steel angles and circular HSS.
    a. Varying the leg length of the angles (L_a);
    b. Varying the thickness of the angles (t_a);
    c. Varying the circular HSS outer diameter (⌀);
    d. Varying the circular HSS thickness (t_c);

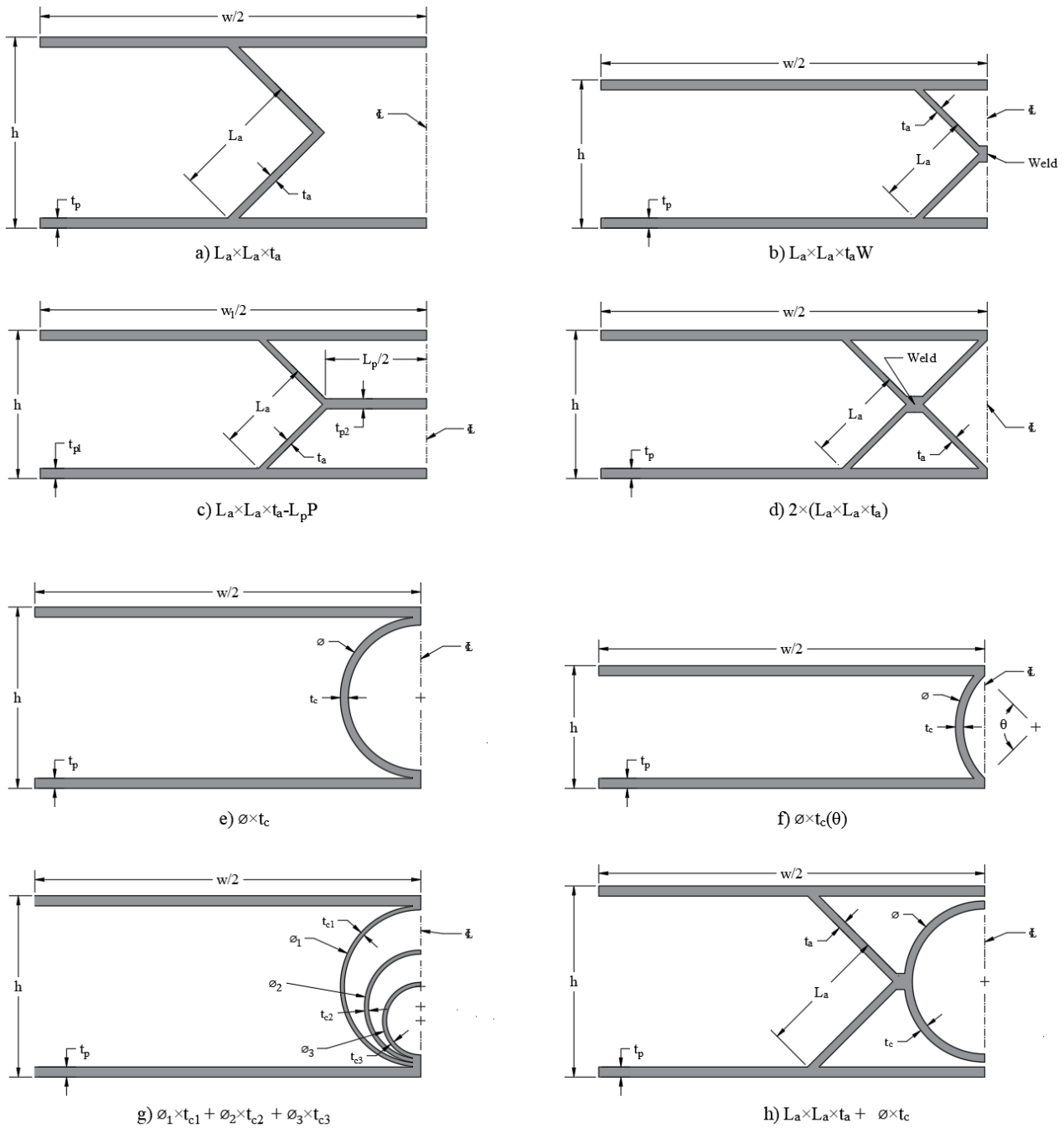

Figure 3.1: Typical EAC cross-sections representing half the shapes, and used for preliminary analysis

3.2.2 Methodology and Procedure

The preliminary FEA was performed with the finite element software Abaqus CAE (Smith 2009). Three dimensional deformable extruded solid elements were used, and sections were defined as solid and homogeneous. Typical material (mechanical) properties for structural steel (mild, hot

rolled) were assumed (Table 3.2), with isotropic behaviour being selected. Also, surface-to-surface contact to the surfaces of the sections was applied. A fixed boundary condition was set at the bottom of the connection, and a symmetry boundary condition was applied at the center cut of the section along the centerline (℄). The symmetry boundary condition was applied to reduce computation time under the assumption that it would not alter the behaviour considerably. An additional boundary condition was applied to the top surface to apply a constant and uniform displacement. This was done to obtain the resulting forces to this applied displacement to generate load-displacement graphs. Meshing was done with hex or hex-dominated elements with a density of meshes that provided at least 3 elements or more along the thickness of the sections. Figure 3.2 shows a sketch of the boundary conditions applied to the model.

Table 3.2: Mild steel material properties (Chapel Steel 2021; CSA 2021)

Material Property	**Value**
Modulus of Elasticity (E)	200 GPa
Poisson's ratio	0.3
Yield stress	300 MPa
Maximum plastic strain	0.4

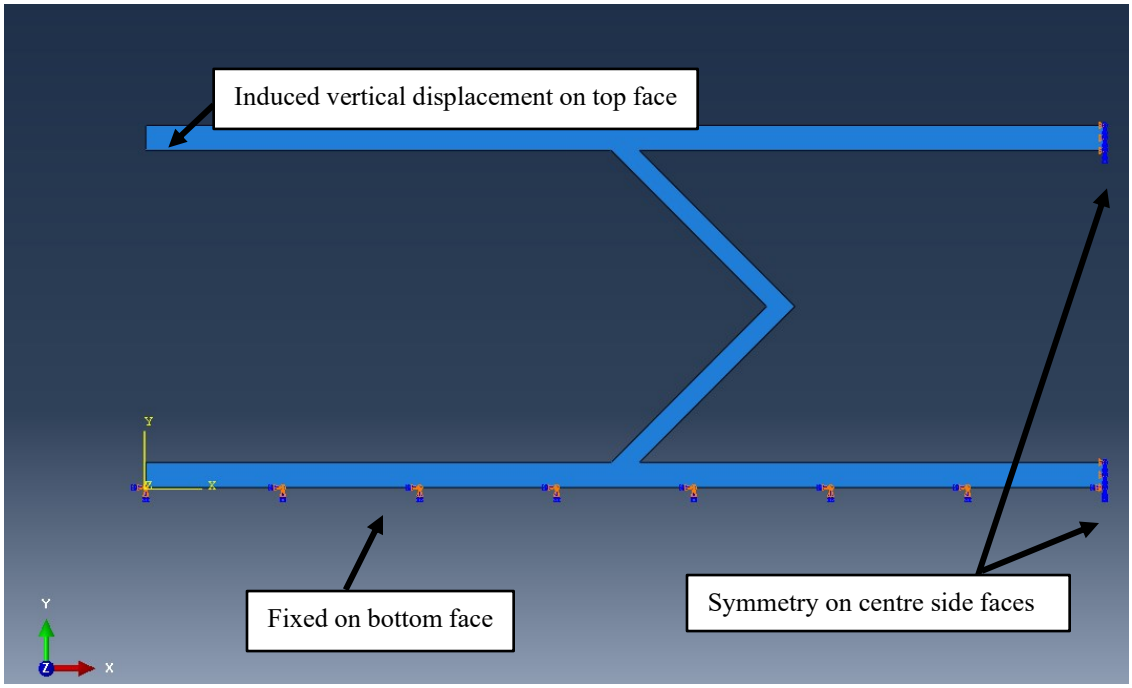

Figure 3.2: Boundary conditions of preliminary FEA model

3.2.3Scalability Verification

The model's scalability was verified to ensure that the results obtained from the FEA model at a specific depth are transferable to any depth. This was done by varying the depth while keeping the cross-section constant. The results were then normalized with respect to the depth to verify that the unit depth load-displacement graphs were approximately identical. Figure 3.3 shows the results for two different cross-sections, each modelled with depths of 50, 75 and 150 mm. The results show near-perfect agreement, which confirms that the results from a specific depth are scalable to accommodate different depths and that the behaviour is consistent. Furthermore, smaller depths can then be used to reduce computing time during the analysis due to the smaller quantity of elements.

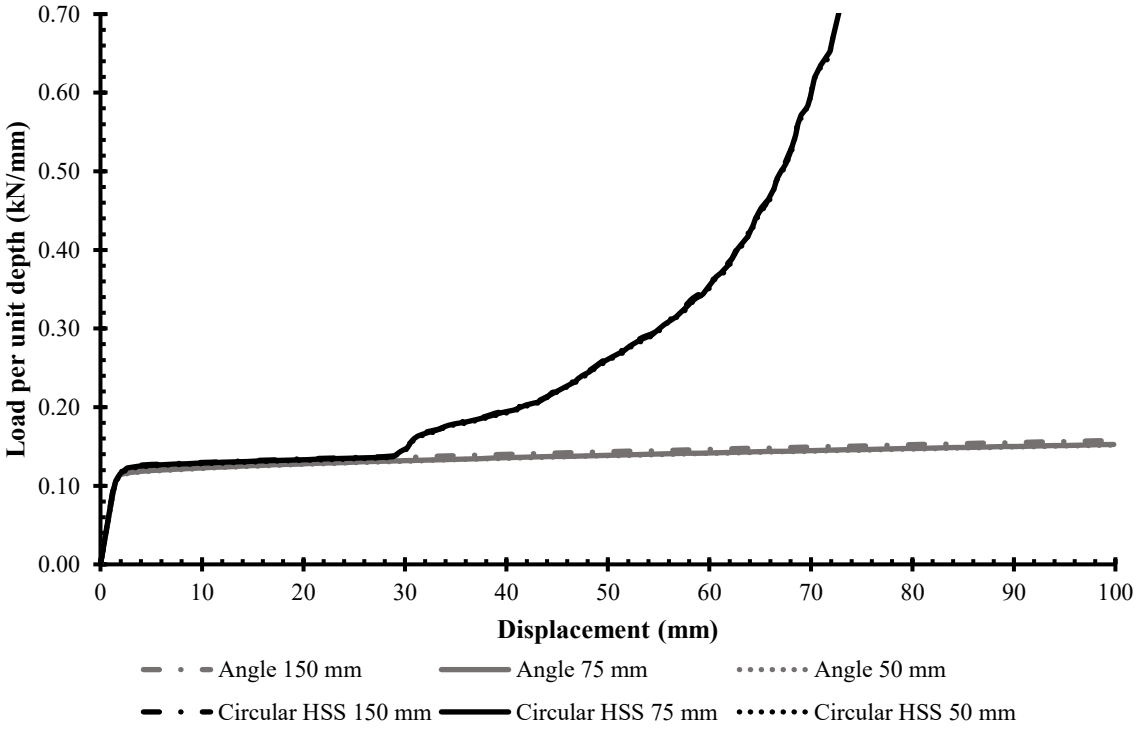

Figure 3.3: Scalability verification

3.2.4 Summary of Preliminary Results

Results obtained from the FEA models are presented based on the cross-sectional shape being analyzed. Individual results of each model can be found in Appendix A with sketches of dimensions and images of the shape before and after analysis. It should be noted that the actual

force in the EAC connection is twice that shown in the load-displacement graphs due to symmetry boundary conditions.

3.2.4.1 Angles

Figure 3.4 shows the results for the EACs consisting of angles only (see Figure 3.1a), where the angle leg length (L_a) and thickness (t_a) was varied.

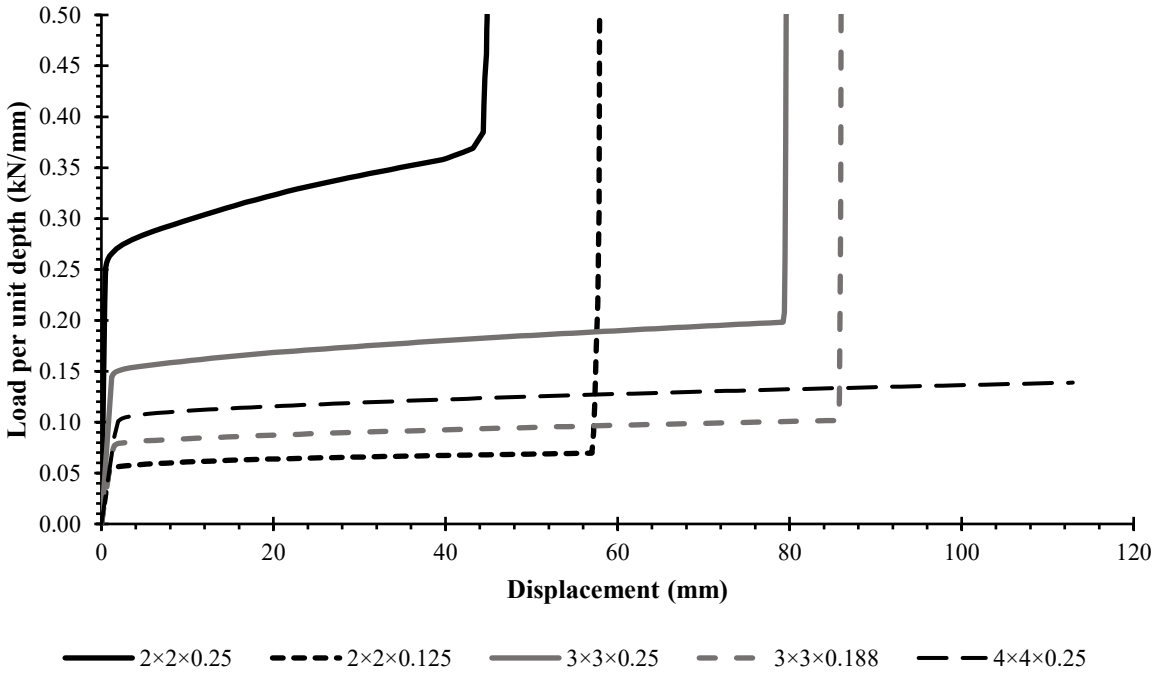

Figure 3.4: FEA results for angles

The observed load-displacement behaviour consisted of an initial elastic region followed by a plateau up to densification following the contact of the angles with the top and bottom steel plates. It is also observed that angles with smaller leg lengths or larger thickness are stiffer and have a larger yield load but have reduced densification displacement.

3.2.4.2 Welded Angles

Figure 3.5 shows the results for EACs constructed with angles that are welded at the center (see Figure 3.1b). A behaviour similar to that documented for angles without a center weld (i.e. Figure 3.3) is observed. Additionally, angles with different plate lengths have almost identical yield load, but increasing these lengths leads to greater densification displacement. Angles with smaller thicknesses have slightly larger densification displacement but a lower yield load.

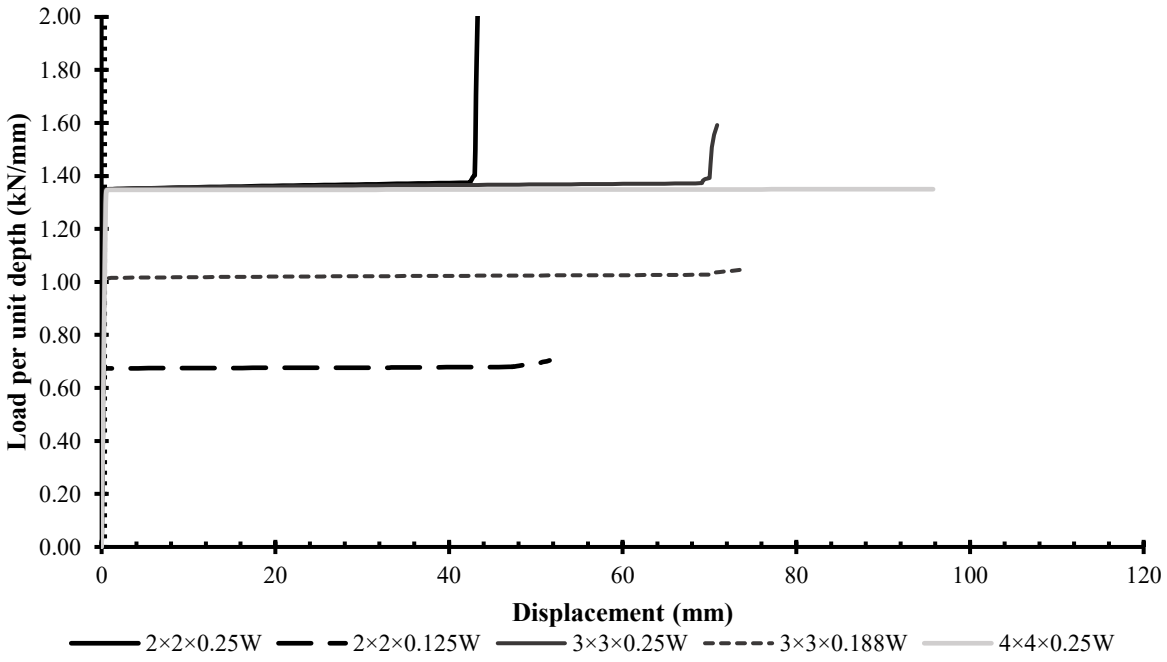

Figure 3.5: FEA results for welded angles

The results obtained for the EACs with angles and central plate (see Figure 3.1c) are presented in Figure 3.6. It is observed when comparing the results from Figure 3.5 and 3.3 that adding a central plate of varying length L_p does not affect the load-displacement behaviour for identical angles.

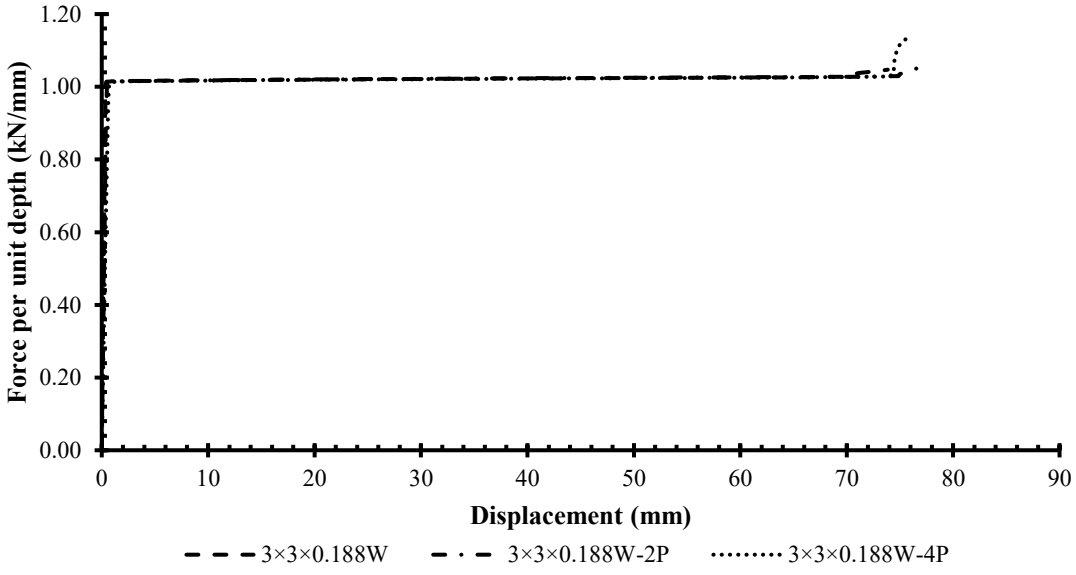

Figure 3.6: FEA results for angles with central plate

Figure 3.7 shows a comparison between EACs made of angles without a central weld, angles with a central weld, and with twice the angles and central welds (see Figure 3.1d). It is observed that EAC with central weld between angles are much stiffer and much stronger but have a slightly lower densification displacement than those without a weld. Yield loads and densification displacements were observed to be approximately 700% and 85%, respectively, when the additional central weld was provided. Doubling the quantity of angles while also providing welds between angles appears to provide similar densification displacement and increase the yield load proportionally by a factor of 2. The behaviour is consistent with additional models of different angle leg lengths, plate lengths and angle thicknesses presented in Appendix A.

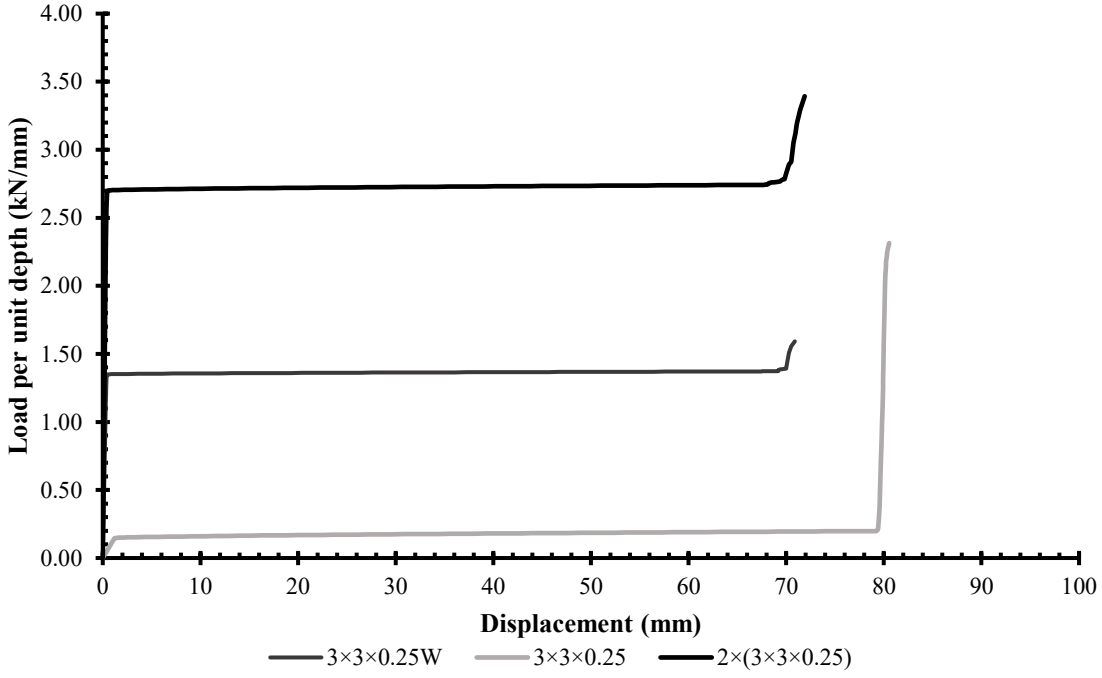

Figure 3.7: Comparison of angle geometry effects on results

3.2.4.3 Circular HSS

Figure 3.8 shows the FEA model results for EACs made of a single circular HSS (see Figure 3.1e) where the circular HSS outer diameters (⌀) and thickness (t_c) were varied.

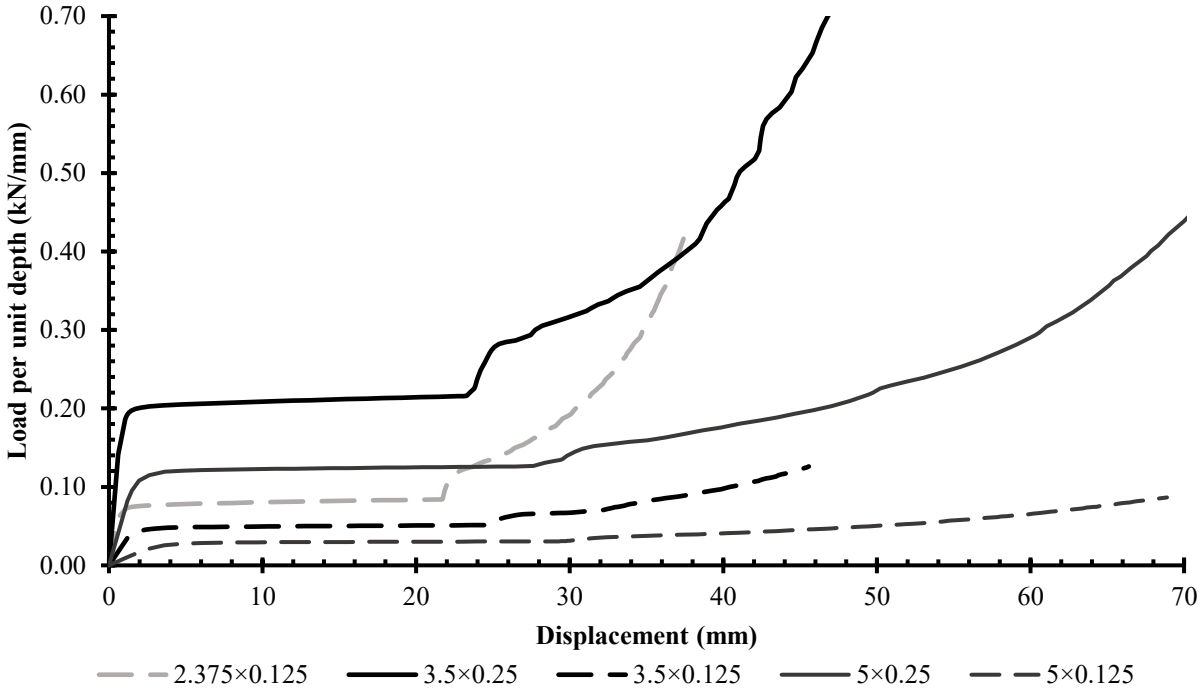

Figure 3.8: FEA results for circular HSS

Typical load-displacement behaviour is observed to consist of an initial elastic region, followed by a plateau. After a certain displacement, an increase in stiffness occurs. This stiffness is smaller than that observed in the elastic region. Stiffness then increases rapidly with densification following significant contact between the steel sections. Circular HSS with a smaller outer diameter or larger thickness is observed to have larger yield load as well as initial elastic and densification stiffnesses but lower densification displacement. The behaviour observed is consistent between different configurations.

Figure 3.9 shows the effect of using an arc of the circular HSS of varying interior angles (θ) as shown in Figure 3.1f. The corresponding results for the full circular HSS, as shown in Figure 3.1e, are also presented in Figure 3.8 for comparison.

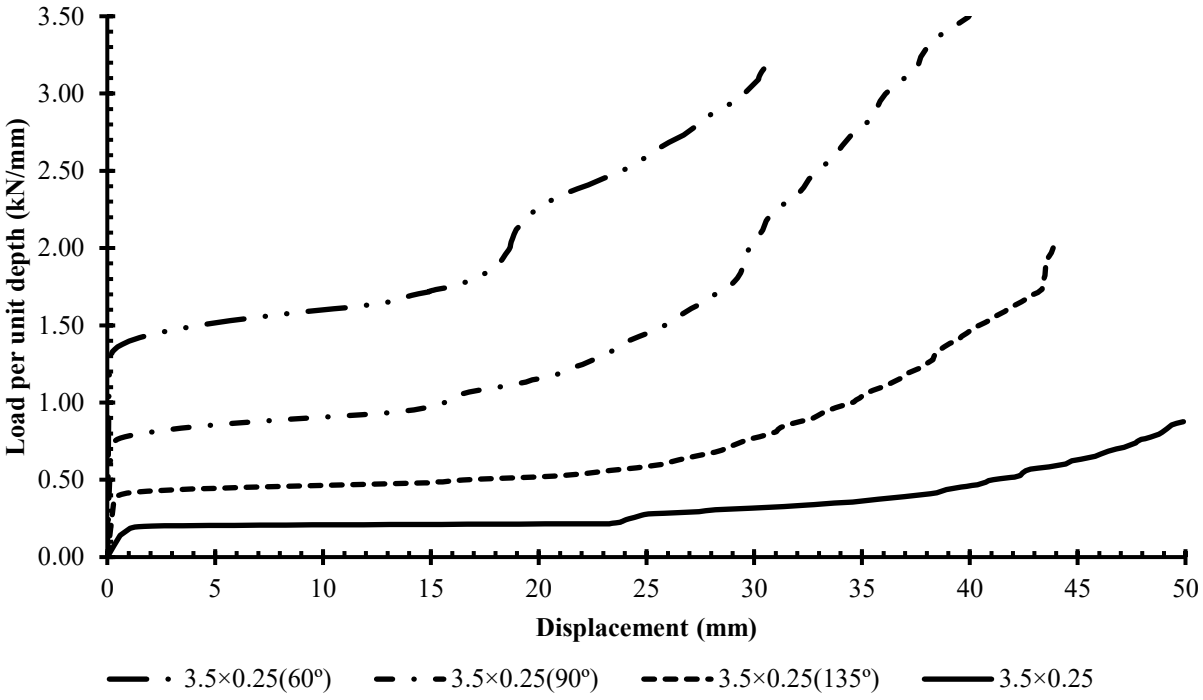

Figure 3.9: FEA results for circular HSS arcs

It can be observed that the EAC manufactured from two arcs of a circular HSS will have similar load-displacement behaviour to the full circular HSS EAC. However, reducing the interior angle results in stiffer initial elastic and densification regions causes an increase in the yield load, and reduces the densification displacement. The observed behaviour is consistent for circular HSS of different outer diameters and thicknesses, as presented in Appendix A.

3.2.4.4 Multiple Circular HSS

Figure 3.10 and Figure 3.11 show the FEA model results for EACs constructed with 2 and 3 circular HSS, respectively (see Figure 3.1g).

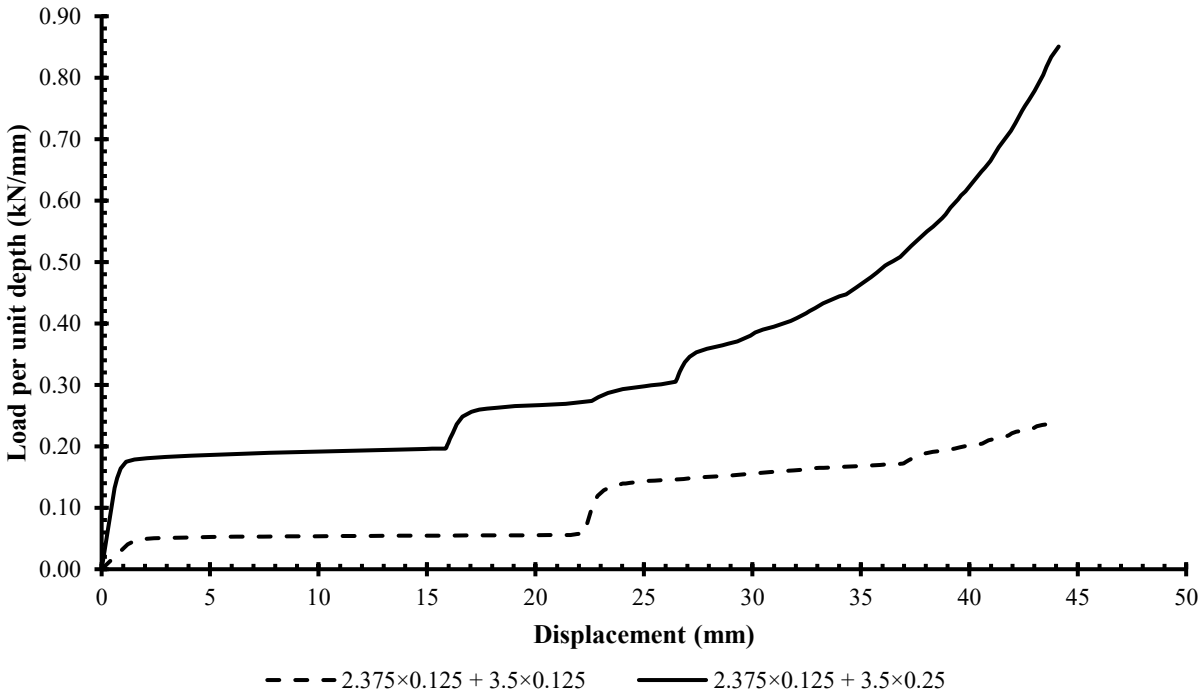

Figure 3.10: FEA results for 2 circular HSS

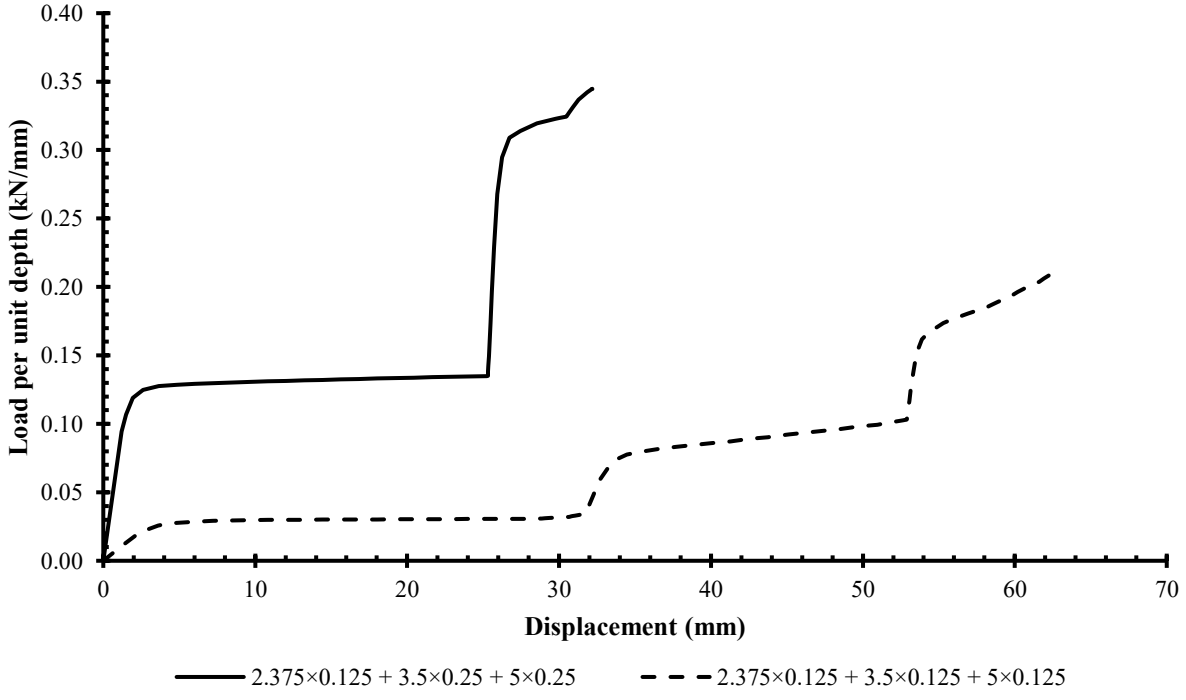

Figure 3.11: FEA results for 3 circular HSS

It can be observed that adding circular HSS will cause a staggered increase in the yield load triggered by the contact of each circular HSS with the section above. Figure 3.12 shows that adding the individual load-displacement curves for each circular HSS approximates the load-displacement curve of the entire model.

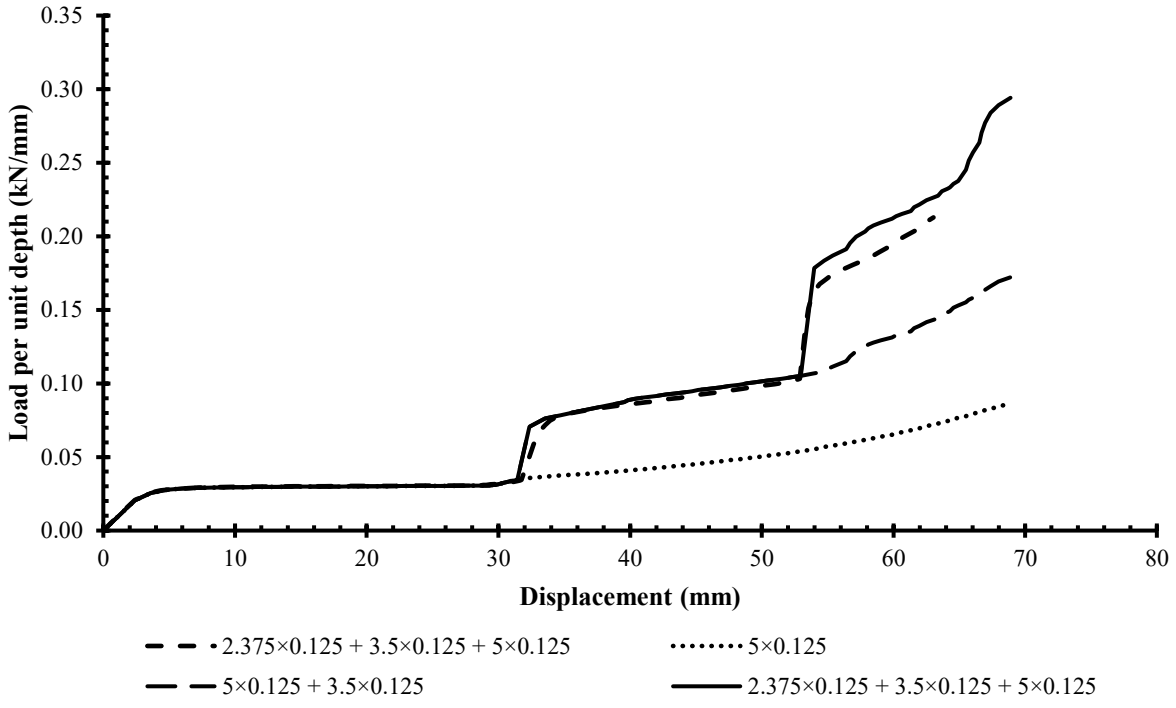

Figure 3.12: Comparison of results for multiple circular HSS

3.2.4.5 Angles and Circular HSS

Figure 3.13 and Figure 3.14 show the FEA results for EACs made of a combination of angles and circular HSS (see Figure 3.1h).

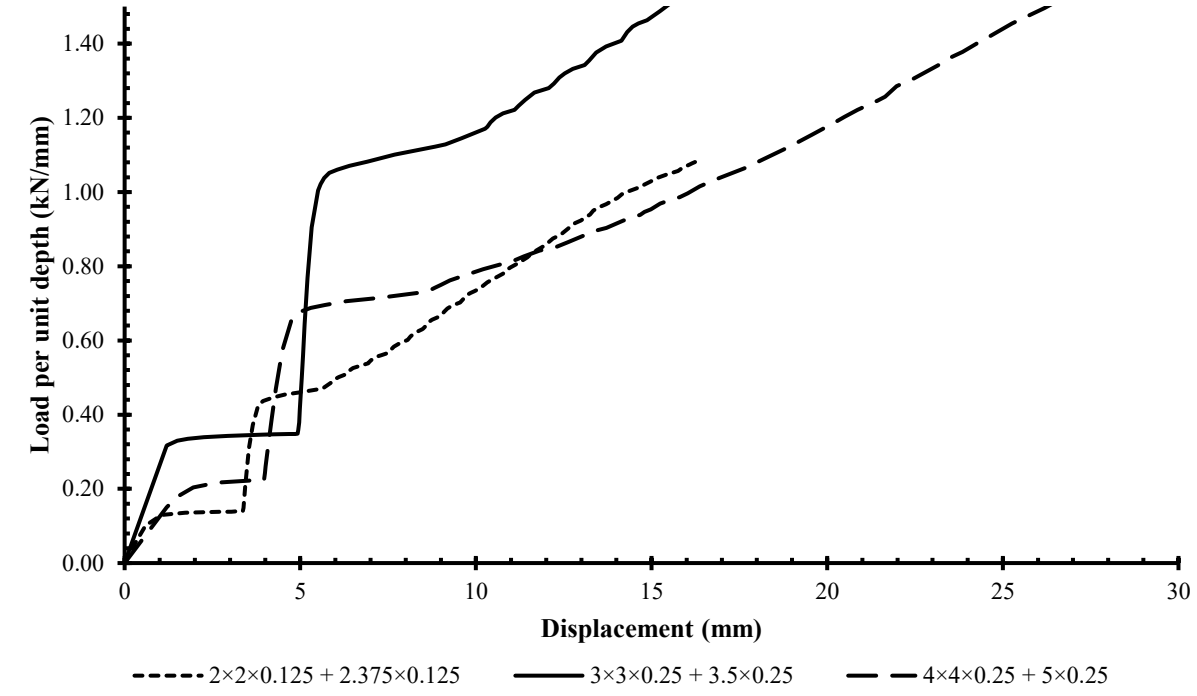

Figure 3.13: FEA results for angles plus circular HSS

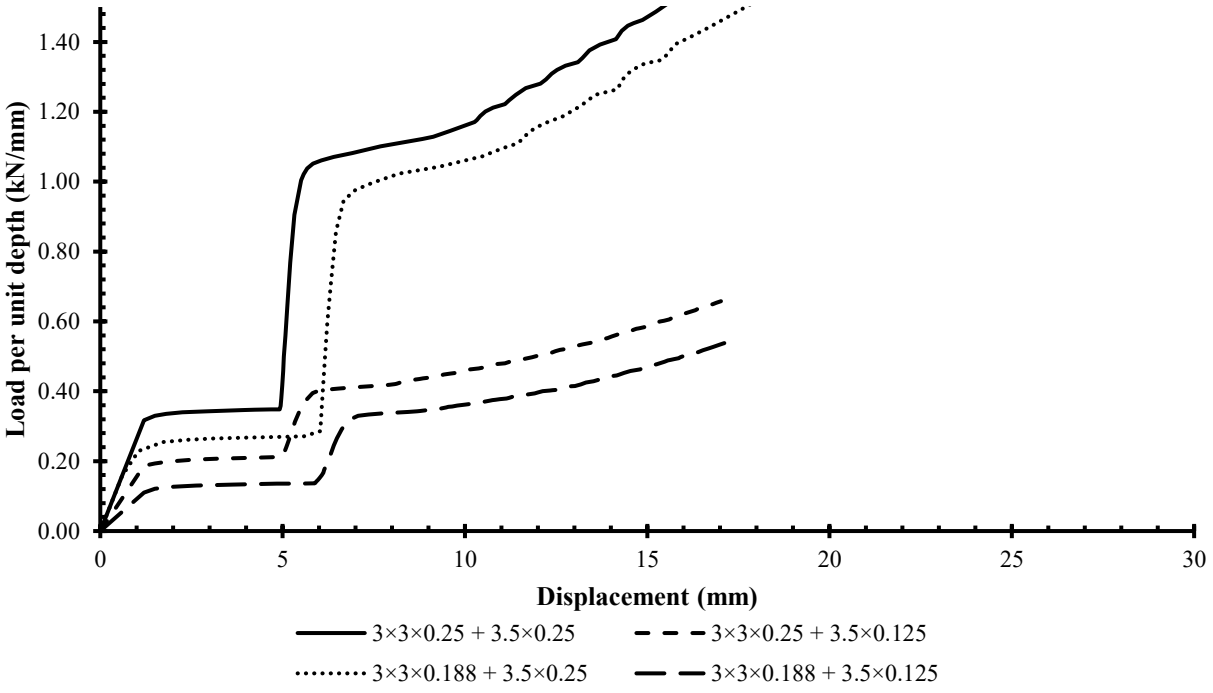

Figure 3.14: Effect of thickness variation

Typical load-displacement behaviour is observed to consist of an initial elastic region followed by an initial plateau. Once the circular HSS comes in contact with the top plate, a secondary elastic region is observed, followed by a short region with stiffness lower than the elastic region but larger than the initial plateau. Densification then occurs, increasing the stiffness of the connection rapidly at large displacements. It can also be observed that increasing thicknesses, decreasing the outer diameter or decreasing the leg length will result in an increase in stiffness and force capacities and a decrease in the densification displacement capacities. This is consistent with additional models of similar geometry presented in Appendix A.

Figure 3.15 shows a comparison of the EAC with both angles and a circular HSS (i.e. Figure 3.1h) with EACs made up of only angles (i.e. Figure 3.1a) or a circular HSS (i.e. Figure 3.1e). It can be observed that the results from the model with both angles and circular HSS do not add up to the sum of an angle and circular HSS on their own, as was the case for EACs with multiple circular HSS. This seems to indicate that the EAC made up of both angles and circular HSS is much stiffer, stronger but has a much lower densification displacement.

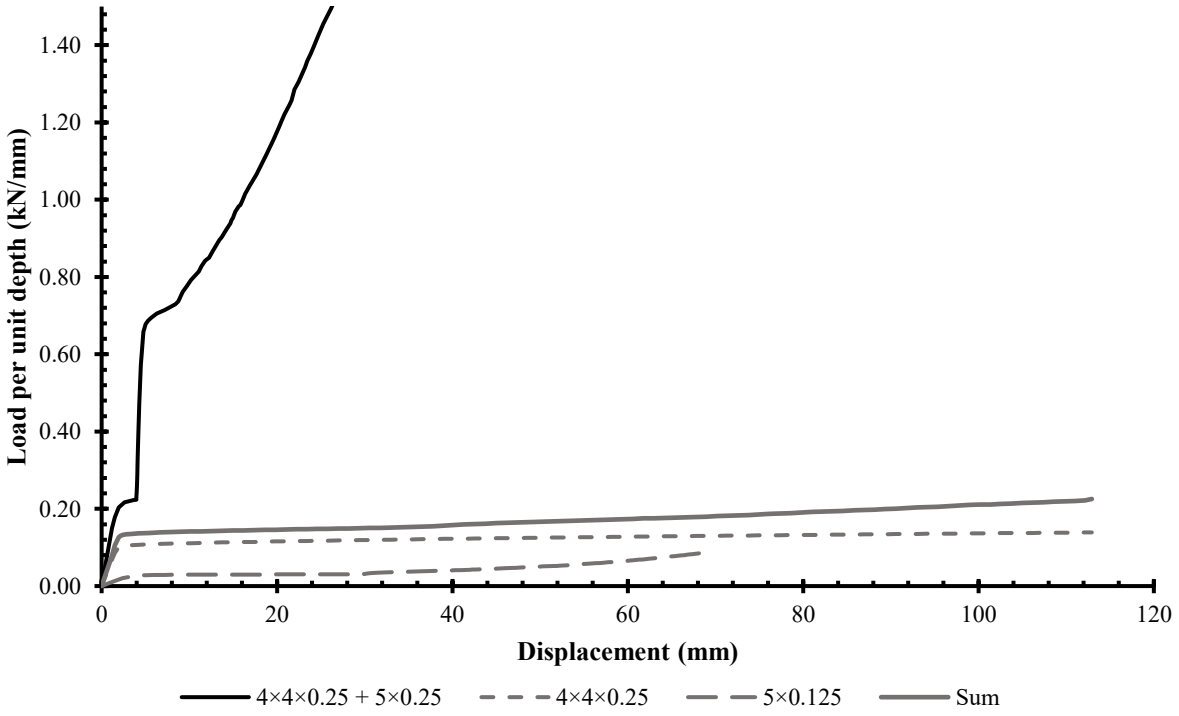

Figure 3.15: Comparison with constituting parts

3.3 Specimen Selection

Based on the preliminary FEA modelling presented in this Chapter, nine connection configurations were selected to experimentally investigate the effects of geometry on the load-displacement behaviour. For this comparison, all connections were chosen to have a depth of 50.8 mm (2”) except where otherwise indicated.

Four EAC specimen were selected to comprise of steel angles based on the observed ductile behaviour, and ease of manufacturing. An angle with a leg length of 76.2 mm [3”] and thickness of 6.35 mm [0.25”] was selected as a baseline reference. The leg length and thicknesses were then varied to 50.8 mm [2”] and 12.7 mm [0.50”] to compare the load-displacement behaviour obtained from these variations with that of the baseline specimen. It should be noted that the 12.7 mm thick angle was not analyzed in the preliminary FEA and was selected based on the availability of steel sections. The fourth specimen consisted of the baseline EAC modified by adding a central weld to investigate potential strengthening effects of the central weld.

EACs with a central plate were not selected due to the preliminary modelling showing that they did not considerably affect the load-displacement behaviour. Similarly, the EACs consisting of four angles were not selected due to the load-displacement behaviour being proportional to the number of pairs of angles.

EACs made of circular HSS were selected for their ductile behaviour and ease of manufacturing. Five specimens were based on this type of connection, with a baseline reference specimen consisting of 50.8 mm [2”] depth, 88.9 mm [3.5”] outer diameter and 6.35 mm [0.25”] thickness. The specimen depth was varied to 101.6 mm [4”] to investigate the experimental scalability of connections based on depth and to verify the FEA scalability. Also, the specimen outer diameter was varied to 127 mm [5”] to investigate its effect on the connection behaviour. EACs consisting of two 90° arcs of 88.9 mm [3.5”] outer diameter circular HSS were selected to investigate the effects of interior angle on the connection behaviour. Finally, EACs made of an additional 60.325 mm [2.375”] outside diameter and 3.175 mm [0.125”] thick circular HSS was selected to investigate the effects of adding multiple circular HSS in a single connection. EACs consisting of both angle and circular HSS were not selected due to the low ductility observed in this connection configuration.

Based on the preliminary analysis and observations made in this Chapter, the selected specimen types for the experimental program are presented in Table 3.3. Drawings of the selected EACs can be found in Appendix B.

Table 3.3: Selected specimen type for experimental program

Specimen type	Description	Sizes*	
Ia	Angle EAC	L_a = 76.2 mm t_a = 6.35 mm	
Ib	Angle EAC	L_a = 50.8 mm t_a = 6.35 mm	
Ic	Angle EAC	L_a = 76.2 mm t_a = 12.7 mm	
Id	Angle EAC welded at the center	L_a = 76.2 mm t_a = 6.35 mm	
IIa	Circular HSS EAC	⌀ = 88.9 mm t_c = 6.35 mm	
IIb	Circular HSS EAC	⌀ = 88.9 mm t_c = 6.35 mm d = 101.6 mm	
IIc	Circular HSS EAC	⌀ = 127.0 mm t_c = 6.35 mm	
IId	Circular HSS 90º arc EAC	⌀ = 88.9 mm t_c = 6.35 mm θ = 90°	
IIe	Two circular HSS EAC	Larger Circular HSS	Smaller Circular HSS
		⌀ = 88.9 mm t_c = 6.35 mm	⌀ = 60.325 mm t_c = 3.175 mm

*Depth (d) is 50.8 mm unless otherwise noted.

3.4 Specimen Design and Manufacturing

Additional design specifications were considered prior to manufacturing. An approximate weld yield load was verified against the maximum yield load of each EAC to ensure that weld failure would not occur. The approximate weld yield load was calculated according to CSA W59-13 equations for statically loaded steel filet welds (Figure 3.16). Each joint would have two welds (one on each side), and all specimens had two joints (two at the bottom plate and two at the top plate). Welds were specified as double fillet welds with complete penetration of the joint. The base

metal (steel sections) shear yield load and the weld shear yield load were calculated according to Equation 3.1 and Equation 3.2, respectively.

$$V_{base} = \min \begin{cases} 0.4 S_1 \ell F_{y1} \\ 0.4 S_2 \ell F_{y2} \end{cases} \quad \text{Equation 3.1}$$

$$V_{weld} = 0.3 t_w \ell X_u \quad \text{Equation 3.2}$$

Where S_1 and S_2 are the effective sizes of leg of fillet for each section material joined together, ℓ is the length of the weld, F_{y1} and F_{y2} are the base metal yield strengths, t_w is the effective throat of the weld, and X_u is the ultimate tensile strength.

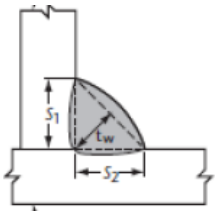

Figure 3.16: Fillet weld cross-section (CSA W59-13)

To compute approximate strength values, S_1 and S_2 were assumed to be 6.35 mm [0.25”], yielding a value for t_w of 4.49 mm [0.176”], while F_{y1} and F_{y2} were approximated at 300 MPa for 44W steel. X_u was assumed to be 490 MPa which was assumed representative of the typical electrode grades used in manufacturing. From these assumptions, the shear force resistance of the weld was found to govern the capacity at a value of 33.5 kN per 50.8 mm long weld. Each connection has four welds to resist the forces being transferred from the plates to the center steel sections. The following table shows the approximate maximum yield load of each specimen selected based on a depth of 50.8 mm, the shear force applied on each weld, and the factor of safety against weld failure prior to connection densification.

Table 3.4: Weld force capacity verification

Specimen	Maximum capacity (kN)	Maximum force per weld (kN)	Factor of safety
Ia	20	5	6.70
Ib	40	10	3.35
Ic	100	25	1.34
Id	140	35	0.96[a]
IIa and IIb	30	7.5	4.47

IIc	20	5	6.70
IId	60	15	2.23
IIe	40	10	3.35

a. This connection had a factor of safety slightly below 1.0. It was assumed to be adequate due to the approximative nature of these calculations and it being close to 1.0.

Steel sections of weldable grade (i.e. 44W/300W) were ordered and cut to length corresponding to the connection depth. To reduce the likelihood of warping during welding due to high temperatures, the steel sections were first spot welded in a jig and then entirely welded at the joints. An example of the jigs is shown in Figure 3.17. This jig was modified for each EAC type and could accommodate multiple geometries. Figure 3.18 and Figure 3.19 show typical welding jig set-up for EACs made of angles and circular HSS, respectively. After welding, the specimens were grinded to ensure that the top surface of the top plate and the bottom surface of the bottom plate were smooth. Connections were finally painted yellow to make them more visible in recordings or pictures during or after testing.

Figure 3.17: Welding jig

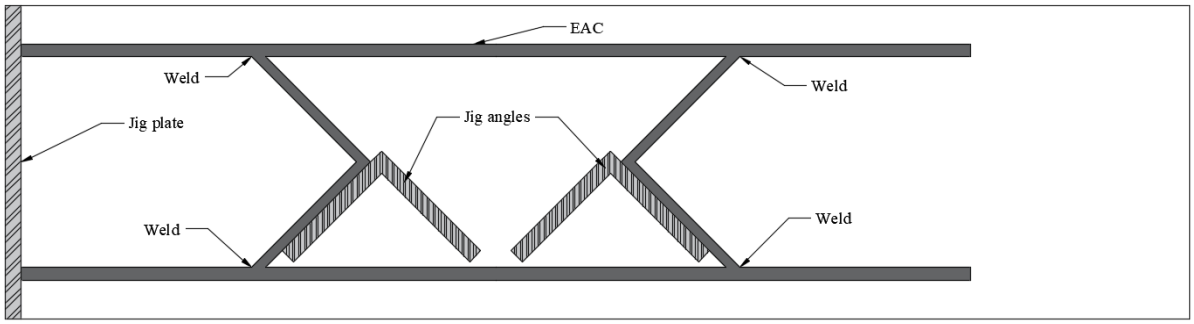

Figure 3.18: Welding jig for angle EAC

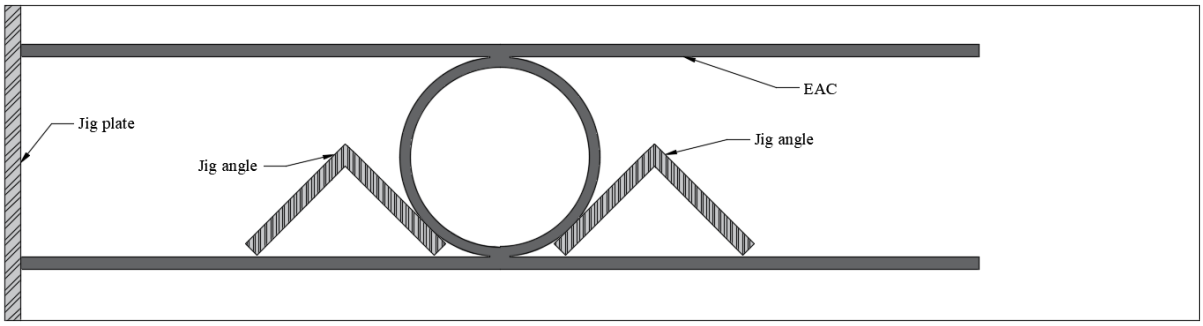

Figure 3.19: Welding jig for circular HSS EAC

CHAPTER 4 - Experimental Program

4.1 General

The experimental component of this project consisted of static and dynamic testing of individual connections. For each of the nine EAC shapes and configurations selected in Chapter 3, two were tested statically, and two were tested dynamically, yielding a total of 36 specimens. Tensile coupon testing of samples of the steel used in manufacturing was also performed. This chapter will present the methodology, description and setup of the testing performed.

4.2 Static Tests

A total of 18 specimens were tested under static loading using the universal testing machine (UTM) at the University of Ottawa structure's lab. The goal of this test was to determine the static force-displacement behaviour and deformed shape of each connection. The specimens were loaded using a displacement-controlled protocol with a constant rate of 4 to 10 mm/min, which was selected to be close to the requirement listed in ASTM E8/E8M (ASTM International 2021) since no standards on the static testing of EACs exist. Loads and displacements were recorded through the UTM systems, while the deformed shape was filmed throughout testing. The dimensions and mass of the specimens were measured and recorded prior to testing. Dimensions were measured with a calliper at an accuracy of ±0.01 mm. Mass was recorded with a scale at an accuracy of ±0.01 kg. Figure 4.1 shows the static test setup with specimen S-Ia-1 as an example.

Figure 4.1: Static test setup with specimen S-Ia-1

4.3 Dynamic tests

4.3.1 General

A total of 18 specimens were tested dynamically in the shock tube facility of the University of Ottawa to simulate blast loading conditions. The experimental setup and methodology of this test will be summarized and described in the following sections. Section 4.3.2 describes the shock tube facility. Section 4.3.3 describes the methodology and test setup.

4.3.2 Shock Tube Test Facility

The shock tube is a device that generates shock waves similar to those generated by far-field detonations of high explosives. The shock waves are generated by rapidly releasing compressed air through a double diaphragm mechanism. This mechanism consists of a spool section separated from the driver and expansion sections by two sets of aluminium sheet foils rated to resist different pressures. These foils are critical to the test since they allow the compressed air to be filled in both the driver and spool sections. A combination of multiple foils can be used to achieve the large pressure resistance required. The first set of foils separates the driver from the spool sections, while

the second set of foils separates the spool from the expansion section. Figure 4.2 and Figure 4.3 shows pictures of the shock tube and its sections.

The pressure rating of the first set of foils is chosen to be lower than the difference in pressure between the spool and driver sections. To execute the test, air that has been compressed in the spool section is first released, thus causing these foils to rupture by a combination of overpressure and suction. This mechanism causes the air in the driver section to travel rapidly towards the expansion section, resulting in the second set of foils to rupture subsequently. The shock wave travels through the 6096 mm [20 ft] long expansion section and applies a reflected pressure onto the end frame. The shock tube is also designed to allow air to evacuate through twelve small vents on its sides, facilitating negative pressures to be generated during testing.

A load transfer device (LTD) is attached to the 2032 mm [6ft 8 in] × 2032 mm [6ft 8 in] end frame in order to transfer the pressure to the specimens. The LTD consists of steel panels connected to the end frame through slotted hinges that can rotate out of plane. When subjected to pressure, rotation of the hinges allows the LTD to translate by up to 200 mm [8 in], which allows the transfer of the pressure onto the mounted specimen.

Storing different amounts of compressed air in the driver section allows for different reflected pressures and impulse combinations to be simulated. This can be achieved by changing the driver length or changing the compressed air pressure. The University of Ottawa shock tube can accommodate driver lengths varying from 305 mm [1 ft] to 5185 mm [17 ft]. Additionally, it can produce reflected pressures and impulses up to about 100 kPa and 2200 kPa-ms, respectively. The positive phase duration of the shock wave generated can range between 5 ms and 70 ms. The driver length used in this project's shock tube testing was 2743 mm [9 ft].

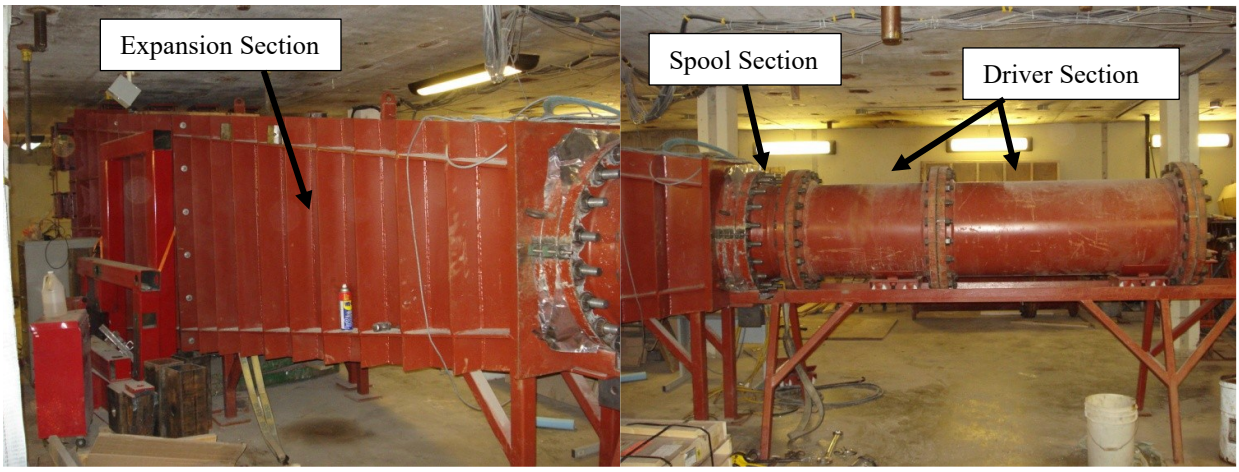

Figure 4.2: Shock tube (Lacroix 2013)

Figure 4.3: Shock tube internal view and end frame

4.3.3 Test Setup

The dynamic test setup, including the LTD and reaction frame to support the specimen, are shown in Figure 4.4 (without specimen) and Figure 4.5 (with specimen). The LTD used included a single load transfer beam at its center, allowing the pressure to be transferred to a single concentrated point load at the center of the load transfer beam. A reaction frame was installed to provide support and the proper boundary conditions for the specimens. A plate was installed between the LTD beam and the specimen to transfer forces while permitting free rotation. Shim plates were also used to ensure that the specimen was snug between the rotating plate and reaction frame. This setup was selected to establish a similar testing methodology to static testing, where forces are transferred through the specimen top and bottom surfaces. Figure 4.6 shows a sketch of the shock tube test setup used in this study.

The steel reaction frame system consisted of two vertical 152.4 mm × 76.2 mm HSS members, each with a top and bottom bracing system consisting of a 76.2 mm × 76.2 mm × 6.4 mm angle cross brace and tension chord. Additionally, the two vertical members are connected near their center by two horizontal 152.6 mm × 152.6 mm HSS beams. The horizontal beams each have a *Revere Model 92/93* compression load cell attached at their center, connected to a stiffened vertical 106 mm W element. This element is in contact with the specimen and supports the force transferred through the specimen to the reaction frame. The vertical members and the ends of the truss system were blocked against the floor and ceiling of the laboratory. Horizontal forces transferred through the reaction frame are partially resisted by friction at the blocking points. For this to work, the blocking must be extremely snug to minimize movement of the reaction frame during testing. The horizontal forces are also resisted by eight steel rods connecting the vertical members to the shock tube.

Since some horizontal movement was anticipated in the supporting frame, the horizontal displacement of the reaction frame was measured during testing with a linear variable differential transducer (LVDT) attached to the W vertical element. Also, the specimen displacement was measured with an LVDT attached to a plate located between the specimen and the LTDs rotating plate. Both LVDTs used to measure the specimen and reaction frame displacements were installed at the center of a post located between the vertical HSS members. Finally, the shock tube displacement was measured with an LVDT attached to the shock tube near the laboratory floor.

The difference between the specimen displacement and the sum of displacements from the reaction frame and shock tube provides the actual displacement of the specimen. The load experienced by the specimen during testing was determined by the load cells. Reflected pressure was measured during testing by two dynamic piezoelectric pressure sensors. These sensors were installed at the bottom and side of the shock tube, near the end frame. All data acquired during testing were recorded at a time interval of 2 ms, equivalent to 2000 sample points per second. Before testing, the dimensions and mass of specimens were measured.

Two *Phantom VEO 410L* high-speed cameras were also used to record the experiment with 2000 frames per second. Three measures were taken to improve clarity during recording. The first measure was to paint the specimens yellow to provide better contrast, while the reaction frame was painted in red. The second measure was to use two *Nila Boxer* 200W LED lighting fixtures (one for each camera) to provide brighter pictures. The cameras were linked to the pressure sensors, and a trigger mechanism was used so that the cameras only started recording when the reflected pressure reached the end frame. Finally, a non-reflecting tape (painter's tape) was applied to the highly reflective reaction frame surfaces to avoid flashes in the picture.

Figure 4.4: Dynamic test setup

Figure 4.5: Specimen in test set up

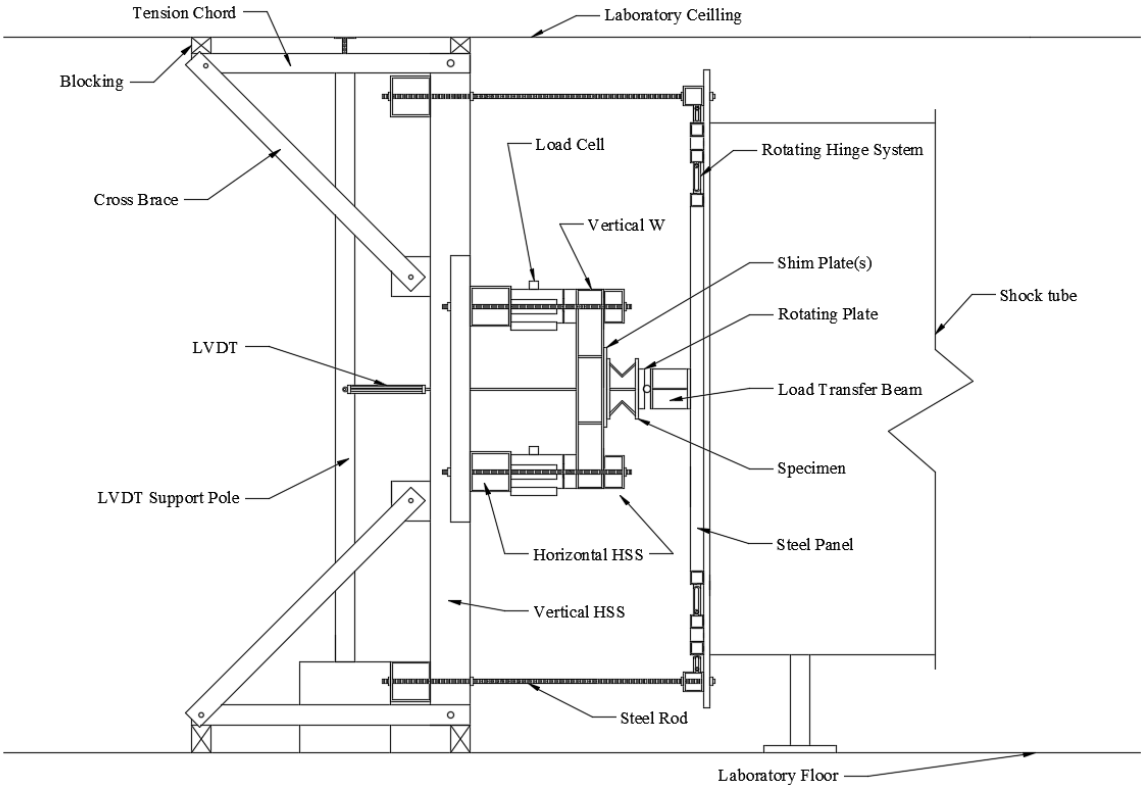

Figure 4.6: Shock tube test setup sketch

4.4 Tensile Coupon Tests

Tensile coupon tests were performed according to ASTM E8/E8M (ASTM International 2021) using the UTM of the University of Ottawa's structures laboratory. A 25 mm strain gauge was used to measure elongation, while loads were measured with the UTM machine. A coupon specimen was taken from each length of steel ordered, except for the plates where only one coupon was taken out of the multiple lengths received. Figure 4.7 shows the tensile coupon test setup with a ruptured specimen.

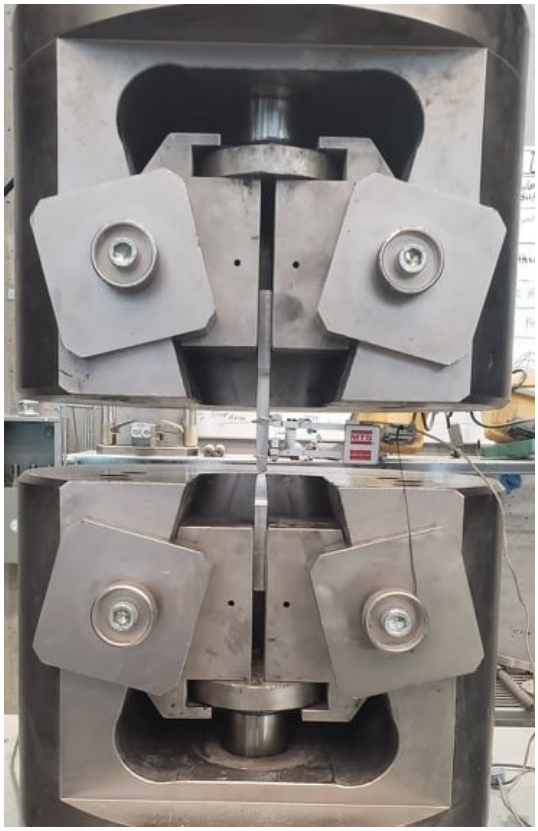

Figure 4.7: Tensile coupon test setup

CHAPTER 5 - Experimental Results

5.1 General

This chapter presents the results of the experimental program described in Chapter 4. Measured dimensions and masses are first presented in Section 5.2, while the experimental results of static and dynamic testing are presented in Section 5.3 and 5.4, respectively.

5.2 As-built Dimension and Mass Measurements

For each specimen type, dimensions were measured for the four replicate specimens (two static and two dynamic) at various locations for width, height, and depth. The average and coefficient of variation (CoV) for the measured dimension are presented for each EAC specimen type in Table 5.1.

Table 5.1: EAC specimen as-built dimensions

Specimen Type	Width - w		Height - h		Depth - d	
	Average (mm)	CoV (%)	Average (mm)	CoV (%)	Average (mm)	CoV (%)
Ia	231.84	0.14	126.33	0.31	50.79	0.24
Ib	205.85	0.30	89.78	0.37	50.79	0.26
Ic	229.96	0.67	125.39	0.59	50.64	0.17
Id	205.96	0.27	125.62	0.83	50.76	0.25
IIa	205.28	0.30	108.32	1.59	50.91	0.60
IIb	205.05	0.36	107.91	1.88	101.83	0.74
IIc	205.52	0.29	147.58	1.31	51.27	1.59
IId	205.17	0.75	107.74	1.19	50.86	0.40
IIe	205.53	0.39	108.72	1.62	51.07	1.03

The actual measured average thickness and respective CoV for each steel section used in the manufacturing of the specimens are presented in Table 5.2.

Table 5.2: Measured thicknesses of steel sections

Steel Section	Specimen Type	Average Thickness (mm)	CoV (%)
76.2×76.2×6.35 Angle	Ia, Id	6.51	2.21
50.8×50.8×6.35 Angle	Ib	6.42	1.99
76.2×76.2×12.70 Angle	Ic	12.79	1.78
9.525 Plate	All specimens	9.66	1.26
88.9×6.35 Circular HSS	IIa, IIb, IIc	6.19	3.60

127.0×6.35 Circular HSS	IIc, IId	6.17	3.58
60.325×3.175 Circular HSS	IIe	3.19	3.66

Table 5.3 presents the mass of each specimen type, the average mass for each specimen type, and the respective CoV.

Table 5.3: Measured mass of specimens

Specimen Type	**Specimen Mass (kg)**				**Average (kg)**	**CoV (%)**
	S-1	**S-2**	**D-1**	**D-2**		
Ia	2.51	2.50	2.50	2.50	2.50	0.17
Ib	2.04	2.04	2.04	2.03	2.04	0.21
Ic	3.14	3.16	3.16	3.16	3.16	0.27
Id	2.32	2.32	2.32	2.34	2.33	0.37
IIa	2.20	2.22	2.1	2.12	2.16	2.36
IIb	4.38	4.4	4.22	4.24	4.31	1.87
IIc	2.52	2.52	2.42	2.42	2.47	2.02
IId	2.02	1.96	2.05	2.06	2.02	1.93
IIe	2.42	2.42	2.34	2.36	2.39	1.50

5.3 Static Test Results

5.3.1 Tensile Coupons Tests Results

Table 5.4 presents the measured yield and ultimate strength for the seven coupon specimens tested in tension, as well as the average and CoV of both parameters for each steel grade. The average yield strength for sections of grade 44W/300W and 1018 were measured to be 390 MPa and 385 MPa, respectively, with a CoV of 4.3% and 14.3%, respectively. The average ultimate strength for sections of grade 44W/300W and 1018 were measured to be 540 MPa and 445 MPa, respectively, with a CoV of 2.8% and 12.4%, respectively.

Table 5.4: Measured yield and ultimate strength

Coupon	Steel Section Shape	Steel Grade	Included in Specimen Type	Yield Strength (MPa)	Ultimate Strength (MPa)
1	101.6 mm Plate	44W/300W	IIa	360	525
2	50.8 mm Plate	44W/300W	All except IIa	390	500
3	76.2×76.2×6.35 mm Angle	44W/300W	I, Ic	400	530
4	50.8×50.8×6.35 mm Angle	44W/300W	Ia	410	540
5	76.2×76.2×12.7 mm Angle	44W/300W	Ib	390	540
			Average	390	527
			CoV (%)	4.3	2.8
6	88.9×6.35 mm Circular HSS	1018	II, IIa, IId	*	*
7	127×6.35 mm Circular HSS	1018	IIb, IIc	440	500
8	60.325×3.175 Circular HSS	1018	IId	330	390
			Average	385	445
			CoV (%)	14.3	12.4

*Coupon did not fit in the test setup, too short.

5.3.2 Connection-level Test Results

A total of 18 static connection-level static tests were conducted, which included two repeats for each of the nine specimen types. The following subsections summarize the experimental observations for each specimen type and present the measured load-displacement relationships. For further details, refer to Appendix C.

5.3.2.1 Specimen S-Ia-1 and S-Ia-2

Figure 5.1 shows the measured static load-displacement relationship for specimens S-Ia-1 and S-Ia-2. These specimens were manufactured from 6.35 mm thick angles with a leg length of 76.2 mm. The initial shape of the specimens, as well as the final deformed shape, are presented in Figure 5.2.

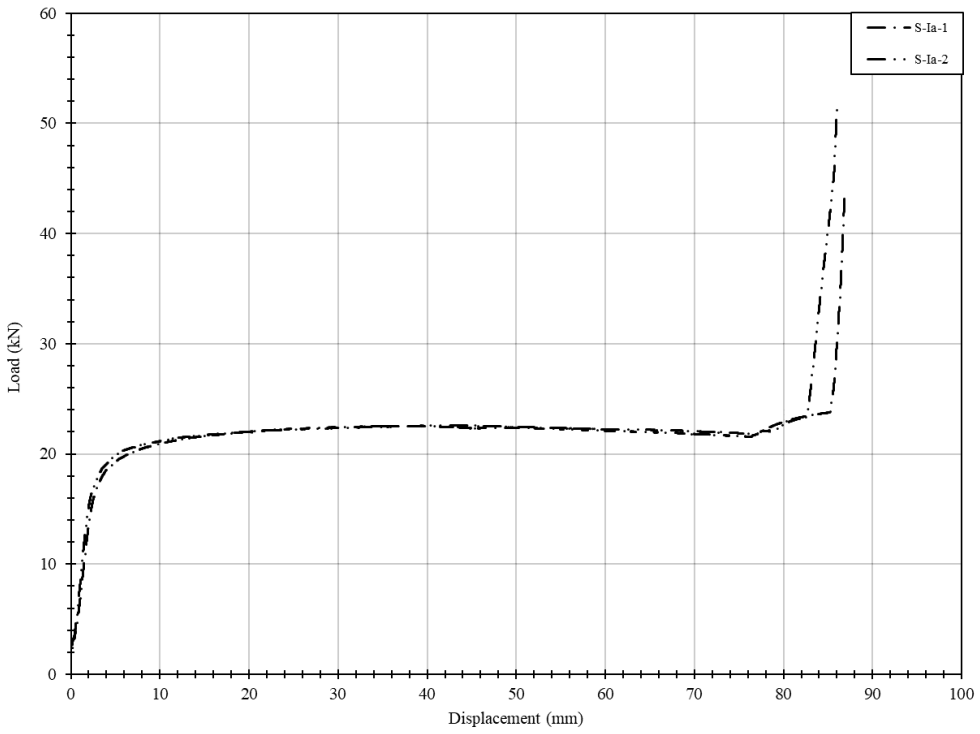

Figure 5.1: Static measured load-displacement curve for specimens S-Ia-1 and S-Ia-2

S-Ia-1 **S-Ia-2**

(i) Initial Shape

(ii) Deformed Shape

Figure 5.2: Initial and deformed shape of specimens S-Ia-1 and S-Ia-2

5.3.2.2 Specimen S-Ib-1 and S-Ib-2

Figure 5.3 presents the measured static load-displacement relationship for specimens S-Ib-1 and S-Ib-2. Specimen type Ib consisted of angles with leg lengths of 50.8 mm instead of the 76.2 mm leg lengths provided in specimen type Ia. The initial shape of the specimens, as well as the final deformed shape, are presented in Figure 5.4. Similar results to specimen type Ia were observed.

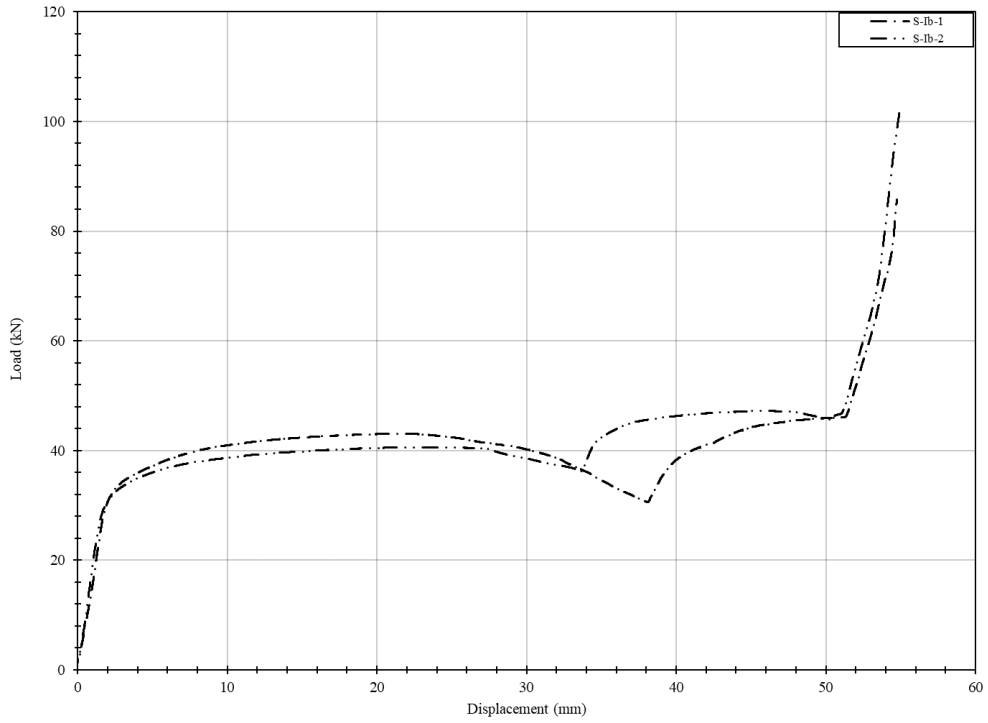

Figure 5.3: Static measured load-displacement curve for specimens S-Ib-1 and S-Ib-2

Ib-S-1 **Ib-S-2**

(i) Initial Shape

(ii) Deformed Shape

Figure 5.4: Initial and deformed shape of specimens S-Ib-1 and S-Ib-2

5.3.2.3 Specimen S-Ic-1 and S-Ic-2

Figure 5.5 shows the measured static load-displacement relationship for specimens S-Ic-1 and S-Ic-2. Specimen type Ic consisted of angles with a thickness of 12.7 mm instead of the 6.35 mm of specimen type Ia. Figure 5.6 shows the typical initial shape and deflected shape of the specimens. Similar behaviour to specimen Ia and Ib was observed.

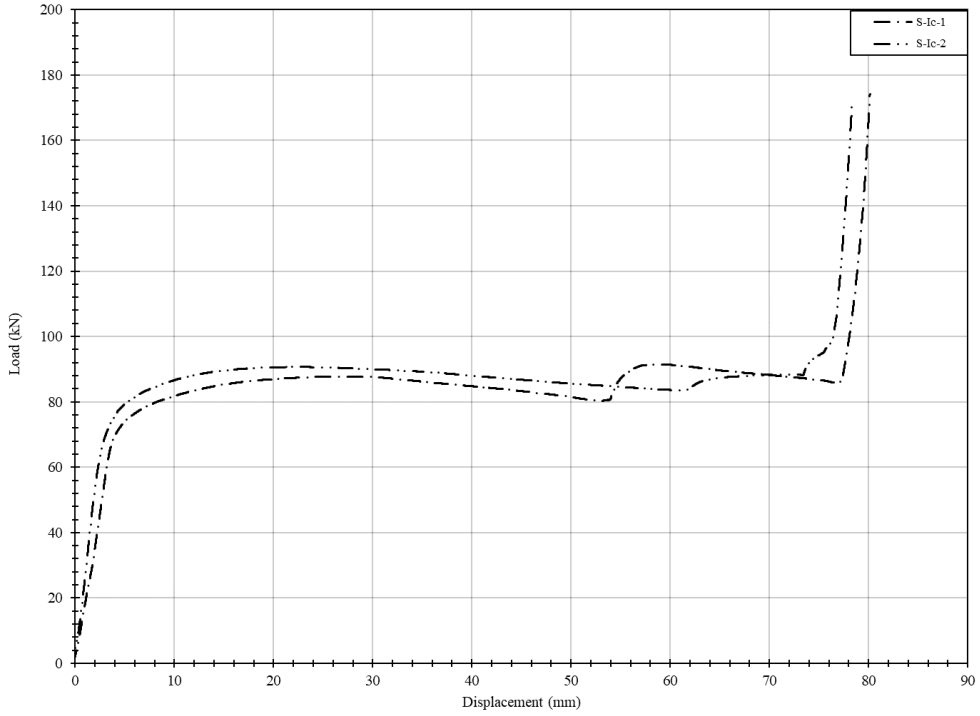

Figure 5.5: Static measured load-displacement curve for specimens S-Ic-1 and S-Ic-2

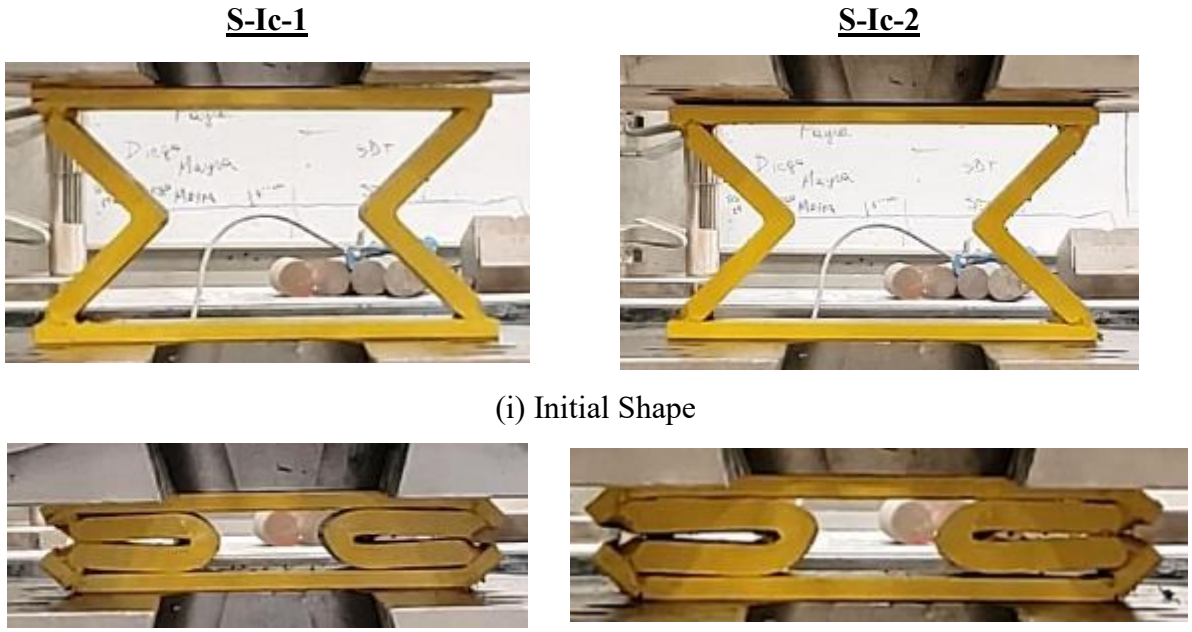

Figure 5.6: Initial and deformed shape of specimens S-Ic-1 and S-Ic-2

5.3.2.4 Specimens S-Id-1 and S-Id-2

Figure 5.7 shows the measured static load-displacement relationship for specimens S-Id-1 and S-Id-2. Specimen type Ic was identical to specimen type Ia, but a centre weld was provided. A significantly different behaviour compared to the previous specimens was observed for this specimen. Figure 5.8 shows the typical initial shape and deflected shape of both specimens.

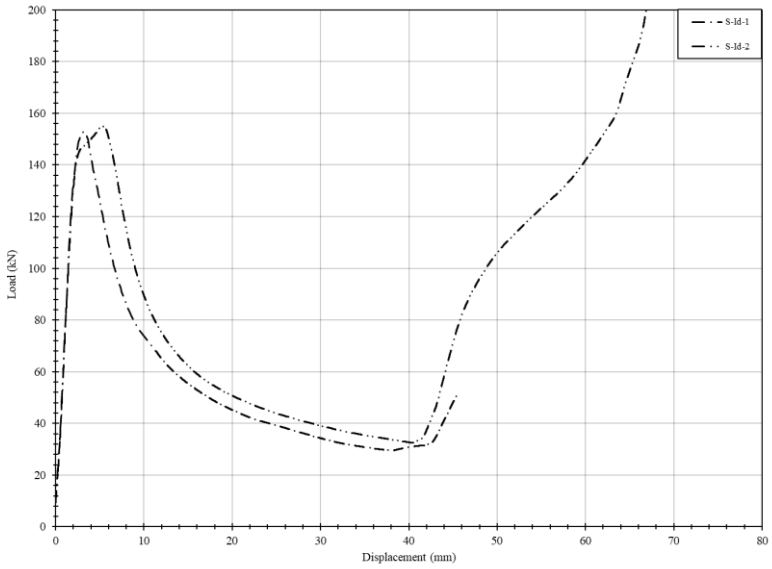

Figure 5.7: Static measured load-displacement curve for specimens S-Id-1 and S-Id-2

S-Id-1 **S-Id-2**

(a) Initial Shape

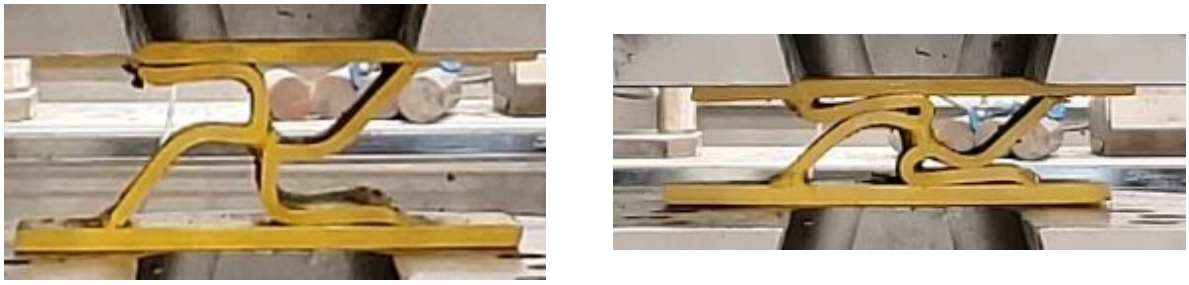

(ii) Deformed Shape

Figure 5.8: Initial and deformed shape of specimens S-Id-1 and S-Id-2

5.3.2.5 Specimens S-IIa-1 and S-IIa-2

Figure 5.9 shows the measured static load-displacement relationship for specimens S-IIa-1 and S-IIa-2. These specimens consisted of a circular HSS with an outer diameter of 88.9 mm. Figure 5.10 shows the initial and deformed shape of both specimens. A slight decrease in load following yielding was observed, which was contrary to specimen types Ia, Ib, and Ic, but this drop was not as significant as specimen type Id.

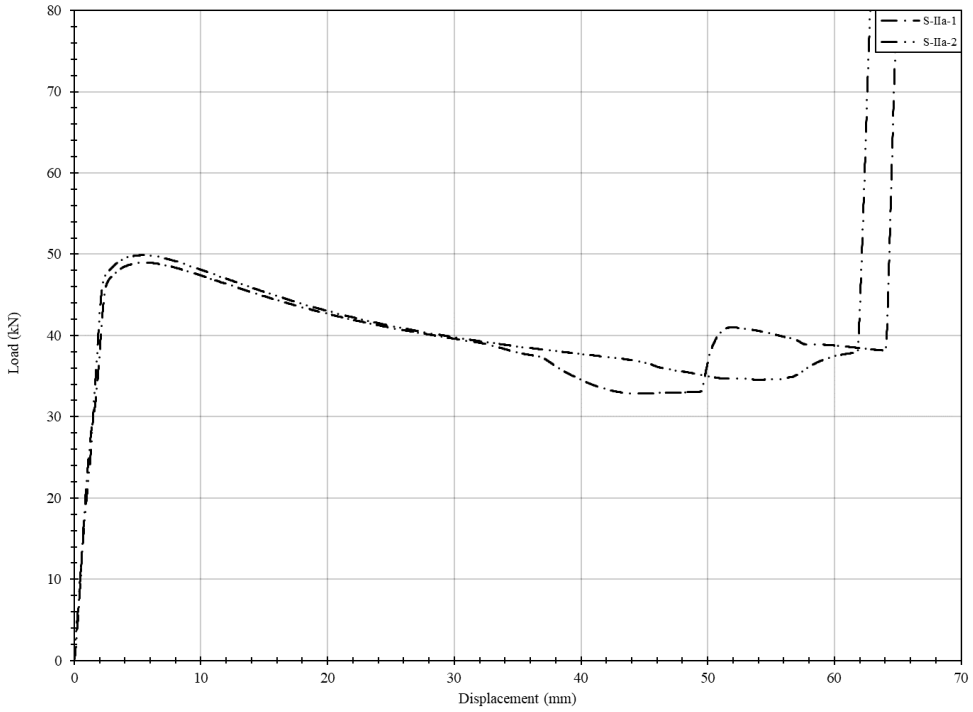

Figure 5.9: Static measured load-displacement curve for specimens S-IIa-1 and S-IIa-2

S-IIa-1 **S-IIa-2**

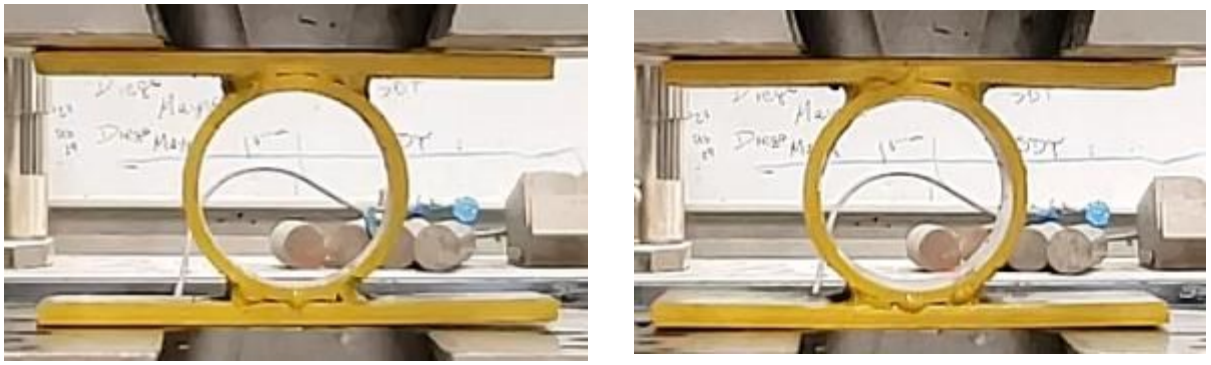

(a) Initial Shape

(ii) Deformed Shape

Figure 5.10: Initial and deformed shape of specimens S-IIa-1 and S-IIa-2

5.3.2.6 Specimens S-IIb-1 and S-IIb-2

Figure 5.11 shows the measured static load-displacement relationship for specimens S-IIb-1 and S-IIb-2. This specimen type had a depth of 101.6 mm, in contrast with the 50.8 mm for all other specimen types, and was otherwise identical to specimen type IIa. Figure 5.12 shows the initial and deformed shape of these specimens. Similar behaviour to specimen type IIa was observed.

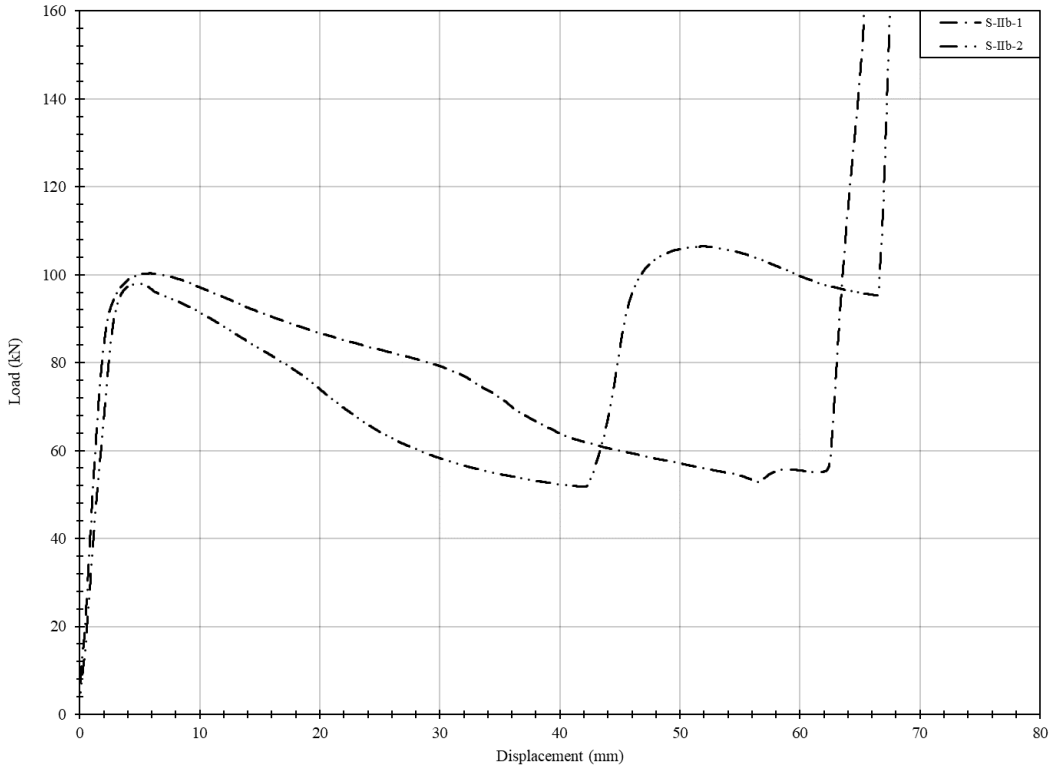

Figure 5.11: Static measured load-displacement curve for specimens S-IIb-1 and S-IIb-2

S-IIb-1 **S-IIb-2**

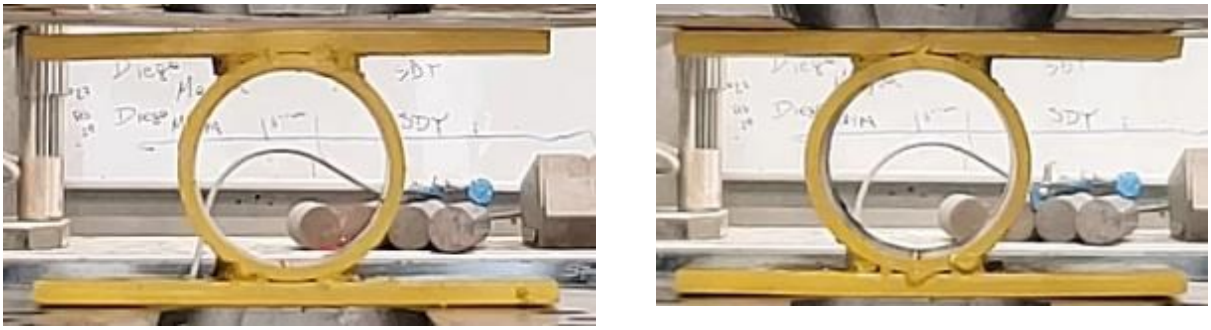

(a) Initial Shape

(ii) Deformed Shape

Figure 5.12: Initial and deformed shape of specimens S-IIb-1 and S-IIb-2

5.3.2.7 Specimens S-IIc-1 and S-IIc-2

Figure 5.13 shows the measured static load-displacement relationship for specimens S-IIc-1 and S-IIc-2. These specimens consisted of a circular HSS with an outer diameter of 127 mm instead of the 88.9 mm of specimen type IIa and IIb. Figure 5.14 shows the initial and deformed shape of both specimens. Similar behaviour to specimen types IIa and IIb was observed.

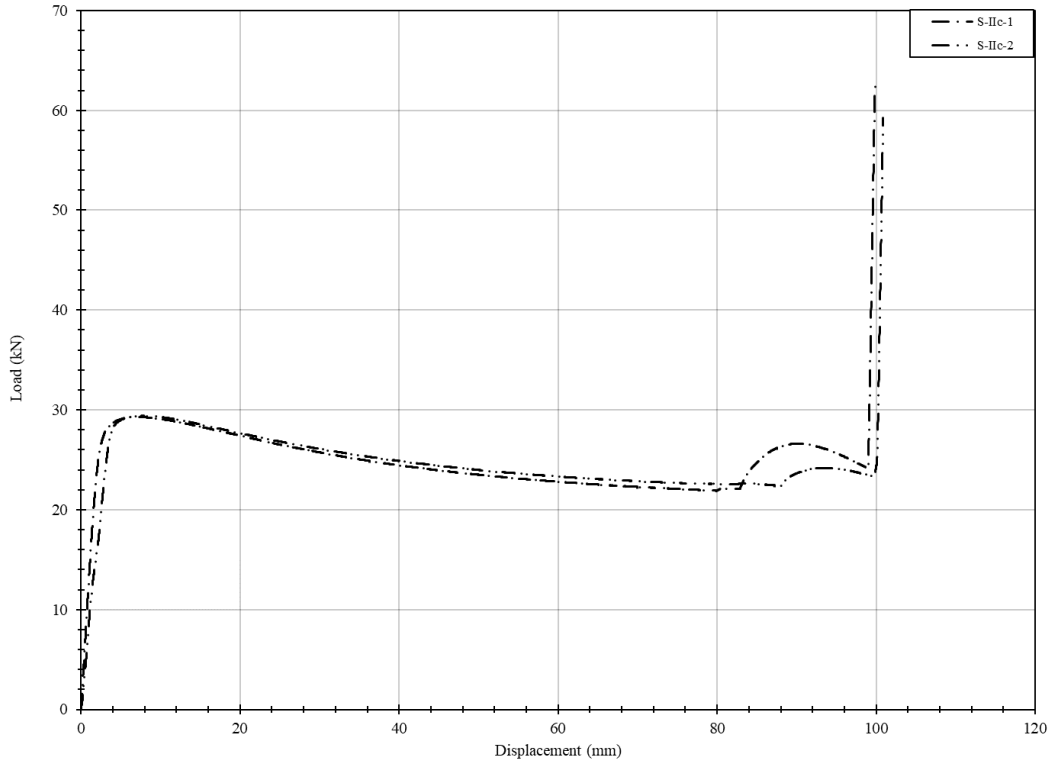

Figure 5.13: Static measured load-displacement curve for specimens S-IIc-1 and S-IIc-2

S-IIc-1 **S-IIc-2**

(a) Initial Shape

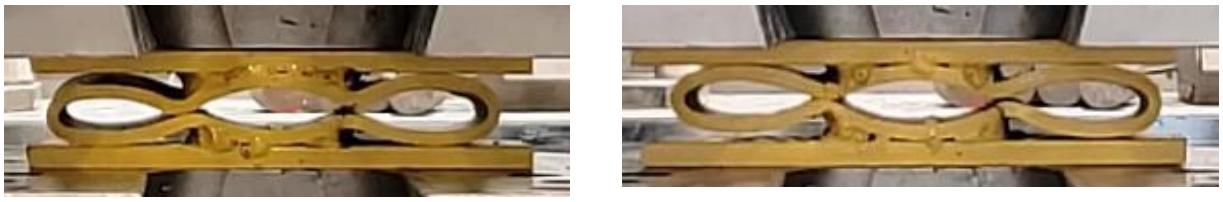

(ii) Deformed Shape

Figure 5.14: Initial and deformed shape of specimens S-IIc-1 and S-IIc-2

5.3.2.8 Specimens S-IId-1 and S-IId-2

Figure 5.15 shows the measured static load-displacement relationship for both specimen S-IId-1 and S-IId-2. This specimen consisted of 90° arcs obtained from the circular HSS of 127 mm in outer diameter. Figure 5.16 shows the initial and deformed shape of these specimens. A much more significant drop in load following yielding was observed for this specimen than for specimen types IIa, IIb, and IIc. In fact, the behaviour is much more similar to the behaviour of specimen type Id.

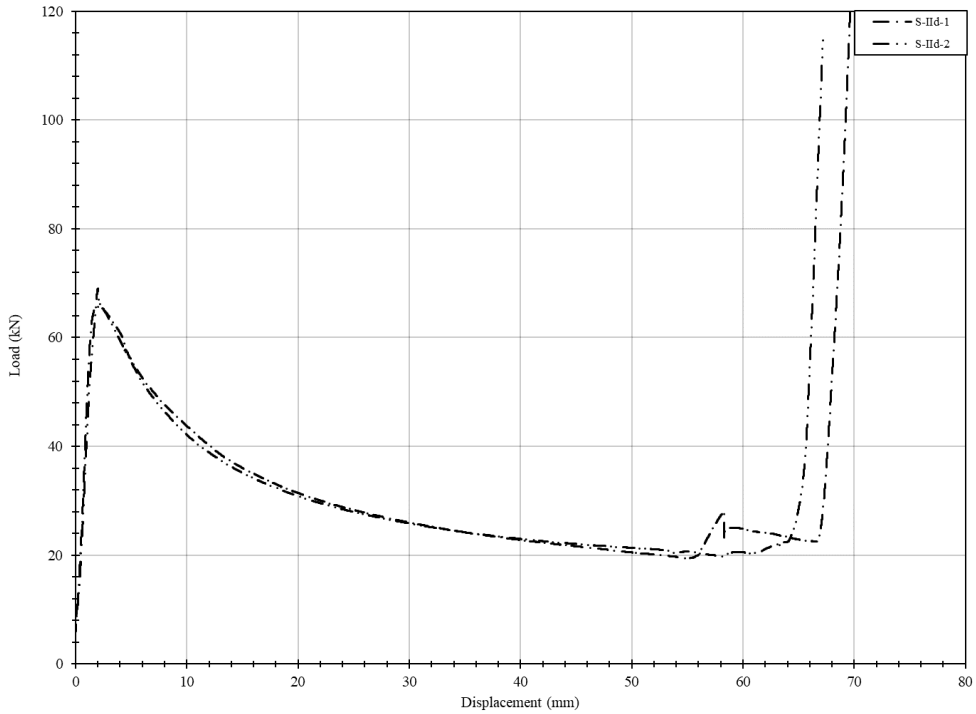

Figure 5.15: Static measured load-displacement curve for specimens S-IId-1 and S-IId-2

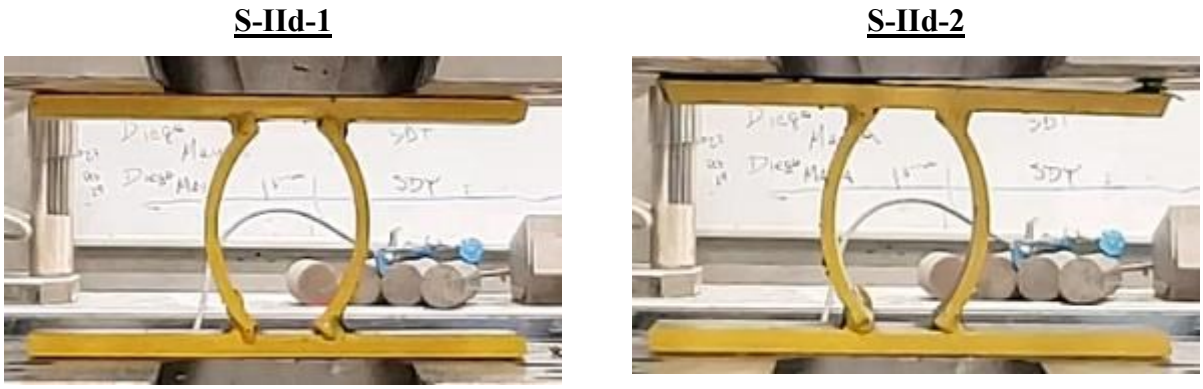

(a) Initial Shape

(ii) Deformed Shape

Figure 5.16: Initial and deformed shape of specimens S-IId-1 and S-IId-2

5.3.2.9 Specimens S-IIe-1 and S-IIe-2

Figure 5.17 shows the measured static load-displacement relationship for both specimen S-IIe-1 and S-IIe-2. This specimen consisted of a circular HSS of identical size to the one used in specimen IIa, however, for this specimen type an additional circular HSS with an outer diameter of 60.325 mm was provided. Figure 5.18 shows the initial and deformed shape of both specimens S-IIe-1 and S-IIe-2. It can be observed that multiple increase in the load were observed following yielding and prior to densification. This behaviour was only observed with this specimen type.

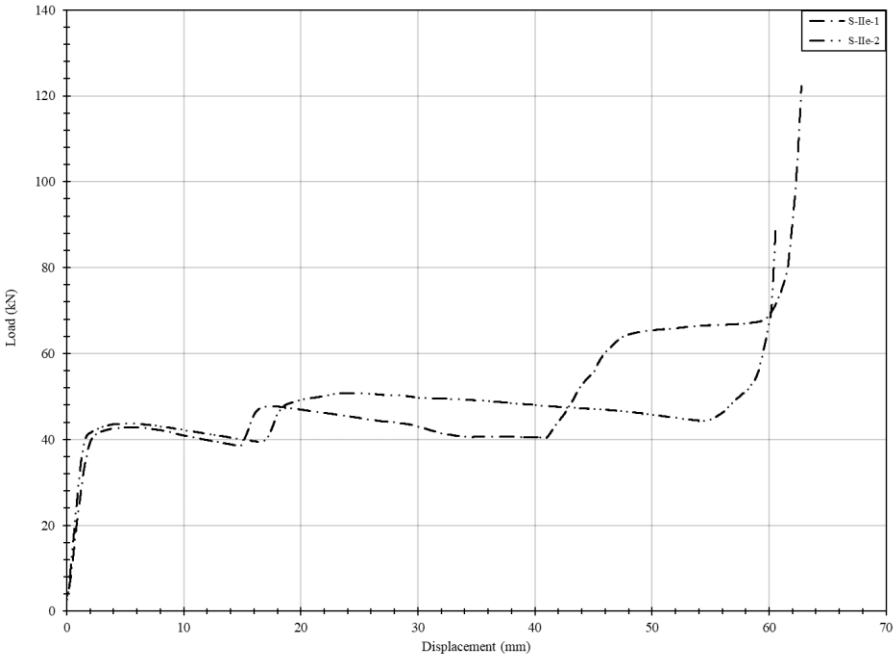

Figure 5.17: Static measured load-displacement curve for specimens S-IIe-1 and S-IIe-2

S-IIe-1 **S-IIe-2**

(a) Initial Shape

(ii) Deformed Shape

Figure 5.18: Initial and deformed shape of specimens S-IIe-1 and S-IIe-2

5.4 Dynamic Test Results

A total of 18 static connection-level dynamic tests were conducted, which included two replicates for each of the nine specimen types. Table 5.5 presents the maximum recorded average reflected pressure and impulse measured during each test, and a typical pressure and impulse time-history graph is presented in Figure 5.19. Additionally, a typical time-history graph for both measured reaction loads and EAC displacement is presented in Figure 5.20. Time-history graphs for reflected pressure, impulse, reaction load and EAC displacement of each specimen are presented in Appendix C. The following sub-sections will summarize the experimental observations for each specimen type and present the measured load-displacement relationships. The initial and deformed shapes that are different from static testing will also be presented, and more pictures of the specimens during testing can be found in Appendix C.

Table 5.5: Maximum reflected pressure and impulse

Specimen Type	Specimen Repeat	Driver Pressure (kPa)	Reflected Pressure - $P_{R,max}$ (kPa)	Reflected Impulse - $I_{R,max}$ (kPa-ms)
Ia	Ia-D-1	270.3	37.3	386.9
	Ia-D-2	275.1	33.7	313.4
Ib	Ib-D-1	279.9	42.5	264.2
	Ib-D-2	268.9	40.7	379.2
Ic	Ic-D-1	563.3	58.0	607.0
	Ic-D-2	573.6	67.1	758.9
Id	Id-D-1	568.8	72.2	644.7
	Id-D-2	569.5	66.5	701.4
IIa	IIa-D-1	244.8	34.8	278.7
	IIa-D-2	250.3	36.6	300.3
IIb	IIb-D-1	413.0	44.1	519.6
	IIb-D-2	415.8	49.2	482.0
IIc	IIc-D-1	260.6	34.2	314.8
	IIc-D-2	261.3	45.7	362.1
IId	IId-D-1	373.7	50.2	493.2
	IId-D-2	376.5	44.3	391.8
IIe	IIe-D-1	233.7	36.0	350.5
	IIe-D-2	233.7	37.8	273.0

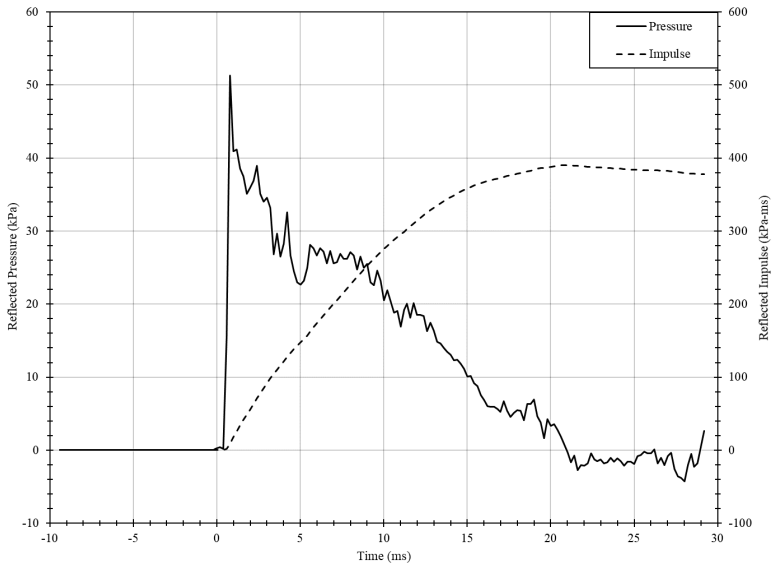

Figure 5.19: Typical pressure and impulse time-history

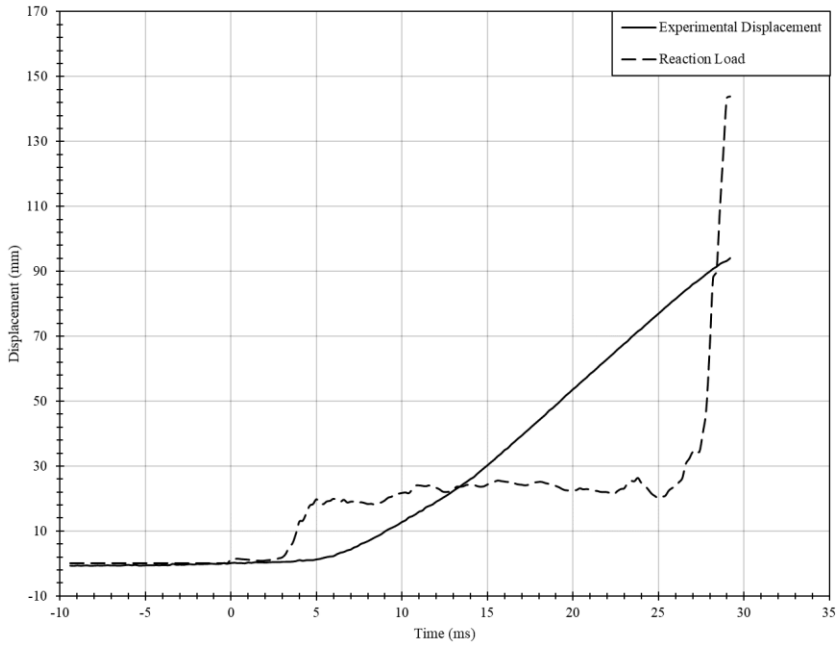

Figure 5.20: Typical time-history for reaction load and displacement

5.4.1 Specimens D-Ia-1 and D-Ia-2

Figure 5.21 shows the measured dynamic load-displacement relationship for both specimen D-Ia-1 and D-Ia-2. A deformed shape similar to static testing was observed in the dynamic testing, and it can be found in Appendix C.

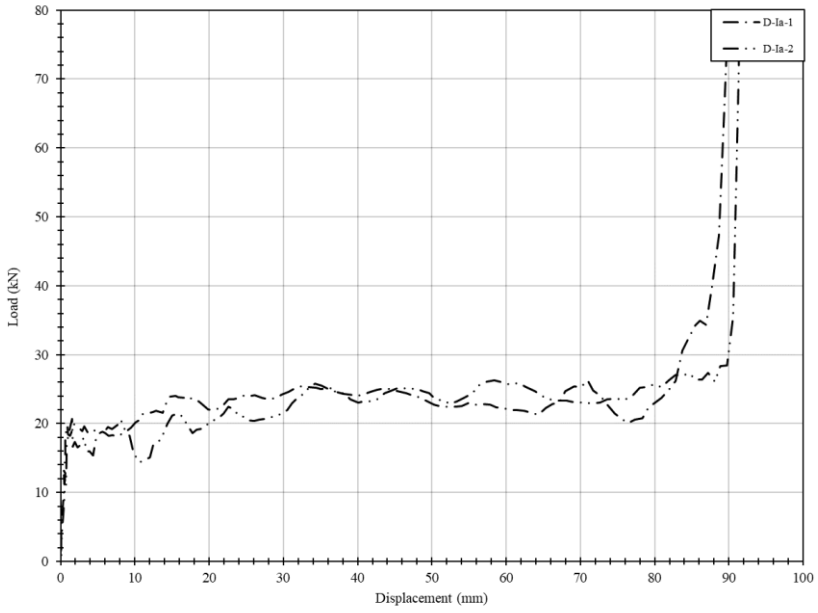

Figure 5.21: Dynamic measured load-displacement curve for specimens D-Ia-1 and D-Ia-2

5.4.2 Specimens D-Ib-1 and D-Ib-2

Figure 5.22 shows the measured dynamic load-displacement relationship for both specimen D-Ib-1 and D-Ib-2. A deformed shape similar to static testing was observed with both specimens, it can be found in Appendix C.

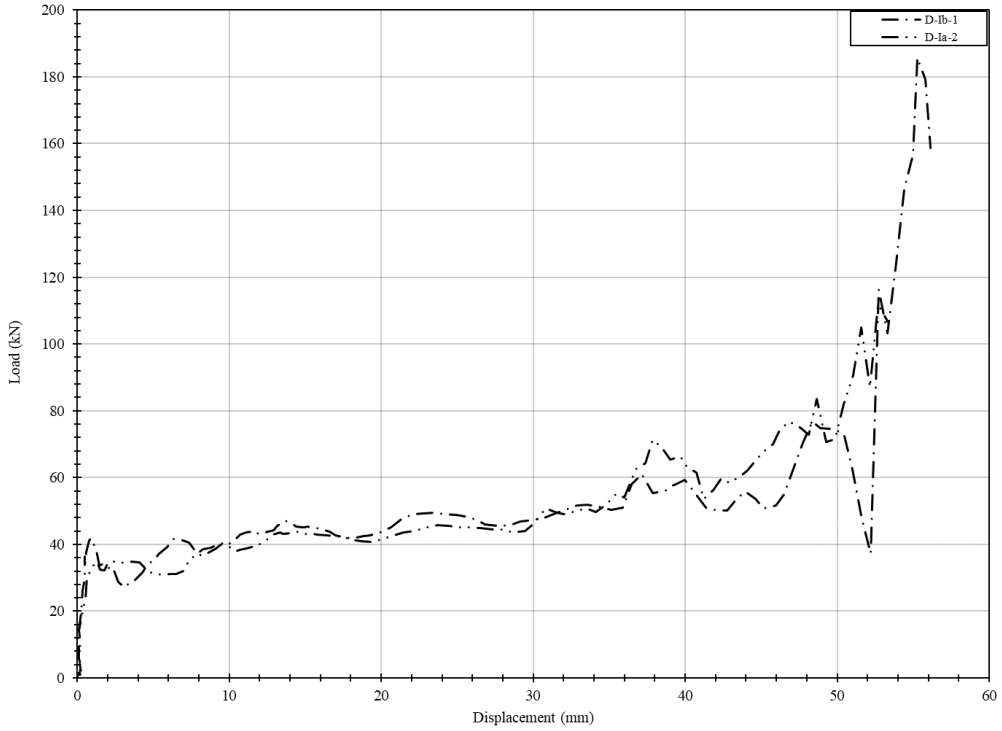

Figure 5.22: Dynamic measured load-displacement curve for specimens D-Ib-1 and D-Ib-2

5.4.3 Specimens D-Ic-1 and D-Ic-2

Figure 5.23 shows the measured dynamic load-displacement relationship for both specimen Ib-D-1 and Ib-D-2. A deformed shape similar to static testing was observed with specimen for both specimens, and can be found in Appendix C.

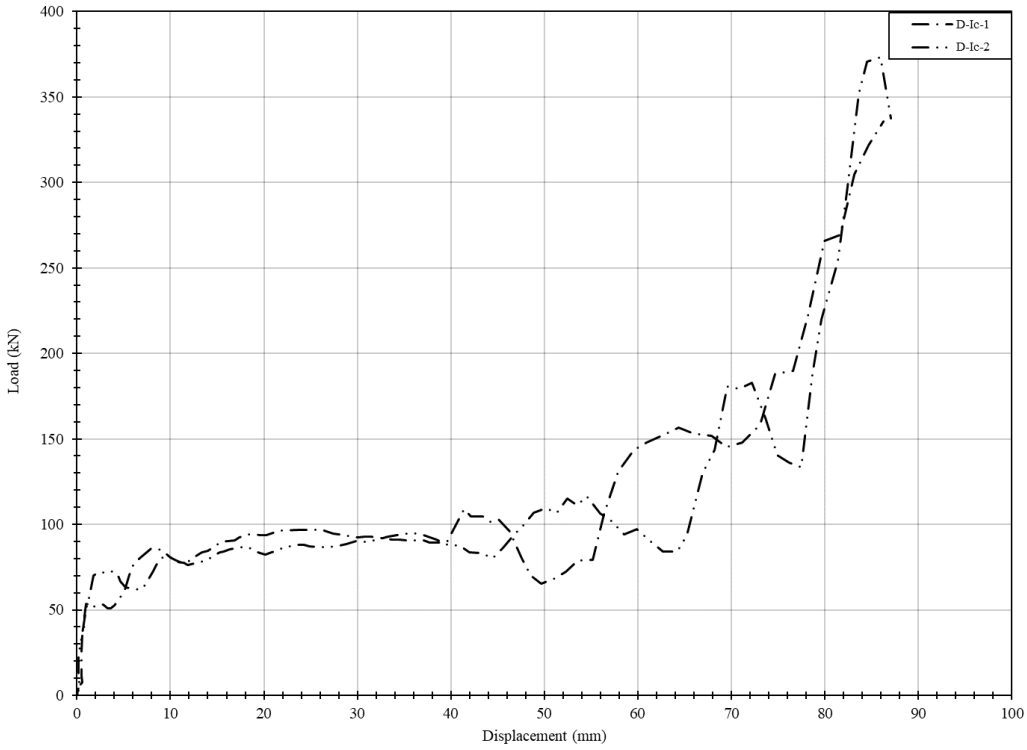

Figure 5.23: Dynamic measured load-displacement curve for specimens D-Ic-1 and D-Ic-2

5.4.4 Specimens D-Id-1 and D-Id-2

Figure 5.24 shows the measured dynamic load-displacement relationship for both specimen D-Id-1 and D-Id-2. A deformed shape similar to static testing was observed also observed with these specimens, they can be found in Appendix C.

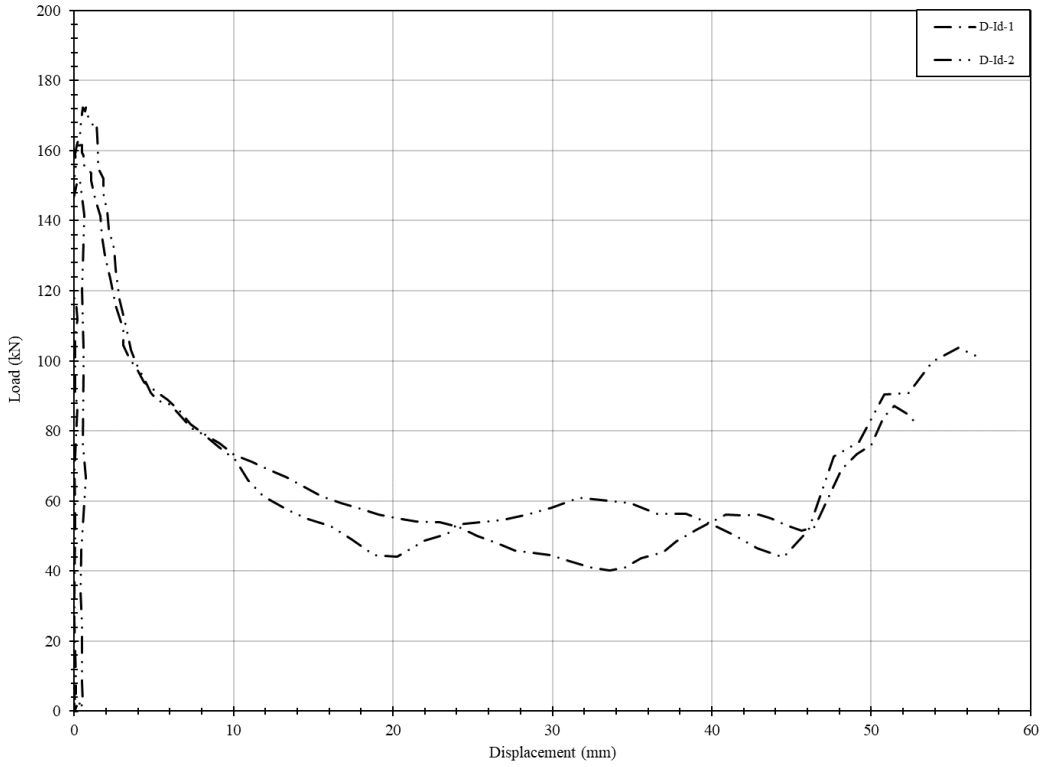

Figure 5.24: Dynamic measured load-displacement curve for specimens D-Id-1 and D-Id-2

5.4.5 Specimens D-IIa-1 and D-IIa-2

Figure 5.25 shows the measured dynamic load-displacement relationship for both specimen D-IIa-1 and D-IIa-2. A deformed shape significantly different from static testing was observed (Figure 5.26). This was attributed to the different weld types in the specimens used for static and dynamic testing during the specimen manufacturing. Also, a significantly different load-displacement behaviour was observed, consisting of an increase in load and stiffness instead of a reduction prior to densification.

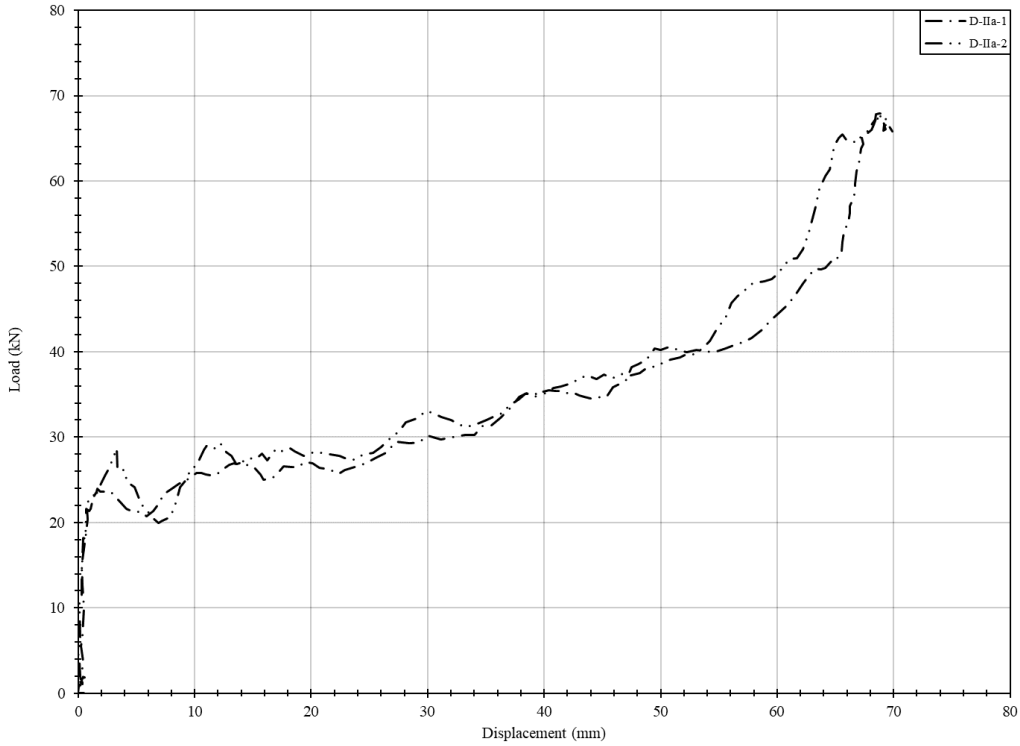

Figure 5.25: Dynamic measured load-displacement curve for specimens D-IIa-1 and D-IIa-2

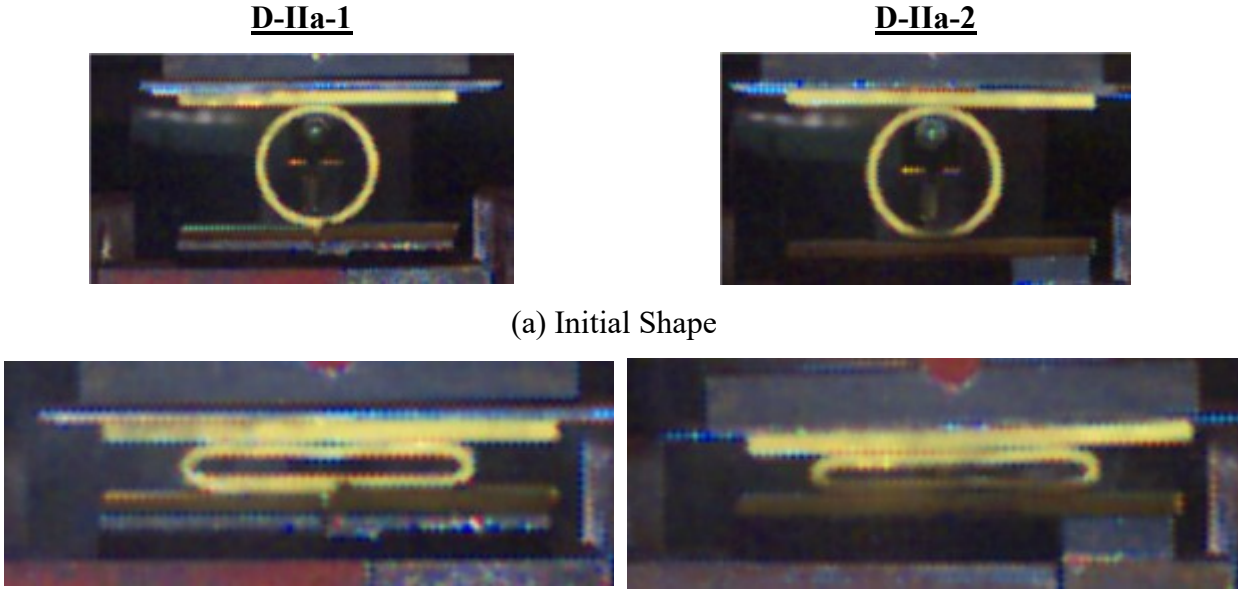

(a) Initial Shape

(ii) Deformed Shape

Figure 5.26: Initial and deformed shape of specimens D-IIa-1 and D-IIa-2

5.4.6 Specimens D-IIb-1 and D-IIb-2

Figure 5.27 shows the measured static load-displacement relationship for both specimen D-IIb-1 and D-IIb-2. A deformed shape similar to specimen type IIa was observed with this specimen, and it can be found in Appendix C. The load-displacement behaviour was similar to the behaviour observed with specimens D-IIa-1 and D-IIa-2.

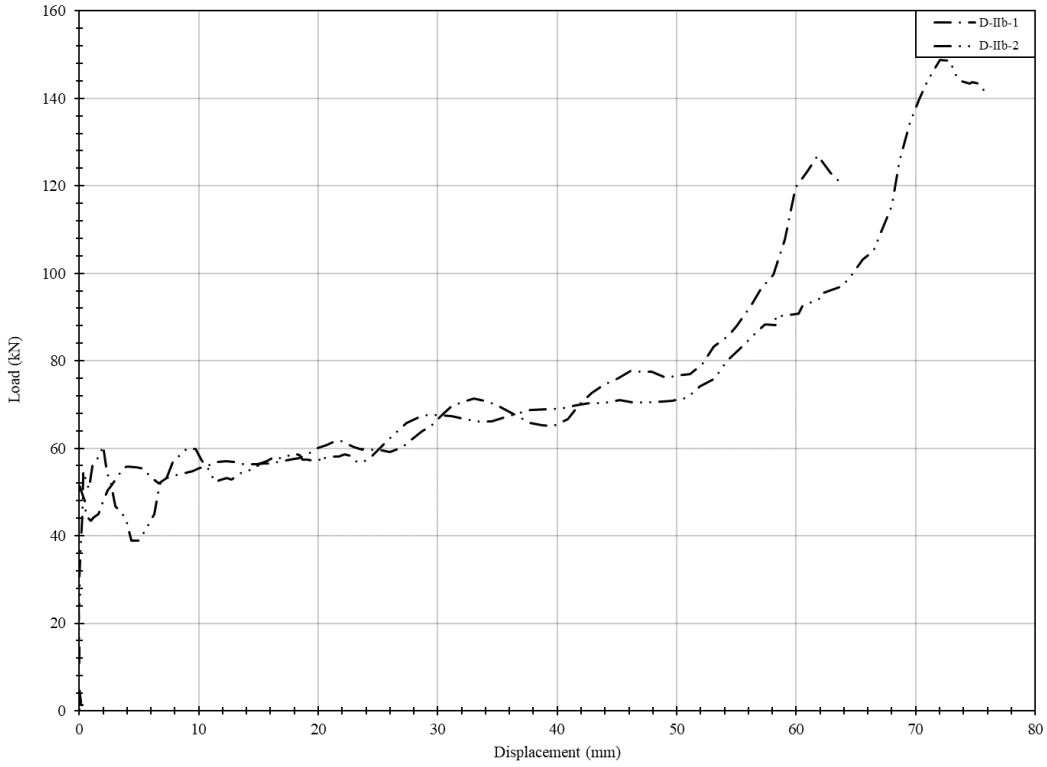

Figure 5.27: Dynamic measured load-displacement curve for specimens D-IIb-1 and D-IIb-2

5.4.7 Specimens D-IIc-1 and D-IIc-2

Figure 5.28 shows the measured dynamic load-displacement relationship for both specimen D-IIc-1 and D-IIc-2. A deformed shape and load-displacement behaviour similar to specimen types IIa and IIb tested dynamically was observed for these specimens.

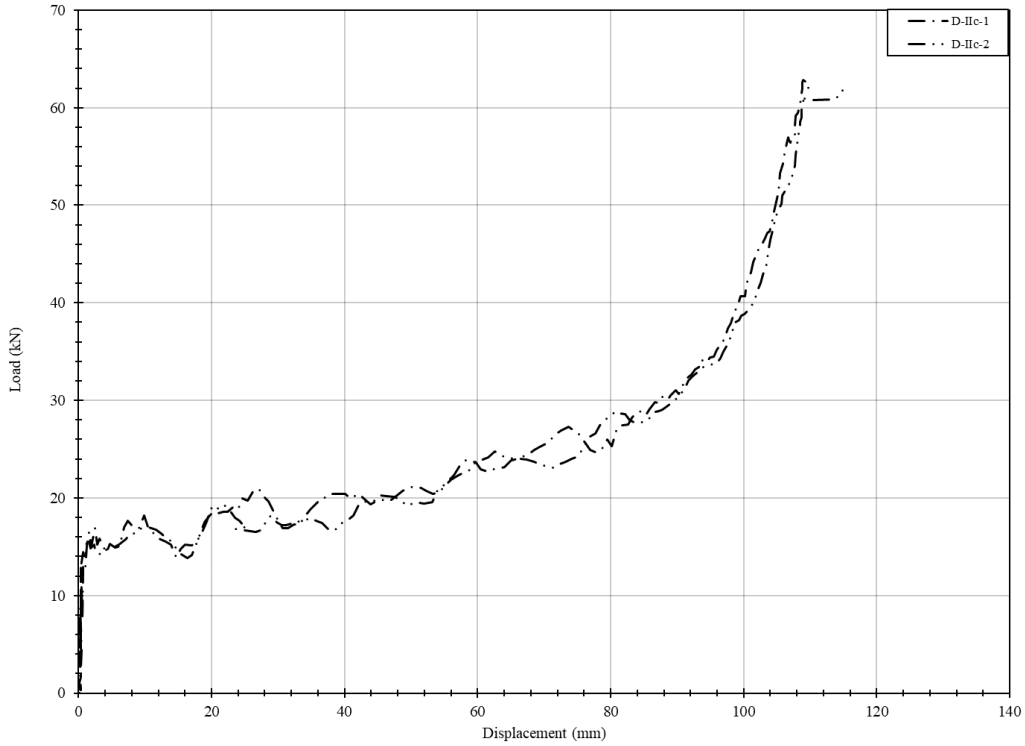

Figure 5.28: Dynamic measured load-displacement curve for specimens D-IIc-1 and D-IIc-2

5.4.8 Specimens D-IId-1 and D-IId-2

Figure 5.29 shows the measured dynamic load-displacement relationship for both specimen D-IId-1 and D-IId-2. Specimen IIc-D-1 and IIc-D-2 had a deformed shape similar to the respective static testing. However, the dynamic load-displacement behaviour was observed to be much more unpredictable for both specimens than the other specimens tested dynamically presented previously.

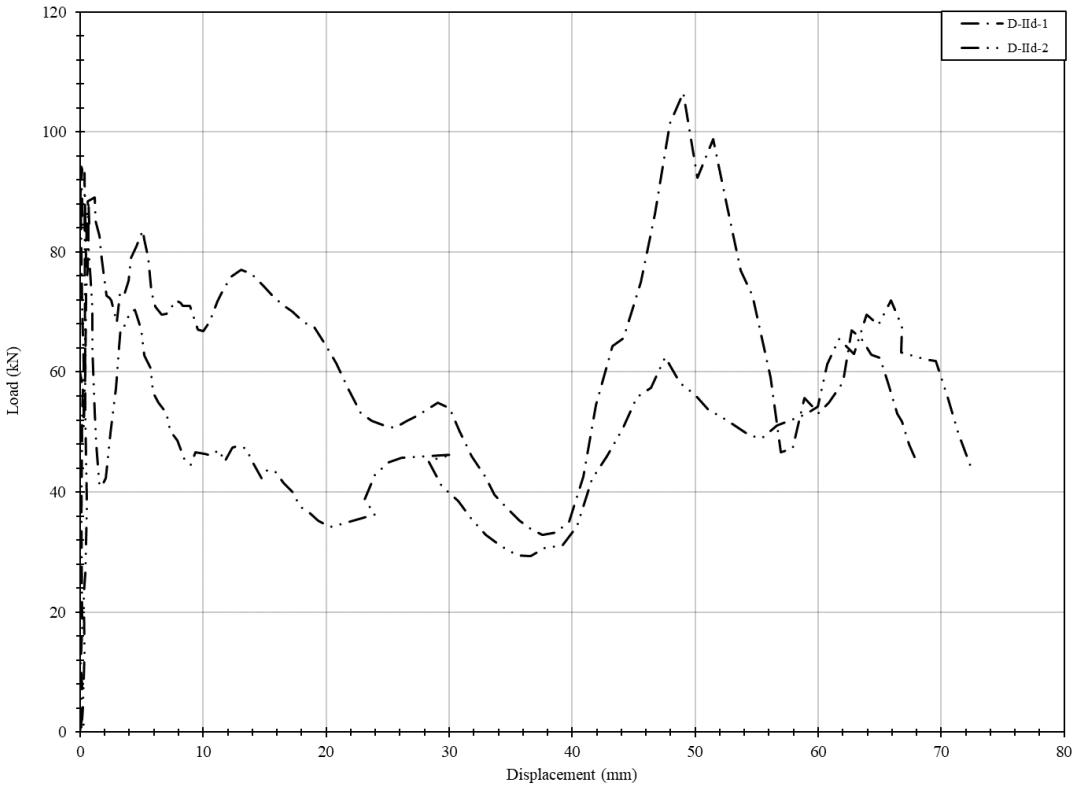

Figure 5.29: Dynamic measured load-displacement curve for specimens D-IId-1 and D-IId-2

5.4.9 Specimens D-IIe-1 and D-IIe-2

Figure 5.30 shows the measured dynamic load-displacement relationship for both specimen D-IIe-1 and D-IIe-2. The deformed shape of both individual circular HSS was similar to the deformed shape of the circular HSS of specimen types IIa, IIb, and IIc. The overall deformed shape, which can be found in Appendix C, was similar to the static deformed shape observed with specimens S-IIe-1 and S-IIe-2.

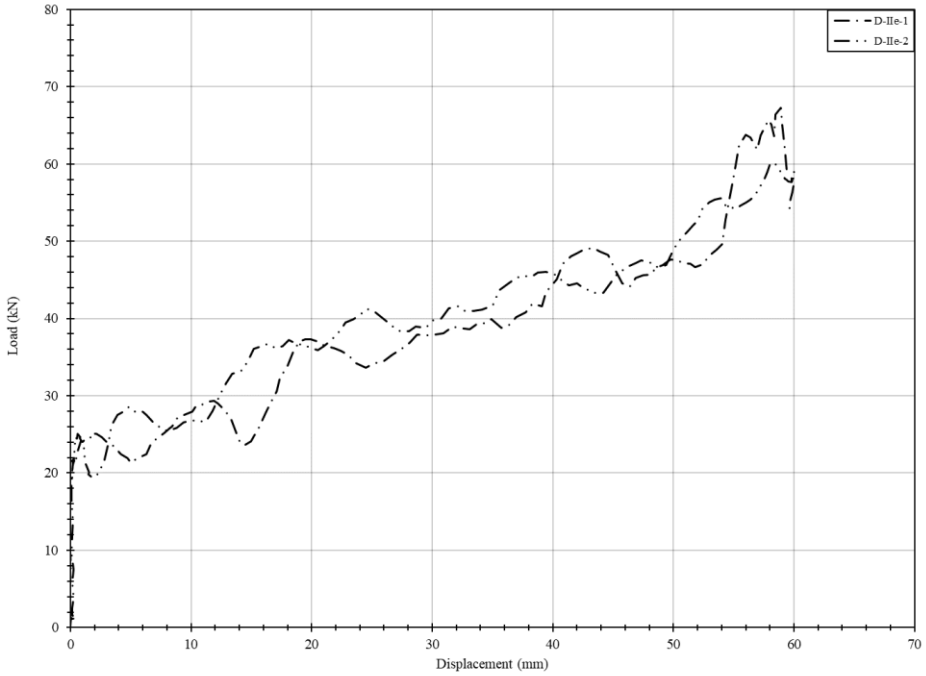

Figure 5.30: Dynamic measured load-displacement curve for specimens D-IIe-1 and D-IIe-2

CHAPTER 6 - Analytical Modelling and Results

6.1 General

This chapter presents the analytical modelling methodology and results. Section 6.2 presents the single degree of freedom (SDOF) analysis performed to model the time-history displacement response of the EACs. Section 0 presents idealized load-displacement curves that are capable of capturing the behaviour of the EAC connections observed during the experimental program. Finally, section 6.4 presents a modified FEA model compared to that presented in Chapter 3, based on actual (measured) mechanical properties of steel and improved modelling techniques.

6.2 SDOF Analysis

SDOF analysis was performed and compared to the experimentally measured dynamic displacement-time histories. The main goal of this comparison is to investigate whether SDOF analysis can sufficiently capture the dynamic behaviour of the EAC connections observed during the experimental testing.

SDOF analysis consists of solving the equation of motion for a given system consisting of mass, stiffness, and loading. An equivalent system, representative of the experimental conditions, was selected and the equation of motion, shown in Equation 6.1, was solved for displacement time-history with stiffness, mass, and loading lumped into a single point.

$$K_{LM} m\ddot{y} + Ky = F(t) \qquad \text{Equation 6.1}$$

A blast analysis software, *RCBlast*® (Jacques 2014), was used to solve this equation. This software has been used and validated by multiple researchers working on various structural components types and materials (Jacques 2011; Lacroix and Doudak 2018b; Viau and Doudak 2016a). The inputs for the SDOF model included the mass, loaded area, measured pressure time-history, and resistance curve of the system. The inputs to the SDOF model are discussed next.

Since the equivalent equation of motion is used, the mass was lumped into a single point to satisfy the equation's requirements. The mass of the system included that of the load-transfer device (LTD), loading arm and specimen. The average mass of the EAC specimens was measured to be 2.6 kg, while the LTD and loading arm masses were taken as 242.0 kg and 7.8 kg, respectively. This resulted in a total mass of approximately 252 kg. Since all inertia forces will be transferred

directly to the specimen at a single point, the total mass was assumed to be already lumped, and thus a K_{LM} of 1.0 was used in the model.

The pressure-time history was taken as the reflected side pressure measured during testing and represents the forcing function on the system. The effective area of the LTD (3.55 m^2) was used to convert the pressure-time history into the forcing function. Figure 6.1 shows the measured reflected pressure-time history of specimen D-Ia-1, representative of typical pressure-time history. It should be noted that only pressure up to the end of the initial positive region was considered in the analysis.

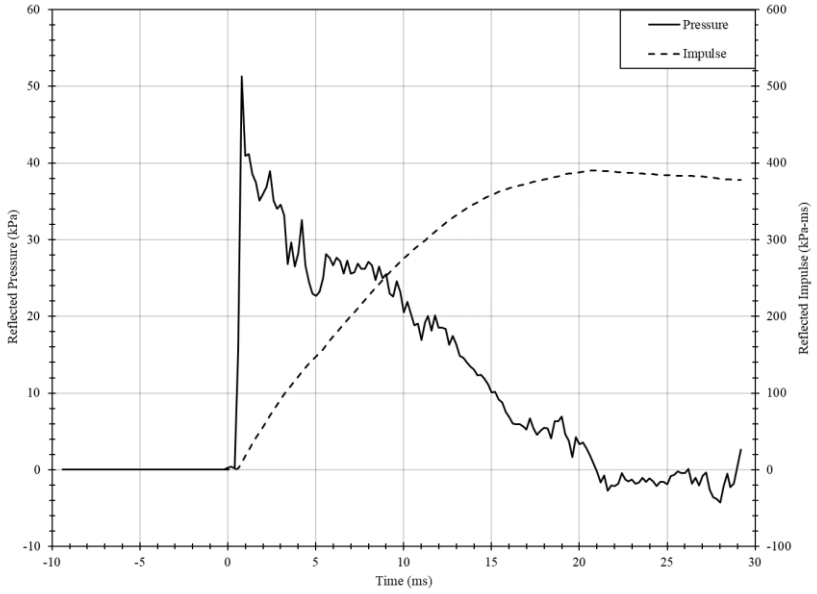

Figure 6.1: Pressure and impulse time histories for specimen D-Ia-1

Due to the non-linear nature observed in the EAC load-displacement response, a resistance curve, representative of the dynamic load-displacement curve of the specimen measured experimentally, was used in the analysis. The curve consisted of the measured dynamic reaction and measured relative displacement of the specimen in relation to the reaction frame. Only the resistance of EAC specimen was assumed to be representative of the system resistance, while the LTD and loading beam were assumed to have a negligible contribution to the resistance and stiffness of the system. Since the reaction load was measured experimentally during dynamic loading, the effects of dynamic increase factors (DIFs) or strength increase factors (SIFs) were assumed to be already incorporated in the resistance curve.

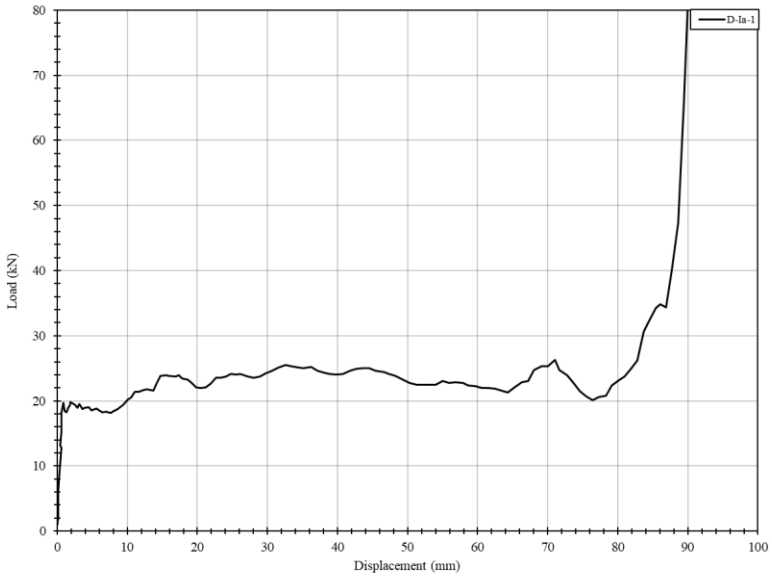

Figure 6.2: Dynamic load-displacement curve of specimen D-Ia-1

6.2.1 SDOF Model Results and Comparison

Figure 6.3 shows the displacement-time histories obtained from the SDOF model and experimental results for specimen D-Ia-1, which presents a representative result for most specimens. It can be observed that reasonably good correlation between the SDOF model and experimental results is obtained. An exception to this was observed with specimen D-Id-1, where good correlation for maximum displacement and time to maximum displacement was observed but did not show a good correlation prior to this point (refer to Appendix D). Displacement-time histories comparison between experimental and SDOF for all specimens is presented in Appendix D.

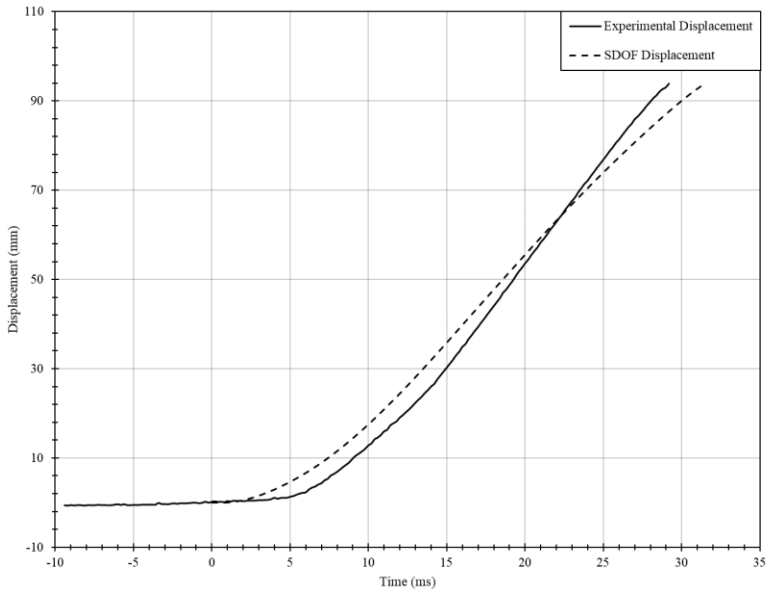

Figure 6.3: Displacement time-histories for specimen D-Ia-1

The maximum displacement and time-to-maximum displacement for each specimen were used to compare the SDOF response with that measured experimentally. Table 6.1 shows the SDOF and experimental maximum displacement and time to maximum displacement for each specimen, while Table 6.2 presents the ratio of SDOF to experimental for both maximum displacement and time to maximum displacement. The SDOF model predicts, on average, values of maximum displacement and time to maximum displacement within 3% and 6% of their experimental counterparts, respectively, with respective coefficients of variations of 4.3% and 8%. Based on the presented results, it can be concluded that SDOF analysis was capable of predicting the connection behaviour accurately.

Table 6.1: Experimental and SDOF maximum displacement and time to maximum displacement

Specimen	Experimental		SDOF	
	Maximum displacement (mm)	**Time to maximum displacement (ms)**	**Maximum displacement (mm)**	**Time to maximum displacement (ms)**
D-Ia-1	94	29.2	94	31.5
D-Ia-2	95.6	29	95.5	31.4
D-Ib-1	55.3	25.8	54.6	27.1
D-Ib-2	52.7	25	51.2	27.4
D-Ic-1	86.3	23.4	73.6	25.5
D-Ic-2	86	22.8	79.2	25.6
D-Id-1	51.4	28	51.4	26.7
D-Id-2	55.5	25	55.2	24.4
D-IIa-1	68.9	31.6	68.9	29.6
D-IIa-2	68.8	30	68.7	28.9
D-IIb-1	61.8	21.8	61.7	22.9
D-IIb-2	72.8	24.8	67.9	28
D-IIc-1	110	39.6	109.9	38.8
D-IIc-2	109.2	38.2	109.1	38.6
D-IId-1	49	23	49	25.4
D-IId-2	90.4	30	81	38.8
D-IIe-1	58.9	28.2	58.1	31.6
D-IIe-2	60	31.8	57.6	31.7

Table 6.2: Ratio of SDOF value to experimental value

Specimen	Ratio of SDOF value to experimental value	
	Maximum Displacement	**Time to maximum displacement**
D-Ia-1	1.00	1.08
D-Ia-2	1.00	1.08
D-Ib-1	0.99	1.05
D-Ib-2	0.97	1.10
D-Ic-1	0.85	1.09
D-Ic-2	0.92	1.12
D-Id-1	1.00	0.95
D-Id-2	0.99	0.98
D-IIa-1	1.00	0.94
D-IIa-2	1.00	0.96
D-IIb-1	1.00	1.05
D-IIb-2	0.93	1.13
D-IIc-1	1.00	0.98
D-IIc-2	1.00	1.01
D-IId-1	1.00	1.10
D-IId-2	0.90	1.29
D-IIe-1	0.99	1.12
D-IIe-2	0.96	1.00
Average	0.97	1.06
CoV (%)	4.3	8.0

6.3 Characterization of EAC Load-displacement Properties

6.3.1 Idealized and Experimental Load-displacement Parameters

The load-displacement behaviour of some of the EAC connections could be idealized into a tri-linear curve which included the elastic stiffness (K_e), yield displacement (Δ_y), yield load (P_y), displacement at the onset of densification (Δ_D), maximum absorbed energy up to densification (W_m), and densification stiffness (K_D). Idealized parameters for all specimens, including static and dynamic testing, were generated and presented in this section. Additionally, the following parameters were used to generate the idealized parameters for comparison with the experimental behaviour: load corresponding to Δ_D (P_D), average plateau load between Δ_y and Δ_D (P_P), maximum load prior to Δ_D (P_{max}), and displacement corresponding to P_{max} (Δ_{Pmax}). Figure 6.4 shows an example of the idealized curve with all parameters.

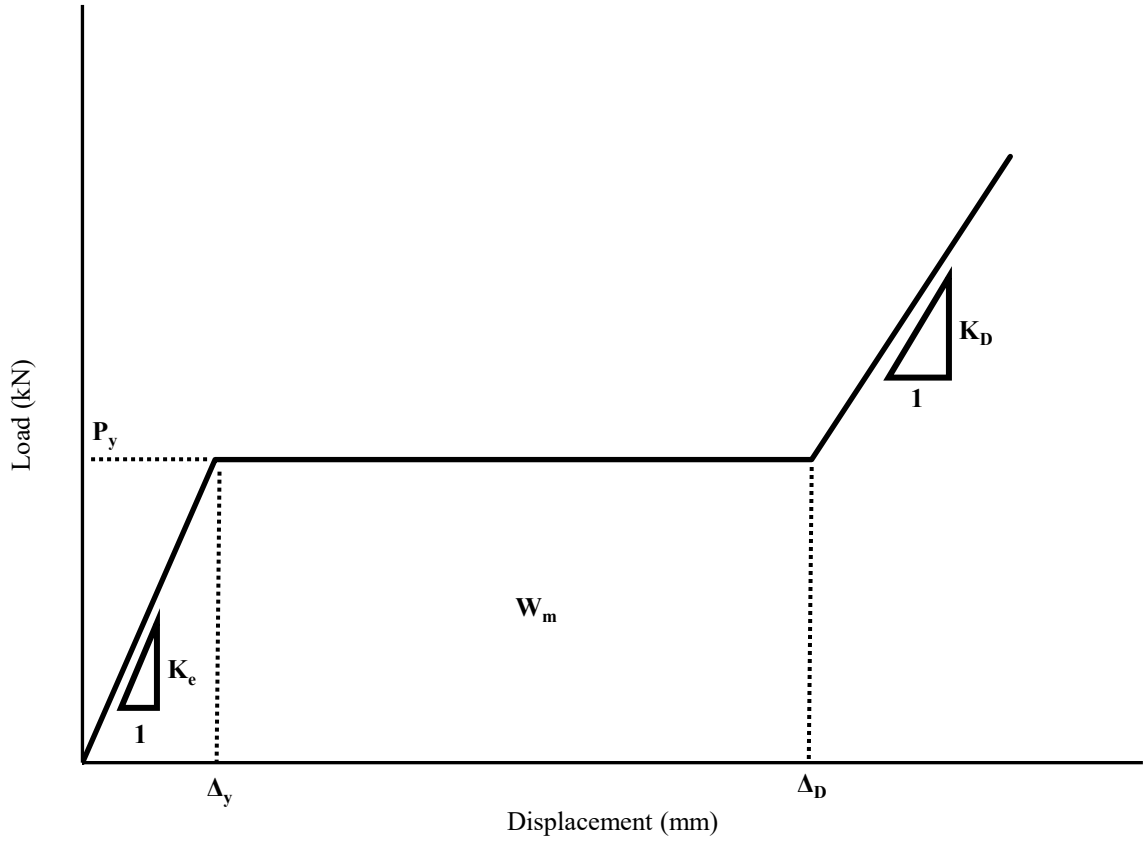

Figure 6.4: Idealized load-displacement curve

The method used to generate the idealized parameters includes the following steps:

- The elastic stiffness (K_e) is determined by calculating the initial stiffness defined by the line connecting the points corresponding to 10% and 40% of the peak load.
- The energy absorption for each displacement value (W_i) is calculated according to Equation 2.7 (Gibson and Ashby 1999), with the load-displacement values measured experimentally.
- The energy absorption efficiency (η) is calculated for all displacements measurements according to Equation 2.4 (Wang et al. 2019).
- The displacement at the onset of densification (Δ_D) is calculated based on the energy absorption efficiency methodology proposed by Wang et al. (2019). Δ_D is thus taken as the displacement corresponding to the local maximum of η near the densification region, as shown in Figure 6.5.

- Similar to K_e, the densification stiffness (K_D) is determined based on a line connecting the point corresponding to the onset of densification (i.e. Δ_D and P_D) to the last measured point in the densification region. This method only provides an approximation of the densification stiffness since the densification region is observed to have an exponentially increasing stiffness with increased load.
- The maximum absorbed energy (W_m) is taken as the energy absorption (W_i) at a displacement value equal to the displacement at the onset of densification (Δ_D).
- The yield load (P_y) and yield displacement (Δ_y) were determined such that the maximum energy absorbed by the EAC (W_m) and elastic stiffness (K_e) remain identical between the experimental and idealized curves.

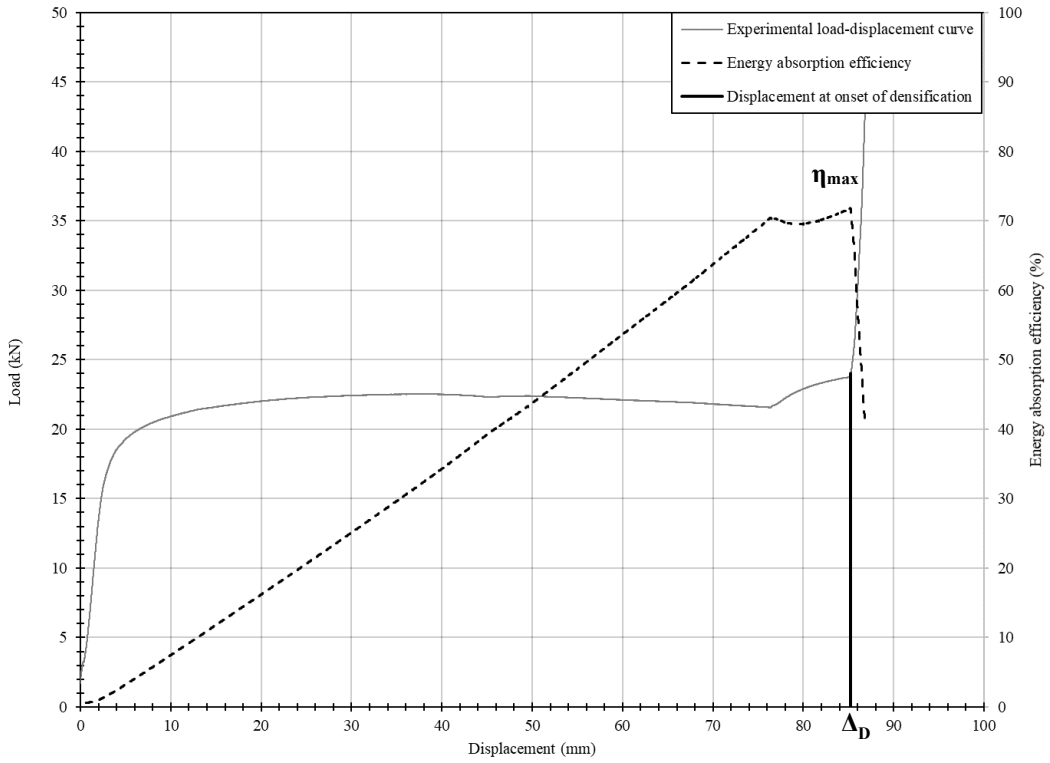

Figure 6.5: Determination of displacement at the onset of densification

Table 6.3 and

Table 6.4 show the idealized and experimental parameters for specimens tested statically and dynamically, respectively. The idealized load-displacement curves for all specimens are presented in Appendix D.

Table 6.3: Idealized and experimental parameters for specimens tested statically

Type	Duplicates	Δ_y (mm)	P_y (kN)	K_y (kN/mm)	P_p (kN)	Δ_{Pmax} (mm)	P_{max} (kN)	Δ_D (mm)	P_D (kN)	W_m (J)	K_D (kN/mm)
Ia	S-Ia-1	3.3	22.0	6.7	22.0	85.2	23.8	85.2	23.8	1839.1	12.0
	S-Ia-2	2.8	22.0	8.0	22.0	82.6	23.3	82.6	23.3	1788.6	8.2
	Average	3.0	22.0	7.4	22.0	83.9	23.6	83.9	23.6	1813.9	10.1
	CoV (%)	8.8	0.0	8.8	0.1	1.5	1.1	1.5	1.1	1.4	18.8
Ib	S-Ib-1	2.4	40.5	16.6	40.6	51.3	46.1	51.3	46.1	2027.9	11.5
	S-Ib-2	2.2	41.2	18.8	41.3	45.4	47.2	51.0	46.7	2055	13.9
	Average	2.3	40.9	17.7	40.9	48.4	46.7	51.2	46.4	2041.5	12.7
	CoV (%)	5.4	0.9	6.2	0.9	6.1	1.2	0.3	0.6	0.7	9.6
Ic	S-Ic-1	4.6	85.7	18.8	85.8	58.9	91.4	77.0	85.8	6403.3	28.6
	S-Ic-2	3.2	87.1	27.2	87.5	22.8	90.7	73.4	88.2	6254.9	16.7
	Average	3.9	86.4	23.0	86.6	40.9	91.1	75.2	87.0	6329.1	22.7
	CoV (%)	17.5	0.8	18.3	1.0	44.2	0.4	2.4	1.4	1.2	26.1
Id	S-Id-1	–[a]	–[a]	80.0	–[a]	3.2	152.9	41.9	31.6	2294	5.5
	S-Id-2	–[a]	–[a]	69.9	–[a]	5.4	155.0	40.4	32.5	2665.2	9.3
	Average	–[a]	–[a]	75.0	–[a]	4.3	154.0	41.2	32.1	2479.6	7.4
	CoV (%)	–[a]	–[a]	6.7	–[a]	25.6	0.7	1.8	1.4	7.5	25.3
IIa	S-IIa-1	2.1	40.4	19.0	40.4	5.0	49.0	64.0	38.1	2543.9	48.6
	S-IIa-2	2.0	40.7	20.6	40.6	5.3	49.9	61.8	37.9	2472.4	40.1
	Average	2.1	40.6	19.8	40.5	5.2	49.5	62.9	38.0	2508.2	44.4
	CoV (%)	3.7	0.4	4.0	0.3	2.9	0.9	1.7	0.3	1.4	9.6
IIb	S-IIb-1	1.6	75.2	46.2	75.2	5.8	100.3	61.9	55.1	4596.9	35.4
	S-IIb-2	2.4	81.4	33.4	81.4	51.5	106.4	66.5	95.3	5316.3	67.4
	Average	2.0	78.3	39.8	78.3	28.7	103.4	64.2	75.2	4956.6	51.4
	CoV (%)	19.9	4.0	16.1	3.9	79.8	3.0	3.6	26.7	7.3	31.2
IIc	S-IIc-1	1.9	25.0	13.2	25.0	6.8	29.3	98.9	24.2	2444.8	41.9
	S-IIc-2	3.2	24.9	7.9	24.9	7.8	29.4	99.7	23.3	2443.4	30.6
	Average	2.5	25.0	10.6	24.9	7.3	29.4	99.3	23.8	2444.1	36.3
	CoV (%)	24.9	0.2	25.1	0.1	6.8	0.2	0.4	1.9	0.0	15.7
IId	S-IId-1	–[a]	–[a]	47.2	–[a]	2.0	65.7	66.7	22.5	2003.9	33.8
	S-IId-2	–[a]	–[a]	40.9	–[a]	2.0	69.1	63.3	21.7	1885.9	23.9
	Average	–[a]	–[a]	44.1	–[a]	2.0	67.4	65.0	22.1	1944.9	28.8
	CoV (%)	–[a]	–[a]	7.2	–[a]	0.0	2.5	2.6	1.8	3.0	17.0
IIe	S-IIe-1	2.1	48.8	22.8	48.8	59.6	67.8	59.6	67.8	2857.6	17.2
	S-IIe-2	1.6	46.3	29.0	46.3	24.2	50.8	54.8	44.4	2502	7.9
	Average	1.9	47.6	25.9	47.6	41.9	59.3	57.2	56.1	2679.8	12.6
	CoV (%)	14.6	2.6	12.0	2.7	42.2	14.3	4.2	20.9	6.6	36.9

[a]No clear plateau behaviour was observed; thus, these values were not calculated.

Table 6.4: Idealized and experimental parameters for specimens tested dynamically

Type	Duplicates	Δ_y (mm)	P_y (kN)	K_y (kN/mm)	P_p (kN)	Δ_{Pmax} (mm)	P_{max} (kN)	Δ_D (mm)	P_D (kN)	W_m (J)	K_D (kN/mm)
Ia	D-Ia-1	0.9	23.5	25.0	22.8	86.1	34.9	86.9	34.3	2028.9	16.6
	D-Ia-2	1.7	23.0	13.7	22.2	87.2	27.3	88.1	26.0	2003.5	27.0
	Average	1.3	23.3	19.4	22.5	86.7	31.1	87.5	30.2	2016.2	21.8
	CoV (%)	28.1	1.1	29.1	1.4	0.6	12.2	0.7	13.7	0.6	23.8
Ib	D-Ib-1	1.1	49.1	46.4	46.9	48.4	76.7	51.6	47.5	2506.3	37.6
	D-Ib-2	1.5	49.6	33.6	47.6	48.7	83.6	49.9	71.6	2437.9	14.4
	Average	1.3	49.4	40.0	47.3	48.6	80.2	50.8	59.6	2472.1	26.0
	CoV (%)	16.5	0.5	16.0	0.7	0.3	4.3	1.7	20.2	1.4	44.6
Ic	D-Ic-1	1.8	99.8	55.8	91.5	64.4	156.5	71.2	147.6	7014.8	12.5
	D-Ic-2	3.1	89.7	28.7	85.6	54.6	116.5	64.2	84.0	5619.3	14.1
	Average	2.5	94.8	42.2	88.6	59.5	136.5	67.7	115.8	6317.0	13.3
	CoV (%)	27.2	5.3	32.1	3.3	8.2	14.7	5.2	27.5	11.0	6.1
Id	D-Id-1	–[a]	–[a]	251.9	–[a]	0.1	170.7	45.6	51.6	2897.0	6.1
	D-Id-2	–[a]	–[a]	319.0	–[a]	0.5	172.3	44.5	43.9	2926.8	5.4
	Average	–[a]	–[a]	285.5	–[a]	0.3	171.5	45.1	47.8	2911.9	5.8
	CoV (%)	–[a]	–[a]	11.8	–[a]	66.7	0.5	1.3	8.1	0.5	5.7
IIa	D-IIa-1	1.0	30.9	30.9	29.8	57.8	41.6	57.8	41.6	1772.1	2.4
	D-IIa-2	1.2	32.7	26.3	31.7	59.5	48.5	59.5	48.5	1924.9	2.1
	Average	1.1	31.8	28.6	30.7	58.7	45.1	58.7	45.0	1848.5	2.2
	CoV (%)	10.7	2.8	7.9	3.1	1.4	7.7	1.5	7.6	4.1	6.5
IIb	D-IIb-1	0.6	64.8	109.0	61.1	46.1	77.7	51.1	77.0	3294.2	4.7
	D-IIb-2	0.4	68.0	152.1	63.0	63.8	97.0	63.8	97.0	4324.8	6.3
	Average	0.5	66.4	130.5	62.1	55.0	87.4	57.5	87.0	3809.5	5.5
	CoV (%)	14.2	2.4	16.5	1.6	16.1	11.0	11.1	11.5	13.5	14.9
IIc	D-IIc-1	1.1	20.3	18.8	19.9	73.7	27.3	80.1	25.3	1617.3	1.3
	D-IIc-2	1.0	21.0	21.2	19.6	80.9	28.9	85.3	27.8	1780.6	1.4
	Average	1.0	20.7	20.0	19.8	77.3	28.1	82.7	26.6	1698.9	1.3
	CoV (%)	4.5	1.7	6.2	0.7	4.7	2.8	3.1	4.7	4.8	4.4
IId	D-IId-1	–[a]	–[a]	130.0	–[a]	49.0	106.6	56.9	46.6	3800.9	3.5
	D-IId-2	–[a]	–[a]	155.0	–[a]	0.4	93.1	55.4	49.0	2780.8	2.2
	Average	–[a]	–[a]	142.5	–[a]	24.7	99.9	56.2	47.8	3290.8	2.8
	CoV (%)	–[a]	–[a]	8.8	–[a]	98.4	6.8	1.4	2.5	15.5	23.4
IIe	D-IIe-1	0.5	36.4	76.0	34.7	43.4	49.1	53.0	48.2	1917.5	3.2
	D-IIe-2	0.6	38.1	66.9	29.5	50.0	48.9	50.0	48.9	1892.5	1.0
	Average	0.5	37.3	71.5	32.1	46.7	49.0	51.5	48.5	1905.0	2.1
	CoV (%)	8.6	2.3	6.4	8.1	7.1	0.2	2.9	0.8	0.7	52.5

[a]No clear plateau behaviour was observed; thus, these values were not calculated.

6.3.2 Comparison of Idealized and Experimental Load-displacement Parameters and Behaviour

For comparison of the idealized and experimental load-displacement behaviours, the idealized yield load was compared to experimental loads, and the overall behaviour was compared graphically. Table 6.5 shows the ratio of idealized yield load to experimental average plateau load (P_p), maximum load prior to Δ_D (P_{max}), and load corresponding to Δ_D (P_D). Cases where the ratio of P_y/P_p are close to 1.0 indicate that the obtained plateau is well-defined and has little variation. It can be noted that the specimens tested statically had ratios of P_y/P_p very close to unity indicating that less variability is observed during that testing regime.

Table 6.5: Ratio of idealized to experimental values

Type	**Dynamic**				**Static**			
	Duplicate	**P_y/P_p**	**P_y/P_{max}**	**P_y/P_D**	**Duplicate**	**P_y/P_p**	**P_y/P_{max}**	**P_y/P_D**
Ia	D-Ia-1	1.03	0.67	0.68	S-Ia-1	1.00	0.92	0.92
	D-Ia-2	1.04	0.84	0.88	S-Ia-2	1.00	0.94	0.94
Ib	D-Ib-1	1.05	0.64	1.03	S-Ib-1	1.00	0.88	0.88
	D-Ib-2	1.04	0.59	0.69	S-Ib-2	1.00	0.87	0.88
Ic	D-Ic-1	1.09	0.64	0.68	S-Ic-1	1.00	0.94	1.00
	D-Ic-2	1.05	0.77	1.07	S-Ic-2	1.00	0.96	0.99
	Average	1.05	0.69	0.84	**Average**	1.00	0.92	0.94
	CoV (%)	1.9	12.4	19.7	**CoV (%)**	0.1	3.6	5.0
IIa	D-IIa-1	1.04	0.74	0.74	S-IIa-1	1.00	0.82	1.06
	D-IIa-2	1.03	0.67	0.67	S-IIa-2	1.00	0.82	1.07
IIb	D-IIb-1	1.06	0.83	0.84	S-IIb-1	1.00	0.75	1.36
	D-IIb-2	1.08	0.70	0.70	S-IIb-2	1.00	0.77	0.85
IIc	D-IIc-1	1.02	0.74	0.80	S-IIc-1	1.00	0.85	1.03
	D-IIc-2	1.07	0.73	0.76	S-IIc-2	1.00	0.85	1.07
IIe	D-IIe-1	1.05	0.74	0.76	S-IIe-1	1.00	0.72	0.72
	D-IIe-2	1.29	0.78	0.78	S-IIe-2	1.00	0.91	1.04
	Average	1.08	0.74	0.76	**Average**	1.00	0.81	1.03
	CoV (%)	7.6	6.1	6.6	**CoV (%)**	0.1	7.2	17.0
Id	D-Id-1	–	–	–	S-Id-1	–	–	–
	D-Id-2	–	–	–	S-Id-2	–	–	–
IId	D-IId-1	–	–	–	S-IId-1	–	–	–
	D-IId-2	–	–	–	S-IId-2	–	–	–

Figure 6.6 shows the experimental static load-displacement behaviour and the corresponding idealized behaviour for specimen S-Ia-1. This specimen had a well-defined plateau and thus showed a typical idealized behaviour where a good correlation is achieved with the experimental behaviour. It can be observed that for both dynamic and static testing, the experimental average plateau load is very close to the idealized yield load. This behaviour was typical of specimens Ia, Ib, and Ic in both static and dynamic testing.

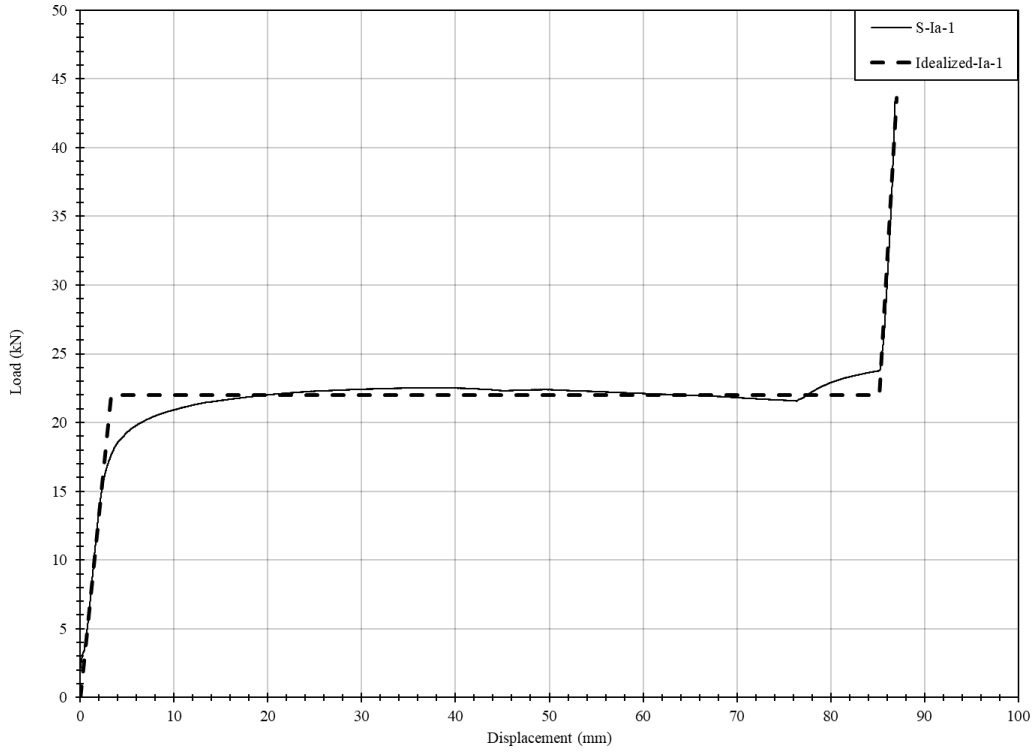

Figure 6.6: Experimental Static and Idealized Load-displacement Curve for Specimen S-Ia-1

Figure 6.7 shows the experimental and idealized curves for specimen S-IIa-1, typical of specimens IIa, IIb, IIc, and IIe tested statically and dynamically. In this case, the idealized behaviour had a reduced correlation with the experimental behaviour. However, it can be observed that the overall idealized behaviour provides a fair representation of the experimental behaviour.

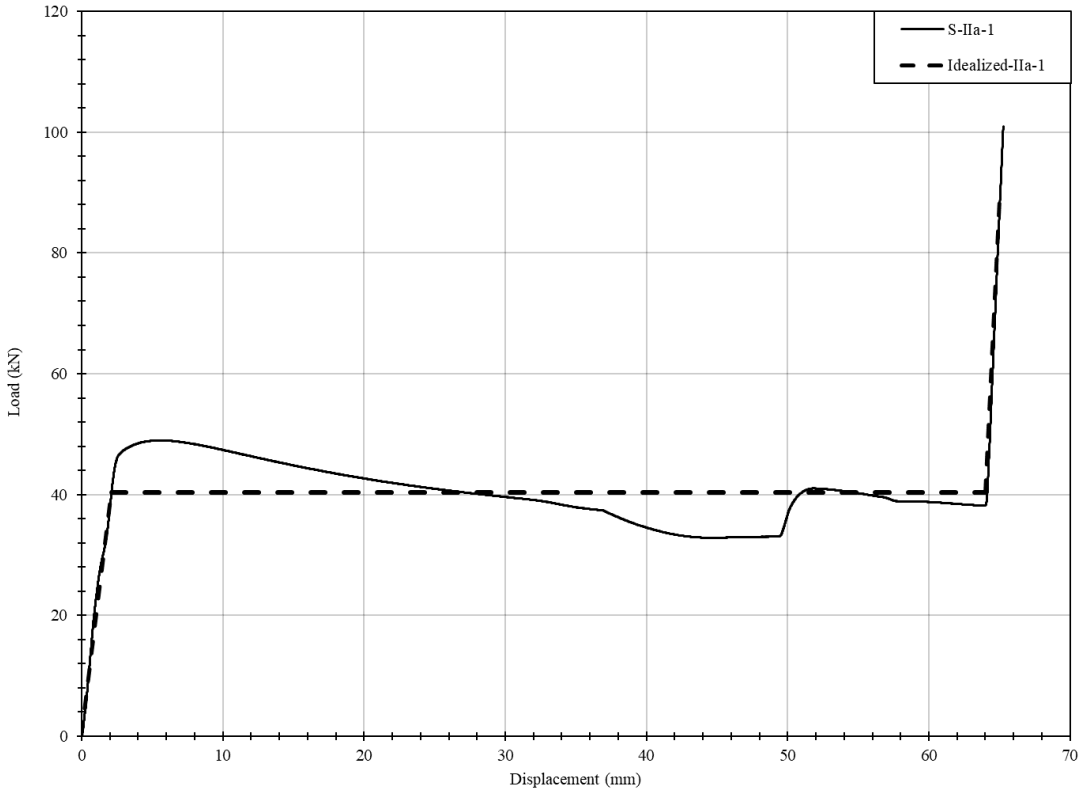

Figure 6.7: Experimental Static and Idealized Load-displacement Curve for Specimen S-IIa-1

Finally, for specimens Id and IId, the idealized behaviour based on the proposed methodology was not able to capture the experimental behaviour, as shown in Figure 6.8. It can be observed that although the absorbed energy up to densification is maintained in the idealized behaviour, the idealized yield load is significantly different from the experimental yield and average plateau load. Thus, no idealized values of yield load or yield displacement have been provided, and further discussion about their applicability as EACs will be made in Chapter 7.

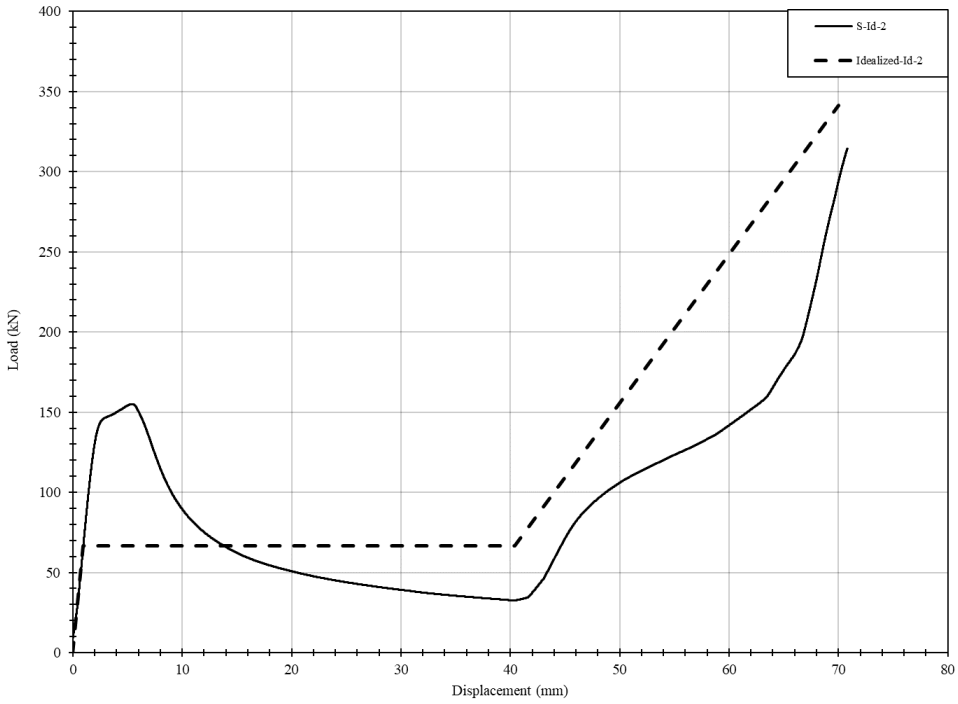

Figure 6.8: Experimental Static and Idealized Load-displacement Curve for Specimen S-Id-1

6.4 Revised FEA Model

6.4.1 Limitations of Preliminary FEA Model and Introduction of the Revised FEA Model

The preliminary FEA model was not able to capture the static behaviour of specimens Id, IIa, IIb, IIc, IId, and IIe, and thus, a revised FEA model was developed with three major modifications. First, since coupon testing resulted in average yield strength of 400 MPa instead of the initially assumed 300 MPa, the yield strength used in the material properties was modified to capture the actual material behaviour. Secondly, since lateral movement of the top plate was observed experimentally, the symmetry boundary condition initially used to simplify the analysis was removed to allow for this lateral movement. Some specimens also experienced rotation, which was not captured in the model. The symmetry boundary condition was most likely preventing this mechanism. Thus, the full EACs were modelled without any symmetry boundary conditions (Figure 6.9) in the revised model. Finally, due to the fact that welds of the circular HSS for specimen IIa were different in the static and dynamic tests, two types of welds, representative of the actual configuration tested were investigated (Figure 6.10 and Figure 6.11). A sketch of the modified boundary conditions is shown in Figure 6.12.

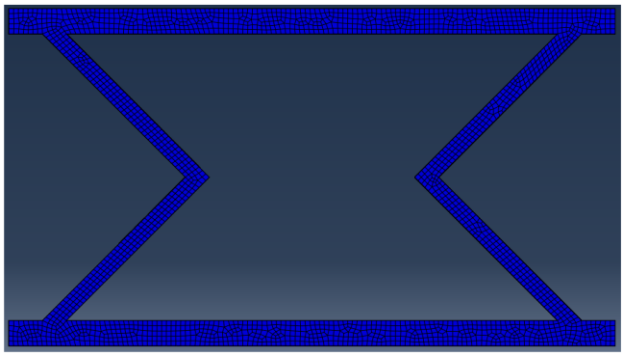

Figure 6.9: Revised FEA mesh for specimen Ia

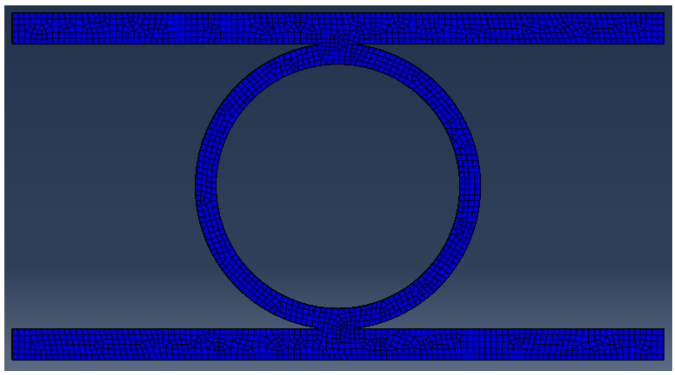

Figure 6.10: Revised FEA mesh for specimen IIa with weld type 1

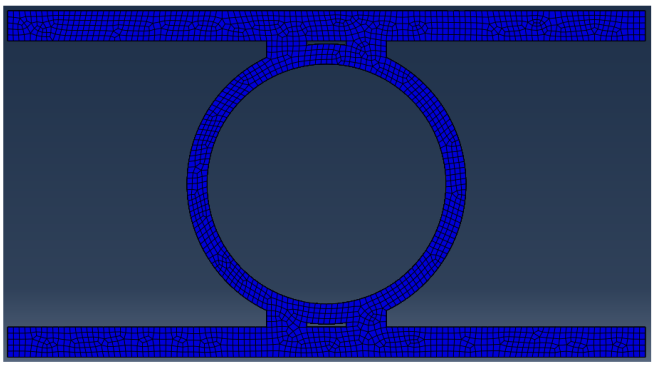

Figure 6.11: Revised FEA mesh for specimen IIa with weld type 2

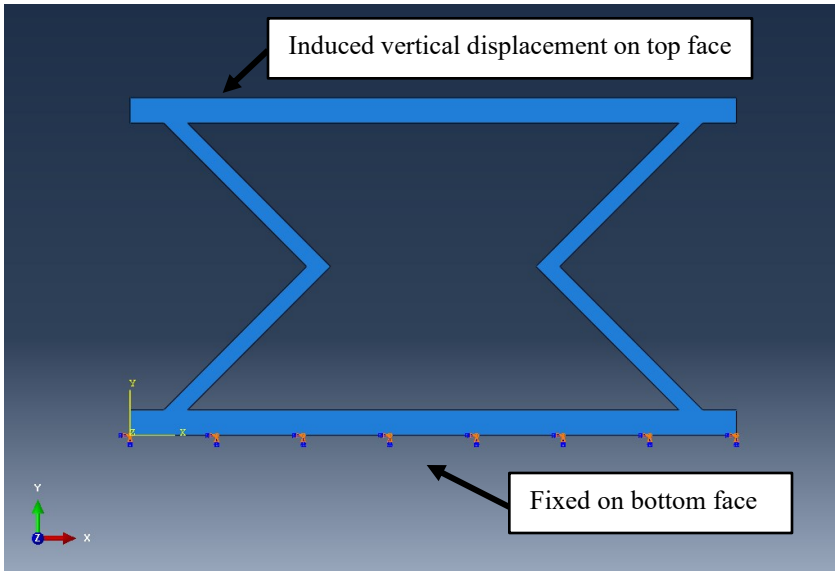

Figure 6.12: Boundary conditions of revised FEA model

6.4.2Mesh Sensitivity Analysis

Prior to performing the FEA analysis, a mesh sensitivity analysis was performed for specimen Ia to determine the number of elements or nodes necessary to produce accurate results. The global size parameter of *Abaqus* (Smith 2009) was varied from 1 to 5, which resulted in a varying number of elements and nodes. Table 6.6 and Figure 6.13 shows the resulting number of elements and nodes for varying values of global size. Figure 6.14 shows the initial mesh for a global size of 2 and 4, respectively, where the latter has a finer mesh.

Table 6.6: Number of elements and nodes for varying global size

Global size	Elements	Nodes
5	2740	4697
4	6695	9856
3	13294	18612
2	45075	56784
1.5	104890	125720
1	366639	413556

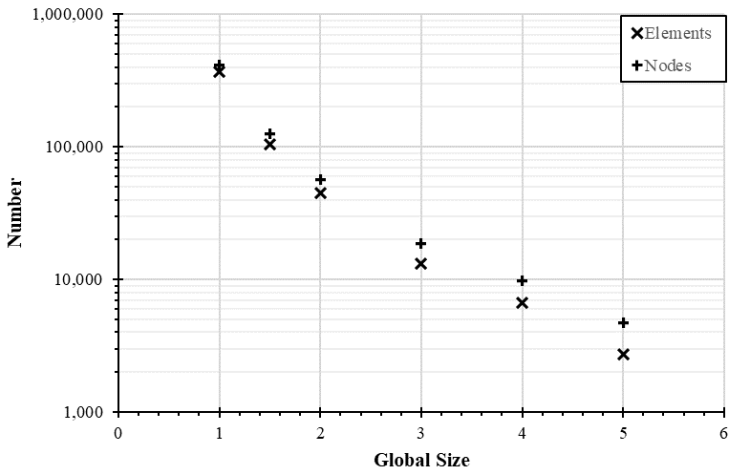

Figure 6.13: Global size and resulting number of elements and nodes

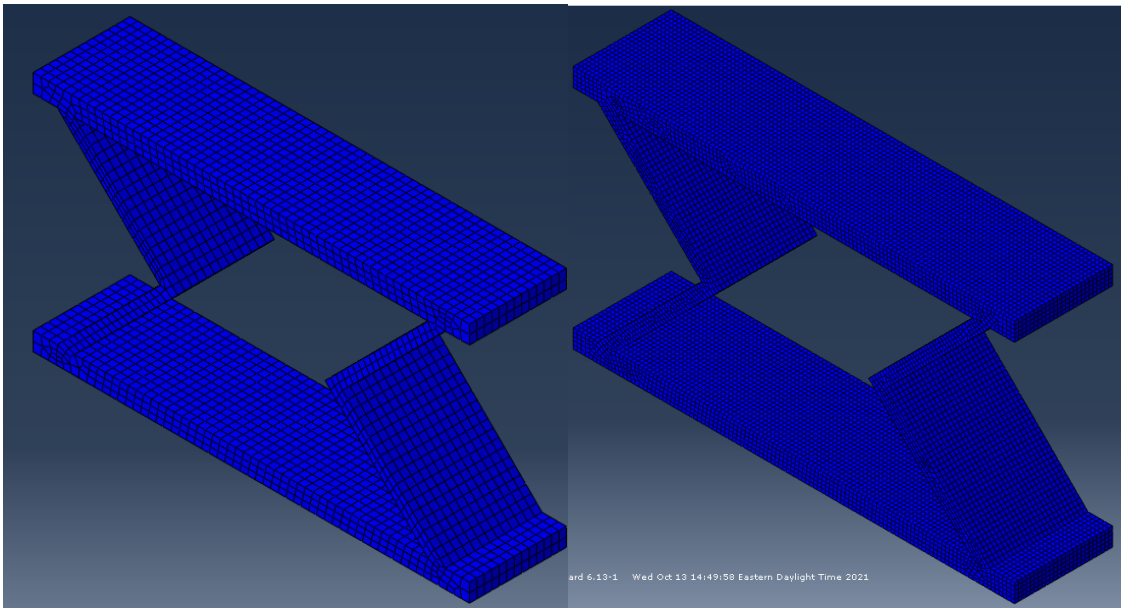

Figure 6.14: Revised FEA model mesh for a global size of 4 (left) and 2 (right), respectively.

For each global size value, the FEA model was run to obtain the load-displacement curve and failure mode, as shown in Figure 6.15. It can be observed that FEA results for global sizes less than three result in mesh-independent load-displacement behaviour. Furthermore, a global size of 1 or less would be more time and computationally demanding. For this reason, a global size between 1 and 3 was used for meshing and was deemed appropriate for all models. The global size was also varied between 1 and 3 until the mesh seemed uniform and well distributed for each model.

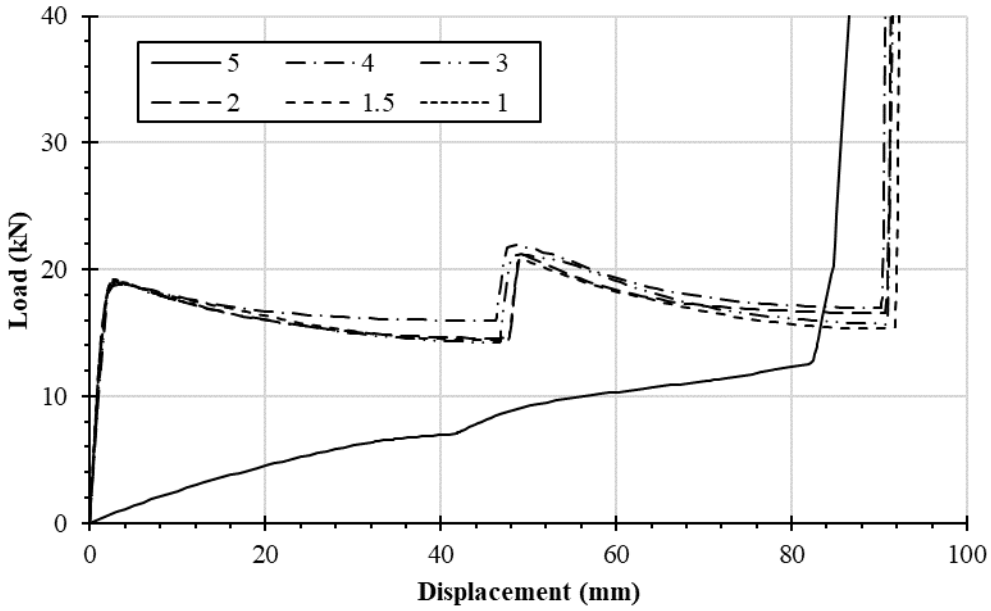

Figure 6.15: Mesh sensitivity analysis of load-displacement FEA model results

6.4.3 Comparison of Revised FEA Model and Experimental Static Results

The revised FEA model results were compared with the experimental static results to validate the revised FEA model. Figures 6.15 to 6.18 presents the experimental static, preliminary FEA model, and revised FEA model results for each specimen type where considerable improvement was achieved from the preliminary FEA model. It can be observed that the revised model is able to capture the overall shape of the static load-displacement curve and offers improved accuracy when compared with the initial FEA model. Also, the overall shape of the load-displacement curve for specimen IIa with two different welds is able to capture the overall behaviour and deflected shape for weld types 1 and 2 (Figure 6.20 and Figure 6.21). The revised model was also able to predict the load reduction experienced following yielding by specimens Id and IId and simulate the rotation of the centre steel section in the deformed shape. Further improvement could be achieved by considering strain-hardening effects, investigating the effects of weld type, and investigating the effect of meshing symmetry on the overall behaviour. More details on the revised FEA model results can be found in Appendix D.

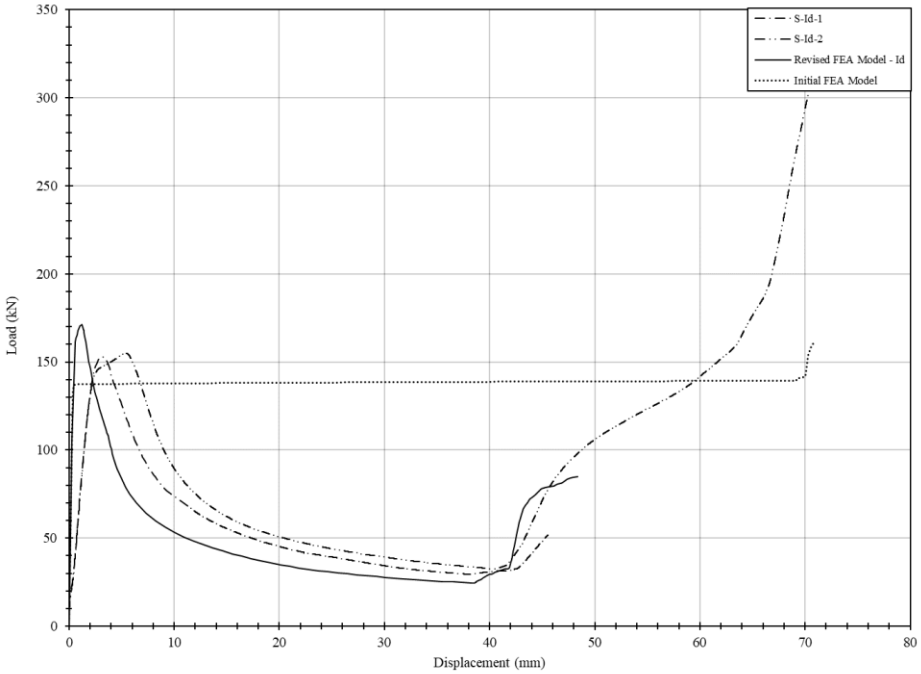

Figure 6.16: Revised FEA model – Id

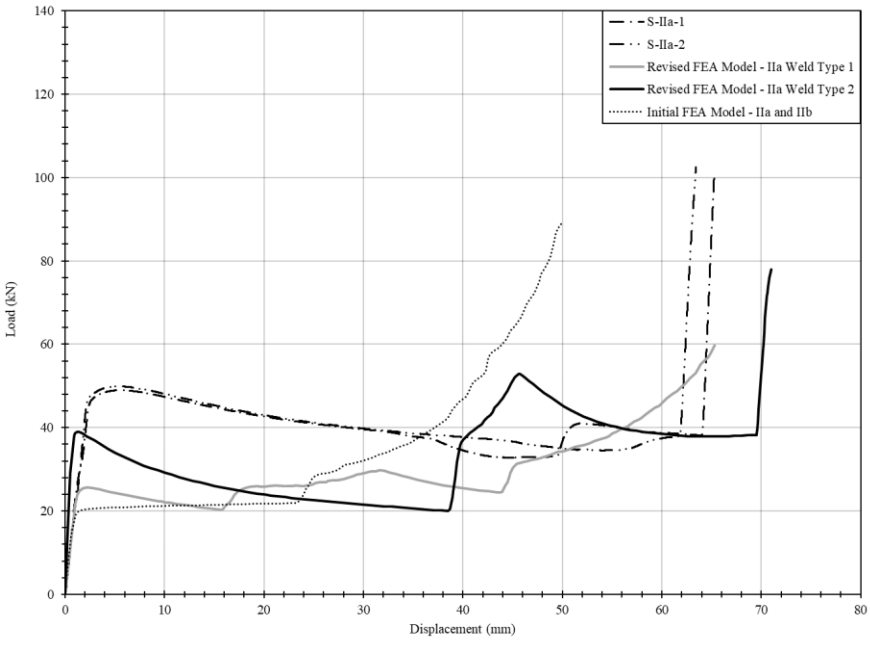

Figure 6.17: Revised FEA model – IIa

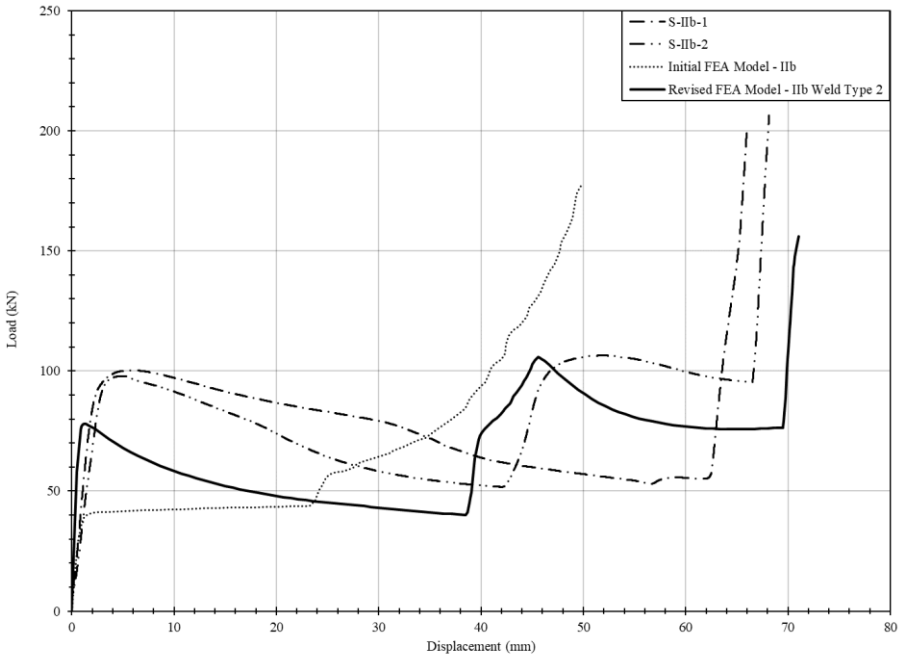

Figure 6.18: Revised FEA model – IIb

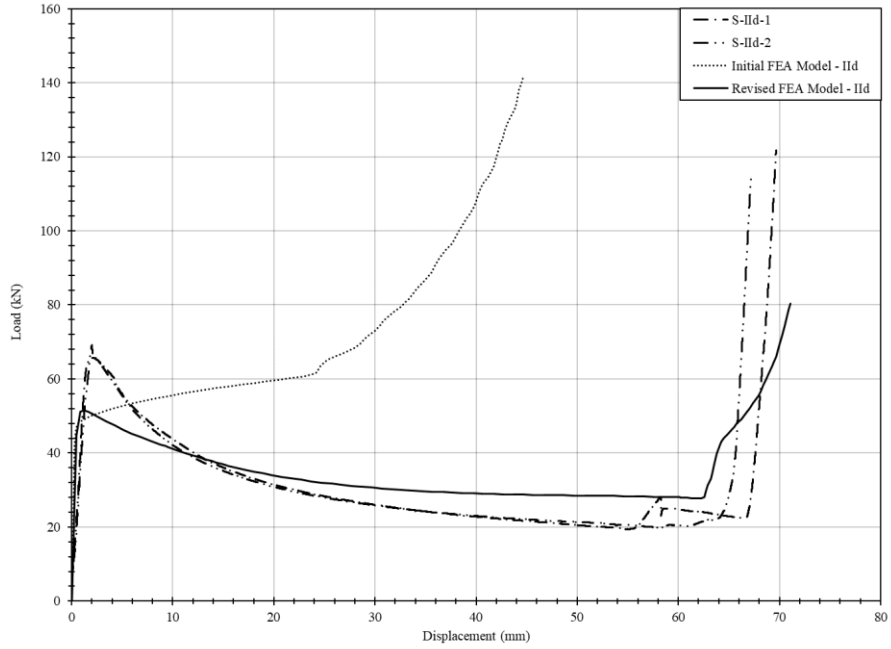

Figure 6.19: Revised FEA model – IId

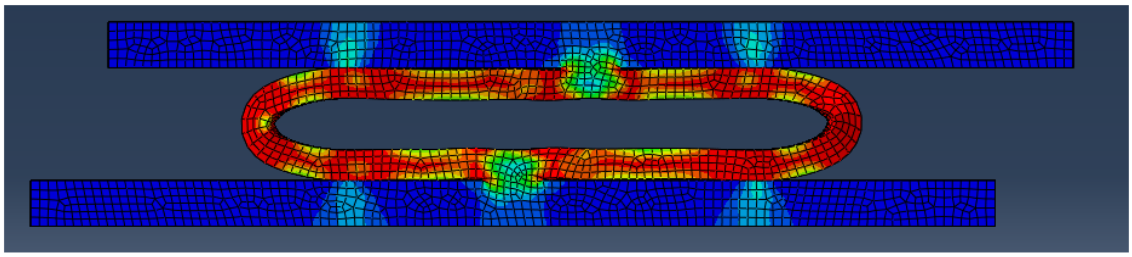

Figure 6.20: Deflected shape for specimen type IIa with weld type 1

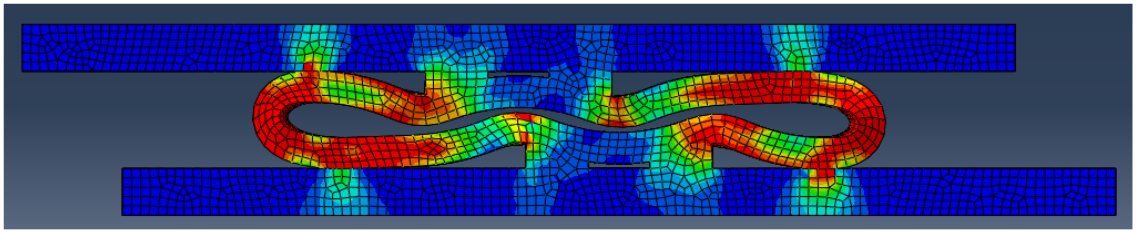

Figure 6.21: Deflected shape for specimen type IIa with weld type 2

CHAPTER 7 - Discussion

7.1 General

This chapter presents the discussion of the experimental and analytical results obtained in the previous chapters. First, a comparison between the static and dynamic test results for specimens of the same type is presented in Section 7.2. This is followed by a discussion of the effects of geometry and weld type on the observed experimental load-displacement behaviour in Section 7.3. Section 7.4 discusses the applicability of EAC for use in timber assemblies, the design process of EAC in timber assemblies with examples, and the potential improvement in the performance of timber assemblies and section 7.4.1 will discuss design considerations.

7.2 Comparison between Static and Dynamic Tests Results

Evaluation of the static and dynamic experimentally measured load-displacement curves showed similar behaviour for specimens with the same manufacturing details, as shown in Figure 7.1. DIFs for yield load and stiffness of 1.12 and 2.3, respectively, were observed for these specimens with a CoV of 6.7% and 38.5%, respectively. This level of dynamic increase on the yield load is typical of steel under high strain rate loading and is already well documented in the literature (i.e. Chen 2010; CSA 2012).

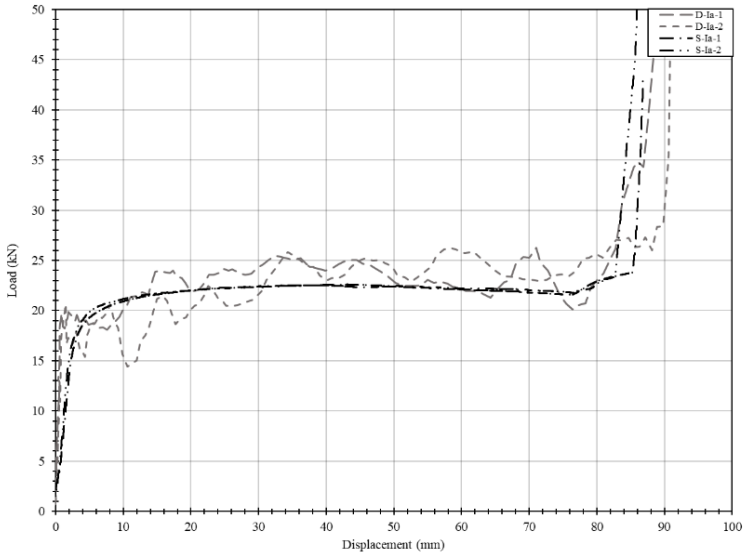

Figure 7.1: Static and dynamic load-displacement curves for specimen type Ia

It should be noted that this comparison is not valid for specimens IIa, IIb, IIc, and IIe since different welds were provided during manufacturing for specimens tested statically and dynamically. Thus, a DIF cannot be determined from the experimental results for these specimens. Further discussion on the effect of welds will be presented in the following section.

7.3 Effect of Geometry and Weld Type on EAC Load-displacement Behaviour

7.3.1 EACs Manufactured from Angles

7.3.1.1 Effect of Angle Thickness and Leg Length

It can be observed from the static or dynamic results that the angular EACs with varying angle thickness and leg length had similar behaviour. Specimen Ia was designed with leg lengths of 76.2 mm [3"] and a thickness of 6.35 mm [0.25"]. Specimen Ib and Ic were designed to be identical to specimen Ia except for one geometrical variable in order to investigate if changing these variables would affect the load-displacement behaviour. For specimen Ib, only the angle leg length was reduced to 50.8 mm [2"], while for specimen Ic, only the angle thickness was increased to 12.7 mm [0.5"]. Figure 7.2 shows the static experimental load-displacement results for specimens Ia, Ib, and Ic. As expected, it can be observed that changing the geometrical properties influenced the experimental load-displacement behaviour.

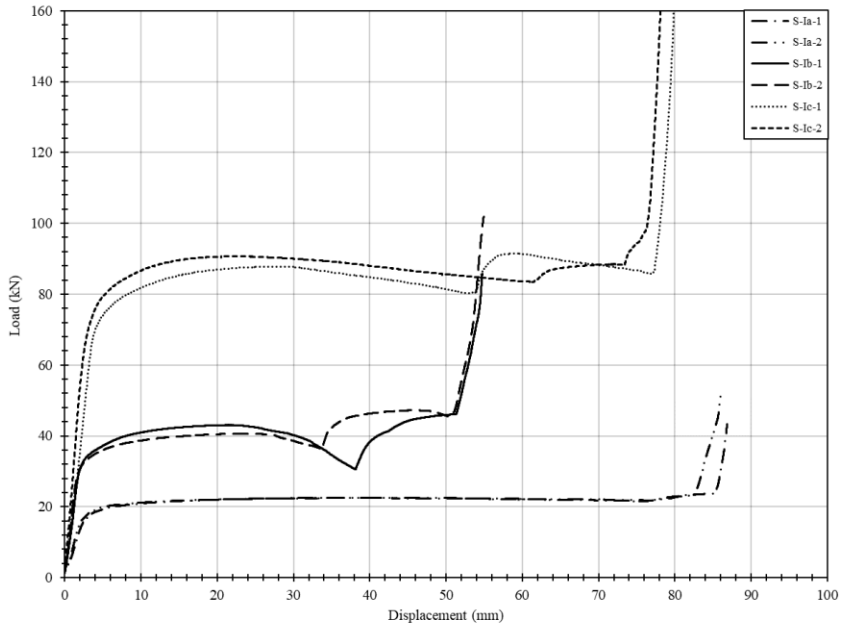

Figure 7.2: Comparison of the static load-displacement results for specimen types Ia, Ib, and Ic

Table 7.1 shows the load-displacement properties and percent change for the changes in geometry investigated in relation to specimen Ia, respectively. The values for yield load, elastic stiffness and densification displacement are based on the idealized load-displacement properties presented in Chapter 6.

Table 7.1: Geometry percent change in relation to specimen type Ia and corresponding property percent change

Specimen Types for Comparison	Test Type	Geometry Percent Change (%)		Corresponding Property Percent Change (%)		
		Thickness	Leg Length	Yield Load	Elastic Stiffness	Densification Displacement
Ia – Ic	Static	100	N.A*	293	213	-10
Ia – Ic	Dynamic	100	N.A.*	308	118	-23
			Average	300	166	-17
Ia – Ib	Static	N.A.*	-33.3	86	141	-39
Ia – Ib	Dynamic	N.A.*	-33.3	112	107	-42
			Average	99	124	-41

*N.A. = Not Applicable

It can be observed that for an increase in thickness of 6.35 mm (100%), from specimen Ia to Ic, the yield load and elastic stiffness increased by approximately 300% and 118%, respectively. Similarly, a reduction in leg length of 25.4 mm (33.3%) from specimen Ia to Ib resulted in the yield load being increased by approximately 99%, while the elastic stiffness increased by approximately 124%. It can also be observed that a reduction in densification displacement is present when the angle thickness increases or the leg length decreases. This reduction in densification displacement is due to the distance between the plates being reduced by providing a shorter EAC depth. This is achieved either through a different angle leg length or thickness.

7.3.1.2 Effect of Centre Weld

A significantly different behaviour was observed for specimen Id, where a reduction in load was observed following yielding and prior to densification. This is contrary to the well-defined plateau observed with specimens Ia, Ib, and Ic (Figure 7.4). Although this connection provided a significantly higher strength, the post-peak behaviour was altered significantly by the weld type alone. In terms of prediction of behaviour, this type of connection is less desirable in blast mitigation strategies since it is difficult to control the post-peak behaviour compared to what was observed in connection types Ia, Ib, or Ic. It can also be noted that a change in the weld type and location for an otherwise identical geometry did cause a significant change in the behaviour.

Although this connection may not be ideal for blast applications, the significant increase in load and stiffness may be advantageous in design situations where inelastic energy dissipation is not required.

Figure 7.3: Specimen type Ia (left) and Id (right)

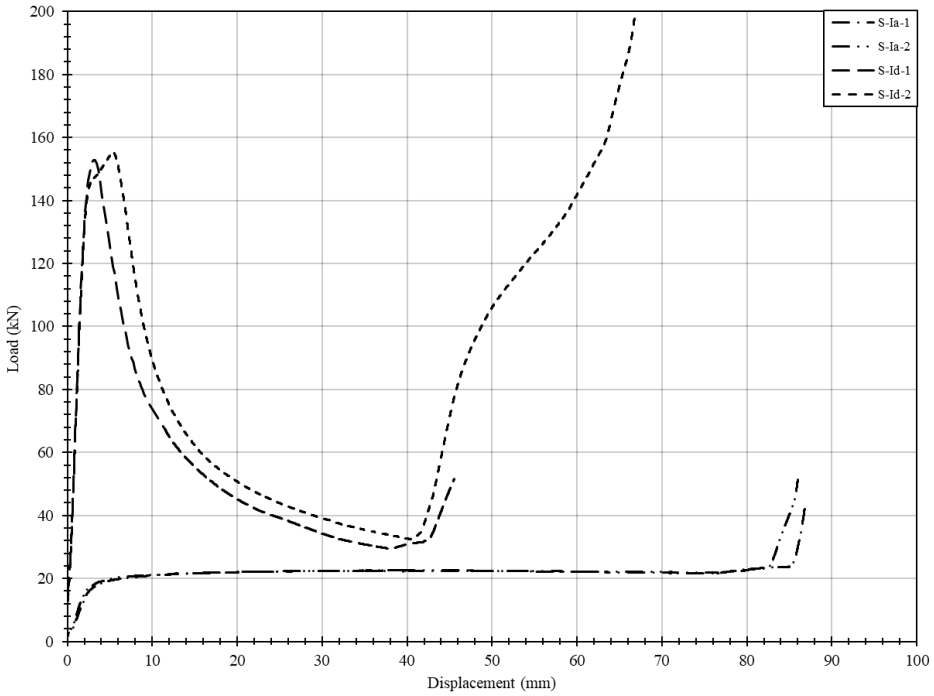

Figure 7.4: Comparison of the static load-displacement results for specimen types Ia and Id

Table 7.2 shows the percent change for the properties of specimen Id in relation to specimen Ia for both static and dynamic experimental results.

Table 7.2: Property percent change due to addition of centre weld

Specimen Types for Comparison	Test Type	Corresponding Property Percent Change (%)		
		Yield Load	Elastic Stiffness	Densification Displacement
Ia – Id	Static	600	920	-51
	Dynamic	638	1374	-49
Average		619	1147	-50

When comparing the maximum load of specimen Id (which is close to the yield load) and the yield load of specimen Ia, it can be observed that an increase of approximately 619% was achieved. A more significant increase of 1147% was observed for the elastic stiffness. A reduction of 50% was observed for densification displacement. Further research is recommended on the effect of weld type for different EAC geometries.

7.3.2 Circular EACs

7.3.2.1 Effect of Weld Type on Load-displacement Behaviour

Different load-displacement behaviours were observed for the circular HSS EACs tested statically and dynamically due to the different weld types provided. Table 7.2 shows the experimental static and dynamic load-displacement behaviour for specimen IIa. It can be observed that the static specimens where welds were provided at the sides of the circular HSS (i.e. weld type 2 presented in Chapter 6) exhibited a reduction in load following the elastic region, up to densification. However, for the specimens tested dynamically (i.e. weld type 1) where only a single weld was provided at the centre, an increase in load was observed up to densification. The yield load is observed to be dramatically affected by the weld types, with the static specimens with weld type 2 having a significantly larger yield load compared to the specimen tested dynamically with weld type 1.

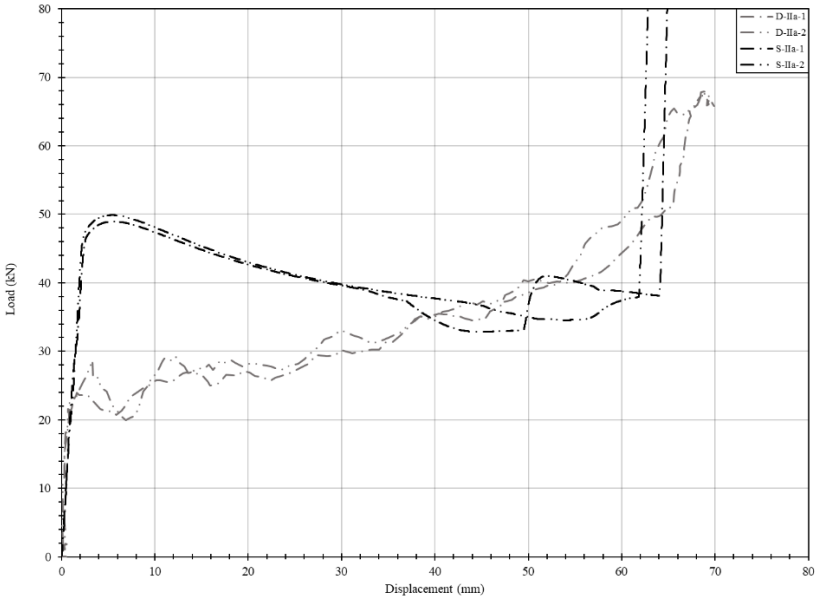

Figure 7.5: Comparison of static (Weld Type 1) and dynamic (Weld Type 2) load-displacement results for specimen type IIa

7.3.2.2 Effect of Circular HSS Diameter and EAC Depth

Circular EACs specimen IIa, IIb, and IIc, had generally similar experimental load-displacement behaviour. Specimen IIa was designed with a circular HSS diameter of 88.9 mm [3.5"] and depth of 50.8 mm [2"]. Specimen IIb and IIc were designed to be identical to specimen IIa except for geometrical variables intended to investigate their effect on the load-displacement behaviour. For specimen IIb, only the depth was increased to 101.6 mm [4"], while for specimen IIc, only the circular HSS diameter was increased to 127.0 mm [5"]. Figure 7.6 shows the static experimental load-displacement results for specimens IIa, IIb, and IIc. It can be observed that changing the geometrical properties influenced the experimental load-displacement behaviour.

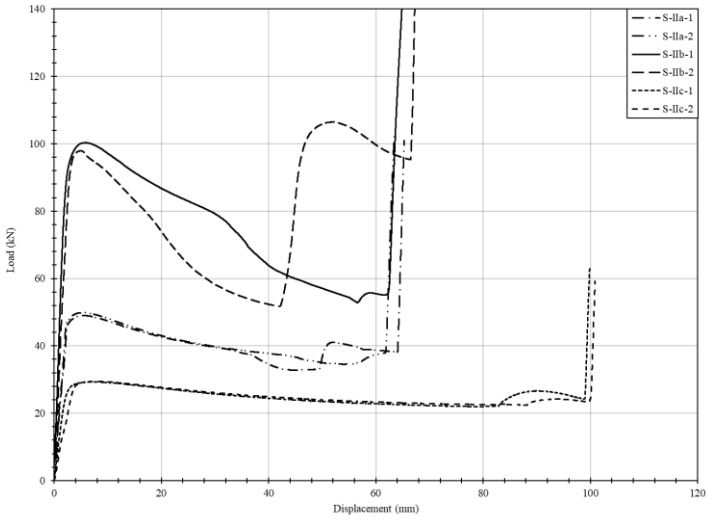

Figure 7.6: Comparison of the static load-displacement results for specimen types IIa, IIb, and IIc

Table 7.3 presents the percent change and corresponding change in mechanical properties based on the idealized experimental load-displacement curves.

Table 7.3: Geometry percent change in relation to specimen IIa and corresponding property percent change

Specimen Types for Comparison	**Test Type**	**Geometry Percent Change (%)**		**Corresponding Property Percent Change (%)**		
		Diameter	**Depth**	**Yield Load**	**Elastic Stiffness**	**Densification Displacement**
IIa - IIb	Static	N.A.	100	93.1	101.0	2.1
	Dynamic	N.A.	100	108.8	356.3	-2.0
IIa - IIc	Static	43	N.A.	-38.5	-46.7	57.9
	Dynamic	43	N.A.	-35.1	-30.1	41.0

It can be observed with specimen IIa and IIb that increasing the depth by 100% caused an increase in yield load of approximately 93% for weld type 2 (i.e. static) and 108% for weld type 1 (i.e. dynamic). Larger increases were observed for elastic stiffness, with 101% and 356% for weld types 2 and 1, respectively. The goal of testing specimen IIb was to identify whether the load-displacement results from specimen IIa would be scalable with the depth (i.e. multiplied by a factor of 2 in this case). Since the increase in depth was accompanied by a proportional increase in yield load and stiffness, scalability is thus confirmed experimentally for the range of dimensions tested.

However, no evidence showed that the densification displacement varied with a change in depth, which indicates that this value remains constant for changes in depth.

It can also be observed with specimen IIa and IIc that increasing the diameter of the EAC from 88.9 mm to 127 mm (43% increase) reduced the idealized yield load and stiffness by 35-38% and 30-47%, respectively. However, this also caused an increase in densification displacement of at least 41%. It is noted that this connection is most likely the most interesting of the circular connections for EAC application since the plateau was much more clearly defined in comparison to the other specimens. It also had a larger densification displacement, delaying the onset of densification and allowing for more energy absorption. Although the yield load is lower, this parameter could be adjusted by adjusting the depth until the desired yield load is achieved, as was demonstrated in specimens IIa and IIb.

7.3.2.3 Effect of Circular HSS Arc

Specimen IIc was manufactured with an arc circumventing 90° of a 127 mm [5"] circular HHS. The goal of testing this specimen was to investigate other possible behaviours that could be used to optimize energy dissipation. Although these connections achieved an increased yield load, it was followed by a greater loss in capacity up to densification (Figure 7.7). As such, the change in arc angle did not seem to maintain a sustained post-peak strength and was therefore not considered an improvement in behaviour for the purpose of optimizing the energy absorption.

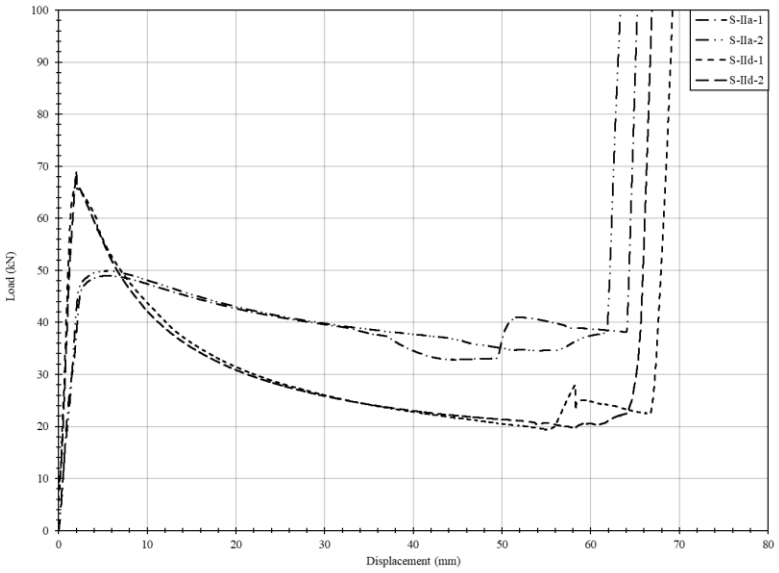

Figure 7.7: Comparison of the static load-displacement results for specimen type IIa and IId

7.3.2.4 Effect of Multiple Circular HSS

Specimen IId was manufactured in an identical manner to specimen IIa, except for the additional circular HSS with a diameter of 60.3 mm [2.375"], which was added to the centre. It is observed from the experimental results that although the initial behaviour was very similar between the two specimen types, following the contact with the secondary circular HSS, a secondary plateau and even tertiary plateau (in the case of specimen S-IIe-1) was generated (Figure 7.8). For the EAC application, this connection was very interesting and should possibly be investigated in more depth. In terms of overall energy absorption, this connection type did not seem to provide any additional advantages over a single circular HSS and the manufacturing was more demanding. However, the interesting aspect of having multiple plateaus is that it could be used in assemblies where multiple failure modes are present. A yielding failure mode could be allowed but other brittle failure modes could be prevented at various displacement levels. This would require future work and research.

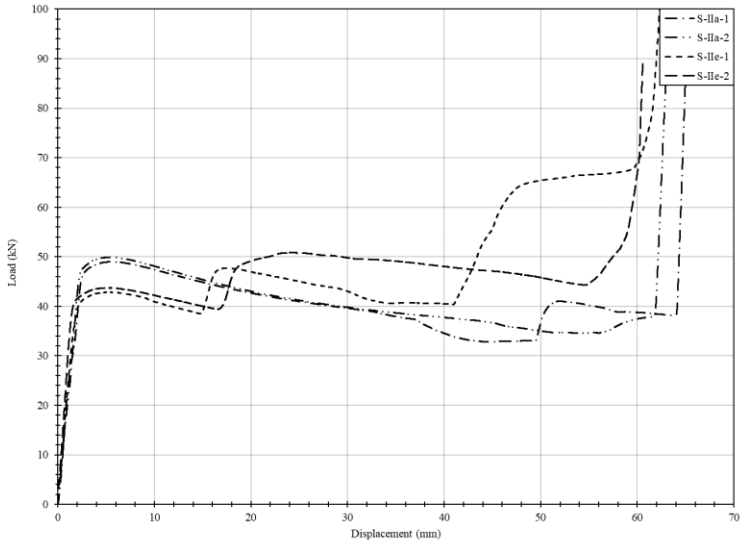

Figure 7.8: Comparison of the static load-displacement results for specimen types IIa and IIe

7.4 Application of EACs to Timber Assemblies and Design Considerations

It is well-established in the literature that wood is brittle when loaded in bending, has limited post-peak behaviour and generally has low mass, which leads to poor performance under blast loading (Lacroix 2017; Viau and Doudak 2016b). To improve the performance of wood elements, connections are introduced to add ductility and energy absorption. Boundary connections such as bolted connections or bearing angles connections can add ductility and energy absorption.

However, this is highly dependent on the adequate design of the timber assembly. If, for example, the connection is designed so that it is stronger than the main timber member, the connection may not improve the system's behaviour (Viau 2020). Even if these connections are properly designed, they often have limited potential to mitigate blast load effects on timber assembly since they do not offer a large amount of added energy absorption potential.

On the other hand, some EACs can offer significant energy absorption potential prior to causing ultimate failure in the main timber member. To illustrate this concept, the performance of a timber assembly where EACs are present is investigated analytically in this section with the results from the present study.

The conceptual timber assembly (Figure 7.9) consists of a spruce-pine 24f-ES, 80 mm wide and 228 mm deep, glulam member with a span of 3000 mm where an energy-absorbing connection is attached at each support. Mechanical properties for the bending design of the glulam member as reported by the manufacturer are shown in Table 7.4.

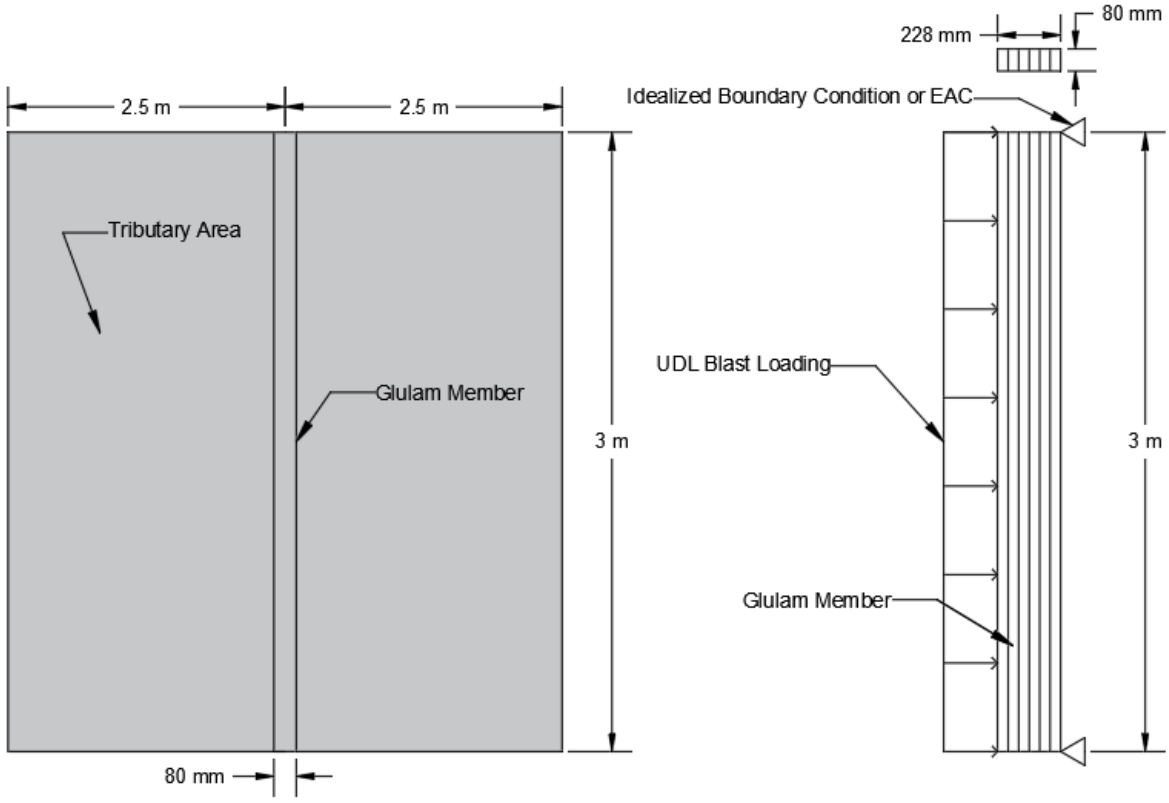

Figure 7.9: Conceptual Scenario

Table 7.4: Manufacturer provided mechanical property for glulam 24f-ES (Nordic 2020)

Mechanical property	Value
Bending moment strength, f_b (MPa)	30.7
Longitudinal shear strength, f_v (MPa)	2.5
Apparent modulus of elasticity, E (MPa)	12400
Density, ρ (kg/m^3)	560

For this investigation, the average dynamic bending moment capacity of the glulam member was determined according to clause 7.5.6.5 of CSA O86 (CSA 2019), as shown in Equation 7.1.

$$M_r = \phi_b f_b (K_D K_H K_{Sb} K_T) S K_x \times \min(K_{Zbg}, K_L) \quad \text{Equation 7.1}$$

Where ϕ_b is the resistance factor for bending, f_b is the specified bending moment strength, K_D is the load duration factor, K_H is the system factor, K_{Sb} is the service condition factor, K_T is the treatment factor, S is the section modulus, K_x is the curvature factor, K_{Zbg} is the size factor in bending for glulam, and K_L is the lateral stability factor. The values for each parameter used in the current investigation and the calculated bending moment capacity are presented in Table 7.5.

Table 7.5: Summary of bending moment capacity calculation

Parameter	Value	Comment
ϕ_b	1.0	Rare event
f_b	30.7 MPa	See Table 7.4
K_D	1.15	Short term loading
$K_H K_{Sb} K_T$	1.0	Single glulam member, dry and untreated
S	6.931×10^6 mm^3	80 mm × 228 mm rectangular section
K_x	1.0	Member without curvature
K_{Zbg}	1.294	Clause 7.5.6.5.1 of CSA O86 (CSA 2019)
K_L	1.0	Clause 7.5.6.4 of CSA O86 (CSA 2019)
M_r	31.67 kN-m	Resulting bending moment capacity (Equation 7.1)

From the specified static bending moment capacity (M_r) of 31.67 kNm, the average dynamic bending moment capacity ($M_{r,D}$) was determined by using a DIF and SIF, as shown in Equation 7.2 (CSA 2012).

$$M_{r,D} = M_r \times SIF \times DIF \quad \text{Equation 7.2}$$

According to the Canadian blast design standard, CSA S850 (CSA 2012), a SIF of 1.2 and a DIF of 1.4 is applicable to glulam. This resulted in an average dynamic bending moment capacity of 53.20 kNm, which coincides for uniformly distributed loading over the 3 m span of the member to a dynamic ultimate failure capacity of 141.88 kN. The elastic stiffness of the glulam member (K_e) was then calculated using Equation 7.3.

$$K_e = \frac{384 E_s I}{5L^3} \quad \text{Equation 7.3}$$

Where L is the length, E_s is the modulus of elasticity corrected by the service condition factor (K_{SE}) and the treatment factor (K_T), and I is the moment of inertia. The values for each parameter used in the current investigation and the elastic stiffness is presented in Table 7.6.

Table 7.6: Summary of elastic stiffness calculation

Parameter	Value	Comment
L	3 m	Length of the glulam member
E_s	12400 MPa	Equal to E since K_{SE} and K_T are equal to 1.0. See Table 7.4.
I	7.902×10^7 mm^4	80 mm × 228 mm rectangular section
K_e	2.78 kN/mm	Resulting elastic stiffness (Equation 7.3)

Thus, the average resistance curve of the glulam member was defined by the dynamic ultimate failure capacity and the elastic stiffness, as shown in Figure 7.10. The timber member was first modelled with idealized boundary conditions using the blast analysis software RCBlast® (Jacques 2014), which utilizes Single-Degree of Freedom (SDOF) analysis. A timber member-EAC assembly was then modelled with BlasTDOF (Viau 2020), a Two-Degree of Freedom (TDOF) blast analysis software. The main goal of both analyses was to determine the minimum peak positive pressure that would cause ultimate failure in the glulam member.

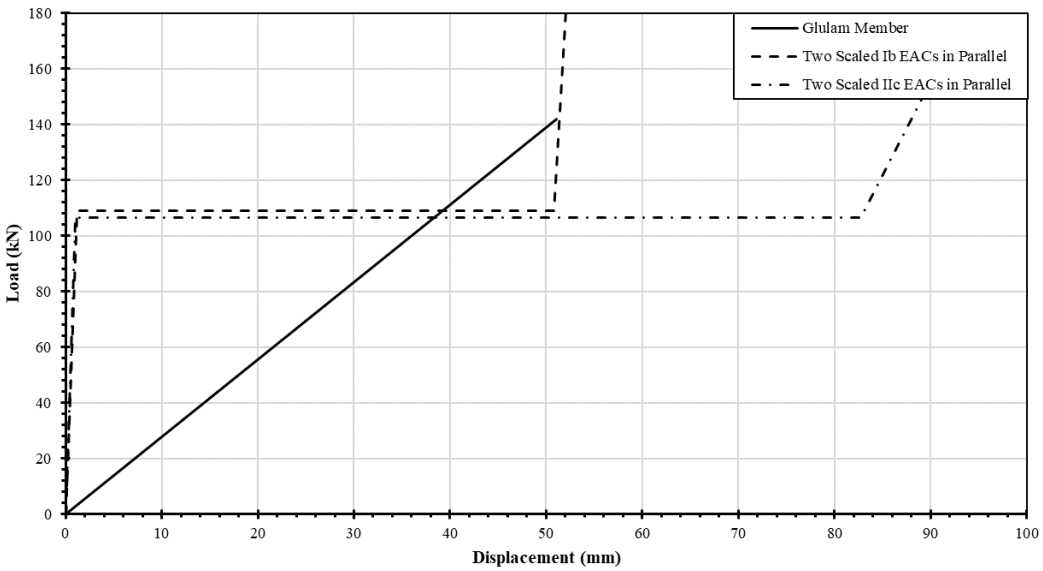

Figure 7.10: Glulam member and EAC resistance curves

Based on the dimensions of the member, the mass of the member for modelling was taken as 25.6 kg based on the manufacturer's provided density shown in Table 7.4. To account for additional mass provided by cladding or elements that are transferring the blast loading to the main timber member, an additional mass equal to the member mass was added for a total of 51.2 kg. This mass could vary; however, it is deemed that this assumption is appropriate since the same mass will be used in all analyses. The loading was assumed to be uniformly distributed, which is typical of blast design, and as such, a load-mass factor of 0.78 is deemed appropriate (Biggs 1964). The loaded area on the cladding member was taken as 15 m^2 considering 2.5 m width on each side of the member. The forcing function on the uniformly loaded area was idealized with a triangular pressure-time history with a constant positive phase duration of 20 ms and an unknown peak positive pressure. The unknown impulse corresponding to the positive peak pressure is thus directly proportional to the positive phase duration. From this analysis, a minimum peak positive pressure of 6.5 kPa, corresponding to an impulse of 65 kPa-ms, caused ultimate failure in the glulam member with idealized boundary conditions.

The EACs selected for the analysis are specimens Ib and IIc. Both specimens have a depth that has been scaled so that the EAC yield load does not exceed the ultimate failure load of the glulam member. This methodology relies on the overdesign factor for yielding, which provides an indication of how much lower the connection yield load should be with respect to the wood

member ultimate failure load for a required probability of failure Viau and Doudak (2021b). By ensuring that the EAC yield load is lower than the main member ultimate failure load with a certain margin, potential variations in the wood member properties (i.e. defects, moisture content variations, etc.) or the connection manufacturing (i.e. errors, poor quality, etc.) are thus considered in the design.

The idealized resistance curve taken for the EAC specimens selected for this investigation was based on the dynamic load-displacement properties presented in Chapter 6, as shown in Figure 7.10 for two connections in parallel. The average values for elastic stiffness, yield load, displacement at the onset of densification, and densification stiffness prior to scaling are presented numerically, with their corresponding CoV, in Table 7.5. It is to be noted that although stiffness values were scaled, the displacements at the onset of densification were not scaled since there was no evidence that this value is affected by the depth, refer to Section 7.3.

Table 7.7: Unscaled and scaled properties for EAC specimens

Property	**Specimen Ib**		**Specimen IIc**	
	Average value	**CoV (%)**	**Average value**	**CoV (%)**
Unscaled depth, d (mm)	50.8	N.A.	50.8	N.A.
Elastic stiffness, K_e (kN/mm)	40.0	16.0	20.0	6.2
Yield load, F_y (kN)	49.4	0.5	20.7	1.7
Displacement at onset of densification, Δ_D (mm)	50.8	1.7	82.7	3.1
Densification stiffness, K_D (kN/mm)	26.0	44.6	1.3	4.4
Scaled depth (mm)	56.1	N.A.	130.9	N.A.
Scaled elastic stiffness (kN/mm)	44.2	N.A.	51.5	N.A.
Scaled yield load (kN)	54.6	N.A.	53.3	N.A.
Scaled densification stiffness, K_D (kN/mm)	28.7	N.A.	3.3	N.A.

The two EACs were selected to compare the effect of varying displacement at the onset of densification on the performance of the assembly when their depths are scaled so that they reach a yield load that gives the same probability of exceedance. The improvement in performance was

assessed by calculating the percent increase in minimum peak positive pressure causing ultimate failure in the glulam member from the case where idealized boundary conditions are provided. For the TDOF analysis, the same glulam member properties and loading assumptions were selected for the member degree-of-freedom. For the second degree-of-freedom, representing the connections, a mass of 2.6 kg was taken for each EACs, which was the average measured mass of the EACs. Since an EAC would be required for each side of the member at the supports, the option "two ends with connections" in the BlasTDOF software was selected. This option considers that the two connections act in parallel. Thus, the resistance curves for both EACs are added together to obtain a total connection resistance curve for the connection degree-of-freedom. No load-mass factor was applied to the connection degree-of-freedom since they are lumped at the supports.

From the TDOF analysis, a minimum peak positive pressure of 8.6 kPa, corresponding to an impulse of 86 kPa-ms, caused ultimate failure in the glulam member for specimen Ib. This represents a 32.3% increase when compared with the glulam member with idealized boundary conditions. For specimen IIc, a minimum peak positive pressure of 9.5 kPa, corresponding to an impulse of 95 kPa-ms, caused ultimate failure, which represents a 46.2% increase. This indicates that both EACs are able to improve the performance of the timber assembly and that the connection with the larger densification displacement (scaled IIc) was able to absorb more energy and offer better performance. The system displacement time-histories for the three cases analyzed in this section are shown in Figure 7.11, while the individual degree-of-freedom (DOF) displacement time-histories for the system with specimen IIc is shown in Figure 7.12. It can be observed that the EAC is only engaged once it yields, at which point the member displacement reduces while the EAC deforms considerably. The EAC was thus able to delay ultimate failure in the glulam member.

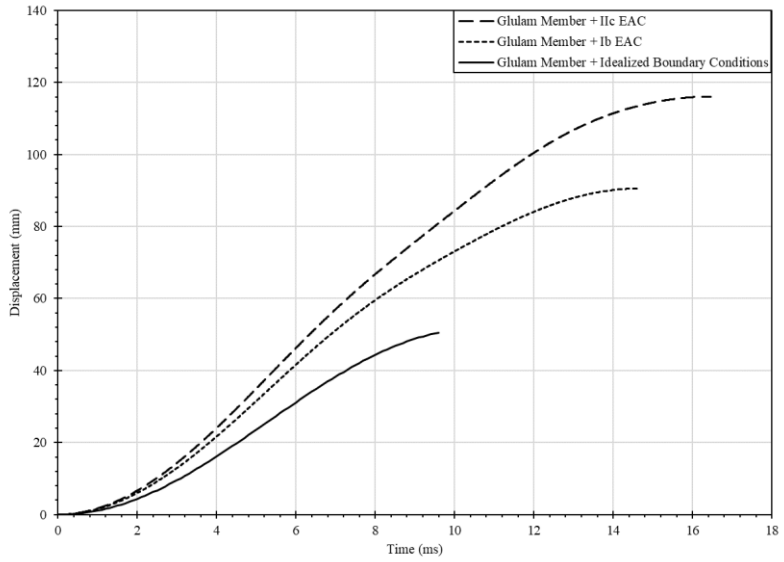

Figure 7.11: System displacement time-histories

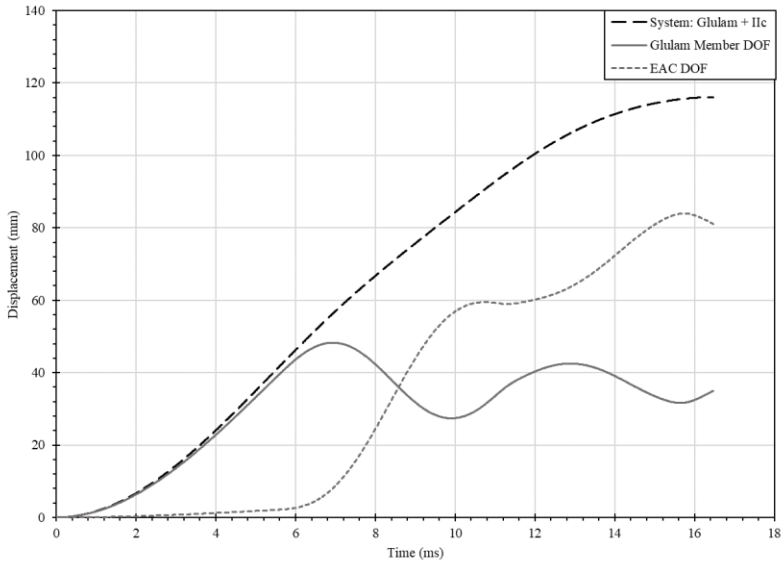

Figure 7.12: Individual DOF displacement time-histories for system with specimen IIc

For specimen IIc, the depths at which optimal yield load is achieved were scaled once again by 50% to show the effects of overdesign of the EAC on the performance of the assembly. For the case where the depth was overdesigned by 50% (i.e. 196.3 mm instead of 130.9 mm), a minimum peak positive pressure of 6.5 kPa caused ultimate failure of the member. This is essentially the same case as for a glulam member with idealized boundary conditions (i.e. no increase in the performance).

In order to investigate whether the EAC stiffness, relative to the stiffness of the timber member, has an impact on the system performance, an additional model was analyzed with the properties of specimen IIc, while varying the EAC stiffness as 0.5, 1.0, or 2.0 times the timber member stiffness. It was shown that the EAC stiffness had little impact on the performance of the assembly containing EACs and glulam members, as shown in Figure 7.13.

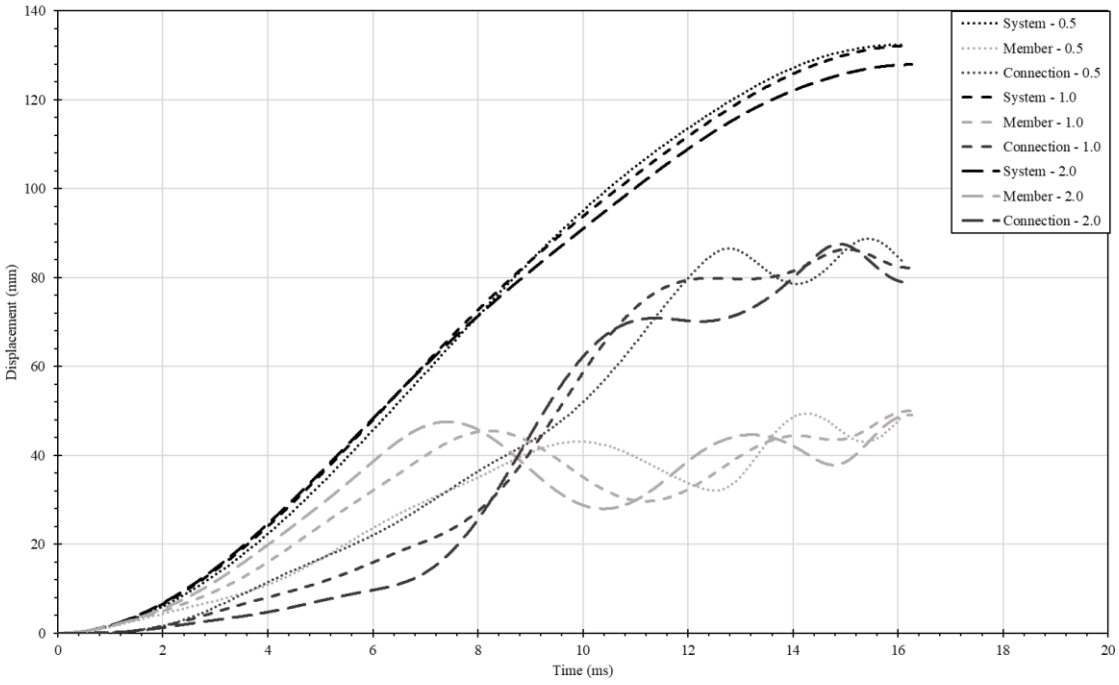

Figure 7.13: Displacement time-histories for EAC-to-wood stiffness ratio of 0.5, 1.0, and 2.0

7.4.1 Design Considerations

For EACs to be effective at mitigating blast loading in timber assemblies, it is crucial that they are designed in such a way that yielding occurs prior to failure of the main member so that energy absorption in the connection can take place. Ensuring that the EAC yield load is less than the member failure load will ensure this for EACs with a well-defined yield plateau. Current practices in the Canadian blast design standard (CSA 2012) requires that failure occurs in the main member prior to connection yielding. This is a reasonable assumption for structural elements that behave in an elastic-plastic manner, however, this is not the case for timber structural elements. Considering the dynamic and strength increase factors on the timber elements, the design should consider the yielding of the EACs at a lower load level than the dynamic strength of the timber member. The influence of strain-hardening in the steel section should also be considered.

It is important to re-emphasize the importance of the manufacturing techniques, especially as it pertains to EAC's geometry and welding details. Although the current study identifies a specific manufacturing process of welding simple structural steel sections together, other manufacturing processes should be investigated. This could be done experimentally on the entire EAC connection or by means of FEA modelling in conjunction with coupon testing results from the same material used in manufacturing.

One key advantage to the proposed methodology for design and manufacturing is that, through the validated scalability of experimental and analytical results, the depth can be varied to achieve any connection yield load. This allows EACs with a well-defined plateau and large densification displacement to be modified as required through a simple manufacturing process. Another design consideration is that the plate thickness is larger than the thickness of the structural steel sections, so deformation is concentrated in the structural steel sections.

CHAPTER 8 - Conclusions

The following conclusions can be drawn from the current research study:

- Decreasing the leg length or increasing the thickness of the steel angles and reducing the diameter of circular HSS cause an increase in yield load and elastic stiffness while reducing the densification displacement.
- Connections with angles and a centre weld resulted in a drastic increase in yield load and elastic stiffness compared to EACs without a centre weld. However, the suitability of those connections for blast mitigation or design is questionable due to the loss in the post-yield capacity.
- EACs manufactured from angles offer a well-defined plateau able to absorb a large quantity of energy, making them particularly suitable for blast mitigation.
- Scalability of the EACs properties based on the depth of the connection is achievable both experimentally and when FEA analysis is used.
- Connections manufactured from an arc of a circular HSS seemed to lose capacity following yielding and were therefore not deemed suitable for the purpose of enhancing the assembly's energy dissipation capabilities.
- EACs manufactured from multiple circular HSS can achieve multiple load-displacement plateaus, and they present an interesting option for systems with multiple failure modes occurring at different levels.
- It is crucial that the welding details used in the manufacturing are similar to those used in testing or design since it was found that varying the weld types had a significant effect on the load-displacement behaviour of EACs.
- SDOF analysis was able to predict the experimental dynamic displacement time-history of the EACs.
- FEA analysis was capable of predicting the load-displacement behaviours of EACs, especially when detailed material properties, based on component level testing, are used in the model.

8.1 Recommendations for Future Work

Based on the current study, the following research topics have been identified for future work:

- This work was limited to EACs at the component level, and only estimates of their effects were investigated analytically. The interaction between EACs and timber members should be investigated both experimentally and analytically before implementation.
- Research on the application of EACs with multiple circular HSS where several load plateaus are achieved should be investigated. These connections could be capable of targeting multiple failure modes, thus possibly improving the behaviour further.
- Further work should investigate the effect of variability of the load-displacement behaviour for EAC of identical manufacturing in more detail since a limited quantity of specimens were investigated in this study.

References

ASTM International. (2021). *Standard Test Methods for Tension Testing of Metallic Materials*. West Conshohocken, PA, USA.

Avalle, M., and Goglio, L. (1997). "Static lateral compression of aluminium tubes: Strain gauge measurements and discussion of theoretical models." <https://journals-sagepub-com.proxy.bib.uottawa.ca/doi/abs/10.1243/0309324971513454> (Jun. 21, 2021).

Baroutaji, A., Morris, E., and Olabi, A. G. (2014). "Quasi-static response and multi-objective crashworthiness optimization of oblong tube under lateral loading." *Thin-Walled Structures*, 82, 262–277.

Biggs, J. M. (1964). *Introduction to Structural Dynamics*. McGraw-Hill, New York, NY.

Blaß, H. J., and Schädle, P. (2011). "Ductility aspects of reinforced and non-reinforced timber joints." *Engineering Structures*, Modelling the Performance of Timber Structures, 33(11), 3018–3026.

Burrell, R. (2012). "Performance of Steel Fibre Reinforced Concrete Columns Under Shock Tube Induced Shock Wave Loading." University of Ottawa, Ottawa, ON.

Burton, R. H., and Craig, J. M. (1963). *An investigation into the energy absorping properties of metal tubes loaded in the transverse direction*. BSc (Eng), University of Bristol, UK.

Cannon, L., and Clubley, S. K. (2021). "Structural response of simple partially-clad steel frames to long-duration blast loading." *Structures*, 32, 1260–1270.

Cao, L., Lu, S., Laflamme, S., Quiel, S., Ricles, J., and Taylor, D. (2018). "Performance-based design procedure of a novel friction-based cladding connection for blast mitigation." *International journal of impact engineering*, Elsevier Ltd, 117, 48–62.

Chapel Steel. (2021). "CSA G40.21 44W / 300W Structural, Carbon & HSLA Steel Plate." *Chapel Steel*, <https://www.chapelsteel.com/csa-g4021-44w.html> (Nov. 13, 2021).

Chen, J. (2010). "AN EXPERIMENTAL STUDY OF STRAIN RATE EFFECTS ON MILD STEEL." Carleton University, Ottawa, Ontario, Canada.

Chopra, A. K. (2017). *Dynamics of Structures Theory and Applications to Earthquake Engineering*. Pearson, University of California at Berkeley.

Corley, W. G., Sr., P. F. M., Sozen, M. A., and Thornton, C. H. (1998). "The Oklahoma City Bombing: Summary and Recommendations for Multihazard Mitigation." *Journal of Performance of Constructed Facilities*, 12(3), 100–112.

Cormie, D., Mays, G., and Smith, P. (2009). *Blast effects on buildings*. Thomas Telford Publishing.

Côté, D., and Doudak, G. (2019). "Experimental investigation of cross-laminated timber panels with realistic boundary conditions subjected to simulated blast loads." *Engineering Structures*, 187, 444–456.

Cowper, G. R., and Symonds, P. S. (1957). *Strain Hardening and Strain-rate Effects in the Impact Loading of Cantilever Beams*. Technical Report-Division of Applied Mathematics, Brown University, Providence.

CSA. (2012). *CSA S850-12 Design and assessment of buildings subjected to blast loads*. CSA Group, Mississauga, ON.

CSA. (2019). *Engineering Design in Wood*. Canadian Standards Association (CSA), 240.

CSA. (2021). *CSA G40.21 General Requirements for Rolled or Welded Structural Quality Steel/Structural Quality Steel*.

CSB. (2007). *INVESTIGATION REPORT: Refinery Explosion and Fire*. Investigation Report, U.S. Chemical Safety And Hazard Investigation Board.

Daneff, G. (1997). "Response of bolted connections to pseudodynamic (cyclic) loading." M.Sc., University of New Brunswick (Canada), Canada.

DeRuntz, J. A., Jr., and Hodge, P. G., Jr. (1963). "Crushing of a Tube Between Rigid Plates." *Journal of Applied Mechanics*, 30(3), 391–395.

DHS. (2011). *Reference Manual to Mitigate Potential Terrorist Attacks Against Buildings*. Department of Homeland Security.

Dinwoodie, J. M. (2017). *Timber: Its nature and behaviour*. CRC Press.

Dusenberry, D. O. (2010). *Handbook for blast-resistant design of buildings*. JWiley & Sons, Hoboken, N.J.

George Grantham Bain Collection. (2021). "Halifax explosion of 1917 | Significance & Facts." *Encyclopedia Britannica*, <https://www.britannica.com/event/Halifax-explosion> (May 19, 2021).

Gibson, L. J., and Ashby, M. F. (1999). *Cellular solids: Structure and properties*. Cambridge University Place, Cambridge, UK.

Gilbertson, C. G., and Bulleit, W. M. (2013). "Load Duration Effects in Wood at High Strain Rates." *Journal of Materials in Civil Engineering*, American Society of Civil Engineers, 25(11), 1647–1654.

Girhammar, U. A., and Andersson, H. (1988). "Effect of Loading Rate on Nailed Timber Joint Capacity." *Journal of Structural Engineering*, American Society of Civil Engineers, 114(11), 2439–2456.

Green, M., and Taggart, J. (2017). *Tall Wood Buildings: Design, Construction and Performance*. Birkhauser.

Gupta, N. K., Sekhon, G. S., and Gupta, P. K. (2005). "Study of lateral compression of round metallic tubes." *Thin-Walled Structures*, 43(6), 895–922.

Jacques, E. (2011). "Blast Retrofit of Reinforced Concrete Walls and Slabs." University of Ottawa, Ottawa, ON.

Jacques, E. (2014). *RCBlast (Version 0.5.1)*.

Jacques, E., Lloyd, A., Braimah, A., Saatcioglu, M., Doudak, G., and Abdelalim, O. (2014). "Influence of high strain-rates on the dynamic flexural material properties of spruce-pine-fir wood studs." *Canadian Journal of Civil Engineering*, 41(1), 56+.

Jacques, E., Lloyd, A., and Saatcioglu, M. (2013). "Predicting reinforced concrete response to blast loads." *Canadian Journal of Civil Engineering*, NRC Research Press, 40(5), 427–445.

Jacques, E., and Saatcioglu, M. (2020). “Uncoupled Compression Membrane Analysis of Reinforced-Concrete Members Subject to Extreme Loads.” *Journal of Structural Engineering*, 146(9), 04020189.

Jansson, B. (1992). “Impact Loading of Timber Beams.” University of British Columbia, Vancouver, B.C.

Jorissen, A., and Fragiacomo, M. (2011). “General notes on ductility in timber structures.” *Engineering Structures*, 33(11), 2987–2997.

Kernaghan, L., and Foot, R. (2017). “Halifax Explosion.” *The Canadian Encyclopedia*, Encyclopedia.

Krauthammer, T. (2008). *Modern Protective Structures*. CRC Press.

Krishnappa, N., Bruneau, M., and Warn, G. P. (2014). “Weak-Axis Behavior of Wide Flange Columns Subjected to Blast.” *Journal of structural engineering (New York, N.Y.)*, American Society of Civil Engineers, 140(5), 4013108-.

Lacroix, D., and Doudak, G. (2020). “Towards enhancing the post-peak performance of glued-laminated timber beams using multi-directional fibre reinforced polymers.” *Engineering Structures*, 215, 110680.

Lacroix, D. N. (2017). “Investigating the Behaviour of Glulam Beams and Columns Subjected to Simulated Blast Loading.” Doctorate of Philosophy, University of Ottawa, Ottawa, ON.

Lacroix, D. N., and Doudak, G. (2015). “Investigation of Dynamic Increase Factors in Light-Frame Wood Stud Walls Subjected to Out-of-Plane Blast Loading.” *Journal of Structural Engineering*, 141(6), 04014159.

Lacroix, D. N., and Doudak, G. (2018a). “Determining the Dynamic Increase Factor for Glued-Laminated Timber Beams.” *Journal of Structural Engineering*, 144(9), 04018160.

Lacroix, D. N., and Doudak, G. (2018b). “Effects of High Strain Rates on the Response of Glulam Beams and Columns.” *Journal of Structural Engineering*, American Society of Civil Engineers, 144(5), 04018029.

Lacroix, D. N., and Doudak, G. (2018c). “Experimental and Analytical Investigation of FRP Retrofitted Glued-Laminated Beams Subjected to Simulated Blast Loading.” *Journal of Structural Engineering*, American Society of Civil Engineers, 144(7), 04018089.

Lacroix, D. N., Doudak, G., and El-Domiaty, K. (2014). “Retrofit Options for Light-Frame Wood Stud Walls Subjected to Blast Loading.” *Journal of Structural Engineering*, 140(4), 04013104.

Lam, F., Wrede, M. S., Yao, C. C., and Gu, J. J. (2008). “Moment resistance of bolted timber connections with perpendicular to grain reinforcements.” *10th World Conference on Timber Engineering*, Miyazaki, Japan.

Lavarnway, D., and Pollino, M. (2015). “Mitigation of Air-Blast Pressure Impulses on Building Envelopes through Blast Resistant Ductile Connectors.” *Journal of Engineering and Architecture*, 3(2).

Li, Y., and Aoude, H. (2020). “Effects of detailing on the blast and post-blast resilience of high-strength steel reinforced concrete (HSS-RC) beams.” *Engineering Structures*, 219, 110869.

Lowak, M. J. (2015). *Static and Dynamic Testing of Cross-Laminated Timber Panels*. Baker Engineering and Risk Consultants, Inc., San Antonio, TX, USA.

Lowak, M. J. (2016). *Additional Static and Dynamic Testing of Cross-Laminated Timber Panels*. Baker Engineering and Risk Consultants, Inc., San Antonio, TX, USA.

Lu, G., and Yu, T. (2003). *Energy Absorption of Structures and Materials*. Woodhead Publishing Limited, Cambridge, UK.

Markwardt, L. J., and Liska, J. A. (1956). “The Influence of Rate of Loading on the Strength of Wood and Wood-Base Materials.” *Symposium on Speed of Testing of Non-Metallic Materials*, ASTM International, 100 Barr Harbor Drive, PO Box C700, West Conshohocken, PA 19428-2959, 3-3–16.

Mays, G. C., Hetherington, J. G., and Rose, T. A. (1999). “Response to Blast Loading of Concrete Wall Panels with Openings.” *Journal of structural engineering (New York, N.Y.)*, American Society of Civil Engineers, 125(12), 1448–1450.

McGrath, A., and Doudak, G. (2021). “Investigating the response of bolted timber connections subjected to blast loads.” *Engineering Structures*, 236, 112112.

Mpidi Bita, H., Currie, N., and Tannert, T. (2018). “Disproportionate collapse analysis of mid-rise cross-laminated timber buildings.” *Structure and Infrastructure Engineering*, Taylor & Francis, 14(11), 1547–1560.

Murphy, S. (2020). “Oklahoma City bombing: Families remember 168 victims with video tribute 25 years later.” *ABC11 Raleigh-Durham*, <https://abc11.com/6115017/> (May 19, 2021).

Nadeau, J., Bennett, R., and Fuller, E. (1982). “An explanation for the rate-of-loading and the duration-of-load effects in wood in terms of fracture mechanics.” *Journal of Materials Science*, Kluwer Academic Publishers, 17(10), 2831–2840.

Nassr, A. A., Razaqpur, A. G., Tait, M. J., Campidelli, M., and Foo, S. (2014). “Dynamic Response of Steel Columns Subjected to Blast Loading.” *Journal of structural engineering (New York, N.Y.)*, American Society of Civil Engineers, 140(7), 4014036-.

NIST. (2005). *Final Report On the Collapse of the World Trade Center Towers*. National Institute of Standards and Technology.

Nolet, V., Casagrande, D., and Doudak, G. (2019). “Multipanel CLT shearwalls: an analytical methodology to predict the elastic-plastic behaviour.” *Engineering Structures*, 179, 640–654.

Nordic. (2020). *Nordic Lam+ Technical Guide*.

NRC. (2018). *National Building Code of Canada 2015*. Canadian Comission on Building and Fire Codes (CCBFC), National Research Council of Canada (NRC).

Office of the Deputy Prime Minister. (2004). “Disproportionate Collapse, The Building Regulations 2000.”

Olabi, A. G., Morris, E., Hashmi, M. S. J., and Gilchrist, M. D. (2008). “Optimised design of nested oblong tube energy absorbers under lateral impact loading.” *International journal of impact engineering*, Elsevier Ltd, Oxford, 35(1), 10–26.

Oswald, C. (2018). “BLAST TESTING OF ENERGY ABSORBING CONNECTORS FOR BLAST RESISTANT DESIGN.” Seville, Spain, 57–67.

Pantelides, C. P., Garfield, T. T., Richins, W. D., Larson, T. K., and Blakeley, J. E. (2014). "Reinforced concrete and fiber reinforced concrete panels subjected to blast detonations and post-blast static tests." *Engineering Structures*, 76, 24–33.

Pearson, C., and Delatte, N. (2005). "Ronan Point Apartment Tower Collapse and its Effect on Building Codes." *Journal of Performance of Constructed Facilities*, 19(2), 172–177.

Pirinen, M. (2014). "Ductility of Wood and Wood Members Connected with Mechanical Fasteners." MSc Thesis, Aalto University.

Poulin, M., Viau, C., Lacroix, D. N., and Doudak, G. (2018). "Experimental and Analytical Investigation of Cross-Laminated Timber Panels Subjected to Out-of-Plane Blast Loads." *Journal of Structural Engineering*, 144(2), 04017197.

Reddy, T. Y., and Reid, S. R. (1979). "On obtaining material properties from the ring compression test." *Nuclear Engineering and Design*, North-Holland, 52(2), 257–263.

Reddy, T. Y., and Reid, S. R. (1980). "Phenomena associated with the crushing of metal tubes between rigid plates." *International Journal of Solids and Structures*, Pergamon, 16(6), 545–562.

Reid, S. R., and Reddy, T. Y. (1978). "Effect of strain hardening on the lateral compression of tubes between rigid plates." *International Journal of Solids and Structures*, Pergamon, 14(3), 213–225.

Shabanlou, M., Moghaddam, H., and Saedi Daryan, A. (2021). "The Effect of Geometry on Structural Behavior of Buildings with Steel Plate Shear Wall System Subjected to Blast Loading." *International Journal of Steel Structures*, 21(2), 650–665.

Silva, P. F., and Lu, B. (2009). "Blast Resistance Capacity of Reinforced Concrete Slabs." *Journal of structural engineering (New York, N.Y.)*, American Society of Civil Engineers, 135(6), 708–716.

Smith, M. (2009). *ABAQUS Standard User's Manual*. Dassault Systèmes Simulia Corp, Providence, RI, USA.

Soroushian, P., and Choi, K.-B. (1987). “Steel Mechanical Properties at Different Strain Rates.” *Journal of structural engineering (New York, N.Y.)*, American Society of Civil Engineers, Reston, VA, 113(4), 663–672.

Spencer, R. (1978). “Rate of Loading Effect in Bending for Douglas-Fir Lumber.” Banff, Alberta, Canada.

Symonds, P. S. (1967). *Survey of Methods of Analysis for Plastic Deformation of Structures under Dynamic Loading, Division of Engineering*. Brown University.

Syron, W. D. (2008). “Strain Rate Dependent Behavior of Laminated Strand Lumber.” University of Maine, Maine.

Tetougueni, C. D., Zampieri, P., and Pellegrino, C. (2020). “Structural performance of a steel cable-stayed bridge under blast loading considering different stay patterns.” *Engineering Structures*, 219, 110739.

Thelandersson, S., and Larsen, H. J. (2003). *Timber Engineering*. Wiley.

TSB. (2014). *Lac-Mégantic runaway train and derailment investigation summary*. Transportation Safety Board of Canada, Gatineau, QC.

USACE. (2008). *Methodology Manual for the Single-Degree-of-Freedom Blast Effects Design Spreadsheets*. U.S. Army Corps of Engineers.

USADD. (2008). *Structures to Resist the Effects of Accidental Explosions*. Department of Defence.

USADD. (2009). *Design of Buildings to Resist Progressive Collapse*. Department of Defence.

Viau, C. (2020). “Investigation and Optimization of Connections in Timber Assemblies Subjected to Blast Loading.” Doctor of Philosophy, University of Ottawa, Ottawa, ON.

Viau, C., and Doudak, G. (2016a). “Investigating the behaviour of typical and designed wall-to-floor connections in light-frame wood stud wall structures subjected to blast loading.” *Canadian journal of civil engineering*, NRC Research Press, 43(6), 562–572.

Viau, C., and Doudak, G. (2016b). “Investigating the Behavior of Light-Frame Wood Stud Walls Subjected to Severe Blast Loading.” *Journal of Structural Engineering*, 142(12), 04016138.

Viau, C., and Doudak, G. (2019). “Behaviour and modelling of cross-laminated timber panels with boundary connections subjected to blast loads.” *Engineering Structures*, 197, 109404.

Viau, C., and Doudak, G. (2021a). “Behavior and Modeling of Glulam Beams with Bolted Connections Subjected to Shock Tube–Simulated Blast Loads.” *Journal of Structural Engineering*, 147(1), 04020305.

Viau, C., and Doudak, G. (2021b). “Energy-Absorbing Connection for Heavy-Timber Assemblies Subjected to Blast Loads–Concept Development and Application.” *Journal of Structural Engineering*, 147(4), 04021027.

Viau, C., and Doudak, G. (2021c). “Dynamic analysis methods for modelling timber assemblies subjected to blast loading.” *Engineering Structures*, 233, 111945.

Wang, M., Song, X., Gu, X., Zhang, Y., and Luo, L. (2015). “Rotational Behavior of Bolted Beam-to-Column Connections with Locally Cross-Laminated Glulam.” *Journal of Structural Engineering*, 141(4), 04014121.

Wang, Y., Pokharel, R., Lu, J., and Zhai, X. (2019). “Experimental, numerical, and analytical studies on polyurethane foam-filled energy absorption connectors under quasi-static loading.” *Thin-walled structures*, Elsevier Ltd, 144, 106257-.

Wang, Y., Zhai, X., and Wang, W. (2017). “Numerical studies of aluminum foam filled energy absorption connectors under quasi-static compression loading.” *Thin-walled structures*, Elsevier Ltd, 116, 225–233.

Warn, G. P., and Bruneau, M. (2009). “Blast Resistance of Steel Plate Shear Walls Designed for Seismic Loading.” *Journal of structural engineering (New York, N.Y.)*, American Society of Civil Engineers, 135(10), 1222–1230.

Weaver, M. K., O’Laughlin, C., and Newberry, C. M. (2017). “Blast Resistance of Cross-Laminated Timber Construction.” *17th ISIEMS*, Federal Office of Bundeswehr Infrastructure, Environmental Protection and Services, Bad Neuenahr, Germany.

Whitney, M. G. (1996). *Blast Damage Mitigation Using Reinforced Concrete Panels and Energy Absorbing Connectors*. Wilfred Baker Engineering, Inc., San Antonio, TX, 25.

WHO. (2020). “Beirut explosion.” *Bulletin of the World Health Organization*, World Health Organization, 98(9), 584–585.

Williams, G. D., and Williamson, E. B. (2011). “Response of Reinforced Concrete Bridge Columns Subjected to Blast Loads.” *Journal of structural engineering (New York, N.Y.)*, American Society of Civil Engineers, 137(9), 903–913.

Wouts, J., Haugou, G., Oudjene, M., Coutellier, D., and Morvan, H. (2016). “Strain rate effects on the compressive response of wood and energy absorption capabilities – Part A: Experimental investigations.” *Composite Structures*, 149, 315–328.

Yonghui, W., Jingyi, L., Ximei, Z., Bowen, X., and Xudong, Z. (2019). “Response of energy absorbing connector with polyurethane foam and multiple pleated plates under impact loading.” *International journal of impact engineering*, Elsevier Ltd, 133, 103356-.

Yu, J., Rinder, T., Stolz, A., Tan, K.-H., and Riedel, W. (2014). “Dynamic Progressive Collapse of an RC Assemblage Induced by Contact Detonation.” *Journal of structural engineering (New York, N.Y.)*, American Society of Civil Engineers, 140(6), 4014014-.

Yu, R., Zhang, D., Chen, L., and Yan, H. (2018). “Non-dimensional pressure–impulse diagrams for blast-loaded reinforced concrete beam columns referred to different failure modes.” <https://journals-sagepub-com.proxy.bib.uottawa.ca/doi/full/10.1177/1369433218768085> (May 18, 2021).

APPENDIX A – Preliminary Finite Element Analysis Results

Name	2×2×0.25	Description	Angle between top and bottom plate

Cross-sectional dimensions

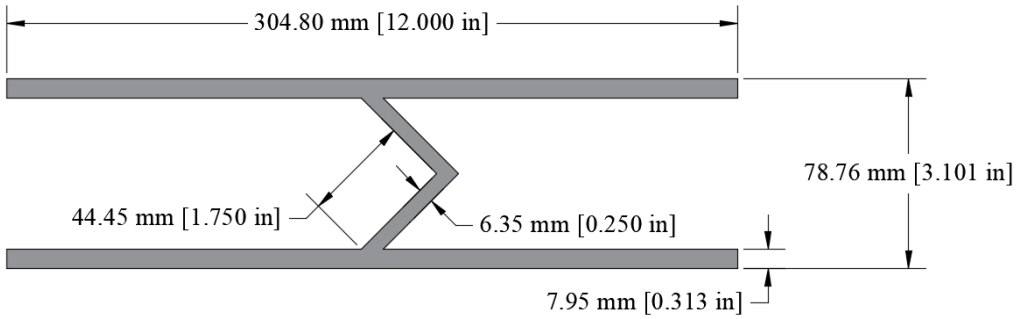

Initial shape	Shape after analysis
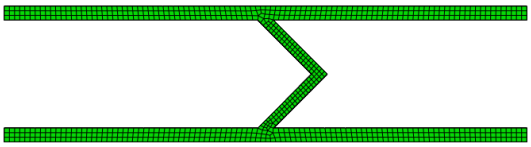	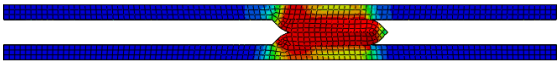

Load-displacement graph (per unit depth)

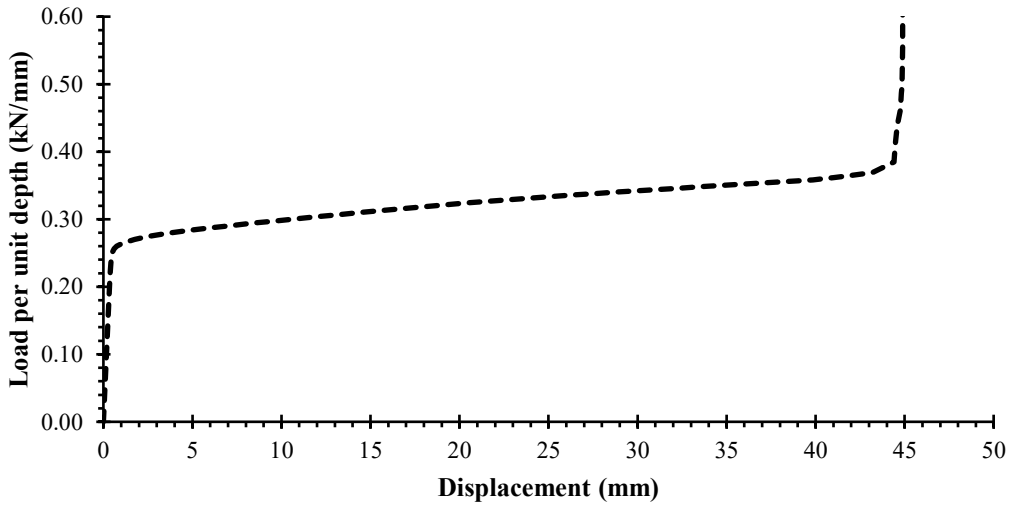

Comments

Depth used in analysis was 50 mm. Initial elastic behaviour is observed up to a displacement of roughly 0.5 mm. A plateau is then experienced from the yield point up to a displacement of roughly 44.4 mm were onset of densification occurs. The capacity of the connection at the onset of densification is roughly 0.38 kN/mm (19.0 kN for 50 mm).

Name	2×2×0.125	Description	Angle between top and bottom plate

Cross-sectional dimensions

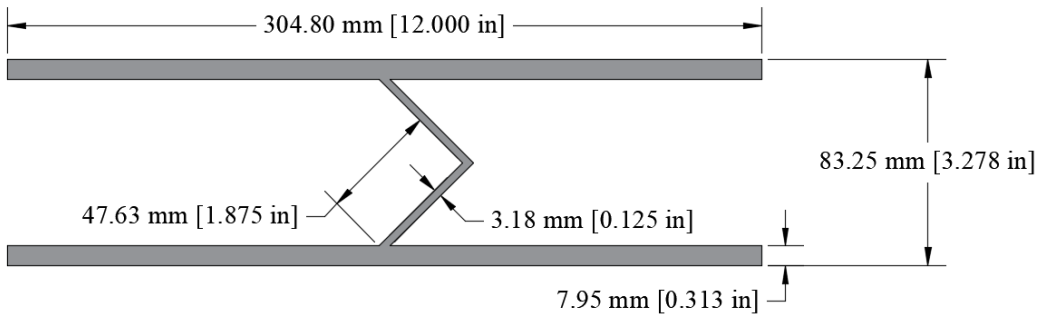

Initial shape	Shape after analysis
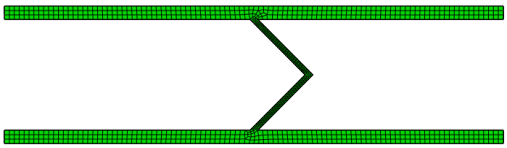	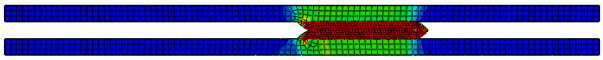

Load-displacement graph (per unit depth)

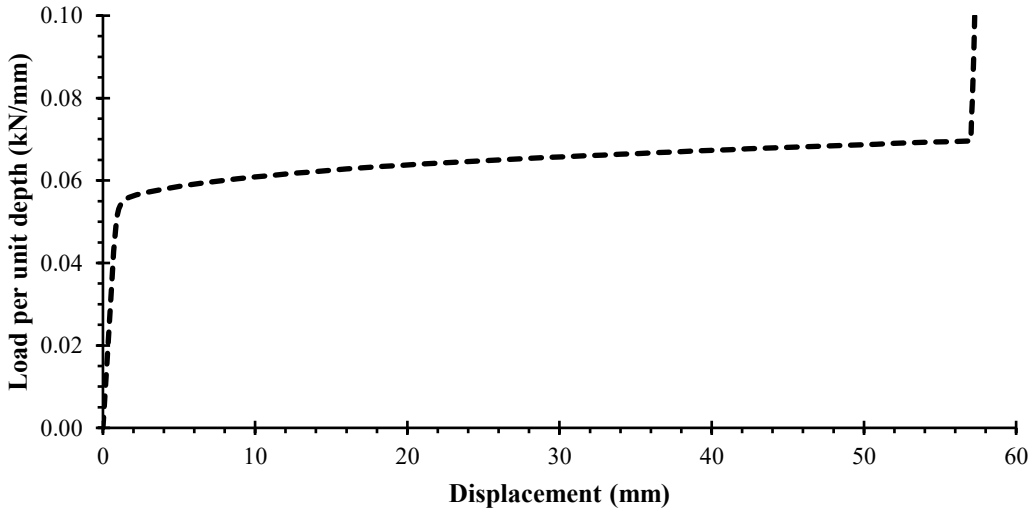

Comments

Depth used in analysis was 50 mm. Initial elastic behaviour is observed up to a displacement of roughly 0.9 mm. A plateau is then experienced from the yield point up to a displacement of roughly 57.1 mm were onset of densification occurs. The capacity of the connection at the onset of densification is roughly 0.07 kN/mm (3.5 kN for 50 mm).

Name	3×3×0.25	Description	Angle between top and bottom plate

Cross-sectional dimensions

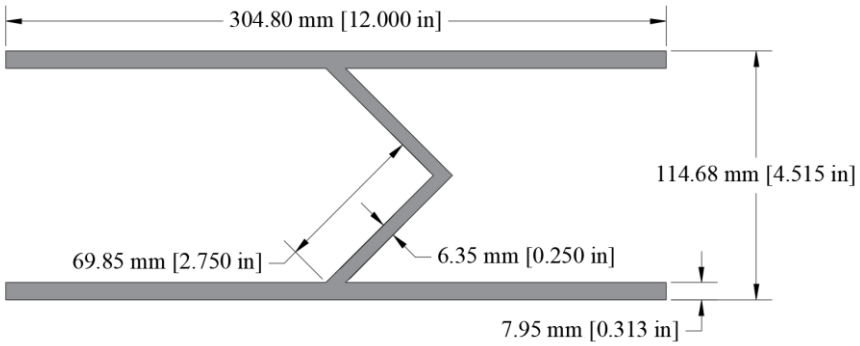

Initial shape	Shape after analysis
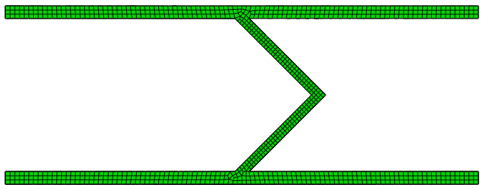	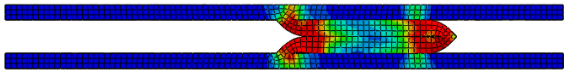

Load-displacement graph (per unit depth)

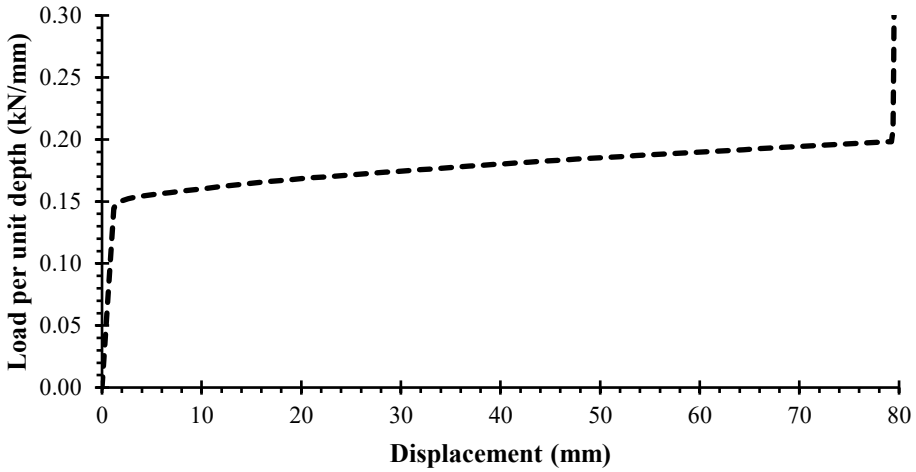

Comments

Depth used in analysis was 50 mm. Initial elastic behaviour is observed up to a displacement of roughly 1.3 mm. A plateau is then experienced from the yield point up to a displacement of roughly 79.2 mm were onset of densification occurs. The capacity of the connection at the onset of densification is roughly 0.20 kN/mm (10.0 kN for 50 mm).

Name	3×3×0.188	Description	Angle between top and bottom plate

Cross-sectional dimensions

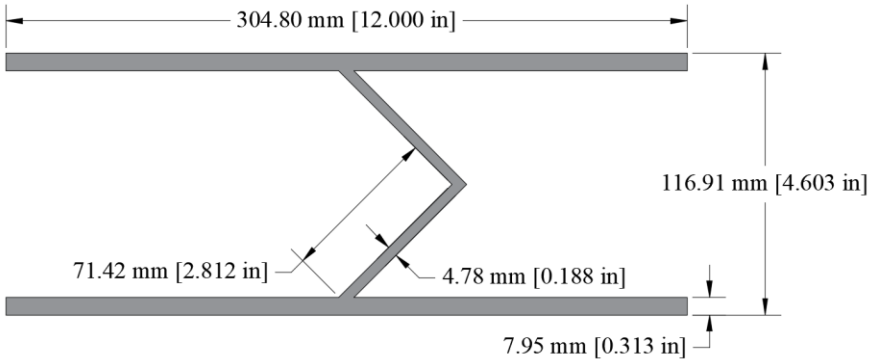

Initial shape	Shape after analysis
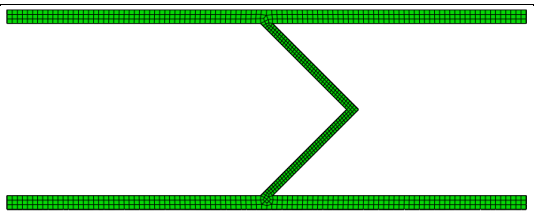	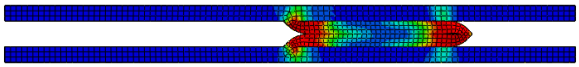

Load-displacement graph (per unit depth)

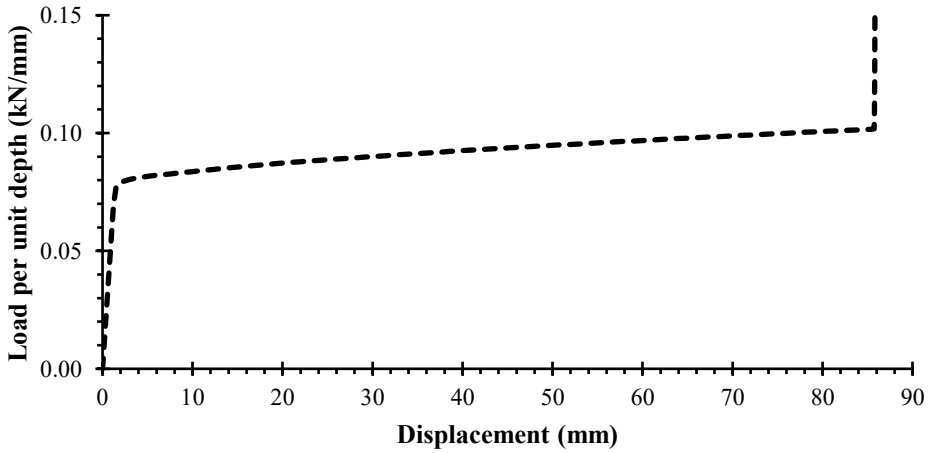

Comments

Depth used in analysis was 50 mm. Initial elastic behaviour is observed up to a displacement of roughly 1.5 mm. A plateau is then experienced from the yield point up to a displacement of roughly 85.7 mm were onset of densification occurs. The capacity of the connection at the onset of densification is roughly 0.10 kN/mm (5.0 kN for 50 mm).

Name	4×4×0.25	Description	Angle between top and bottom plate

Cross-sectional dimensions

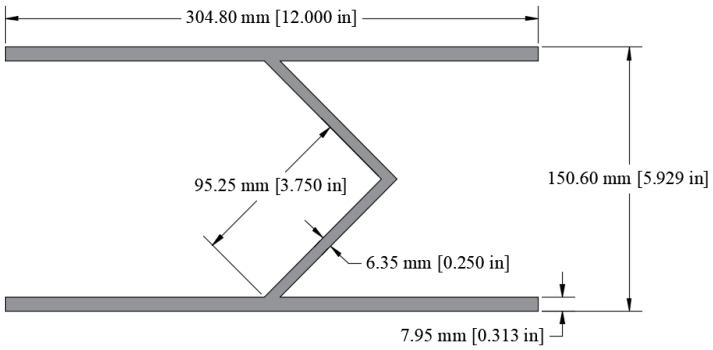

Initial shape	Shape after analysis
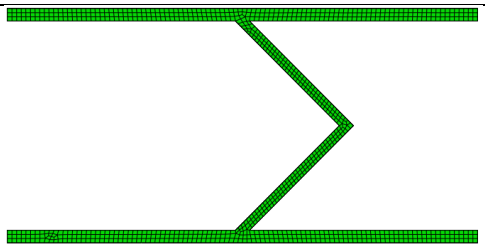	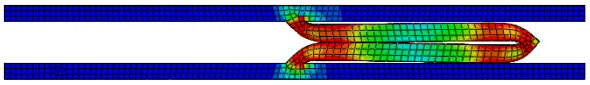

Load-displacement graph (per unit depth)

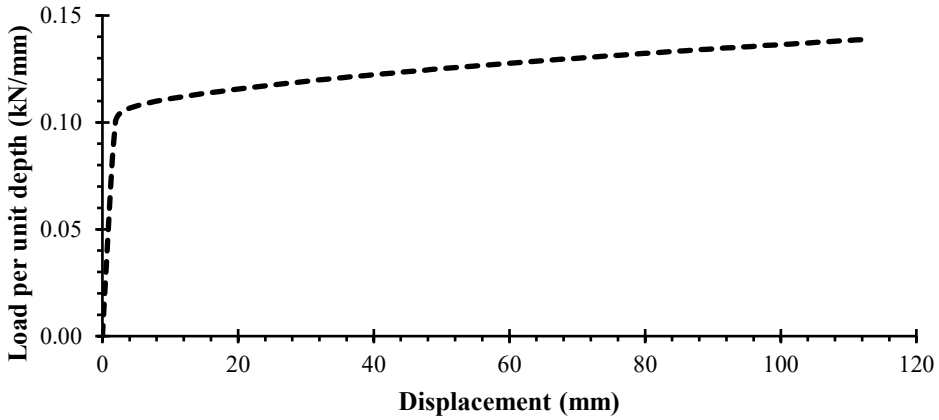

Comments

Depth used in analysis was 50 mm. Initial elastic behaviour is observed up to a displacement of roughly 1.9 mm. A plateau is then experienced from the yield point up to a displacement of 112.9 mm were the analysis ended. The capacity of the connection at the end of analysis was roughly 0.14 kN/mm (7.0 kN for 50 mm).

Name	2.375×0.125	Description	Circular HSS between top and bottom plate

Cross-sectional dimensions

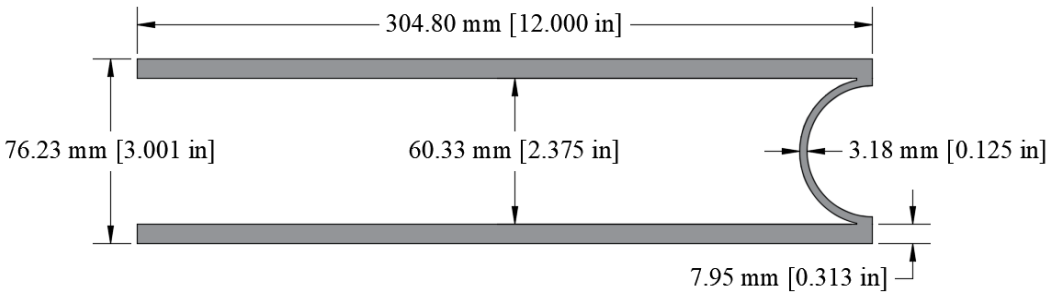

Initial shape	Shape after analysis
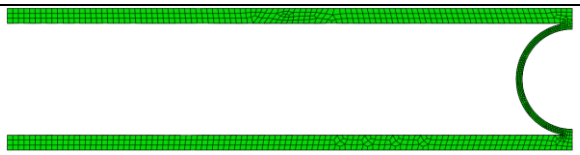	

Load-displacement graph (per unit depth)

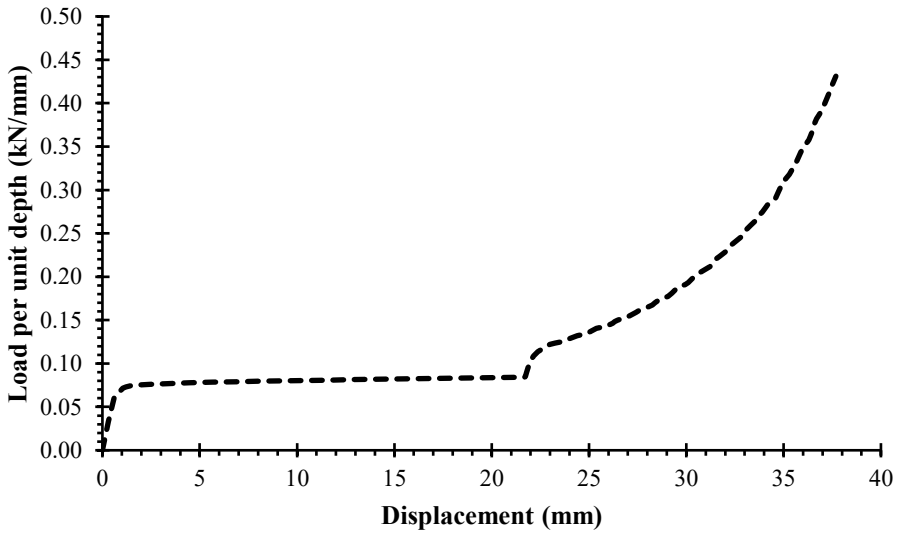

Comments

Depth used in analysis was 10 mm. Initial elastic behaviour is observed up to a displacement of roughly 0.6 mm. A plateau is then experienced from the yield point up to a displacement of roughly 21.7 mm were Load starts increasing rapidly with increasing displacement. The capacity of the connection at this point is roughly 0.08 kN/mm (0.8 kN for 10 mm).

Name	2.375×0.125(90º)	Description	Arc of Circular HSS between top and bottom plate

Cross-sectional dimensions

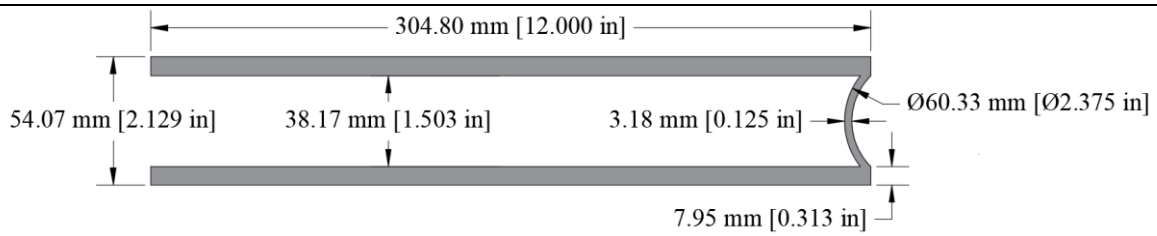

Initial shape	Shape after analysis
	

Load-displacement graph (per unit depth)

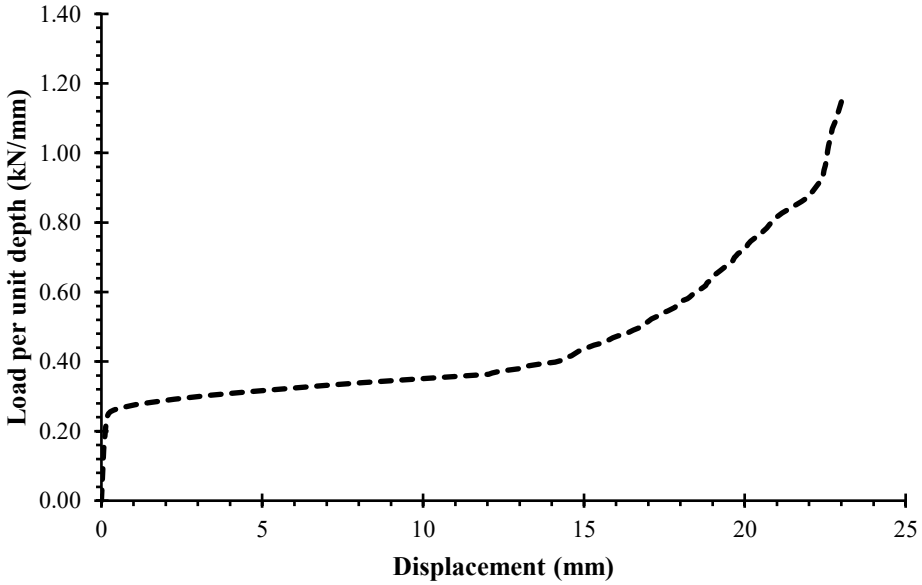

Comments

Depth used in analysis was 10 mm. Initial elastic behaviour is observed up to a displacement of roughly 0.2 mm. A plateau is then experienced from the yield point up to a displacement of roughly 14.4 mm were Load increases more rapdily with increased displacement. The capacity of the connection at the end of this plateau is roughly 0.41 kN/mm (4.1 kN for 10 mm).

Name	2.375×0.125(135º)	Description	Arc of Circular HSS between top and bottom plate

Cross-sectional dimensions

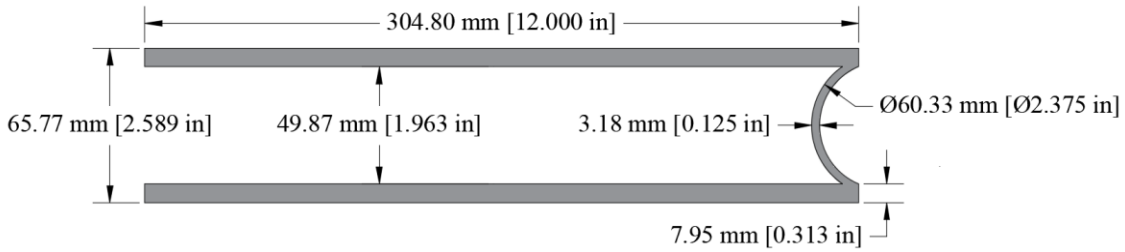

Initial shape	Shape after analysis
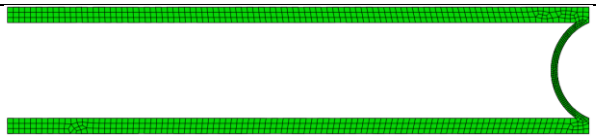	

Load-displacement graph (per unit depth)

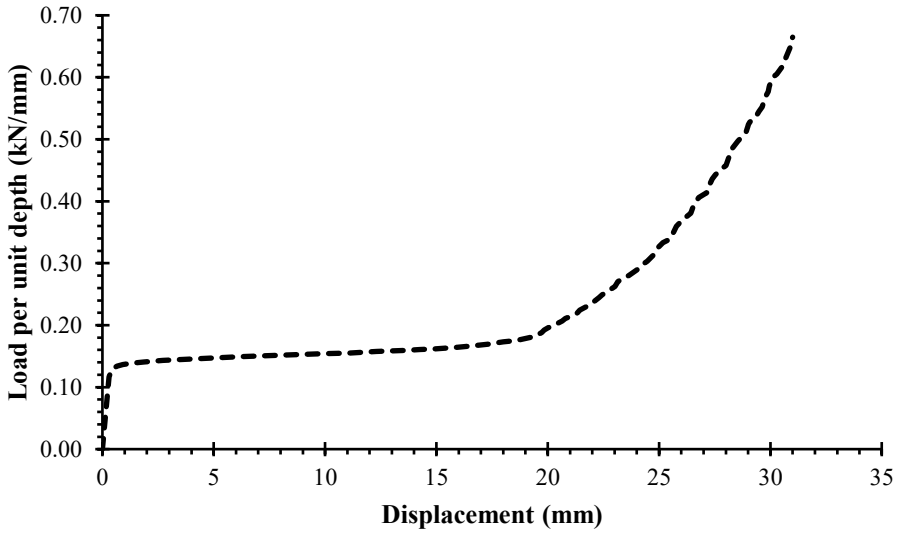

Comments

Depth used in analysis was 10 mm. Initial elastic behaviour is observed up to a displacement of roughly 0.3 mm. A plateau is then experienced from the yield point up to a displacement of roughly 19.7 mm were Load starts rapidly increasing with increased displacement. The capacity of the connection at this point is roughly 0.19 kN/mm (1.9 kN for 10 mm).

Name	3.5×0.25	Description	Circular HSS between top and bottom plate

Cross-sectional dimensions

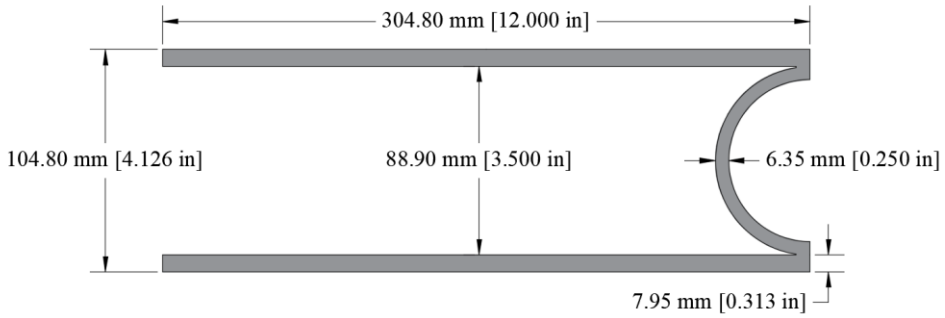

Initial shape	Shape after analysis
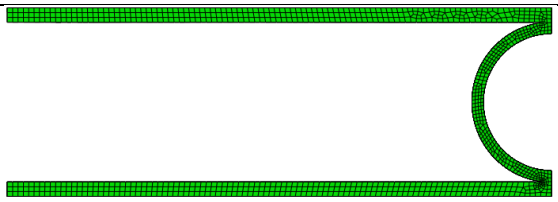	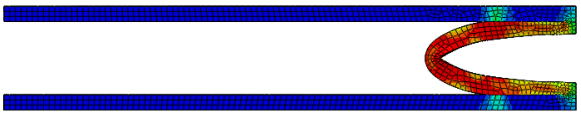

Load-displacement graph (per unit depth)

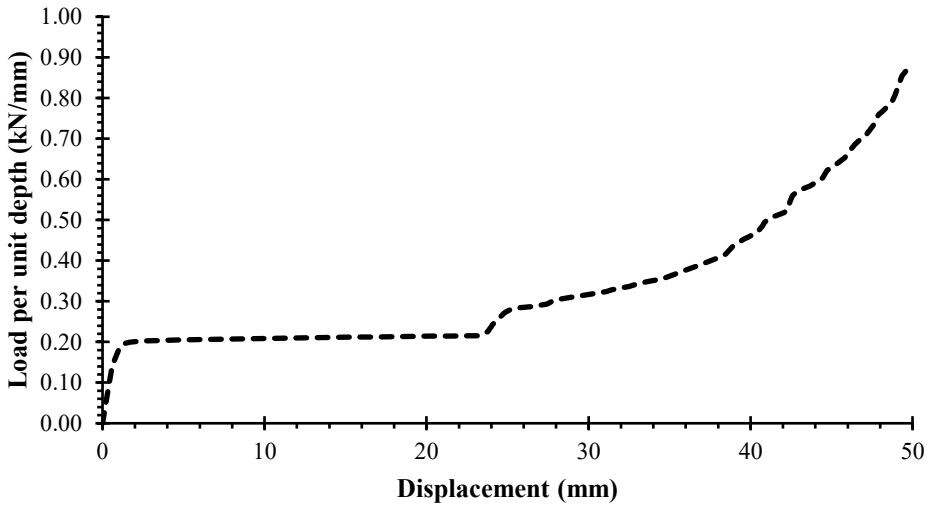

Comments

Depth used in analysis was 50 mm. Initial elastic behaviour is observed up to a displacement of roughly 1.3 mm. A plateau is then experienced from the yield point up to a displacement of roughly 23.4 mm were Load starts rapidly increasing with strength. The capacity of the connection at this point is roughly 0.23 kN/mm (11.5 kN for 50 mm).

Name	3.5×0.25(90º)	Description	Arc of Circular HSS between top and bottom plate

Cross-sectional dimensions

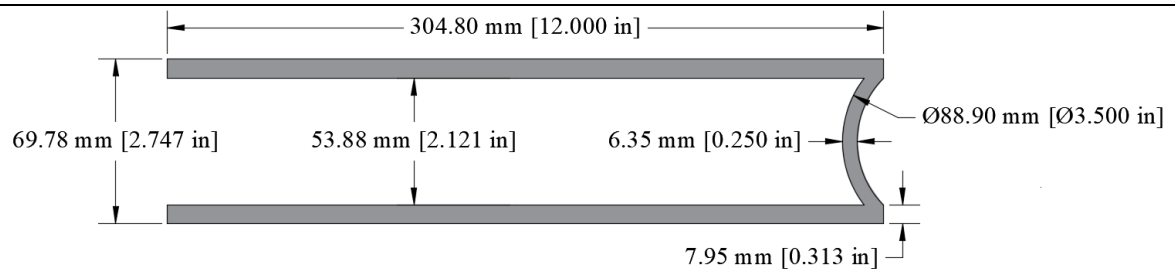

Initial shape	Shape after analysis
	

Load-displacement graph (per unit depth)

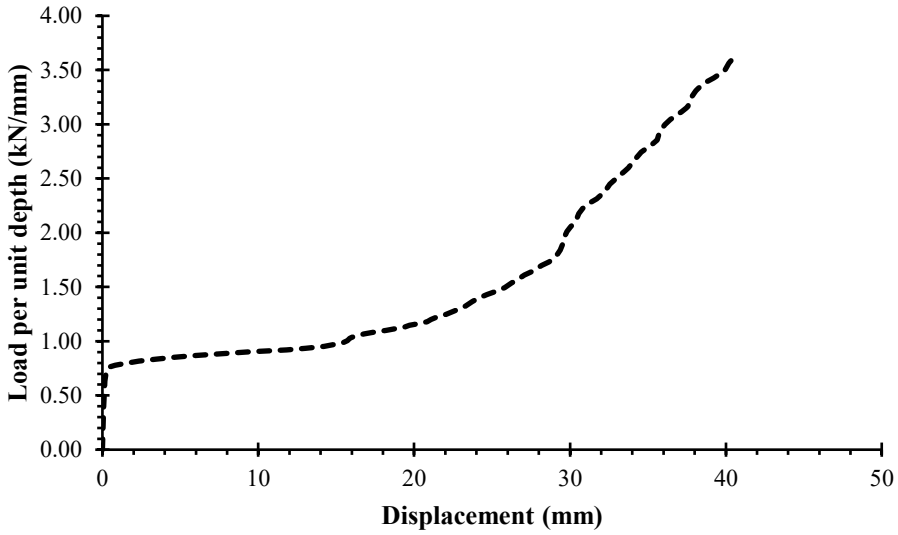

Comments

Depth used in analysis was 10 mm. Initial elastic behaviour is observed up to a displacement of roughly 0.2 mm. A plateau is then experienced from the yield point up to a displacement of roughly 15.4 mm were Load starts rapidly increasing with increased displacement. The capacity of the connection at this point is roughly 1.0 kN/mm (10 kN for 10 mm).

Name	3.5×0.25(60º)	Description	Arc of Circular HSS between top and bottom plate

Cross-sectional dimensions

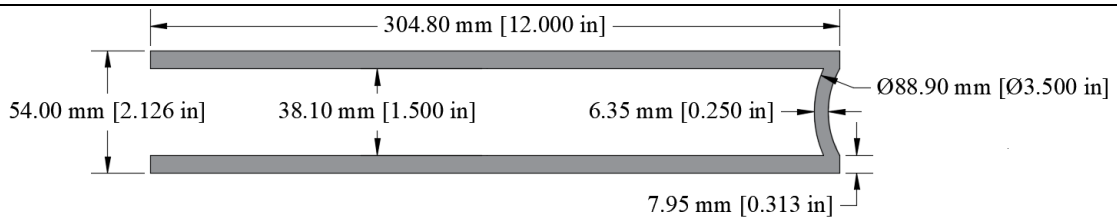

Initial shape	Shape after analysis
	

Load-displacement graph (per unit depth)

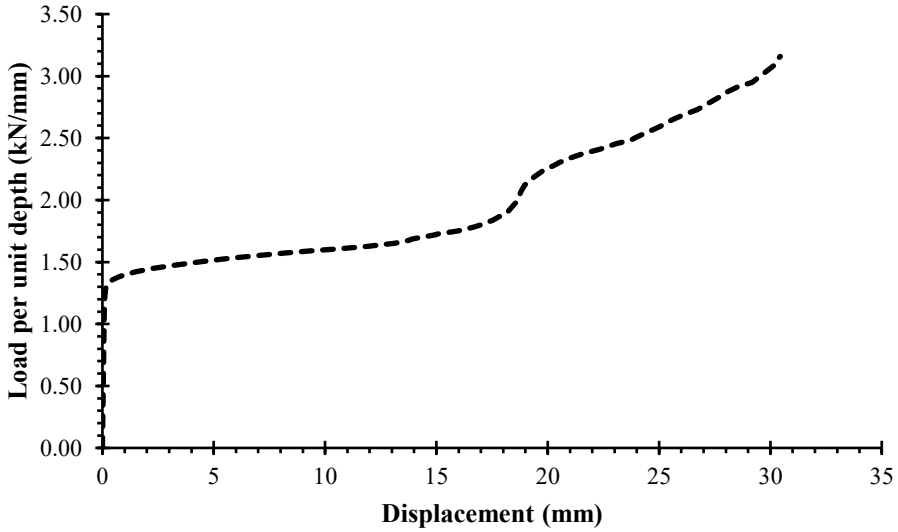

Comments

Depth used in analysis was 50 mm. Initial elastic behaviour is observed up to a displacement of roughly 0.1 mm. A plateau is then experienced from the yield point up to a displacement of roughly 17.1 mm were Load starts rapidly increasing with increased displacement, with a notable jump in the Load. The capacity of the connection at this point is roughly 1.8 kN/mm (90 kN for 50 mm).

Name	3.5×0.25(135º)	Description	Arc of Circular HSS between top and bottom plate

Cross-sectional dimensions

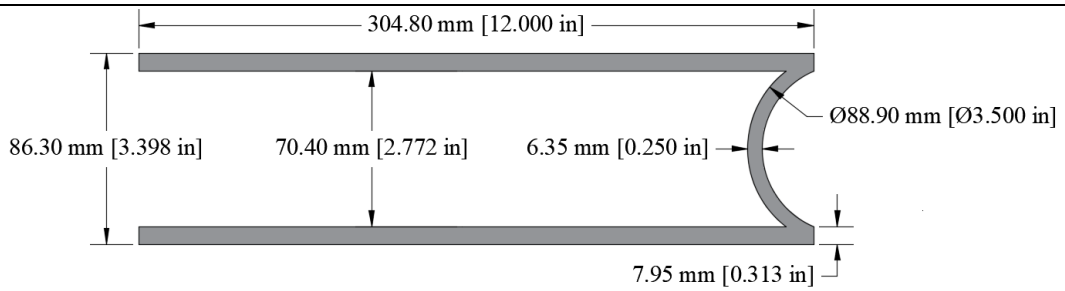

Initial shape	Shape after analysis
	

Load-displacement graph (per unit depth)

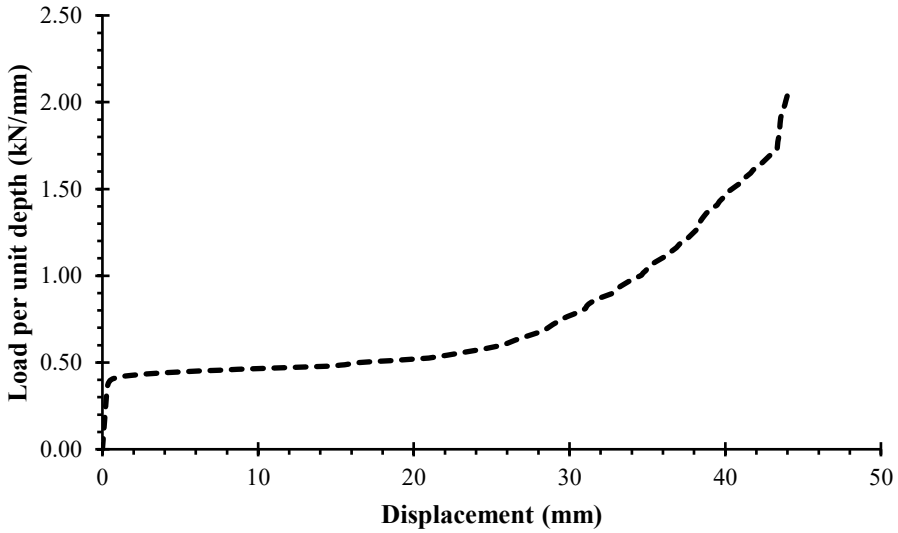

Comments

Depth used in analysis was 10 mm. Initial elastic behaviour is observed up to a displacement of roughly 0.3 mm. A plateau is then experienced from the yield point up to a displacement of roughly 26.0 mm were Load starts rapidly increasing with increased displacement. The capacity of the connection at this point is roughly 0.61 kN/mm (6.1 kN for 10 mm).

Name	3.5×0.125	Description	Circular HSS between top and bottom plate

Cross-sectional dimensions

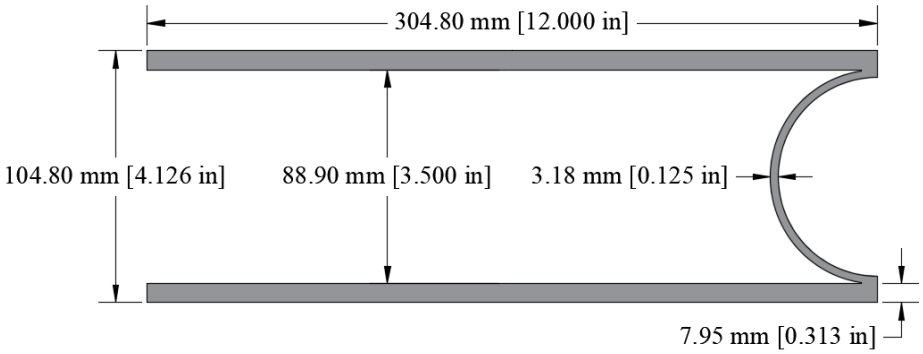

Initial shape

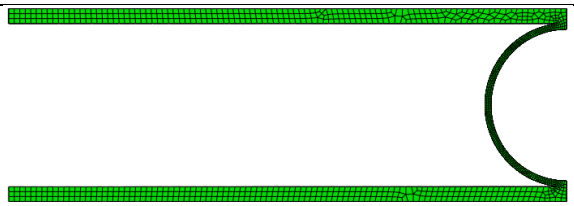

Shape after analysis

Load-displacement graph (per unit depth)

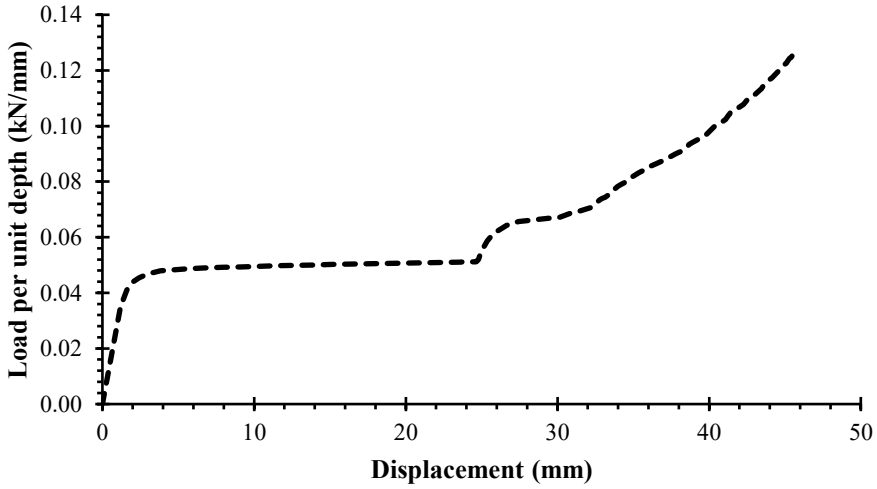

Comments

Depth used in analysis was 50 mm. Initial elastic behaviour is observed up to a displacement of roughly 1.6 mm. A plateau is then experienced from the yield point up to a displacement of roughly 24.6 mm were Load starts rapidly increasing with increased displacement, with a notable jump in the Load. The capacity of the connection at this point is roughly 0.05 kN/mm (2.5 kN for 50 mm).

Name	3.5×0.125(90º)	Description	Arc of Circular HSS between top and bottom plate

Cross-sectional dimensions

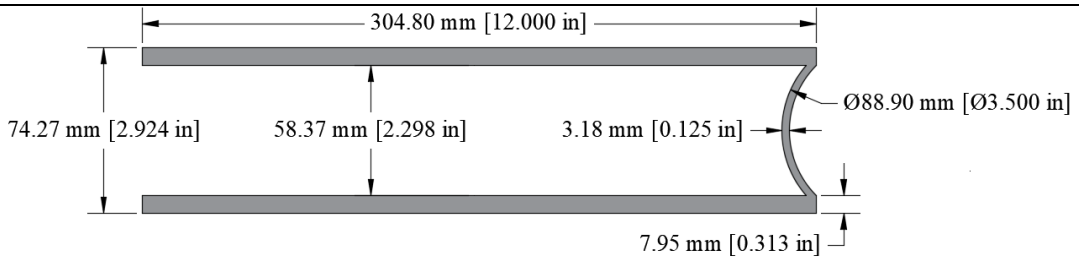

Initial shape	Shape after analysis
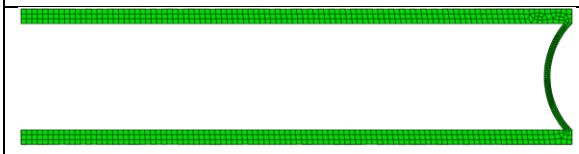	

Load-displacement graph (per unit depth)

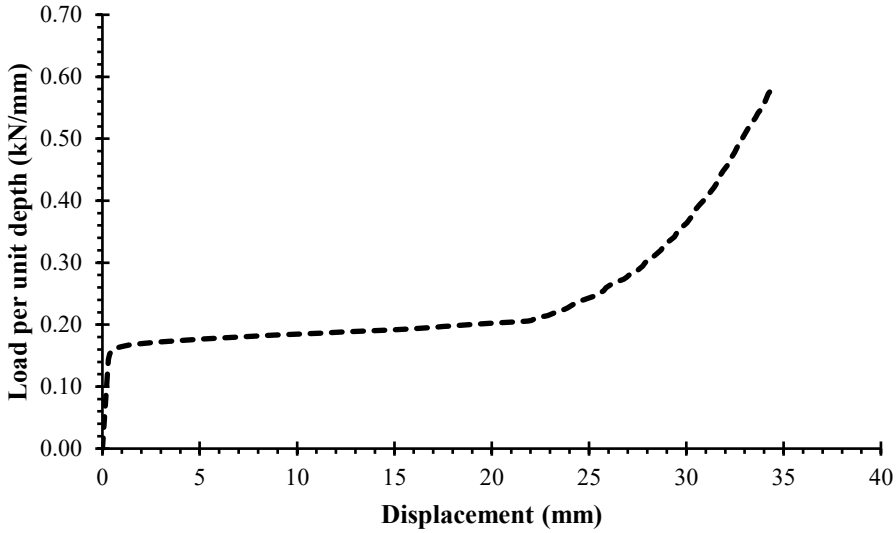

Comments

Depth used in analysis was 10 mm. Initial elastic behaviour is observed up to a displacement of roughly 0.3 mm. A plateau is then experienced from the yield point up to a displacement of roughly 22.6 mm were Load starts increasing rapidly with increasing displacement. The capacity of the connection at this point is roughly 0.21 kN/mm (2.1 kN for 10 mm).

Name	3.5×0.125(135º)	Description	Arc of Circular HSS between top and bottom plate

Cross-sectional dimensions

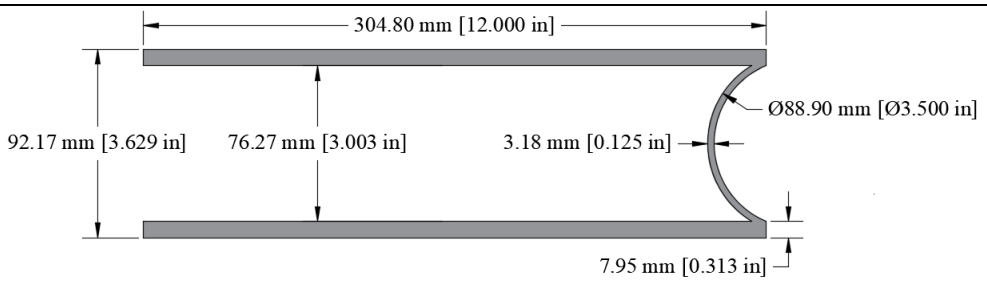

Initial shape	Shape after analysis
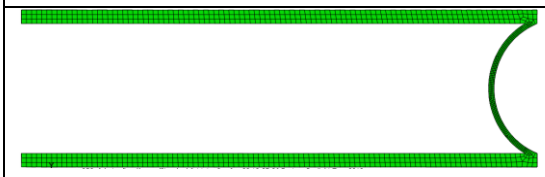	

Load-displacement graph (per unit depth)

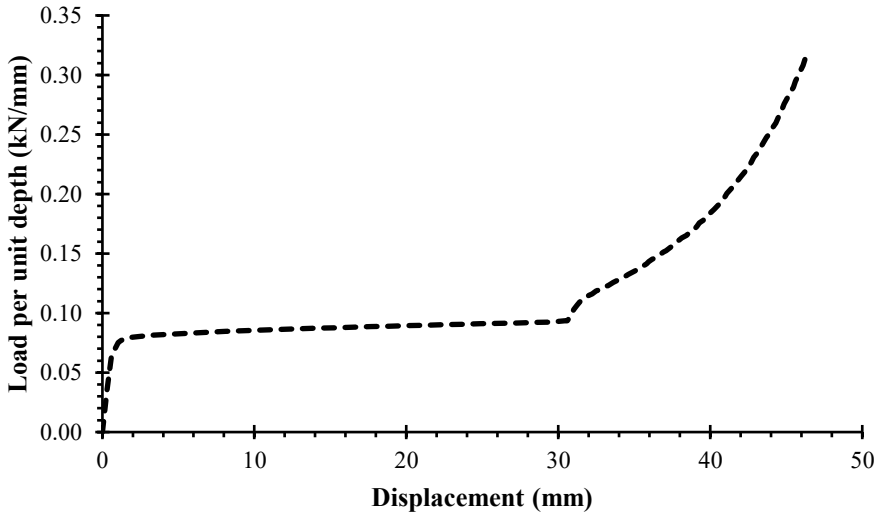

Comments

Depth used in analysis was 10 mm. Initial elastic behaviour is observed up to a displacement of roughly 0.6 mm. A plateau is then experienced from the yield point up to a displacement of roughly 30.6 mm were Load starts increasing rapidly with increasing displacement. The capacity of the connection at this point is roughly 0.10 kN/mm (1.0 kN for 10 mm).

Name	5×0.25	Description	Circular HSS between top and bottom plate

Cross-sectional dimensions

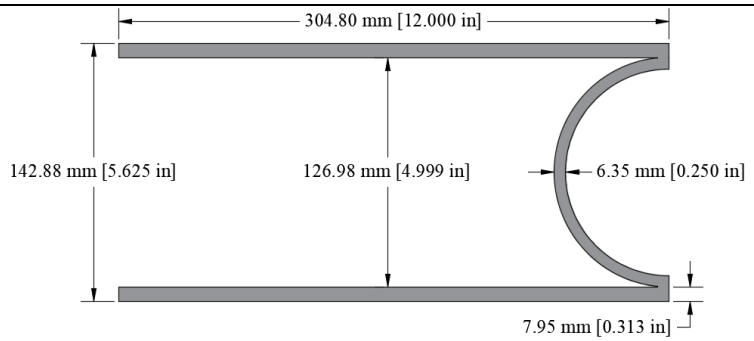

Initial shape	Shape after analysis
	

Load-displacement graph (per unit depth)

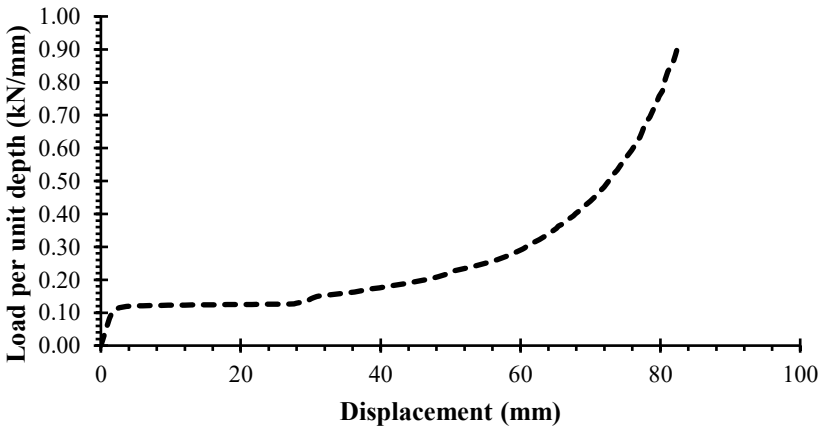

Comments

Depth used in analysis was 50 mm. Initial elastic behaviour is observed up to a displacement of roughly 1.5 mm. A plateau is then experienced from the yield point up to a displacement of roughly 30.0 mm were Load starts increasing rapidly with increasing displacement. The capacity of the connection at this point is roughly 0.13 kN/mm (6.5 kN for 50 mm).

Name	5×0.25 (90º)	Description	Arc of Circular HSS between top and bottom plate

Cross-sectional dimensions

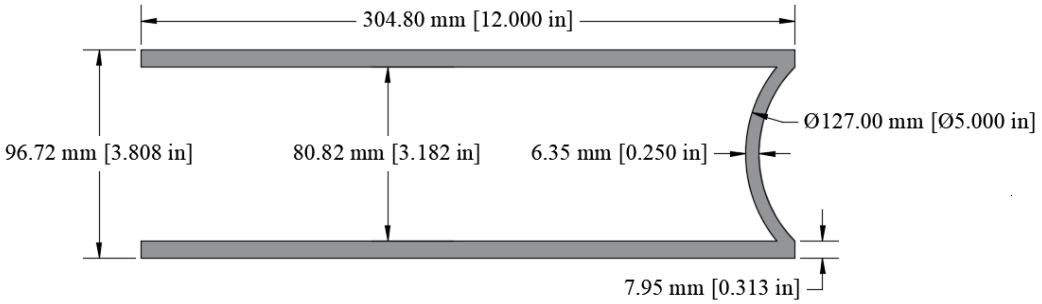

Initial shape	Shape after analysis
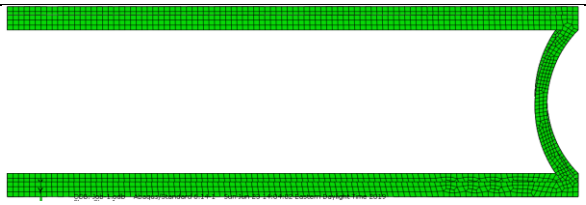	

Load-displacement graph (per unit depth)

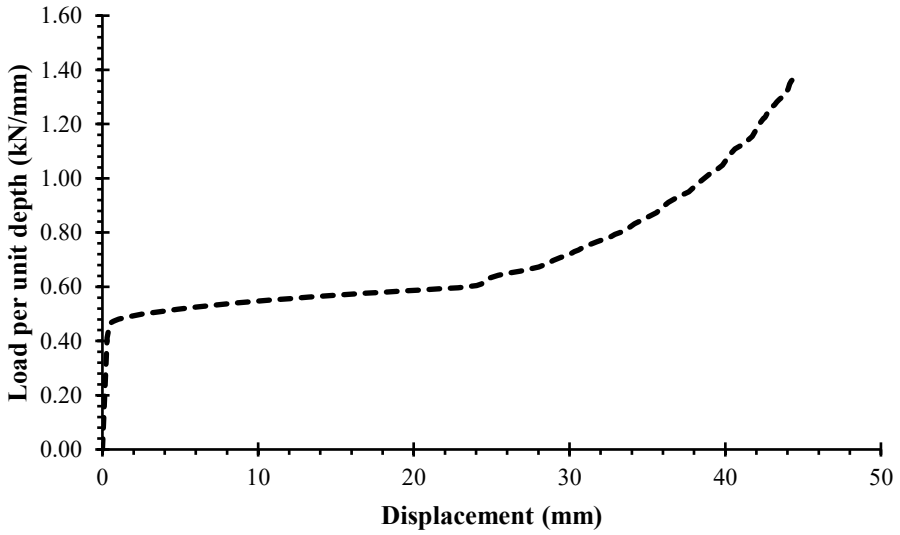

Comments

Depth used in analysis was 10 mm. Initial elastic behaviour is observed up to a displacement of roughly 0.3 mm. A plateau is then experienced from the yield point up to a displacement of roughly 24.8 mm were Load starts increasing rapidly with increasing displacement. The capacity of the connection at this point is roughly 0.61 kN/mm (6.1 kN for 10 mm).

Name	5×0.25 (135º)	Description	Arc of Circular HSS between top and bottom plate

Cross-sectional dimensions

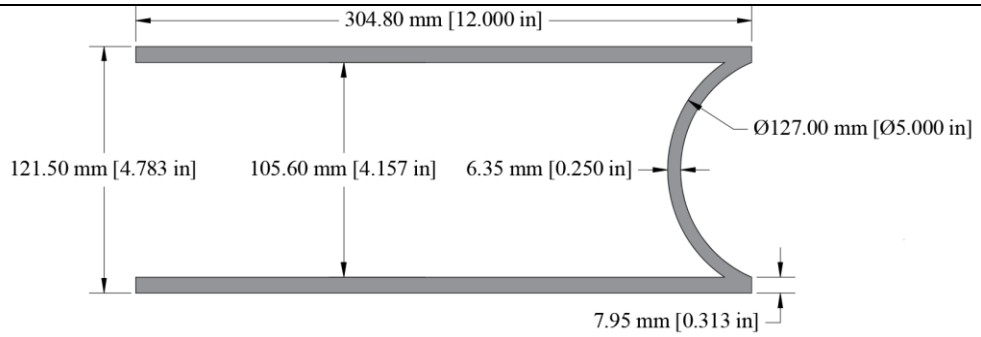

Initial shape	Shape after analysis
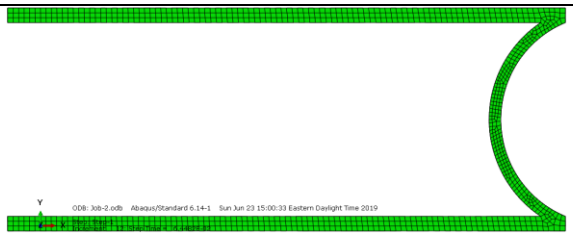	

Load-displacement graph (per unit depth)

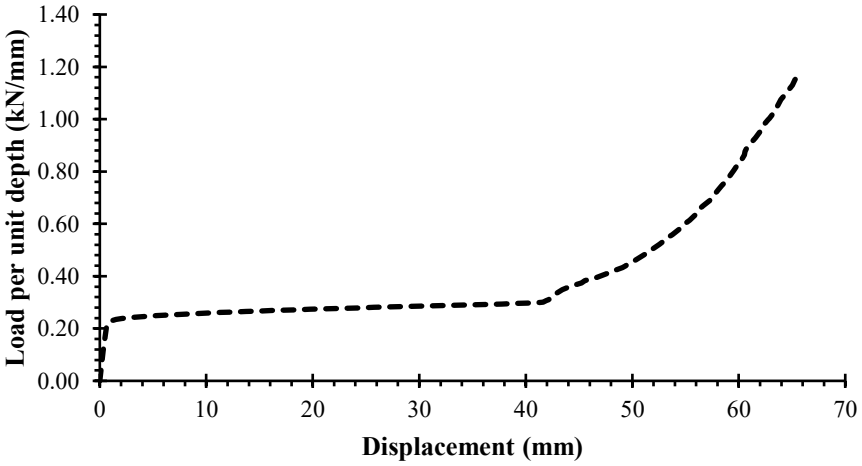

Comments

Depth used in analysis was 10 mm. Initial elastic behaviour is observed up to a displacement of roughly 0.6 mm. A plateau is then experienced from the yield point up to a displacement of roughly 30.0 mm were Load starts increasing rapidly with increasing displacement. The capacity of the connection at this point is roughly 0.09 kN/mm (0.9 kN for 10 mm).

Name	5×0.125	Description	Circular HSS between top and bottom plate

Cross-sectional dimensions

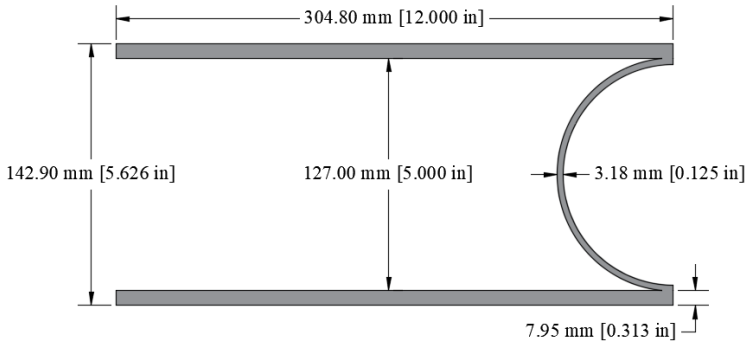

Initial shape	Shape after analysis
	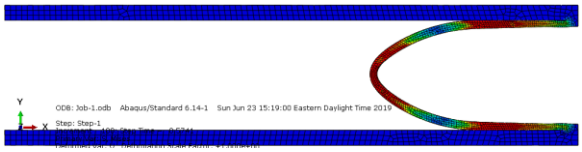

Load-displacement graph (per unit depth)

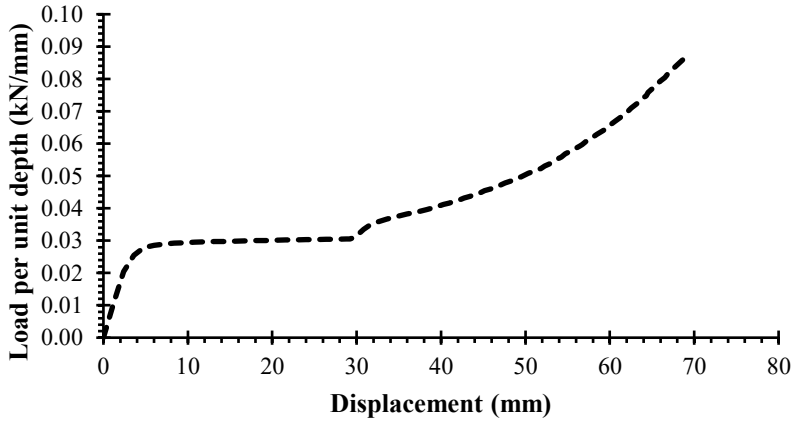

Comments

Depth used in analysis was 50 mm. Initial elastic behaviour is observed up to a displacement of roughly 3.6 mm. A plateau is then experienced from the yield point up to a displacement of roughly 28.8 mm were Load starts increasing rapidly with increasing displacement. The capacity of the connection at this point is roughly 0.03 kN/mm (1.5 kN for 50 mm).

Name	5×0.125 (90º)	Description	Arc of Circular HSS between top and bottom plate

Cross-sectional dimensions

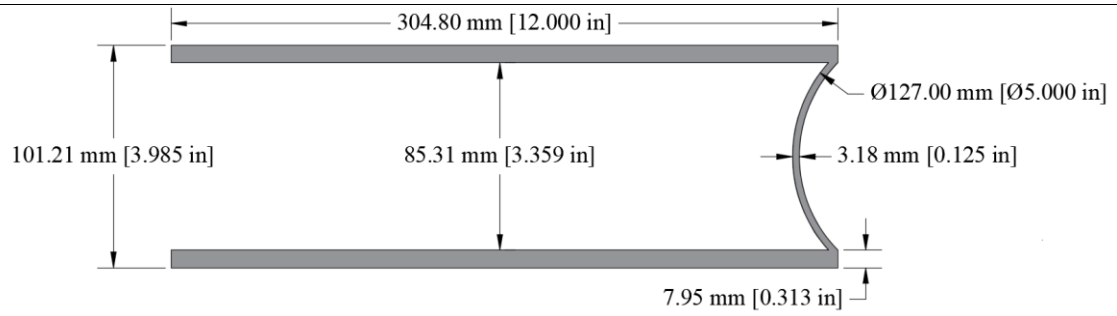

Initial shape

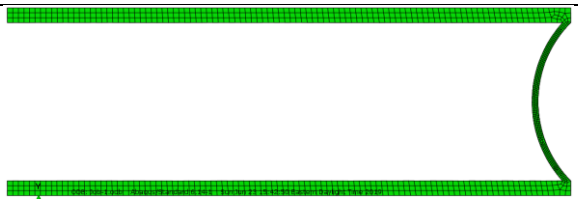

Shape after analysis

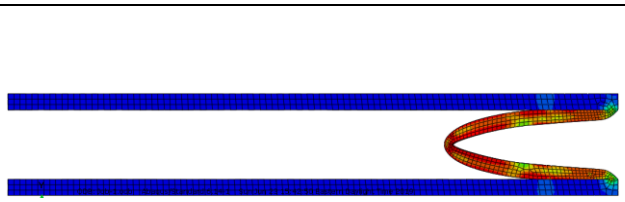

Load-displacement graph (per unit depth)

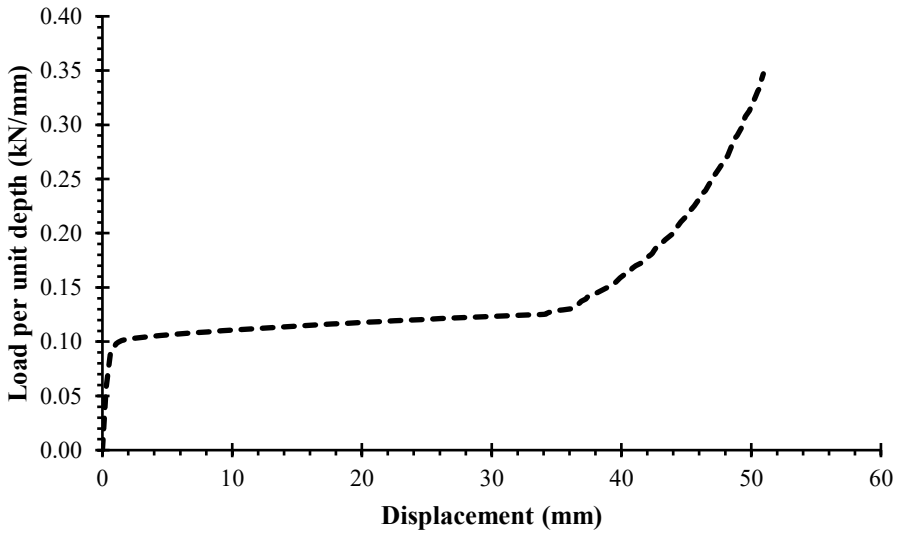

Comments

Depth used in analysis was 10 mm. Initial elastic behaviour is observed up to a displacement of roughly 0.6 mm. A plateau is then experienced from the yield point up to a displacement of roughly 35.2 mm were Load starts increasing rapidly with increasing displacement. The capacity of the connection at this point is roughly 0.12 kN/mm (1.2 kN for 10 mm).

Name	5×0.125 (135º)	Description	Arc of Circular HSS between top and bottom plate

Cross-sectional dimensions

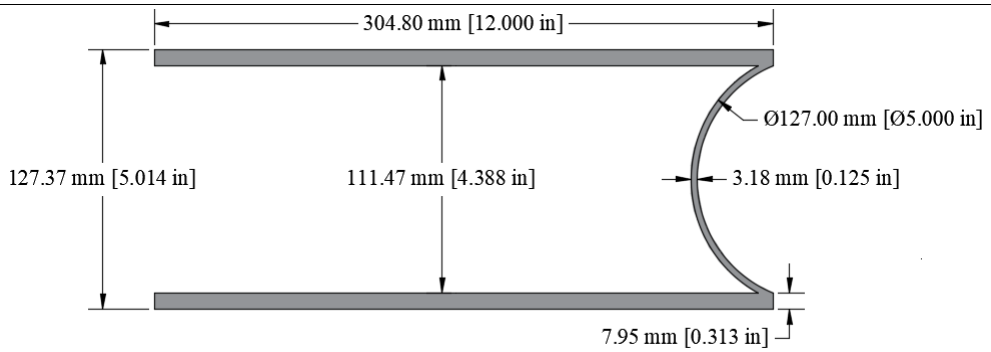

Initial shape	Shape after analysis
	

Load-displacement graph (per unit depth)

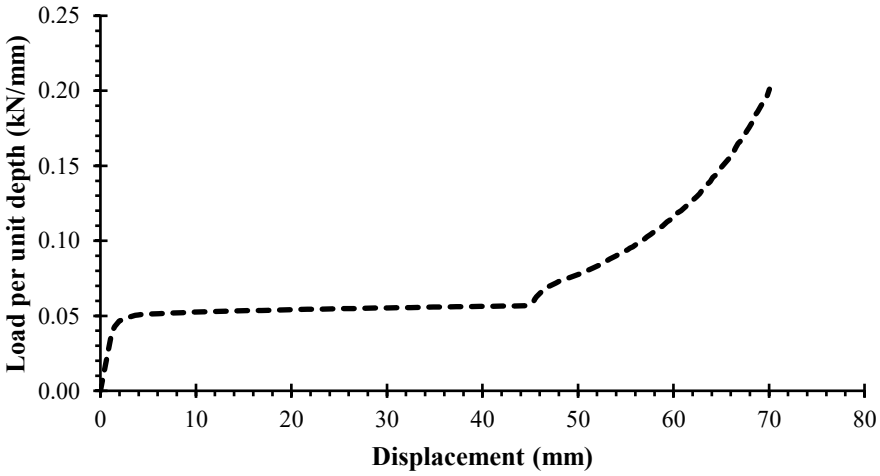

Comments

Depth used in analysis was 10 mm. Initial elastic behaviour is observed up to a displacement of roughly 1.2 mm. A plateau is then experienced from the yield point up to a displacement of roughly 44.4 mm were Load starts increasing rapidly with increasing displacement. The capacity of the connection at this point is roughly 0.05 kN/mm (0.5 kN for 10 mm).

Name	2×2×0.25W	Description	Angle welded at center between top and bottom plates

Cross-sectional dimensions

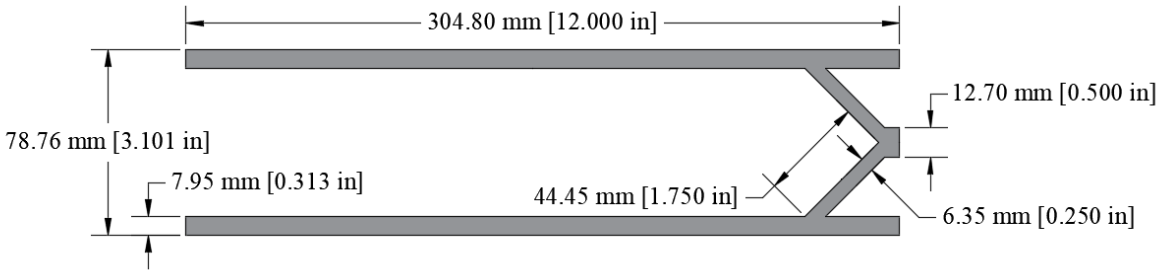

Initial shape	Shape after analysis
	

Load-displacement graph (per unit depth)

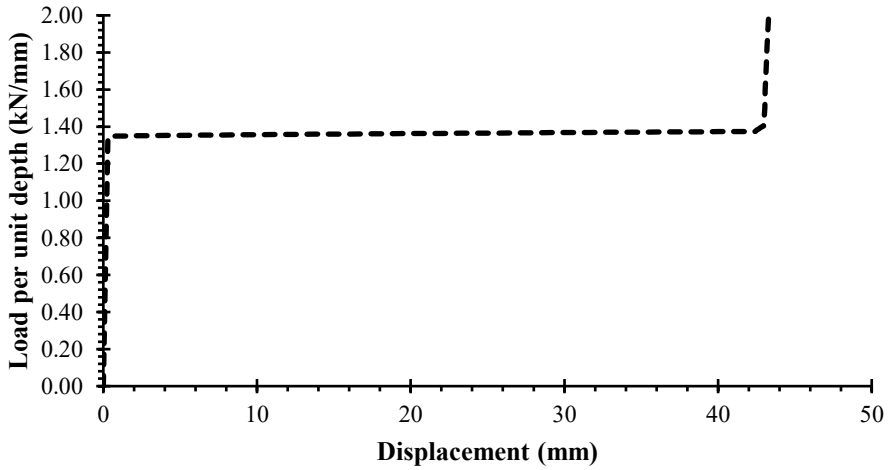

Comments

Depth used in analysis was 10 mm. Initial elastic behaviour is observed up to a displacement of roughly 0.3 mm. A plateau is then experienced from the yield point up to a displacement of roughly 42.3 mm were onset of densification occurs. The capacity of the connection at the onset of densification is roughly 1.37 kN/mm (13.7 kN for 10 mm).

Name	2×2×0.125W	Description	Angle welded at center between top and bottom plates

Cross-sectional dimensions

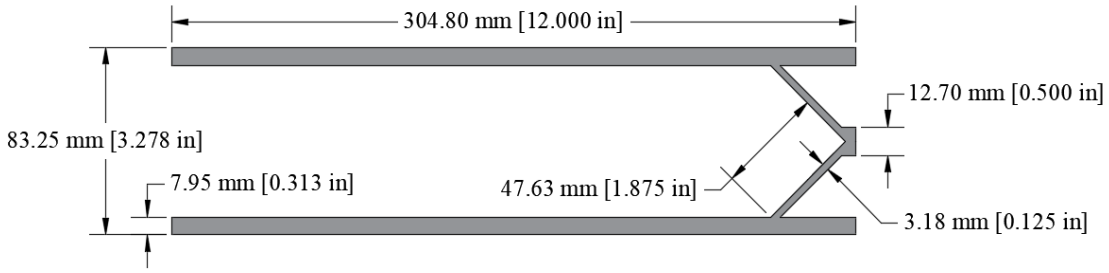

Initial shape	Shape after analysis
	

Load-displacement graph (per unit depth)

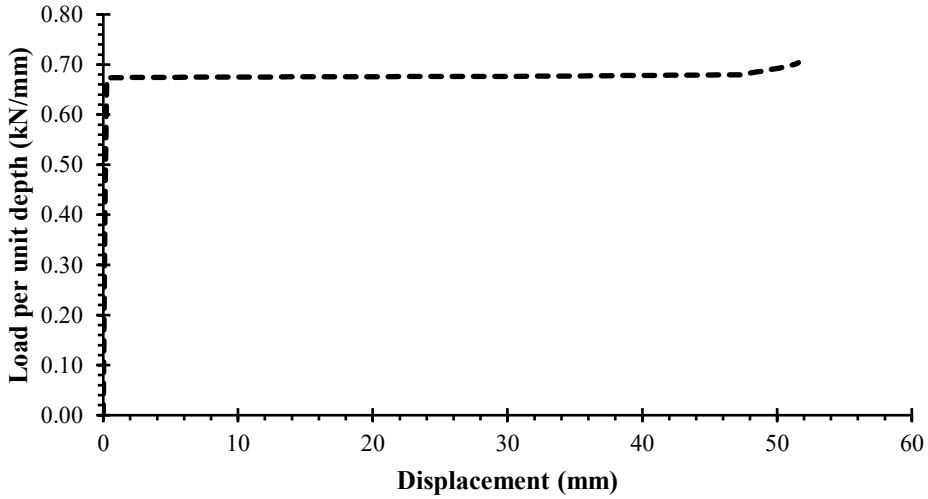

Comments

Depth used in analysis was 10 mm. Initial elastic behaviour is observed up to a displacement of roughly 0.3 mm. A plateau is then experienced from the yield point up to a displacement of roughly 47.2 mm were onset of densification occurs. The capacity of the connection at the onset of densification is roughly 0.68 kN/mm (6.8 kN for 10 mm).

Name	3×3×0.25W	Description	Angle welded at center between top and bottom plates

Cross-sectional dimensions

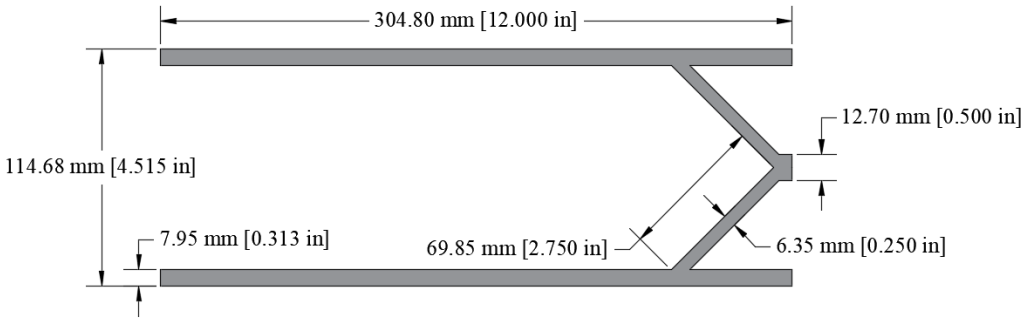

Initial shape	Shape after analysis
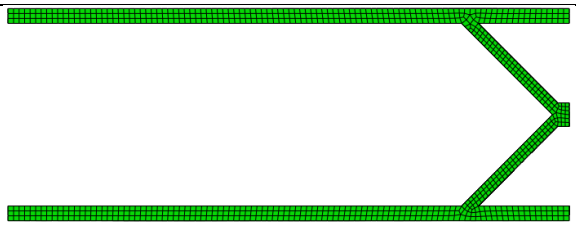	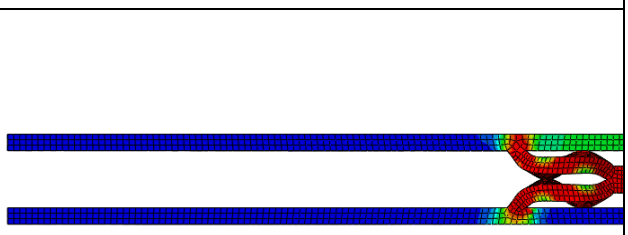

Load-displacement graph (per unit depth)

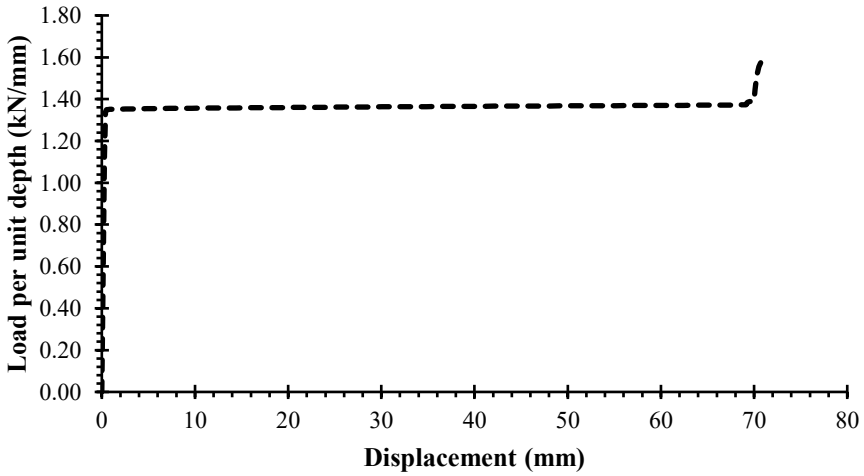

Comments

Depth used in analysis was 50 mm. Initial elastic behaviour is observed up to a displacement of roughly 0.4 mm. A plateau is then experienced from the yield point up to a displacement of roughly 69.0 mm were onset of densification occurs. The capacity of the connection at the onset of densification is roughly 1.37 kN/mm (68.5 kN for 50 mm).

Name	3×3×0.25W-2P	Description	Angle connected with center plate between top and bottom plates

Cross-sectional dimensions

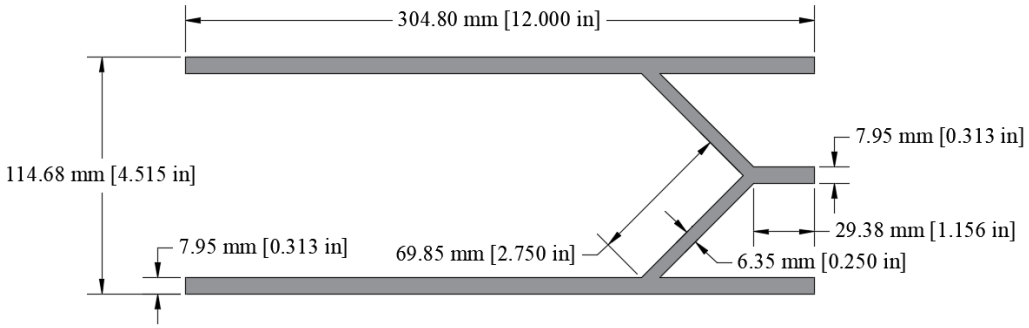

Initial shape	Shape after analysis
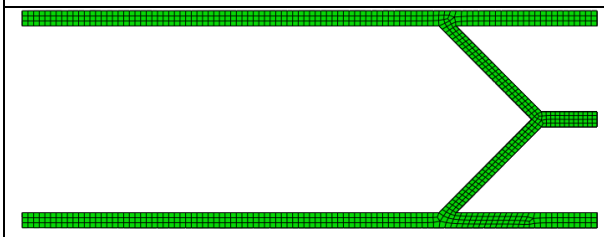	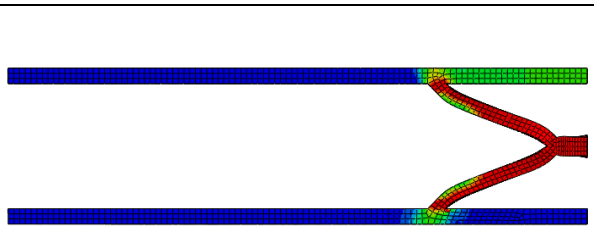

Load-displacement graph (per unit depth)

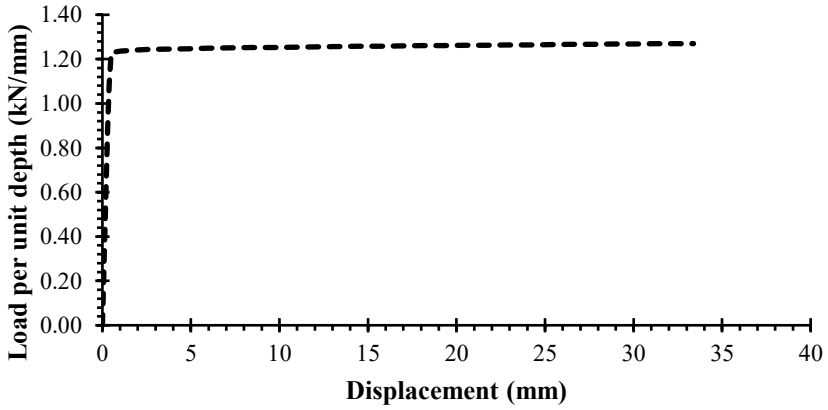

Comments

Depth used in analysis was 50 mm. Initial elastic behaviour is observed up to a displacement of roughly 0.5 mm. A plateau is then experienced from the yield point up to a displacement of roughly 33.3 mm were the analysis eneded. The capacity of the connection is roughly 1.27 kN/mm (63.5 kN for 50 mm) at the end of the analysis.

Name	3×3×0.25W-4P	Description	Angle connected with center plate between top and bottom plates

Cross-sectional dimensions

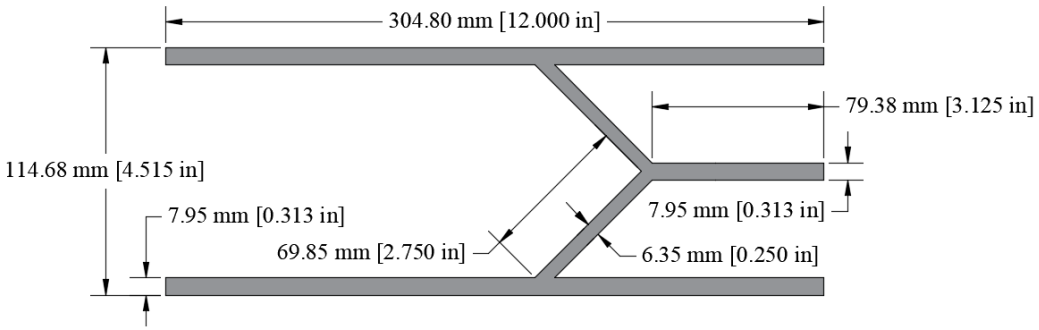

Initial shape	Shape after analysis
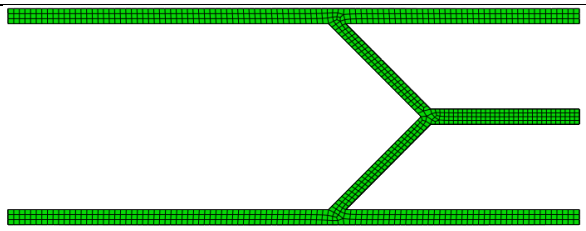	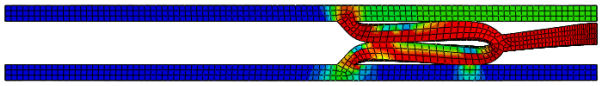

Load-displacement graph (per unit depth)

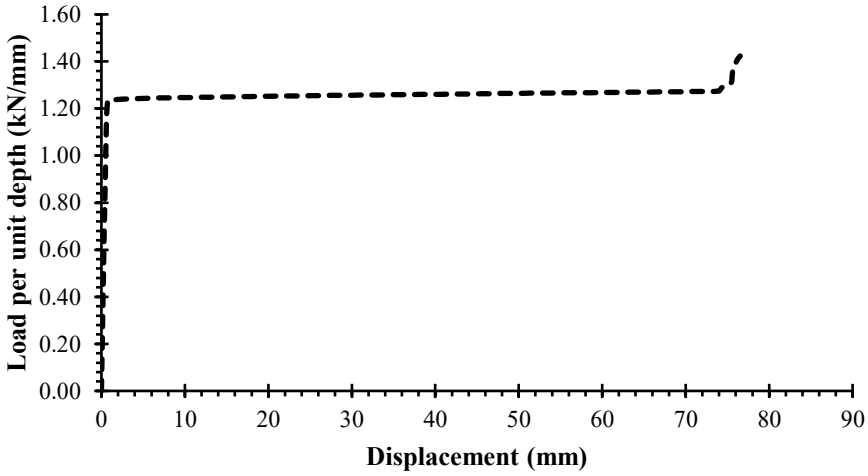

Comments

Depth used in analysis was 50 mm. Initial elastic behaviour is observed up to a displacement of roughly 0.6 mm. A plateau is then experienced from the yield point up to a displacement of roughly 73.3 mm were onset of densification occurs. The capacity of the connection at the onset of densification is roughly 1.27 kN/mm (63.5 kN for 50 mm).

Name	3×3×0.188W	Description	Angle welded at center between top and bottom plates

Cross-sectional dimensions

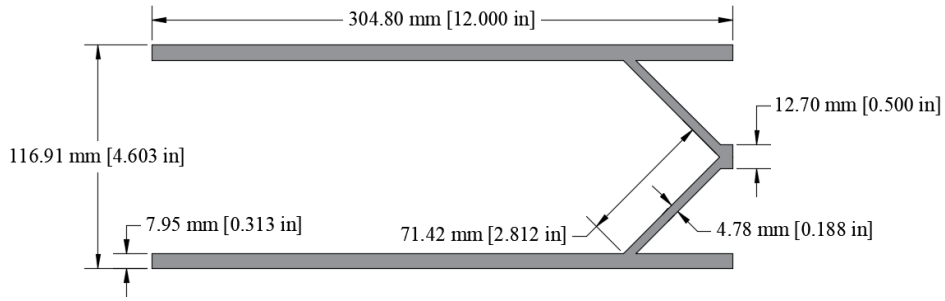

Initial shape

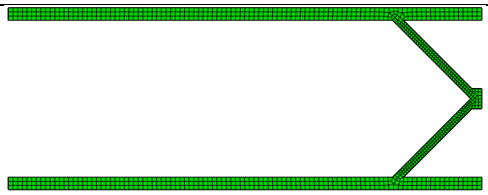

Shape after analysis

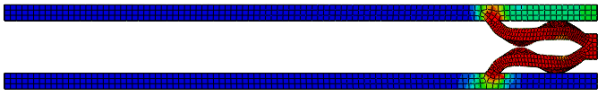

Load-displacement graph (per unit depth)

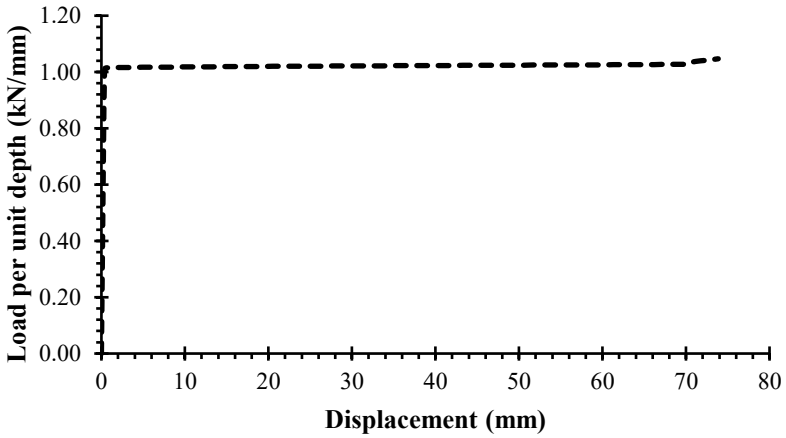

Comments

Depth used in analysis was 50 mm. Initial elastic behaviour is observed up to a displacement of roughly 0.4 mm. A plateau is then experienced from the yield point up to a displacement of roughly 73.8 mm were the analysis ended. The capacity of the connection at the end of the analysis is roughly 1.03 kN/mm (51.5 kN for 50 mm).

Name	3×3×0.188W-2P	Description	Angle connected with center plate between top and bottom plates

Cross-sectional dimensions

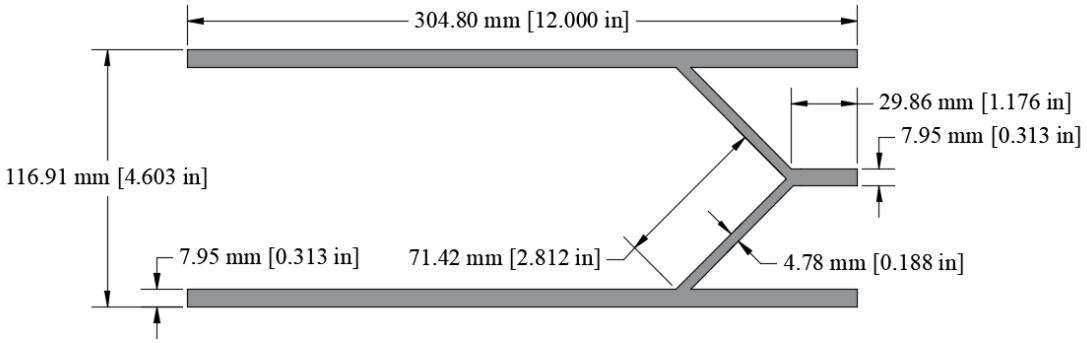

Initial shape	Shape after analysis
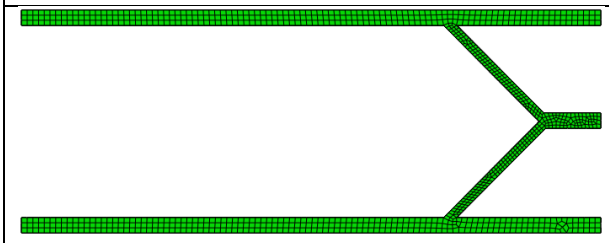	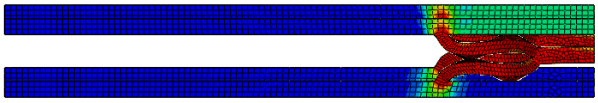

Load-displacement graph (per unit depth)

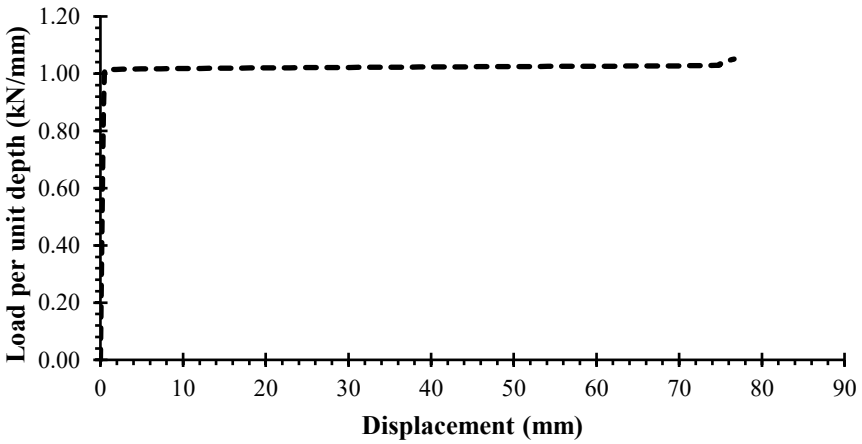

Comments

Depth used in analysis was 50 mm. Initial elastic behaviour is observed up to a displacement of roughly 0.5 mm. A plateau is then experienced from the yield point up to a displacement of roughly 75.9 mm were the analysis ended. The capacity of the connection at the end of the analysis is roughly 1.04 kN/mm (52.0 kN for 50 mm).

Name	3×3×0.188W-4P	Description	Angle connected with center plate between top and bottom plates

Cross-sectional dimensions

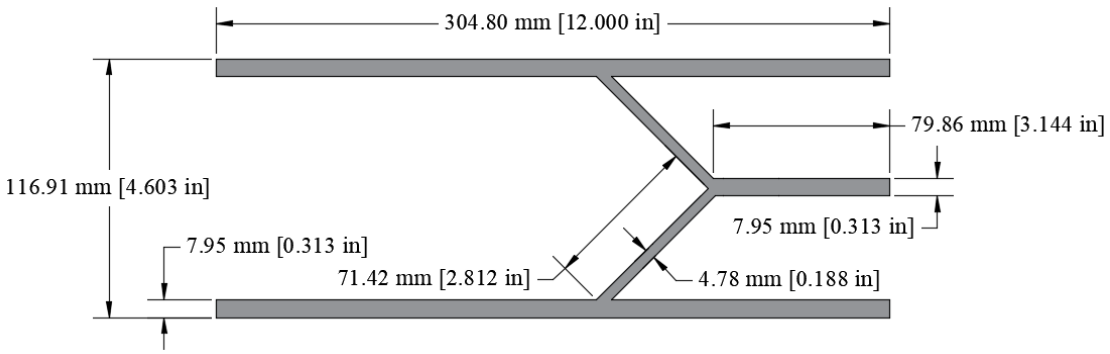

Initial shape	Shape after analysis
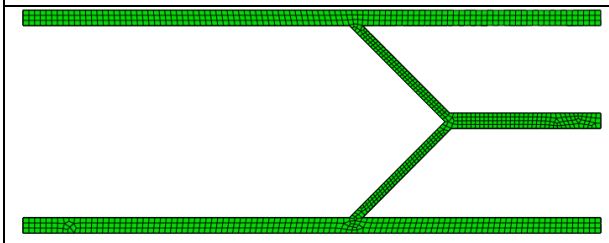	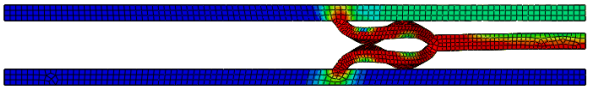

Load-displacement graph (per unit depth)

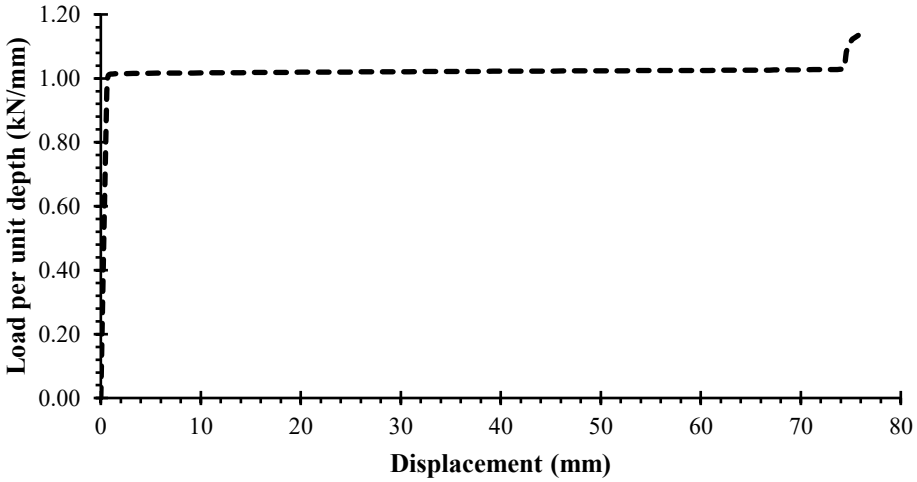

Comments

Depth used in analysis was 50 mm. Initial elastic behaviour is observed up to a displacement of roughly 0.6 mm. A plateau is then experienced from the yield point up to a displacement of roughly 73.6 mm were onset of densification occured. The capacity of the connection at this point is roughly 1.02 kN/mm (51.0 kN for 50 mm).

Name	4×4×0.25W	Description	Angle welded at center between top and bottom plates

Cross-sectional dimensions

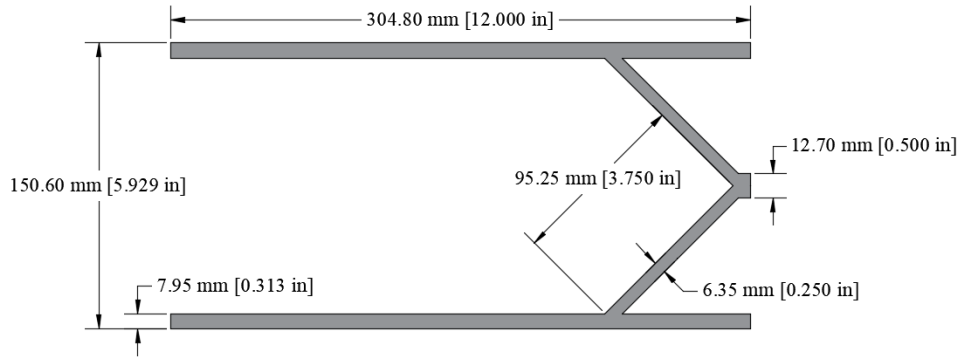

Initial shape	Shape after analysis
	

Load-displacement graph (per unit depth)

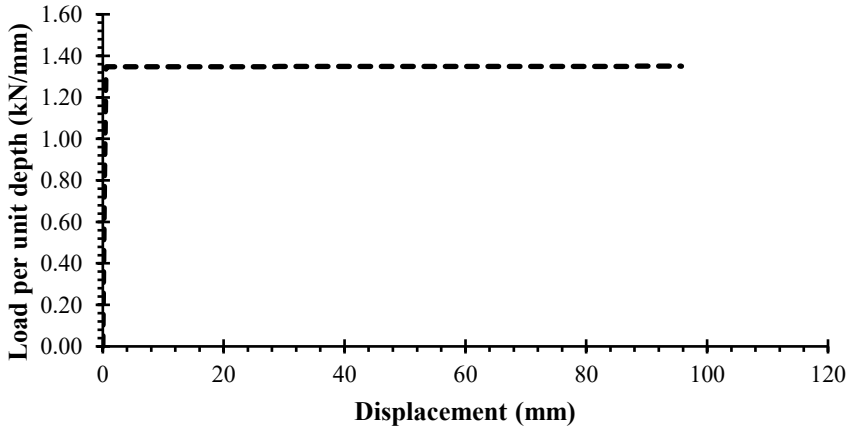

Comments

Depth used in analysis was 10 mm. Initial elastic behaviour is observed up to a displacement of roughly 0.5 mm. A plateau is then experienced from the yield point up to a displacement of roughly 95.6 mm were the analysis ended. The capacity of the connection at the end of the analysis is roughly 1.34 kN/mm (13.4 kN for 10 mm).

Name	2(2×2×0.25)	Description	Two angle per side between top and bottom plates

Cross-sectional dimensions

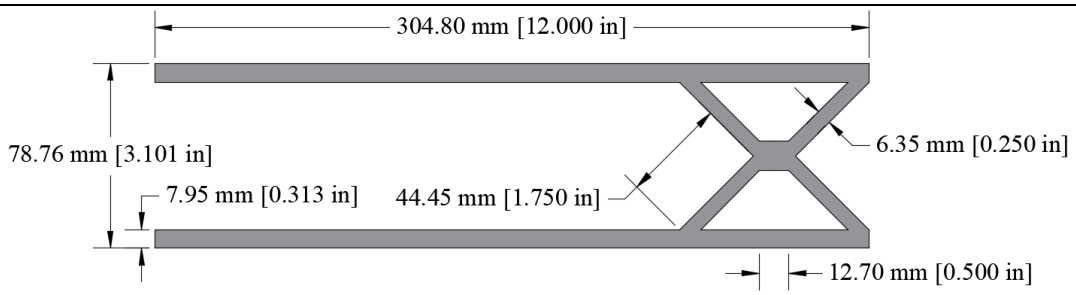

Initial shape	Shape after analysis
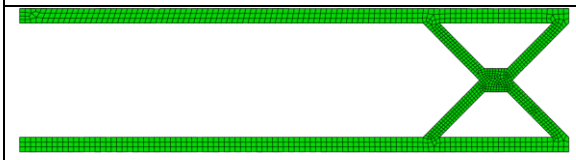	

Load-displacement graph (per unit depth)

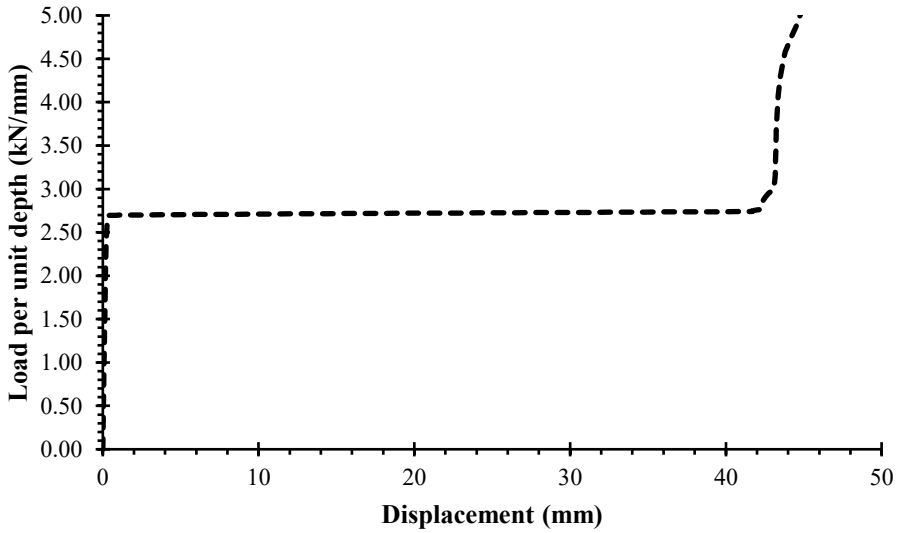

Comments

Depth used in analysis was 10 mm. Initial elastic behaviour is observed up to a displacement of roughly 0.3 mm. A plateau is then experienced from the yield point up to a displacement of roughly 42.2 mm were onset of densification occured. The capacity of the connection at this point is roughly 2.76 kN/mm (27.6 kN for 10 mm).

Name	2(2×2×0.125)	Description	Two angle per side between top and bottom plates

Cross-sectional dimensions

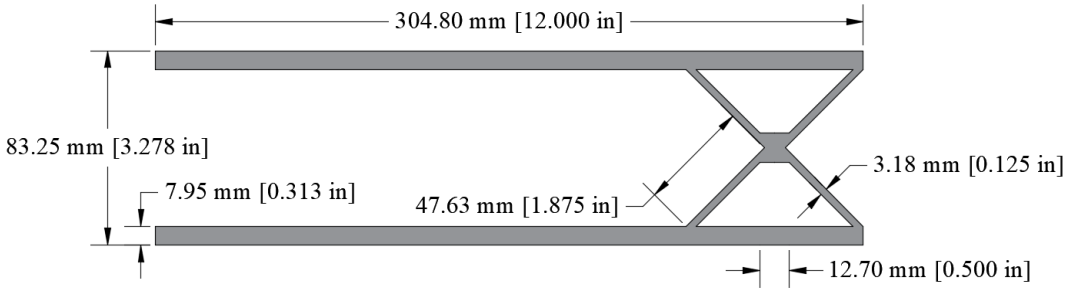

Initial shape	Shape after analysis
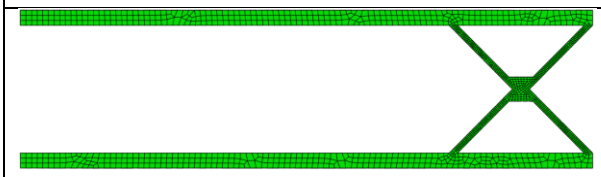	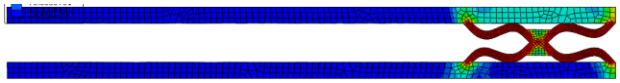

Load-displacement graph (per unit depth)

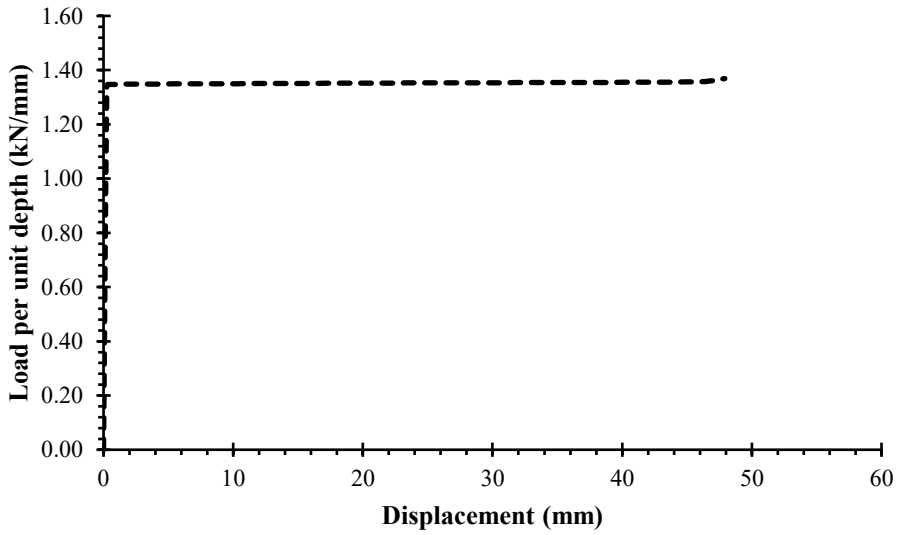

Comments

Depth used in analysis was 10 mm. Initial elastic behaviour is observed up to a displacement of roughly 0.3 mm. A plateau is then experienced from the yield point up to a displacement of roughly 47.9 mm were the analysis ended. The capacity of the connection at the end of the analysis is roughly 1.37 kN/mm (13.7 kN for 10 mm).

Name	2(3×3×0.25)	Description	Two angle per side between top and bottom plates

Cross-sectional dimensions

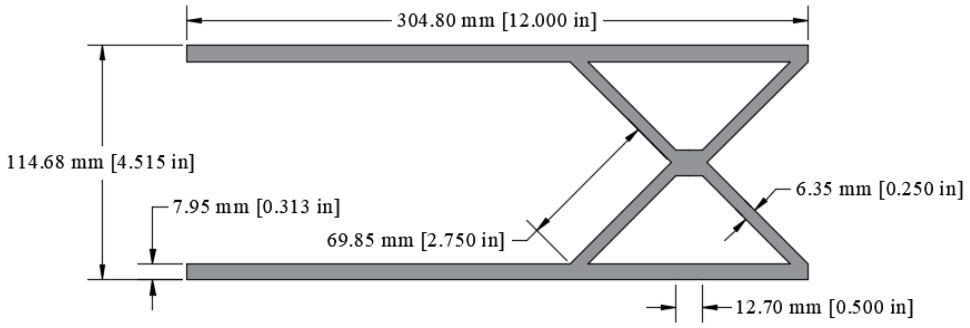

Initial shape

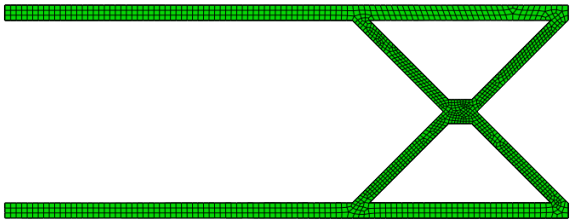

Shape after analysis

Load-displacement graph (per unit depth)

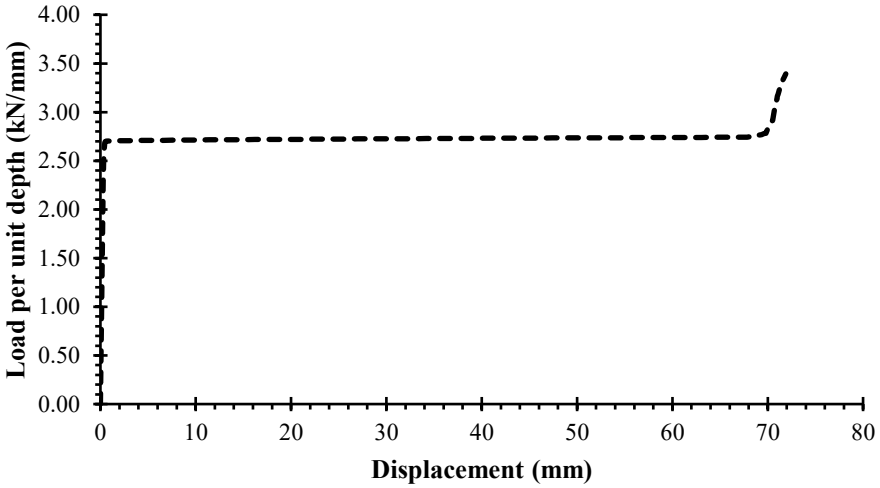

Comments

Depth used in analysis was 50 mm. Initial elastic behaviour is observed up to a displacement of roughly 0.4 mm. A plateau is then experienced from the yield point up to a displacement of roughly 68.0 mm were onset of densification occured. The capacity of the connection at this point is roughly 2.74 kN/mm (137 kN for 50 mm).

Name	2(3×3×0.188)	Description	Two angle per side between top and bottom plates

Cross-sectional dimensions

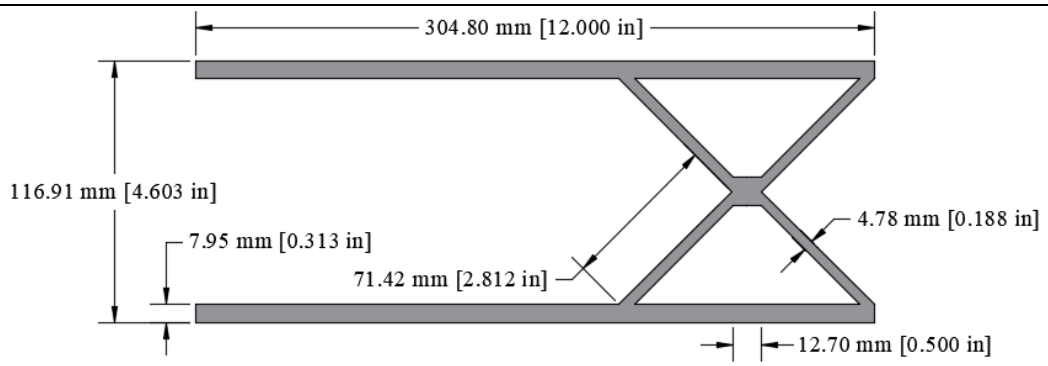

Initial shape	Shape after analysis
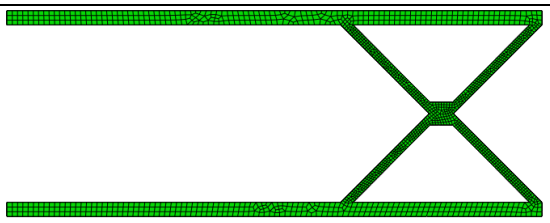	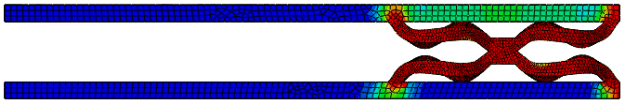

Load-displacement graph (per unit depth)

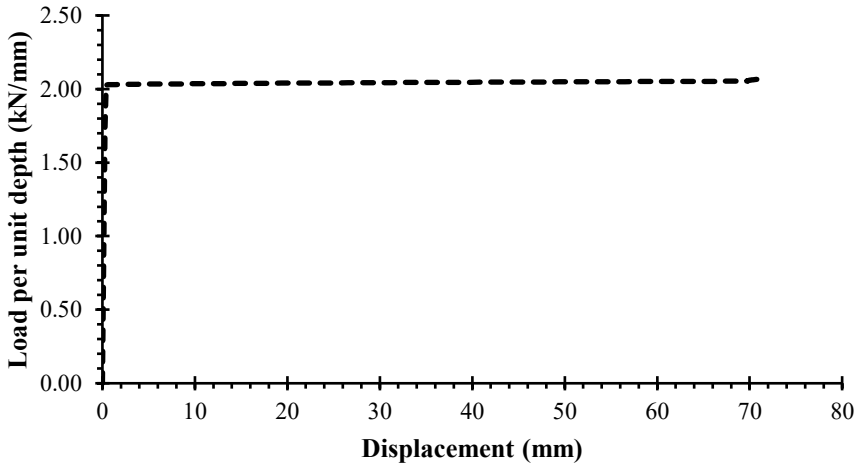

Comments

Depth used in analysis was 50 mm. Initial elastic behaviour is observed up to a displacement of roughly 0.4 mm. A plateau is then experienced from the yield point up to a displacement of roughly 71.0 mm were the analysis ended. The capacity of the connection at the end of the analysis is roughly 2.06 kN/mm (103 kN for 50 mm).

Name	2(4×4×0.25)	Description	Two angle per side between top and bottom plates

Cross-sectional dimensions

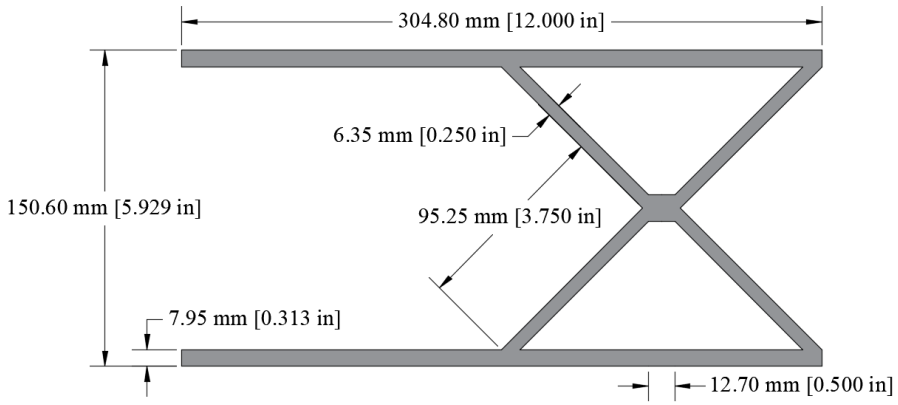

Initial shape

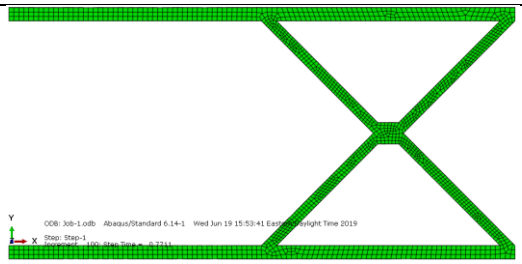

Shape after analysis

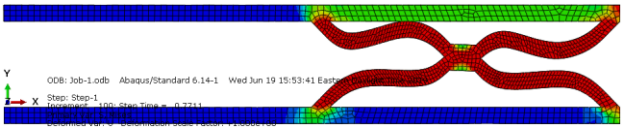

Load-displacement graph (per unit depth)

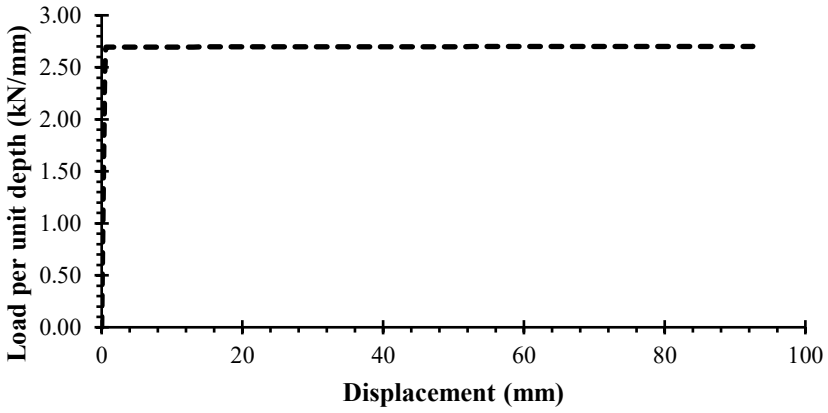

Comments

Depth used in analysis was 10 mm. Initial elastic behaviour is observed up to a displacement of roughly 0.5 mm. A plateau is then experienced from the yield point up to a displacement of roughly 92.5 mm were the analysis ended. The capacity of the connection at the end of the analysis is roughly 2.70 kN/mm (27 kN for 10 mm).

Name	2×2×0.25 + 2.375×0.125	Description	Angle plus circular HSS between top and bottom plates

Cross-sectional dimensions

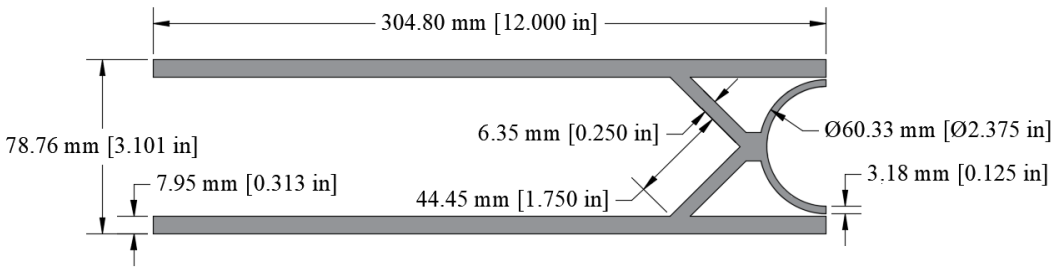

Initial shape	Shape after analysis
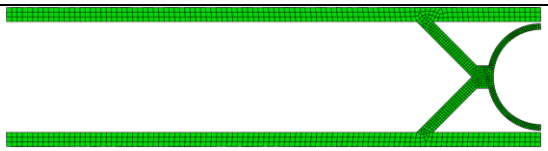	

Load-displacement graph (per unit depth)

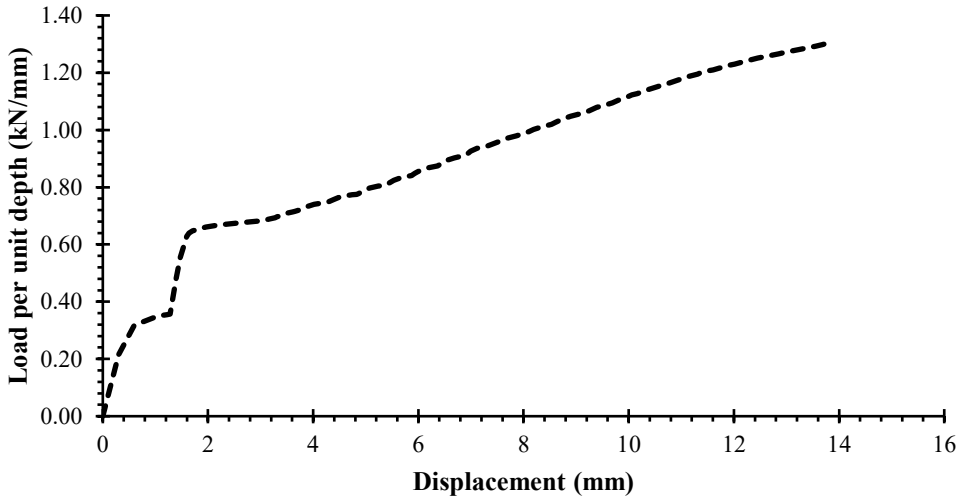

Comments

Depth used in analysis was 10 mm. Initial elastic behaviour is experienced up to a displacement of 0.6 mm. Afterwards, a short plateau is experienced up to a displacement of 1.3 mm. A second elastic zone is experienced up to a displacment of 1.6 mm, due to contact being made between the top and bottom plates and the central circular HSS. Following the second elastic zone, the connection stiffness decreases and Load increases at a mostly constant rate up to a displacement of 13.7 mm where the analysis was ended. The capacity at this point is 1.31 kN/mm (13.1 kN for 10 mm).

Name	2×2×0.125 + 2.375×0.125	Description	Angle plus circular HSS between top and bottom plates

Cross-sectional dimensions

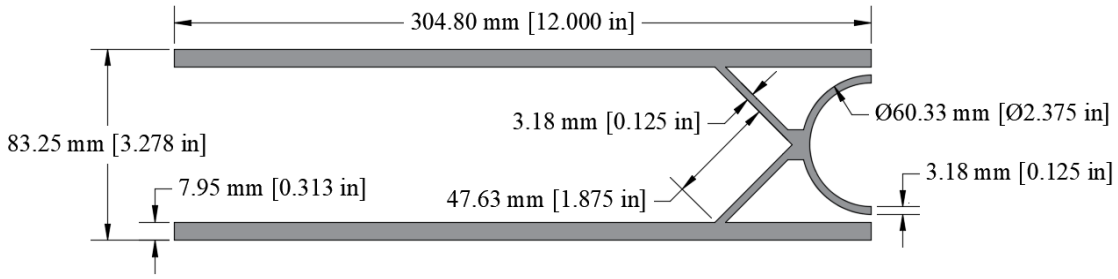

Initial shape	Shape after analysis
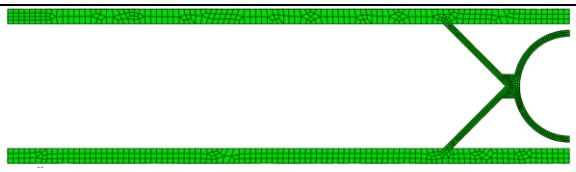	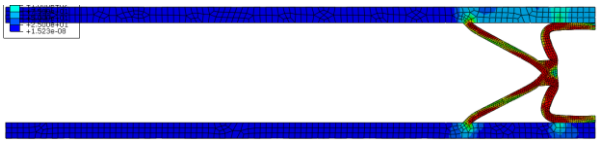

Load-displacement graph (per unit depth)

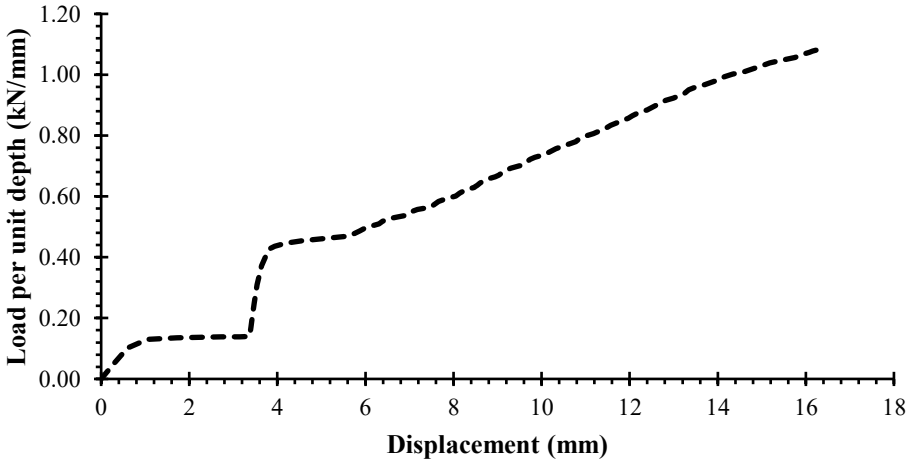

Comments

Depth used in analysis was 10 mm. Initial elastic behaviour is experienced up to a displacement of 0.9 mm. Afterwards, a short plateau is experienced up to a displacement of 3.4 mm. A second elastic zone is experienced up to a displacment of 3.8 mm, due to contact being made between the top and bottom plates and the central circular HSS. Following the second elastic zone, the connection stiffness decreases and Load increases at a mostly constant rate up to a displacement of 16.2 mm where the analysis was ended. The capacity at this point is 1.08 kN/mm (10.8 kN for 10 mm).

Name	3×3×0.25 + 3.5×0.25	Description	Angle plus circular HSS between top and bottom plates

Cross-sectional dimensions

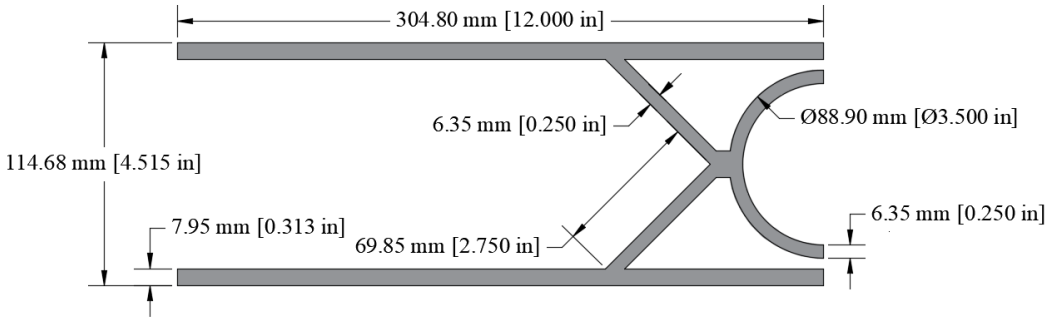

Initial shape	Shape after analysis
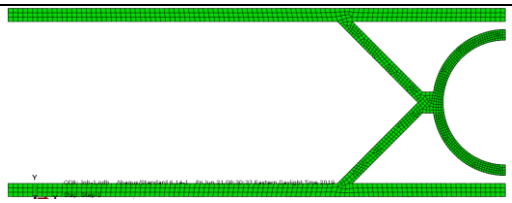	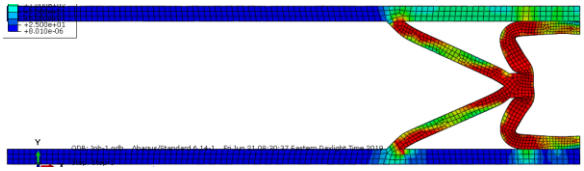

Load-displacement graph (per unit depth)

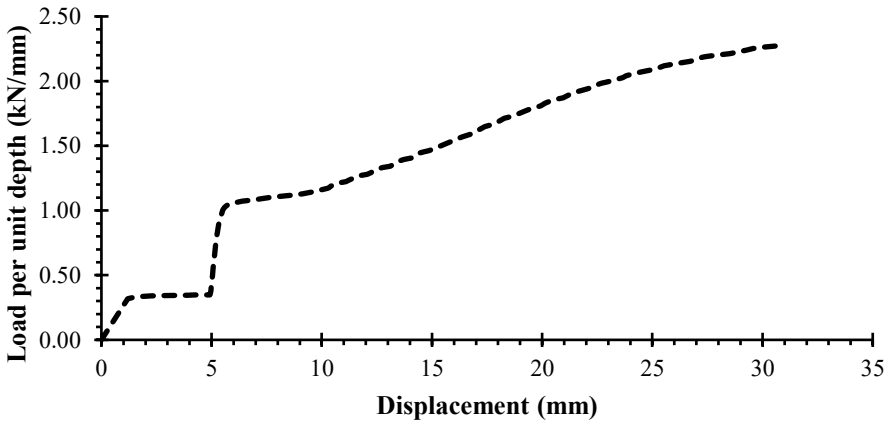

Comments

Depth used in analysis was 50 mm. Initial elastic behaviour is experienced up to a displacement of 1.2 mm. Afterwards, a short plateau is experienced up to a displacement of 5.0 mm. A second elastic zone is experienced up to a displacment of 5.6 mm, due to contact being made between the top and bottom plates and the central circular HSS. Following the second elastic zone, the connection stiffness decreases and Load increases at a mostly constant rate up to a displacement of 30.6 mm where the analysis was ended. The capacity at this point is 2.27 kN/mm (113.5 kN for 50 mm).

Name	3×3×0.25 + 3.5×0.125	Description	Angle plus circular HSS between top and bottom plates

Cross-sectional dimensions

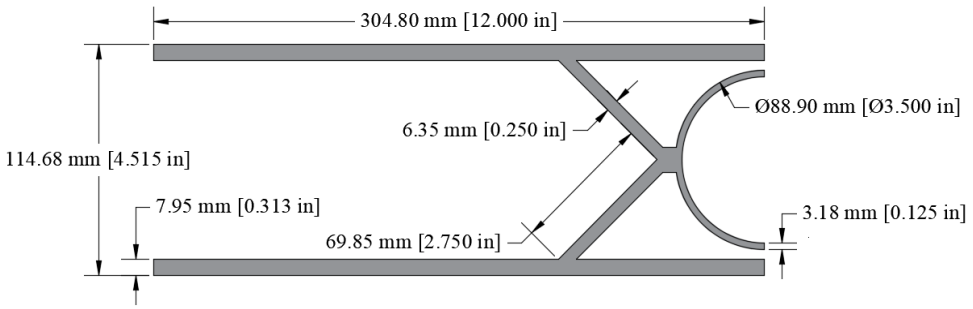

Initial shape

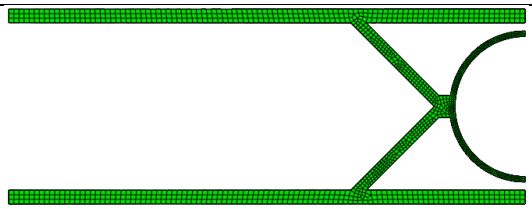

Shape after analysis

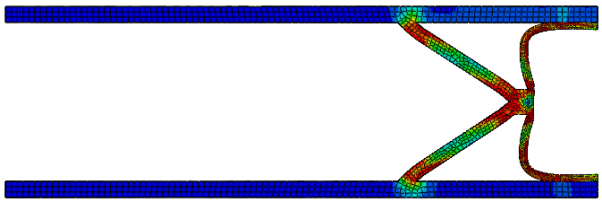

Load-displacement graph (per unit depth)

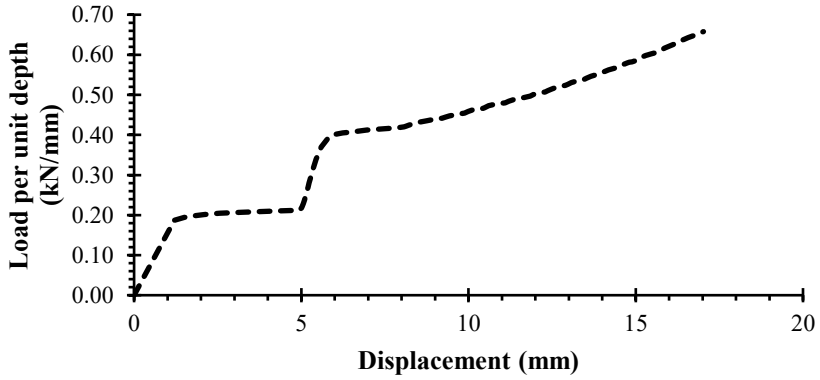

Comments

Depth used in analysis was 10 mm. Initial elastic behaviour is experienced up to a displacement of 1.1 mm. Afterwards, a short plateau is experienced up to a displacement of 6.0 mm. A second elastic zone is experienced up to a displacment of 6.7 mm, due to contact being made between the top and bottom plates and the central circular HSS. Following the second elastic zone, the connection stiffness decreases and Load increases at a mostly constant rate up to a displacement of 39.8 mm where the analysis was ended. The capacity at this point is 2.43 kN/mm (24.3 kN for 10 mm).

Name	3×3×0.188 + 3.5×0.25	Description	Angle plus circular HSS between top and bottom plates

Cross-sectional dimensions

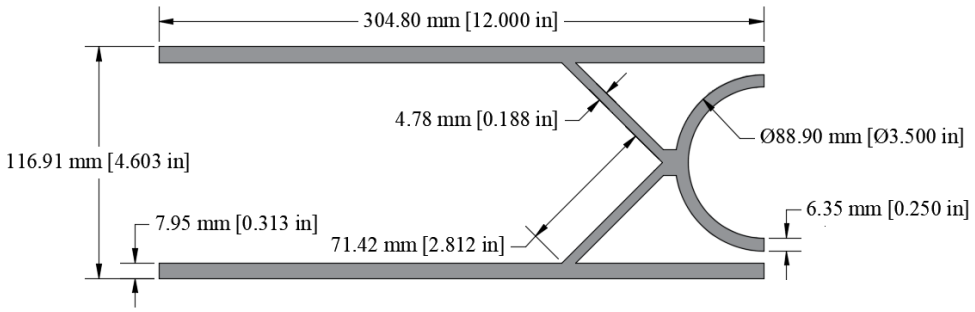

Initial shape	Shape after analysis
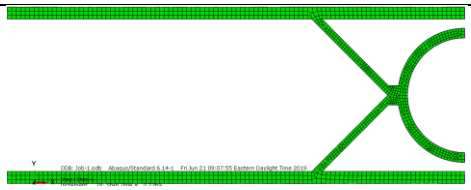	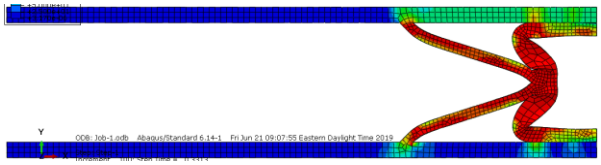

Load-displacement graph (per unit depth)

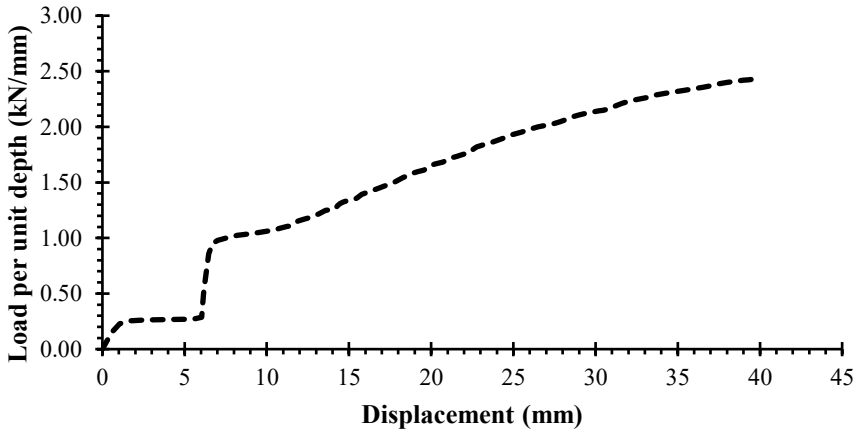

Comments

Depth used in analysis was 10 mm. Initial elastic behaviour is experienced up to a displacement of 1.1 mm. Afterwards, a short plateau is experienced up to a displacement of 6.0 mm. A second elastic zone is experienced up to a displacment of 6.7 mm, due to contact being made between the top and bottom plates and the central circular HSS. Following the second elastic zone, the connection stiffness decreases and Load increases at a mostly constant rate up to a displacement of 39.8 mm where the analysis was ended. The capacity at this point is 2.43 kN/mm (24.3 kN for 10 mm).

Name	3×3×0.188 + 3.5×0.125	Description	Angle plus circular HSS between top and bottom plates

Cross-sectional dimensions

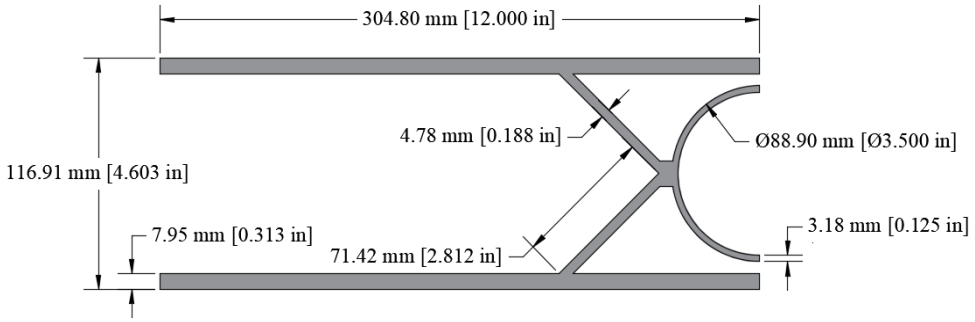

Initial shape

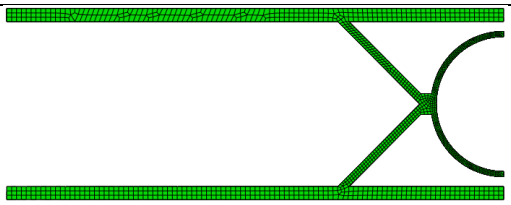

Shape after analysis

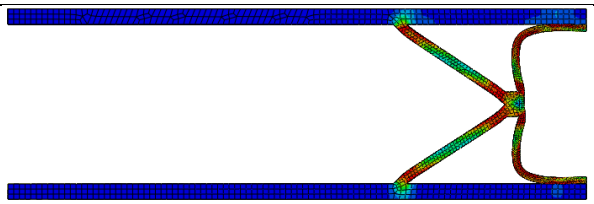

Load-displacement graph (per unit depth)

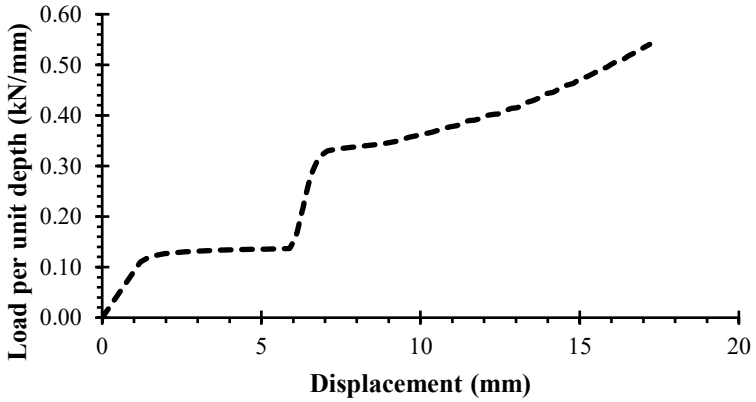

Comments

Depth used in analysis was 50 mm. Initial elastic behaviour is experienced up to a displacement of 1.4 mm. Afterwards, a short plateau is experienced up to a displacement of 5.9 mm. A second elastic zone is experienced up to a displacment of 6.9 mm, due to contact being made between the top and bottom plates and the central circular HSS. Following the second elastic zone, the connection stiffness decreases and Load increases at a mostly constant rate up to a displacement of 17.2 mm where the analysis was ended. The capacity at this point is 0.54 kN/mm (27 kN for 50 mm).

Name	4×4×0.25 + 5×0.25	Description	Angle plus circular HSS between top and bottom plates

Cross-sectional dimensions

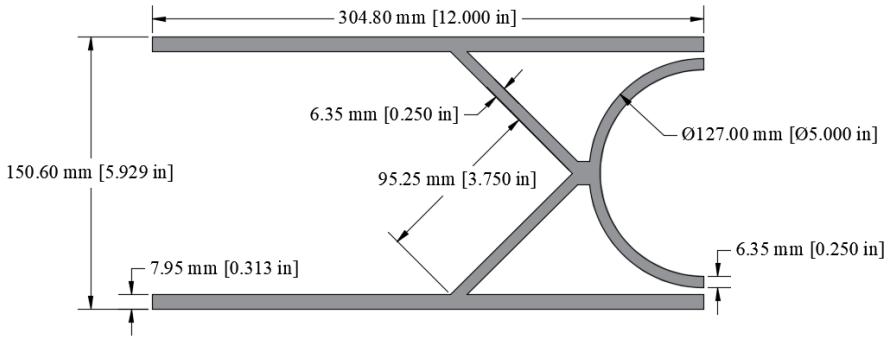

Initial shape

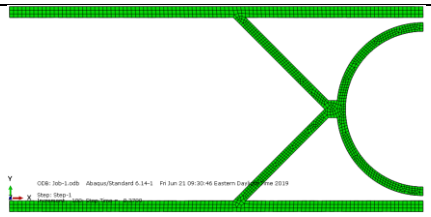

Shape after analysis

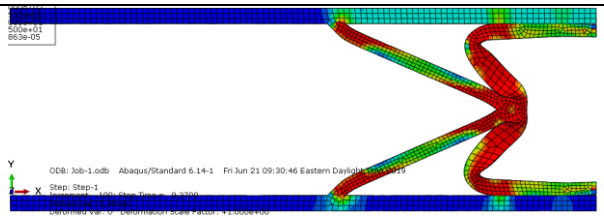

Load-displacement graph (per unit depth)

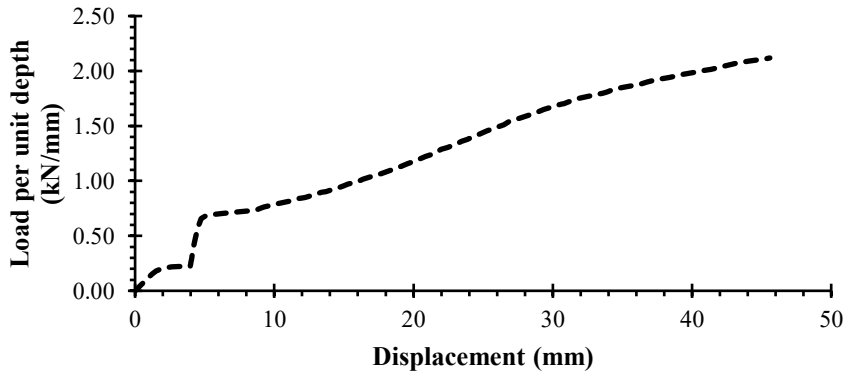

Comments

Depth used in analysis was 10 mm. Initial elastic behaviour is experienced up to a displacement of 1.5 mm. Afterwards, a short plateau is experienced up to a displacement of 4.0 mm. A second elastic zone is experienced up to a displacment of 4.8 mm, due to contact being made between the top and bottom plates and the central circular HSS. Following the second elastic zone, the connection stiffness decreases and Load increases at a mostly constant rate up to a displacement of 45.6 mm where the analysis was ended. The capacity at this point is 2.11 kN/mm (21.1 kN for 10 mm).

Name	4×4×0.25 + 5×0.125	Description	Angle plus circular HSS between top and bottom plates

Cross-sectional dimensions

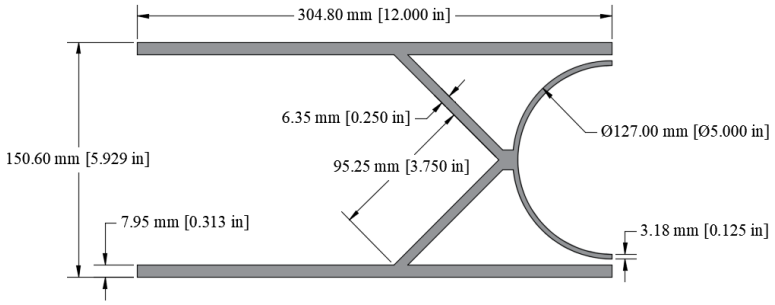

Initial shape	Shape after analysis
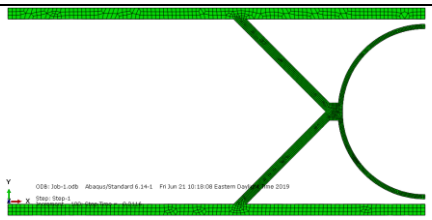	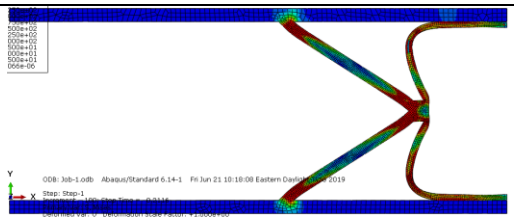

Load-displacement graph (per unit depth)

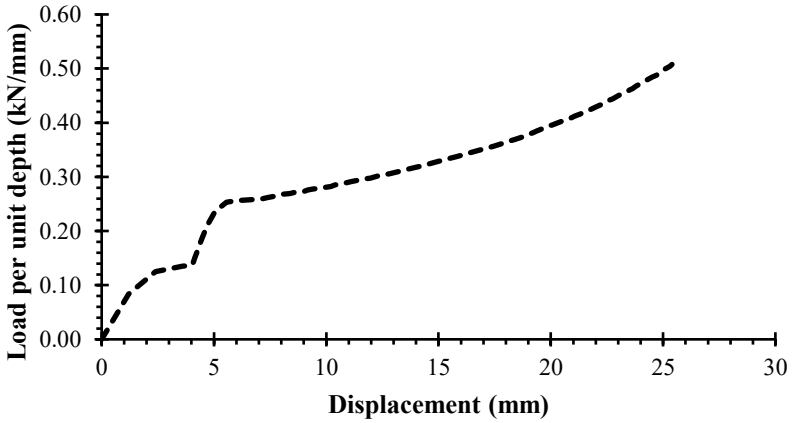

Comments

Depth used in analysis was 10 mm. Initial elastic behaviour is experienced up to a displacement of 2.4 mm. Afterwards, a short plateau is experienced up to a displacement of 4.0 mm. A second elastic zone is experienced up to a displacment of 5.5 mm, due to contact being made between the top and bottom plates and the central circular HSS. Following the second elastic zone, the connection stiffness decreases and Load increases at a mostly constant rate up to a displacement of 25.3 mm where the analysis was ended. The capacity at this point is 0.50 kN/mm (5.0 kN for 10 mm).

Name	2.375×0.125 + 3.5×0.125	Description	Two nested circular HSS between top and bottom plate

Cross-sectional dimensions

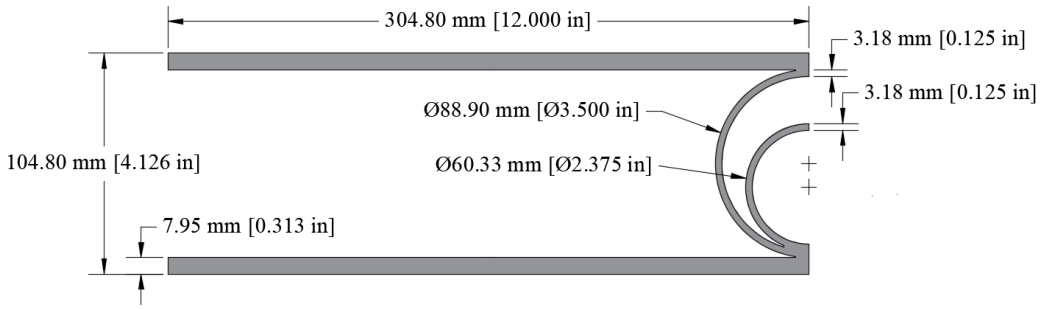

Initial shape	Shape after analysis
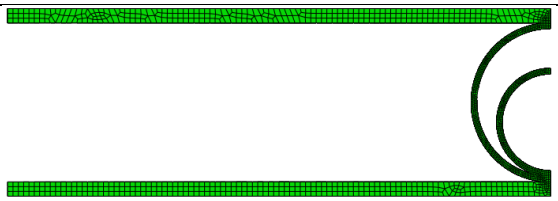	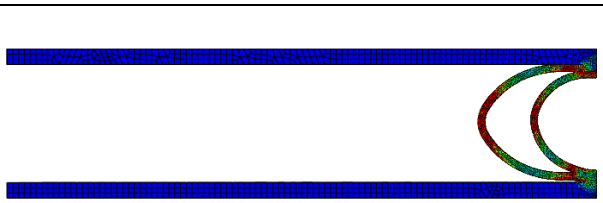

Load-displacement graph (per unit depth)

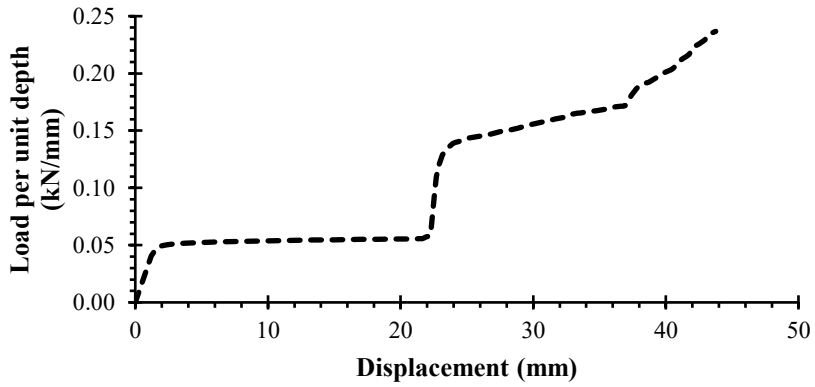

Comments

Depth used in analysis was 50 mm. Initial elastic behaviour is experienced up to a displacement of 1.5 mm. Afterwards, a short plateau is experienced up to a displacement of 22.2 mm. A second elastic zone is experienced up to a displacment of 23.7 mm, due to contact being made between the top and bottom plates and the central circular HSS. Following the second elastic zone, Load increases at a mostly constant rate up to a displacement of 37.0 mm where onset of densification occurs. The capacity at this point is 0.17 kN/mm (8.5 kN for 50 mm).

Name	2.375×0.125 + 3.5×0.25	Description	Two nested circular HSS between top and bottom plate

Cross-sectional dimensions

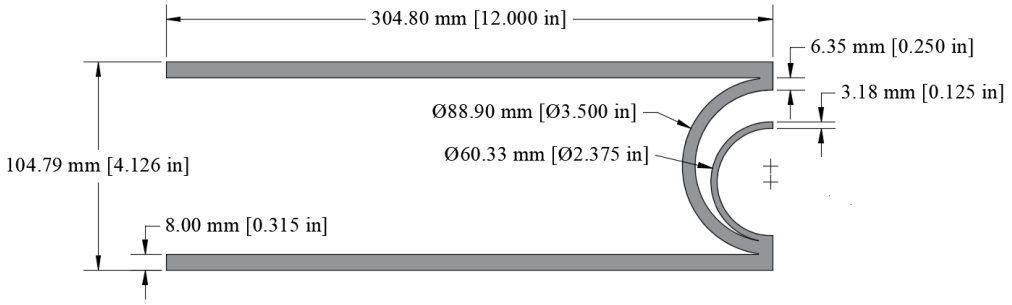

Initial shape	Shape after analysis
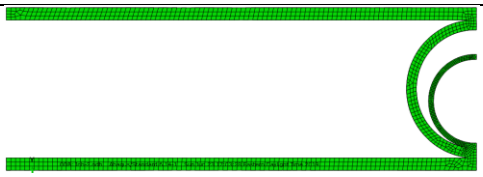	

Load-displacement graph (per unit depth)

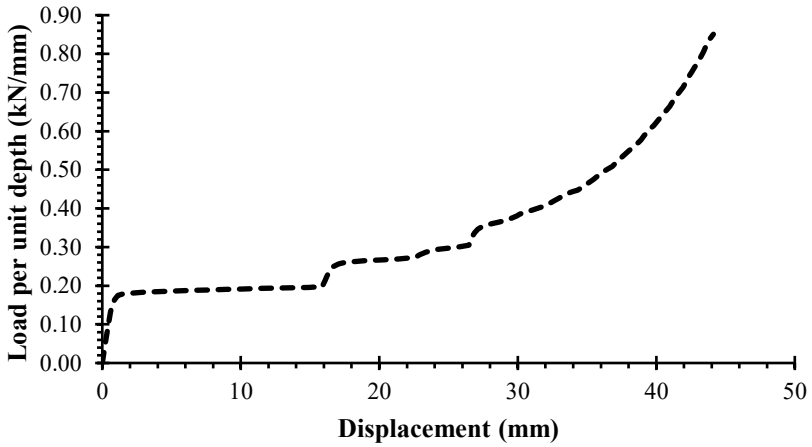

Comments

Depth used in analysis was 50 mm. Initial elastic behaviour is experienced up to a displacement of 1.5 mm. Afterwards, a short plateau is experienced up to a displacement of 22.2 mm. A second elastic zone is experienced up to a displacment of 23.7 mm, due to contact being made between the top and bottom plates and the central circular HSS. Following the second elastic zone, Load increases at a mostly constant rate up to a displacement of 37.0 mm where onset of densification occurs. The capacity at this point is 0.17 kN/mm (8.5 kN for 50 mm).

Name	2.375×0.125 + 3.5×0.25 + 5×0.25	**Description**	Three nested circular HSS between top and bottom plates

Cross-sectional dimensions

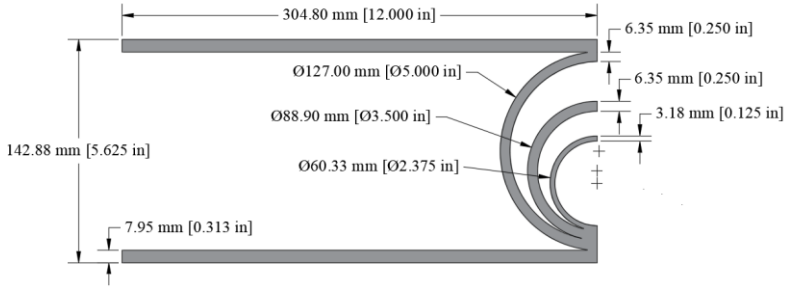

Initial shape	**Shape after analysis**
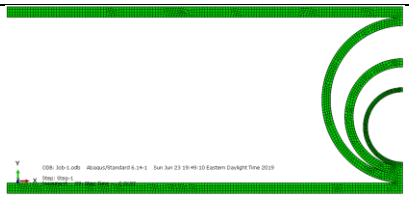	

Load-displacement graph (per unit depth)

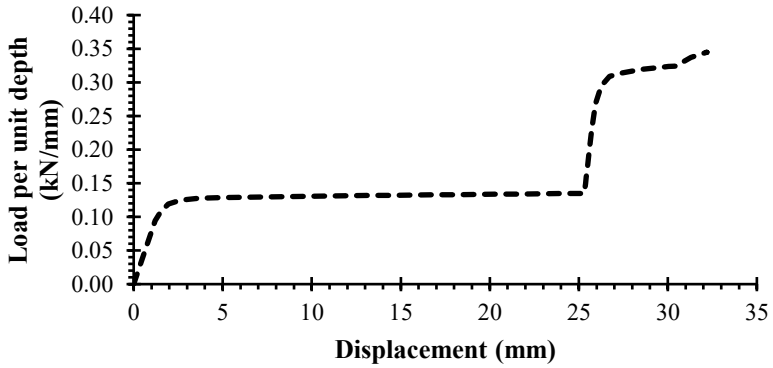

Comments

Depth used in analysis was 10 mm. Initial elastic behaviour is experienced up to a displacement of 1.8 mm. Afterwards, a short plateau is experienced up to a displacement of 25.3 mm. A second elastic zone is then experienced shorlty, due to contact being made between the top and bottom plates and the central circular HSS. Following the second elastic zone, a secondary plateau is experienced up to a displacement of 31.9 mm where the analysis ended. The capacity of the connection at that point is 0.34 kN/mm (3.4 kN for 10 mm). The smaller circular HSS did not make contact with the other sections before the end of the analysis.

Name	2.375×0.125 + 3.5×0.125 + 5×0.125	Description	Three nested circular HSS between top and bottom plates

Cross-sectional dimensions

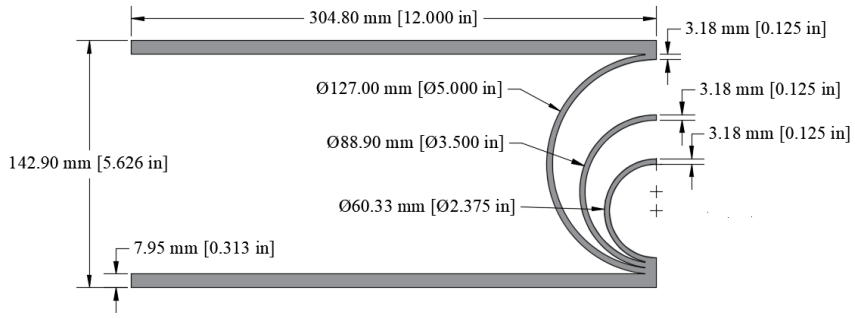

Initial shape

Shape after analysis

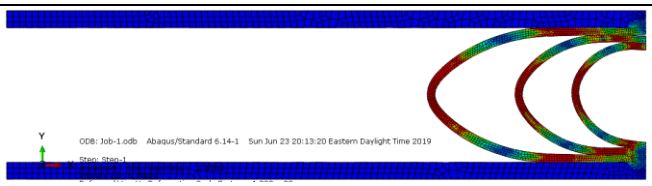

Load-displacement graph (per unit depth)

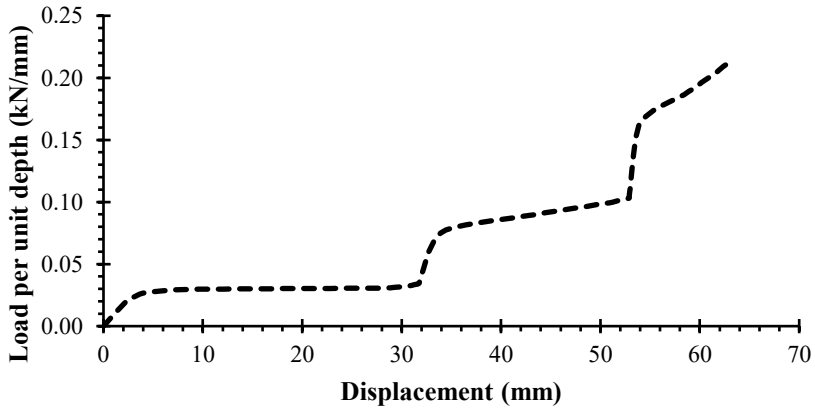

Comments

Depth used in analysis was 10 mm. The behaviour of this connection consists of three subsequent elastic zone followed by plateaus explained by the contact of each nested circles with another steel section. The first, second and third plateau are experienced from displacements of 4.0 mm to 31.3 mm, 34.4 mm to 52.9 mm, and 54.4 mm to 63.0 mm, respecitvely. The stiffness of the elastic zones and plateaus increase in respect to their previous elastic zones and plateau. The capacity of the connection at the end of the analysis is 0.21 kN/mm (2.1 kN for 10 mm)

APPENDIX B – Drawings of Specimens

Specimen Type Ia

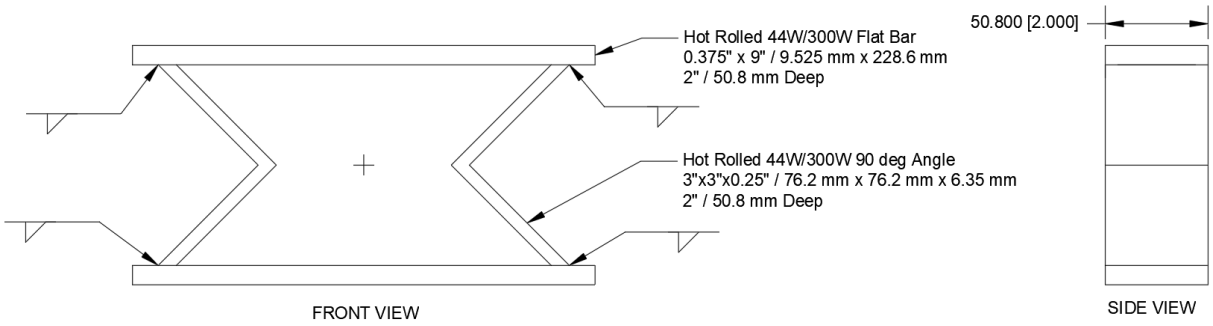

Specimen Type Ib

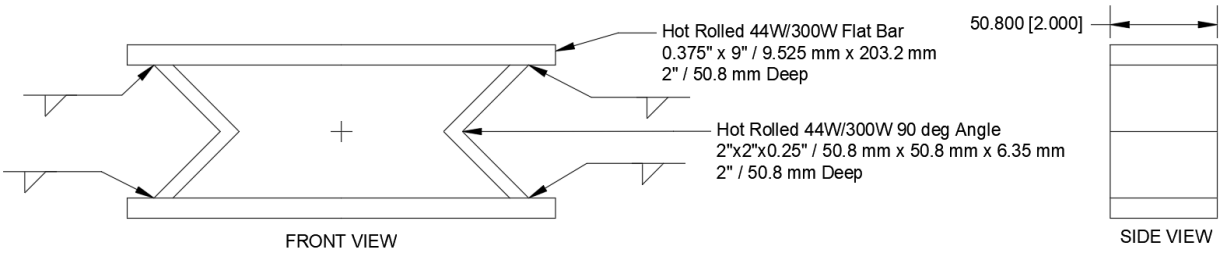

Specimen Type Ic

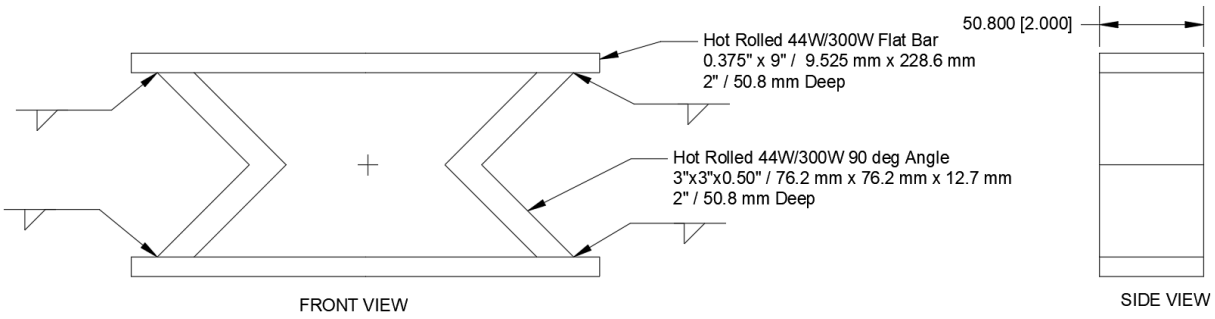

Specimen Type Id

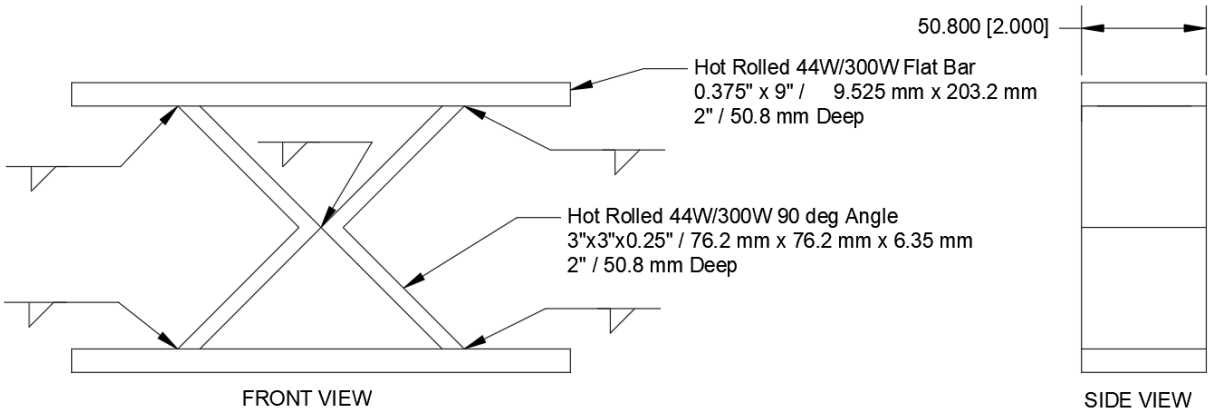

Specimen Type IIa

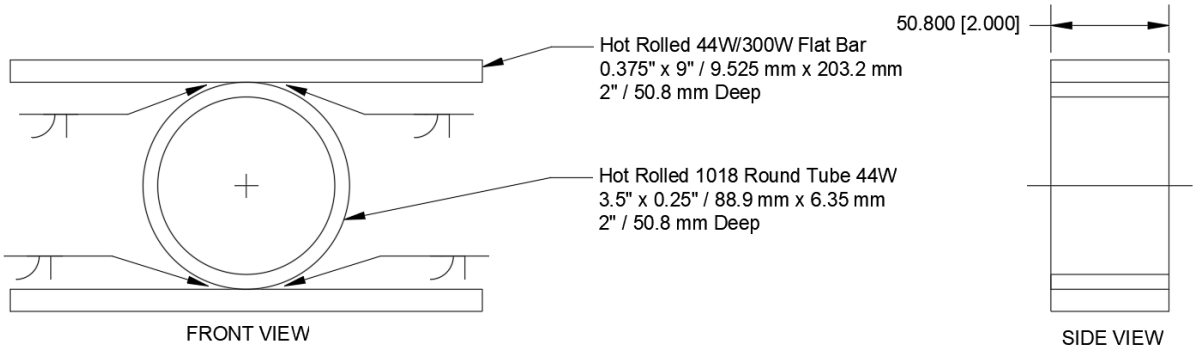

Specimen Type IIb

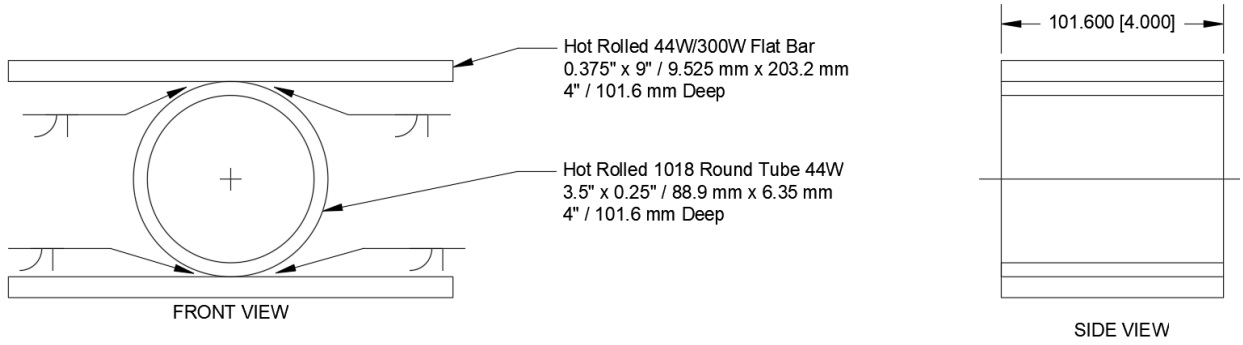

Specimen Type IIc

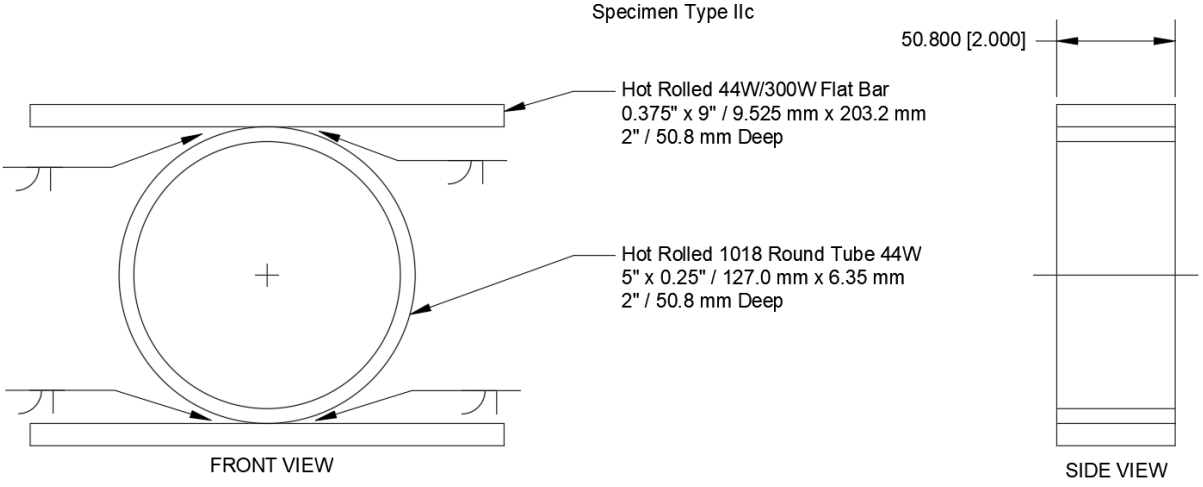

Specimen Type IId

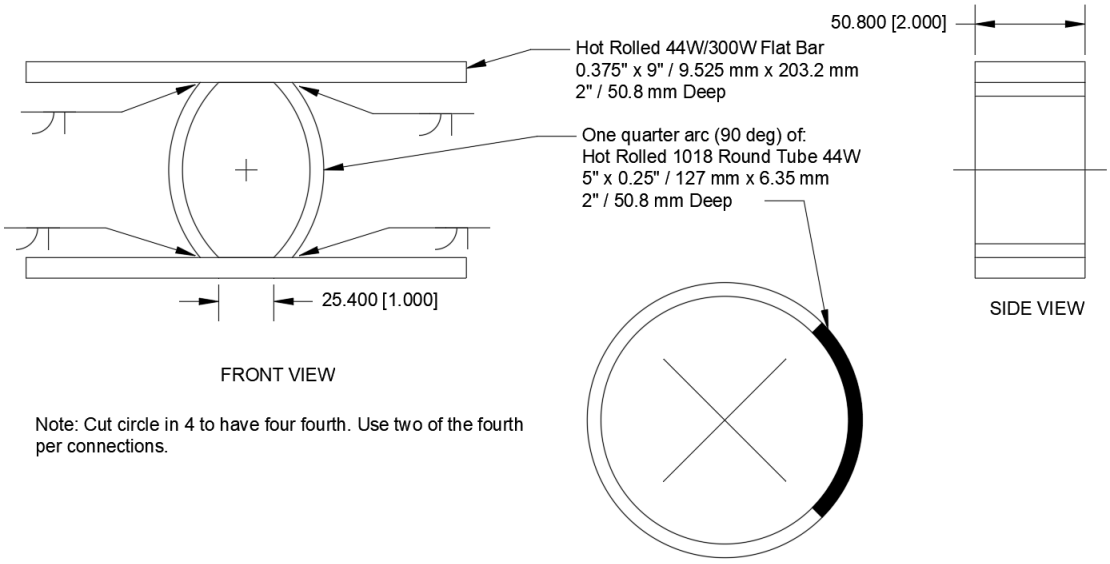

Note: Cut circle in 4 to have four fourth. Use two of the fourth per connections.

Specimen Type IIe

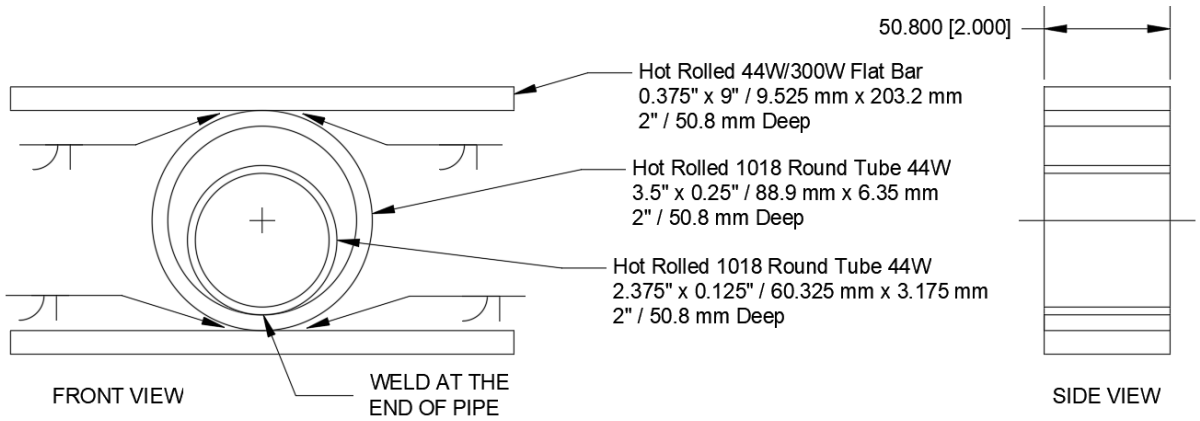

APPENDIX C – Static and Dynamic Connection Level Test Results

Specimen	S-Ia-1	**Description**	Angles with leg lengths of 76.2 mm and thickness of 6.35 mm

Load-displacement graph

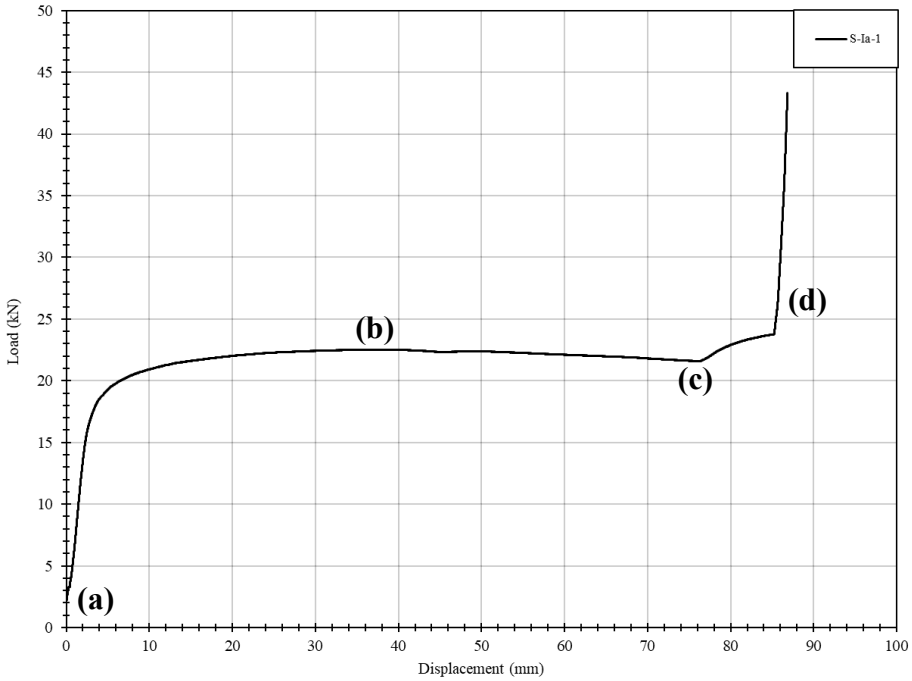

(a) Initial

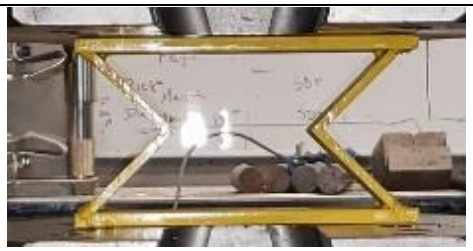

(b) Plateau, prior to contact

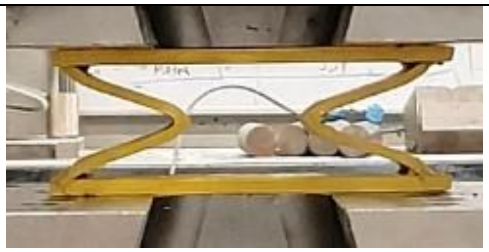

(c) Contact of left angle with bottom plate

(d) Contact of right angle with top plate

Comments

Minimal deformation occurred during the initial elastic region, however, following yielding, large deformation occurred at almost constant load. Typical deformation shape is shown in picture (picture b). An increase in load occurred at the point of initial contact between an angle and plate occurred (picture c). Once further contact between the angle and the plate occurred (picture d), a significant increase in stiffness was observed.

Specimen	S-Ia-2	Description	Angles with leg lengths of 76.2 mm and thickness of 6.35 mm

Load-displacement graph

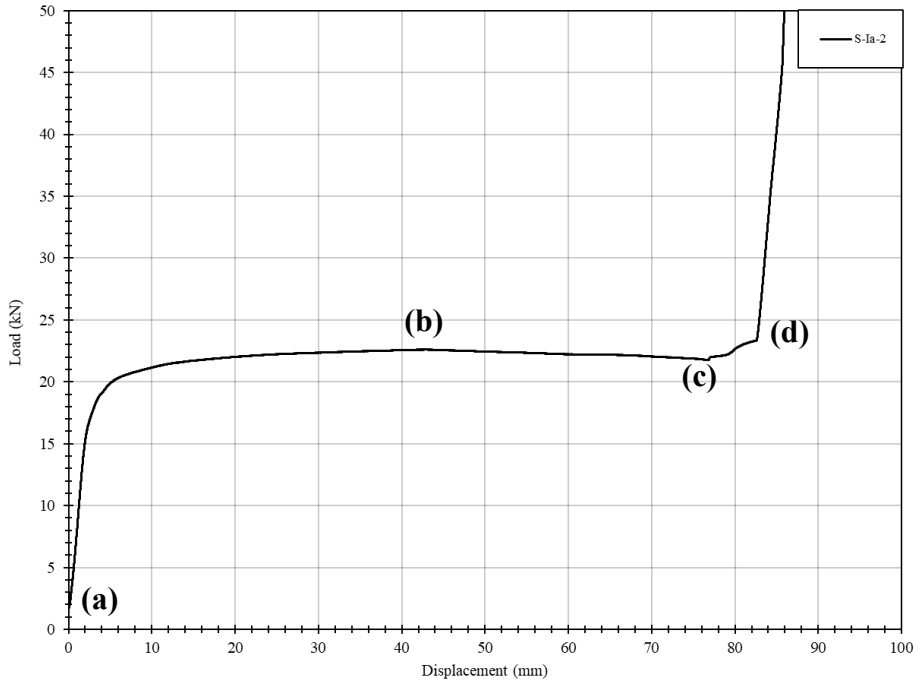

(a) Initial

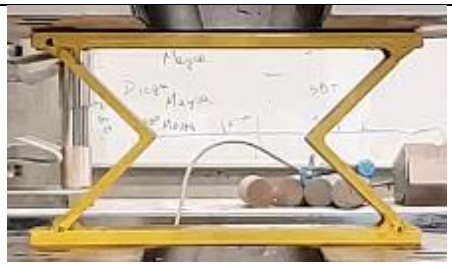

(b) Plateau, prior to contact

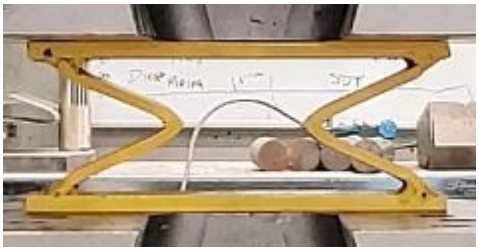

(c) Contact of right angle with top plate

(d) Contact of left angle with top plate

Comments

Minimal deformation occurred during the initial elastic region, however, following yielding, large deformation occurred at almost constant load. Typical deformation shape is shown in picture (picture b). An increase in load occurred at the point of initial contact between an angle and plate occurred (picture c). Once further contact between the angle and the plate occurred (picture d), a significant increase in stiffness was observed.

Specimen	S-Ib-1	**Description**	Angles with leg lengths of 50.8 mm and thickness of 6.35 mm

Load-displacement graph

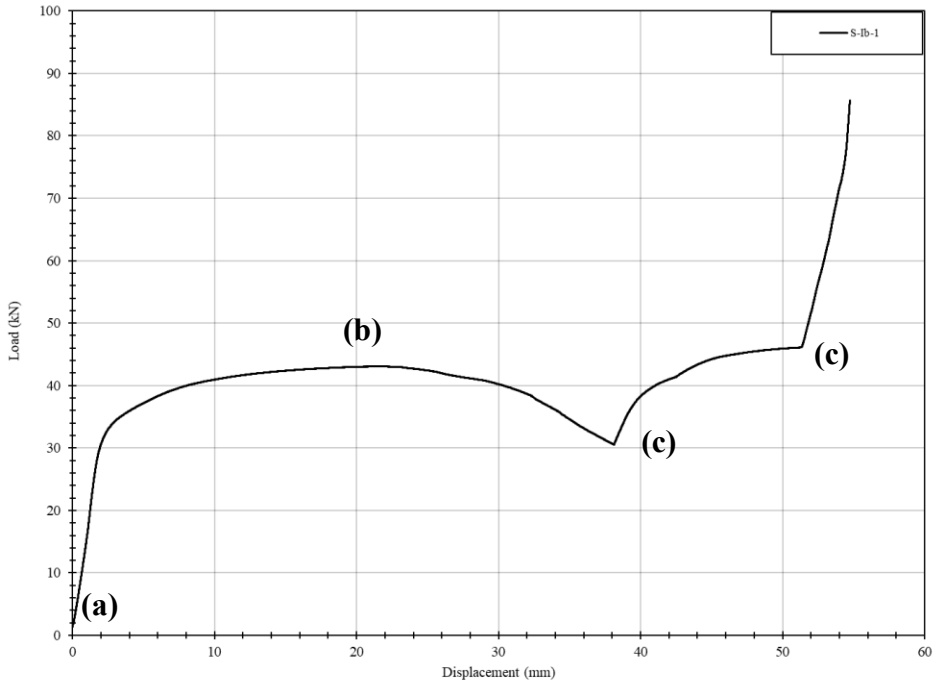

(a) Initial	(b) Plateau, prior to contact
	
(c) Contact of right angle with top plate and left angle with bottom plate	(d) Contact of left angle with top plate
	

Comments

Unequal deformation of the angles during the plateau (i.e. picture c) caused a dip in the load measured until further contact was achieved.

Specimen	S-Ib-2	**Description**	Angles with leg lengths of 50.8 mm and thickness of 6.35 mm

Load-displacement graph

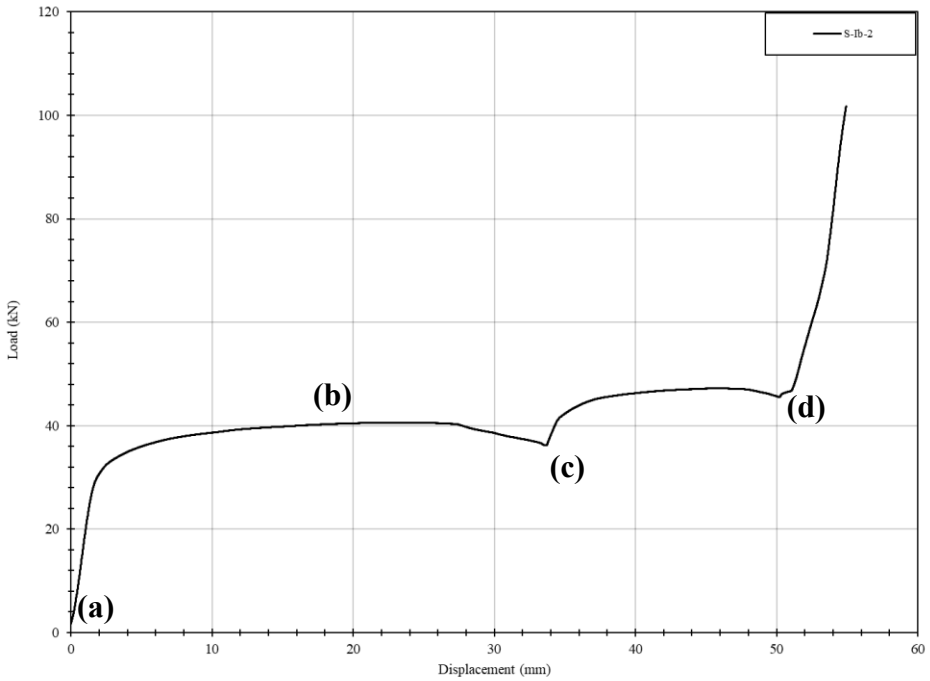

(a) Initial

(b) Plateau, prior to contact

(c) Contact of right angle with top plate

(d) Contact of left angle with top and bottom plate

Comments

Unequal deformation of the angles during the plateau (i.e. picture c) caused a dip in the load measured until further contact was achieved.

Specimen	S-Ic-1	**Description**	Angles with leg lengths of 76.2 mm and thickness of 12.7 mm

Load-displacement graph

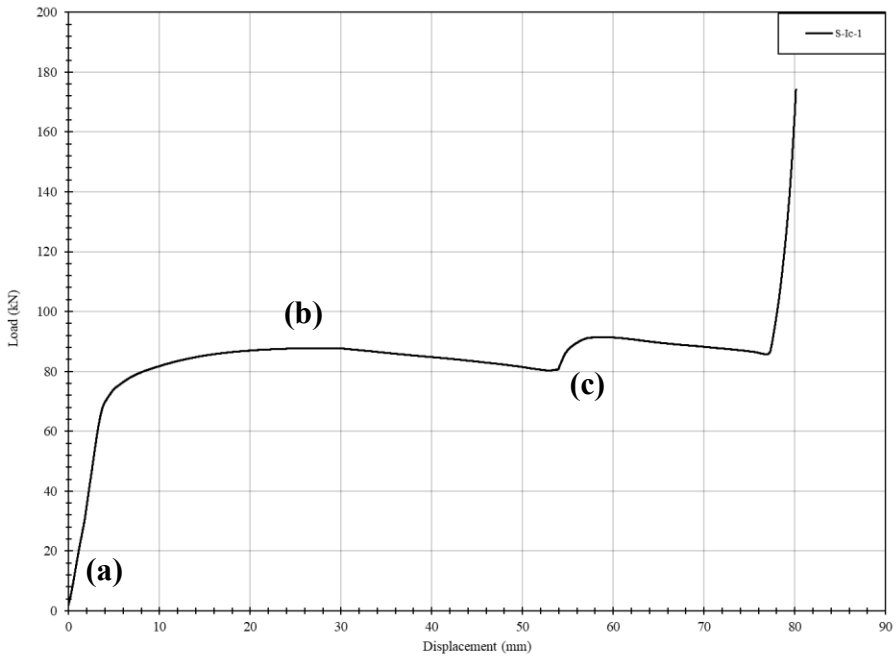

(a) Initial

(b) Plateau, prior to contact

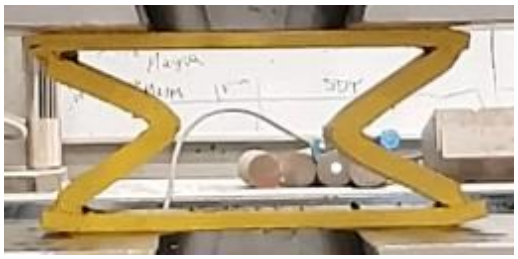

(c) Contact of left angle with top plate and right angle with bottom plate

(d) Further contact between angles and plates

Comments

Unequal deformation of the angles during the plateau (i.e. picture c) caused a dip in the load measured until further contact was achieved.

Specimen	S-Ic-2	**Description**	Angles with leg lengths of 76.2 mm and thickness of 12.7 mm

Load-displacement graph

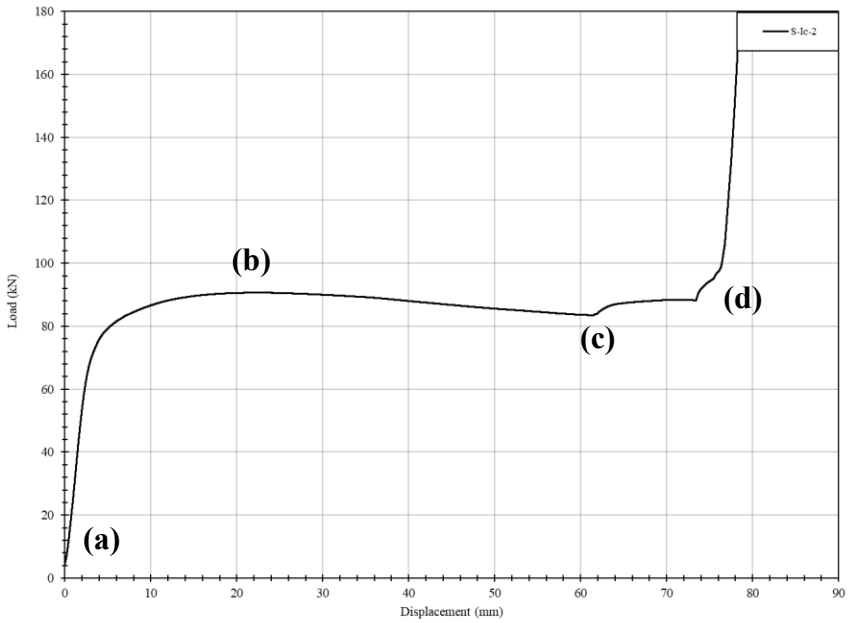

(a) Initial	(b) Plateau, prior to contact
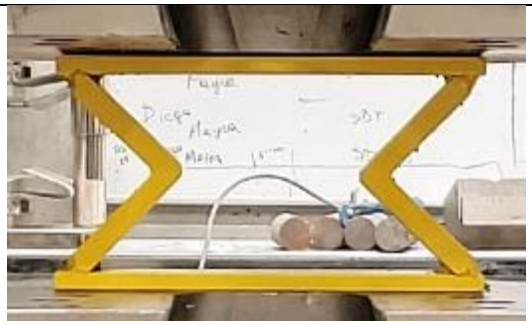	
(c) Contact of right angle with top plate and left angle with bottom plate	(d) Further contact between angles and plates
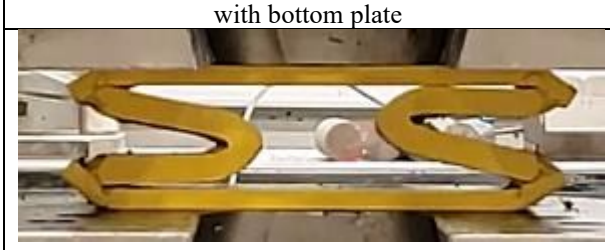	

Comments

The angles deformed more symetrically than specimen S-Ic-1, and no significant dip in the load was observed.

Specimen	S-Id-1	**Description**	Angles with leg lengths of 76.2 mm and thickness of 6.35 mm. Additional centre weld.

Load-displacement graph

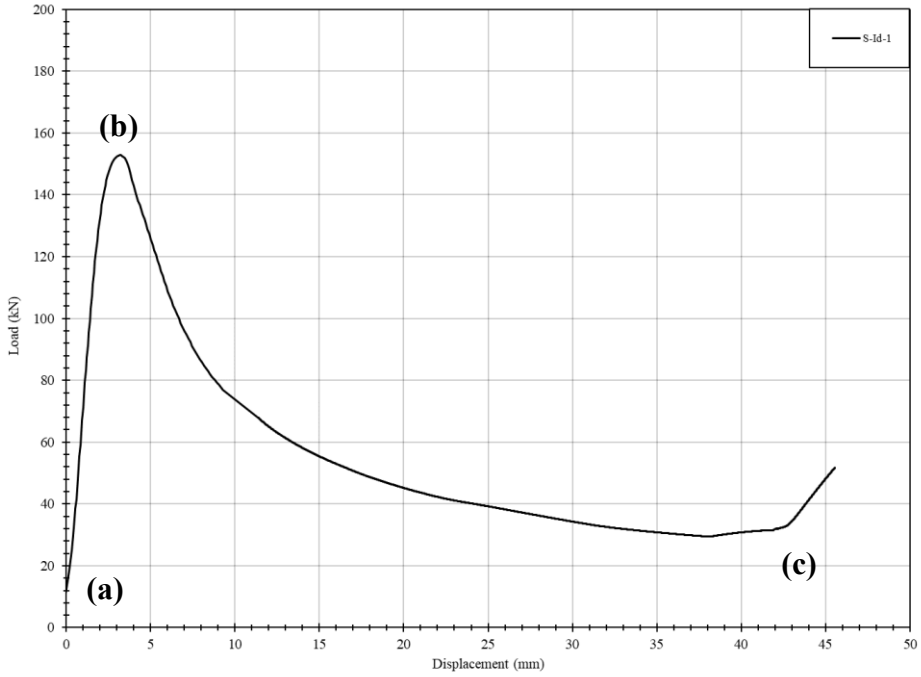

(a) Initial

(b) Post-yield, prior to contact

(c) Contact between angles and plates

Comments

A significant drop in the load was observed following yielding.

Specimen	S-Id-2	**Description**	Angles with leg lengths of 76.2 mm and thickness of 6.35 mm. Additional centre weld.

Load-displacement graph

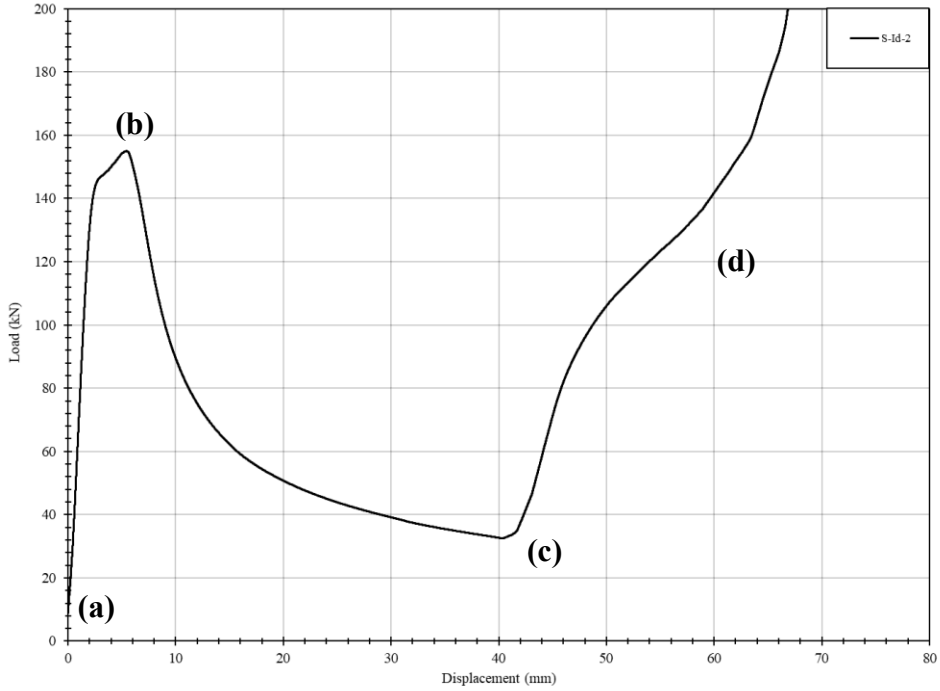

(a) Initial	(b) Post-yield, prior to contact
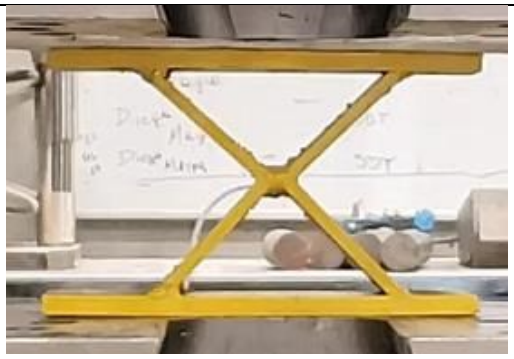	
(c) Contact between angles and plates	(c) Further contact between angles and plates
	

Comments

A significant drop in the load was observed following yielding.

Specimen	S-IIa-1	**Description**	Circular HSS with outer diameter of 88.9 mm and thickness of 6.35 mm

Load-displacement graph

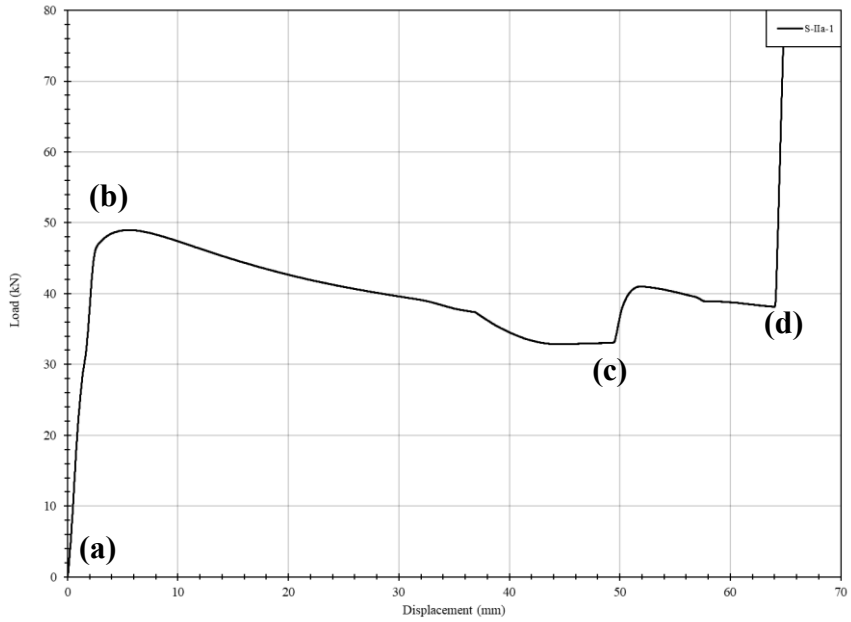

(a) Initial

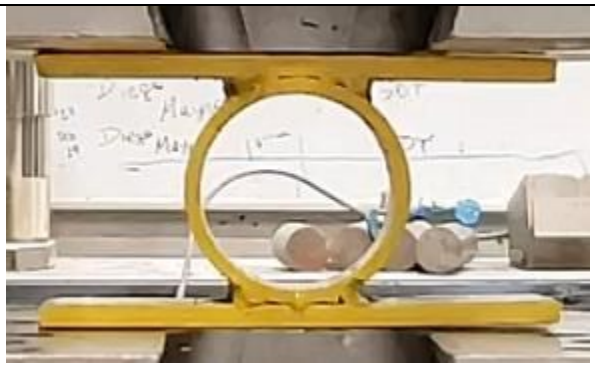

(b) Plateau, prior to contact

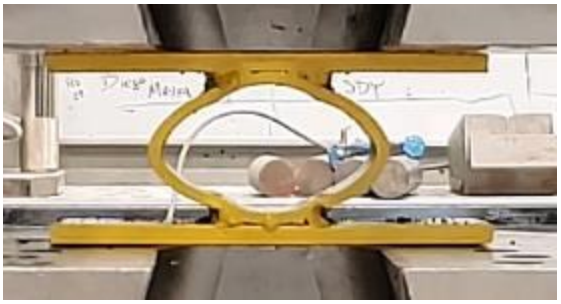

(c) Contact with bottom plate

(d) Further contact

Comments

A slight drop in load following yielding was observed.

Specimen	S-IIa-2	**Description**	Circular HSS with outer diameter of 88.9 mm and thickness of 6.35 mm

Load-displacement graph

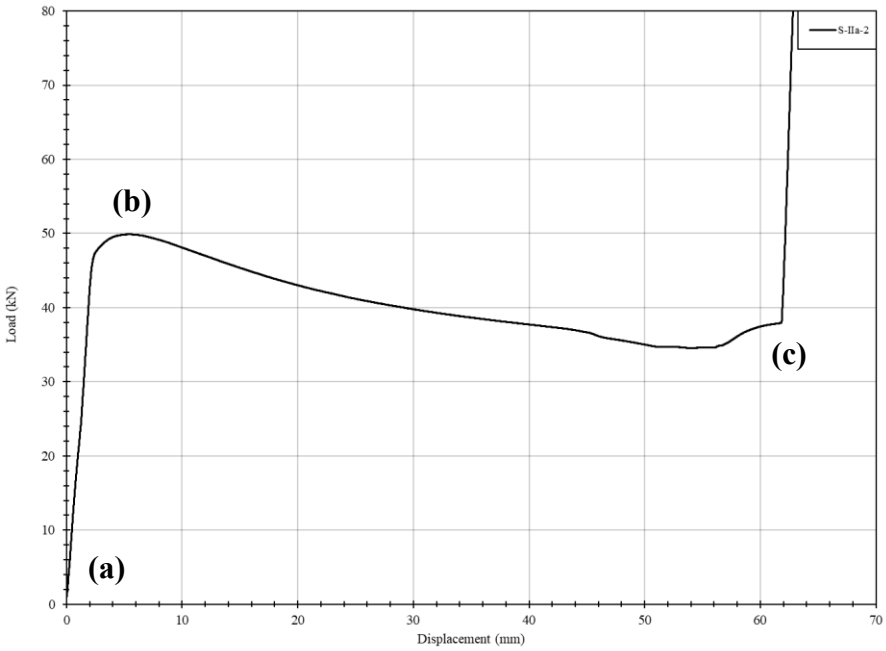

(a) Initial

(b) Plateau, prior to contact

(c) Contact with plates

Comments

A slight drop in load following yielding was observed.

Specimen	S-IIb-1	**Description**	Circular HSS with outer diameter of 88.9 mm and thickness of 6.35 mm Depth of 101.6 mm

Load-displacement graph

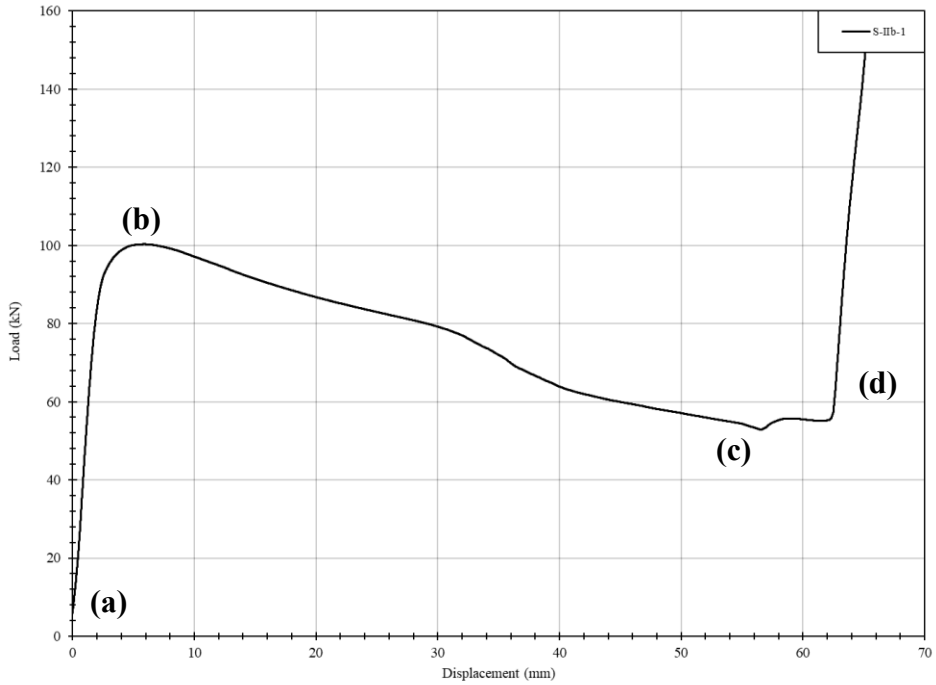

(a) Initial

(b) Plateau, prior to contact

(c) Contact with plates

(d) Further contact with plates

Comments

A slight drop in load following yielding was observed.

Specimen	S-IIb-2	**Description**	Circular HSS with outer diameter of 88.9 mm and thickness of 6.35 mm Depth of 101.6 mm

Load-displacement graph

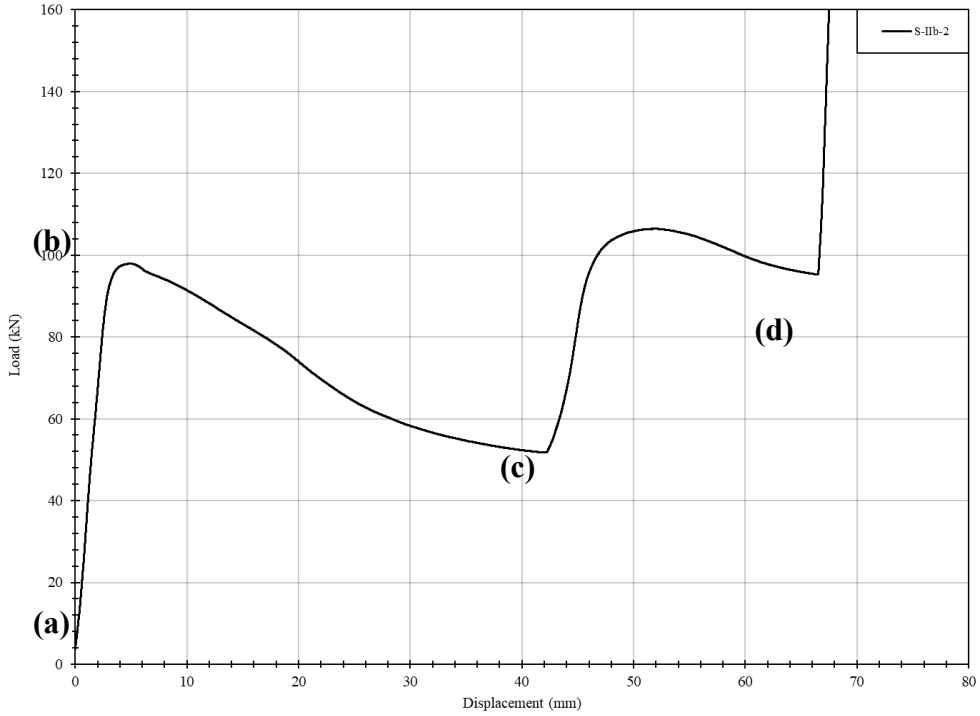

(a) Initial

(b) Plateau, prior to contact

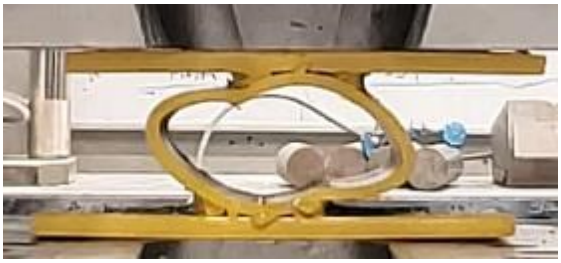

(c) Contact with plates

(d) Further contact with plates

Comments

A slight drop in load following yielding was observed. Deformation of the circular HSS was much more non uniform.

Specimen	S-IIc-1	**Description**	Circular HSS with outer diameter of 127 mm and thickness of 6.35 mm

Load-displacement graph

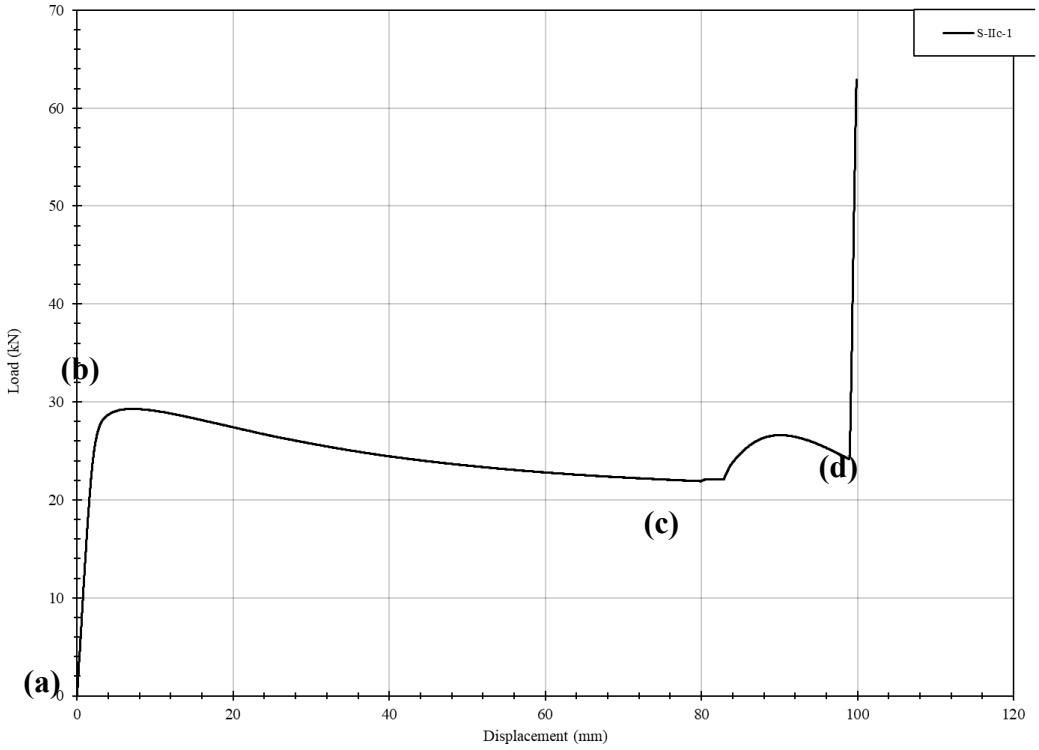

(a) Initial	(b) Plateau, prior to contact
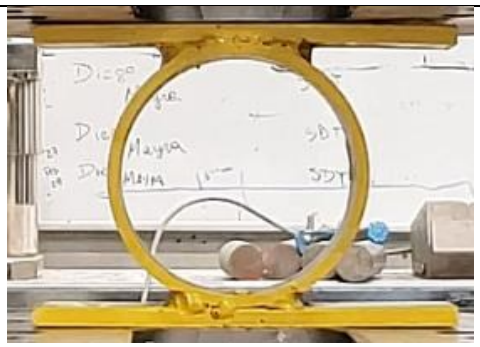	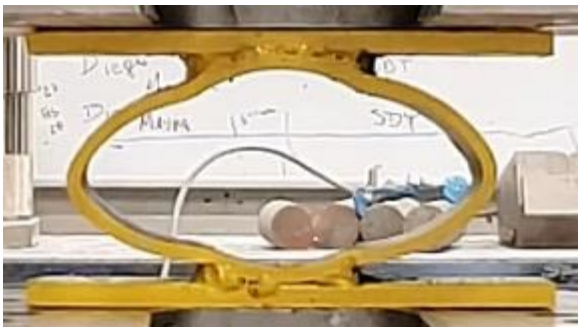
(c) Contact with plates	(d) Further contact with plates
	

Comments

A slight drop in load following yielding was observed.

Specimen	S-IIc-2	**Description**	Circular HSS with outer diameter of 127 mm and thickness of 6.35 mm

Load-displacement graph

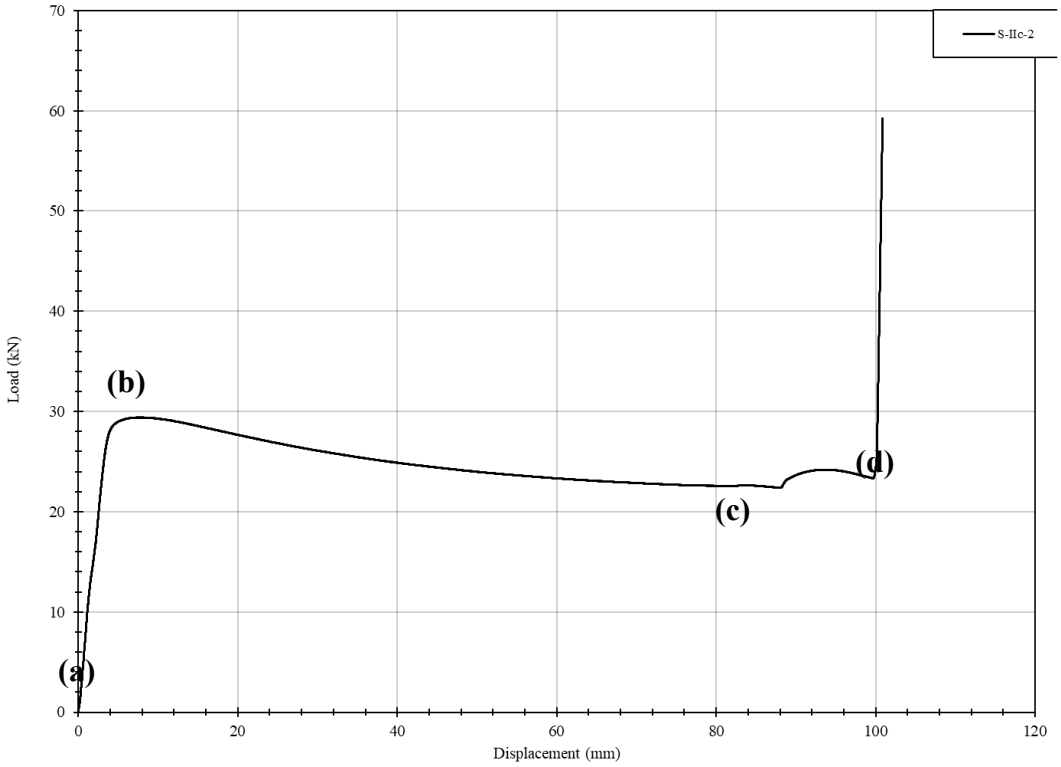

(a) Initial

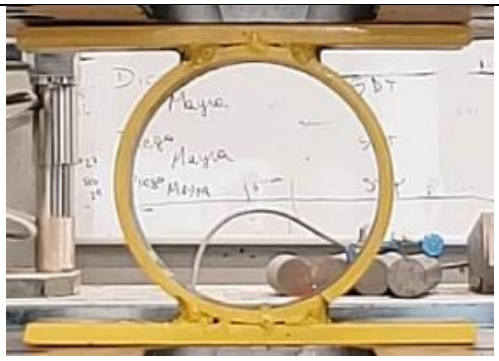

(b) Plateau, prior to contact

(c) Contact with plates

(d) Further contact with plates

Comments

A slight drop in load following yielding was observed.

Specimen	S-IId-1	**Description**	Arcs from circular HSS of outer diameter of 127 mm and thickness of 6.35 mm.

Load-displacement graph

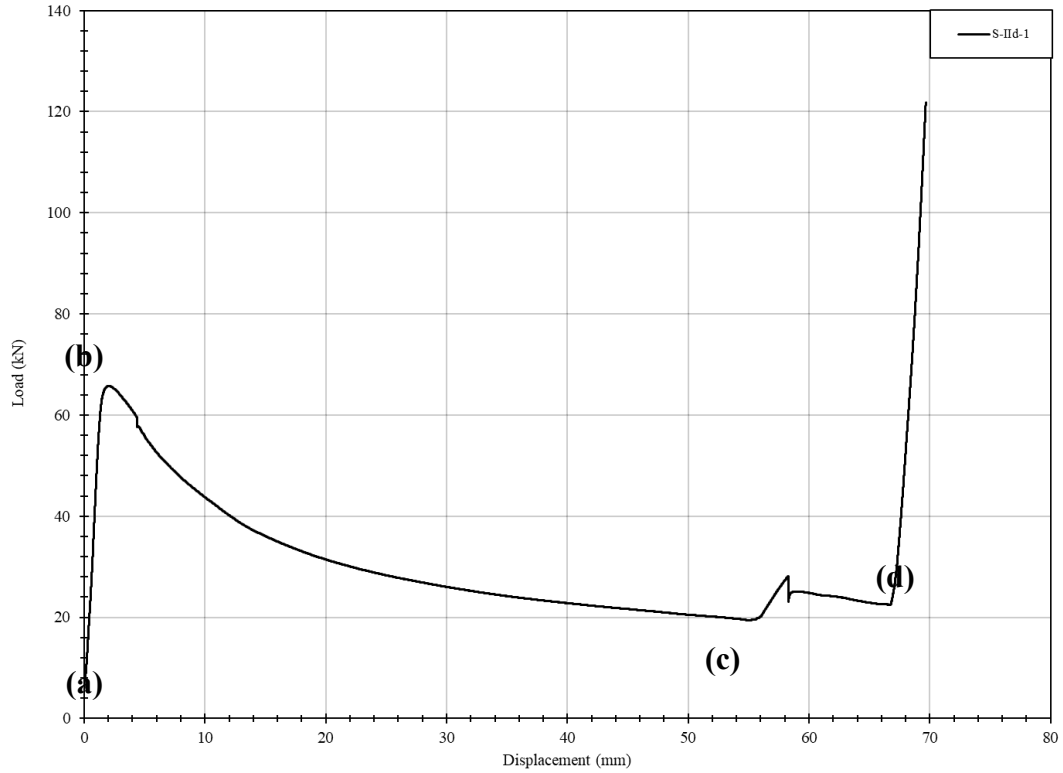

(a) Initial

(b) Post-yield, prior to contact

(c) Contact with plates

(d) Further contact with plates

Comments

A substantial drop in load following yielding was observed.

Specimen	S-IId-2	**Description**	Arcs from circular HSS of outer diameter of 127 mm and thickness of 6.35 mm.

Load-displacement graph

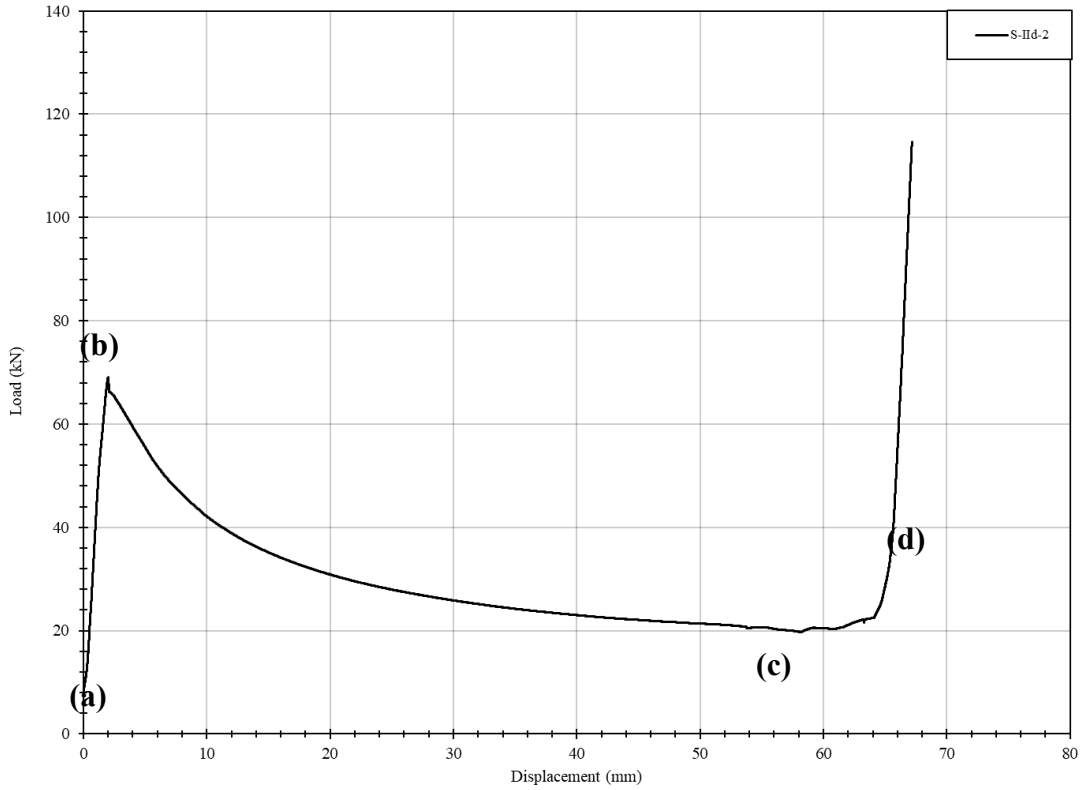

(a) Initial

(b) Post-yield, prior to contact

(c) Contact with plates

(d) Further contact with plates

Comments

A substantial drop in load following yielding was observed.

Specimen	S-IIe-1	**Description**	Circular HSS with outer diameter of 88.9 mm and thickness of 6.35 mm

			Circular HSS with outer diameter of 60.325 mm and thickness of 3.175 mm

Load-displacement graph

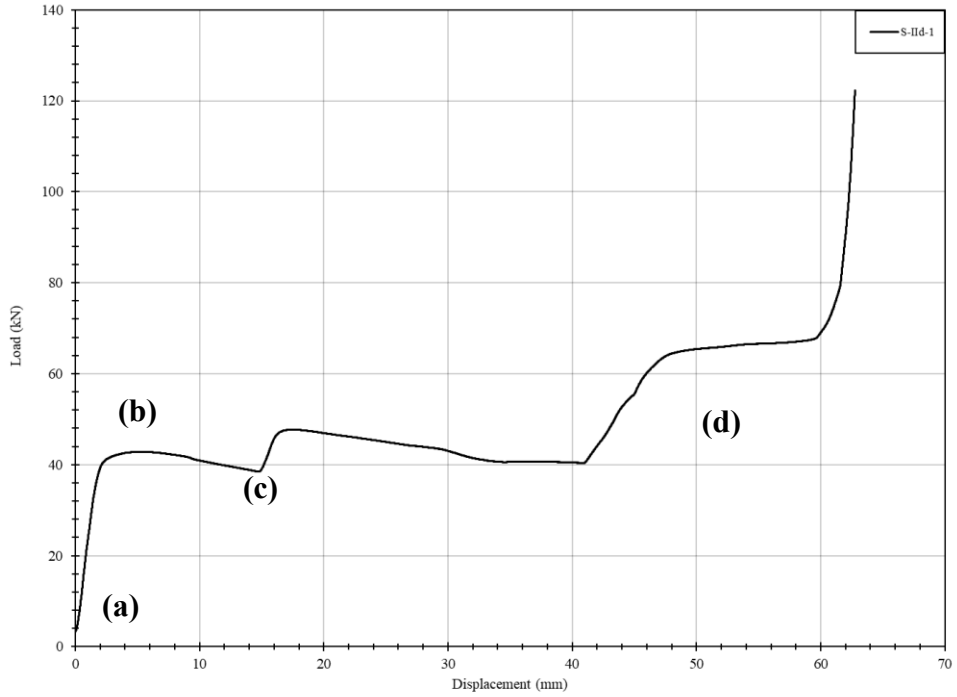

(a) Initial	(b) Plateau, prior to contact
	
(c) Contact with plates	(d) Further contact with plates
	

Comments

Multiple increases and decreases in load were observed during deformation.

Specimen	S-IIe-2	**Description**	Circular HSS with outer diameter of 88.9 mm and thickness of 6.35 mm Circular HSS with outer diameter of 60.325 mm and thickness of 3.175 mm

Load-displacement graph

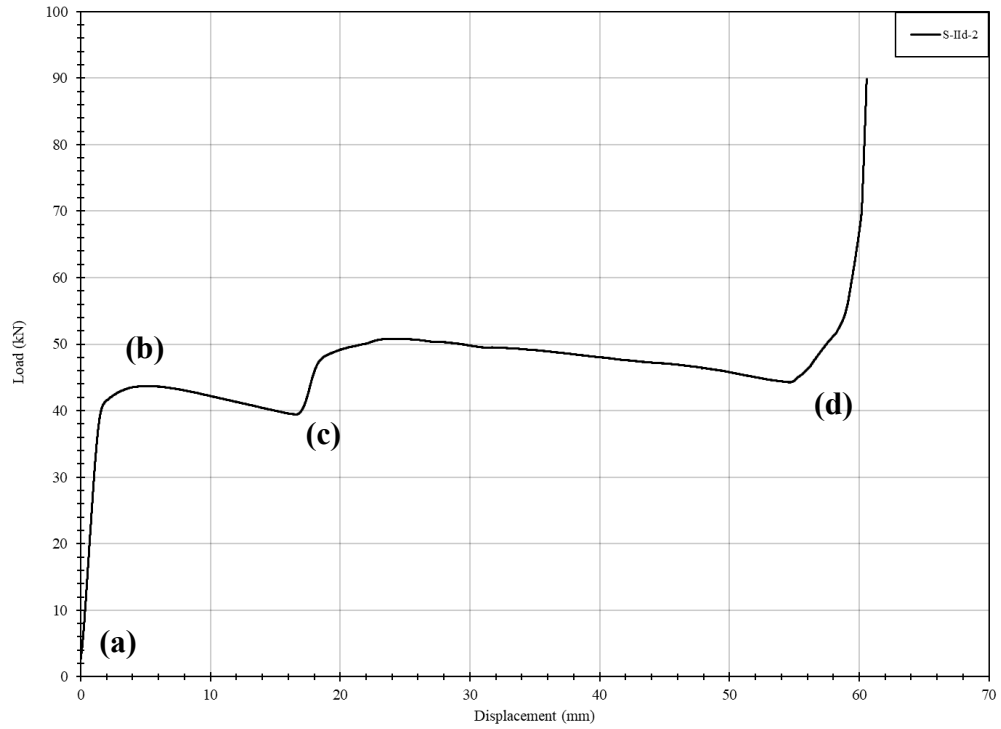

(a) Initial

(b) Plateau, prior to contact

(c) Contact with plates

(d) Further contact with plates

Comments

Multiple increases and decreases in load were observed during deformation.

Specimen	D-Ia-1	Description	Angles with leg lengths of 76.2 mm and thickness of 6.35 mm

Pressure and impulse time-histories

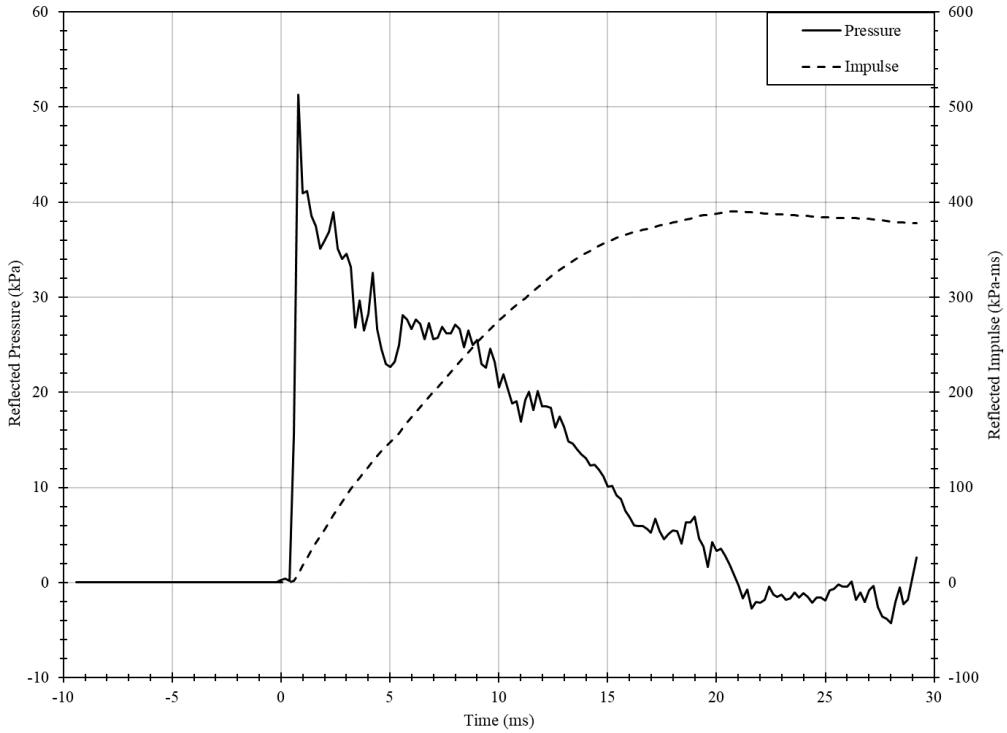

Experimental displacement and reaction loading time-histories

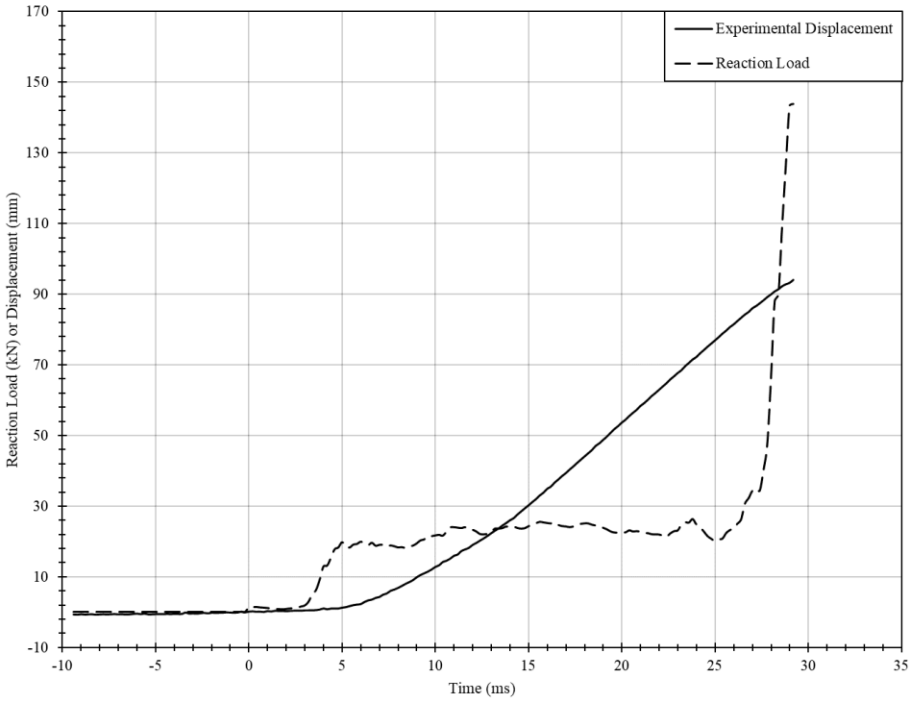

Load-displacement graph

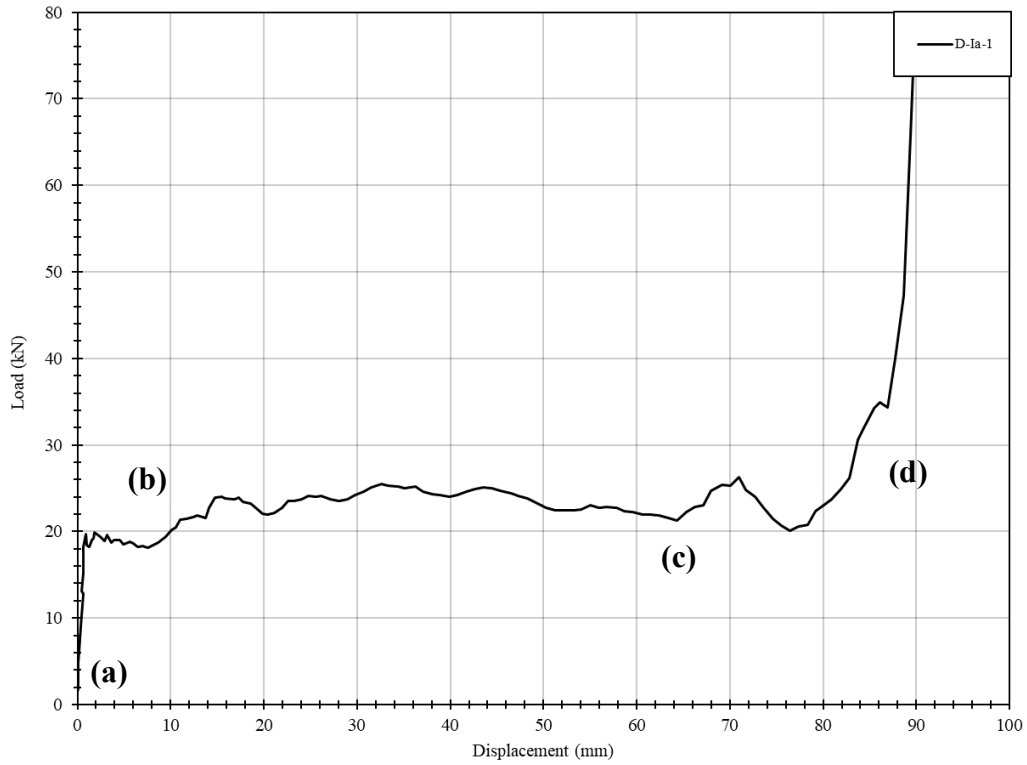

(a) Initial	(b) Plateau, prior to contact
	
(c) Contact with plates	(d) Further contact with plates
	

Comments

Similar behaviour to the static specimens was observed. The driver pressure was 270.3 kPa which resulted in a maximum reflected pressure of 37.3 kPa and impulse of 386.9 kPa-ms.

Specimen	D-Ia-2	Description	Angles with leg lengths of 76.2 mm and thickness of 6.35 mm

Pressure and impulse time-histories

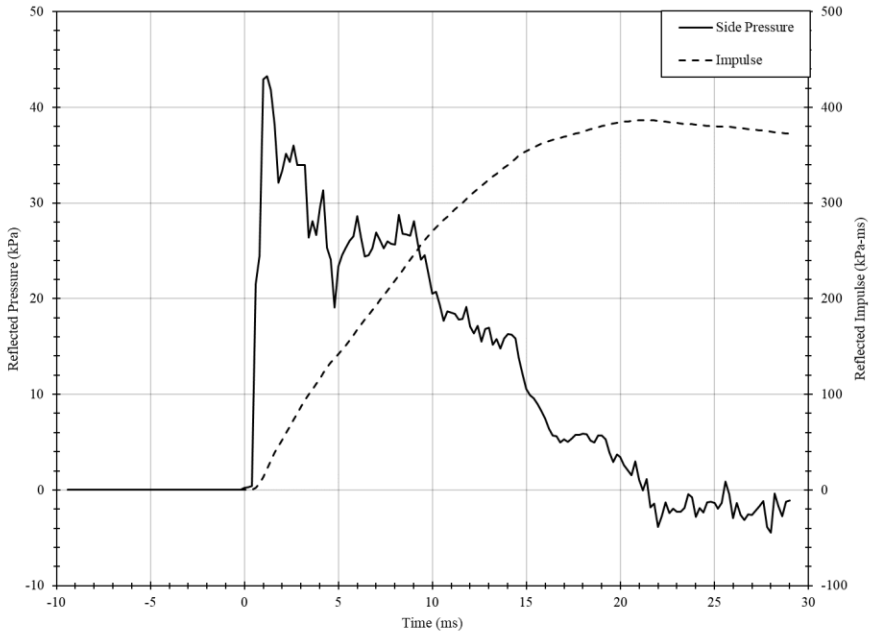

Experimental displacement and reaction loading time-histories

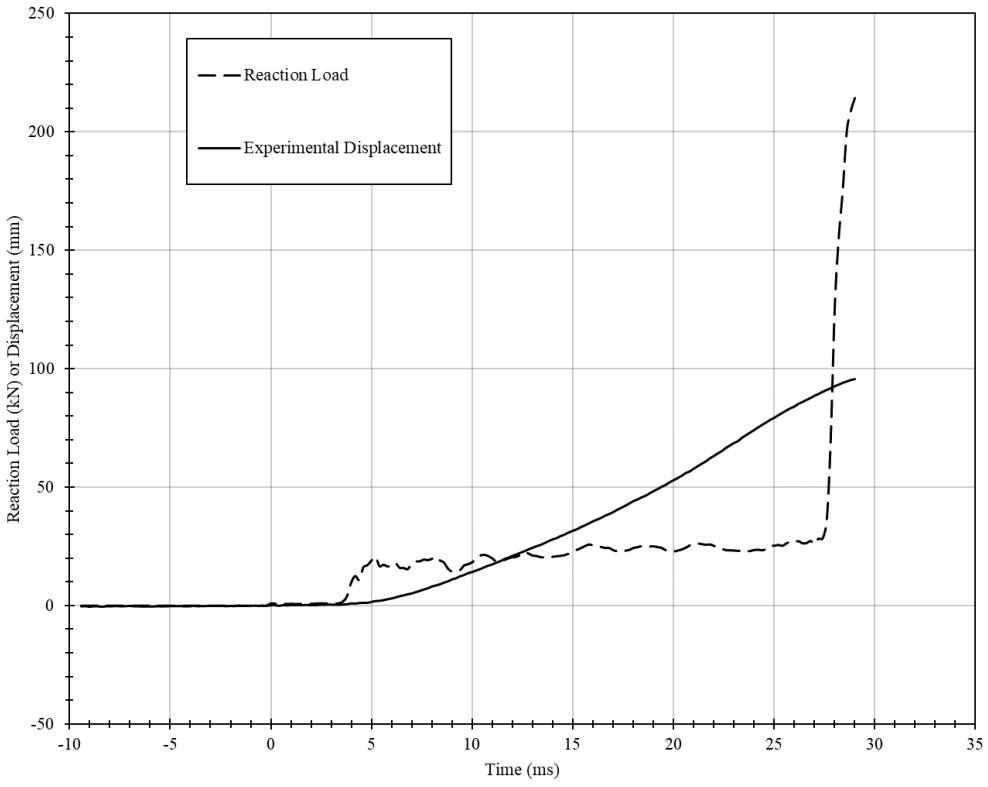

Load-displacement graph

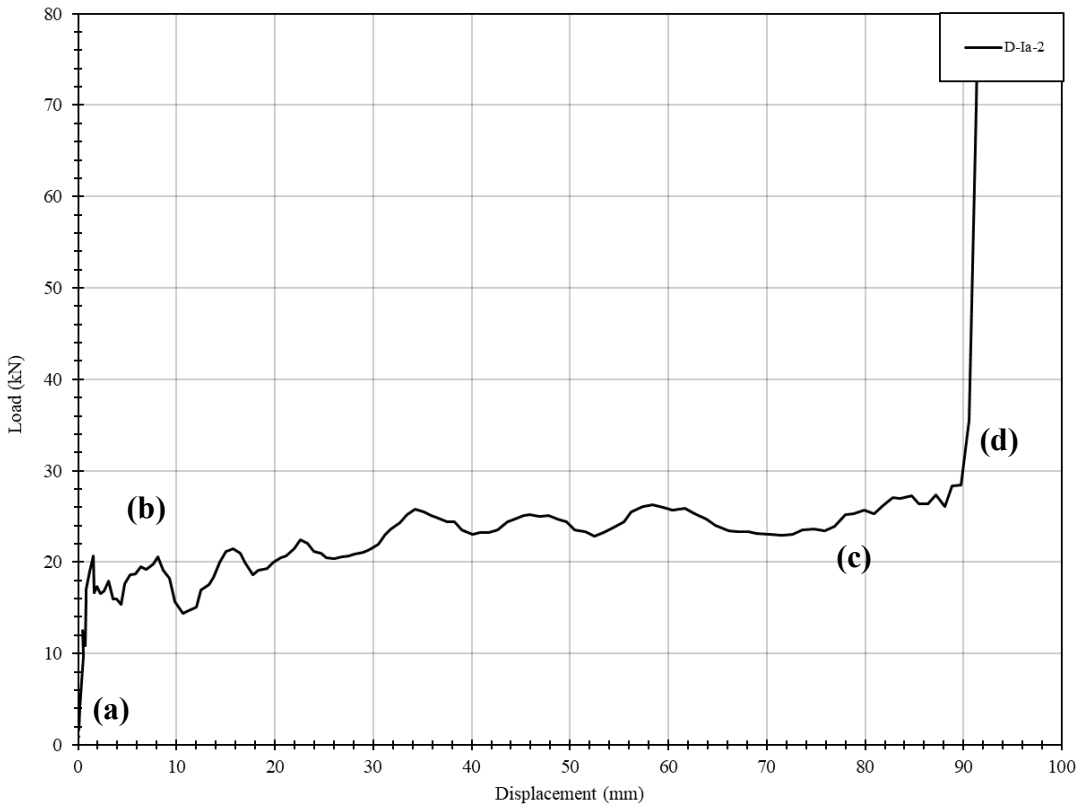

(a) Initial	(b) Plateau, prior to contact
	
(c) Contact with plates	(d) Further contact with plates
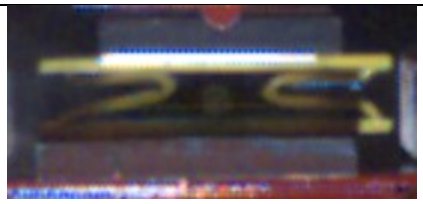	

Comments

Similar behaviour to the static specimens was observed. The driver pressure was 275.1 kPa which resulted in a maximum reflected pressure of 33.7 kPa and impulse of 313.4 kPa-ms.

Specimen	D-Ib-1	Description	Angles with leg lengths of 50.8 mm and thickness of 6.35 mm

Pressure and impulse time-histories

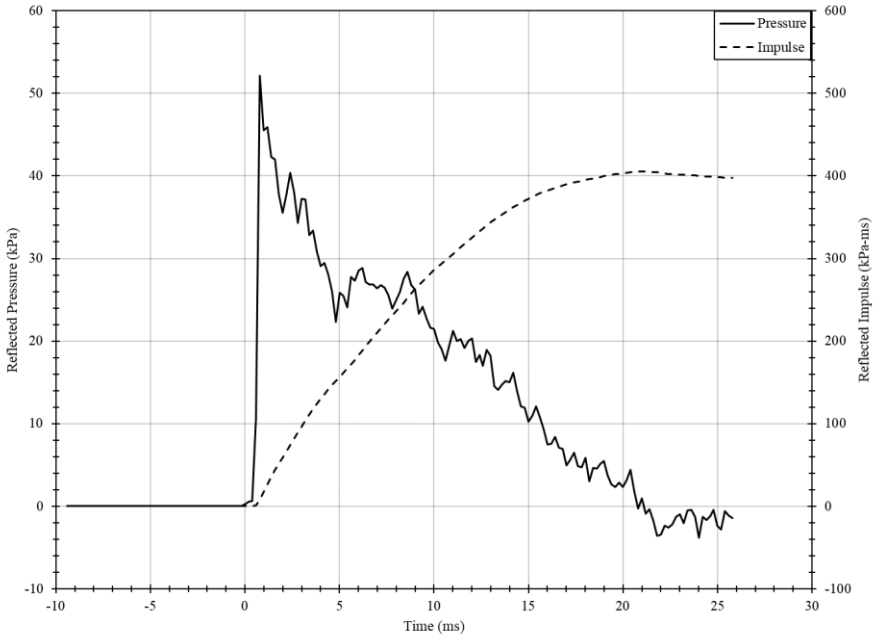

Experimental displacement and reaction loading time-histories

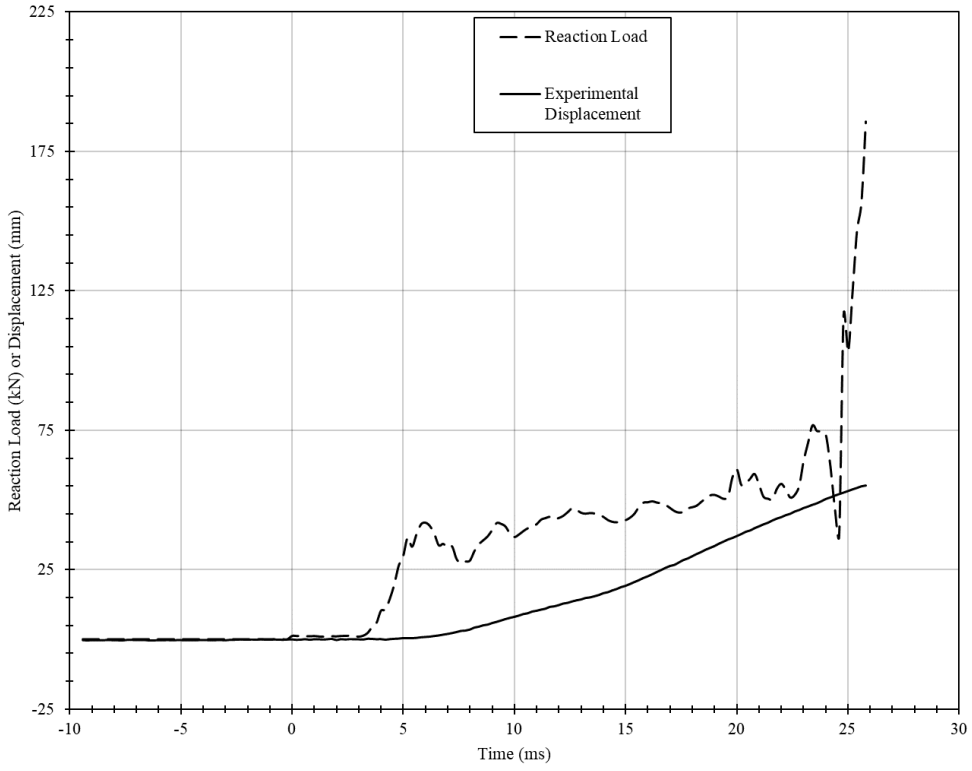

Load-displacement graph

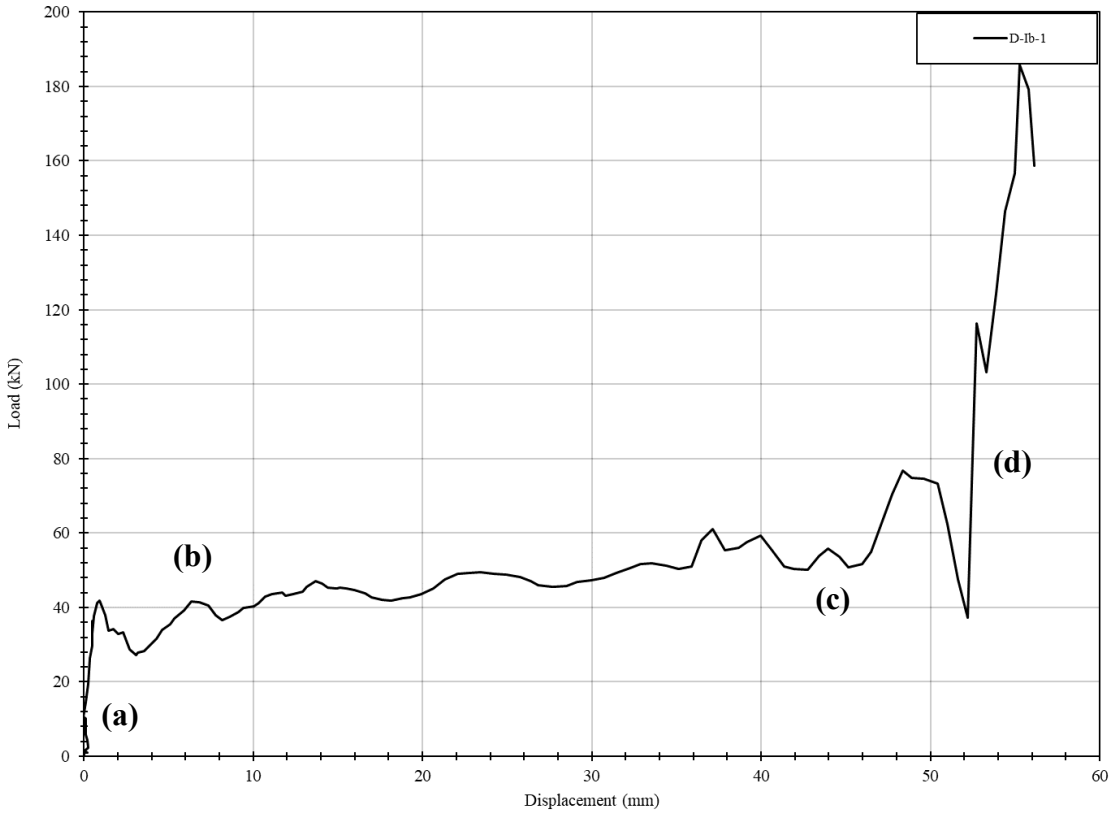

(a) Initial	(b) Plateau, prior to contact
	
(c) Contact with plates	(d) Further contact with plates
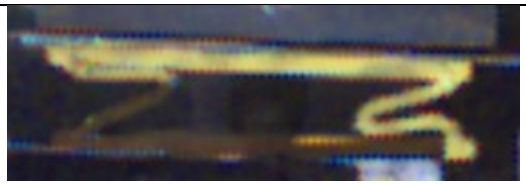	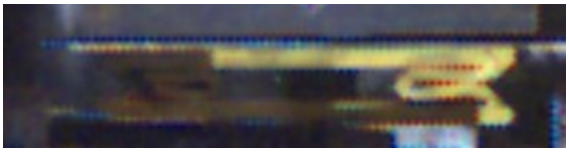

Comments

Similar behaviour to the static specimens was observed. The driver pressure was 279.9 kPa which resulted in a maximum reflected pressure of 42.5 kPa and impulse of 264.2 kPa-ms.

Specimen	D-Ib-2	Description	Angles with leg lengths of 50.8 mm and thickness of 6.35 mm

Pressure and impulse time-histories

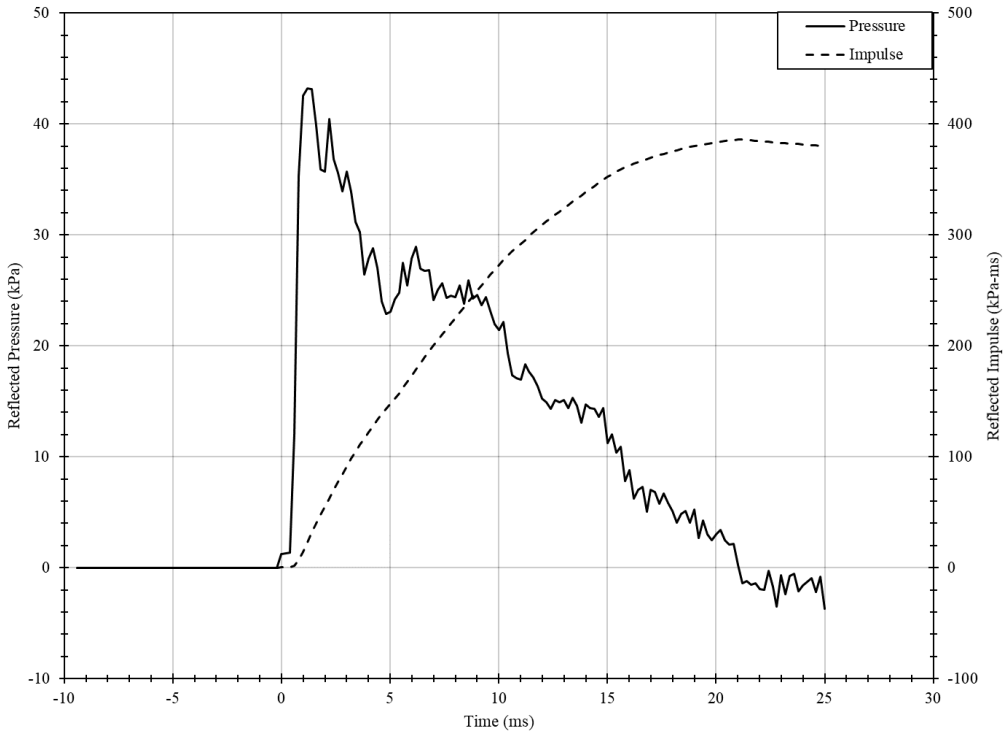

Experimental displacement and reaction loading time-histories

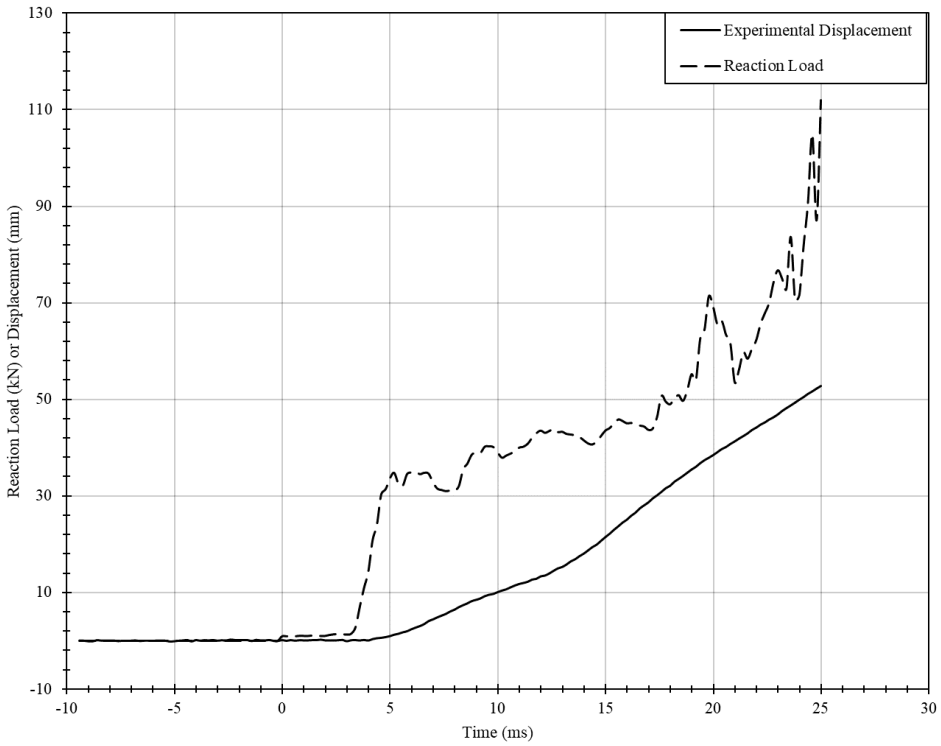

Load-displacement graph

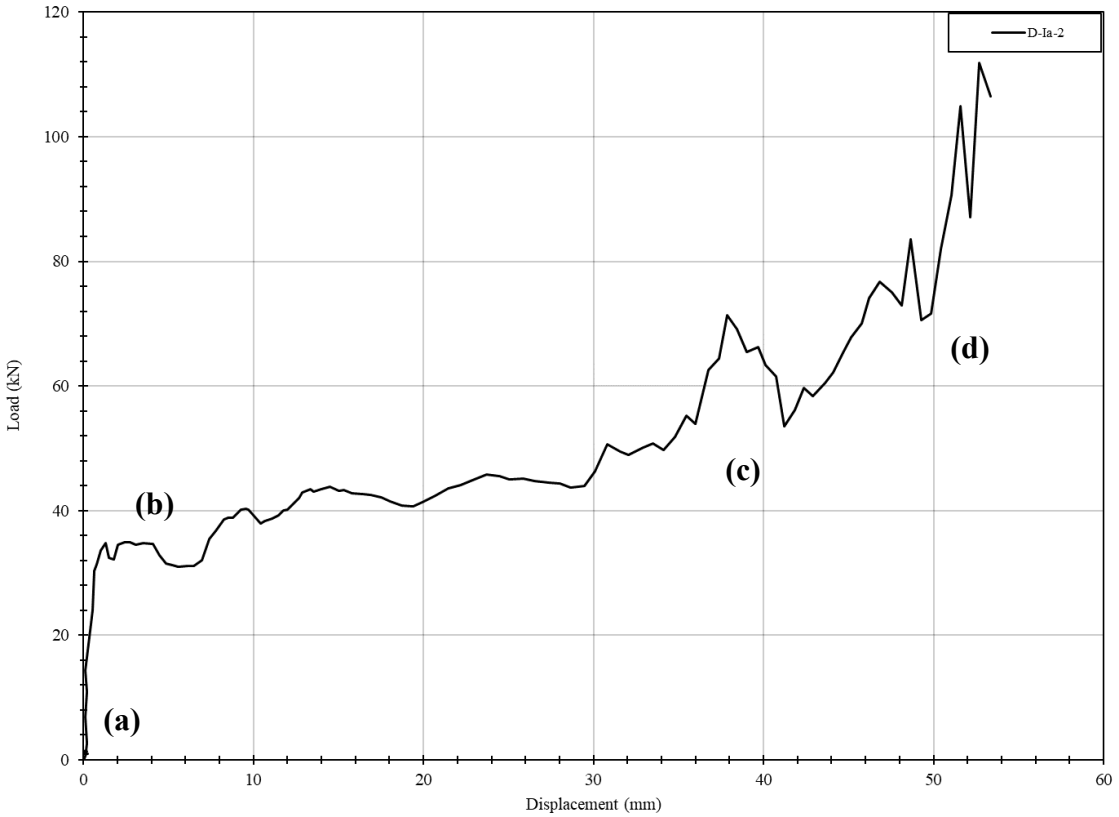

(a) Initial	(b) Plateau, prior to contact
	
(c) Contact with plates	(d) Further contact with plates
	

Comments

Similar behaviour to the static specimens was observed. The driver pressure was 268.9 kPa which resulted in a maximum reflected pressure of 40.7 kPa and impulse of 379.2 kPa-ms.

Specimen	D-Ic-1	Description	Angles with leg lengths of 76.2 mm and thickness of 12.7 mm

Pressure and impulse time-histories

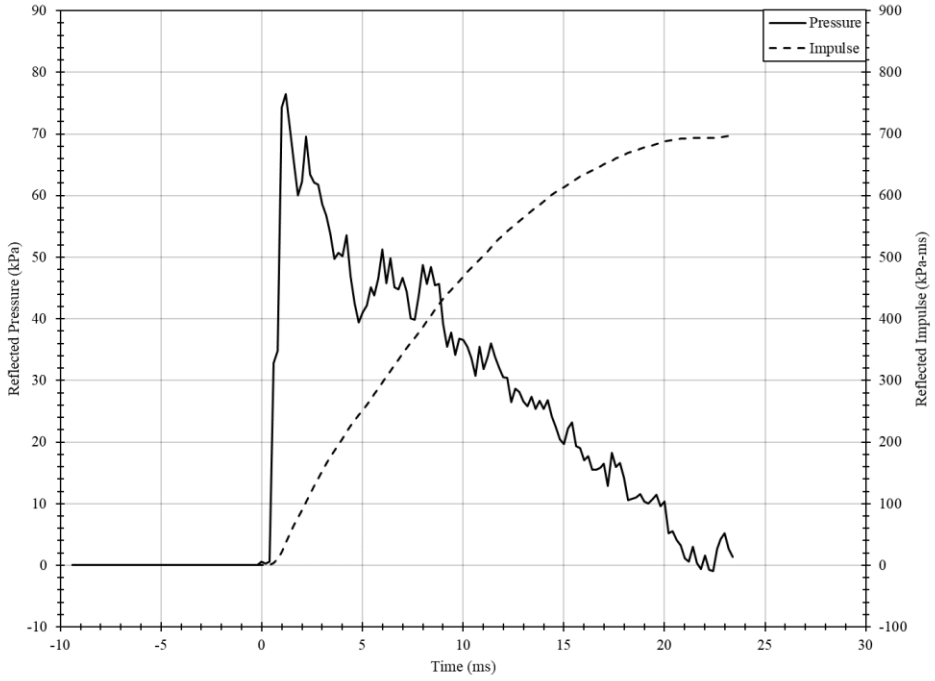

Experimental displacement and reaction loading time-histories

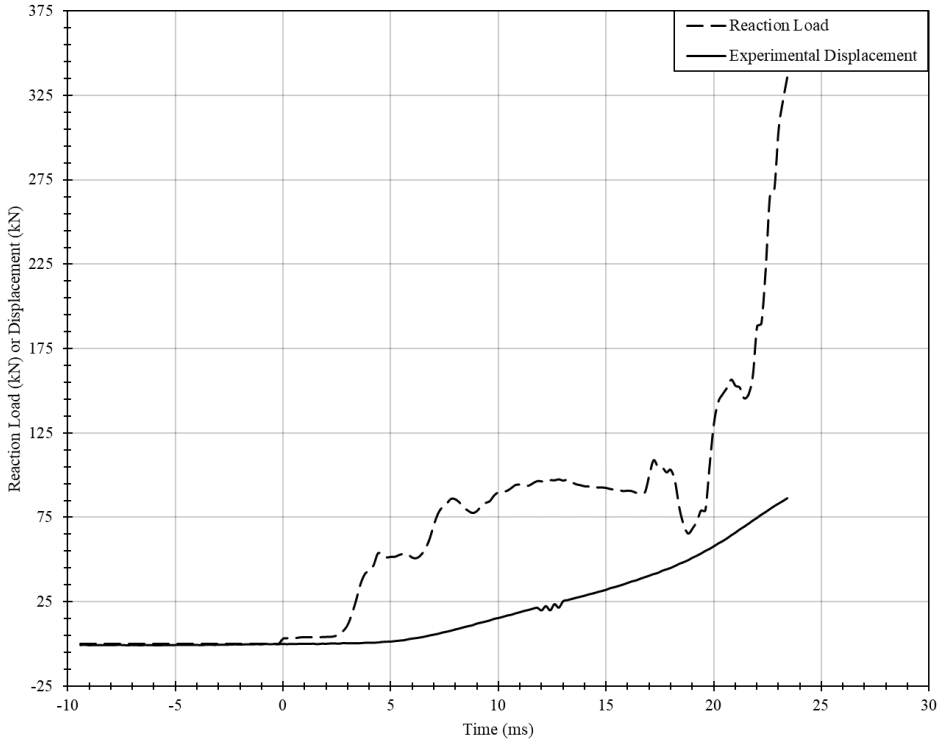

Load-displacement graph

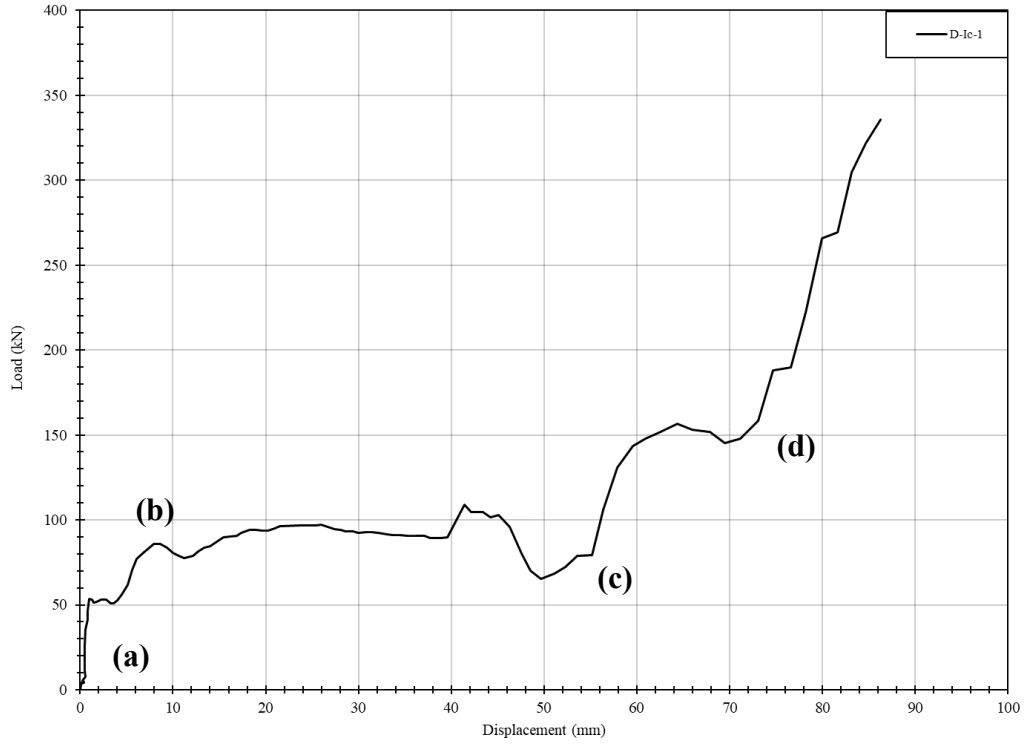

(a) Initial

(b) Plateau, prior to contact

(c) Contact with plates

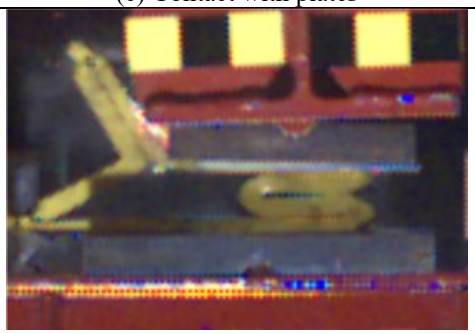

Comments

The right angle was not deformed, however, this did not seem to affect the load-displacement behaviour. The driver pressure was 563.3 kPa which resulted in a maximum reflected pressure of 58.0 kPa and impulse of 607.0 kPa-ms.

Specimen	D-Ic-2	Description	Angles with leg lengths of 76.2 mm and thickness of 12.7 mm

Pressure and impulse time-histories

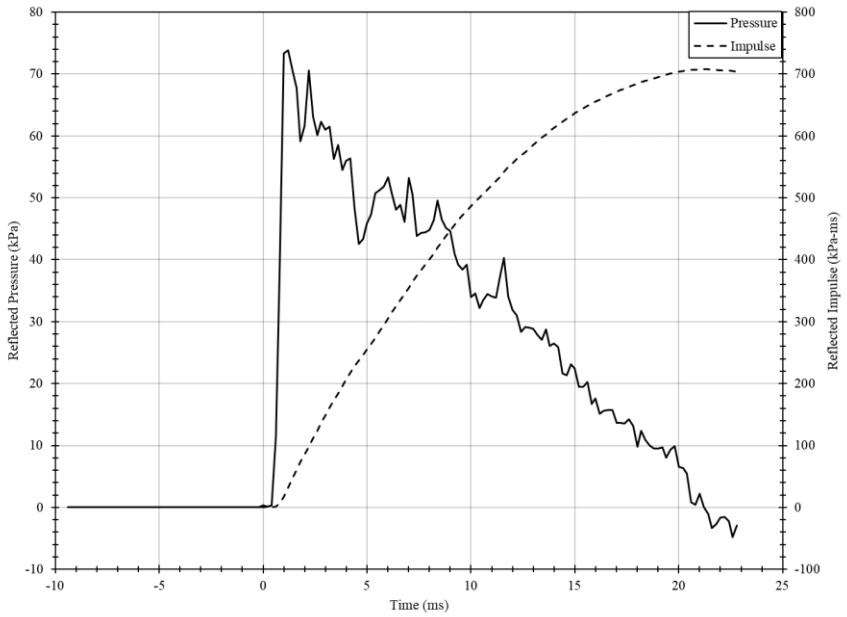

Experimental displacement and reaction loading time-histories

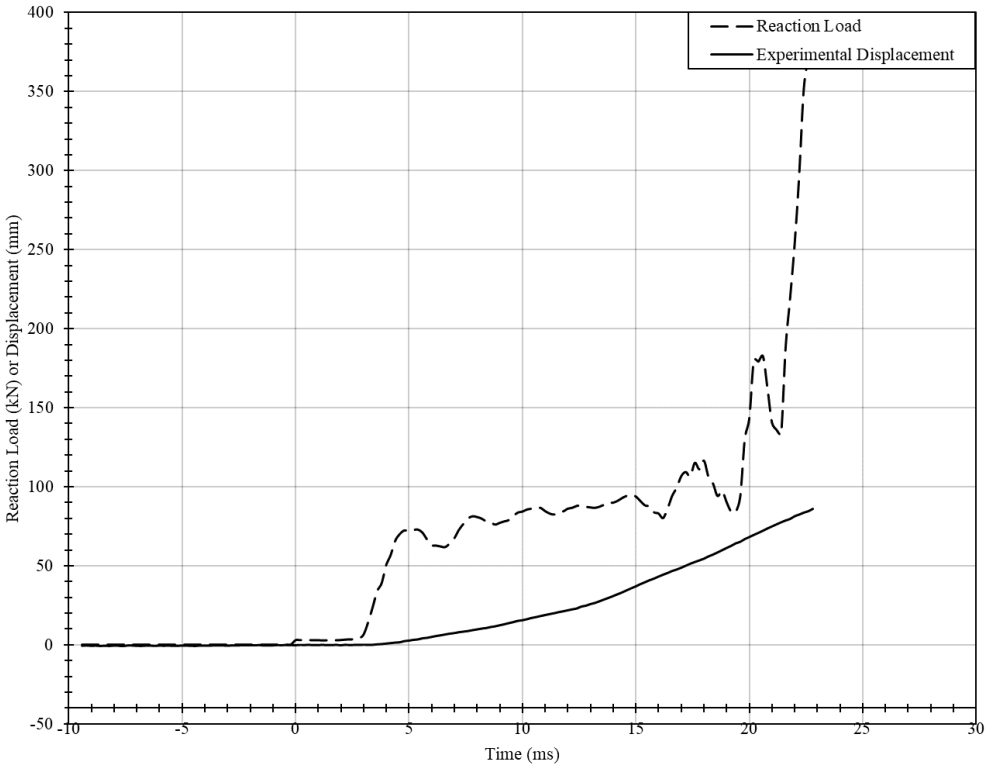

Load-displacement graph

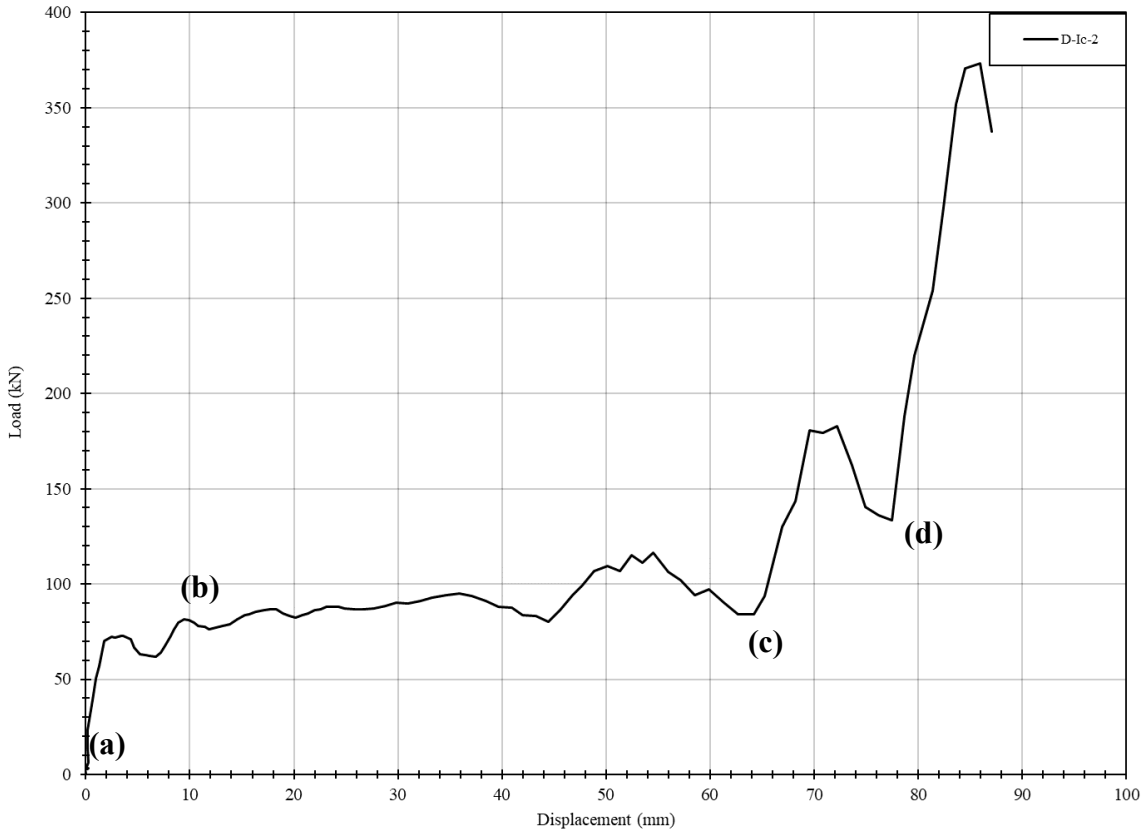

(a) Initial	(b) Plateau, prior to contact
	
(c) Contact with plates	(d) Further contact with plates
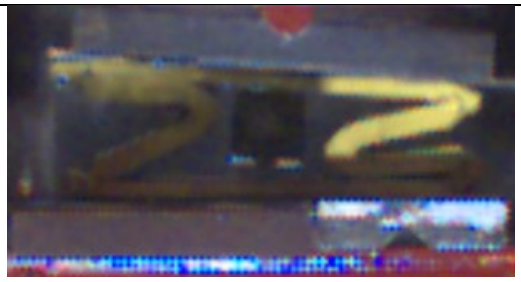	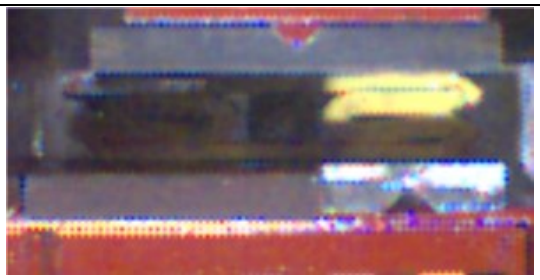

Comments

Similar behaviour to the static specimens was observed. The driver pressure was 573.6 kPa which resulted in a maximum reflected pressure of 67.1 kPa and impulse of 758.9 kPa-ms.

Specimen	D-Id-1	Description	Angles with leg lengths of 76.2 mm and thickness of 6.35 mm. Additional centre weld.

Pressure and impulse time-histories

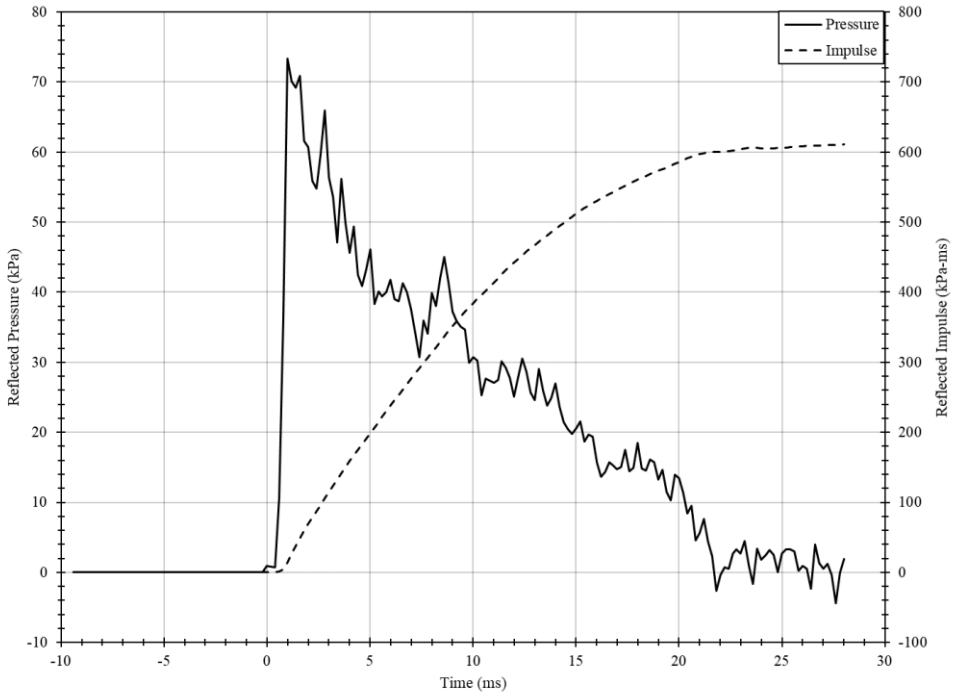

Experimental displacement and reaction loading time-histories

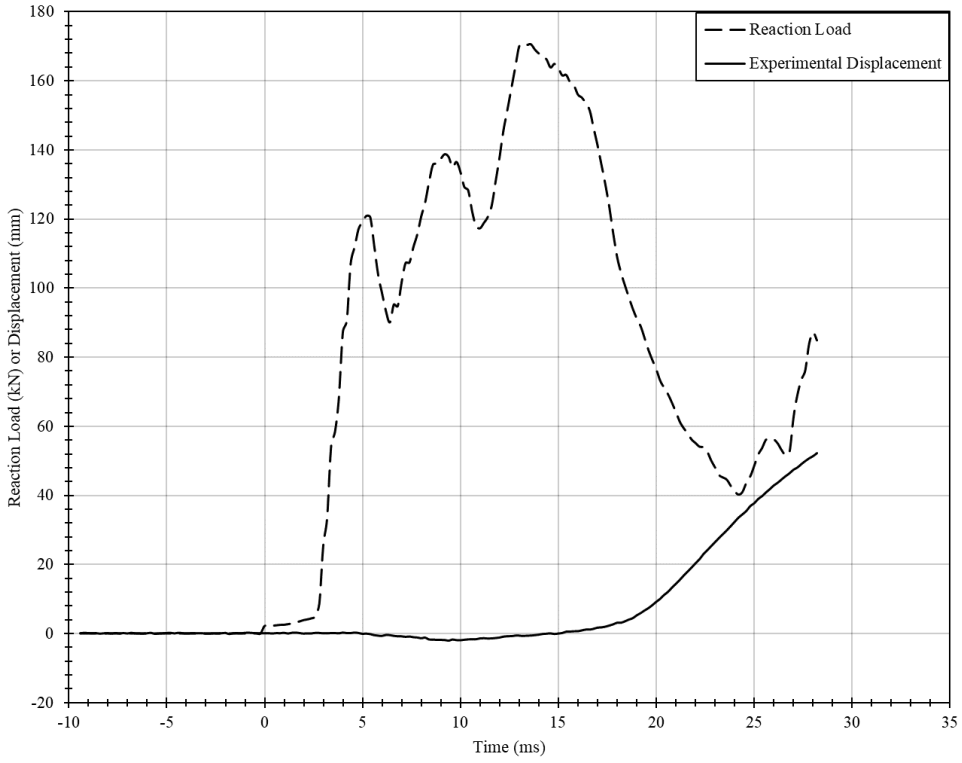

Load-displacement graph

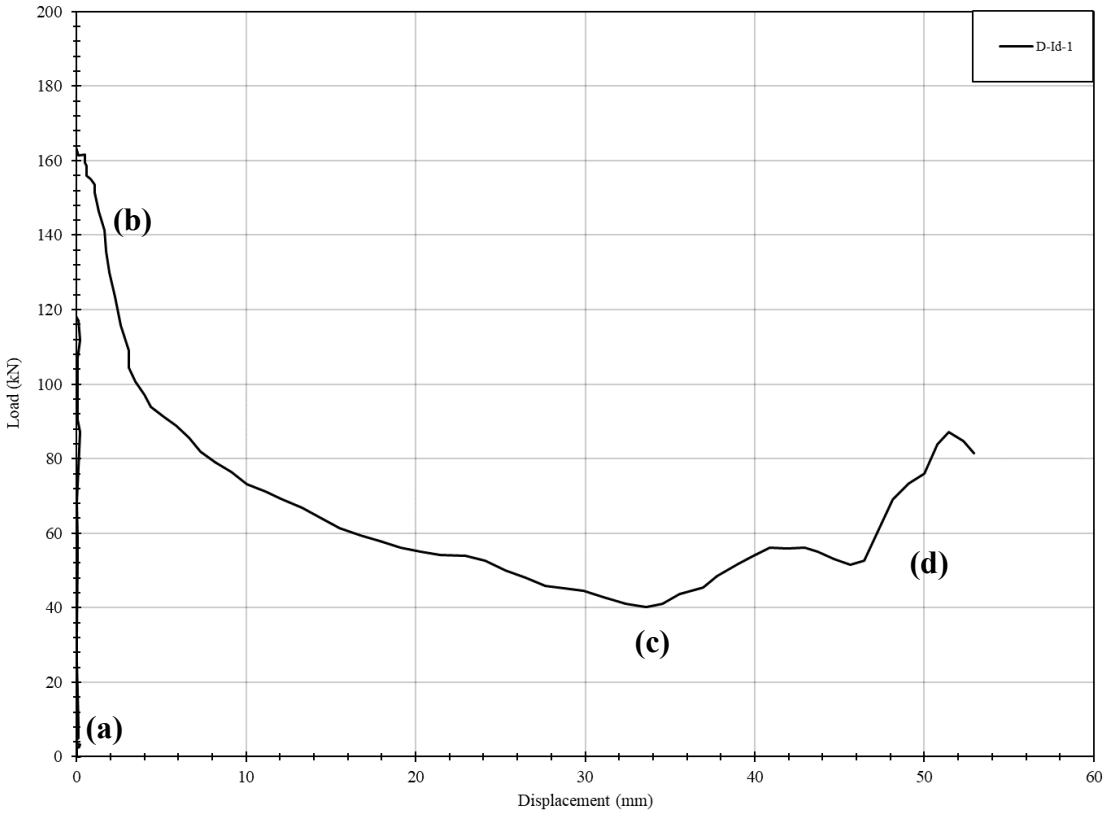

(a) Initial

(b) Plateau, prior to contact

(c) Contact with plates

(d) Further contact with plates

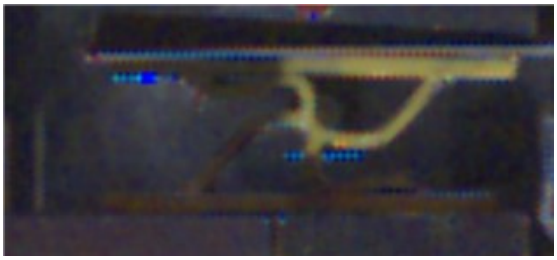

Comments

Similar behaviour to the static specimens was observed. The driver pressure was 568.8 kPa which resulted in a maximum reflected pressure of 72.2 kPa and impulse of 644.7 kPa-ms.

Specimen	D-Id-2	**Description**	Angles with leg lengths of 76.2 mm and thickness of 6.35 mm. Additional centre weld.

Pressure and impulse time-histories

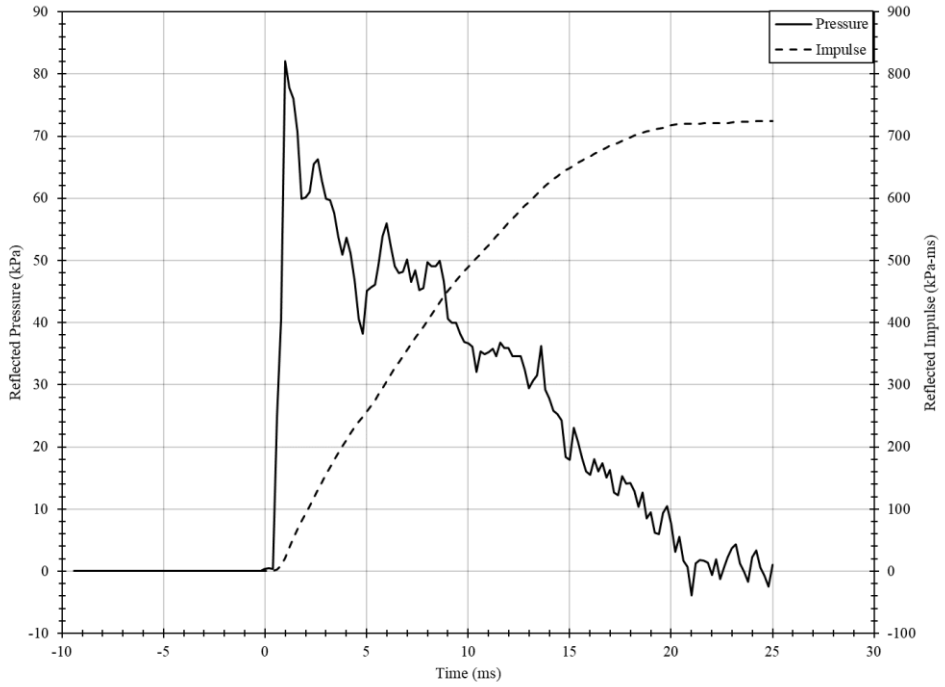

Experimental displacement and reaction loading time-histories

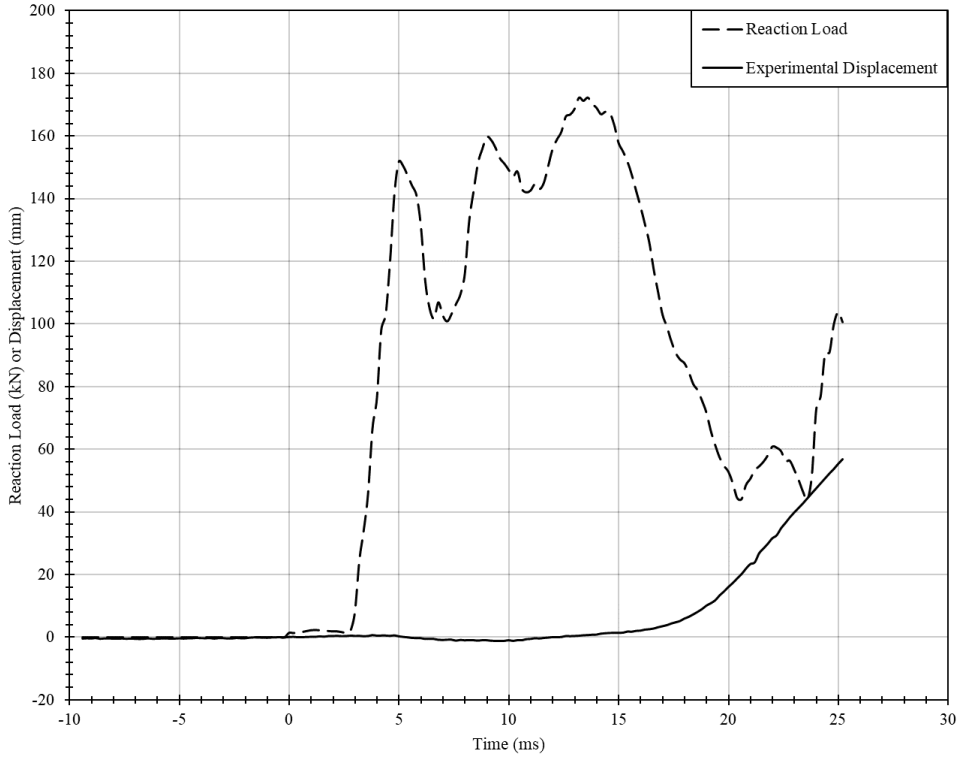

Load-displacement graph

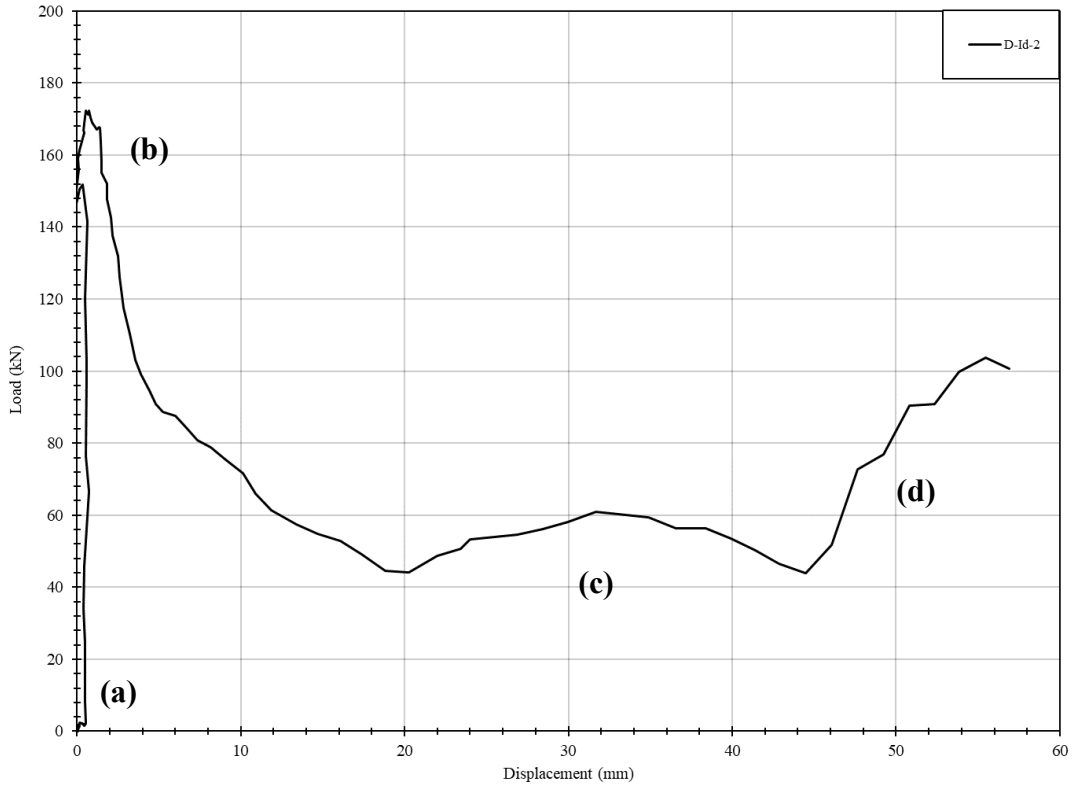

(a) Initial	(b) Plateau, prior to contact
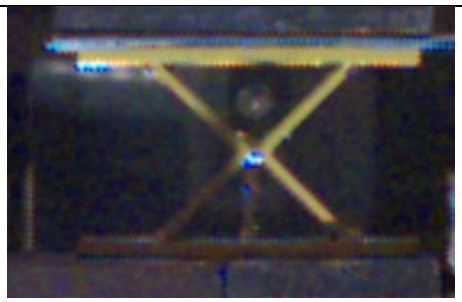	
(c) Contact with plates	(d) Further contact with plates
	

Comments

Similar behaviour to the static specimens was observed. The driver pressure was 569.5 kPa which resulted in a maximum reflected pressure of 66.5 kPa and impulse of 701.4 kPa-ms.

Specimen	D-IIa-1	Description	Circular HSS with outer diameter of 88.9 mm and thickness of 6.35 mm

Pressure and impulse time-histories

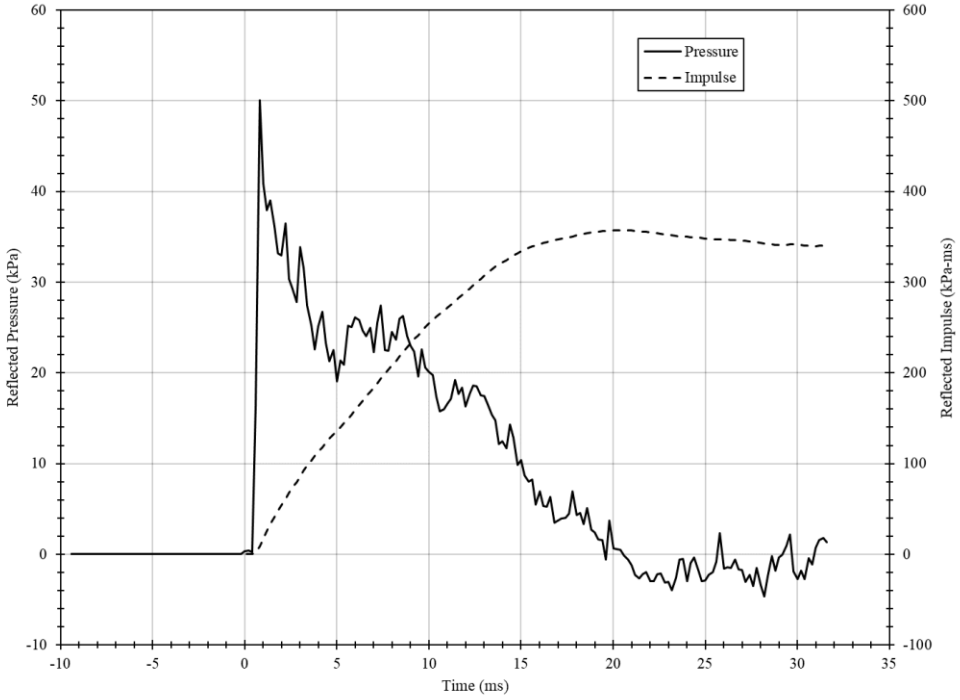

Experimental displacement and reaction loading time-histories

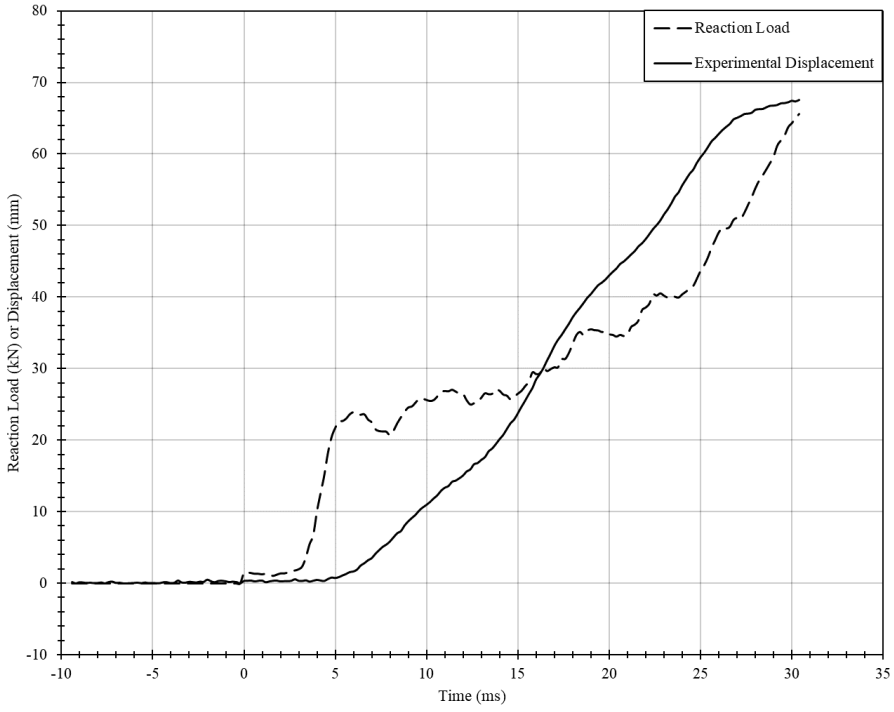

Load-displacement graph

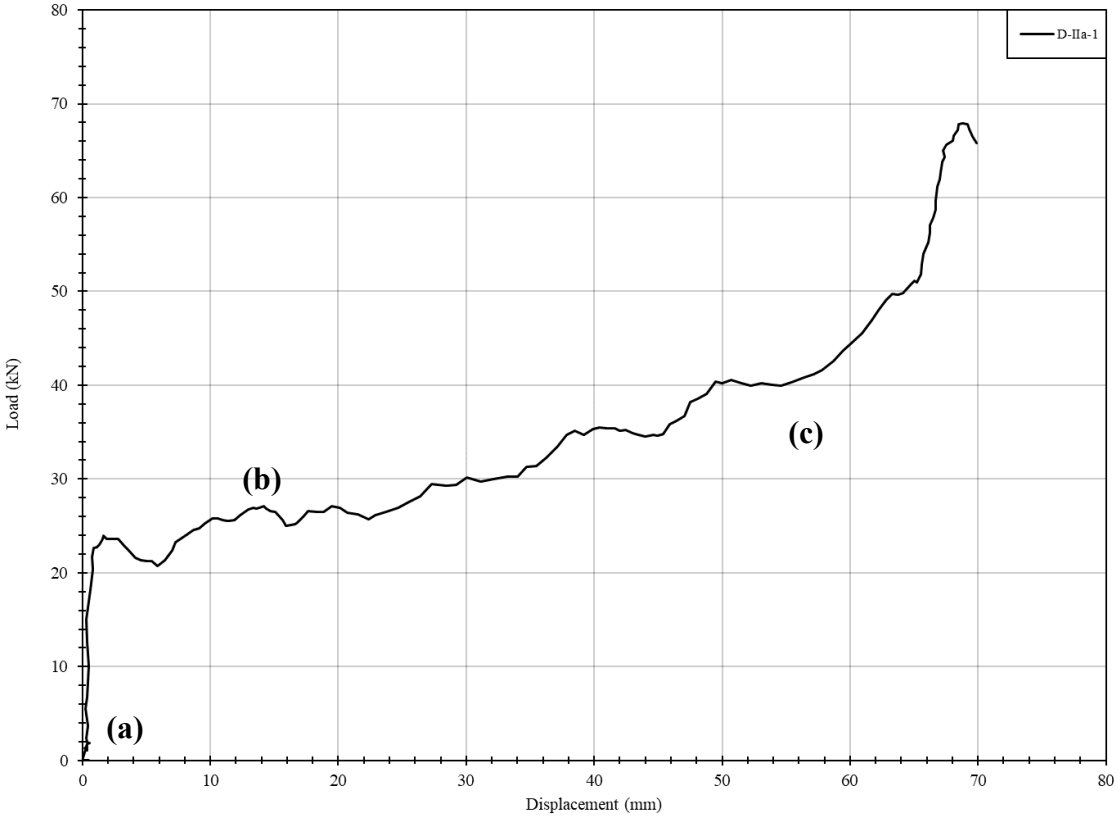

(a) Initial

(b) Plateau, prior to contact

(c) Further contact with plates

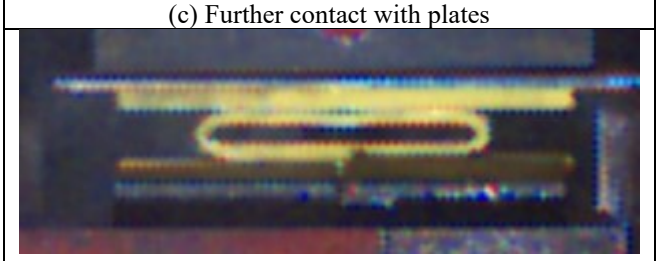

Comments

The behaviour was not similar to the static specimen, this is attributed to the different welds provided. The driver pressure was 244.8 kPa which resulted in a maximum reflected pressure of 34.8 kPa and impulse of 278.7 kPa-ms.

Specimen	D-IIa-2	**Description**	Circular HSS with outer diameter of 88.9 mm and thickness of 6.35 mm

Pressure and impulse time-histories

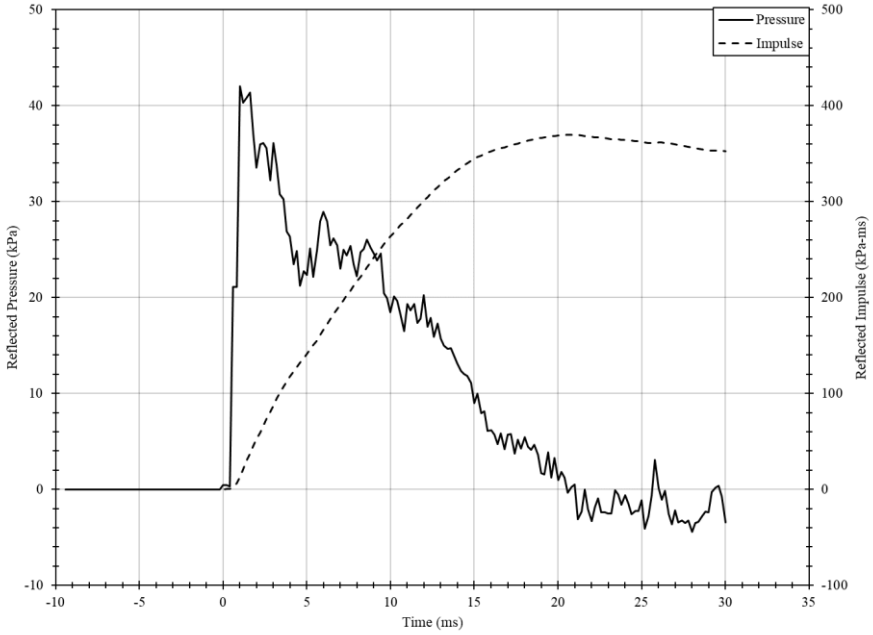

Experimental displacement and reaction loading time-histories

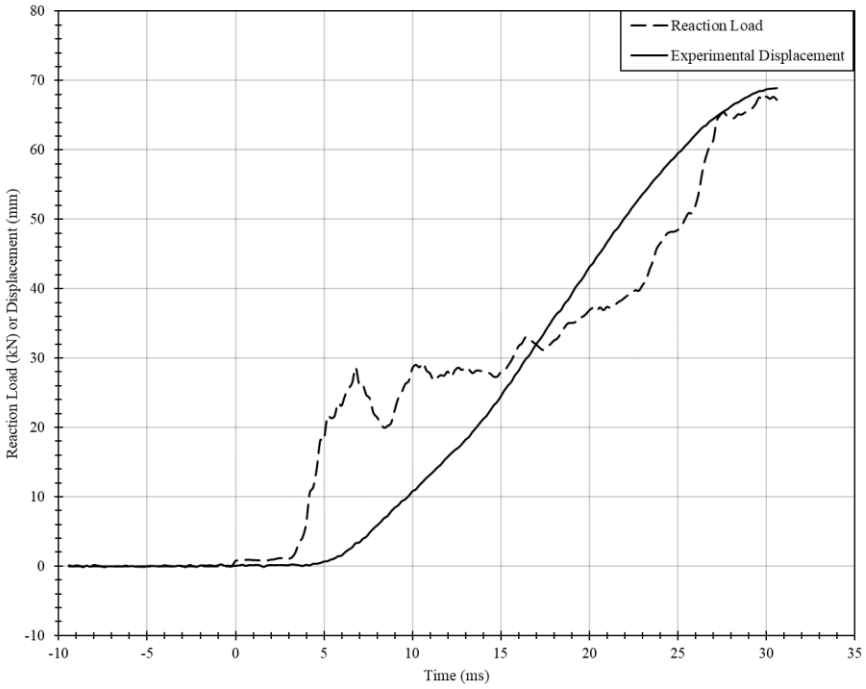

Load-displacement graph

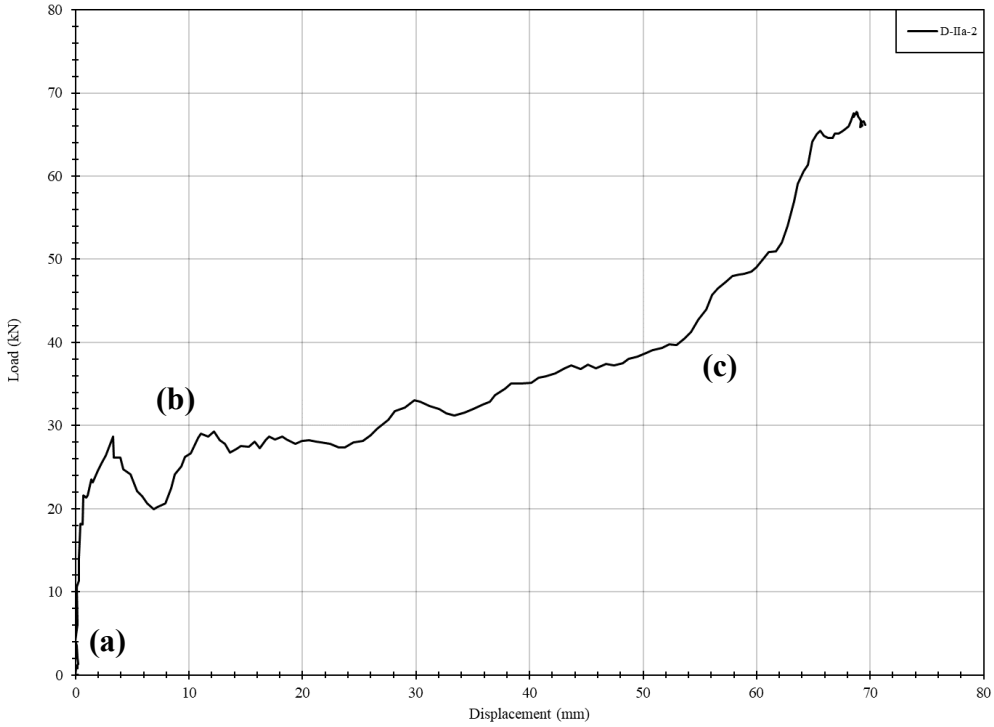

(a) Initial

(b) Plateau, prior to contact

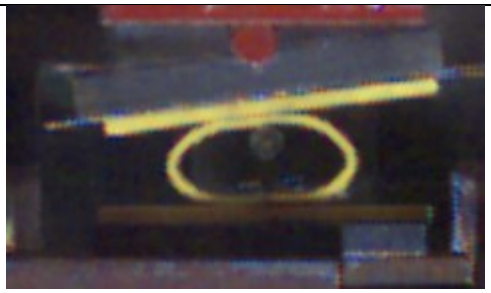

(c) Further contact with plates

Comments

The behaviour was not similar to the static specimen, this is attributed to the different welds provided. The driver pressure was 250.3 kPa which resulted in a maximum reflected pressure of 36.6 kPa and impulse of 300.3 kPa-ms.

Specimen	D-IIb-1	Description	Circular HSS with outer diameter of 88.9 mm and thickness of 6.35 mm Depth of 101.6 mm

Pressure and impulse time-histories

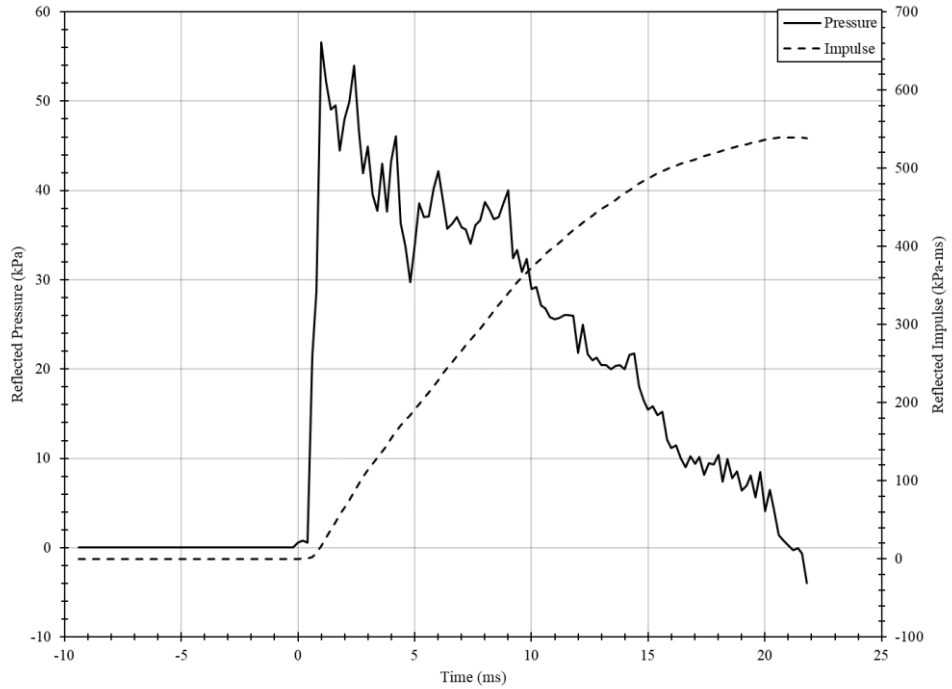

Experimental displacement and reaction loading time-histories

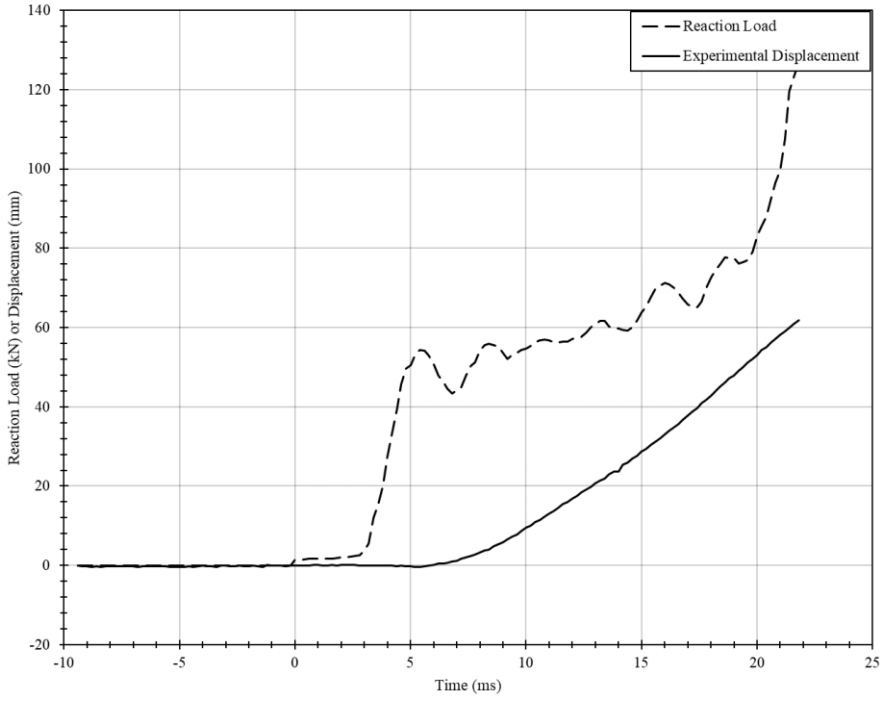

Load-displacement graph

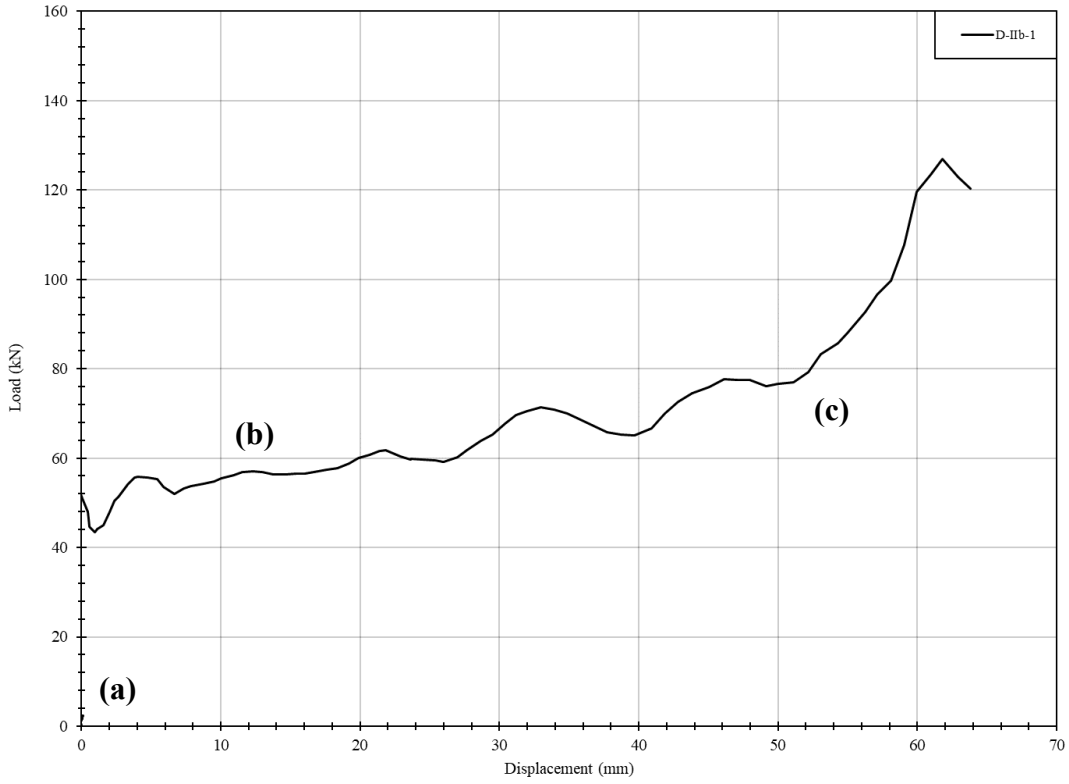

(a) Initial

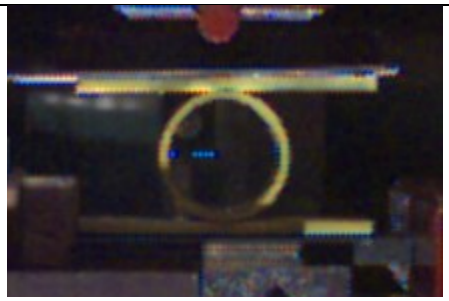

(b) Plateau, prior to contact

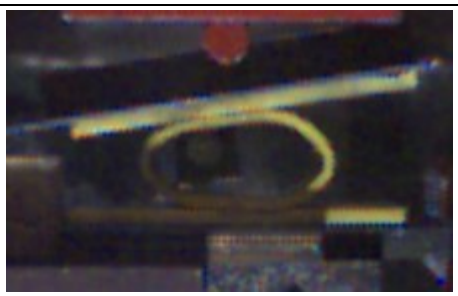

(c) Further contact with plates

Comments

The behaviour was not similar to the static specimen, this is attributed to the different welds provided. The driver pressure was 413.0 kPa which resulted in a maximum reflected pressure of 44.1 kPa and impulse of 519.6 kPa-ms.

Specimen	D-IIb-2	Description	Circular HSS with outer diameter of 88.9 mm and thickness of 6.35 mm Depth of 101.6 mm

Pressure and impulse time-histories

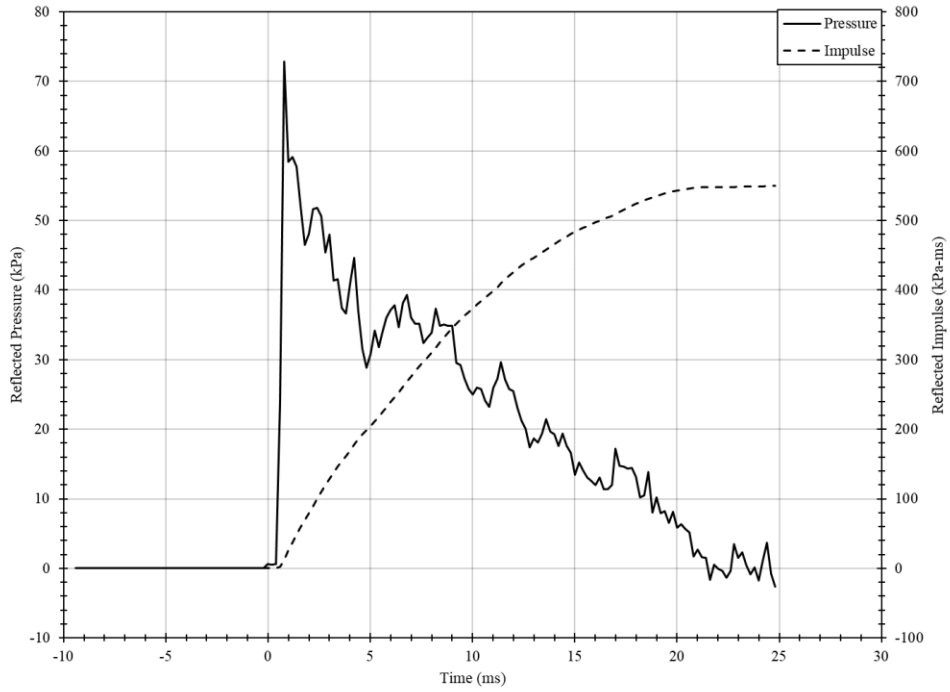

Experimental displacement and reaction loading time-histories

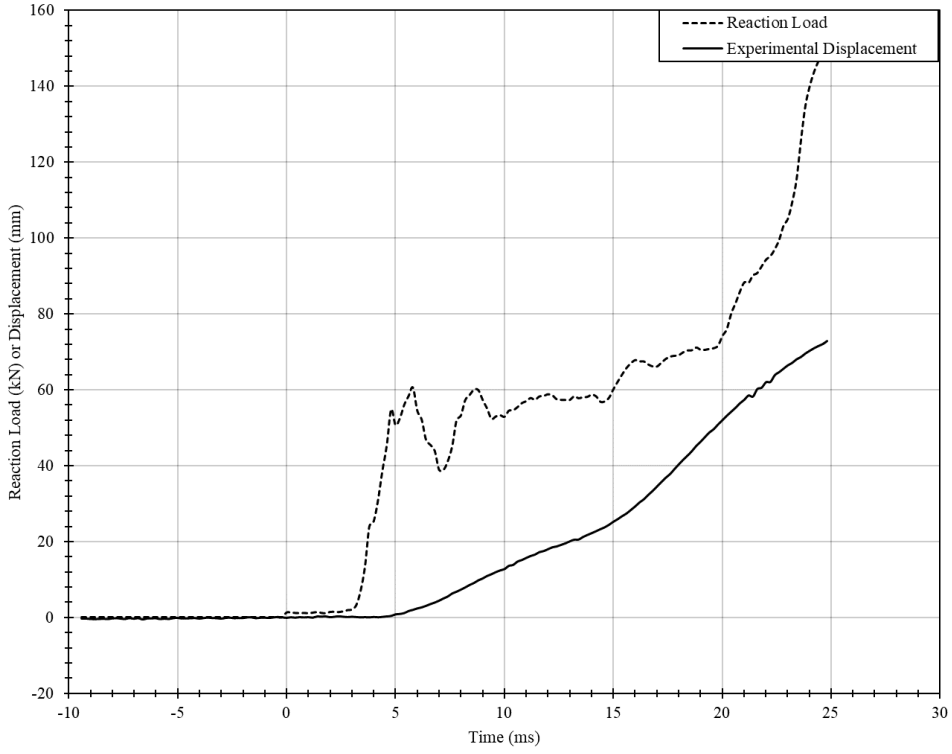

Load-displacement graph

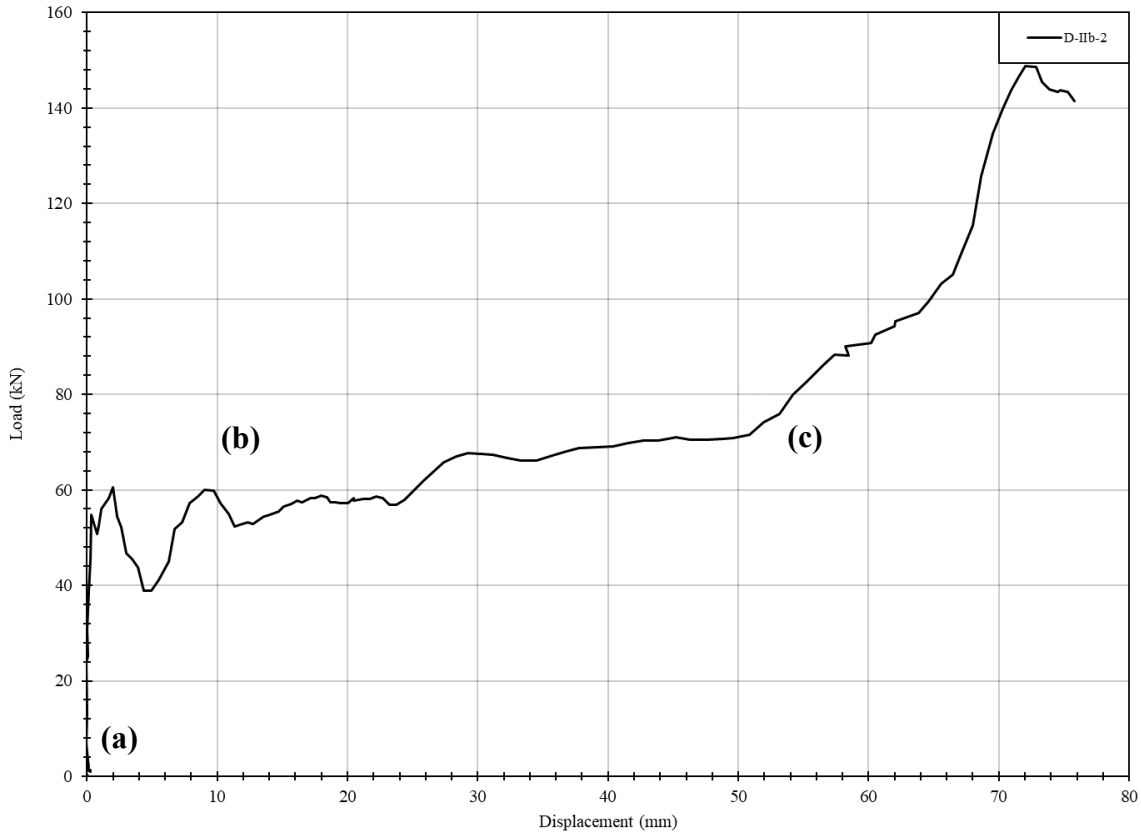

(a) Initial

(b) Plateau, prior to contact

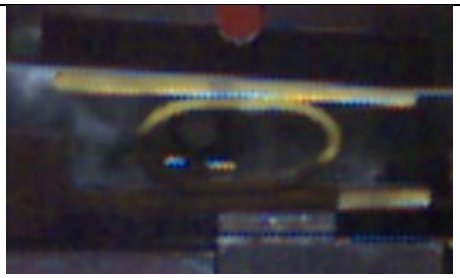

(c) Further contact with plates

Comments

The behaviour was not similar to the static specimen, this is attributed to the different welds provided. The driver pressure was 415.8 kPa which resulted in a maximum reflected pressure of 49.2 kPa and impulse of 482.0 kPa-ms.

Specimen	D-IIc-1	**Description**	Circular HSS with outer diameter of 127 mm and thickness of 6.35 mm

Pressure and impulse time-histories

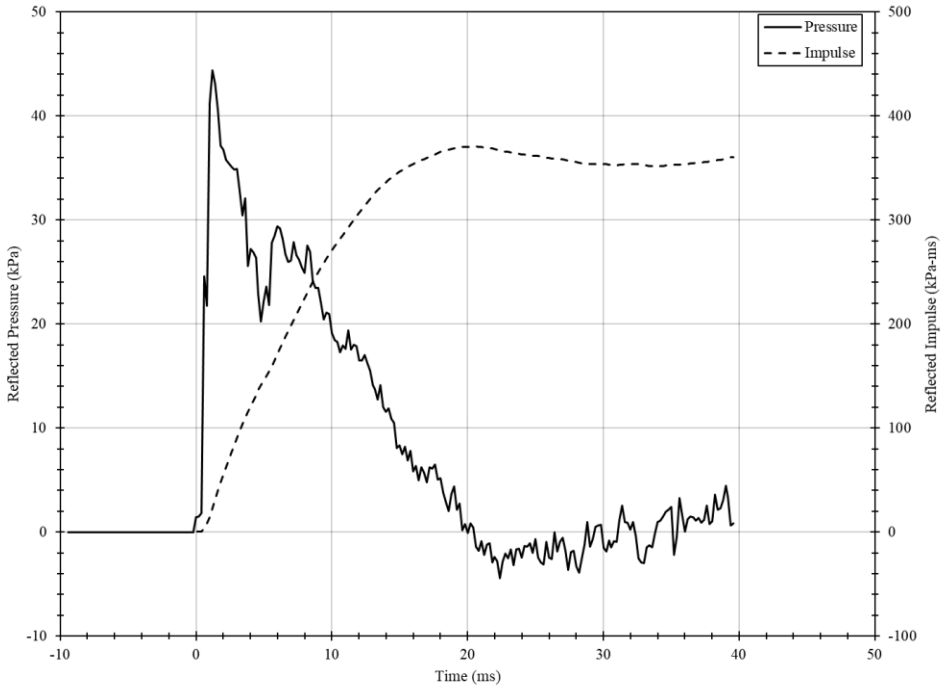

Experimental displacement and reaction loading time-histories

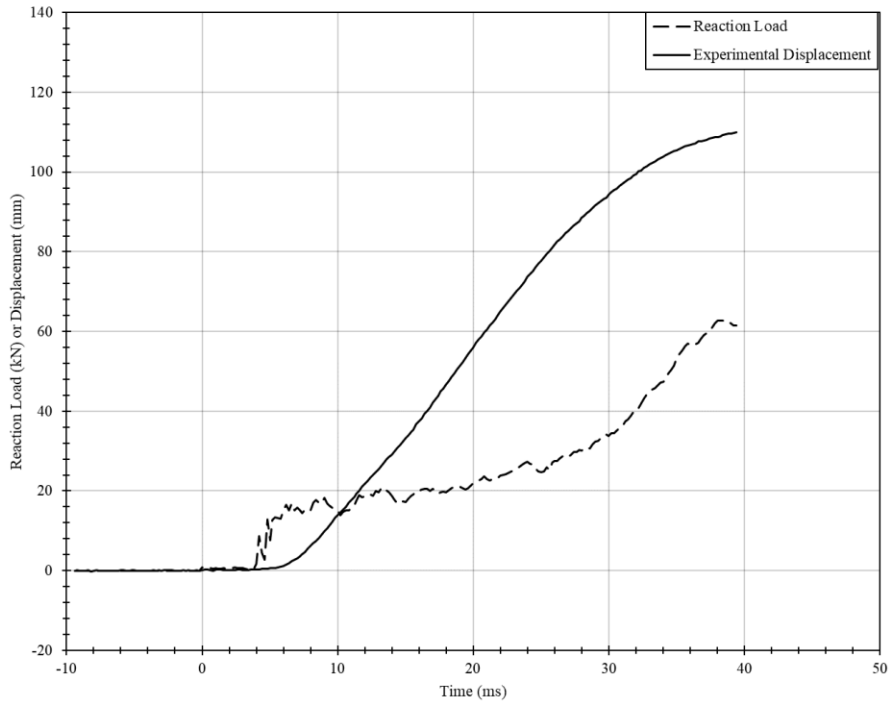

Load-displacement graph

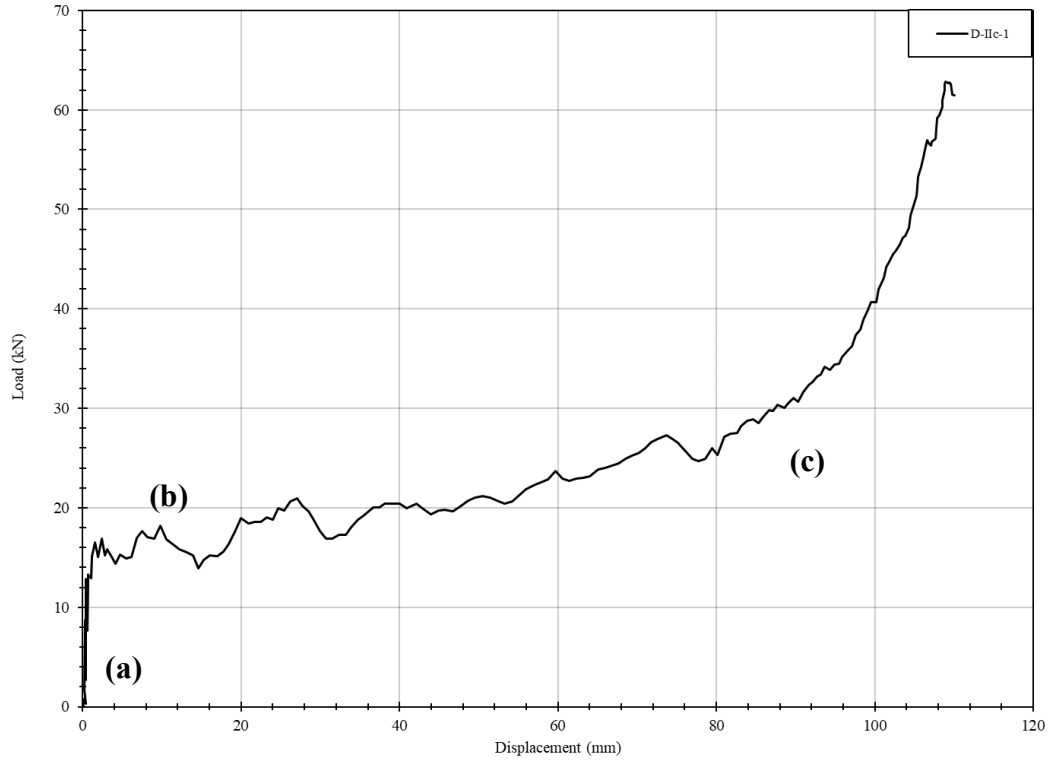

(a) Initial

(b) Plateau, prior to contact

(c) Further contact with plates

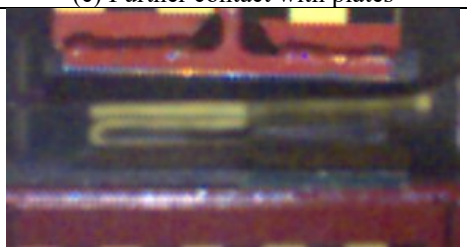

Comments

The behaviour was not similar to the static specimen, this is attributed to the different welds provided. The driver pressure was 260.6 kPa which resulted in a maximum reflected pressure of 34.2 kPa and impulse of 314.8 kPa-ms.

Specimen	D-IIc-2	Description	Circular HSS with outer diameter of 127 mm and thickness of 6.35 mm

Pressure and impulse time-histories

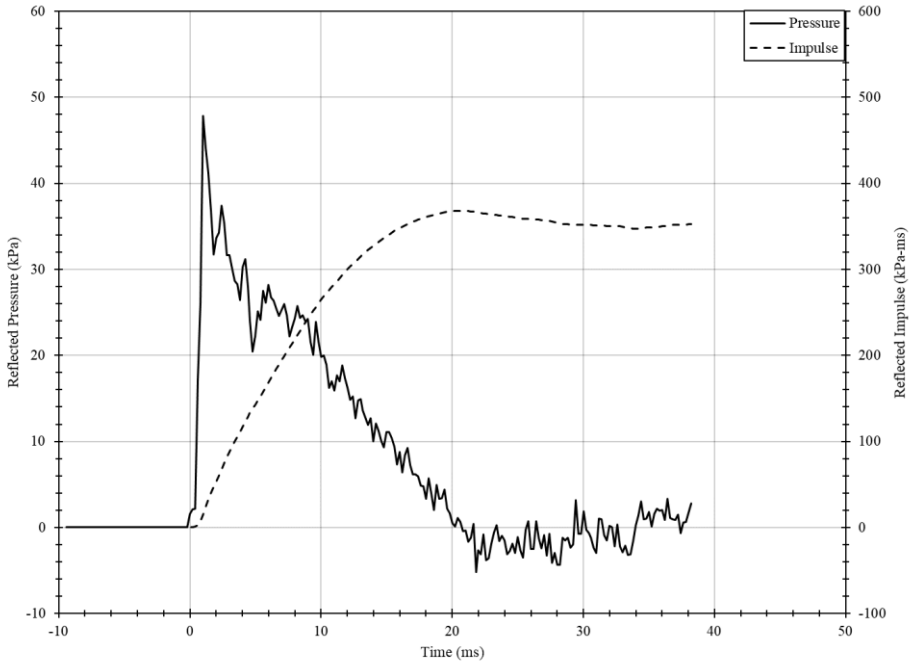

Experimental displacement and reaction loading time-histories

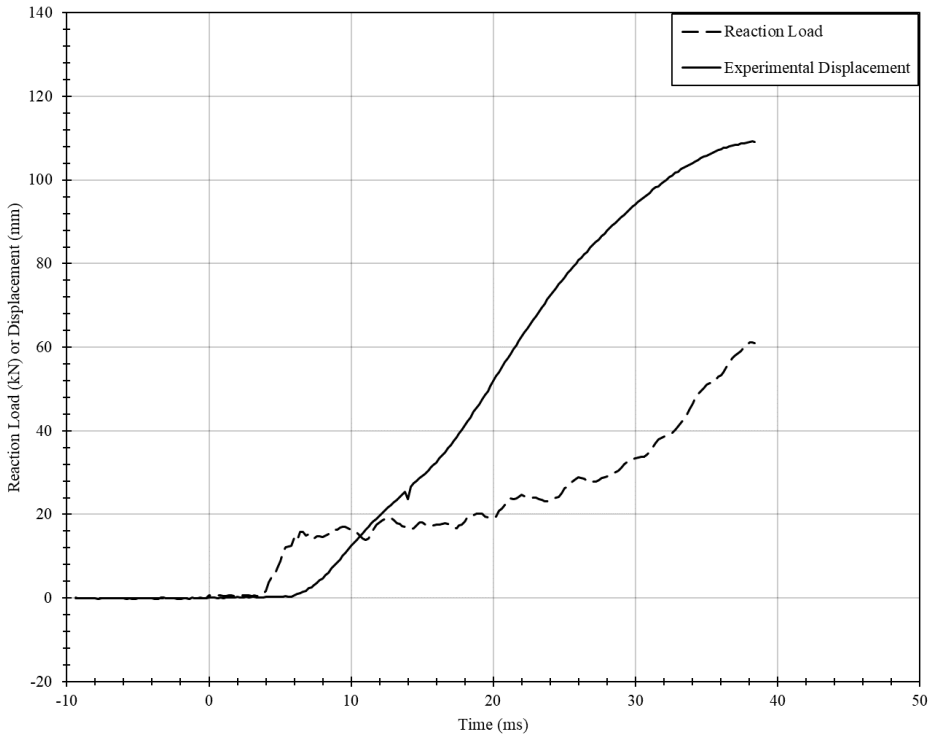

Load-displacement graph

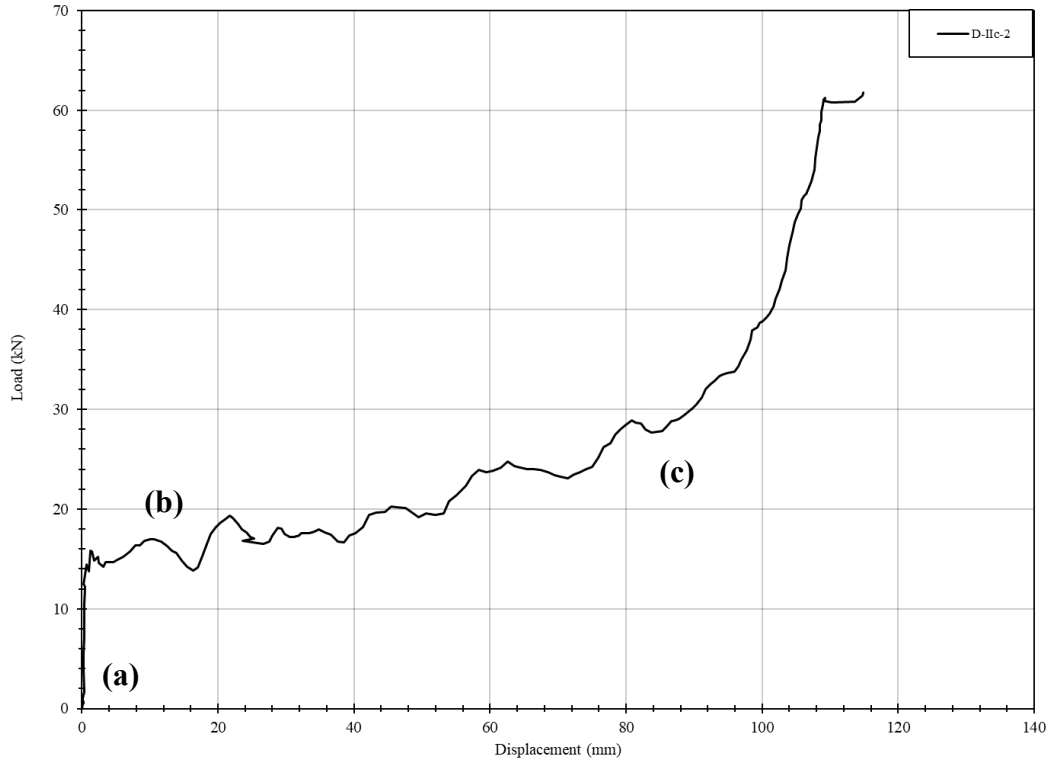

(a) Initial

(b) Plateau, prior to contact

(c) Further contact with plates

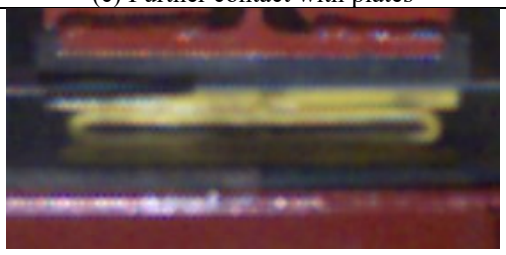

Comments

The behaviour was not similar to the static specimen, this is attributed to the different welds provided. The driver pressure was 261.3 kPa which resulted in a maximum reflected pressure of 45.7 kPa and impulse of 362.1 kPa-ms.

Specimen	D-IId-1	**Description**	Arcs from circular HSS of outer diameter of 127 mm and thickness of 6.35 mm.

Pressure and impulse time-histories

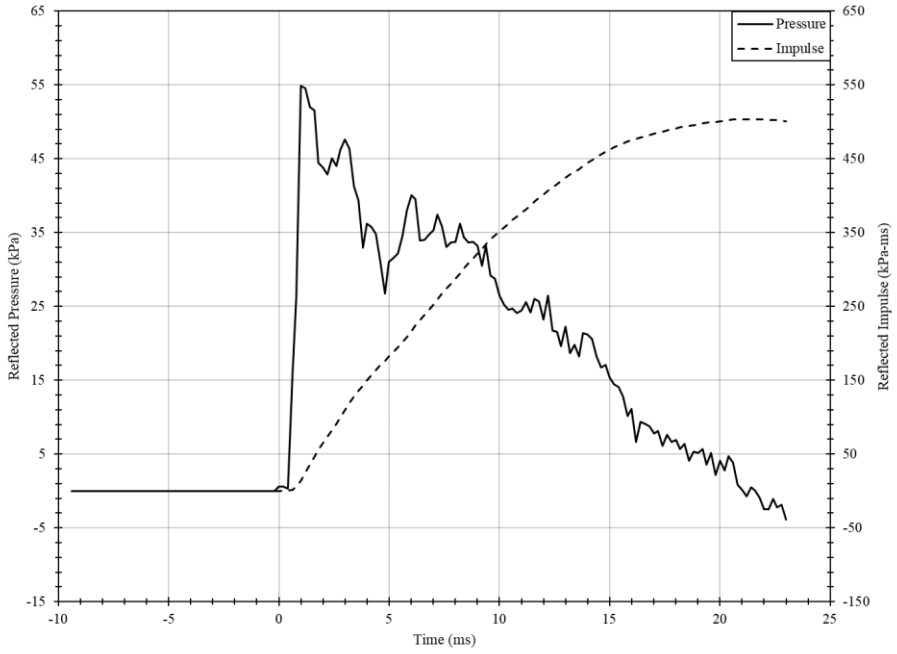

Experimental displacement and reaction loading time-histories

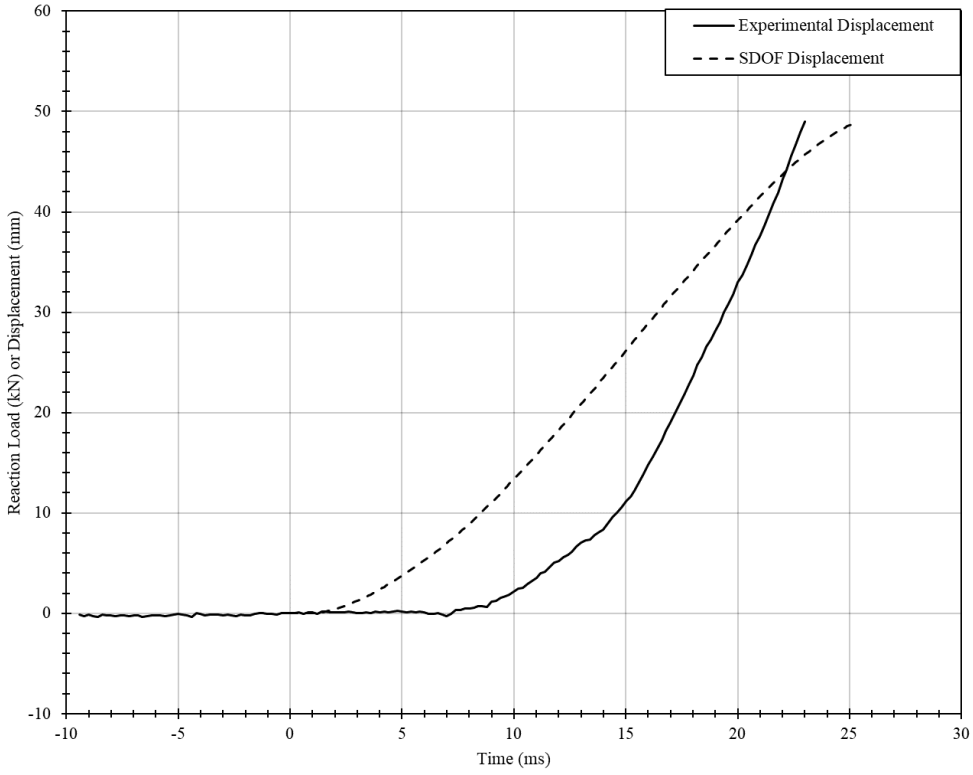

Load-displacement graph

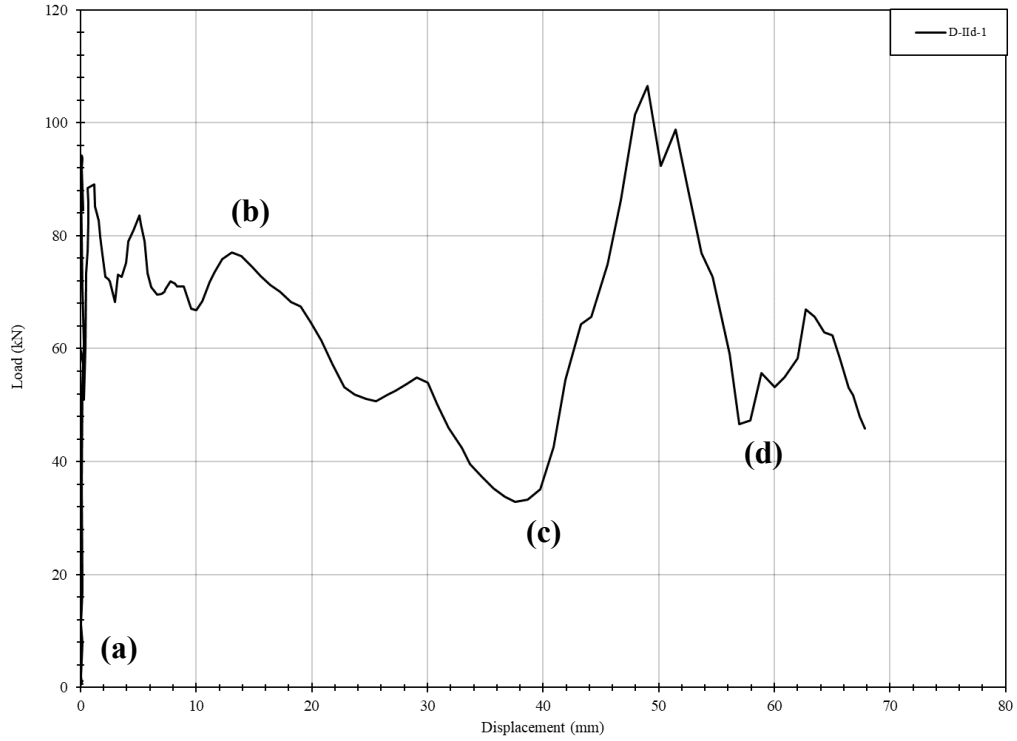

(a) Initial	(b) Plateau, prior to contact
	
(c) Contact with plates	(d) Further contact with plates
	

Comments

The deflected shape was similar to the static specimen. The driver pressure was 373.7 kPa which resulted in a maximum reflected pressure of 50.2 kPa and impulse of 493.2 kPa-ms.

Specimen	D-IId-2	Description	Arcs from circular HSS of outer diameter of 127 mm and thickness of 6.35 mm.

Pressure and impulse time-histories

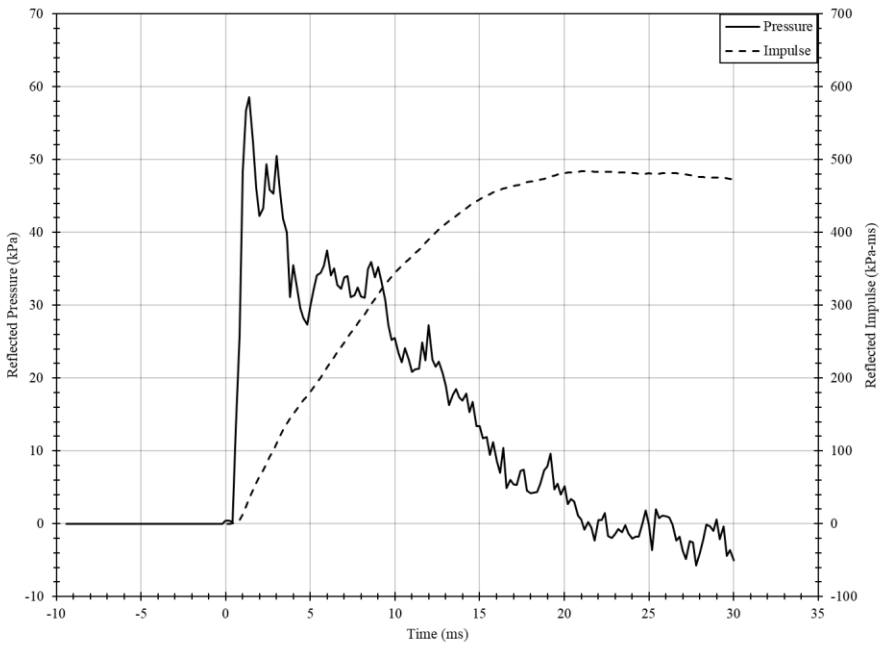

Experimental displacement and reaction loading time-histories

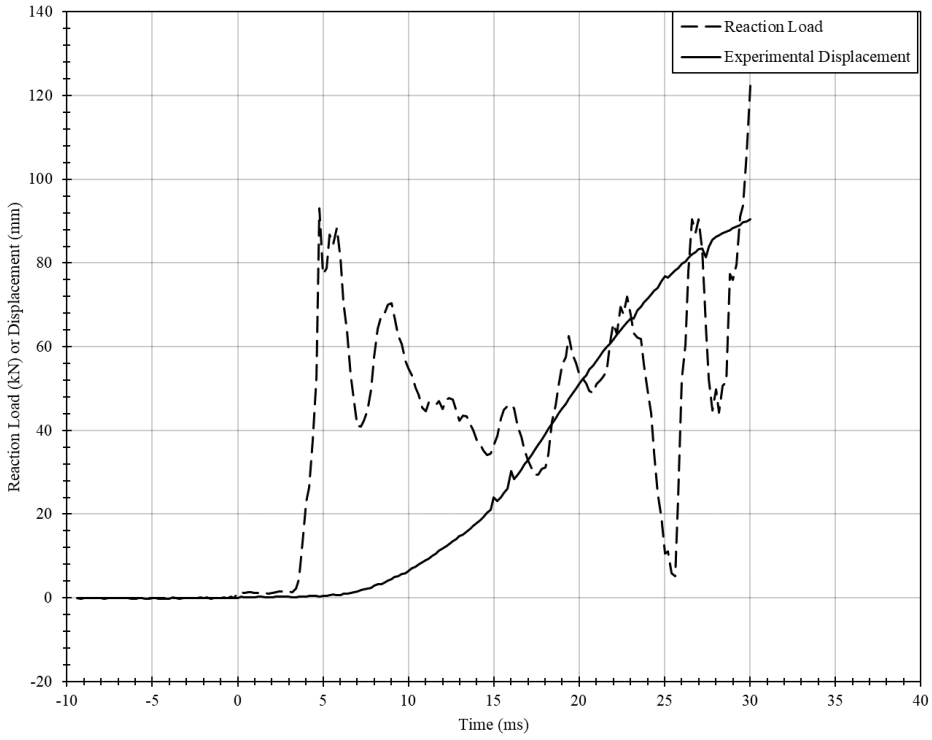

Load-displacement graph

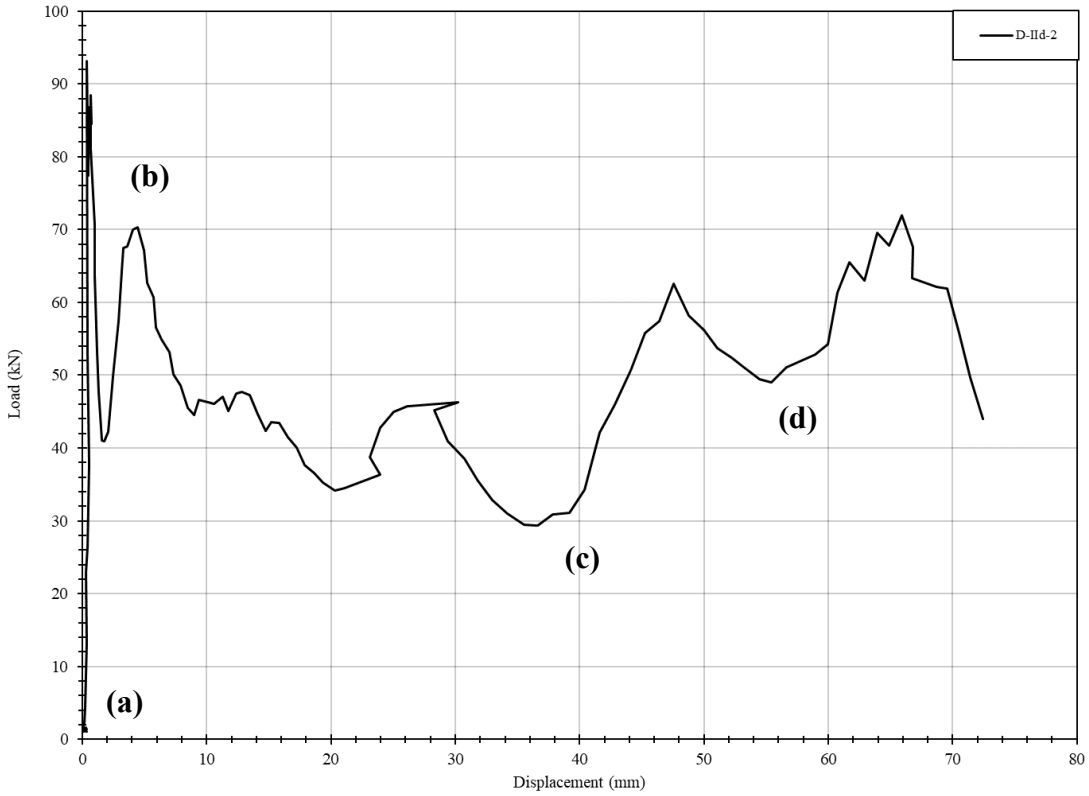

(a) Initial

(b) Plateau, prior to contact

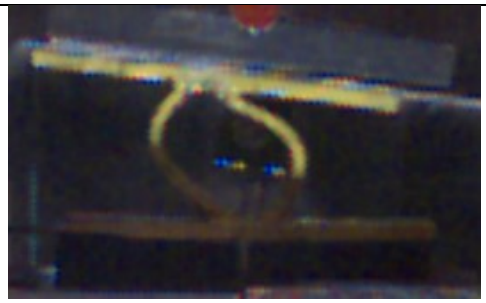

(c) Contact with plates

Comments

The deflected shape was similar to the static specimen. The driver pressure was 376.5 kPa which resulted in a maximum reflected pressure of 44.3 kPa and impulse of 391.8 kPa-ms.

Specimen	D-IIe-1	**Description**	Circular HSS with outer diameter of 88.9 mm and thickness of 6.35 mm Circular HSS with outer diameter of 60.325 mm and thickness of 3.175 mm

Pressure and impulse time-histories

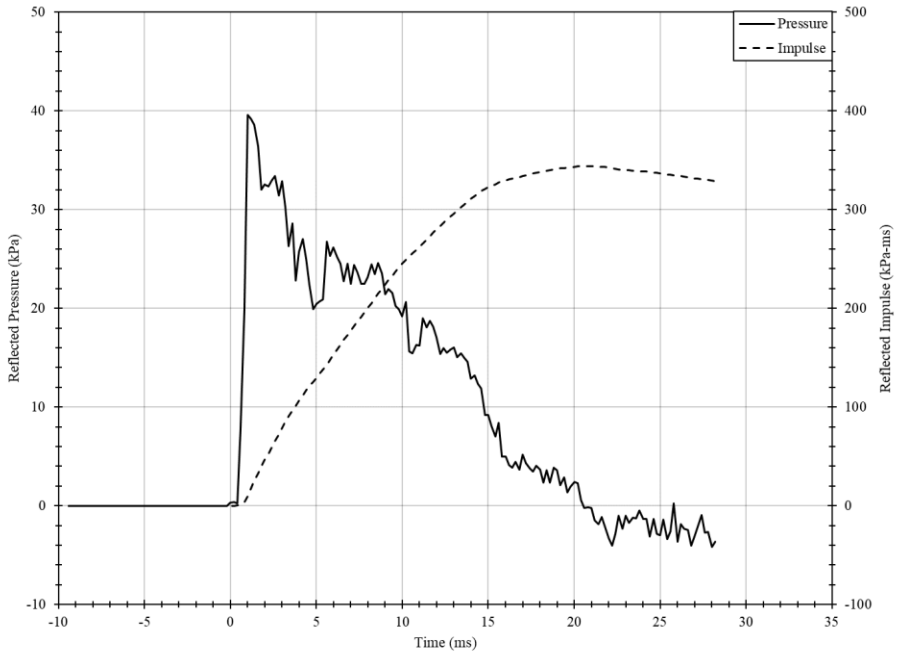

Experimental displacement and reaction loading time-histories

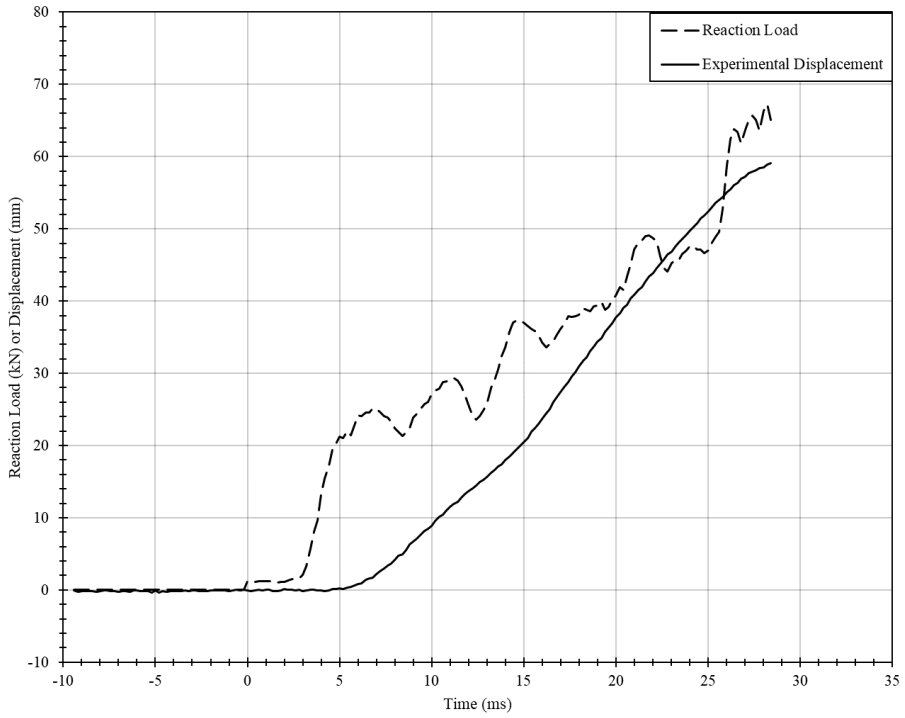

Load-displacement graph

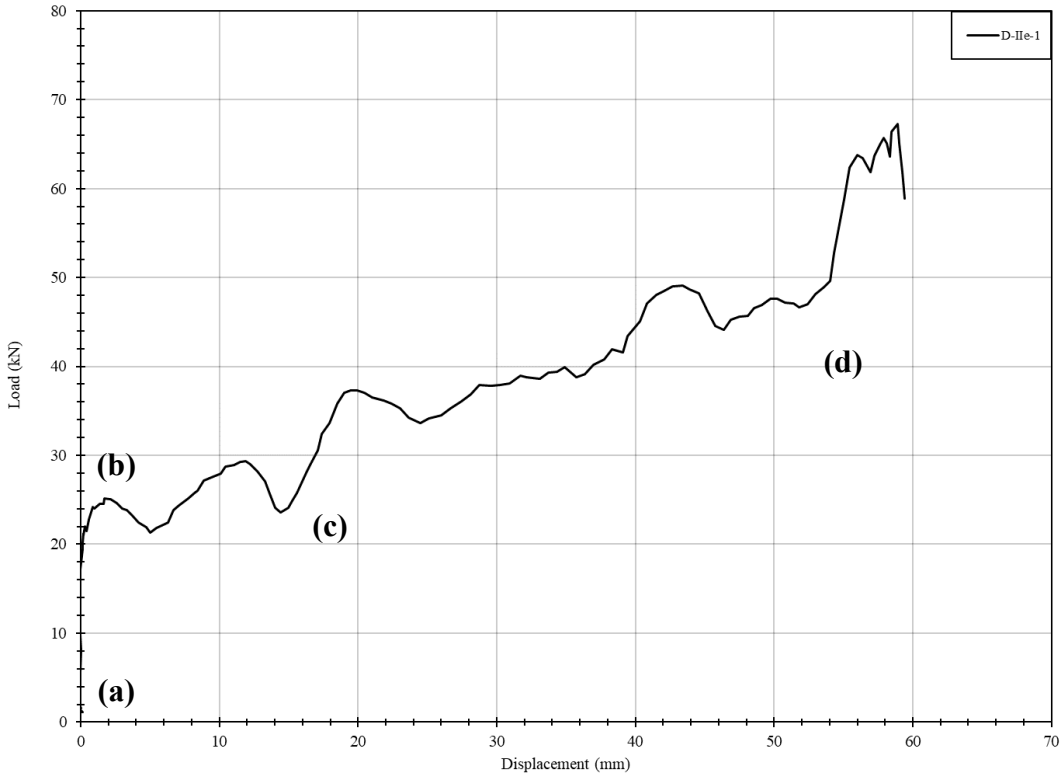

(a) Initial	(b) Plateau, prior to contact
	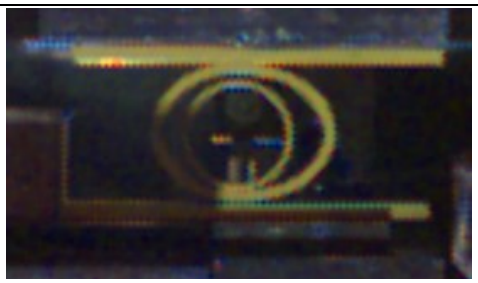
(c) Contact between both circular HSS	(d) Contact with plates
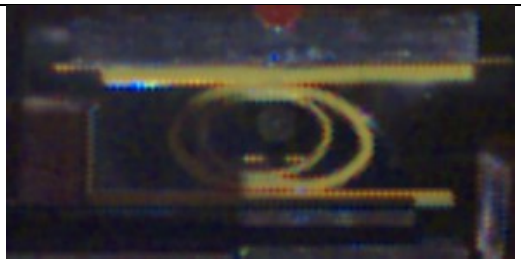	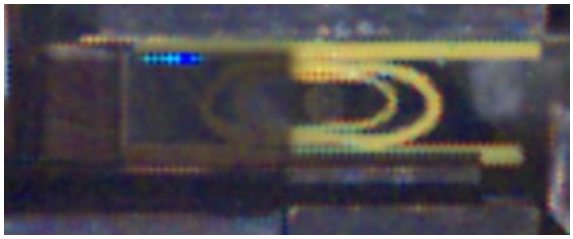

Comments

The dynamic behaviour was significantly different from the static behaviour, this is attributed to the different welds provided. The driver pressure was 233.7 kPa which resulted in a maximum reflected pressure of 36.0 kPa and impulse of 350.5 kPa-ms.

Specimen	D-IIe-2	**Description**	Circular HSS with outer diameter of 88.9 mm and thickness of 6.35 mm Circular HSS with outer diameter of 60.325 mm and thickness of 3.175 mm

Pressure and impulse time-histories

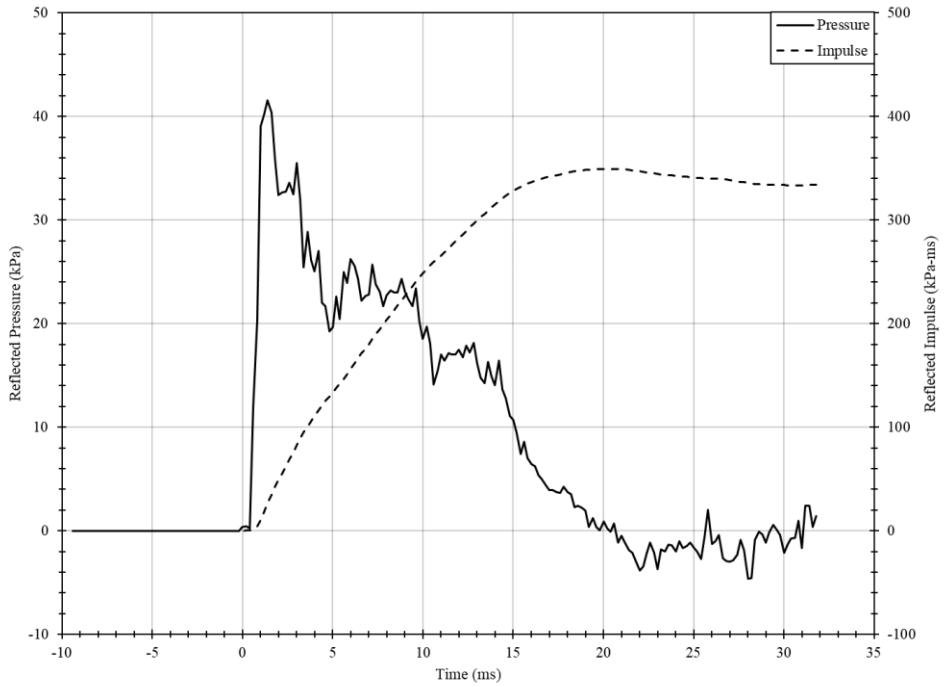

Experimental displacement and reaction loading time-histories

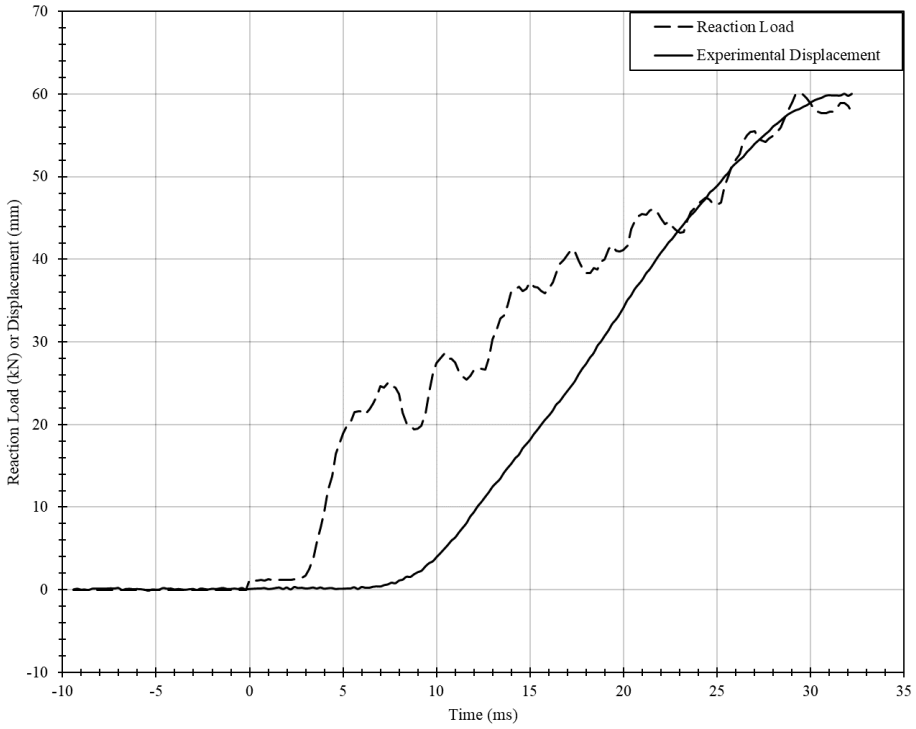

Load-displacement graph

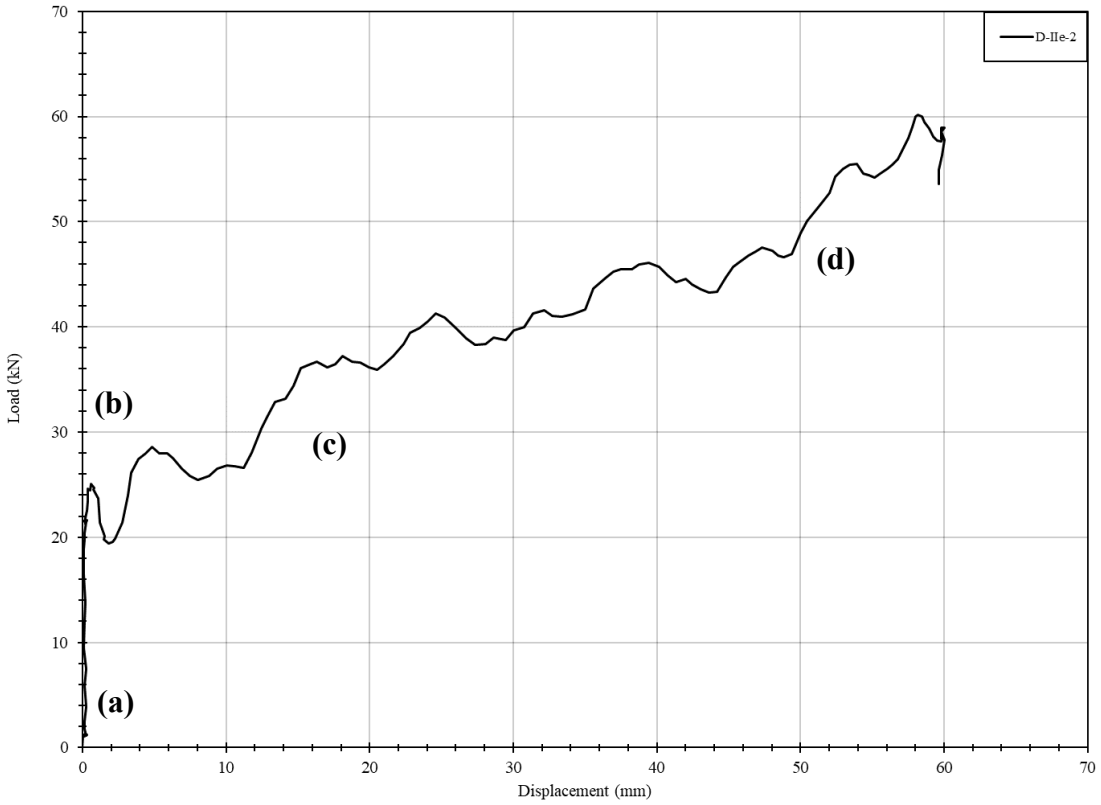

(a) Initial

(b) Plateau, prior to contact

(c) Contact between both circular HSS

(d) Contact with plates

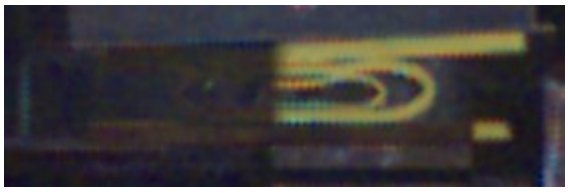

Comments

The dynamic behaviour was significantly different from the static behaviour, this is attributed to the different welds provided. The driver pressure was 233.7 kPa which resulted in a maximum reflected pressure of 37.8 kPa and impulse of 273.0 kPa-ms.

APPENDIX D – Analytical Results

Specimen	S-Ia-1	Description	Angles with leg lengths of 76.2 mm and thickness of 6.35 mm

Energy absorption efficiency, and experimental and idealized load-displacement relationships

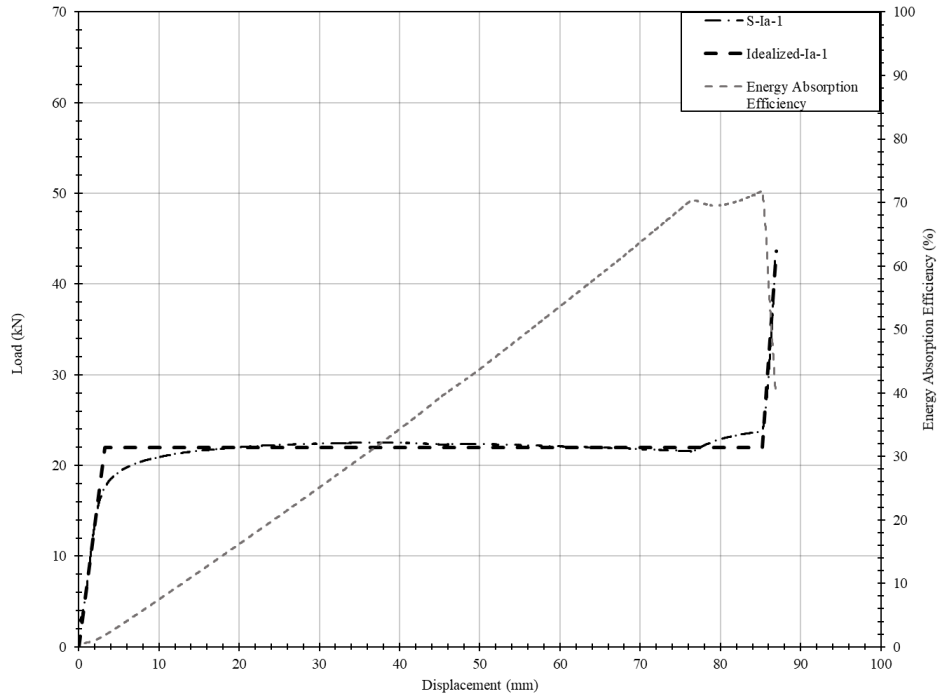

Experimental load-displacement, preliminary FEA model, and revised FEA model

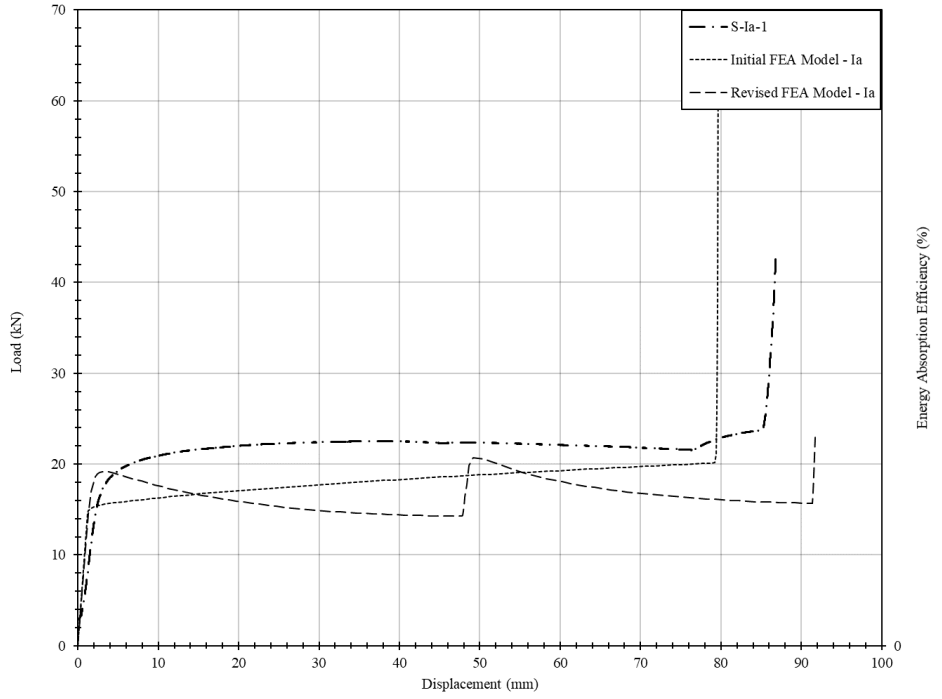

Specimen	S-Ia-2	Description	Angles with leg lengths of 76.2 mm and thickness of 6.35 mm

Energy absorption efficiency, and experimental and idealized load-displacement relationships

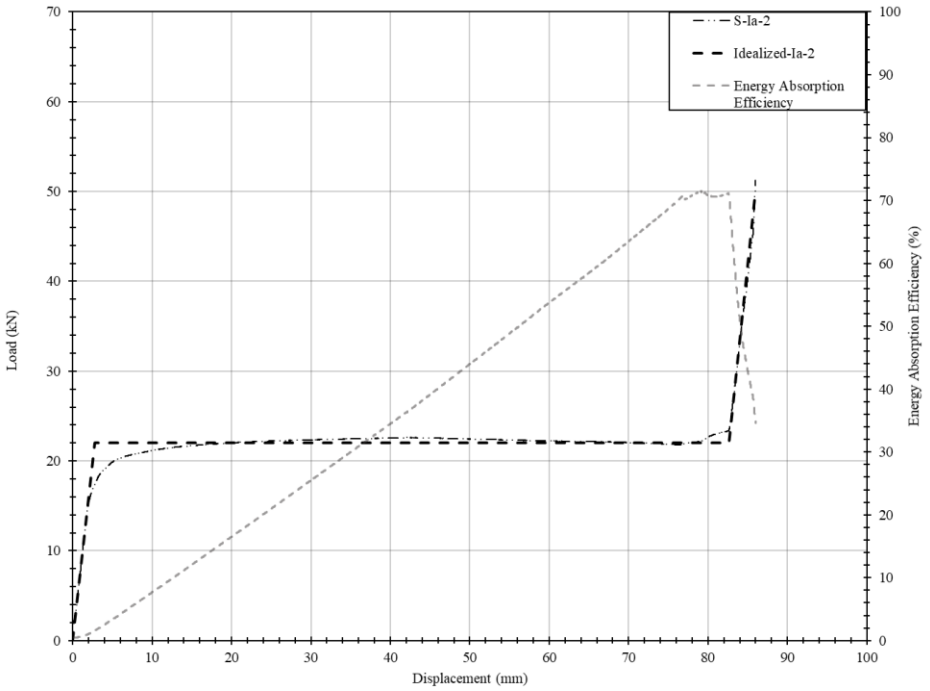

Experimental load-displacement, preliminary FEA model, and revised FEA model

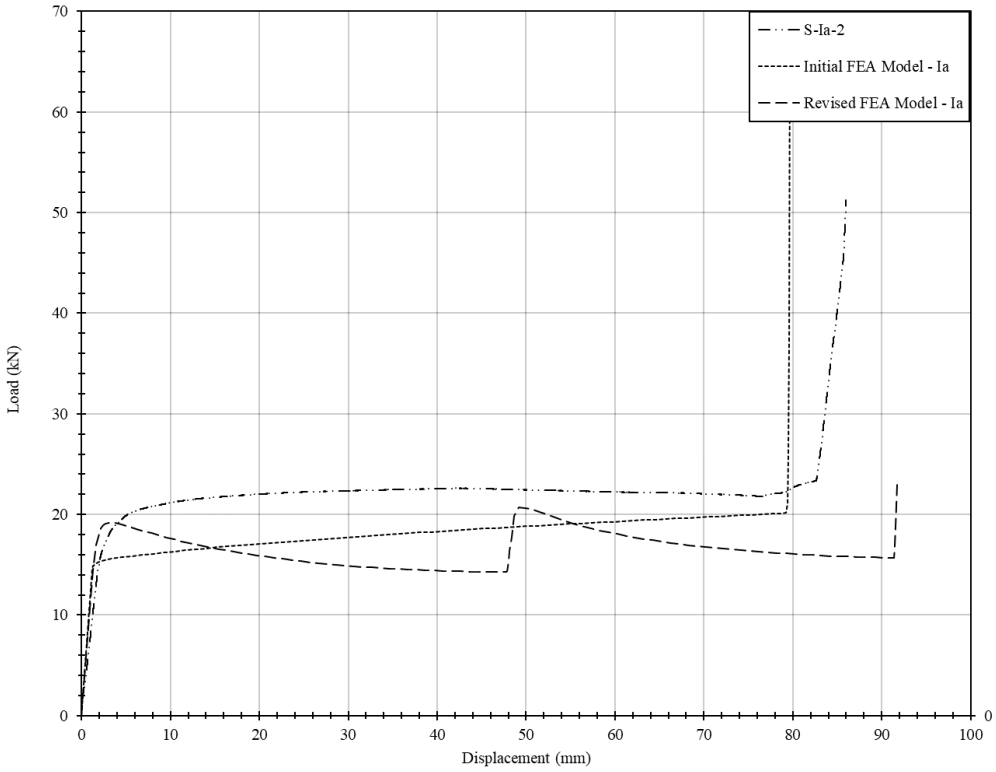

Specimen	S-Ib-1	Description	Angles with leg lengths of 50.8 mm and thickness of 6.35 mm

Energy absorption efficiency, and experimental and idealized load-displacement relationships

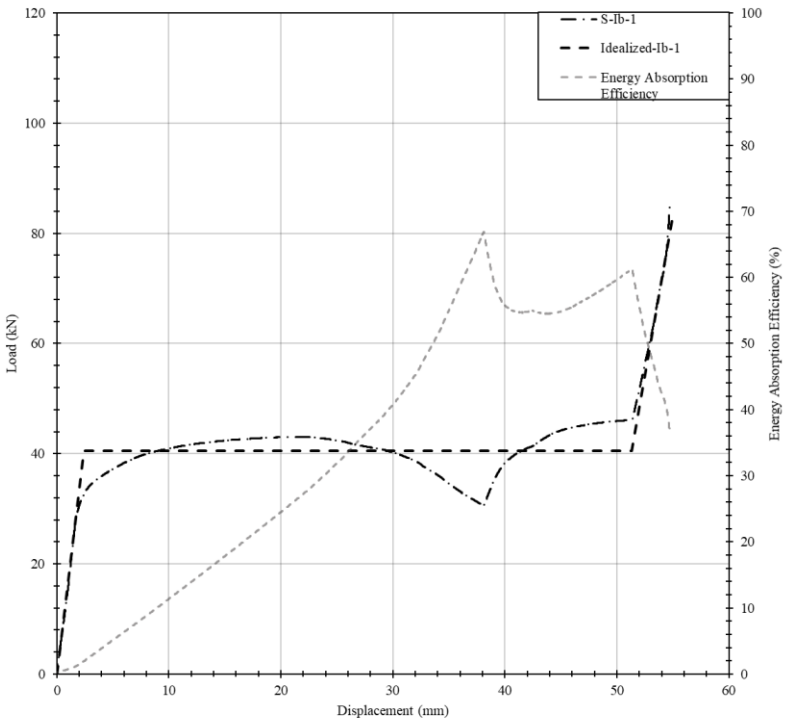

Experimental load-displacement, preliminary FEA model, and revised FEA model

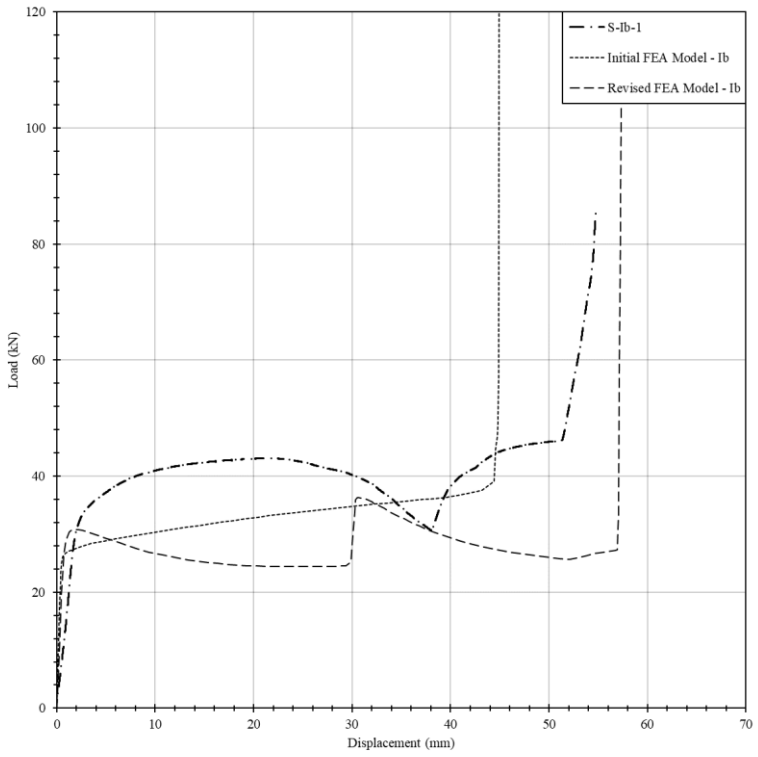

Specimen	S-Ib-2	Description	Angles with leg lengths of 50.8 mm and thickness of 6.35 mm

Energy absorption efficiency, and experimental and idealized load-displacement relationships

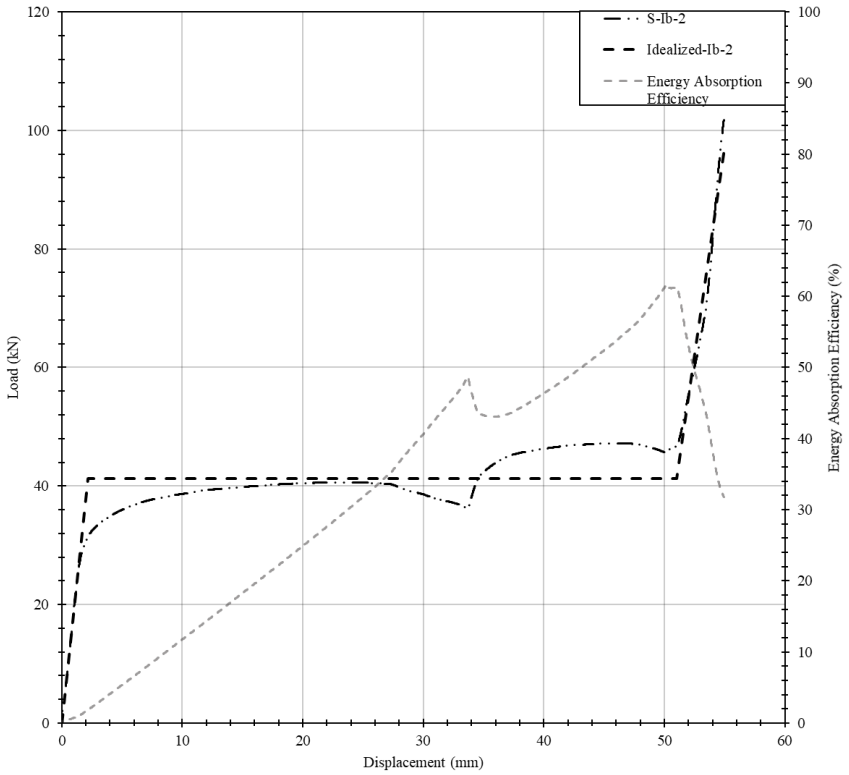

Experimental load-displacement, preliminary FEA model, and revised FEA model

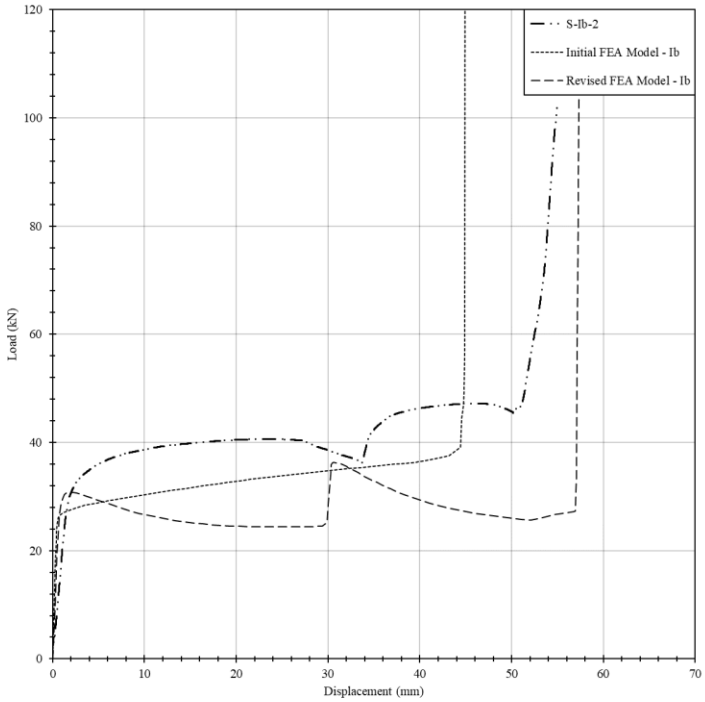

Specimen	S-Ic-1	Description	Angles with leg lengths of 76.2 mm and thickness of 12.7 mm

Energy absorption efficiency, and experimental and idealized load-displacement relationships

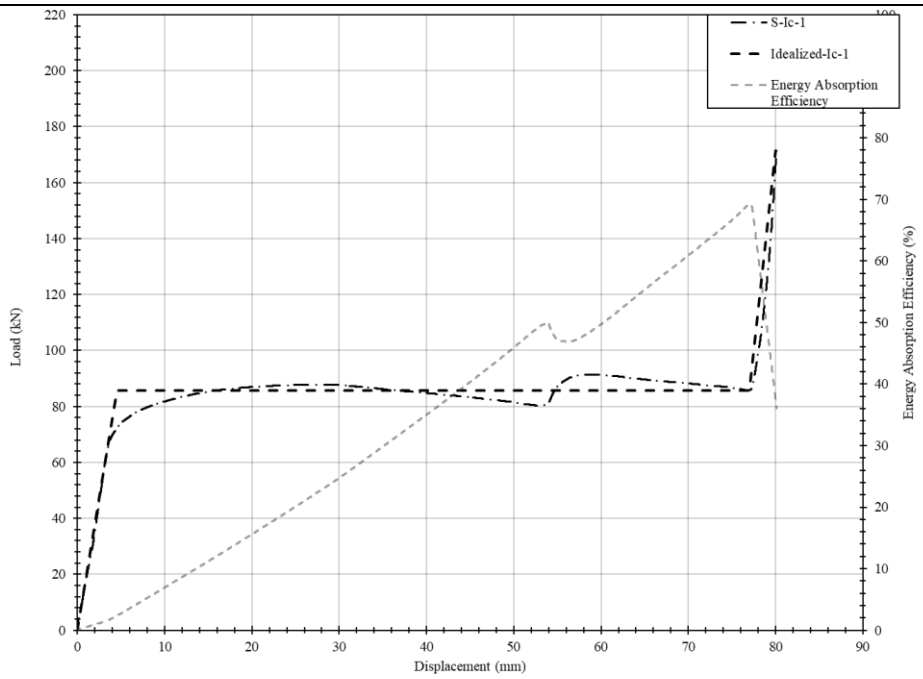

Experimental load-displacement, preliminary FEA model, and revised FEA model

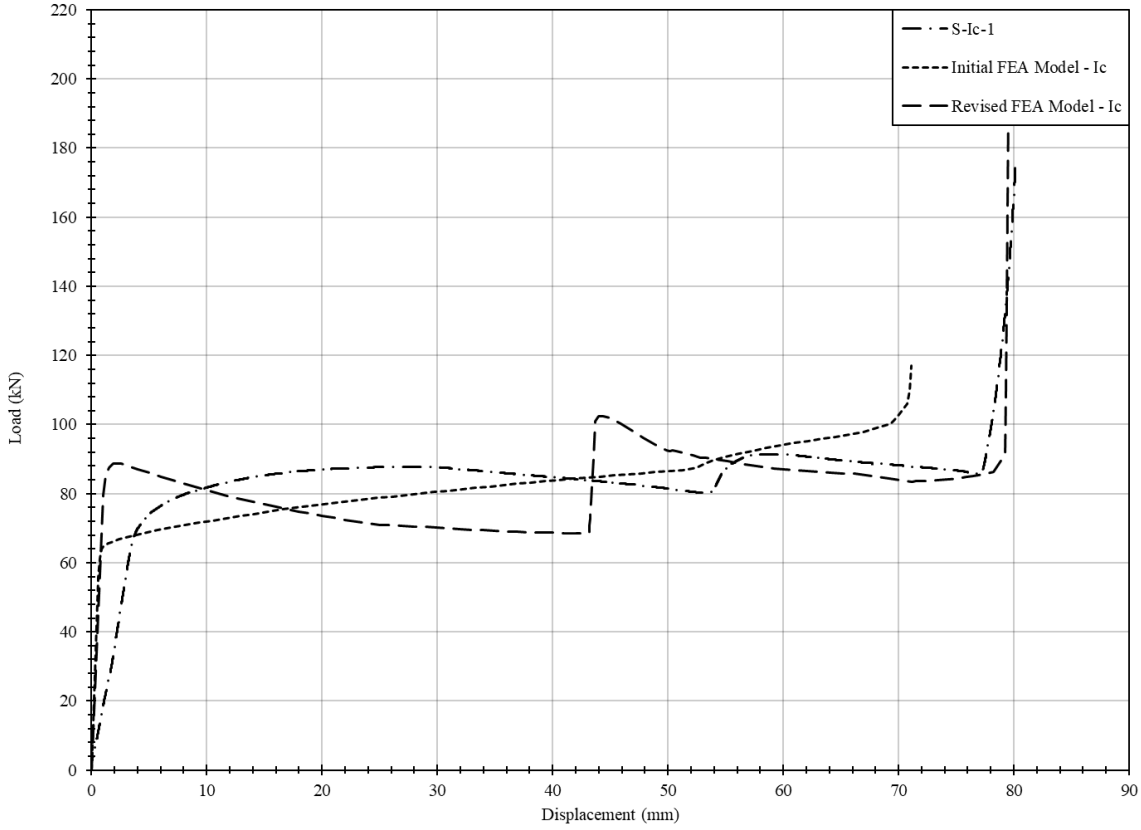

Specimen	S-Ic-2	Description	Angles with leg lengths of 76.2 mm and thickness of 12.7 mm

Energy absorption efficiency, and experimental and idealized load-displacement relationships

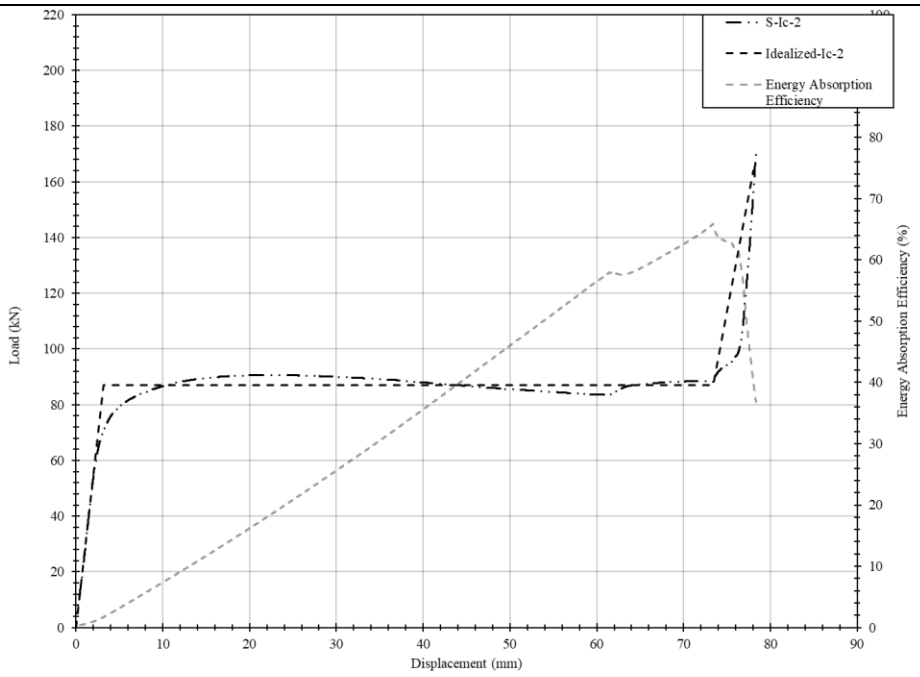

Experimental load-displacement, preliminary FEA model, and revised FEA model

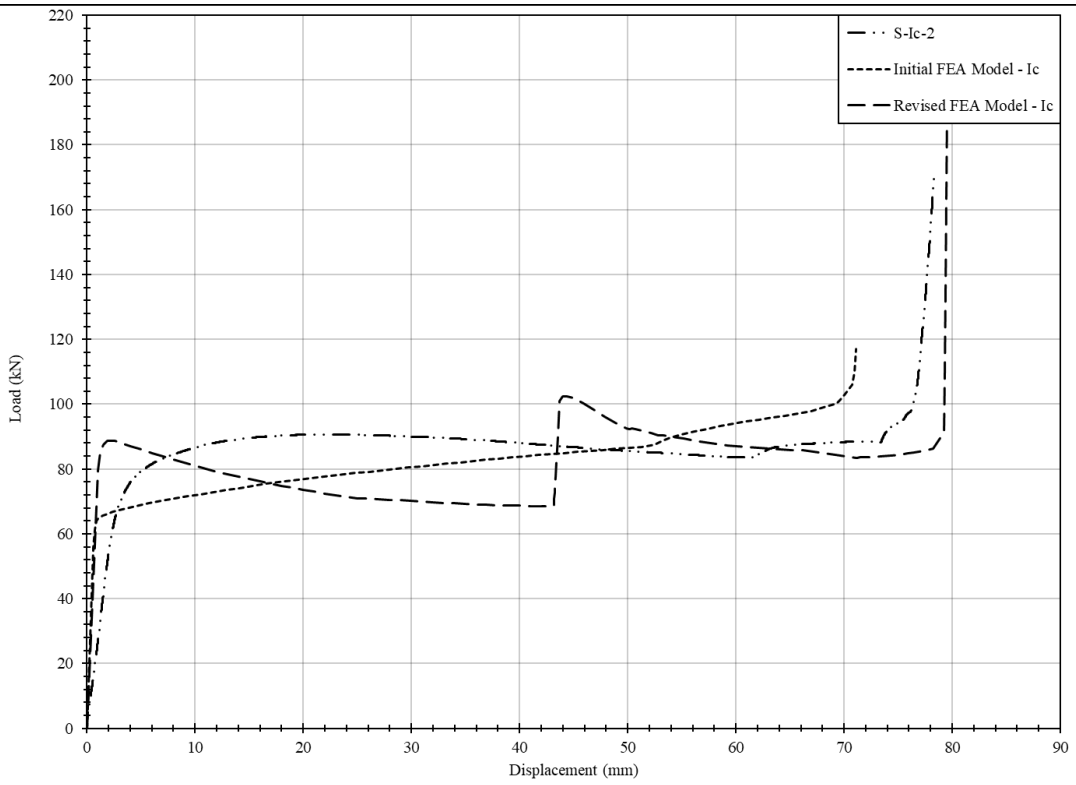

Specimen	S-Id-1	Description	Angles with leg lengths of 76.2 mm and thickness of 6.35 mm. Additional centre weld.

Energy absorption efficiency and experimental load-displacement relationships

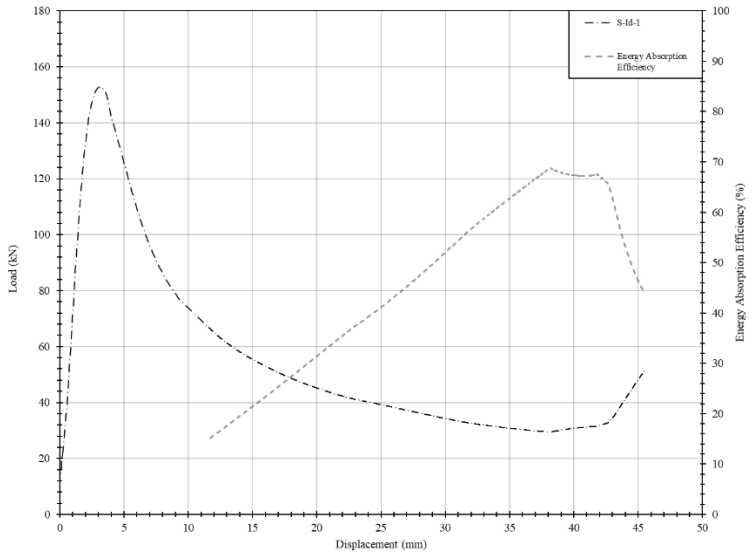

Experimental load-displacement, preliminary FEA model, and revised FEA model

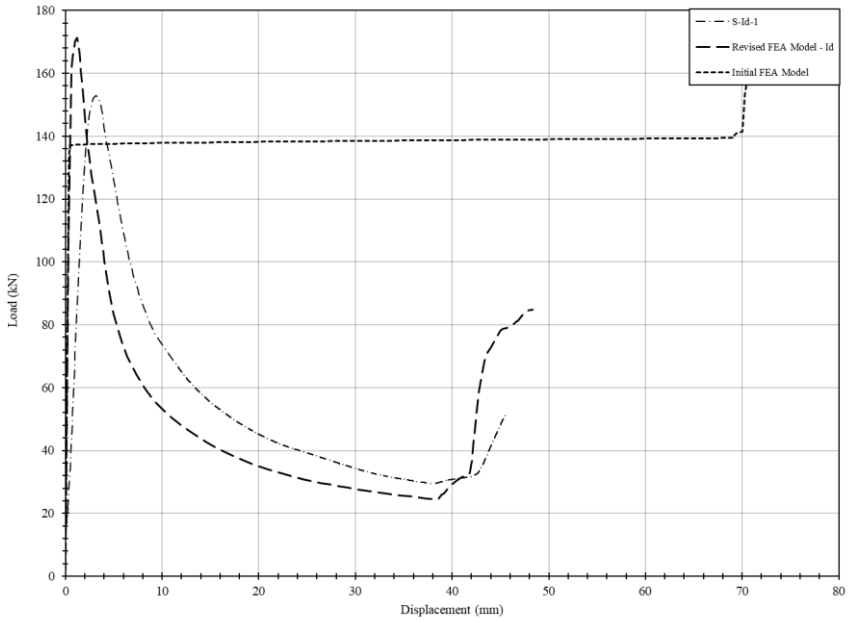

Specimen	S-Id-2	Description	Angles with leg lengths of 76.2 mm and thickness of 6.35 mm. Additional centre weld.

Energy absorption efficiency, and experimental and idealized load-displacement relationships

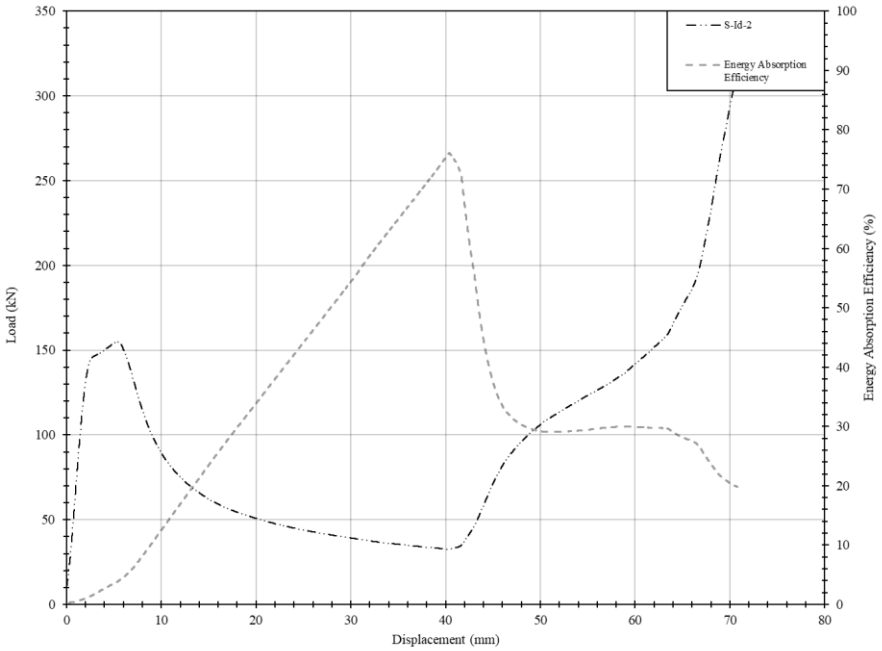

Experimental load-displacement, preliminary FEA model, and revised FEA model

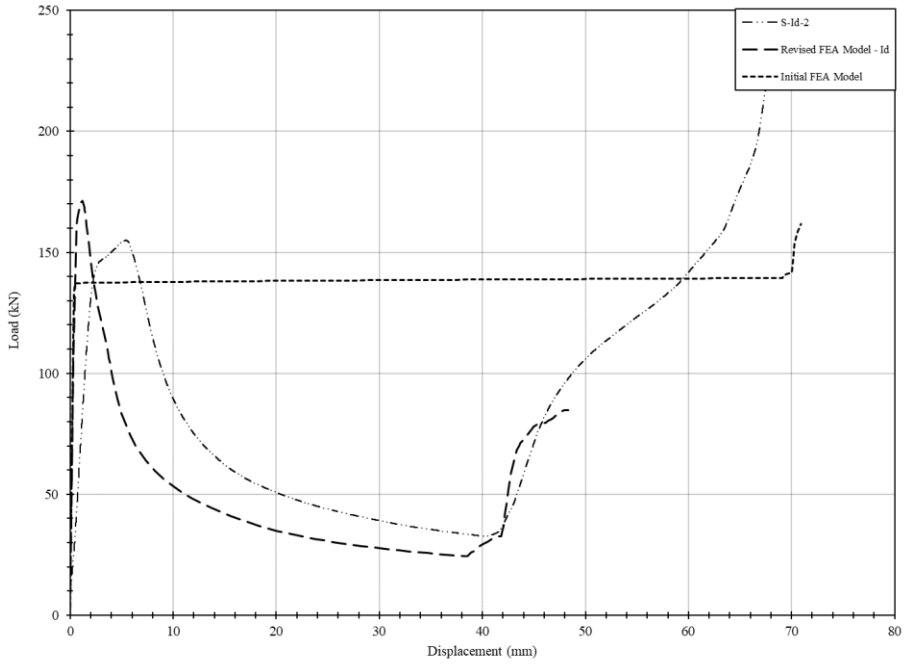

Specimen	S-IIa-1	Description	Circular HSS with outer diameter of 88.9 mm and thickness of 6.35 mm

Energy absorption efficiency, and experimental and idealized load-displacement relationships

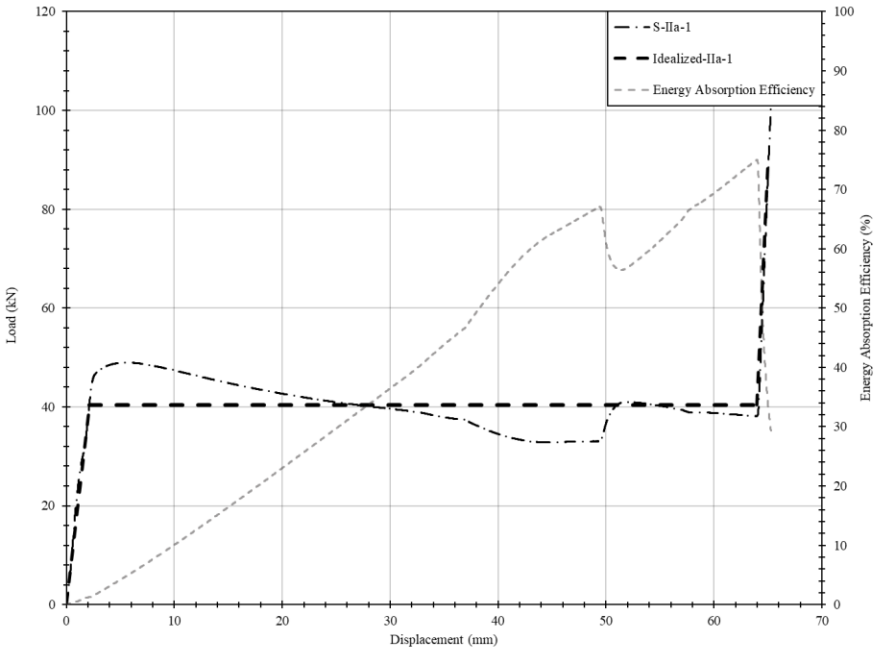

Experimental load-displacement, preliminary FEA model, and revised FEA model

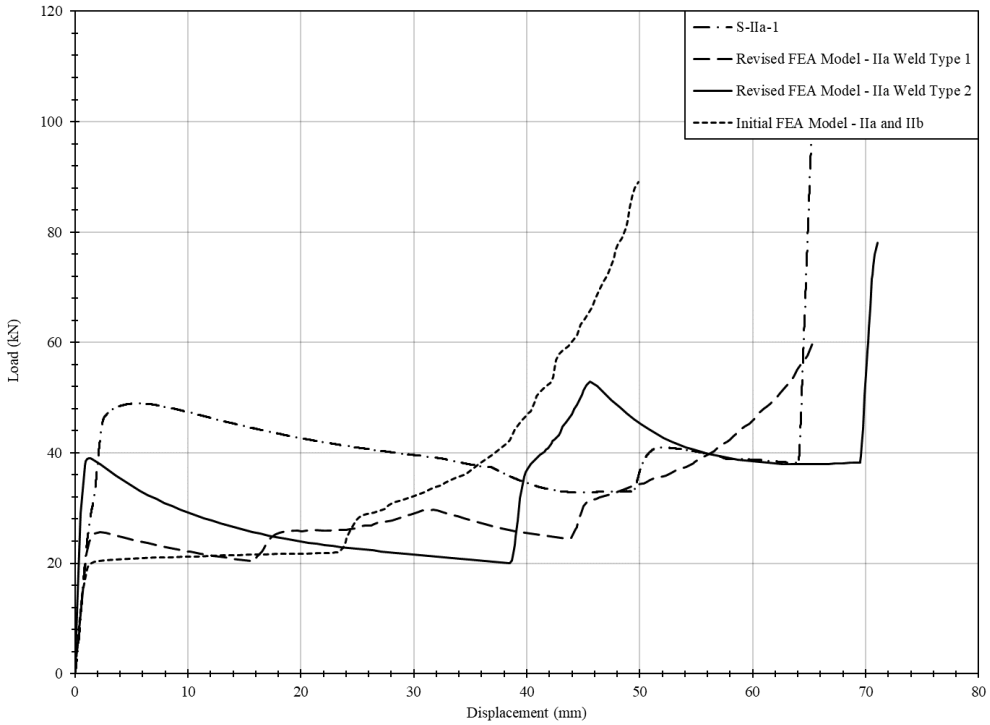

Specimen	S-IIa-2	Description	Circular HSS with outer diameter of 88.9 mm and thickness of 6.35 mm

Energy absorption efficiency, and experimental and idealized load-displacement relationships

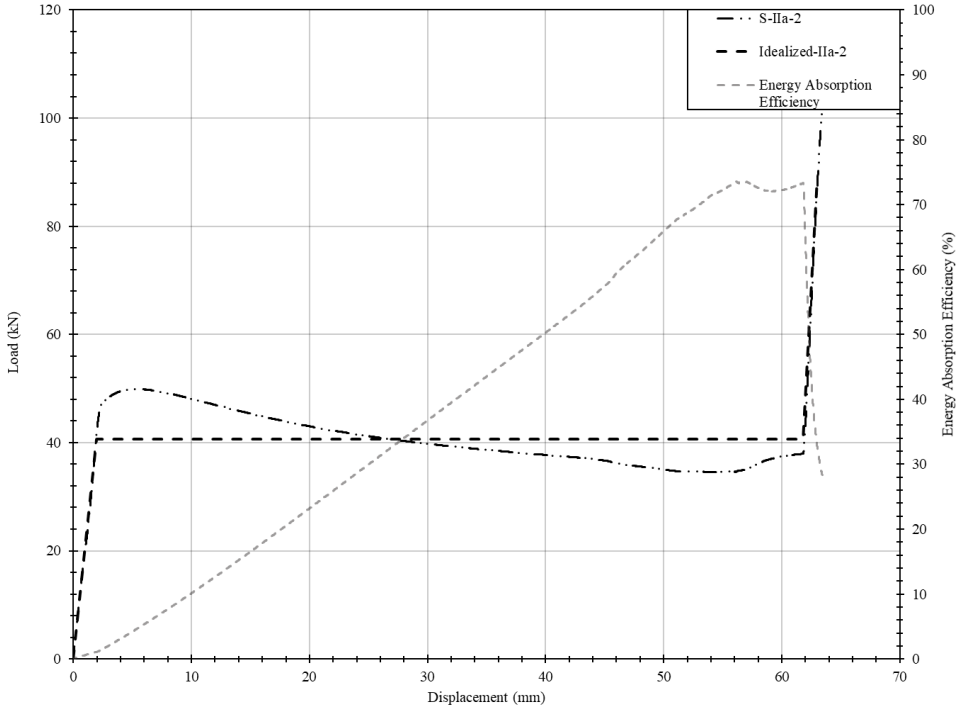

Experimental load-displacement, preliminary FEA model, and revised FEA model

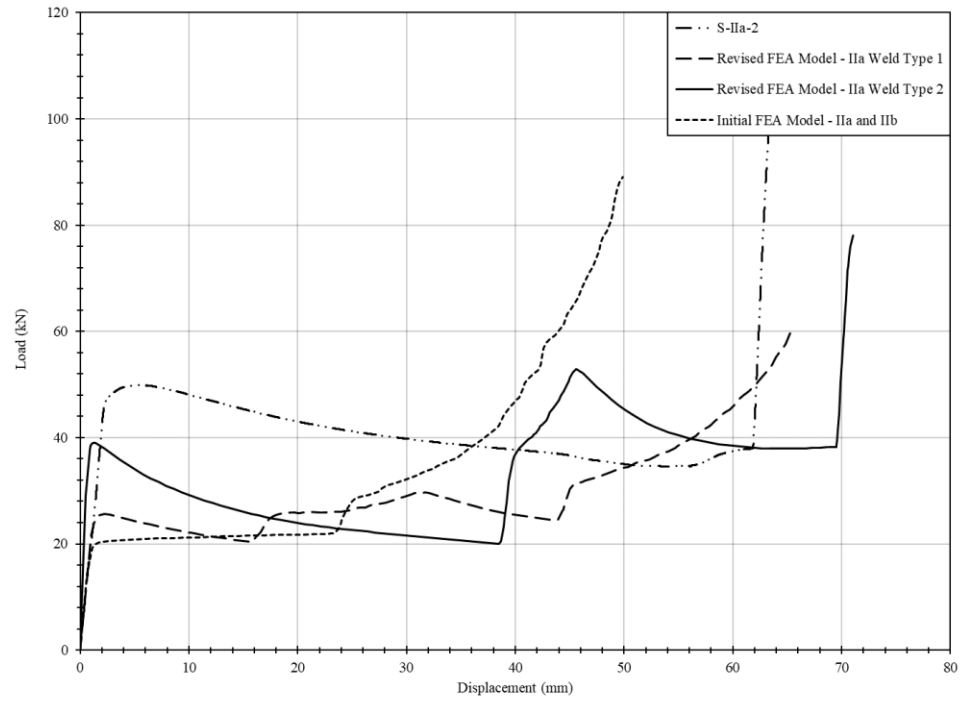

Specimen	S-IIb-1	**Description**	Circular HSS with outer diameter of 88.9 mm and thickness of 6.35 mm Depth of 101.6 mm

Energy absorption efficiency, and experimental and idealized load-displacement relationships

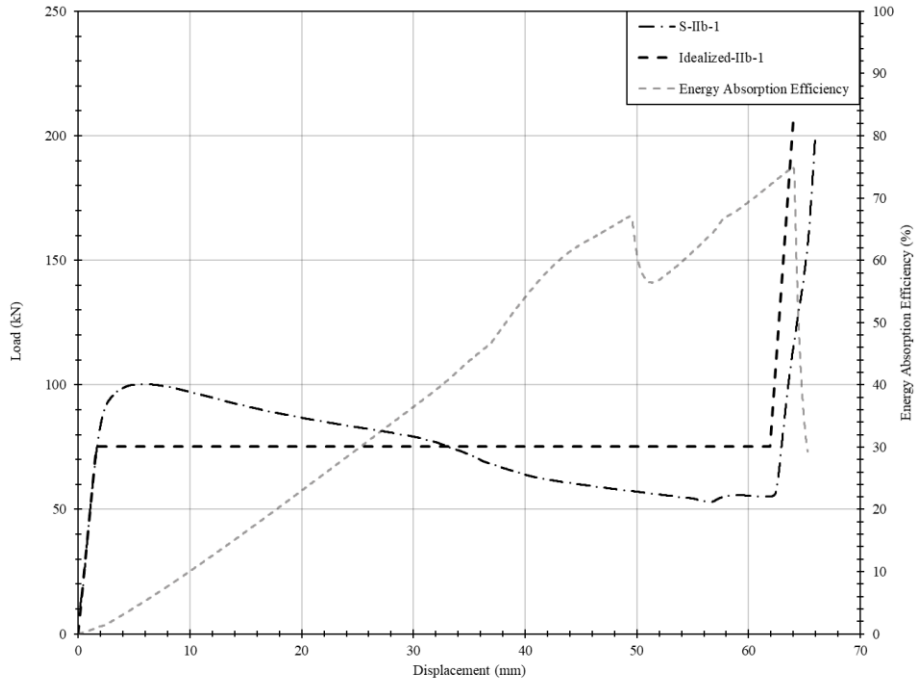

Experimental load-displacement, preliminary FEA model, and revised FEA model

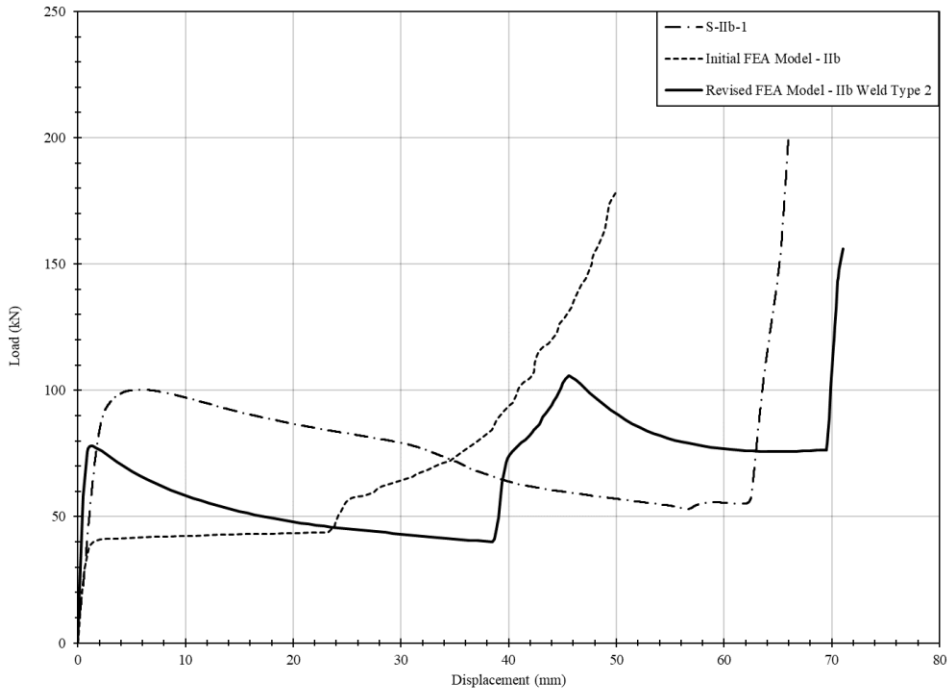

Specimen	S-IIb-2	**Description**	Circular HSS with outer diameter of 88.9 mm and thickness of 6.35 mm Depth of 101.6 mm

Energy absorption efficiency, and experimental and idealized load-displacement relationships

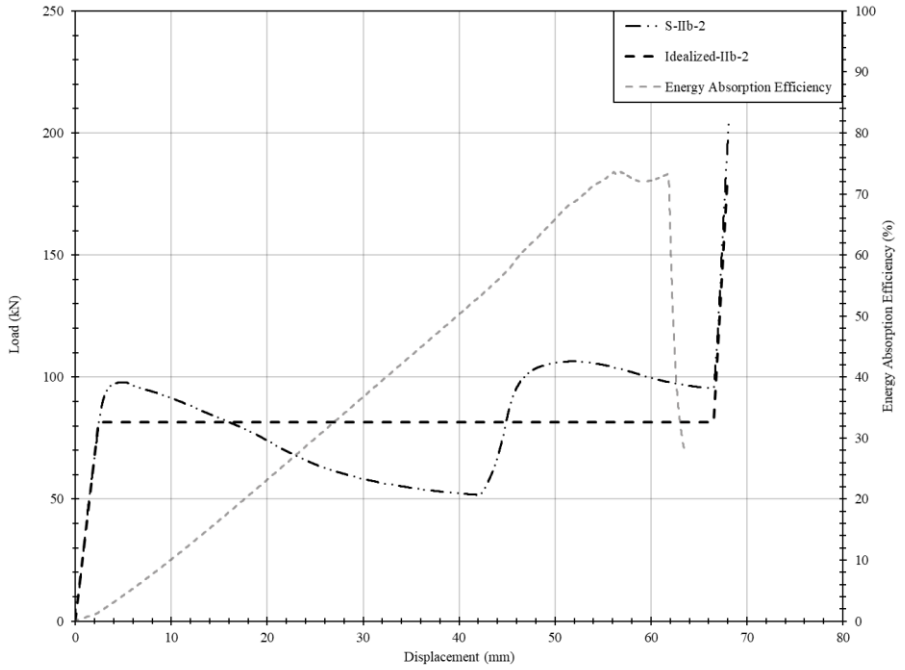

Experimental load-displacement, preliminary FEA model, and revised FEA model

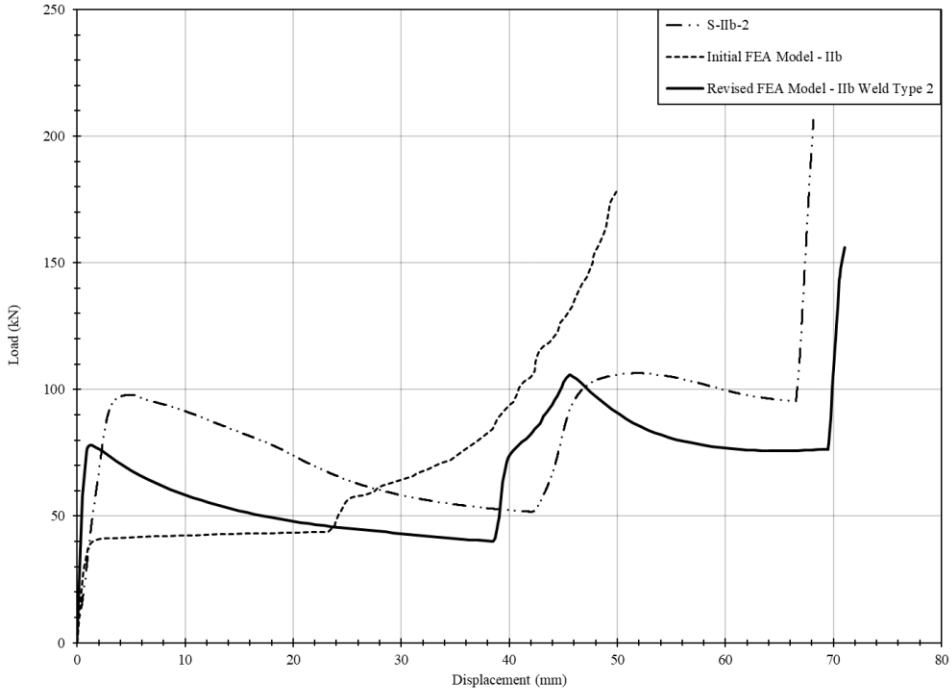

Specimen	S-IIc-1	Description	Circular HSS with outer diameter of 127 mm and thickness of 6.35 mm

Energy absorption efficiency, and experimental and idealized load-displacement relationships

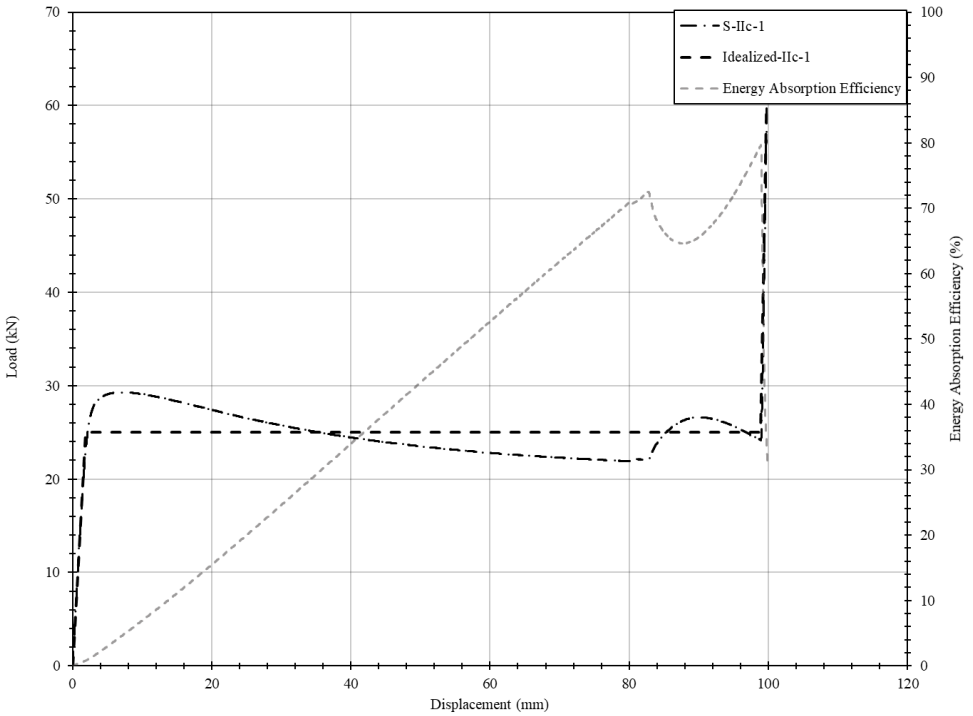

Experimental load-displacement, preliminary FEA model, and revised FEA model

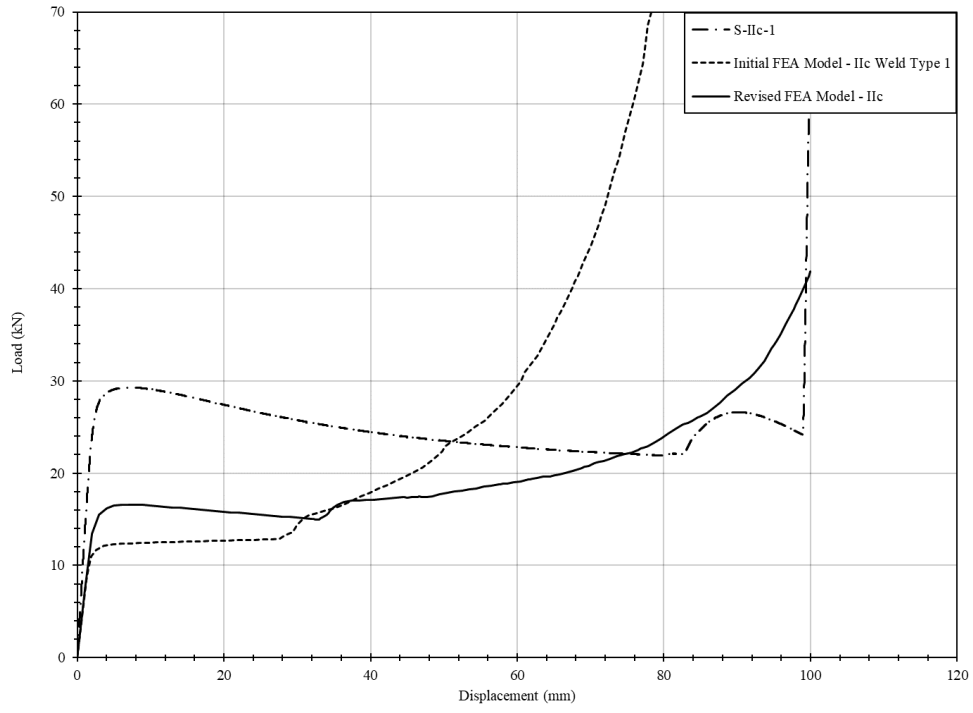

Specimen	S-IIc-2	Description	Circular HSS with outer diameter of 127 mm and thickness of 6.35 mm

Energy absorption efficiency, and experimental and idealized load-displacement relationships

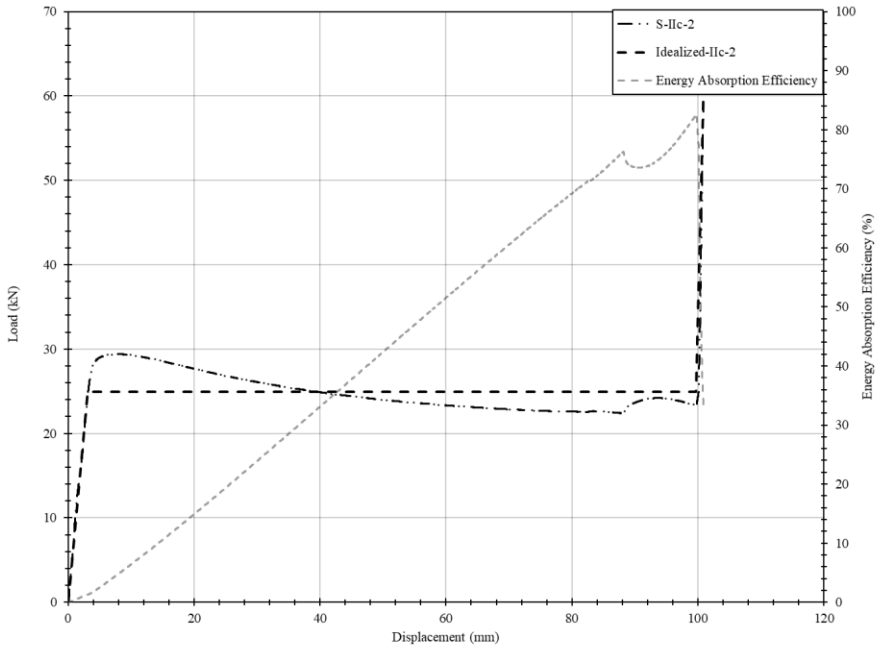

Experimental load-displacement, preliminary FEA model, and revised FEA model

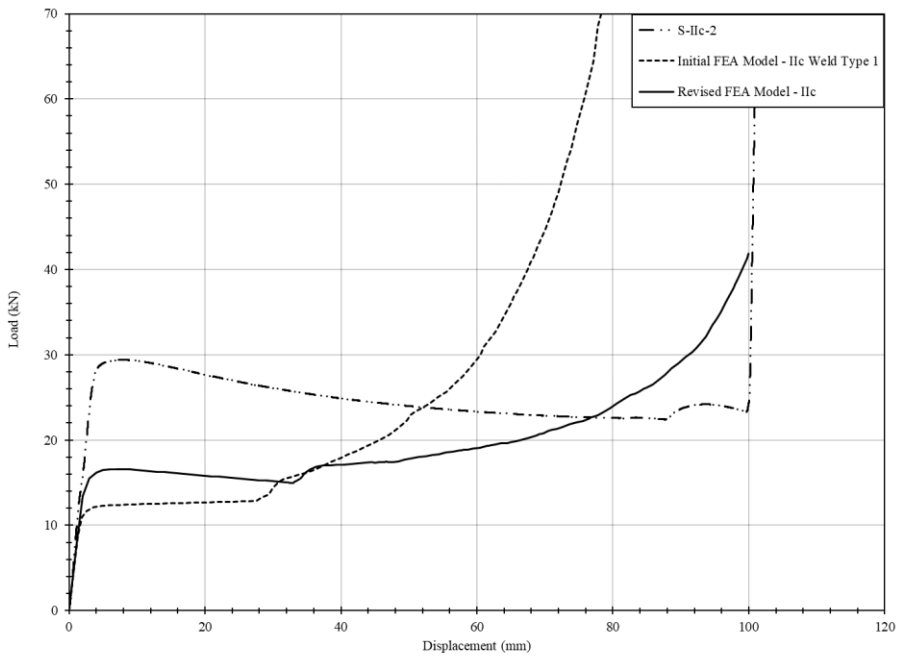

Specimen	S-IId-1	**Description**	Arcs from circular HSS of outer diameter of 127 mm and thickness of 6.35 mm.

Energy absorption efficiency and experimental load-displacement relationships

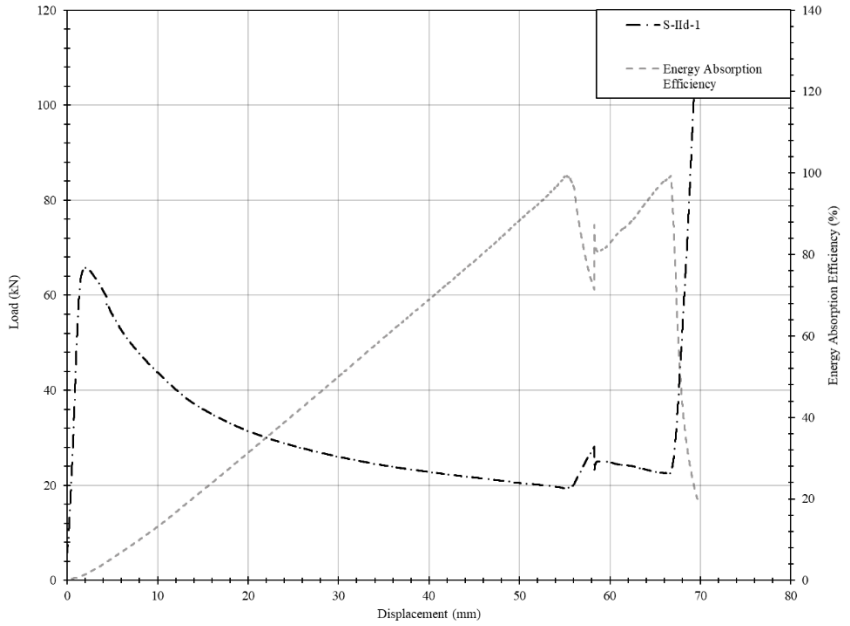

Experimental load-displacement, preliminary FEA model, and revised FEA model

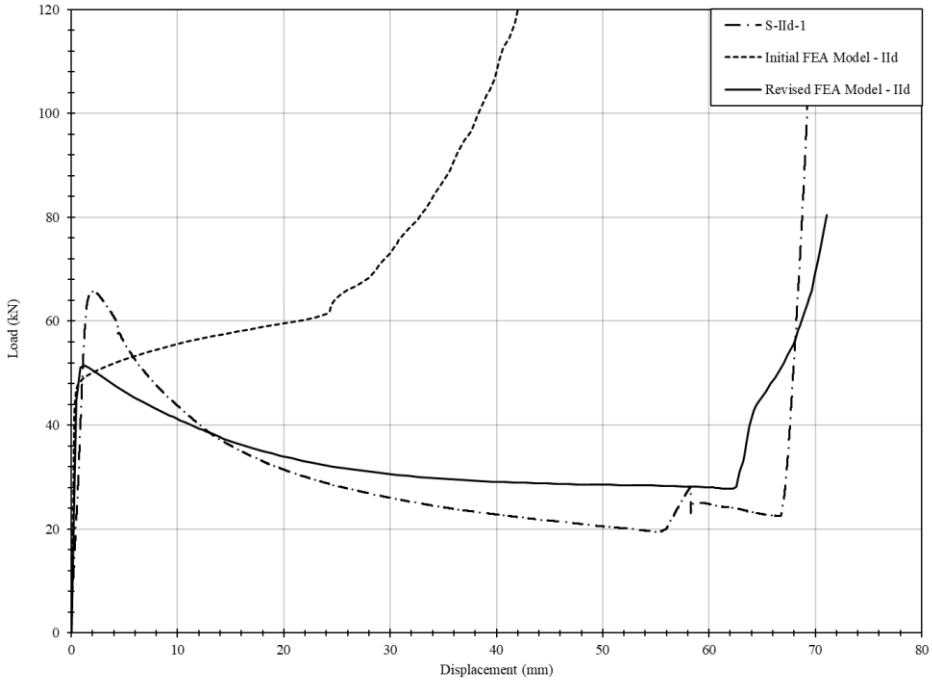

Specimen	S-IId-2	**Description**	Arcs from circular HSS of outer diameter of 127 mm and thickness of 6.35 mm.

Energy absorption efficiency, and experimental and idealized load-displacement relationships

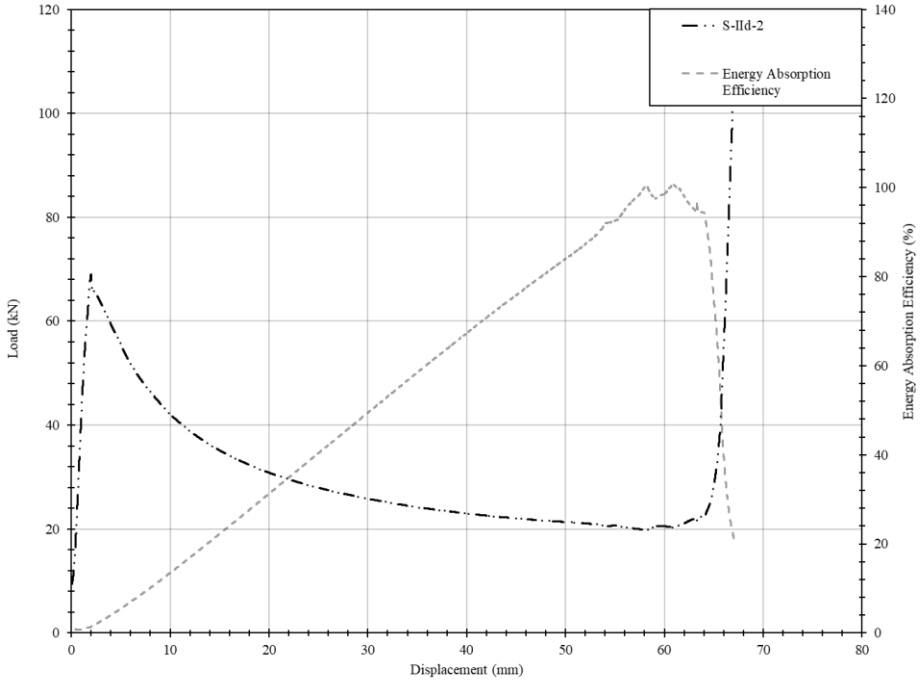

Experimental load-displacement, preliminary FEA model, and revised FEA model

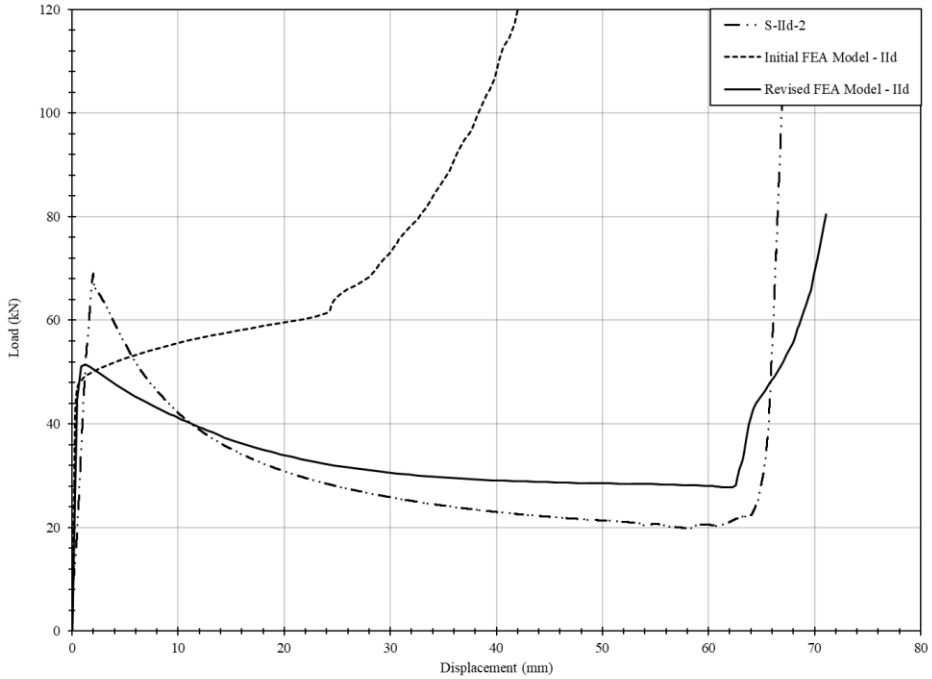

Specimen	S-IIe-1	**Description**	Circular HSS with outer diameter of 88.9 mm and thickness of 6.35 mm Circular HSS with outer diameter of 60.325 mm and thickness of 3.175 mm

Energy absorption efficiency, and experimental and idealized load-displacement relationships

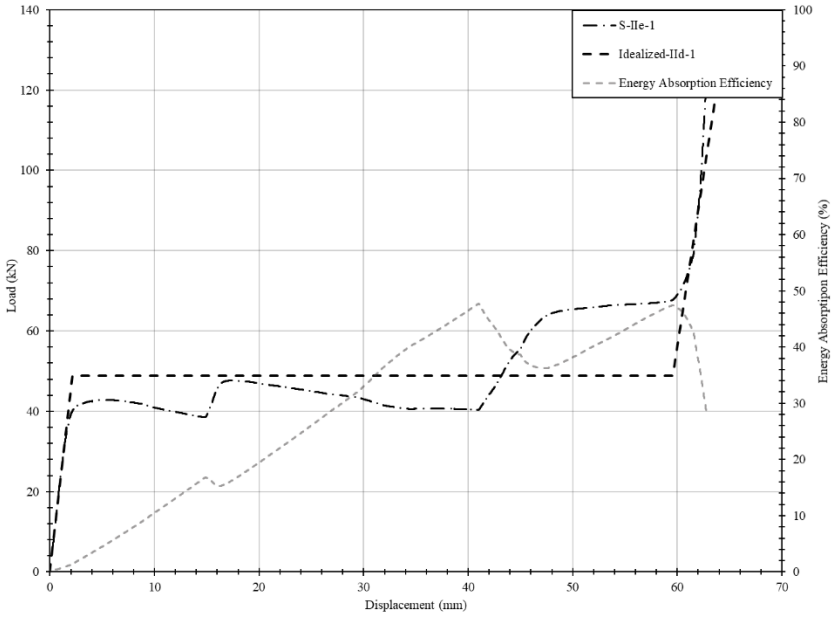

Experimental load-displacement, preliminary FEA model, and revised FEA model

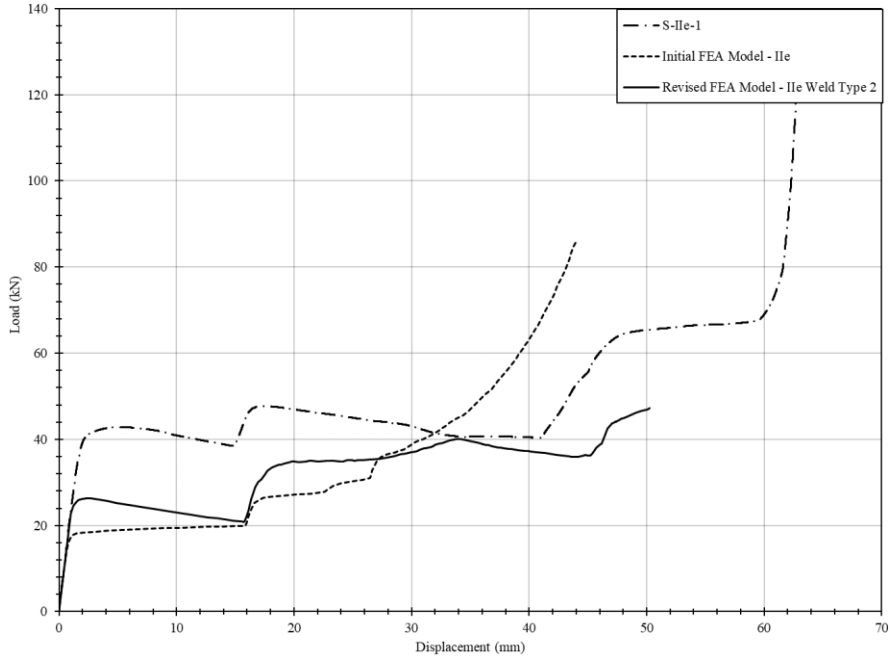

Specimen	S-IIe-2	**Description**	Circular HSS with outer diameter of 88.9 mm and thickness of 6.35 mm Circular HSS with outer diameter of 60.325 mm and thickness of 3.175 mm

Energy absorption efficiency, and experimental and idealized load-displacement relationships

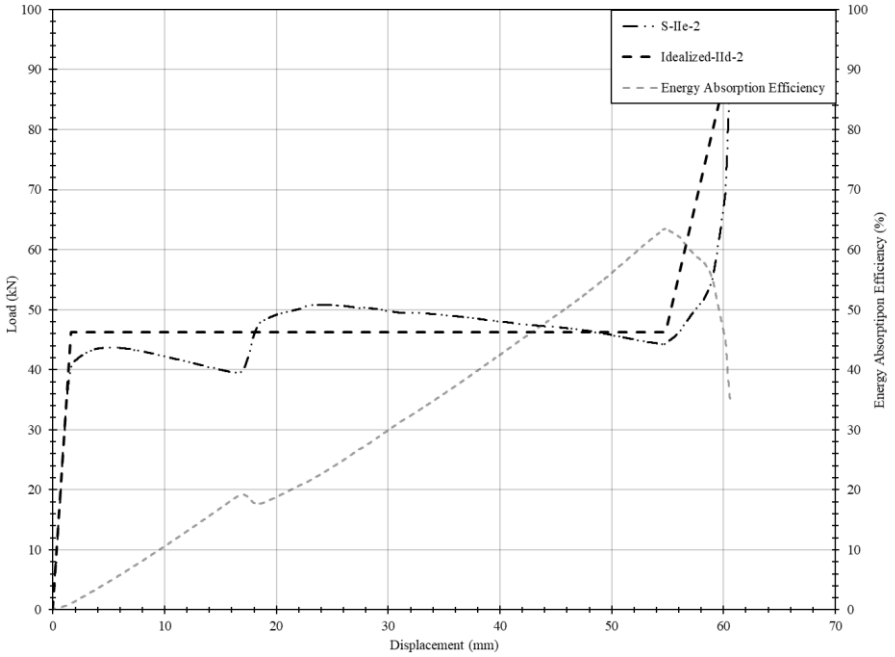

Experimental load-displacement, preliminary FEA model, and revised FEA model

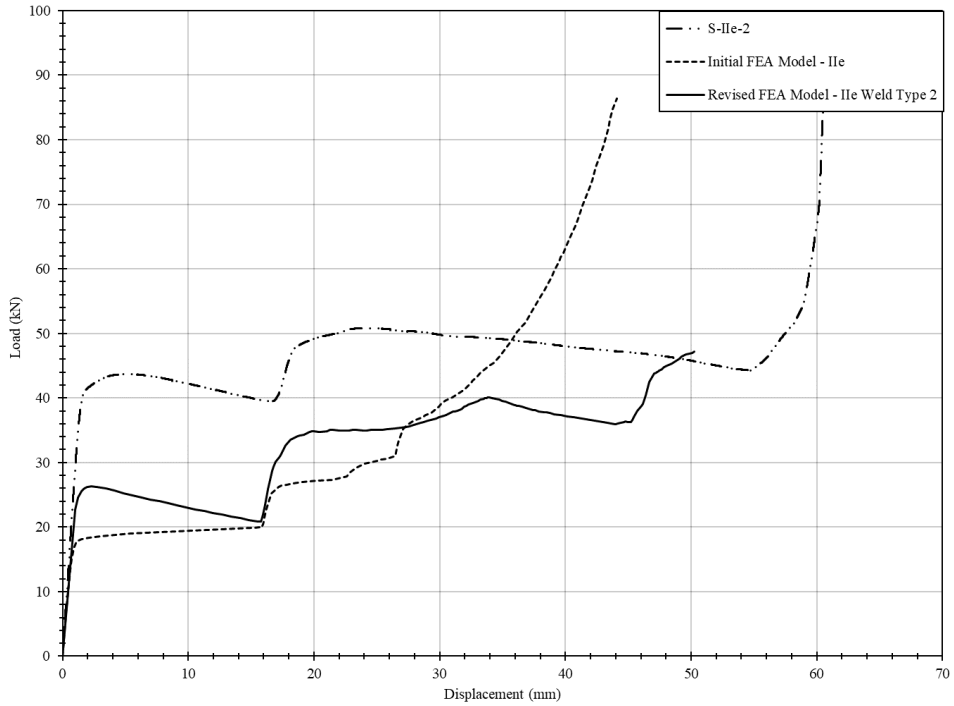

Specimen	D-Ia-1	Description	Angles with leg lengths of 76.2 mm and thickness of 6.35 mm

SDOF and experimental displacement time-histories

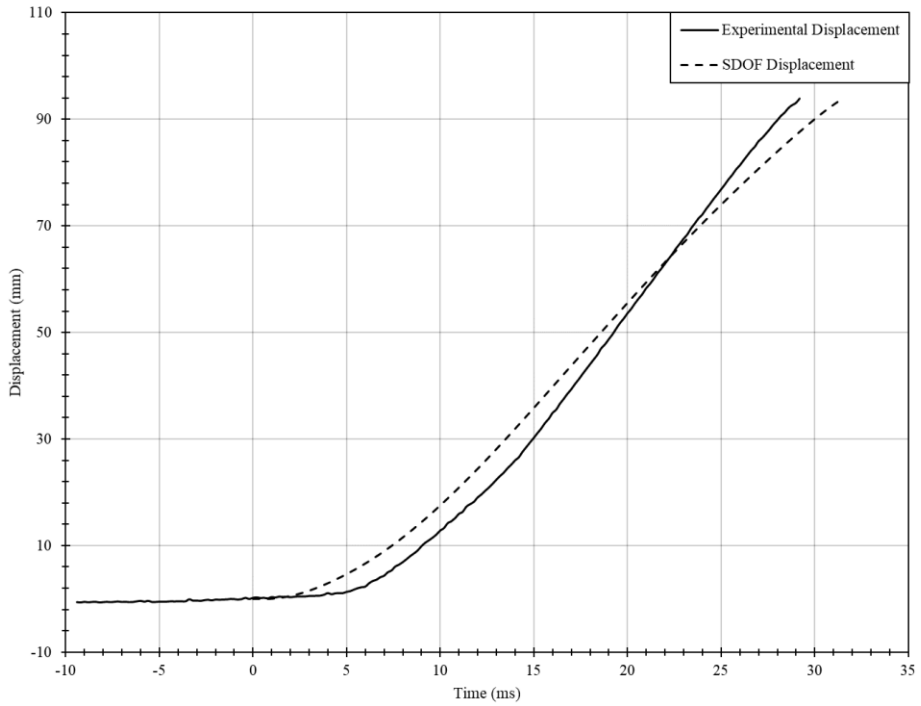

Energy absorption efficiency, and experimental and idealized load-displacement relationships

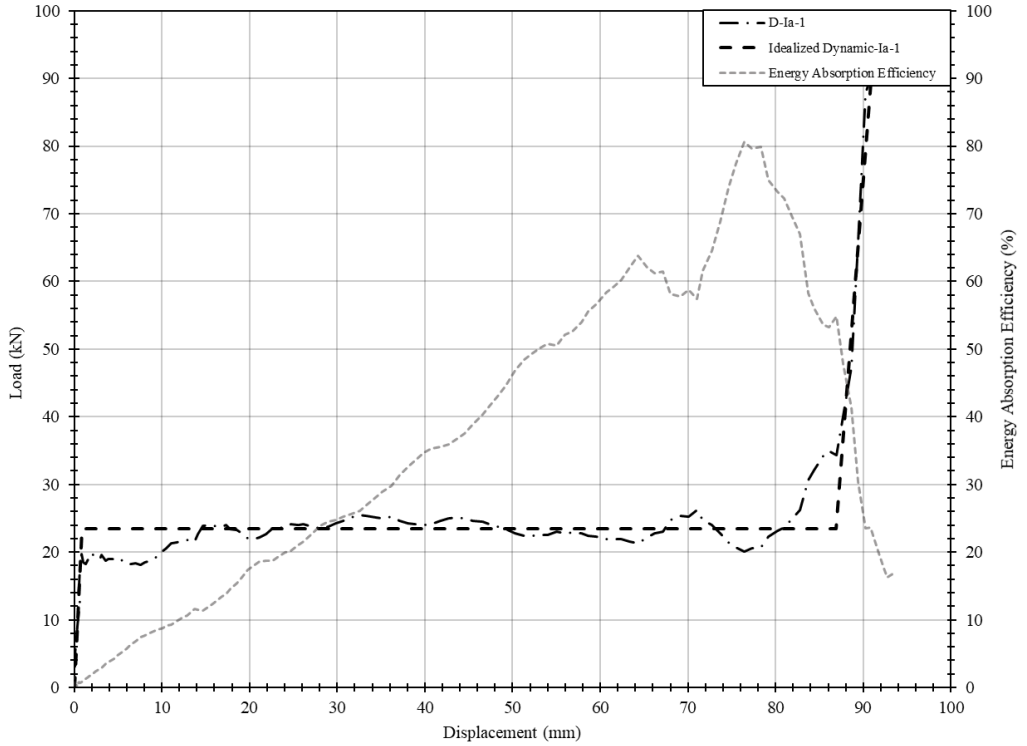

Specimen	D-Ia-2	Description	Angles with leg lengths of 76.2 mm and thickness of 6.35 mm

SDOF and experimental displacement time-histories

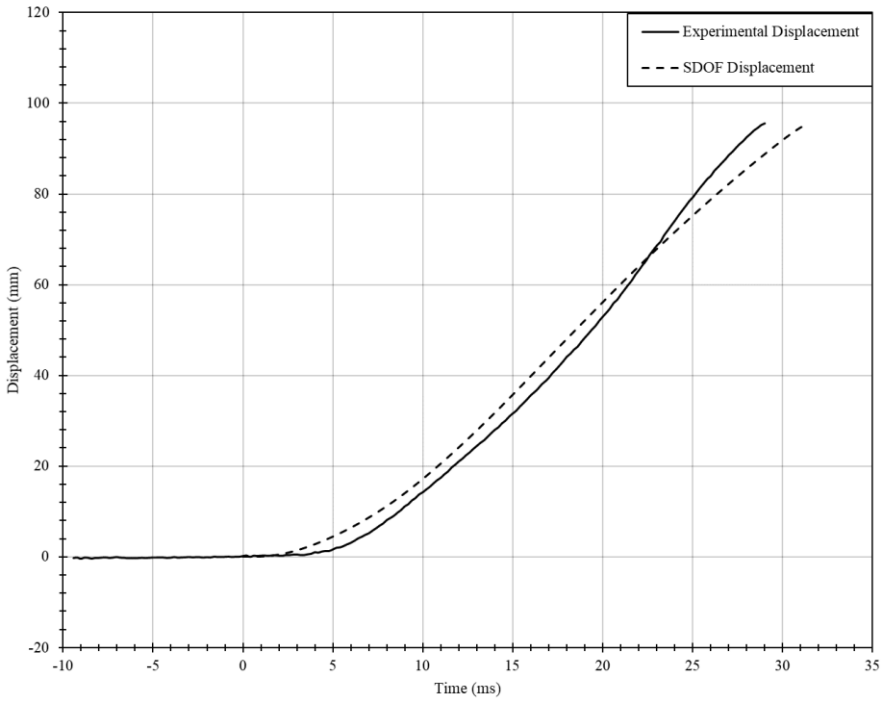

Energy absorption efficiency, and experimental and idealized load-displacement relationships

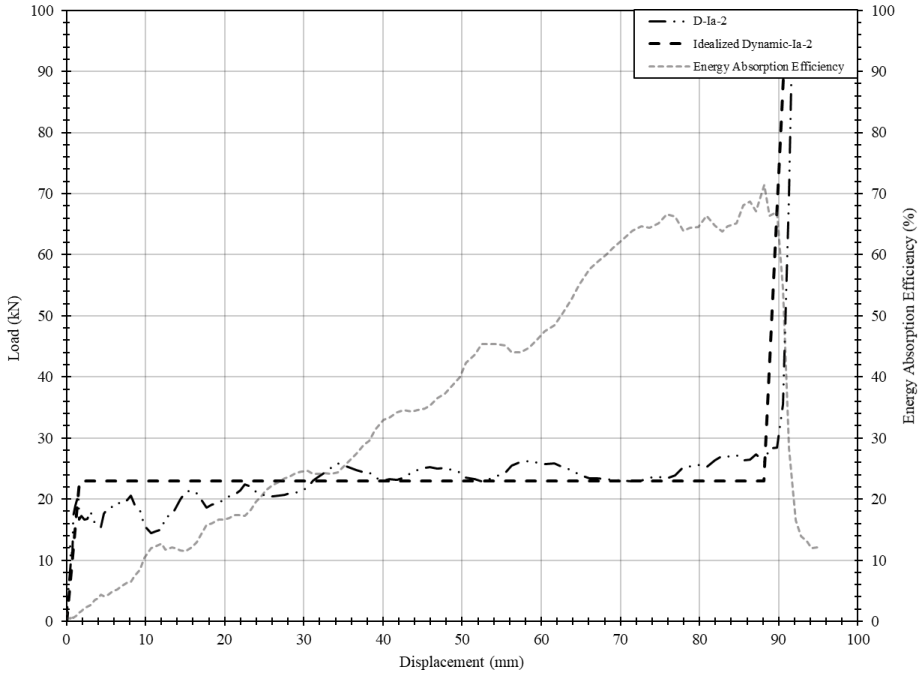

Specimen	D-Ib-1	Description	Angles with leg lengths of 50.8 mm and thickness of 6.35 mm

SDOF and experimental displacement time-histories

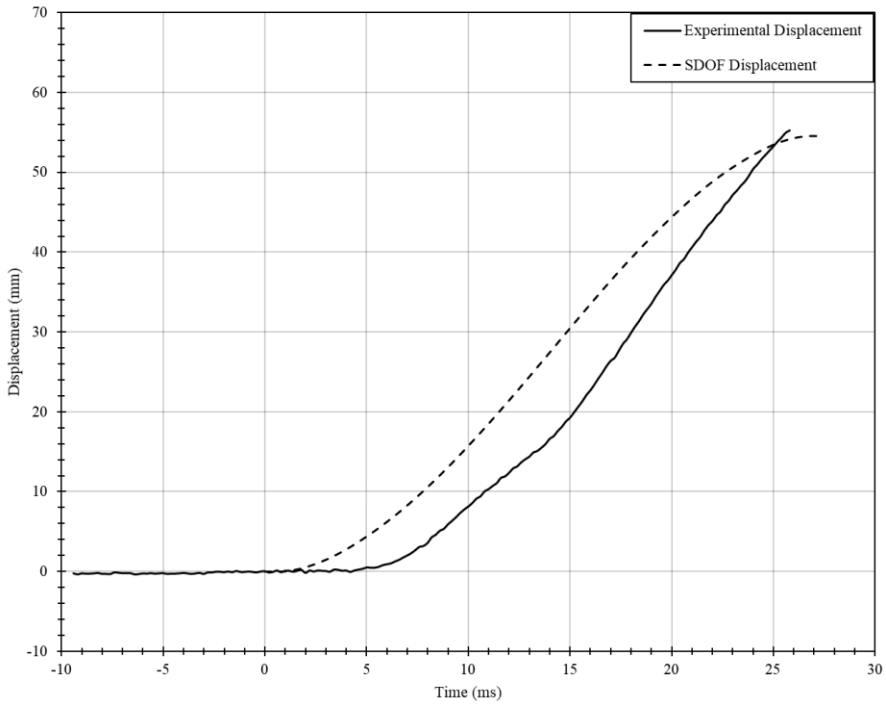

Energy absorption efficiency, and experimental and idealized load-displacement relationships

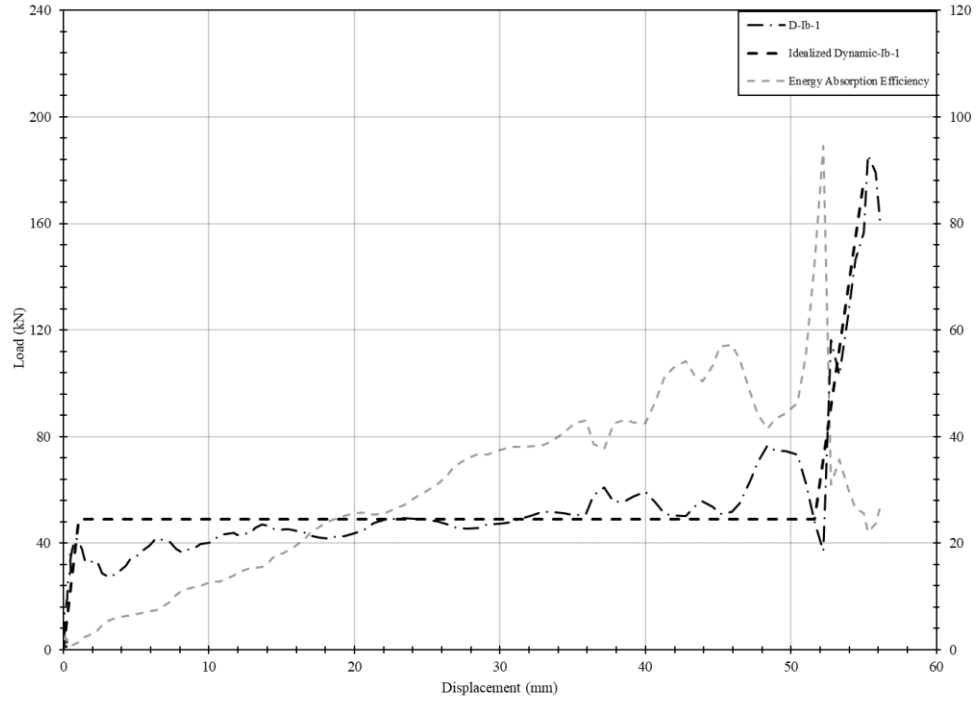

Specimen	D-Ib-2	Description	Angles with leg lengths of 50.8 mm and thickness of 6.35 mm

SDOF and experimental displacement time-histories

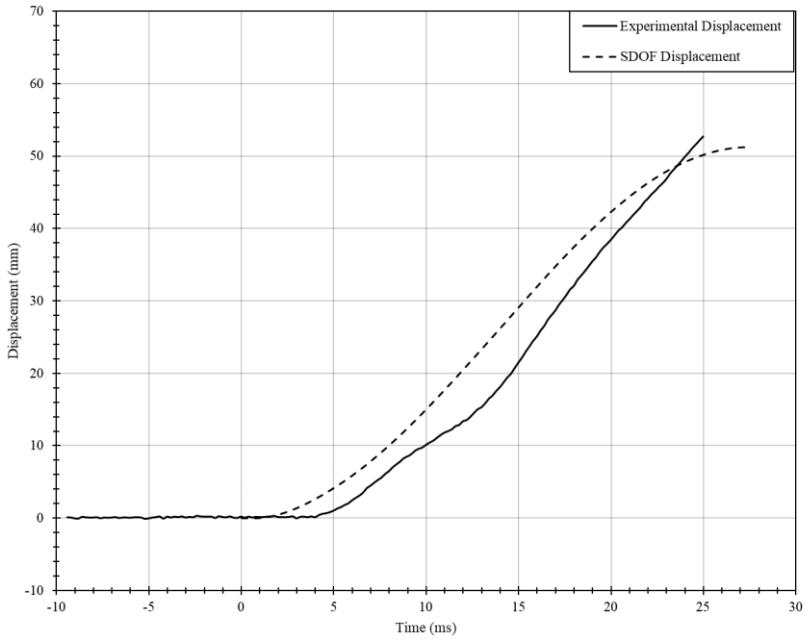

Energy absorption efficiency, and experimental and idealized load-displacement relationships

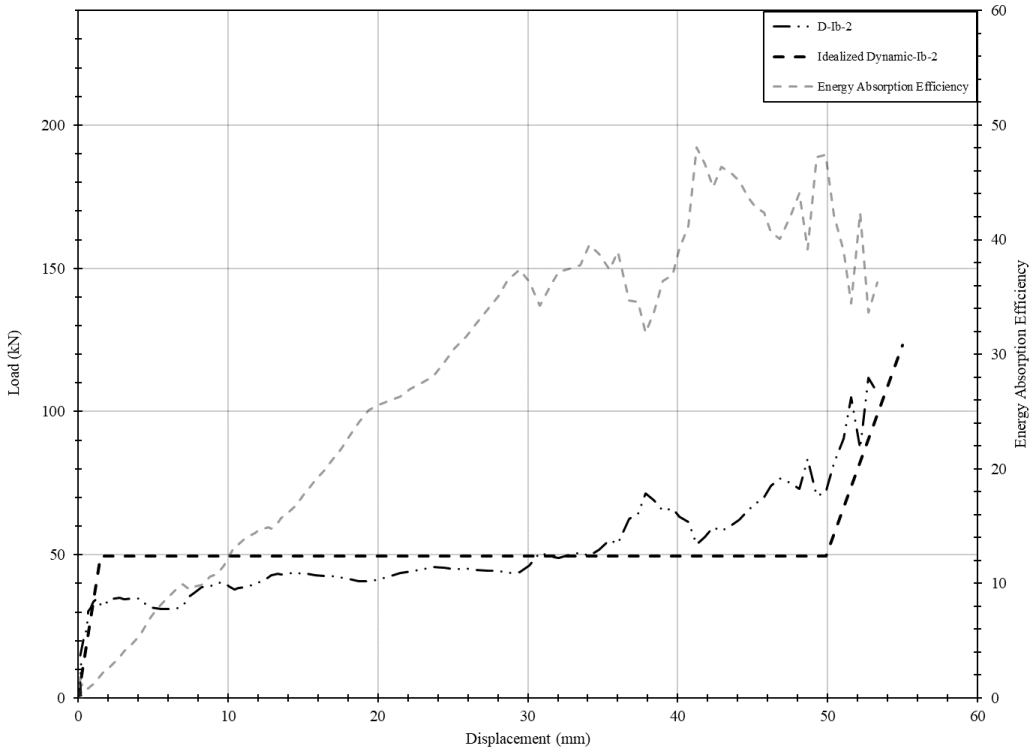

Specimen	D-Ic-1	Description	Angles with leg lengths of 76.2 mm and thickness of 12.7 mm

SDOF and experimental displacement time-histories

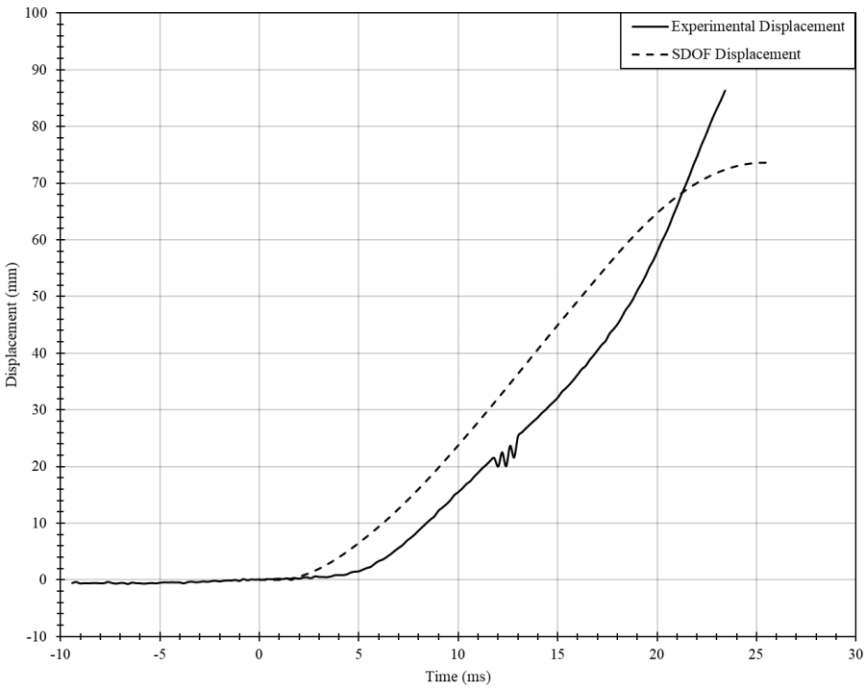

Energy absorption efficiency, and experimental and idealized load-displacement relationships

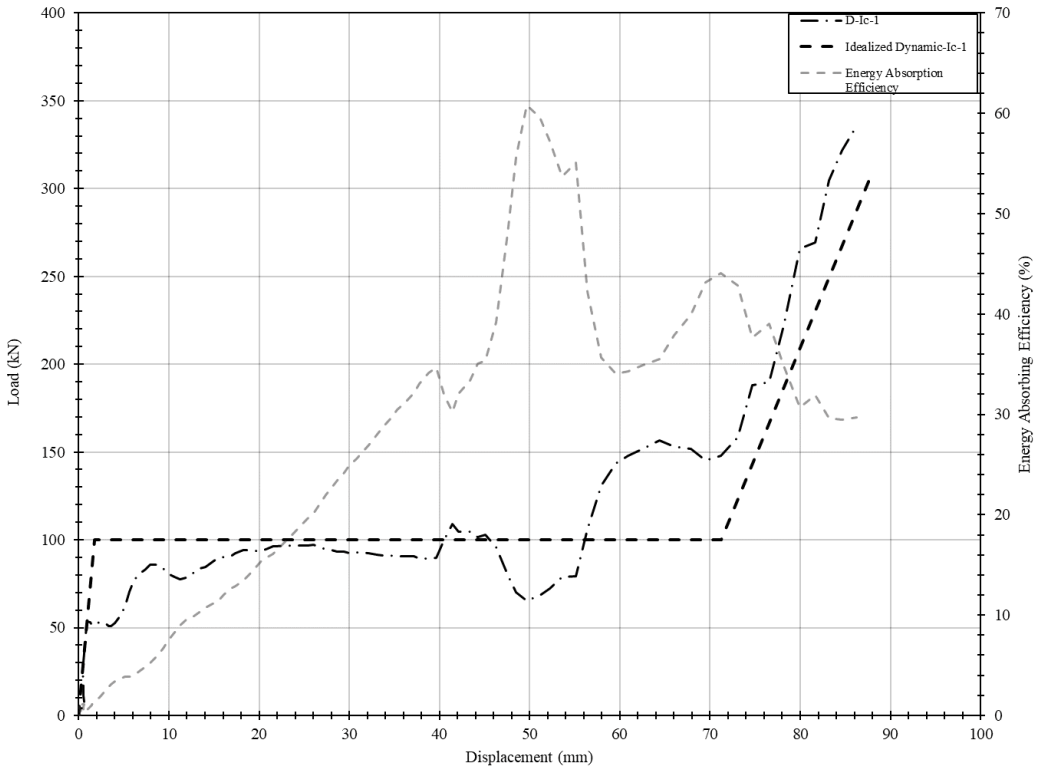

Specimen	D-Ic-2	Description	Angles with leg lengths of 76.2 mm and thickness of 12.7 mm

SDOF and experimental displacement time-histories

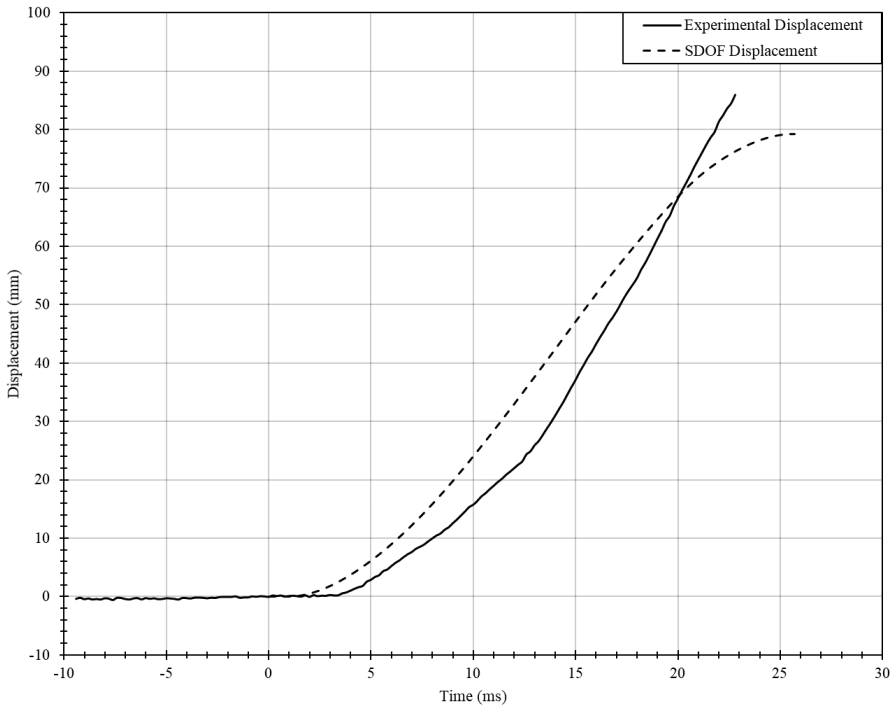

Energy absorption efficiency, and experimental and idealized load-displacement relationships

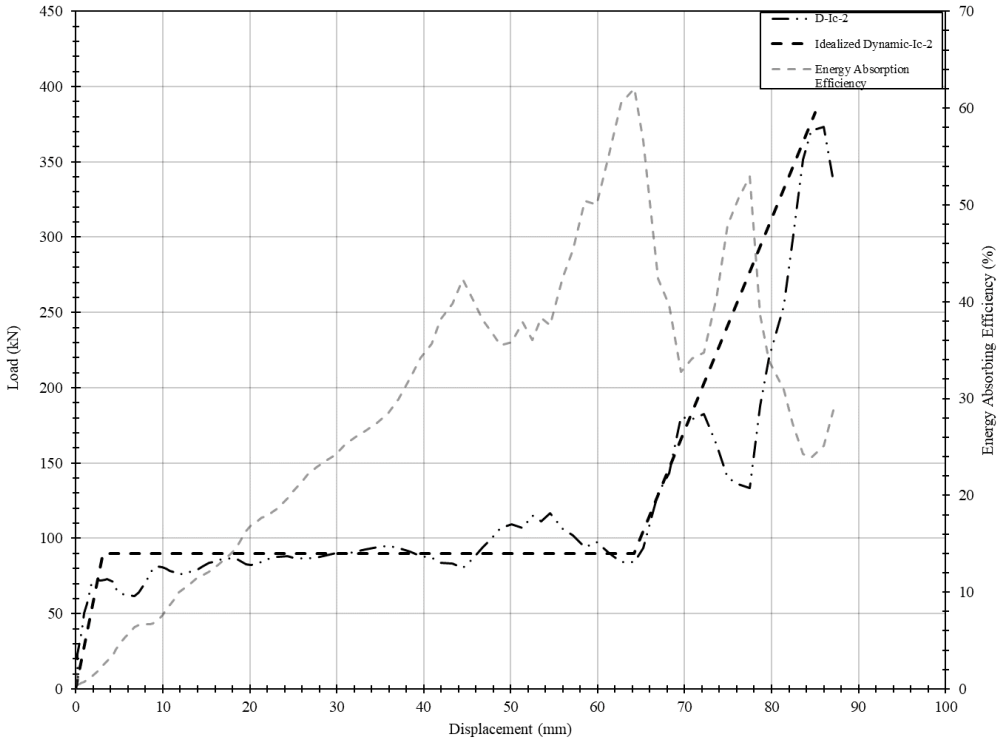

Specimen	D-Id-1	Description	Angles with leg lengths of 76.2 mm and thickness of 6.35 mm. Additional centre weld.

SDOF and experimental displacement time-histories

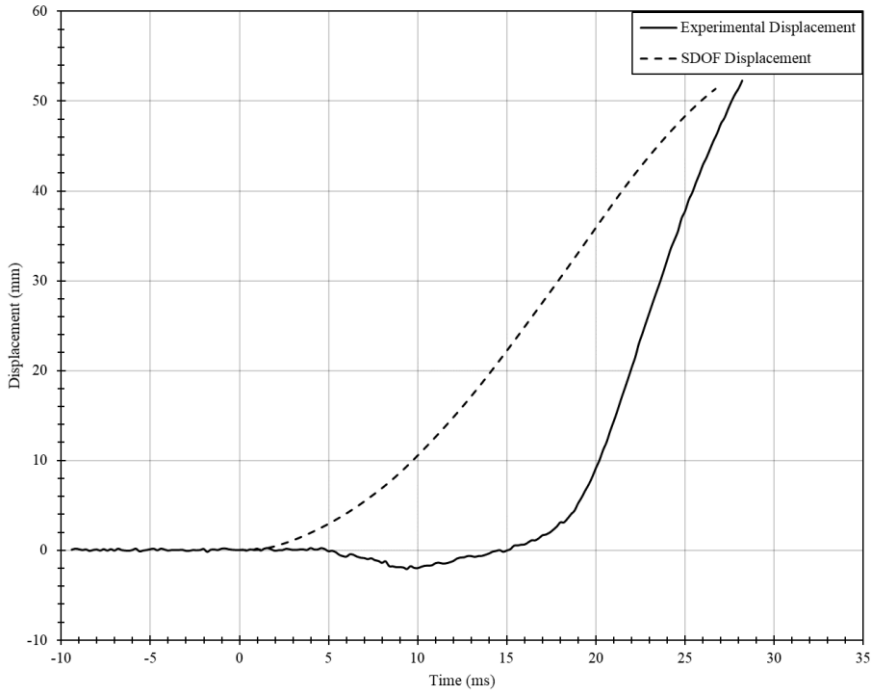

Energy absorption efficiency, and experimental and idealized load-displacement relationships

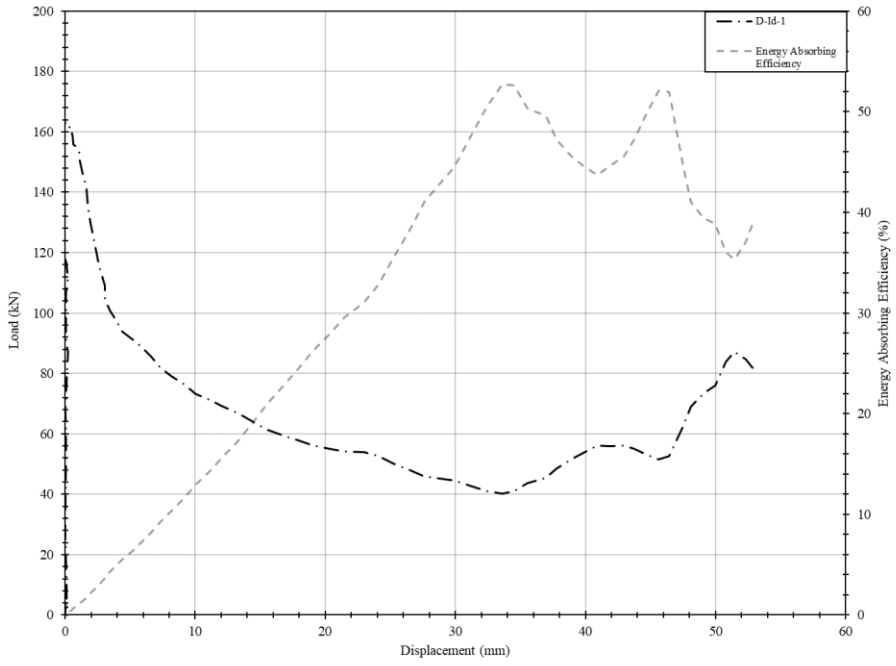

Specimen	D-Id-2	Description	Angles with leg lengths of 76.2 mm and thickness of 6.35 mm. Additional centre weld.

SDOF and experimental displacement time-histories

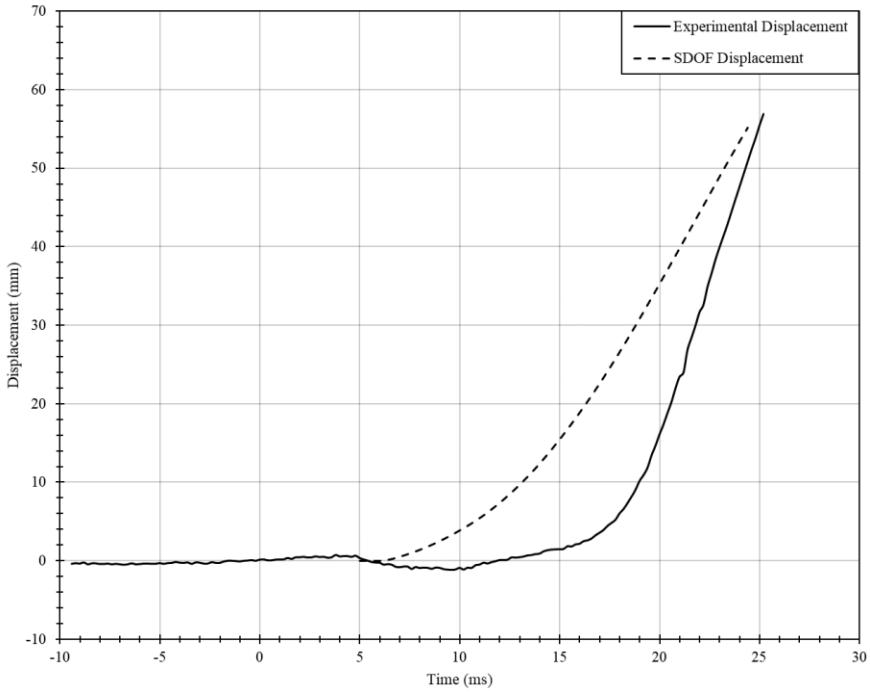

Energy absorption efficiency, and experimental and idealized load-displacement relationships

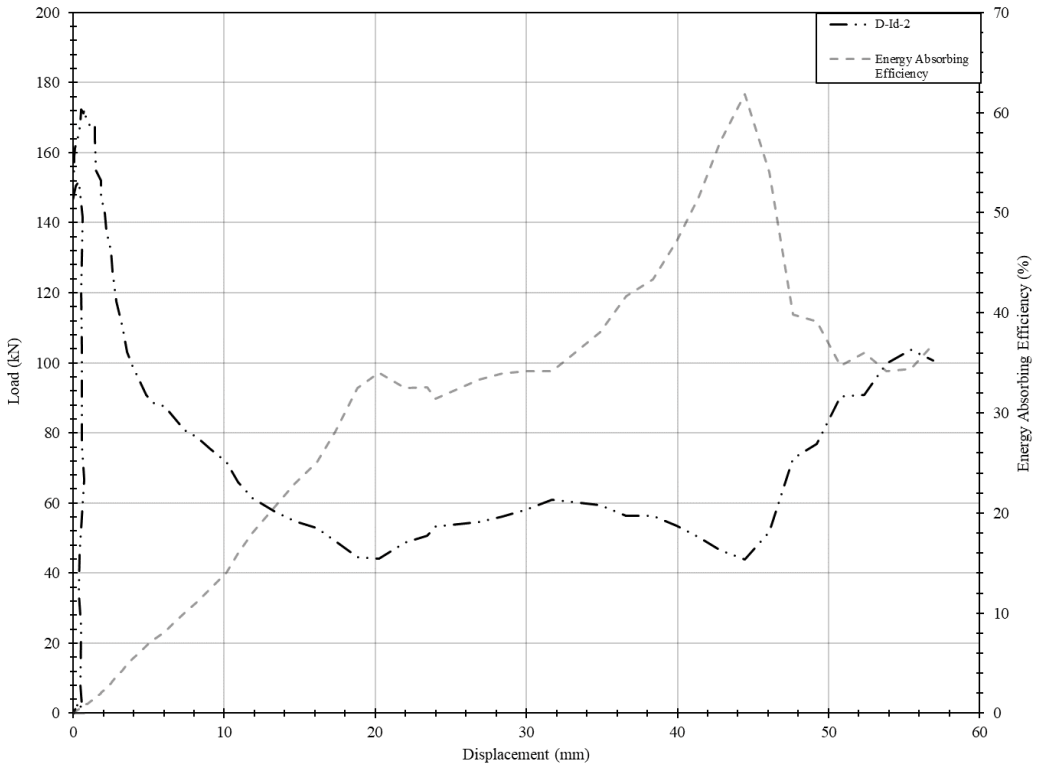

Specimen	D-IIa-1	Description	Circular HSS with outer diameter of 88.9 mm and thickness of 6.35 mm

SDOF and experimental displacement time-histories

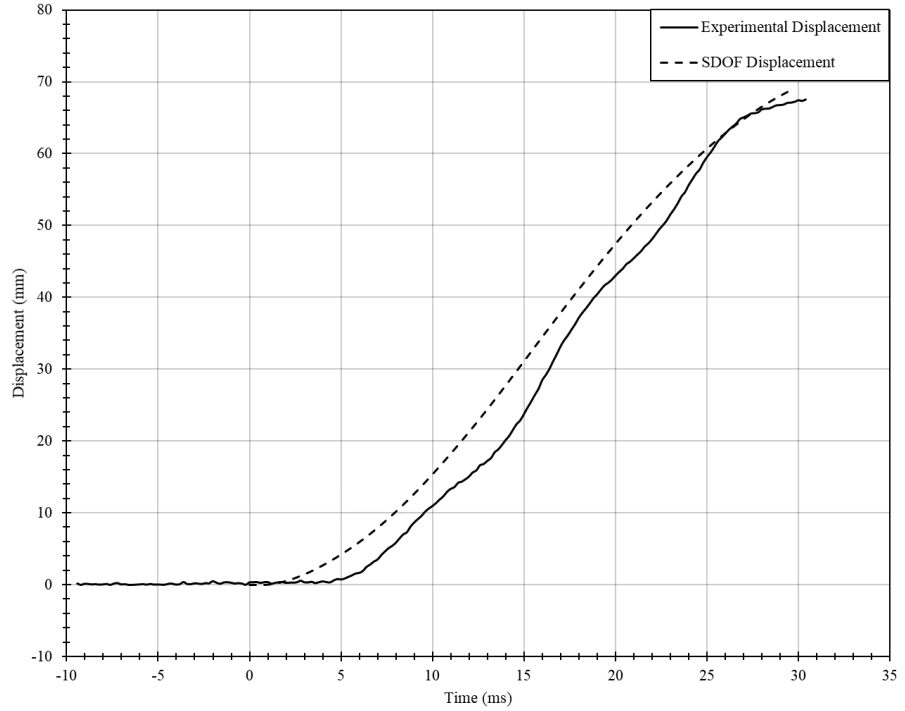

Energy absorption efficiency, and experimental and idealized load-displacement relationships

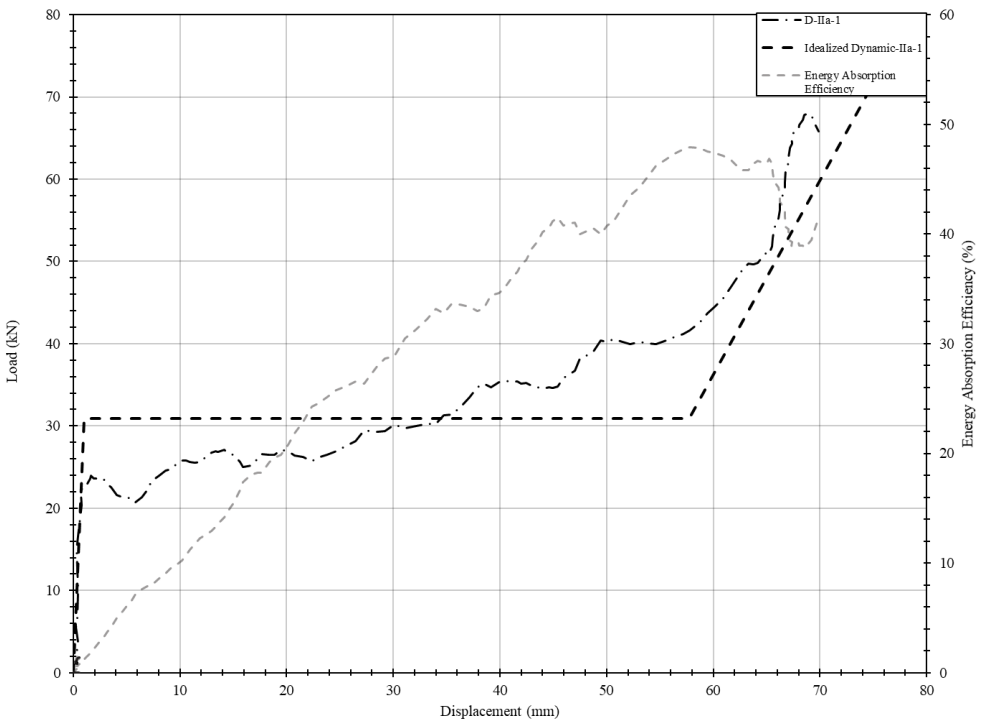

Specimen	D-IIa-2	Description	Circular HSS with outer diameter of 88.9 mm and thickness of 6.35 mm

SDOF and experimental displacement time-histories

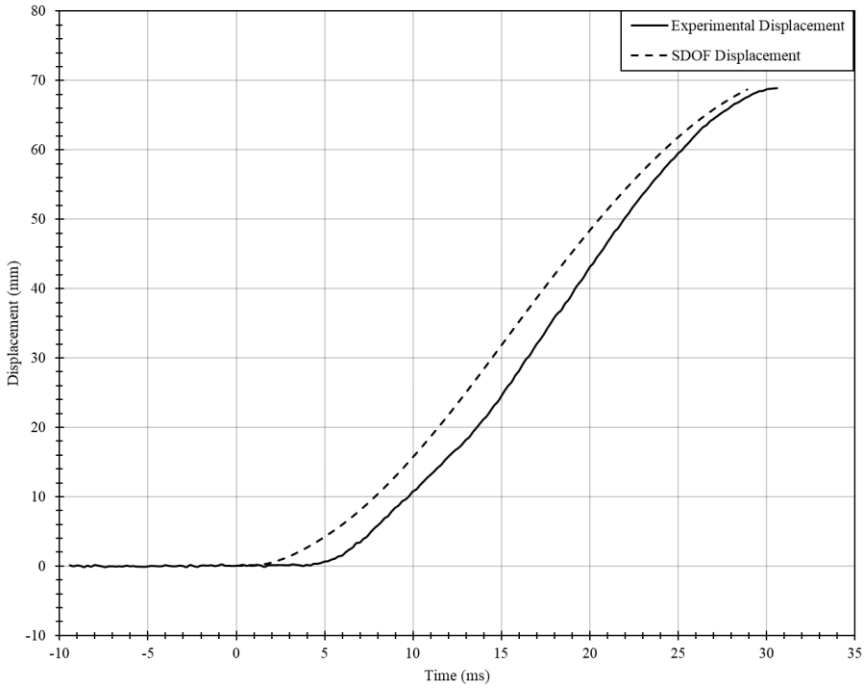

Energy absorption efficiency, and experimental and idealized load-displacement relationships

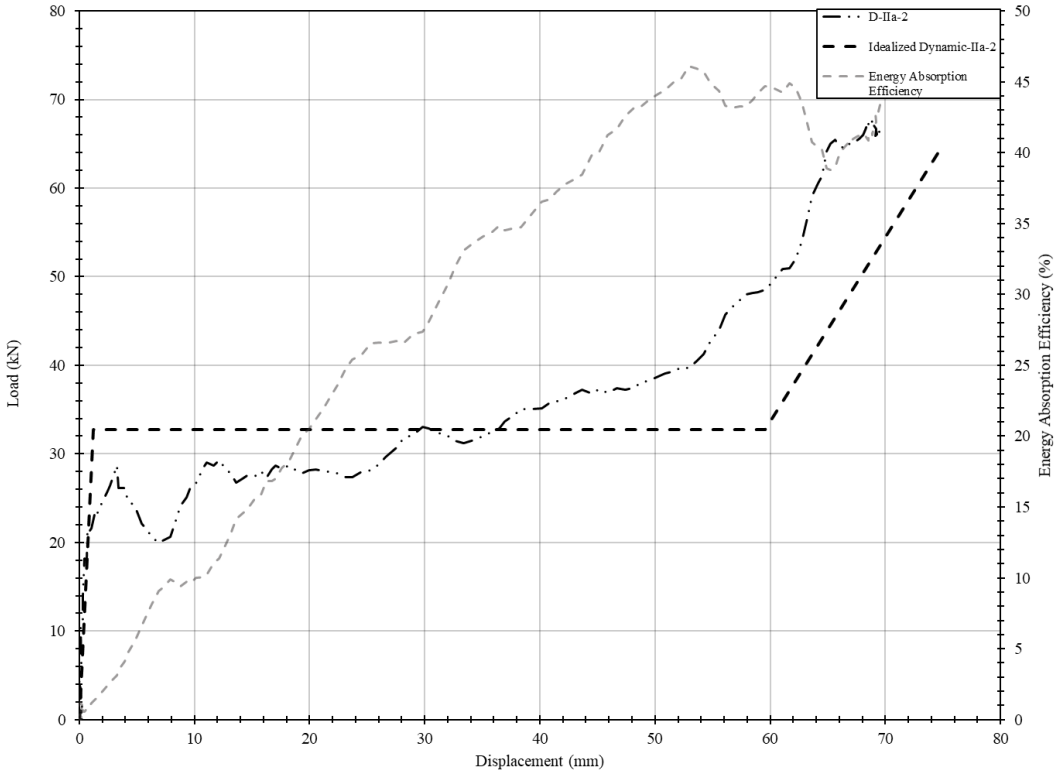

Specimen	D-IIb-1	**Description**	Circular HSS with outer diameter of 88.9 mm and thickness of 6.35 mm Depth of 101.6 mm

SDOF and experimental displacement time-histories

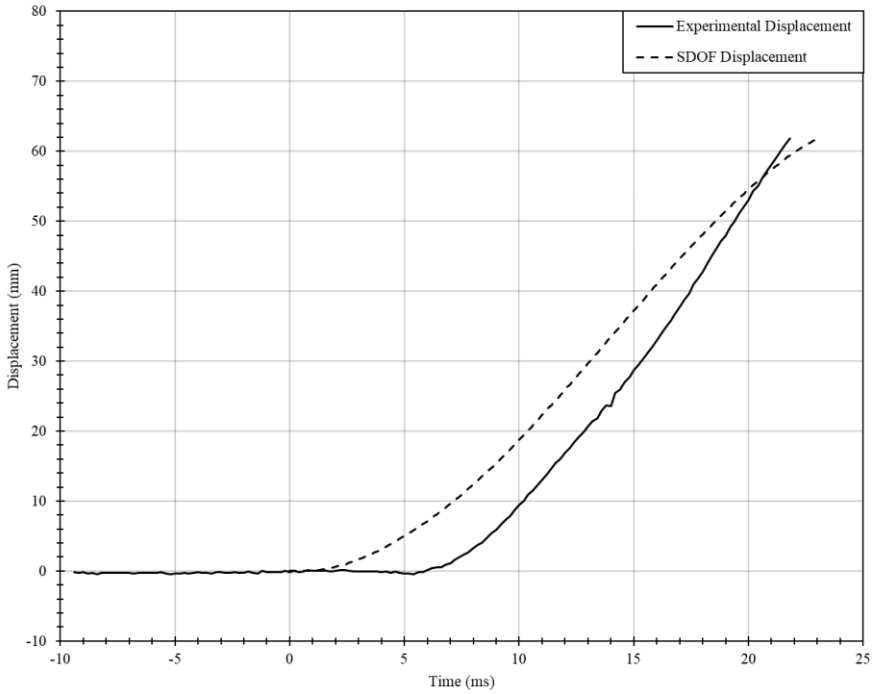

Energy absorption efficiency, and experimental and idealized load-displacement relationships

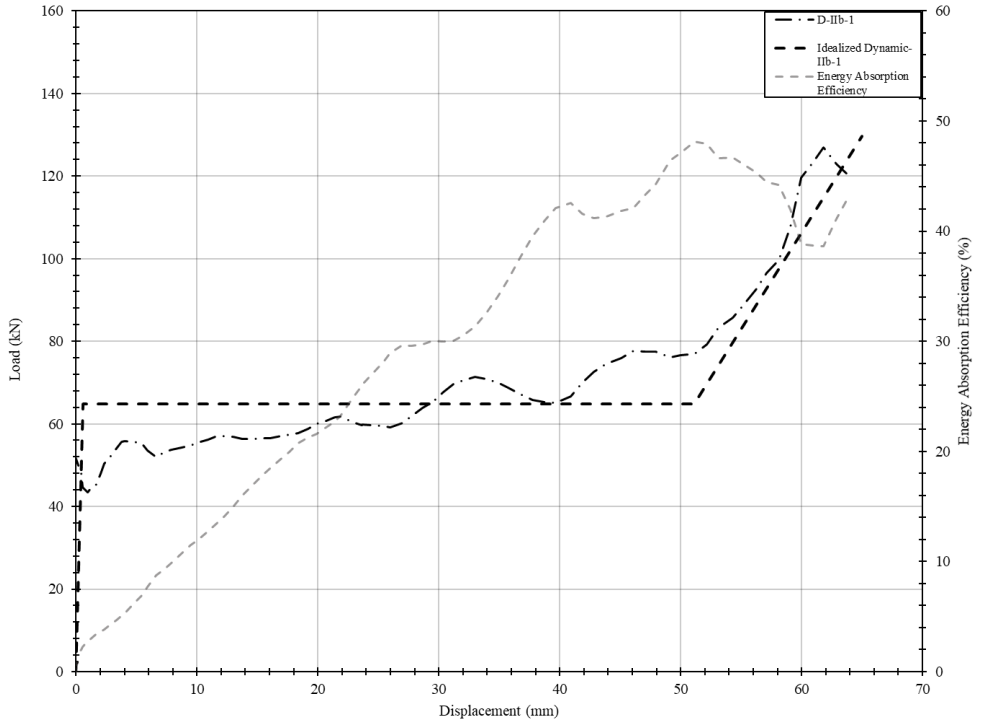

Specimen	D-IIb-2	**Description**	Circular HSS with outer diameter of 88.9 mm and thickness of 6.35 mm Depth of 101.6 mm

SDOF and experimental displacement time-histories

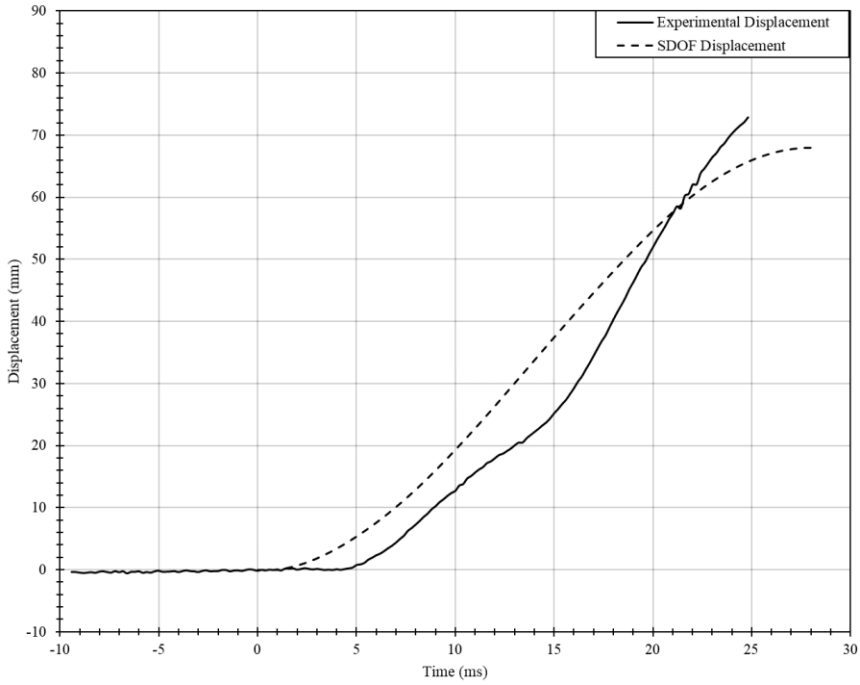

Energy absorption efficiency, and experimental and idealized load-displacement relationships

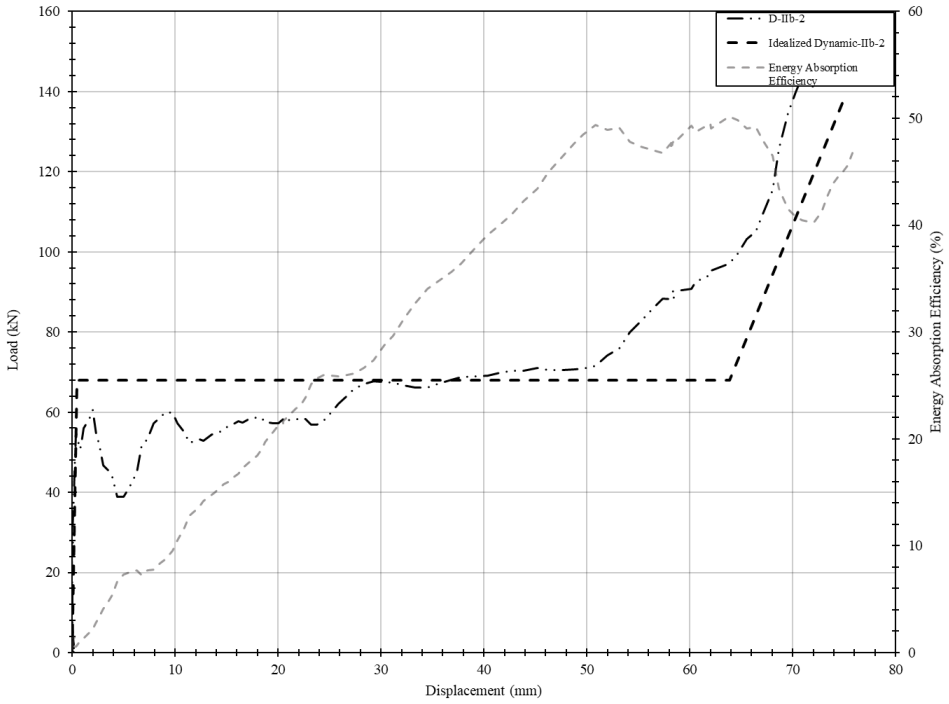

Specimen	D-IIc-1	Description	Circular HSS with outer diameter of 127 mm and thickness of 6.35 mm

SDOF and experimental displacement time-histories

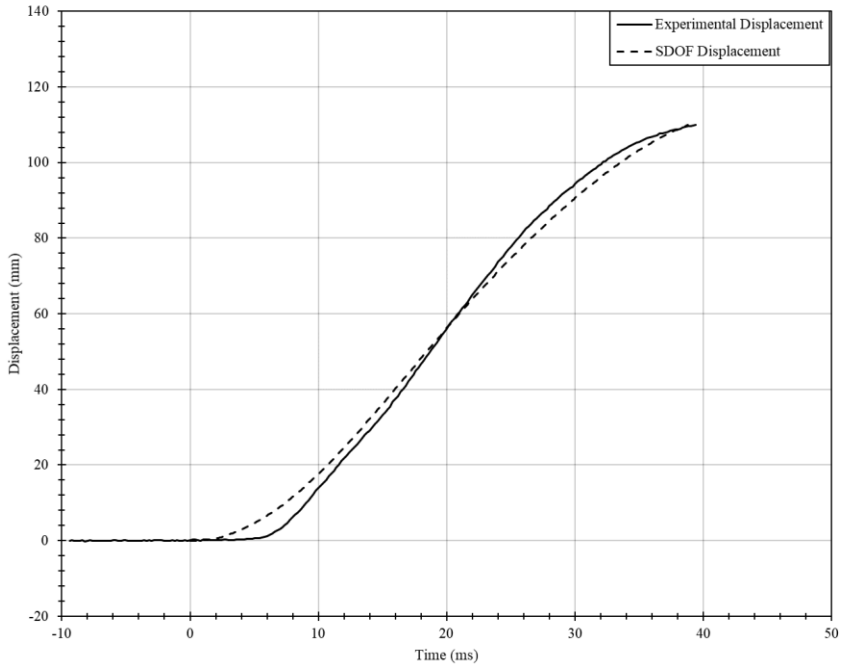

Energy absorption efficiency, and experimental and idealized load-displacement relationships

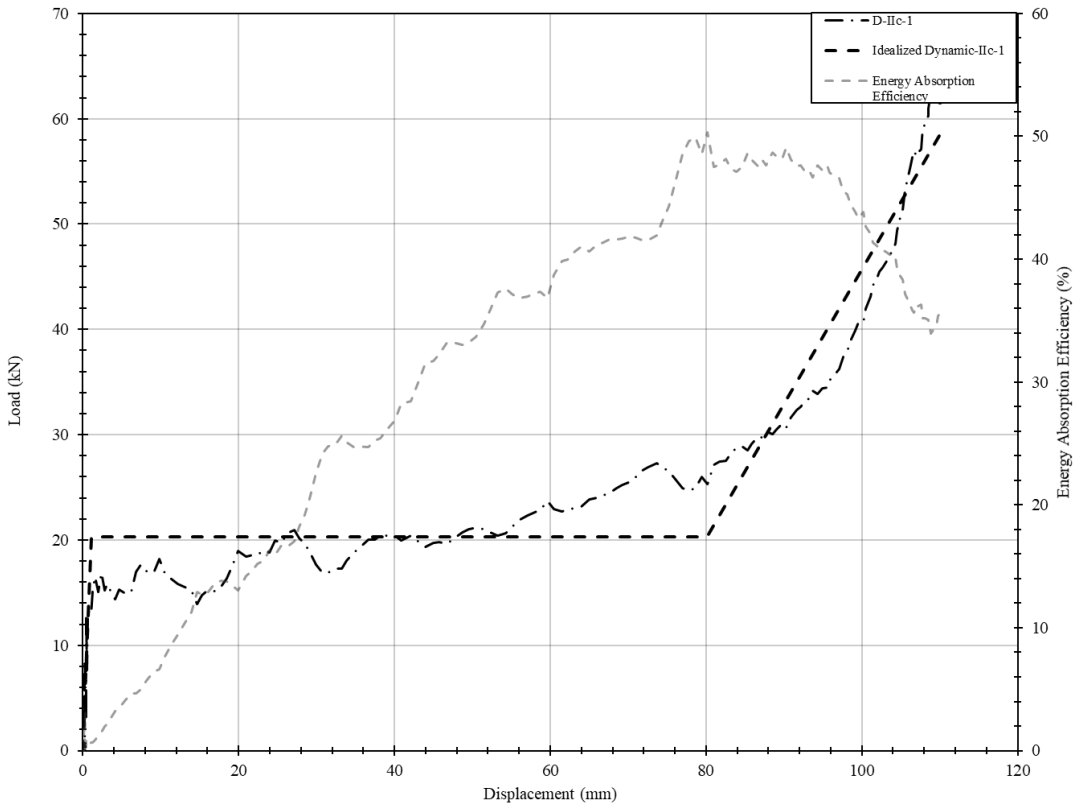

Specimen	D-IIc-2	Description	Circular HSS with outer diameter of 127 mm and thickness of 6.35 mm

SDOF and experimental displacement time-histories

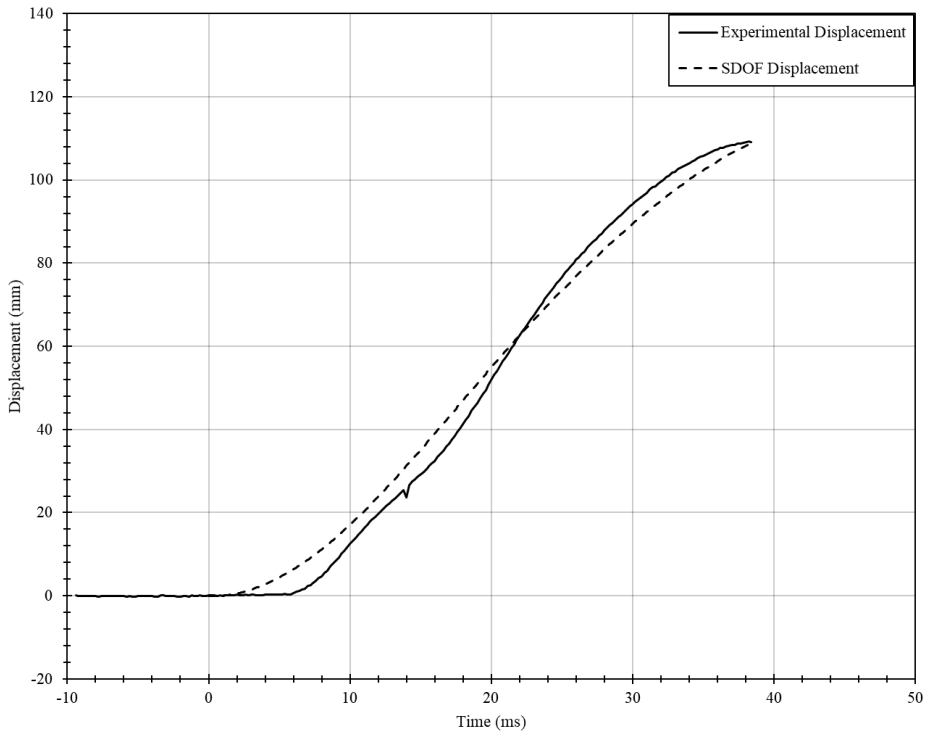

Energy absorption efficiency, and experimental and idealized load-displacement relationships

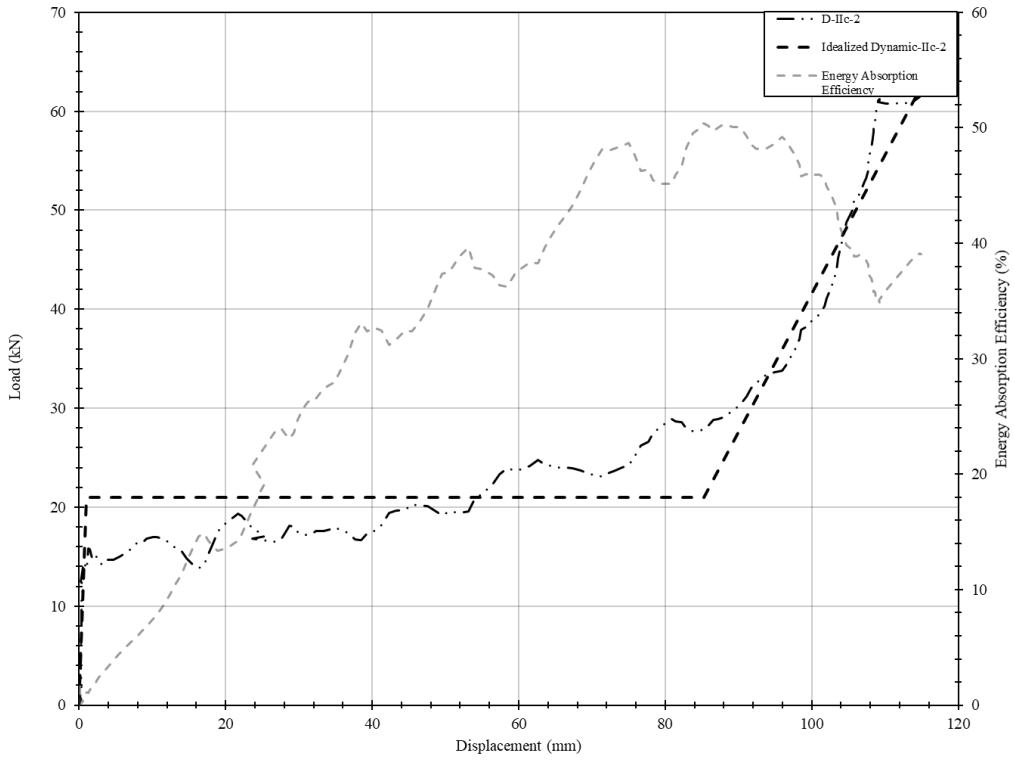

Specimen	D-IId-1	Description	Arcs from circular HSS of outer diameter of 127 mm and thickness of 6.35 mm.

SDOF and experimental displacement time-histories

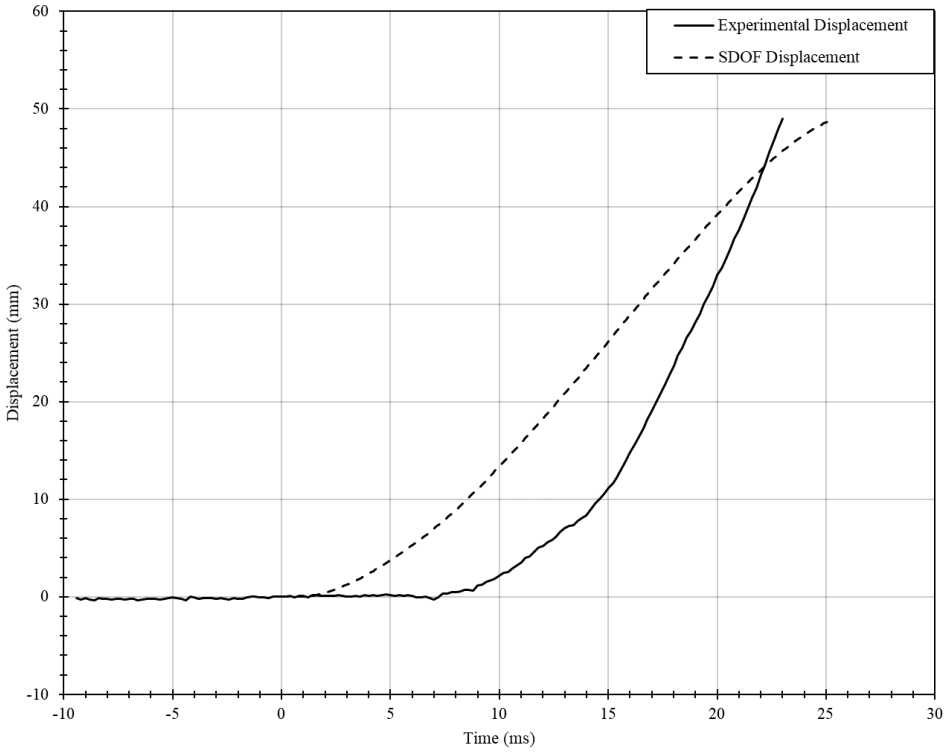

Energy absorption efficiency, and experimental and idealized load-displacement relationships

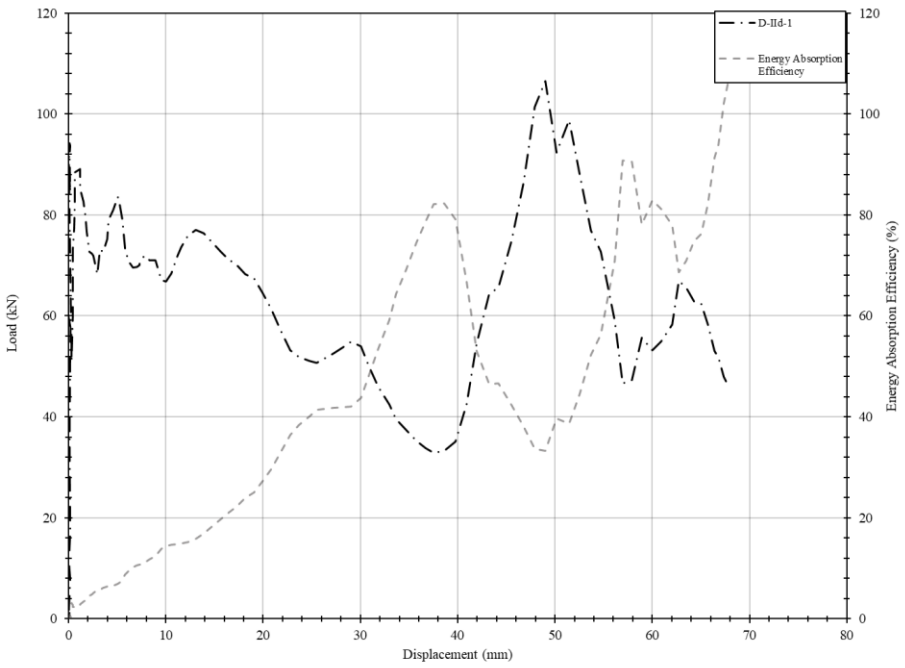

Specimen	D-IId-2	Description	Arcs from circular HSS of outer diameter of 127 mm and thickness of 6.35 mm.

SDOF and experimental displacement time-histories

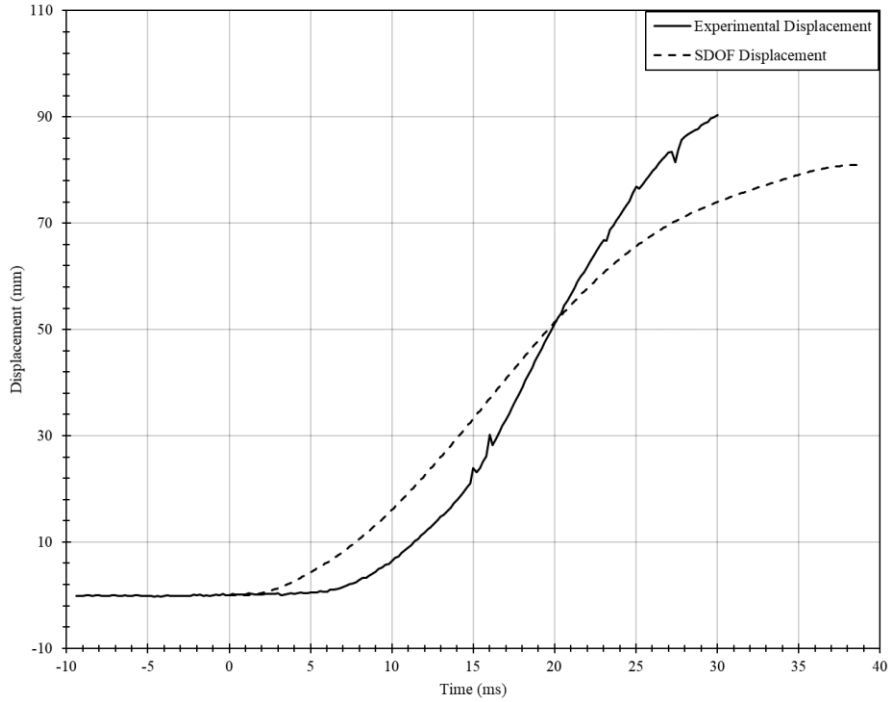

Energy absorption efficiency, and experimental and idealized load-displacement relationships

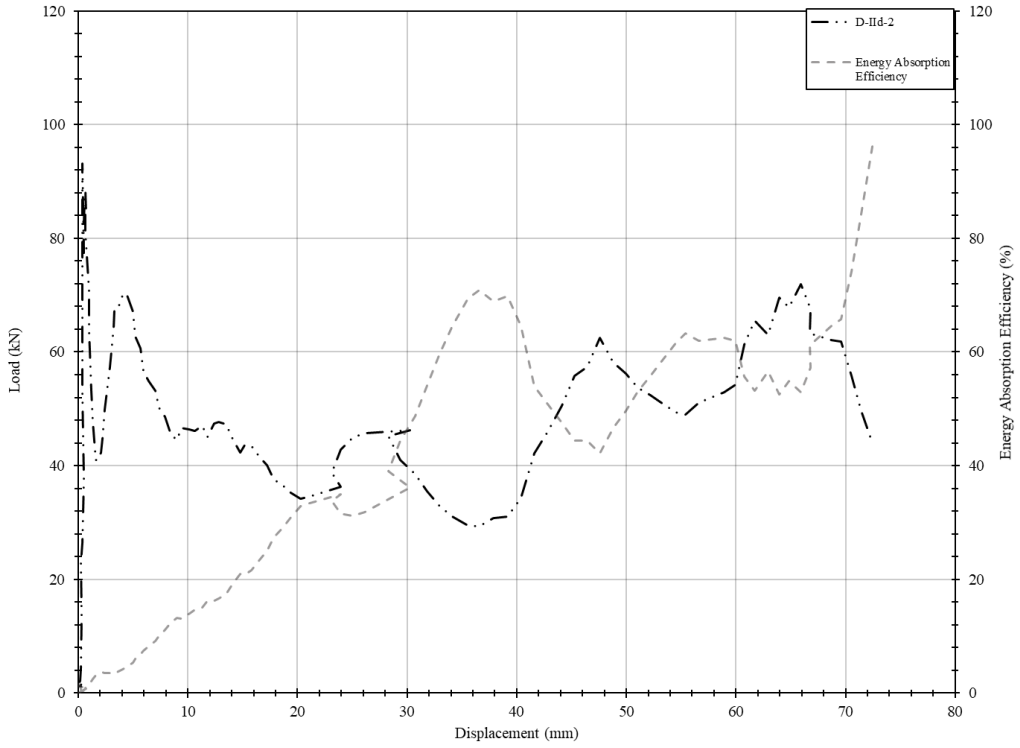

Specimen	D-IIe-1	**Description**	Circular HSS with outer diameter of 88.9 mm and thickness of 6.35 mm Circular HSS with outer diameter of 60.325 mm and thickness of 3.175 mm

SDOF and experimental displacement time-histories

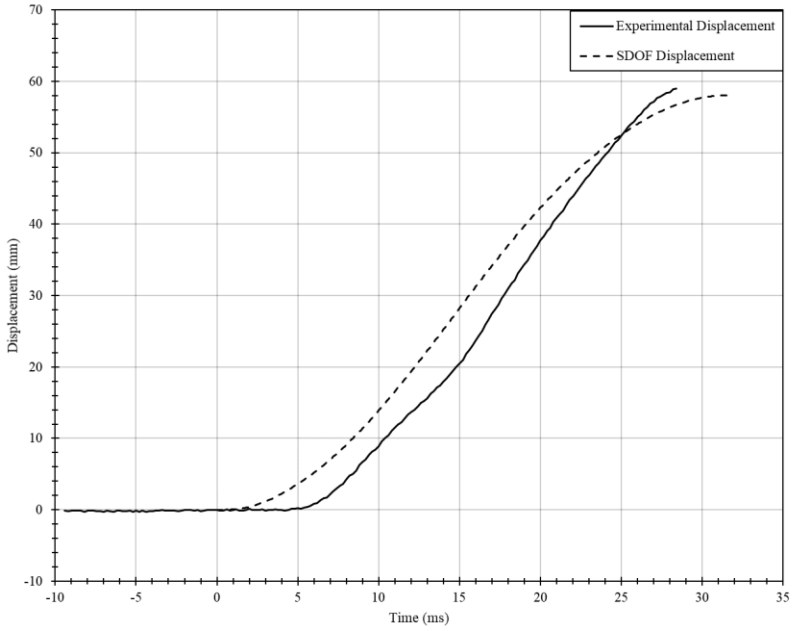

Energy absorption efficiency, and experimental and idealized load-displacement relationships

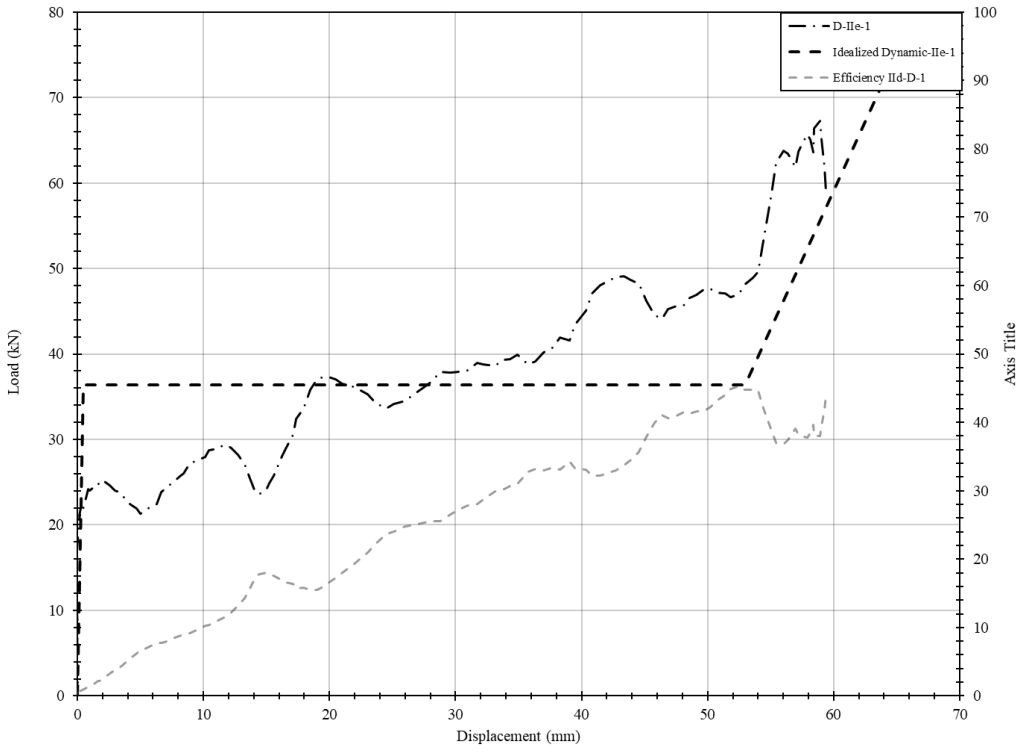

Specimen	D-IIe-2	**Description**	Circular HSS with outer diameter of 88.9 mm and thickness of 6.35 mm Circular HSS with outer diameter of 60.325 mm and thickness of 3.175 mm

SDOF and experimental displacement time-histories

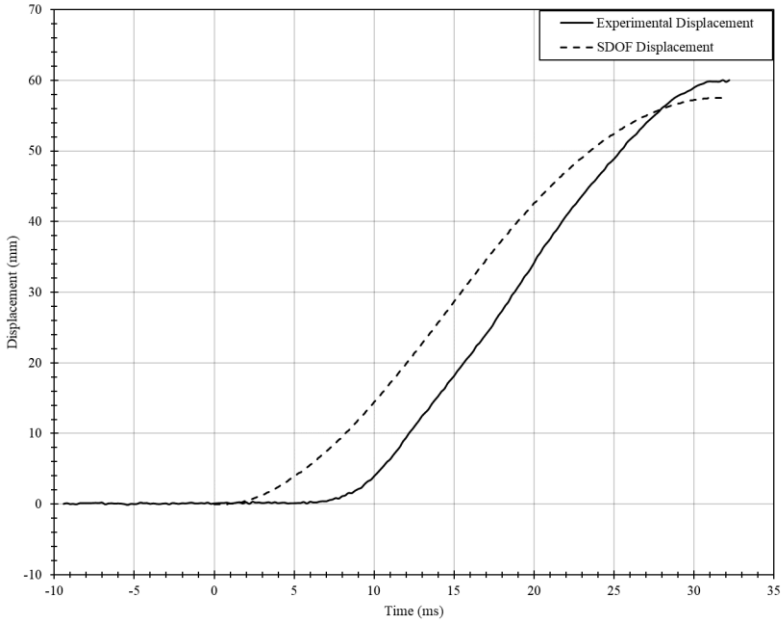

Energy absorption efficiency, and experimental and idealized load-displacement relationships